NASA
Reference
Publication
1170

October 1986

Preliminary Design of Turbopumps and Related Machinery

George F. Wislicenus

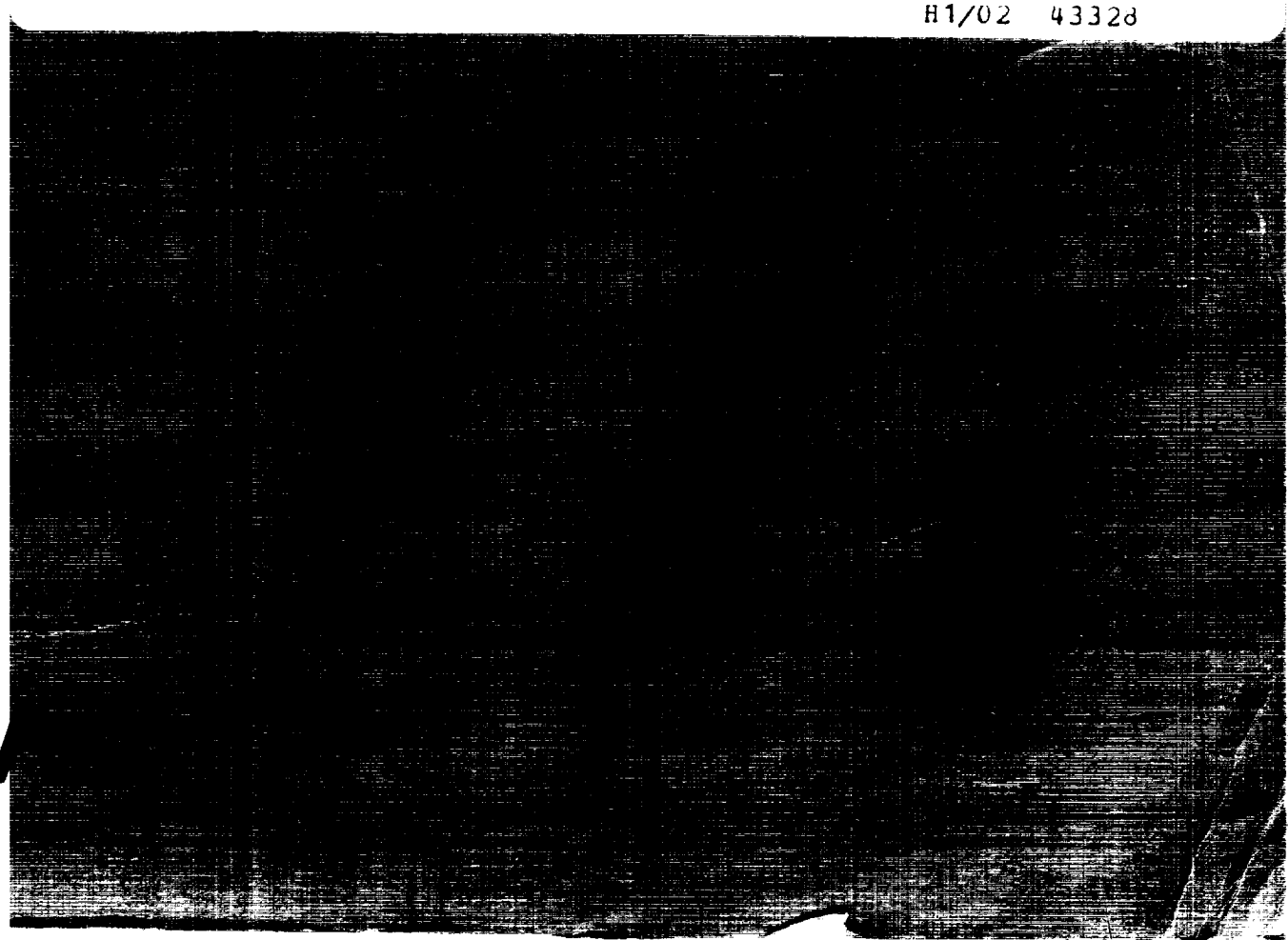

NA

NASA Reference Publication 1170

1986

Preliminary Design of Turbopumps and Related Machinery

George F. Wislicenus

Santa Rosa, California

NASA

National Aeronautics and Space Administration

Scientific and Technical Information Branch

Preface

This compendium on preliminary design of turbopumps and related machinery pertains primarily to the pumps used in connection with large liquid-fuel rocket engines. As a design study, its general purpose is similar to that of the NASA monographs on space vehicle design criteria. However, while these monographs are primarily intended to record established design practices in their respective fields, this compendium is intended to contribute also to future developments and improvements in this and related fields of turbomachinery.

In the title of this compendium, the word "preliminary" denotes the initial phases of design, where the general shape and characteristics of the machine are to be determined. Therefore this compendium does not apply primarily to machines for which the general form and method of design are well established, for example, axial-flow turbojet engines. It also does not apply to the final analysis of an approximately established design, usually carried out by specialists in such fields as fluid mechanics, stress analysis, rotor dynamics, and the like, where one must employ much more accurate methods than presented in this compendium.

Thus the word "design" in the title denotes primarily the initial, creative or form-finding phases of the design process. The design engineer responsible for these early phases cannot be expected to be an expert in all the special fields of knowledge involved in the design process, but should have a dependable, although simplified, knowledge of these fields to the extent to which they determine the general form and characteristics of the machine to be designed and developed. While the subsequent detailed analysis by specialists may call for improvements in the initial design, this analysis can rarely be allowed to change the fundamental design characteristics, since that would probably lead to major delays or compromises. Therefore the initial design must be dependable in its broad, overall characteristics, and accuracy in detail cannot be its primary objective. It is to this initial design phase that this compendium is intended to make a modest contribution.

The first requirements for achieving dependability in the initial design process are physical simplicity and transparency of reasoning. Furthermore it is desirable to converge as early as possible to a fairly definite geometric form of the machine to be developed, because major errors are often visible by geometric inconsistencies or abnormalities. Obviously the experience of the engineer in designing forms that are desirable with respect to hydrodynamic or mechanical considerations is of major importance and is, therefore, cultivated in this compendium as much as possible.

The relation between the prescribed operating conditions (rate of flow, pump head, speed of rotation, etc.) and the geometric form characteristics of the machine, such as its flow cross sections, is particularly simple and dependably determined for incompressible fluids. Therefore it should be understandable that the pumping part of the turbopump has received primary attention, since it is concerned essentially with incompressible fluids. However, the importance of the driver, usually a gas turbine, makes it necessary during the preliminary design phase to consider also the flow principles of compressible fluids. These compressible flow principles must also be considered in cases where the pumped fluid changes its volume significantly.

As much as possible, the simplicity and reliability of incompressible flow considerations are retained by treating the mechanics of compressible fluids as a departure from the theory of incompressible fluids. This is accomplished by changing the fluid volume per unit of mass as a function of a dimensionless velocity of the compressible fluid flow (suggested by Prandtl and Busemann). Although one must expect objections to this treatment from a broader, scientific point of view, its simplicity justifies its use to meet the limited objectives of this compendium, not to mention the authority of the authors just cited.

Because of the inherent theoretical simplicity of axial-flow machines compared with radial-flow machines, axial-flow machines are treated in the theoretical background (ch. 2) as well as in the description of the design methods (ch.3) before the older radial-flow machines. The treatment of axial-flow machines departs markedly from the classical approach, which describes primarily the fluid mechanical action of various standard vane sections when arranged as a straight system of parallel vanes. This approach is inadequate for the design of vane systems exposed to the danger of cavitation. This occurs because the classical vane shapes in pumping (i.e., retarding) vane systems usually have the greatest vane pressure differences near the low-pressure inlet side of the system and lead to unacceptable pressure reductions below the inlet pressure of the (rotor) vane system. The so-called mean streamline method for the analysis of experimental cascade data (ch. 2) as well as for the design of axial-flow cascades with prescribed vane pressure distributions (ch. 3) has overcome this cavitation problem in axial-flow vane systems. The axial-flow-compressor designer will find it interesting to observe that the vane shapes developed in this manner, in order to minimize cavitation, have a striking resemblance to those used in axial-flow compressor or fan stages for high, often supersonic, inlet Mach numbers of the relative flow. There compressibility effects subject the vane surface pressures and velocities to the same restrictions as the danger of cavitation in axial-flow pumps.

The design limitations to prevent separation or stall, first recognized and described with respect to radial- and axial-flow machines in 1928 and 1934, were most clearly established in the late forties on the basis of axial-flow cascade test data. Therefore this subject occupies an important place in this compendium in the treatment of axial-flow machines and has led to a uniform presentation of the various separation criteria or diffusion factors suggested since 1928.

The fundamental difference between radial- and axial-flow turbomachinery rotors emphasized in this compendium is the inherent vorticity of the relative flow in radial-flow rotors. Equally inherent and important is the fundamentally three-dimensional form of the flow and vane shape between the axial inlet and the radial discharge of the rotor of large radial-flow pumps. It is interesting that already in the thirties (and before) overall pump efficiencies of about 90 percent were reliably and repeatedly achieved with pumps having the previously mentioned complications, almost as consistently as with hydraulic turbines of essentially the same type. In spite of the fact that these favorable results were obtained mainly on empirical and geometric bases, it seems necessary that these pumps and their design principles receive careful attention in this compendium (ch. 4).

Scientific curiosity as well as occasional disappointment in the performance of pumps designed by means of the aforementioned principles have led to investigations in search of some simple rationale for the empirical design methods developed during or before the thirties. These efforts were carried out first with respect to separation or stall limits of rotor vane systems and later with regard to design for a prescribed pressure distribution along the rotor vanes. While these attempts are as yet not supported by test results, they are outlined in chapter 4 in the hope that this presentation will stimulate further work toward a firmer basis for the design of radial-flow turbomachinery rotors.

Knowledgeable readers may be disappointed in the mathematically rather elementary treatment of theoretical considerations presented in this compendium. This type of treatment may be regrettable, but is unavoidable because of the primarily physical and geometric orientation of this writer, whose experience in the field of turbomachinery design was obtained chiefly at the drawing board and in the shop serving the development of turbomachines. As a consequence, this compendium is intended primarily to meet the needs of the design engineer who is concerned with the practical development problems of turbomachinery and to encourage him in this undertaking. The reader is not required to have advanced mathematical methods at his command.

It may be of interest that in recent years some of the design operations described in this compendium have, on the basis of these elementary descriptions, been translated into computer language. This important step has been fairly well completed for the design of axial-flow vane systems for pumps by the mean streamline method. It has also been extended to the design of pump rotors with an axial inlet and a more or less radial discharge. The Applied Research Laboratory of the

Pennsylvania State University can give information on these developments. However, these computer-aided design methods have not been included in this compendium. The design methods described here can be, and have been, carried out with fair success by means of the drawing board and small hand calculator alone.

This writer is greatly indebted to NASA for sponsoring this work and for providing the needed critical reviews. In particular, the writer would like to thank Mr. Melvin J. Hartmann, Director of Aeronautics at the Lewis Research Center, for encouraging the writing of this compendium and, together with Mr. Calvin L. Ball, for supporting its completion. In the beginning the technical review was directed effectively by Mr. Cavour H. Hauser and carried out by Mr. Werner R. Britsch. Later the technical review was continued by Mr. Mark R. Laessig, Mr. Michael J. Pierzga, and Mr. Donald M. Sandercock. These reviewers made constructive suggestions and improved many of the technical descriptions. The general editorial work was done by Ms. Margaret J. Mallette, whose careful review resulted in numerous improvements in the form of presentation. This compendium could not have been completed without the constructive collaboration of the NASA staff members just mentioned and probably of others whose contributions did not come to the direct attention of this writer. To aid in future developments of the work reported here, constructive suggestions and corrections by readers and users of this compendium will be very much appreciated.

George F. Wislicenus

Contents

Page

Units of Measurement

The design and operating characteristics of turbomachines developed throughout this compendium are generally expressed in dimensionless form. To these one may, of course, apply any consistent system of units. For those cases where a dimensional form is used for specific reasons, both International System (SI) units and U.S. customary units may be observed. The author endorses the primary use of SI units. Infrequently, however, U.S. customary units appear in illustrative examples, on figures of general characteristic curves, and as alternative units. The U.S. customary units are retained in order to ease the understanding for those accustomed to this system of units and to relate certain figures to the original work which supports them. The following discussion makes some comparisons of the two unit systems.

The units used in the International System are

length (L)	measured in meters (m)
time (T)	measured in seconds (sec)
force (F)	measured in newtons (N)
mass (M)	measured in kilograms (kg)

In contrast, the traditional units of measurement customarily used in the United States of America are

length (L)	measured in feet (ft)
time (T)	measured in seconds (sec)
force (F)	measured in pounds (lb)
mass (M)	also measured in pounds (lb)

It is immediately evident that the U.S. customary system has a serious weakness in that it uses the same unit (pound) for force as well as for mass. The original metric system had the same weakness, because it used kilogram for mass as well as for force. (This weakness was eliminated in the International System by introducing a new unit (newton) for force.)

The common weakness of the U.S. customary system and the original metric system permitted, for over a hundred years, the use of the concept of head (in German Fallhoehe or Foerderhoehe) with the dimension of a length for the ability to do or to absorb hydrodynamic work, measured in force times length. The concept of head was obviously suggested in the field of hydraulic engineering to describe a difference in elevation of the free water levels on the two sides of a hydraulic installation such as a powerplant with its penstocks. This physical justification of length as the dimension of head can be supported algebraically by writing this dimension in the form (ft)(lb)/lb or (m)(kg)/kg and cancelling lb against lb or kg against kg, ignoring the fact that in both cases one cancels the dimension of a force against the dimension of a mass. This traditional mistake means that mass is measured by a force, specifically its weight, which is still usually the simplest way to measure mass rather than by comparison with a standard mass.

In the International System, the equivalent of head has the dimensions of force times length (work) per unit of mass, which is (N)(m)/kg. Since force equals mass times acceleration, one can write the equivalent of head in the International System in the form

$$\text{(mass)(acceleration)(length)/mass}$$

or, expressed in unit abbreviations,

$$\text{(kg)(m/sec}^2\text{)(m)/kg} = \text{m}^2/\text{sec}^2$$

This means the equivalent of head in the International System has the dimension of a velocity squared.

In order to avoid a conflict between the International System and the traditional systems mentioned previously, this compendium retains the term and concept of head (denoted by the symbol H or h) with the dimension of a length. However, this concept is always used in combination with the standard gravitational acceleration, $g_o = 9.81$ m/sec^2 in the original metric system or $g_o = 32.2$ ft/sec^2 in the U.S. customary system. It is immediately clear that the product Hg_o has the dimension of a velocity squared, that is, the

same dimension as the equivalent of head in the International System (provided H has the dimension of a length). The product Hg_o (or hg_o) has also the same physical meaning as required in the International System, insofar as the standard gravitational acceleration g_o is obviously the ratio of a unit of weight to a unit of mass. Therefore multiplication by g_o changes mechanical work per unit of weight to mechanical work per unit of mass. The use of the product Hg_o (or hg_o) for work per unit of mass, in place of a single, new symbol, is justified mainly to retain the relation to the traditional concept of head (H or h) and to avoid confusion with other symbols already in use. (One may expect that any future edition of this compendium will depart from this practice of its first edition.)

It may be well to mention here that capital H for head is used in this compendium for total or stagnation head as measured by an upstream-pointing pitot tube, whereas lower case h is used for the so-called static head as measured by a piezometer hole in a surface parallel to the flow (approximately). In connection with compressible fluids, the same symbols are used in the same manner for stagnation and static enthalpy.

In closing this discussion on units of measurement, it is desirable to illustrate what are described previously as consistent and inconsistent applications of units of measurement. The most common case of inconsistent use of such units is the use of revolutions per minute (rpm) with cubic feet per second (ft^3/sec) or (worse) gallons per minute (gal/min) or the use of head (in ft) without multiplication by g_o. These inconsistencies are so common when using the U.S. customary system (particularly in the field of pump cavitation) that this compendium uses the inconsistent value of suction specific speed in parentheses behind the consistent (dimensionless) value in order to assist older engineers. The conversion of specific speeds from the consistent (dimensionless) to traditional inconsistent values is given in sections 1.2.1 and 1.2.2 of chapter 1.

In this compendium, the speed of rotation of a machine is expressed in revolutions per second, which is consistent with cubic feet per second, and head is expressed in feet times g_o. Equally consistent with these additional units would be radians per second as a measure of the rotation of a machine or shaft and the conversion factor 2π, which must be considered properly when dealing with the peripheral velocity.

Symbols

Designations of units of measurement: length, L; mass, M; time, T; force, $F = MLT^{-2}$; temperature, t

A	area	L^2
A,B,C,D	stations across or along streamlines; stations along contour or any line	
A_{th}	throat area of volute or diffuser (fig. 1-11)	L^2
a	axial width of rotating element (fig. 1-30)	L
a	acoustic velocity; velocity of sound	LT^{-1}
b	width of passage or impeller; width (or depth) of flow normal to plane of flow considered; blade span normal to meridional flow	L
b	length of section line normal to meridional streamlines, and coordinate along such a line (fig. 2-1)	L
b_o	width of impeller at outer periphery	L
C	Coriolis force	$F = MLT^{-2}$
C_L	lift coefficient	
$C_{L,1}$	lift coefficient referred to inlet velocity of vane system or cascade considered	
$C_{L,\infty}$	lift coefficient referred to vectorial mean w_∞ or V_∞ of relative inlet and discharge velocities of vane system	
C_p	local vane surface pressure coefficient, usually $(p_{ref} - p)/(V_{ref}^2/2g_o)$	
C_p	specific heat at constant pressure in mechanical units	Lt^{-1}
C_v	specific heat at constant volume in mechanical units	Lt^{-1}
C_1	coefficient in eq. (1-42)	
D	diameter or any representative linear dimension of machine or characteristic linear dimension of system	L
D	diffusion factor (see eq. (2-70))	
D_h	hub diameter	L
$D_{h,1}, D_{h,2}$	hub diameters at inlet and discharge, respectively, of axial-flow rotor (fig. 1-20)	L
D_i	inlet diameter of pump or compressor rotor; inside diameter of any turbomachinery rotor or vane system (figs. 1-7, 1-20, and 1-25)	L
D_{loc}	local diffusion factor (see eq. (2-63))	
D_o	outside discharge diameter (figs. 1-7 and 1-25)	L
D_s	specific diameter, $D(g_oH)^{1/4}/Q^{1/2}$	
D_{th}	twice distance of center of throat area from axis of rotation (fig. 1-11)	L
d	vane distance normal to flow relative to given vane system; generally, distance	L
d	distance between streamlines and distance from vane edges to contour (see fig. 2-11)	L
d_o	normal vane distance near outside diameter of system	L

d_y	normal vane distance at place other than measurement location of d_o	L
E	modulus of elasticity	$FL^{-2} = ML^{-1}T^{-2}$
F	Froude number, U^2/gD or V^2/gD	
F	force	$F = MLT^{-2}$
F_a	axial force per unit span, i.e., force per unit span normal to vane-to-vane extent of straight, two-dimensional cascade (fig. 2-9)	$FL^{-1} = MT^{-2}$
F_U	circumferential force per unit span, i.e., force per unit span in vane-to-vane direction of straight, two-dimensional cascade (fig. 2-9)	$FL^{-1} = MT^{-2}$
F_1	force per unit span or unit distance normal to plane of flow	$FL^{-1} = MT^{-2}$
f	frequency; frequency of vibration	T^{-1}
g	acceleration of system as a whole	LT^{-2}
g_o	standard gravitational acceleration (of system as a whole)	LT^{-2}
H	total (static plus velocity) head; net pump work per unit of weight of fluid	$FLF^{-1} = L$
H_r	rotor head; total work per unit of weight of fluid, exchanged between rotor and fluid	L
H_{sv}	total (static plus velocity) head above vapor pressure at low-pressure side of hydrodynamic rotor	L
h	static head; static pressure divided by weight per unit volume of fluid	L
h	thickness of vane normal to the general direction of vane	L
h	enthalpy per unit weight in mechanical units; $h = C_pT$ in thermal units	L
h_a	atmospheric or ambient pressure divided by weight per unit volume of liquid	L
h_o	Busemann head correction factor (fig. 2-47)	
h_{SA}	Stodola head correction	
h_{sv}	static head above vapor pressure of liquid at low-pressure side of turbomachinery rotor	L
h_v	vapor pressure of liquid divided by weight per unit volume of liquid	L
I	moment of inertia of cross-sectional area	L^4
K	cascade-effect coefficient, defined by eq. (2-56)	
K	heat-transfer coefficient	tM^{-1}
K_A	Ackeret separation or diffusion factor (eq. (2-62))	
K_∞	Wislicenus separation or diffusion factor (eq. (2-68))	
L	lift (force)	$F = MLT^{-2}$
L	characteristic linear dimension of system	L
l	length; chord length of vane	L
l	linear spacing between cavitation nuclei	L
M	moment, torque; bending moment	$FL = ML^2T^{-2}$

m	coefficient in eq. (2-93) determining direction of straight line	
m_s	section modulus, section moment of inertia I divided by maximum distance from neutral axis	L^3
N	number of vanes; number of stages	
N	number of cavitation nuclei per unit volume	L^{-3}
Nn	exciting frequency of rotating system	T^{-1}
$N_{s,P}$	dimensional specific speed referred to power (eq. (1-20))	consistent units
n	number of revolutions per unit of time (sec)	T^{-1}
n	linear coordinate normal to meridional streamlines	L
n	term in eq. (2-93) determining location of straight line	
n	exponent between 0 and 1	
Δn	distance between mean camber line and mean streamline	L
n_a	compressibility specific speed (table 1-I)	
n_g	gravity specific speed (table 1-I)	
n_s	basic specific speed (table 1-I)	
n_v	vibration specific speed (table 1-I)	
$n_{(v)}$	general form of specific speeds (table 1-II)	
n_ν	viscosity specific speed (table 1-I)	
n_σ	stress specific speed (table 1-I)	
$n_{\sigma,c}$	stress specific speed related to centrifugal stresses	
Δn_1	distance Δn for unit lift coefficient ($C_{L,\infty}=1$)	L
P	power	$FLT^{-1}=ML^2T^{-3}$
Pe	Peclet number	
p	pressure; static or local pressure	$FL^{-2}=ML^{-1}T^{-2}$
Δp	pressure difference	$FL^{-2}=ML^{-1}T^{-2}$
p_a	ambient or atmospheric pressure	$FL^{-2}=ML^{-1}T^{-2}$
p_g	gage pressure	$FL^{-2}=ML^{-1}T^{-2}$
p_g	partial pressure of gas in liquid	$FL^{-2}=ML^{-1}T^{-2}$
p_o	total (static plus velocity) pressure	$FL^{-2}=ML^{-1}T^{-2}$
p_v	vapor pressure	$FL^{-2}=ML^{-1}T^{-2}$
Q	volume flow rate	L^3T^{-1}
q	parameter relating bending moment in beam to moments of applied forces (eq. (1-102))	
q	defined by eq. (2-61)	
R	Reynolds number	
R	radius of curvature of streamlines	L
R	gas constant; $R=C_p-C_v$	Lt^{-1}
r	radius, distance from axis of rotation	L
r	radius of gyration, $\sqrt{I/A}$	L^2
r_n	radius normal to conical wall	L
S	suction specific speed	
s	coordinate along given curve or contour	L

T	absolute temperature	t
t	time	T
t	wall thickness	L
t	circumferential spacing of vanes	L
t_o	circumferential vane spacing at outer periphery	L
U	peripheral velocity of solid parts of machine (rotor)	LT^{-1}
U_i	peripheral velocity of solid parts at inlet or inside diameter D_i (figs. 1-7 and 1-20)	LT^{-1}
U_o	peripheral velocity of solid parts at outer diameter D_o (figs. 1-7 and 1-25)	LT^{-1}
U_1, U_2	peripheral velocities of solid parts at inlet and discharge, respectively, of vane system (for axial flow $U_1 = U_2 = U$)	LT^{-1}
u	x-component of fluid velocity in Cartesian system x,y,z	LT^{-1}
V	absolute fluid velocity, i.e., velocity relative to stationary parts of machine (whole machine being assumed stationary); for propeller, velocity relative to propelled vehicle	LT^{-1}
V_i	absolute fluid velocity at inlet or inside diameter D_i (fig. 1-7)	LT^{-1}
$V_{i,1} V_{i,2}$	absolute fluid velocities at diameter D_i and at inlet and discharge, respectively, of vane system (fig. 1-20)	LT^{-1}
V_m	meridional component of absolute fluid velocity in machine, i.e., component parallel to radial and axial planes	LT^{-1}
$V_{m,i}$	meridional component of absolute fluid velocity at diameter D_i (fig. 1-7)	LT^{-1}
$V_{m,i,1}, V_{m,i,2}$	meridional component of absolute fluid velocity at diameter D_i and at inlet and discharge, respectively, of system (fig. 1-20); if V_m is radially constant, $V_{m,i,1} = V_{m,1}$ and $V_{m,i,2} = V_{m,2}$	LT^{-1}
V_o	absolute fluid velocity at outer diameter D_o (fig. 1-7)	LT^{-1}
V_o	fictitious velocity of ideal gas, reached by isentropic expansion to zero pressure and zero absolute temperature	LT^{-1}
V_U	peripheral component of absolute fluid velocity in machine	LT^{-1}
ΔV_U	change in peripheral component of absolute fluid velocity	LT^{-1}
$V_{U,i}$	peripheral component of absolute fluid velocity at diameter D_i (fig. 1-7)	LT^{-1}
$V_{U,i,1}, V_{U,i,2}$	peripheral components of absolute fluid velocities at diameter D_i and at inlet and discharge, respectively, of system (fig. 1-20)	LT^{-1}
V_1	absolute fluid velocity at inlet to vane system at any diameter (fig. 1-21)	LT^{-1}
V_2	absolute fluid velocity at discharge from vane system at any diameter (fig. 1-21)	LT^{-1}
v	specific volume, volume per unit weight	$L^3F^{-1} = L^2T^2M^{-1}$
v	y-component of fluid velocity in Cartesian system x,y,z	LT^{-1}
(v)	representative velocity listed in table 1-III	LT^{-1}
W	weight	$F = MLT^{-2}$

w	load on beam per unit area	$FL^{-2} = ML^{-1}T^{-2}$
w	relative fluid velocity, i.e., velocity relative to rotating parts of machine (rotor)	LT^{-1}
w	z-component of fluid velocity in Cartesian system x,y,z	LT^{-1}
w_i	relative fluid velocity at inner (or inlet) diameter D_i (fig. 1-7)	LT^{-1}
$w_{i,1}, w_{i,2}$	relative fluid velocities at diameter D_i and at inlet and discharge, respectively, of vane system (fig. 1-20)	LT^{-1}
w_o	relative fluid velocity at outer diameter D_o (fig. 1-7)	LT^{-1}
w_{SA}	Stodola correction of peripheral component of relative velocity at discharge of radial-flow rotors (fig. 2-48)	LT^{-1}
w_U	peripheral component of relative fluid velocity	LT^{-1}
w_1	relative fluid velocity at inlet to vane system (fig. 1-21)	LT^{-1}
w_2	relative fluid velocity at discharge from vane system (fig. 1-21)	LT^{-1}
w_∞	vectorial mean between incoming and discharging relative velocities of vane system (fig. 1-21)	LT^{-1}
x,y,z	Cartesian coordinates	L
x	coordinate in vane-to-vane direction in straight cascade of parallel vanes	L
x	index	
y	coordinate designating a radial position, particularly close to inside diameter of radial-flow system	L
y	coordinate in meridional (axial) direction in straight cascade of parallel vanes	L
y	coordinate normal to surface, e.g., surface of cavitation void	L
Z	number of vanes in Busemann diagram (fig. 2-47) and accompanying relations	
z	elevation; vertical coordinate	L
z	axial coordinate in cylindrical flow system	L
α	angle of attack	
α	cone angle in fig. 1-37	
α	Mach angle; $\sin \alpha = a/V$	
α_o	angle of attack measured from zero-lift direction	
β	angle between velocity vector relative to vane system and meridional direction, except when applying to Busemann's results (fig. 2-47), when it is measured from peripheral direction	
β_v	vane angle measured from meridional (axial, radial) direction	
Γ	circulation; $\Gamma = \oint v_s \, ds$	L^2T^{-1}
Γ_v	circulation about a vane	L^2T^{-1}
γ	ratio of specific heats; $\gamma = C_p/C_v$; exponent for isentropic, ideal gas changes	
δ	elastic deformation of solid parts	L
δ	boundary-layer thickness	L

δ_g	elastic deformation of solid parts under influence of a general acceleration g of entire system	L
ζ	vorticity	T^{-1}
ζ_c	component of bound vane vorticity in meridional planes (fig. 2-70)	T^{-1}
ζ_m	meridional vorticity component, describing vorticity of flow in surfaces of revolution normal to meridional flow (usually circumferential flow)	T^{-1}
ζ_U	circumferential vorticity component, describing vorticity of meridional flow	T^{-1}
η	efficiency	
η_h	hydraulic efficiency, H/Hr for pumps and compressors, Hr/H for turbines	
θ	angular coordinate in vane systems of turbomachinery	
θ	angle between ζ_c (fig. 2-70) and axial direction	
$\Delta\theta$	change in direction of supersonic flow	
λ	angle between ζ_c and resultant, bound vane vorticity ζ (fig. 2-70)	
λ	latent heat of vaporization	L
μ	viscosity	$FTL^{-2} = ML^{-1}T^{-1}$
ν	kinematic viscosity, μ/ρ	L^2T^{-1}
ρ	mass per unit volume	ML^{-3}
ρ_f	mass of fluid per unit volume	ML^{-3}
ρ_s	mass of structural material per unit volume	ML^{-3}
σ	stress in solid parts	$FL^{-2} = ML^{-1}T^{-2}$
σ_c	stress in solid parts induced by centrifugal forces	$FL^{-2} = ML^{-1}T^{-2}$
σ_f	stress in solid parts induced by fluid forces	$FL^{-2} = ML^{-1}T^{-2}$
σ_H	Thoma cavitation parameter, H_{sv}/H	
σ_p	cavitation number, $(p_{ref}-p)/(\rho V_{ref}^2/2)$	
$\sigma_{p,d}$	cavitation number with respect to desinent cavitation	
σ_R	cavitation number resulting from combined effects of average (smooth) boundary curvature and boundary roughness	
σ_1	cavitation number of local surface irregularity (roughness) alone	
τ	shear stress	$FL^{-2} = ML^{-1}T^{-2}$
τ	vane thickness in circumferential direction	L
φ	flow coefficient, V/U	
φ	angular coordinate of polar coordinate system and of radial-flow vane system	
φ	inclination of meridional streamline (stream surface) against axial direction	
ψ	head coefficient, $2g_oH/U^2$	
ω	angular velocity	T^{-1}

Subscripts:

a	axial
av	average
d	desinent cavitation
g	general acceleration of system as a whole
h	hub diameter
i	inlet diameter of pump or compressor rotor; inside diameter of any turbomachinery vane or volute system
i	incipient cavitation
L	boundary layer
l	liquid
m	meridional; location in axial and radial plane
max	maximum
min	minimum
o	reference of any type; free stream; outer diameter of turbomachinery vane or flow system
o	zero velocity (stagnation condition) except in V_o
o	undisturbed local conditions on smooth surface or parent body
R	resultant
r	radial
rel	relative
SA	Stodola correction of flow discharging from radial-flow rotors
s	suction; low-pressure side of machine or rotor
s	direction s along contour
st	static
sv	suction and vapor pressure
th	throat area of volute or vane diffuser
U	peripheral component or direction
v	vane or blade
v	vapor
x	vane-to-vane (circumferential) direction in straight cascade of parallel vanes
x,y,z	directions of Cartesian coordinates x,y,z
y	radial direction
y	axial (meridional) direction in straight cascade of parallel vanes (normal to x-direction)
z	elevation; vertical direction
z	axial direction (or component) in cylindrical flow system (three-dimensional axial-flow system)
1	unity; first in series of stations; inlet to vane system
1	unit width or depth normal to plane of flow considered, unit span
2	second in series of stations; discharge from vane system

Chapter 1

Survey of the Field of Turbomachinery in Dimensionless Form

1.1 Principles of Similarity Considerations in Turbomachinery

1.1.1 Introduction

Any presentation of the design of machinery or structures naturally deals with the relation between the design and the prescribed or expected behavior or performance of the machines or structures considered. Thus a survey of a field of machinery or structures is a survey of designs in relation to the behavior or performance of the machines or structures. In this compendium, the behavior or performance is called here the performance or operating characteristics of the machine or structure. This chapter, therefore, presents a survey of the design and performance or operating characteristics of turbomachinery.

The term design form (or form of design) means the geometric form of design, whereas the term design (used as a noun) includes, besides the design form, the structural material and anything else that has an influence on, or relation to, the performance or operating characteristics of the machine.

Furthermore all geometrically similar machines or structures of different absolute size or dimensions are considered as having only one and the same design form, so that mere scaling up or down of a machine or structure, without changing the ratio of its various dimensions relative to each other, is not considered changing the design form. With this definition, a survey of design forms is automatically dimensionless, as every single item of the survey comprises all geometrically similar machines or structures concerned, irrespective of absolute size.

The term scaling is applied to the linear dimensions of a structure or machine, meaning that all linear dimensions are changed by the same ratio, so that geometric similarity is preserved. The term scaling may apply also to quantities other than dimensions, for example, to velocities and forces. If in a fluid the magnitudes of all velocities and of their components are changed by the same ratio, the velocity field is said to be scaled, and the flow is considered to remain similar. An exactly analogous statement can be made with respect to forces.

It is well known that geometrically similar machines or structures of different sizes do not in general have the same performance or operating characteristics. Obviously turbomachines such as pumps or turbines generally have different rates of flow if they have different absolute dimensions or velocities, although they may be geometrically similar (i.e., they may have the same design form). However, if the rate of flow Q were made dimensionless by division by a velocity V times an area (the square of a linear dimension D), then all machines of the same design form might have the same dimensionless rate of flow Q/VD^2. It is shown later in this section that this is not always true for turbomachines. For this to be true, both the machines and the flow in the machines would have to be similar. Thus a survey of a field of machines or structures is dimensionless only if both the design forms and the performance or operating characteristics are related by similarity considerations.

Considerations of this type are certainly not limited to turbomachines. For instance, such considerations are regularly used in the field of general fluid mechanics. The flow over an airplane wing or airfoil is an example. Geometrically similar airfoils generally do not produce the same lift, which obviously depends on the absolute size of the airfoil, the velocity of flow, and the angle of attack α (see fig. 1-1). Only at the same angle of attack can the flow over an airfoil be similar and permit the application of similarity considerations.

The performance (lift L) of an airfoil is usually expressed in dimensionless form by the so-called lift coefficient

$$C_L = \frac{L}{(\rho V^2/2)A}$$

or

$$L = C_L \frac{\rho V^2}{2} A \qquad (1\text{-}1)$$

This relation expresses the fact that a dynamic force such as the lift L must be proportional to the mass per unit volume ρ, to the square of the velocity of flow V, and to a characteristic area A. In the usual definition of C_L, this area A is the area of the airfoil measured normal to the lift force L.

If the flow over geometrically similar airfoils is indeed similar, their lift coefficients have one and the same value (dimensionless performance or operating characteristics are the same). It should be mentioned that similarity of flow requires not only the same angle of attack but also similarity with respect to viscosity (Reynolds number), compressibility (Mach number), cavitation (cavitation number), and gravity (Froude number).

This relation among the dimensionless performance characteristics (lift coefficient), the design form (dimensionless shape of the airfoil), and the form of flow (angle of attack), which is the essence of the application of similarity considerations to the design of machines or structures, is discussed in this chapter with respect to turbomachinery.

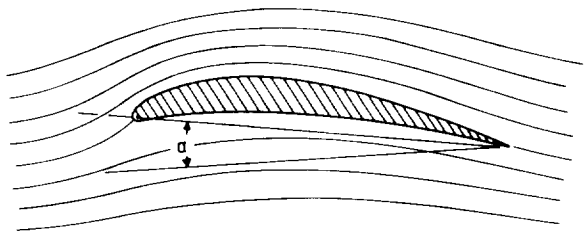

Figure 1-1.—Flow-deflecting vane or airfoil showing effect of angle of attack α on form of flow.

If both the aerodynamic or hydrodynamic characteristics and the mechanical performance characteristics (such as the load carrying capacity, deflection, etc.) are to be considered, then mechanical characteristics of the solid material (such as allowable stress and modulus of elasticity) have to be taken into account together with the structural form of the element considered (e.g., the wing). These must then be related to corresponding performance characteristics of the structure or machine.

The simplest relation of this type obviously is the one which states that the internal forces per unit area, called stresses, are under similar conditions proportional to the forces per unit area applied to the structure, such as aerodynamic or hydrodynamic pressures.

In other cases, the forces applied to the structure (such as gravitational forces) are proportional to its volume or weight, so that the applied force is proportional to $\rho g_o D^3$, where D is any representative linear dimension of the system. If compared with dynamically applied forces, which are proportional to $\rho V^2 D^2$, the ratio of dynamic to gravitational forces is $\rho V^2 D^2 / \rho g_o D^3 = V^2/g_o D$, which is the square of the Froude number.

This extension of similarity considerations into the field of mechanics of solids applies, of course, also to the field of turbomachinery and is discussed in detail in sections 1.2.3, 1.3.3, and 1.3.4.

1.1.2 Basic Similarity Considerations on Turbomachinery

To apply similarity considerations to turbomachinery, it is necessary to describe first the most essential characteristics whereby turbomachines can be distinguished from other types of machinery. A more detailed description of turbomachines is developed throughout this compendium.

Turbomachines are fluid-handling machines, such as turbines, centrifugal- or axial-flow pumps or compressors, and propellers. A turbomachine comprises one or more rotating elements equipped with the means, usually vanes, whereby forces are transmitted from the rotating elements to the fluid flowing through or past these elements. It is essential that there is at all times at least one

significant open passage from the inlet to the discharge of the machine. This requirement distinguishes a turbomachine from positive-displacement (rotating) machinery. The force action exerted by the elements of a turbomachine must, therefore, be fluid dynamic, in contrast with those acting in positive-displacement machinery. This force may be either of the inertial type, that is, generated according to Newton's law of motion, where force equals mass times acceleration, or of the viscous type, obeying Newton's law of viscous shear forces or the laws of turbulent shear forces in fluids. It is not certain that machinery using primarily viscous shear forces should be included under the term turbomachinery. This compendium is concerned only with turbomachinery in which the force action between the rotating elements and the fluid is primarily, but not exclusively, of the type in which force equals mass times acceleration. All considerations are based on this assumption.

Another consequence of the preceding description of turbomachinery results from the fact that there is always at least one open fluid passage between the inlet and the discharge of the machine, namely, that there is no rigid relation between the motion (speed of rotation) of the machine and the rate of flow through the machine. In contrast, the rate of flow of positive-displacement machinery is proportional to the speed of the machine (within the limits of changes in internal leakages and of the effects of compressibility of the fluid). With turbomachinery, on the other hand, substantial departures from this proportionality between the rate of flow and the speed of the machine are to be expected. In fact, the rate of flow has no rigid relation to the rotative speed of the machine. In order to analyze this situation further, it is necessary to define more closely the concept of similarity of flow.

Similarity of flow in two geometrically similar machines or other flow structures is defined by the condition that the velocities of flow at all pairs of geometrically similarly located points in the machines being compared have one and the same ratio to each other throughout the two machines and have the same direction relative to the machines (i.e., that the proportionality of all velocities applies also to all directional components of the velocities relative to the machines compared) (see fig. 1-2).

For the designer, the most useful application of this definition is that the flow velocity diagrams at geometrically similarly located points in the

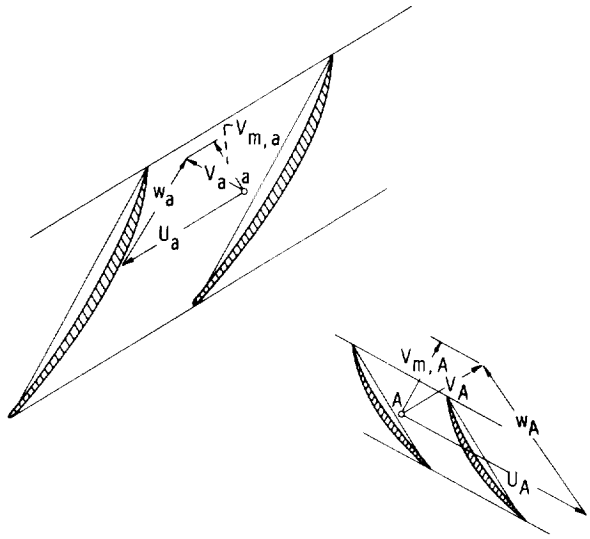

Figure 1-2.—Similarity of flow, shown by similar velocity diagrams at any pair of similarly located points A and a.

machines must be geometrically similar for the two machines compared (fig. 1-2). In fact, the application of this definition may be considered as a valid test of similarity. This, of course, applies also to three-dimensional flow conditions and velocity diagrams.

The accuracy of the foregoing definition depends on the accuracy with which the fluid velocities are defined. First, the flow through turbomachinery is known to be unsteady, that is, to fluctuate at frequencies related to the frequency of the vanes of the rotating systems passing the stationary vanes or other stationary parts of the machine. Thus any fluid velocity quoted without reference to time is necessarily time-averaged over a reasonable length of time compared with the period of fluctuations. Arriving at this average is not a simple problem, as it may involve an averaging of the rate, momentum, or energy of the flow. Fortunately, for small fluctuations, these averages do not differ a great deal from each other. Second, turbulent velocity fluctuations have to be disregarded, because their random nature makes a rational process of averaging impractical at present. Usually a mean velocity has to be defined by the time-averaged rate of flow through a limited, that is, finite, cross section of the flow field.

The problem of similarity of flow conditions may best be described by the following question (ref. 1, p. 6): Under what conditions will a geometrically similar flow of liquid or gas occur around or within geometrically similar boundaries? The general

answer to this question has two parts. First, as stated by the aforementioned condition of similarity of flow, for a single airfoil in an infinitely extended straight stream, the airfoil must be geometrically similar and the angle of attack must be the same. Second, the forces acting on the fluid must be similarly arranged, because otherwise the fluid would be forced off the geometrically similar path in spite of the similarity of the fluid passages.

Similar velocity distributions are accompanied by similar force distributions only if the forces have the same relation to the fluid velocities at all corresponding points of the systems compared. This is the case if mass (or inertia) forces are the only forces considered. It follows that, under this condition, geometrically similar flow boundaries and inflow conditions always produce geometrically similar flow conditions.

In the presence of forces other than inertia, similarity of flow may still be maintained if the forces change proportionally to the inertial forces, for example, if viscous forces are kept proportional to inertial forces by maintaining the same Reynolds number in the machines compared.

If the flow boundaries have no motion relative to each other, inertial forces only do not constitute any significant problem, as geometrically similar flow boundaries with similar inflow and discharge conditions (i.e., similar flows at infinity) always lead to similar flow, as defined previously. Therefore similarity considerations in general fluid mechanics usually deal with the departures from incompressible flow controlled by inertial forces only.

In the field of turbomachinery, one is confronted with an additional condition of similarity when dealing exclusively with inertial forces. This condition is most easily understood on the basis of the similarity requirement of having similar fluid velocity diagrams at all similarly located points in the machines compared. In turbomachines, these velocity diagrams contain meridional fluid velocities V_m which are dependent primarily on the rate of volume flow Q divided by a representative area D^2. The same velocity diagrams also contain peripheral velocities of the rotating solid parts U which are proportional to a representative diameter D times the speed of rotation n. Therefore, to satisfy the requirement of similarity of velocity diagrams, it is necessary that the so-called flow coefficient $\varphi = V_m/U$ have the same value at similarly located points in the machines compared. This necessary condition of similarity can also be made to be a sufficient condition by replacing the meridional fluid velocity V_m by any fluid velocity in the machine V, which leads to an almost self-evident condition of similarity: fluid velocities V and peripheral velocities U of the solid parts must have the same ratio at all similarly located points in the machines compared. This condition at similarly located points is expressed by the equation

$$\frac{V}{U} = \text{constant} \tag{1-2}$$

and is called the kinematic condition of similarity of flow in turbomachines.

The flow coefficient $\varphi = V_m/U$ assumes a very definite physical meaning if applied to a point where the absolute velocity V has no peripheral component, as shown in figure 1-3 for the inlet. In this case, $\varphi = \cot \beta$, where β is the angle between the meridional direction (the direction lying in an axial and radial plane) and the relative velocity vector, and φ alone determines the form of the velocity diagram. But the meaning of the flow coefficient is not limited to this particular simple case. The

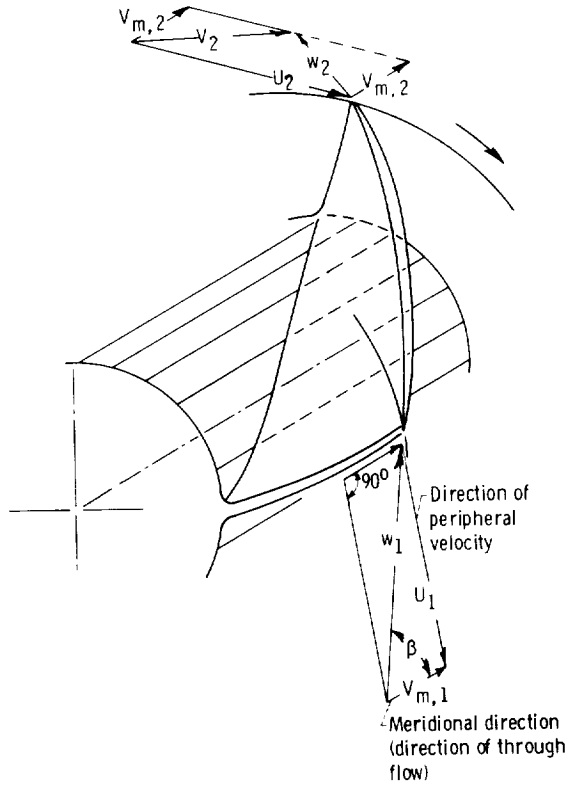

Figure 1-3.—Velocity diagrams of axial-flow pump rotor blade.

equation $\varphi = V_m / U$ is a dimensionless expression of the depth of any velocity vector diagram in the meridional direction.

From the interpretations given previously, $V = \text{constant} \times Q/D^2$ and $U = \text{constant} \times nD$, the kinematic condition of similarity may be written in the form

$$\frac{Q}{D^2}\,\frac{1}{nD} = \frac{Q}{D^3 n} = \text{constant} \tag{1-3}$$

which applies throughout the machines being compared. Accordingly the aforementioned limitation to similarly located points becomes unnecessary as long as D has the same meaning for all machines being compared.

The next step consists of applying the fact that force action between the machine and the fluid and a corresponding exchange of work between the rotor and the fluid are dominated by inertial forces. (This assumption is valid if forces such as viscous or gravitational forces are kept either negligible or proportional to inertial forces by keeping the Reynolds number and the Froude number constant.) With this assumption, all fluid pressure differences Δp in the machine are given, under similar flow conditions and for incompressible fluids, by the relation

$$\Delta p = \text{constant} \times \frac{\rho V^2}{2} \tag{1-4}$$

where ρ is the mass per unit volume of the fluid and V is any well defined fluid velocity. This relation follows immediately from the well-known Bernoulli equation, which also explains the factor 1/2. The right side of equation (1-4) can also be interpreted as the mass flow per unit area ρV times any change in velocity (which under similar flow conditions is proportional to V), so that this side of the equation is proportional to a change in momentum of the flow per unit area.

The pressure difference Δp may also be interpreted as work or energy per unit volume (ft-lb/ft^3 or lb/ft^2) if the unit of volume is displaced under the pressure difference Δp. By dividing by the weight per unit volume $g_o \rho$, where $g_o = 32.2$ feet per second squared, one obtains the work or energy per unit weight, called a difference in head:

$$\Delta h = \frac{\Delta p}{\rho g_o} = \text{constant} \times \frac{V^2}{2g_o} \tag{1-5}$$

For gases, Δh (without its relation to Δp) is a difference in enthalpy measured in mechanical units (ft-lb/lb) instead of thermal units (Btu/lb). The total exchange of mechanical energy between a turbomachine and each unit of fluid weight passing through the machine is called the head of the machine. It obeys the same similarity relation as any Δh:

$$\left.\begin{aligned} H &= \text{constant} \times \frac{V^2}{2g_o} \\ &\text{or} \\ \frac{2g_o H}{V^2} &= \text{constant} \end{aligned}\right\} \tag{1-6}$$

Thus this ratio has the same value at similarly located points in similar machines with similar flow conditions.

In terms of the rate of volume flow Q (with $V \approx Q/D^2$), equation (1-6) can be written in the form

$$\frac{g_o H D^4}{Q^2} = \text{constant} \tag{1-7}$$

This expression also has the same value for all similar machines with similar flows. The one-quarter power of this expression is sometimes called the specific diameter:

$$D_s = \frac{D(g_o H)^{1/4}}{Q^{1/2}} \tag{1-8}$$

Considering the condition of kinematic similarity (eq. (1-2)), one can replace the representative fluid velocity V by a representative peripheral velocity of the rotor U and thus obtain a new expression in place of equation (1-6):

$$\left.\begin{aligned} H &= \text{constant} \times \frac{U^2}{2g_o} \\ &\text{or} \\ \frac{2g_o H}{U^2} &= \psi = \text{constant} \end{aligned}\right\} \tag{1-9}$$

where the constant of proportionality ψ is called the head coefficient and may be considered as a dimensionless expression of the head of the

machine or of the corresponding change in enthalpy. It always has the same value for similar flow conditions in similar machines provided that U is defined in the same manner in the machines compared. Both U and ψ are referred to some diameter of the machine, for example, the outside diameter of its rotor, so that one can write $\psi_o = 2g_oH/U_o^2$.

If the same relation is desired in terms of the linear dimension D and the speed of rotation n of the machine, with $U = \text{constant} \times Dn$, an equivalent dimensionless expression of the head can be written:

$$\frac{g_oH}{D^2n^2} = \text{constant} \tag{1-10}$$

The energy exchange between the rotor and the fluid, expressed in dimensionless form by the head coefficient ψ or by g_oH/D^2n^2, can also be described by Euler's equation of the exchange of angular momentum between the rotor and the fluid. This equation is derived in detail in chapter 2. For axial-flow machines, this equation leads to the relation

$$H = \eta_h \Delta V_U \frac{U}{g_o} \tag{1-10a}$$

where ΔV_U is the change in the peripheral velocity component of the flow passing through the rotor (change in peripheral momentum), and η_h is the hydraulic efficiency, which expresses only head losses and not losses due to leakage and drag (which only increase the torque). The hydraulic efficiency is, therefore, somewhat higher than the overall efficiency.

Substituting equation (1-10a) into equation (1-9) results in an expression for axial-flow machines:

$$\psi = 2\eta_h \frac{\Delta V_U}{U} \tag{1-11}$$

(For axial-flow turbines, one simply replaces η_h by $1/\eta_h$.) Equation (1-11) shows that ψ describes not only the energy exchange but also the circumferential deflection of the flow by the rotors in dimensionless form. The greater ψ, the greater the deflection ΔV_U. For example, $\psi = 1$ describes approximately the maximum conventional deflection of the flow in axial-flow pump or compressor rotors. A relation similar to equation (1-11) can also be written for radial-flow rotors.

Figure 1-4 shows the so-called characteristic curves of a centrifugal (or axial-flow) pump at two speeds of rotation, and figure 1-5 the same curves for two geometrically similar pumps of different sizes at the same speed of rotation n. Included are curves of power consumption, which are obviously proportional to $\rho Q g_o H/\eta$, where η denotes the overall efficiency.

The coordinates of the curves of head as a function of flow may be expressed in the dimensionless forms Q/D^3n and g_oH/D^2n^2, according to equations (1-3) and (1-10). If Q/D^3n

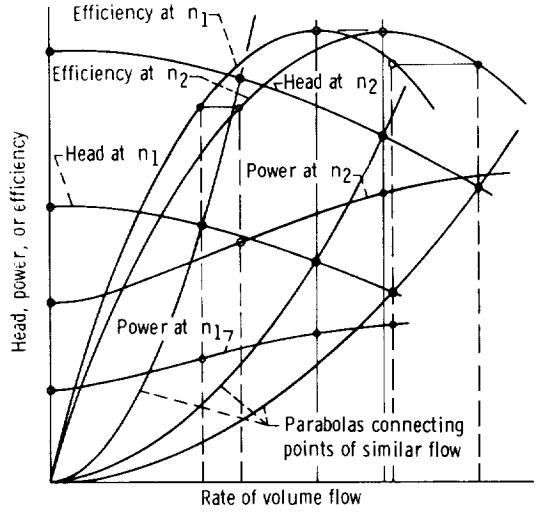

Figure 1-4.—Characteristic curves of centrifugal pump at two speeds of rotation n_1 and n_2.

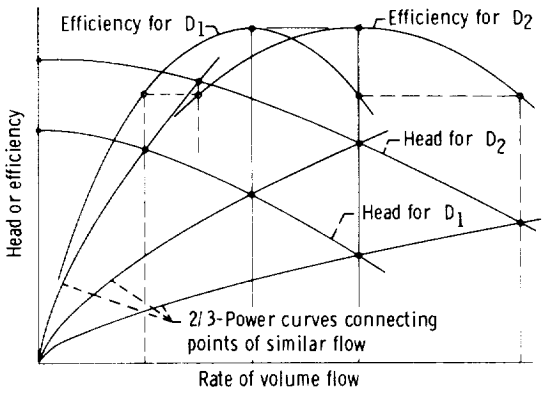

Figure 1-5.—Characteristic curves of two similar centrifugal pumps with linear dimensions D_1 and D_2 operating at same speed n.

has the same value for similar machines, then $g_o H/D^2n^2$ also has one and the same value, provided that the effects of viscosity, compressibility, cavitation, and gravity are either negligible or kept proportional to the head H by using constant values of their respective dimensionless expressions (Reynolds number, Mach number, etc.).

For the similar flow conditions described by

$$\left.\begin{aligned} &\frac{Q}{D^3 n} = \text{constant} \\ &\text{and} \\ &\frac{g_o H}{D^2 n^2} = \text{constant} \end{aligned}\right\} \qquad (1\text{-}12)$$

Q changes linearly, and H changes with the square of the speed of rotation. However, at a constant speed of rotation n, Q changes with the cube and H with the square of the linear dimension D of the machine. The corresponding square parabola connecting points of similar flow conditions of the head-capacity curves for different speeds is shown in figure 1-4, and the corresponding 2/3-power curve for different dimensions of the machines is shown in figure 1-5.

It should be evident that the characteristic curves (e.g., the head-capacity curves) do not connect points of similar flow conditions and, therefore, cannot be derived by similarity considerations. Generally the characteristic curves must be determined by tests. Only their slopes at the points of best efficiency can be approximated by theoretical means.

The head-capacity (and other characteristic) curves shown in figures 1-4 and 1-5 can be reduced to one curve by using the dimensionless coordinates Q/D^3n and $g_o H/D^2n^2$ or equivalent expressions such as $\varphi = V/U$ and $\psi = 2g_o H/U^2$. This was done to obtain the curve shown in figure 1-6 for an axial-flow pump. Different data point symbols refer to different speeds of the same pump. The scatter of these points is practically within the test accuracy, which indicates that for a pump of this size (impeller diameter, 15 in.) and the speeds listed, the test fluid (water) did not show any effects of viscosity (Reynolds number) or compressibility. The test was conducted at a sufficiently high absolute pressure to practically eliminate cavitation.

The type of curve shown in figure 1-6 is, therefore, a valid dimensionless expression of the head-capacity curves of all geometrically similar pumps of this design form, irrespective of speed and size, provided that, for example, the Reynolds number remains above certain lower limits.

As mentioned previously, the similarity relations discussed in this chapter are valid if either of two conditions is satisfied: if inertial forces are dominating to the extent that all other forces, such as viscous and gravitational forces, are negligible or if these other forces have a constant ratio to inertial forces and thus satisfy the Reynolds law of similarity and the Froude law of similarity, respectively. An analagous statement can be made relative to cavitation, that is, that similarity can be maintained if the absolute pressure is adjusted so that the difference between all local pressures and the vapor pressure of the liquid is proportional to all other pressure differences in the machine caused by inertial forces.

Although the effects of compressibility can also be described by force actions, these effects are more directly characterized by the changes in the volume of the fluid handled in the machine. This means that the volume flow Q at similarly located flow cross sections in the machines being compared must have the same ratio to the volume flow at some standard place (e.g., the inlet to the machines). It turns out that this similarity of volume flow is very closely satisfied if the local Mach number is the same at similarly located points in the machines being compared.

A distinction is made previously between

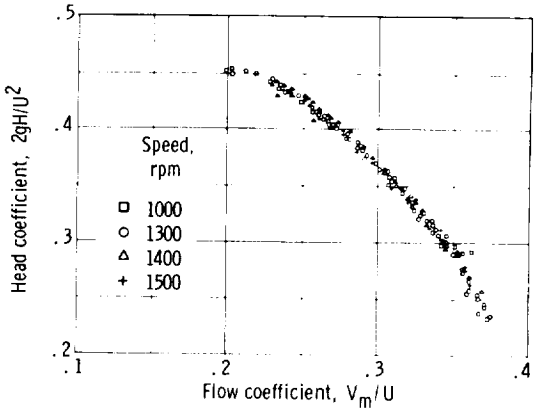

Figure 1-6.—Dimensionless head-capacity curve of axial-flow pump.

similarity relations using local velocities such as $\varphi = V/U = \text{constant}$ and those using overall operating characteristics such as $Q/D^3n = \text{constant}$. The relation $V/U = \text{constant}$ means that V/U has the same value only at similarly located points in the machines compared, and the relation $Q/D^3n = \text{constant}$ means that this ratio has the same value throughout the machines compared. For compressible fluids, however, the relation $Q/D^3n = \text{constant}$ also has a definite meaning if it is applied only to similarly located regions in the machines compared. A region is defined as that portion of the flow passages within a machine through which the volume flow Q is essentially constant.

1.1.3 Review

A design form comprises all geometrically similar designs regardless of absolute size. Thus design forms are dimensionless.

Geometrically similar machines have something in common, but their performance or operating characteristics may obviously be different because of differences in absolute size, velocities, forces, etc. However, size, velocity, and force can be combined into a dimensionless performance characteristic, for example, the lift coefficient of an airfoil:

$$C_L = \frac{L}{(\rho V^2/2)A}$$

Geometrically similar airfoils have the same lift coefficient only if the flow over the airfoil is similar. Similarity of flow requires not only geometrically similar flow boundaries but also a kinematic flow criterion of similarity, in this case, the angle of attack between the flow and the airfoil. Similarity considerations may be extended to apply to mechanical characteristics such as stresses or elastic deformations.

Similarity of flow, particularly in turbomachinery, may be defined by the similarity of velocity vector diagrams at all geometrically similarly located points in the two or more geometrically similar machines or flow structures being compared. Similarity of flow requires that all forces within the flow change proportionally to each other. If inertial forces dominate, as is the case in turbomachinery and flow over an airplane wing, other forces such as viscous and gravitational forces must change proportionally to the inertial forces; this leads to the requirement of constant Reynolds number, constant Froude number, etc., unless viscous and gravitational forces are negligible. Furthermore changes in the volume of a gas must have the same ratio between pairs of similarly located points in the machines compared, so that the Mach number must be the same at similarly located points. Finally, the pressure at similarly located points in liquids must have the same dimensionless relation to the vapor pressure; that is, it must have the same cavitation number.

The velocity vector diagrams in turbomachines generally contain fluid velocities $V = \text{constant} \times Q/D^2$ and peripheral velocities of the solid parts $U = \text{constant} \times nD$. To maintain similarity of the velocity vector diagrams, the flow coefficient $\varphi = V/U$ must have the same value at similarly located points; therefore $(Q/D^2)/nD = Q/D^3n$ must have the same value to obtain similar flow in geometrically similar machines.

If Q/D^3n has the same value for geometrically similar machines (if the flow in such machines is similar), the head H (energy exchange per unit weight of fluid), or the change in enthalpy, is proportional to the square of the velocities of the rotating parts U and of the fluid V in the machine. Thus, for similar flow, the head coefficient $\psi = 2g_oH/U^2$ and the equivalent ratio $2g_oH/V^2$ have the same value at similarly located points in similar machines, and g_oH/n^2D^2 as well as g_oHD^4/Q^2 have the same values for similar machines operating with the same value of Q/D^3n. The ratios Q/D^3n and g_oH/n^2D^2 or g_oHD^4/Q^2 may be considered as dimensionless, fluid-dynamic operating or performance characteristics of turbomachines. Other dimensionless fluid-dynamic and mechanical characteristics are introduced in section 1.2.

1.2 Relations Between Operating Characteristics and Design Characteristics

1.2.1 Basic Specific Speed

In section 1.1, the performance or operating characteristics of turbomachines are expressed in the following dimensionless forms:

Flow coefficient in the form

$$\varphi = \frac{V_m}{U}$$

or as the ratio

$$\frac{Q}{nD^3} \qquad (1\text{-}13)$$

Head coefficient referred to peripheral velocity in the form

$$\psi = \frac{2g_oH}{U^2}$$

or as the equivalent ratio

$$\frac{g_oH}{n^2D^2} \qquad (1\text{-}14)$$

Head coefficient referred to fluid velocity as the ratio

$$\frac{2g_oH}{V^2}$$

or

$$\frac{g_oHD^4}{Q^2} \qquad (1\text{-}15)$$

Head coefficient in the form of the so-called specific diameter

$$D_s = \frac{D(g_oH)^{1/4}}{Q^{1/2}} \qquad (1\text{-}16)$$

Similarity of flow in geometrically similar turbomachines depends primarily on the kinematic condition of similarity:

$$\frac{V}{U} = \text{constant}$$

which has the same value at similarly located points in similar machines, or

$$\frac{Q}{D^3n} = \text{constant} \qquad (1\text{-}17)$$

which has the same value throughout similar machines.

If this condition for similar flow is satisfied (along with some additional conditions given in sec. 1.1),

$$\psi = \frac{2g_oH}{U^2} = \text{constant}$$

or

$$\frac{g_oH}{n^2D^2} = \text{constant} \qquad (1\text{-}18)$$

and

$$\frac{2g_oH}{V^2} = \text{constant}$$

or

$$D_s = \frac{(g_oH)^{1/4}}{Q^{1/2}} = \text{constant} \qquad (1\text{-}18a)$$

The dimensionless operating or performance characteristics Q/D^3n, g_oH/n^2D^2, etc. can be calculated only if the size of the machine D is known, which means at least one of the machines to be compared must have a known design form and known dimensions.

It is evident from equations (1-17) and (1-18) that, when the speed n of a machine with fixed form and size is changed while similarity of flow is maintained, the rate of flow Q changes with the first power of the speed of rotation n and the head H changes with the second power of the speed of rotation n^2 and of the rate of flow Q^2. The resulting parabolic relation between H and Q is shown in figure 1-4. The same equations show that, when the size D of a machine is changed while its speed, similarity of geometric form, and similarity of flow are maintained, the rate of flow Q changes with the third power of the linear dimension D^3 and the head H changes with the second power of the linear dimension D^2. The resulting 2/3-power relation between H and Q is shown in figure 1-5. Consequently, any values of H and Q can be obtained without changing the form of the machine or of the flow by merely changing the size D and the speed n of the machine. For example, in a diagram of H as a function of Q, similar flow can be maintained by following successively along a parabola $H = \text{constant} \times Q^2$ while holding the diameter constant and along a curve of $H = \text{constant} \times Q^{2/3}$ while holding speed constant (figs. 1-4 and 1-5).

If Q, H, and n are considered as the given operating conditions of the machine, not every pair of values of Q and H can be reached with a given speed n, as one can follow without restriction only a curve $H = \text{constant} \times Q^{2/3}$ (fig. 1-5) and can change only the size D at will.

It is then natural to ask the following question: What field of operating conditions of n, Q, and H can be covered by turbomachines of the same geometric design form operating under similar flow conditions? This question can be answered by eliminating from equations (1-17) and (1-18) the linear dimension D. It is customary to accomplish this by dividing $(Q/D^3n)^{1/2}$ by $(g_oH/n^2D^2)^{3/4}$:

$$\frac{Q^{1/2}}{D^{3/2}n^{1/2}} \frac{n^{3/2}D^{3/2}}{(g_oH)^{3/4}} = \frac{nQ^{1/2}}{(g_oH)^{3/4}} = \text{constant}$$

which satisfies, of course, the condition $H = \text{constant} \times Q^{2/3}$ at $n = \text{constant}$. The resulting expression for the basic specific speed, or more concisely, the specific speed n_s, is

$$n_s = \frac{nQ^{1/2}}{(g_oH)^{3/4}} \tag{1-19}$$

which is defined by the following statement: Any fixed value of the basic specific speed describes all operating conditions (n, Q, and H) that can be satisfied by similar flow conditions in geometrically similar turbomachines.

This definition is, of course, valid only if inertial forces dominate the flow and if the flow is kept similar also with respect to the effects of viscosity, compressibility, cavitation, and gravity or if these effects are negligible.

The particular form of the specific speed given by equation (1-19) has primarily a historic rationale, although it differs from the conventional forms by the fact that it is dimensionless if consistent units are used for n, Q, H, and g_o. The concept of the specific speed was first introduced by Camerer in the second decade of this century in the form of the turbine specific speed:

$$N_{s,P} = \frac{nP^{1/2}}{H^{5/4}} \tag{1-20}$$

where the power P is given as

$$P = \frac{\eta \rho g_o QH}{550} = \text{constant} \times QH$$

The early definition of this concept was that $N_{s,P}$ is the speed of rotation of a geometrically similar turbine delivering 1 horsepower under a head of 1 meter. The equivalence of expressions (1-19) and (1-20) is demonstrated by multiplying the top and bottom expression (1-19) by $H^{1/2}$.

It should be evident from the derivation and definition of n_s that any power of expression (1-19) would correspond to the same definition and would have the same practical meaning. For example, the 2/3 power of n_s would be the ratio of a kinematically determined (fictitious) velocity $(nQ^{1/2})^{2/3}$ to a dynamically determined velocity $(g_oH)^{1/2}$ and might thus have a clearer physical significance than the form (1-19). On the other hand, the specific speed may also be written as a ratio of two linear dimensions $|Q/(g_oH)^{1/2}|^{1/2}$ and $n/(g_oH)^{1/2}$. The first one is given by the rate of flow and the second by the speed of rotation, both in relation to the dynamic velocity $(g_oH)^{1/2}$. Evidently there is more than one physical interpretation of the specific speed, and thus there is no good reason for departing from the conventional form of the specific speed except for making it dimensionless as is done in equation (1-19).

There are various dimensional specific speeds in use. All of them eliminate the standard gravitational acceleration g_o, because it is constant, and measure n in rpm. The conventional pump specific speed in the United States, with Q in gallons per minute, is

$$\frac{n(\text{rpm})[Q(\text{gal/min})]^{1/2}}{[H(\text{ft})]^{3/4}} = \left(g_o \frac{\text{ft}}{\text{sec}^2}\right)^{3/4} \times \left(60 \frac{\text{sec}}{\text{min}}\right)^{3/2} \left(7.481 \frac{\text{gal}}{\text{ft}^3}\right)^{1/2} n_s = 17\,200\, n_s \tag{1-21}$$

Another form is

$$\frac{n(\text{rpm})[Q(\text{ft}^3/\text{sec})]^{1/2}}{[H(\text{ft})]^{3/4}} = \left(g_o \frac{\text{ft}}{\text{sec}^2}\right)^{3/4} \left(60 \frac{\text{sec}}{\text{min}}\right) n_s = 812\, n_s \tag{1-22}$$

The turbine specific speed used in the United States is

$$\frac{n(\text{rpm})[P(\text{hp})]^{1/2}}{[H(\text{ft})]^{5/4}} = g_o^{3/4}\left(60\,\frac{\text{sec}}{\text{min}}\right)\left(\frac{g_o\rho\eta}{550}\right)^{1/2} n_s$$

$$= 259\, n_s \qquad (1\text{-}23)$$

where the efficiency η is equal to 0.9.

There are, of course, still other specific speeds used in countries having the metric system, which gives ample reason for using a dimensionless expression for this inherently dimensionless number.

It should be evident that the specific speed of any given machine and of geometrically similar machines can be varied over a wide range by operating with dissimilar flow conditions, that is, at different values of the dimensionless rate of flow Q/D^3n. However, this is generally not advisable because the efficiency and other operating characteristics are favorable only over a limited range of Q/D^3n.

It has become customary to associate a turbomachine or a class of geometrically similar turbomachines with its basic specific speed at the Q/D^3n value of best efficiency. In this restricted sense the basic specific speed becomes a dimensionless operating characteristic of any class of geometrically similar turbomachines. Turbomachines having the same specific speed at the best efficiency do not have to be geometrically similar (since the same operating condition can be satisfied by different design forms). But turbomachines of different specific speeds at the best efficiency cannot be geometrically similar (except in the rare case when the efficiency curve plotted against Q/D^3n has a completely flat top). Thus the basic specific speed at the best efficiency is regularly used as an index of turbomachinery design despite the fact that in its original form the specific speed contains only operating characteristics, not design characteristics.

The specific speed at best efficiency does not determine the design of a turbomachine uniquely. Nevertheless, there is a relation between the design form and the specific speed so defined, particularly after certain design choices have been made such as radial or axial flow, inward or outward flow, and the number of stages to be used. Before relations between the basic specific speed and the design form are derived, it is well to consider a much simpler use of the concept of the specific speed.

Evidently the specific speed can be calculated as soon as the operating characteristics n,Q, and H of a new machine are known, before any decisions regarding the design of the machine are made. One may then search the records of existing machines for a machine having the desired specific speed near its point of best efficiency and having characteristics which are acceptable for the machine to be designed (number of stages, axial or radial flow, etc.). If such a machine is found, the problem reduces to simply scaling the known machine up or down in size D and speed n according to equations (1-17) and (1-18) until the desired performance is obtained. This performance may, of course, depend on variables not contained in the specific speed, which may very well determine the choices between radial and axial flow, single-stage and multistage machines, and so on. Sections 1.2.2 and 1.2.3 elaborate further on this aspect.

The next step is obviously to establish a relation between the basic specific speed at the best efficiency and the design form. The desired relation is first derived for radial- or mixed-flow centrifugal pumps (or compressors), with particular reference to the rotor or impeller design. These considerations are limited to single-stage machines. In other words, the head H is the head of the particular single stage considered. The specific speed is, therefore, the specific speed of that particular stage.

Evidently

$$Q = V_{m,i}\left(\frac{D_i^2\pi}{4} - \frac{D_h^2\pi}{4}\right) = V_{m,i}\frac{D_i^2\pi}{4}\left(1 - \frac{D_h^2}{D_i^2}\right)$$

and

$$n = \frac{U}{D}\,\frac{1}{\pi}$$

in the notation given in figure 1-7. Hence

$$n_s = \frac{nQ^{1/2}}{(g_o H)^{3/4}} = \frac{U}{D\pi}\left[\frac{V_{m,i} D_i^2 \pi}{4} \times \left(1 - \frac{D_h^2}{D_i^2}\right)\right]^{1/2} \frac{1}{(g_o H)^{3/4}}$$

and

$$n_s = \frac{1}{2^{1/4}\pi^{1/2}}\left(\frac{U^2}{2g_o H}\right)^{3/4}\left(\frac{V_{m,i}}{U_i}\right)^{1/2} \times \left(\frac{D_i}{D}\right)^{3/2}\left(1 - \frac{D_h^2}{D_i^2}\right)^{1/2} \qquad (1\text{-}24)$$

This equation may be evaluated according to figure 1-7 with respect to $D = D_{o,max}$ and $U = U_{o,max}$, $D = D_{o,min}$ and $U = U_{o,min}$, or any other associated D and U values. The most critical value of $\psi = 2g_o H/U^2$ is its maximum value at $D = D_{o,min}$ and $U = U_{o,min}$ because the Euler turbomachinery momentum equation derived in chapter 2, section 2.3, states that the change in the product of the peripheral flow velocity component V_U and the peripheral rotor velocity U is proportional to the head. Thus, the lower U, the greater the change in V_U (the greater the deflection of the flow in the peripheral direction).

Figure 1-8 shows the evaluation of equation (1-24) with $D = D_{o,min}$ and $U = U_{o,min}$ under the empirical assumptions that $V_{m,i}/U_i = 0.36 = \text{constant}$ and $U_{o,min}^2/2g_o H = 1 = \text{constant}$. These assumptions are reasonable for centrifugal pump impellers with backward-bent vanes.

Equation (1-24) appears in a simplified form if one selects $D = D_i$ and $U = U_i$ (see fig. 1-7), so that

$$n_s = \frac{nQ^{1/2}}{(g_o H)^{3/4}} = \frac{1}{2^{1/4}\pi^{1/2}}\left(\frac{U_i^2}{2g_o H}\right)^{3/4} \times \left(\frac{V_{m,i}}{U_i}\right)^{1/2}\left(1 - \frac{D_h^2}{D_i^2}\right)^{1/2} \qquad (1\text{-}25)$$

This form of equation (1-24) is particularly useful for axial-flow rotors where D_i and U_i apply to both the high-pressure and the low-pressure sides of the rotor (see fig. 1-20). In this case, $D_h = D_{h,1}$.

As mentioned previously, the minimum diameter on the high-pressure side of the rotor is critical with respect to the value of $\psi = 2g_o H/U^2$. For axial-flow rotors, the hub diameter $D_{h,2}$ on the high-pressure

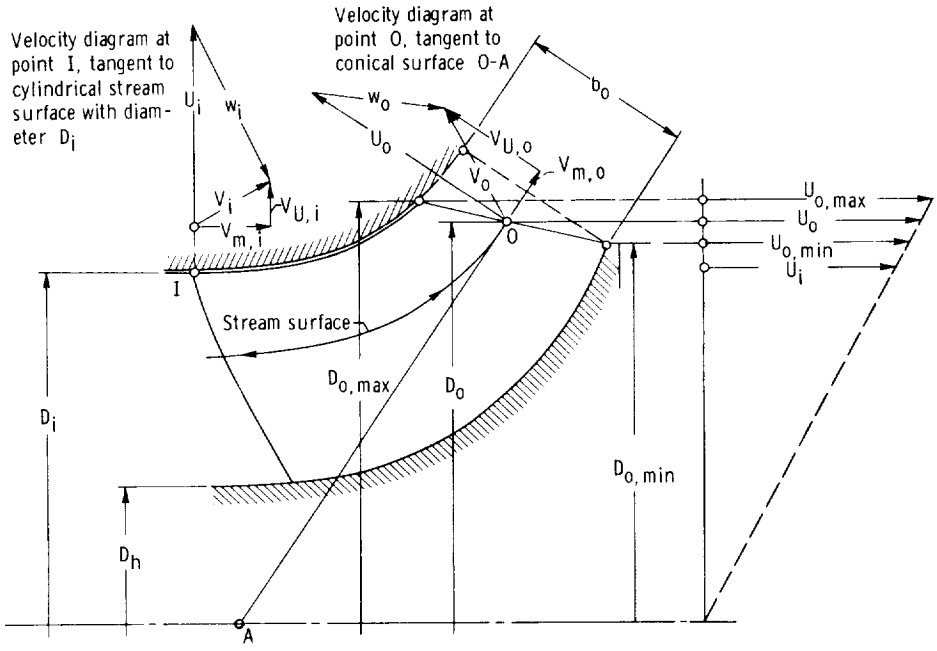

Figure 1-7.—Mixed-flow rotor profile defining notation.

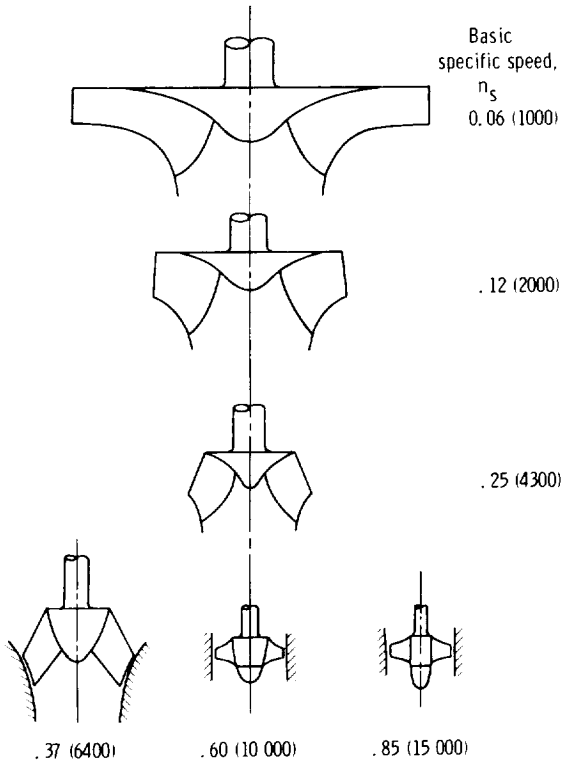

Figure 1-8.—Pump impeller profiles as function of basic specific speed. (Values in parentheses are dimensional specific speeds with flow rate in gal/min.)

side is the minimum diameter on that side. Using the notation in figure 1-20, one may write equations (1-24) and (1-25) in the form

$$n_s = \frac{1}{2^{1/4}\pi^{1/2}}\left(\frac{U_{h,2}^2}{2g_oH}\right)^{3/4}\left(\frac{D_i}{D_{h,2}}\right)^{3/2} \times\left(\frac{V_{m,1}}{U_i}\right)^{1/2}\left(1-\frac{D_{h,1}^2}{D_i^2}\right)^{1/2} \qquad (1\text{-}26)$$

This equation was evaluated for $2g_oH/U_{h,2}^2 = \text{constant} = 1$ and 4 and for $V_{m,1}/U_i = 0.36$. The results are shown in figure 1-9. The first value $n_{s,1}$ is derived from $2g_oH/U_{h,2}^2 = 1$ and applies approximately to pump and compressor rotors of conventional design. The second value $n_{s,4}$ is derived from $2g_oH/U_{h,2}^2 = 4$ and applies primarily to impulse type turbine rotors. It is possible that much larger values than $\psi_{h,2} = 1$ may also apply to pump and compressor rotors (see sec. 1.3.2.1).

Equation (1-25), which applies primarily to axial-flow machines, was evaluated in general form, and the results are presented in figure 1-10. Included in this diagram are lines for $2g_oH/V_{m,1}^2 = \text{constant}$, where the meridional velocity component $V_{m,1}$ is obviously the axial velocity component at the low-pressure side of the rotor (see fig. 1-20). With these lines figure 1-10 represents also an evaluation of the equation

$$n_s = \frac{nQ^{1/2}}{(g_oH)^{3/4}} = \frac{1}{2^{1/4}\pi^{1/2}}\left(\frac{V_{m,1}^2}{2g_oH}\right)^{3/4} \times\frac{U_i}{V_{m,1}}\left(1-\frac{D_{h,1}^2}{D_i^2}\right)^{1/2} \qquad (1\text{-}27)$$

where $V_{m,1} = V_{m,i}$. Equation (1-27) is equivalent to equation (1-25) and is useful with respect to cavitation considerations (see sec. 1.2.2).

Equation (1-24), with its modifications for axial-flow rotors, is by no means the only relation between the basic specific speed and the design characteristics of the machine. Equation (1-24) refers particularly to the inlet conditions of a pump or compressor impeller (discharge conditions of a turbine rotor) and uses the pump inlet flow coefficient $V_{m,i}/U_i$. Only the head coefficient $2g_oH/U_o^2$ refers to the outside (high-pressure side) of the rotor.

Referring instead primarily to the outside (high-pressure) cross section of the rotor, one may write the rate of flow in the form $Q = V_{m,o}D_o\pi b_o$, where b_o is the rotor width at the outside diameter D_o measured normal to the outside meridional velocity

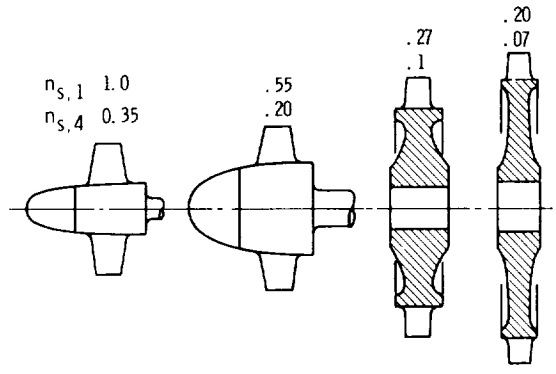

Figure 1-9.—Axial-flow rotor profiles as function of basic specific speed n_s ($n_{s,1}$ for head coefficient $2g_oH/U_h^2 = 1$; $n_{s,4}$ for $2g_oH/U_h^2 = 4$).

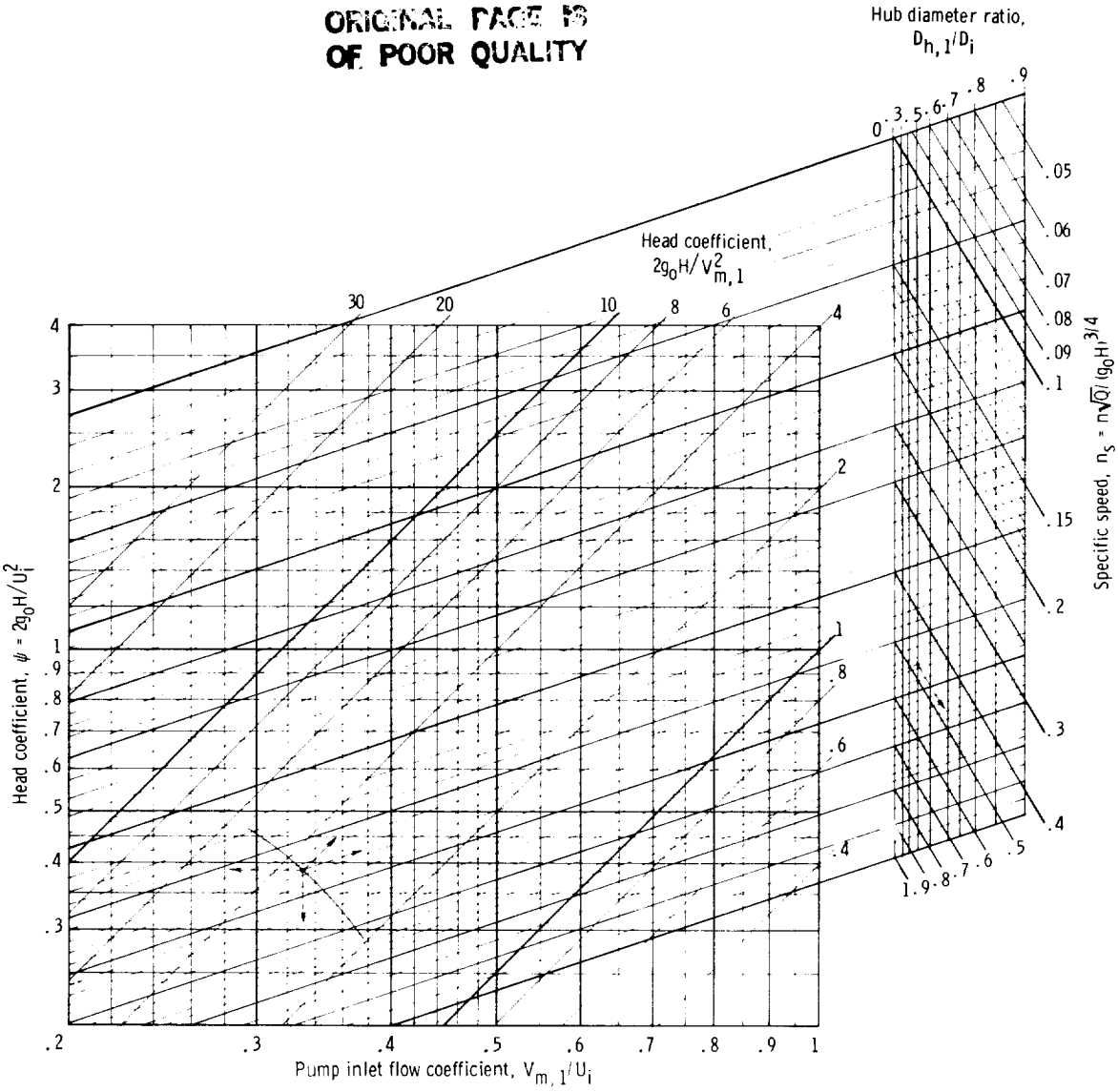

Figure 1-10.—Characteristic diagram for axial-flow turbomachinery. (See fig. 1-20 for notation.)

$V_{m,o}$ (see fig. 1-7). With this expression of Q, the basic specific speed assumes the form

$$n_s = \frac{nQ^{1/2}}{(g_oH)^{3/4}} = \frac{U_o}{D_o\pi}\frac{(V_{m,o}D_o\pi b_o)^{1/2}}{(g_oH)^{3/4}}$$

$$= \frac{2^{3/4}}{\pi^{1/2}}\left(\frac{U_o^2}{2g_oH}\right)^{3/4}$$

$$\times\left(\frac{V_{m,o}}{U_o}\right)^{1/2}\left(\frac{b_o}{D_o}\right)^{1/2} \qquad (1\text{-}28)$$

Instead of limiting this relation to impeller characteristics, one can examine the flow conditions in the stationary passages surrounding the outside diameter of the rotor (see fig. 1-11). Here $Q = V_{th}A_{th}$, where A_{th} is the total area (so-called throat area) of the stationary passages, that is, the total stationary vane passage area closest to the rotor. If the radial dimension of this passage is d_{th} and its average width normal to the meridional velocity is b_{th}, then $A_{th} = N\,d_{th}b_{th}$, where N is the number of stationary passages for one stage. Thus $N=1$ for a single volute, $N=2$ for a twin volute, and $N=10$ for 10 guide vanes.

Furthermore, from the law of constant angular

momentum,

$$V_{th} = V_{U,o} \frac{D_o}{D_{th}}$$

where D_{th} is the diameter corresponding to the distance of the centroid of the throat cross section from the axis of rotation (see fig. 1-11) and $V_{U,o}$ is the peripheral fluid velocity at the outside diameter D_o of the rotor (see fig. 1-7). With

$$Q = V_{th} A_{th} = V_{U,o} \frac{D_o}{D_{th}} A_{th}$$

and

$$n = \frac{U_o}{\pi D_o}$$

one finds

$$n_s = \frac{nQ^{1/2}}{(g_o H)^{3/4}} = \frac{U_o}{\pi D_o} \times \left(V_{U,o} \frac{D_o}{D_{th}} A_{th} \right)^{1/2} \frac{1}{(g_o H)^{3/4}}$$

$$= \frac{2^{3/4}}{\pi} \left(\frac{U_o^2}{2 g_o H} \right)^{3/4} \times \left(\frac{V_{U,o}}{U_o} \frac{D_o}{D_{th}} \frac{A_{th}}{D_o^2} \right)^{1/2} \qquad (1\text{-}29)$$

Assuming zero absolute rotation of the fluid at the low-pressure side of the rotor (i.e., $V_{U,i} = 0$), one can derive from Euler's turbomachinery equation (e.g. 2-18)) an equation for radial-flow pumps which is analogous to equation (1-11):

$$\psi_o = \frac{2 g_o H}{U_o^2} = 2 \eta_h \frac{V_{U,o}}{U_o} \qquad (1\text{-}30)$$

so that

$$\frac{V_{U,o}}{U_o} = \frac{1}{2 \eta_h} \frac{2 g_o H}{U_o^2}$$

Substituting this into equation (1-29) leads, for $V_{U,i} = 0$, to the relation

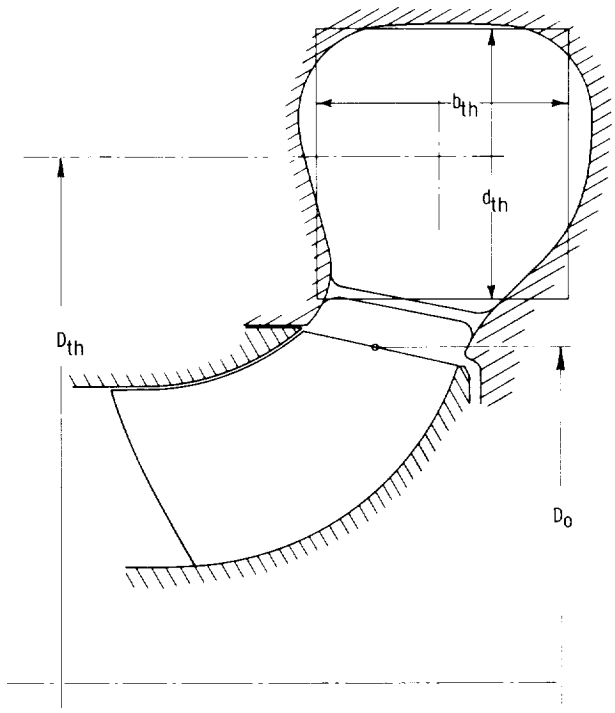

Figure 1-11.—Radial casing section defining notation. Throat area $A_{th} = d_{th} \times b_{th}$.

$$n_s = \frac{2^{1/4}}{\pi} \left(\frac{U_o^2}{2 g_o H} \right)^{1/4} \left(\frac{1}{\eta_h} \frac{D_o}{D_{th}} \frac{A_{th}}{D_o^2} \right)^{1/2} \qquad (1\text{-}31)$$

(For turbines $1/\eta_h$ is replaced by η_h.)

It is thus apparent that the basic specific speed, which is the dimensionless expression of the operating conditions n, Q, and H, can be translated into dimensionless design parameters in many ways, partly by changing the peripheral velocity of the rotor to which it refers and partly by changing the way in which the rate of volume flow Q is expressed in terms of the dimensions of and the velocities in the machine.

It should be obvious that the relations between equation (1-24) and the subsequent equations (1-28) and (1-29) are based on the condition of continuity of an incompressible fluid with the volume rate of flow Q considered constant throughout the machine.

Other generalizations are possible regarding, for example, the diameters D or peripheral velocities U of the solid rotating parts. The relation between

equations (1-25) and (1-26) is an example. This second type of generalization applies in principle to compressible as well as incompressible fluids. There is no reason to believe that the types of generalization mentioned here exhaust the possibilities for such relations between the basic specific speed (the operating conditions n, Q, and H) and the corresponding design parameters ($2g_oH/U^2$, V/U, and several ratios of linear dimensions).

Figure 1-8 shows examples of impeller profiles determined from equation (1-24) for the same head and capacity. It should be noted that the size of the rotor decreases rapidly with increasing basic specific speed. In the absence of other restrictions, one should thus select the maximum basic specific speed in order to minimize the size and, presumably, the cost of the machine for a given volume flow rate Q and head H.

In the commercial pump field, the most obvious upper limit in the speed of rotation stems from the restriction of standard electric motor speeds to 3600 rpm for 60 hertz, which frequently leads to very low basic specific speeds for pumps with low flow rates and fairly high head values. This restriction does not apply to steam or gas turbine drive or to geared drive. However, the most fundamental restrictions in the speed of rotation result from cavitation, compressibility effects, and centrifugal stresses in solid rotating parts. These restrictions are discussed in sections 1.2.2, 1.2.3, 1.3.2.1, 1.3.2.2., and 1.3.3.1.

There exist also practical lower limits for the specific speed per stage of a turbomachine, which result from excessive skin-friction and leakage losses. Figure 1-12 shows optimum values of the efficiencies of single-stage turbomachines (particularly pumps) as a function of the single-stage basic specific speed. These values represent so-called stage efficiencies (sometimes called bowl efficiencies), that is, they do not include losses due to ducting the flow to and from the active vane systems of the machine, which are of particular importance for single-stage machines with high specific speeds.

The efficiencies shown in figure 1-12, which gives specific speeds per stage, fall off significantly at the low end of the specific speed scale. Thus this drop in efficiency determines the specific speed of the entire unit where a change from a single-stage to a multistage pump may be appropriate. If this lower limit of specific speed per stage is applied to multistage units, it may also set, with a practical upper limit on the number of stages, a limit where transition from hydrodynamic machines to hydrostatic machines (positive-displacement machines) is appropriate.

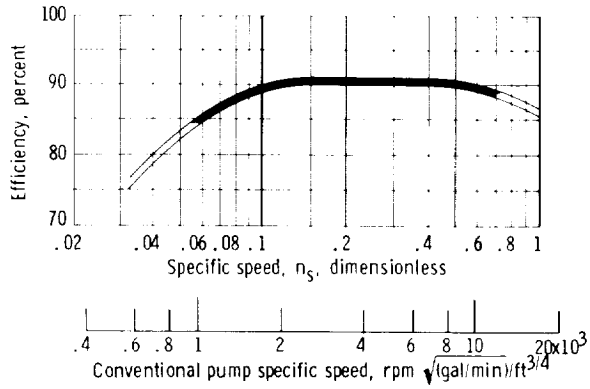

Figure 1-12.—Estimated optimum pump stage efficiencies.

In review, then, the relation of the fluid velocities V to the peripheral velocities U of the rotating parts, called the flow coefficient

$$\frac{V_{m,i}}{U_i} = \text{constant} \times \frac{Q}{D^3 n}$$

and the corresponding relation of velocities to the head of the machine

$$\psi = \frac{2g_oH}{U^2} = \text{constant} \times \frac{g_oH}{D^2n^2}$$

are related to the operating conditions n, Q, and H by eliminating the linear dimension, or diameter, D from $Q/D^3n = \text{constant}$ and $g_oH/D^2n^2 = \text{constant}$. The resulting dimensionless combination of operating conditions n, Q, and H is called the basic specific speed:

$$n_s = \frac{nQ^{1/2}}{(g_oH)^{3/4}} \tag{1-19}$$

The resulting similarity relation $n_s = \text{constant}$ supplements the relations $Q/D^3n = \text{constant}$ and $g_oH/D^2n^2 = \text{constant}$ (derived in the preceding sec. 1.1). The new relation defines the requirement of

similarity of flow in similar machines with respect to the operating conditions n, Q, and H only.

The three relations $Q/D^3n = \text{constant}$, $g_oH/D^2n^2 = \text{constant}$, and $n_s = nQ^{1/2}/(g_oH)^{3/4} = \text{constant}$, which result from similar flow in similar machines, are, of course, interdependent. Any two of these relations are sufficient to determine the third.

The application of the basic specific speed is usually limited to the values of n, Q, and H at which a particular machine has its best efficiency (see fig. 1-4). It is expected that this condition exists always under similar flow conditions, that is, at only one value of Q/D^3n (with effects of viscosity and compressibility disregarded). Thus there is only one basic specific speed at the best efficiency point associated with one class of geometrically similar machines, and it is called the specific speed of that form of machine.

The same basic specific speed at the best efficiency point can be achieved with machines of different geometric forms, but different basic specific speeds at the best efficiency point require corresponding differences in the geometric design form of the machines compared. Thus the basic specific speed at the best efficiency point, itself depending on operating conditions only, becomes an index of the design forms of turbomachines. Figures 1-8 and 1-9 show such relations. They are achieved analytically by substituting

$$n = \frac{U_o}{\pi D_o}$$

and

$$Q = \left(\frac{V_{m,i} D_i^2 \pi}{4}\right)\left(1 - \frac{D_h^2}{D_i^2}\right)$$

into the specific speed equation (eq. (1-19)). The resulting equations (eqs. (1-24) to (1-31)) establish relations between the dimensionless expression of the operating conditions n, Q, and H and design parameters such as diameter ratios like D_o/D_i, head coefficients of the general form $2g_oH/U^2$, and flow coefficients of the form V_m/U.

The head coefficients and flow coefficients together determine, under certain assumptions, the velocity vector diagrams that form the bases for the vane shapes of turbomachines.

The basic specific speed has a dramatic effect on the size of the impeller, as shown by the pump impeller profiles in figure 1-8. An increase in basic specific speed is, therefore, usually desirable. Such increases are necessarily connected with corresponding increases in the fluid velocities and in the peripheral velocities of the rotating parts. The limitations of the increases in velocities due to cavitation, compressibility of the fluid, and stresses in the solid parts of the machine are discussed in the following sections.

1.2.2 Cavitation Characteristics Described by Similarity Considerations

The first generalization of similarity considerations of turbomachinery going beyond the flow considerations outlined in sections 1.1 and 1.2.1 involves cavitation in turbomachinery handling liquids.

Cavitation is the local vaporization of a flowing liquid caused by local pressure reductions due to the dynamic action of the flowing liquid. The term cavitation usually also includes the subsequent condensation when the liquid moves from the low-pressure zone into a zone of higher pressure. However, the eroding effects (on the solid boundaries) of this condensation of vapor in a rapid stream of liquid should not be called cavitation but rather cavitation damage.

The formation and existence of cavitation voids (vapor- and gas-filled regions) can be related to the vapor pressure and the pressures in the flowing liquid in a reasonably straightforward fashion. This section does so on the basis of simple similarity considerations. The rate of cavitation damage is probably determined by the forces connected with the collapse of cavitation voids, rather than by the overall hydrodynamic behavior and design of the machine. Since only the latter are the principal subjects of this compendium, the complex problem of the forces connected with condensation in a rapidly moving stream of liquid is not considered. Also, these forces have not yet been described by simple similarity considerations.

The usual so-called classical assumption on the occurrence of cavitation states that cavitation takes place instantaneously whenever and wherever the local static pressure in the liquid drops to the vapor pressure of the liquid as given in its vapor tables (e.g., the familiar steam tables for water). Departures from this classical behavior are discussed in chapter 2, section 2.8. Although there are good reasons for such departures, it is nevertheless true that most liquids satisfy the

classical assumption very closely under most conditions existing in turbomachinery. The present analysis, using similarity considerations to describe cavitation, is carried out under the classical assumption, along with the assumption that the local temperature and vapor pressure of the liquid at the point of cavitation are known.

The occurrence of cavitation in turbomachines is usually described by means of a so-called net positive suction head NPSH, which is the total head above the vapor pressure at the low-pressure side of the machine outside the rotor. In this compendium, the NPSH is designated by H_{sv}, where H denotes total head (including the velocity head) and the subscript sv refers to suction and vapor pressure. Thus

$$H_{sv} = h_s + \frac{V_s^2}{2g_o} - \frac{p_v}{g_o \rho} \pm \Delta z \qquad (1\text{-}32)$$

where h_s is the static head equal to the static pressure divided by the weight per unit volume of the fluid $g_o\rho$, V_s is the fluid velocity at the place where h_s is measured, p_v is the vapor pressure (usually at the bulk temperature of the liquid), and Δz is the difference in elevation between the point where h_s and V_s are measured and the point of cavitation.

Whenever cavitation occurs somewhere in the machine, vapor pressure exists at that point in the machine. Thus H_{sv} is the difference in head between the point of cavitation and a convenient place on the suction side of the machine where the head h_s and the velocity V_s are measured. The difference in elevation Δz can be eliminated by converting h_s and thereby H_{sv} to the elevation of the point of cavitation (which may have to be estimated). If this is done, the head difference H_{sv} is controlled by inertial forces in the same sense as H and therefore, obeys the same laws of similarity as H or any other dynamic head difference in the machine. One may write for H_{sv}, then, the same similarity relations and dimensionless expressions as derived in sections 1.1 and 1.2.1 with respect to H and apply them to any other dynamic head or pressure difference in turbomachinery.

It is stated previously that H_{sv} is a head difference in the machine only if vapor pressure and thus cavitation exist somewhere in the machine. Therefore, H_{sv} is useful only in connection with cavitation and the observation of certain effects of cavitation.

The best method of observing cavitation is the optical method because, with experienced observers, it is the most sensitive method and because it discloses the location and form of the cavitation voids. The value of H_{sv} can be recorded in relation to the size, location, and form of the cavitation voids observed and thus assumes a definite meaning.

Obviously optical observation is possible only with specially equipped machines. As such machines are rarely available, it is customary to observe cavitation in turbomachines indirectly by its effect on the performance of the machine. Figure 1-13 shows the effect of cavitation on the head-capacity curve. In this figure, H_{sv} can be correlated definitely only with the maximum capacity achievable with a given (reduced) value of H_{sv}. The slight drop in performance that usually exists over the entire capacity range is difficult to measure by this method. For this reason, it is customary to test a machine at constant capacity Q and speed n and to observe other performance variables such as head, power, or efficiency as a function of H_{sv}. The value of H_{sv} is reduced in small steps from high values, where (because of the absence of cavitation) no effects are expected, to low values, where the performance deteriorates drastically. On a curve so obtained (fig. 1-14), one may then mark the H_{sv} value at which the first effects of cavitation are observed, that is, the value at which the first clear deviation from the horizontal (zero-effect) part of the curve occurs (point A), and one may consider this a safe lower limit of H_{sv} at the particular capacity Q and speed n of the test. (The actual safety of operation at this point is not assured, as

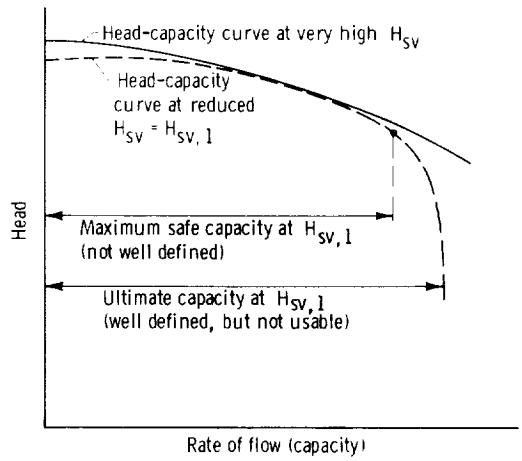

Figure 1-13.—Pump head-capacity curve under influence of cavitation.

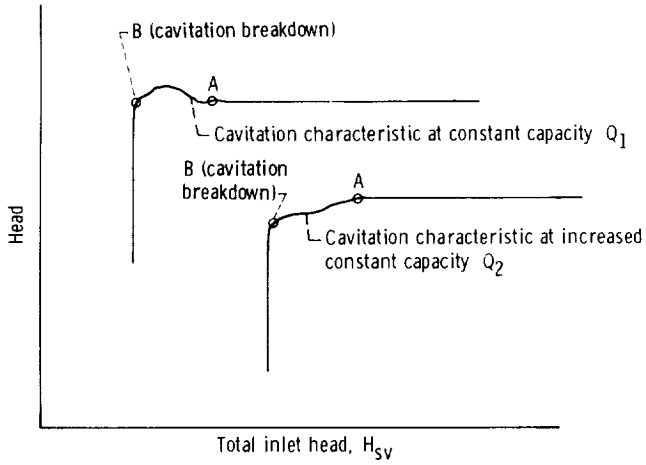

Figure 1-14.—Typical effects of cavitation on head of pump at two constant capacities and one constant speed of rotation.

local cavitation can be observed optically or acoustically well before cavitation has any effect on the performance of the machine (see also ch. 2, sec. 2.8).

Furthermore one may mark a second value of H_{sv} (point B) at which the performance begins to deteriorate very rapidly (cavitation breakdown), and one may consider this the ultimate lower limit of H_{sv}. Figure 1-15 shows results of an actual cavitation test of this type (performed by the Worthington Pump and Machinery Corp.) on an axial-flow pump which indicate that the initial effect of cavitation may be an increase, instead of the usual decrease, in head and power consumption. This phenomenon is not yet fully understood but is usually explained as being caused by a local reduction in skin friction at the onset of cavitation. An increase in head with the onset of cavitation is most frequently observed at capacities below that of the best efficiency point, where the flow has some tendency toward instabilities (separation, stall).

In figure 1-15, the total inlet head above the vapor pressure H_{sv} is made dimensionless by division by the total pump head H. This ratio, called the Thoma cavitation parameter σ_H, is one of the first methods of making H_{sv} dimensionless. Because the resulting changes in head and power are also plotted in dimensionless form, a set of cavitation curves of this form should not change with the speed of rotation or the absolute size of the machine if tests are performed under similar flow conditions (i.e., with geometrically similar machines at the same value of Q/nD^3 (see secs. 1.1 and 1.2.1)). If this type of dimensionless cavitation curve changes under supposedly similar flow conditions as a function of size or speed, one must

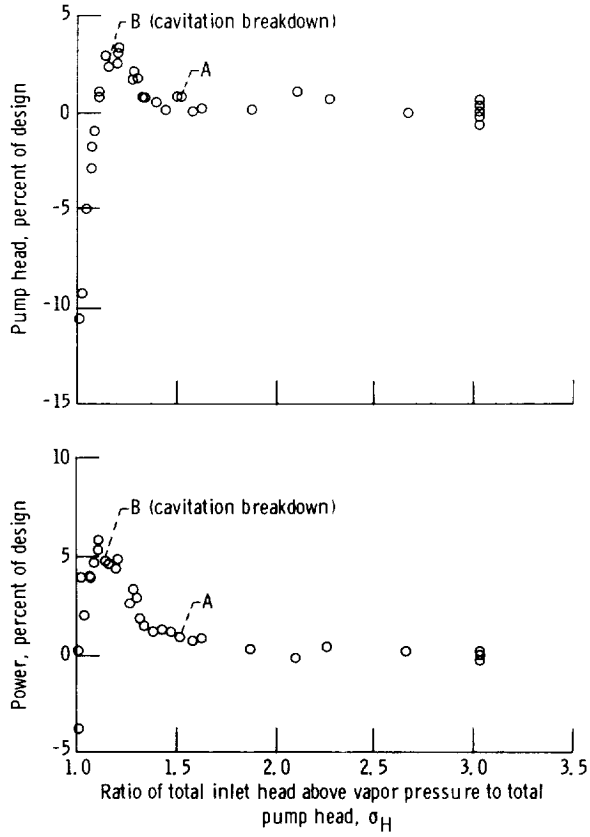

Figure 1-15.—Cavitation test points for axial-flow pump. Specific speed, 0.755.

conclude that the flow is not truly similar at the same σ_H. Such departures from similarity under conditions where the flow should be similar under the classical assumptions are called scale effects and are further discussed in chapter 2, section 2.8.

Besides using the Thoma cavitation parameter

$$\sigma_H = \frac{H_{sv}}{H} \tag{1-33}$$

one may introduce H_{sv} instead of H directly into the similarity parameters presented in sections 1.1 and 1.2.1. This yields the following sets of ratios:

$$\left.\begin{array}{l} \dfrac{2g_o H_{sv}}{U^2} \\ \text{or} \\ \dfrac{g_o H_{sv}}{n^2 D^2} \end{array}\right\} \tag{1-34}$$

and

$$\left.\begin{array}{l} \dfrac{2g_o H_{sv}}{V^2} \\ \text{or} \\ \dfrac{g_o H_{sv} D^4}{Q^2} \end{array}\right\} \tag{1-35}$$

The flow coefficient, or dimensionless capacity,

$$\left.\begin{array}{l} \varphi = \dfrac{V_m}{U} \\ \text{or the ratio} \\ \dfrac{Q}{nD^3} \end{array}\right\} \tag{1-13}$$

is, of course, identical to that used previously. In the very same manner as described in section 1.2.1, the dimensionless capacity $Q/D^3 n$ can be combined with either expression (1-34) or (1-35) to eliminate the linear dimension D and, thus, obtain the so-called suction specific speed:

$$S = \frac{nQ^{1/2}}{(g_o H_{sv})^{3/4}} \tag{1-36}$$

Any fixed value of the suction specific speed (S = constant) describes all suction operating conditions (n, Q, and H_{sv}) that can be satisfied by similar flow and cavitation conditions in geometrically similar suction passages of turbomachines. (Compare this definition with that of the basic specific speed given with eq. (1-19).)

The dimensionless expressions (1-34) and (1-35) of H_{sv} are found in the field of cavitation to be even more important than the corresponding expressions of the head of the machine H, which are discussed in sections 1.1.2 and 1.2.1. With respect to cavitation, these expressions and the flow coefficient φ are usually used in connection with the velocities $V_{m,i}$ and U_i, because these velocities exist on the low-pressure side of the rotor, where cavitation is expected to start.

Figures 1-16 and 1-17 show the inception value (curve A) as well as the breakdown value (curve B) of H_{sv} in its two nondimensional forms $2gH_{sv}/V_{m,i}^2$ and $2gH_{sv}/U_i^2$ plotted against the flow coefficient $V_{m,i}/U_i$. Generally the minimum value of $2gH_{sv}/V_{m,i}^2$ (i.e., the condition where the disturbing effect of the rotating vanes is a minimum) coincides with the flow coefficient of the best efficiency point, although one can design for departures from this rule if desired. Nevertheless these plots, like plots of airfoil characteristics, particularly pressure distributions, clearly show an optimum in performance as a function of the direction of the relative flow in relation to its design direction.

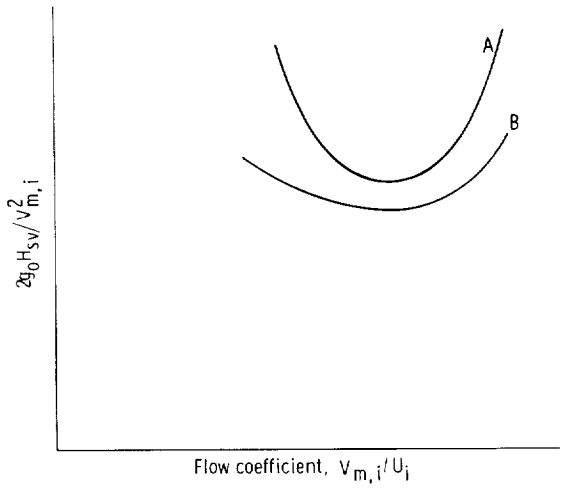

Figure 1-16.—Cavitation characteristics of centrifugal pump made dimensionless by means of $V_{m,i}^2$ and U_i.

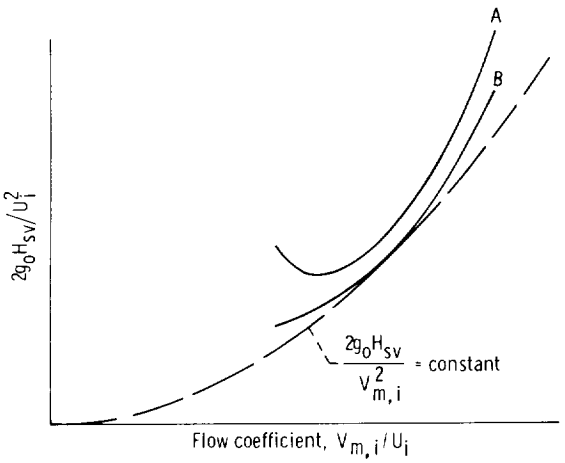

Figure 1-17.—Cavitation characteristics of centrifugal pump made dimensionless by means of U_i^2 and U_i.

It is desirable to investigate the behavior of individual elements of turbomachines, particularly their vanes, relative to the pressure distribution and the resulting cavitation performance as a function of the angle of attack. This was done in water tunnels, and a remarkably good correlation between the changes in theoretical pressure distribution and corresponding changes in the optically observed cavitation performance was obtained, particularly regarding the onset of cavitation.

During these investigations it was desirable to define a cavitation number that is independent of the particular conditions existing in turbomachines. This number is

$$\sigma_p = \frac{p - p_v}{\rho V^2/2} \tag{1-37}$$

where p is the static pressure in the flow, measured on a surface parallel to the flow away from the influence of the tested body (vane or airfoil), p_v is the vapor pressure in the flowing liquid, ρ is the mass per unit volume of the liquid, and V is the free-stream velocity relative to the tested body, measured at the same place as p. Obviously σ_p is included in the classical assumption of cavitation and is equal to the minimum pressure coefficient of the object tested, defined as

$$C_{p,min} = \frac{p - p_{min}}{\rho V^2/2} \tag{1-38}$$

In terms used in the turbomachinery field, this cavitation coefficient assumes the form

$$\sigma_p = \frac{h_{sv}}{\rho w_i^2/2} \tag{1-39}$$

where h_{sv} is the static head above the head corresponding to the vapor pressure. Hence

$$h_{sv} = H_{sv} - \frac{V^2}{2g_o} \tag{1-40}$$

where V is the local velocity of flow at the point where h_{sv} and H_{sv} are being measured or evaluated. At the low-pressure side of the rotor

$$H_{sv} = \frac{V_i^2}{2g_o} + \sigma_p \frac{w_i^2}{2g_o} \tag{1-41}$$

(see fig. 1-7).

Since V_i is a local fluid velocity, it cannot be related directly to a rate of flow and a cross section of the machine. To achieve this relation, one has to use average velocities defined by some simple relations, primarily the condition of continuity and perhaps a conclusion from a prescribed angular momentum. Defining V_i by the equation $V_i^2 = V_{U,i}^2 + V_{m,i}^2$, one can obtain the desired relation by determining an average $V_{m,i}$ from the condition of continuity and $V_{U,i}$ from the angular momentum that the flow is intended to have at the cross section considered.

However, V_i so defined does not include flow losses, in particular the existence of a boundary layer on the walls of the space of revolution in which V_i is defined. To consider this, one introduces a correction factor C_1 which takes into account nonuniformities in the velocity distribution in the low-pressure passage of the rotor as well as pressure losses between this passage and the section where h_{sv} and H_{sv} are being measured. With this correction factor, equation (1-41) appears in the form

$$H_{sv} = C_1 \frac{V_i^2}{2g_o} + \sigma_p \frac{w_i^2}{2g_o} \tag{1-42}$$

The suction specific speed can be related to certain design and flow parameters in the same manner as the basic specific speed n_s of the machine (in sec. 1.2.1). The expression exactly corresponding to equation (1-24) is

$$S=\frac{nQ^{1/2}}{(g_oH_{sv})^{3/4}}=\frac{1}{2^{1/4}\pi^{1/2}}\left(\frac{U^2}{2g_oH_{sv}}\right)^{3/4}$$
$$\times\left(\frac{V_{m,i}}{U_i}\right)^{1/2}\left(\frac{D_i}{D}\right)^{3/2}\left(1-\frac{D_h^2}{D_i^2}\right)^{1/2} \quad (1\text{-}43)$$

With $D=D_o$ and $U=U_o$, this relation is not as useful as the corresponding relation for the basic specific speed (eq. (1-24)), because H_{sv} is not as directly related to U_o as the total head H of the machine (or stage). Rather, H_{sv} may be related to the peripheral rotor velocity in the low-pressure passage (for pumps, the inlet), which is $U_i=U(D_i/D)$. Substituting this into equation (1-43) leads to

$$S=\frac{nQ^{1/2}}{(g_oH_{sv})^{3/4}}=\frac{1}{2^{1/4}\pi^{1/2}}\left(\frac{U_i^2}{2g_oH_{sv}}\right)^{3/4}$$
$$\times\left(\frac{V_{m,i}}{U_i}\right)^{1/2}\left(1-\frac{D_h^2}{D_i^2}\right)^{1/2} \quad (1\text{-}44)$$

Further analysis of the cavitation behavior of turbomachines shows that $2g_oH_{sv}/U_i^2$, corresponding to the head coefficient ψ_i, is not the most useful suction head coefficient. Instead, the head coefficient referred to the absolute inlet velocity $2g_oH_{sv}/V_i^2$ (as used in sec. 1.2.1, eq. (1-27)) is very significant. With this coefficient, equation (1-44) assumes the form

$$S=\frac{nQ^{1/2}}{(g_oH_{sv})^{3/4}}=\frac{1}{2^{1/4}\pi^{1/2}}\left(\frac{V_i^2}{2g_oH_{sv}}\right)^{3/4}$$
$$\times\left(\frac{V_{m,i}}{V_i}\right)^{3/2}\frac{U_i}{V_{m,i}}\left(1-\frac{D_h^2}{D_i^2}\right)^{1/2} \quad (1\text{-}45)$$

It is evident that this expression may also be written in the form

$$S=\frac{1}{2^{1/4}\pi^{1/2}}\left(\frac{V_{m,i}^2}{2g_oH_{sv}}\right)^{3/4}$$
$$\times\frac{U_i}{V_{m,i}}\left(1-\frac{D_h^2}{D_i^2}\right)^{1/2} \quad (1\text{-}46)$$

As demonstrated in section 1.2.1, the relation of a dimensionless expression of an operating condition, such as n_s or S, to design and flow parameters can assume many different forms depending on the parameters that are considered most useful. Equations (1-43) to (1-46) demonstrate this fact with respect to the suction specific speed. Other forms for the suction specific speed can readily be obtained.

For example, with respect to cavitation, the relative velocity on the low-pressure side of the rotor may well be of major importance. The velocity diagrams shown in figure 1-7 indicate that

$$w_i^2=(U_i-V_{U,i})^2+V_{m,i}^2=U_i^2$$
$$-2U_iV_{U,i}+V_{U,i}^2+V_{m,i}^2$$

Hence

$$\frac{w_i^2}{U_i^2}=1-2\frac{V_{U,i}}{U_i}+\frac{V_{U,i}^2}{U_i^2}+\frac{V_{m,i}^2}{U_i^2} \quad (1\text{-}47)$$

Obviously equation (1-44) can be written in the form

$$S=\frac{1}{2^{1/4}\pi^{1/2}}\left(\frac{w_i^2}{2g_oH_{sv}}\right)^{3/4}$$
$$\times\left(\frac{U_i}{w_i}\right)^{3/2}\left(\frac{V_{m,i}}{U_i}\right)^{1/2}\left(1-\frac{D_h^2}{D_i^2}\right)^{1/2} \quad (1\text{-}48)$$

Substituting for U_i/w_i from equation (1-47) yields

$$S=\frac{1}{2^{1/4}\pi^{1/2}}\left(\frac{w_i^2}{2g_oH_{sv}}\right)^{3/4}$$
$$\times\frac{(V_{m,i}/U_i)^{1/2}(1-D_h^2/D_i^2)^{1/2}}{[1-2(V_{U,i}/U_i)+V_{U,i}^2/U_i^2+V_{m,i}^2/U_i^2]^{3/4}} \quad (1\text{-}49)$$

which may be of considerable value since, according to equation (1-42),

$$\frac{2g_oH_{sv}}{w_i^2}=C_1\frac{V_i^2}{w_i^2}+\sigma_p \quad (1\text{-}50)$$

Thus $w_i^2/2g_oH_{sv}$ is calculable for given velocity diagrams (see fig. 1-18).

The general combination of equation (1-42) with the specific speed equations involves the following steps:

$$\frac{2g_oH_{sv}}{U_i^2}=C_1\frac{V_i^2}{U_i^2}+\sigma_p\frac{w_i^2}{U_i^2} \quad (1\text{-}50a)$$

and $V_i^2 = V_{U,i}^2 + V_{m,i}^2$, according to the velocity diagrams in figure 1-7. Hence combining the last expressions with equation (1-47) gives

$$\frac{2g_o H_{sv}}{U_i^2} = C_1\left(\frac{V_{U,i}^2}{U_i^2} + \frac{V_{m,i}^2}{U_i^2}\right) + \sigma_p\left(1 - 2\frac{V_{U,i}}{U_i} + \frac{V_{U,i}^2}{U_i^2} + \frac{V_{m,i}^2}{U_i^2}\right)$$

or

$$\frac{2g_o H_{sv}}{U_i^2} = (C_1 + \sigma_p)\left(\frac{V_{U,i}^2}{U_i^2} + \frac{V_{m,i}^2}{U_i^2}\right) + \sigma_p\left(1 - 2\frac{V_{U,i}}{U_i}\right)$$

By substitution of the last expression into equation (1-44), one obtains

$$S = \frac{1}{2^{1/4}\pi^{1/2}} \times \frac{(V_{m,i}/U_i)^{1/2}(1 - D_h^2/D_i^2)^{1/2}}{\left\{(C_1 + \sigma_p)(V_{U,i}^2/U_i^2 + V_{m,i}^2/U_i^2) + \sigma_p[1 - 2(V_{U,i}/U_i)]\right\}^{3/4}} \tag{1-50b}$$

For zero prerotation (i.e., $V_{U,i} = 0$), equation (1-50b) reduces to

$$S = \frac{1}{2^{1/4}\pi^{1/2}} \times \frac{(V_{m,i}/U_i)^{1/2}(1 - D_h^2/D_i^2)^{1/2}}{[(C_1 + \sigma_p)V_{m,i}^2/U_i^2 + \sigma_p]^{3/4}} \tag{1-50c}$$

and equation (1-49) assumes the form

$$S = \frac{1}{2^{1/4}\pi^{1/2}}\left(\frac{w_i^2}{2g_o H_{sv}}\right)^{3/4} \times \frac{(V_{m,i}/U_i)^{1/2}(1 - D_h^2/D_i^2)^{1/2}}{(1 + V_{m,i}^2/U_i^2)^{3/4}} \tag{1-49a}$$

which follows in this case immediately from $w_i^2 = U_i^2 + V_{m,i}^2$.

It should be clear that equations (1-43) to (1-50c) and (1-49a) represent simultaneous and interdependent relations. Figure 1-18 represents these relations in one diagram for $V_{U,i} = 0$ and $C_1 = 1.1$. For any particular value of C_1 and of σ_p, the suction specific speed reaches a maximum at one particular flow coefficient. This relation changes relatively little with moderate rotation of the absolute flow on the suction side of the rotor.

It may be of interest to review briefly the way in which the concept of suction specific speed was originally developed in the United States (the earlier derivation by Bergeron in France was not published and is therefore not known to this writer). This part of section 1.2.2 is not used later and may therefore be skipped in reading this chapter.

It is stated previously that the Thoma parameter $\sigma_H = H_{sv}/H$ was the first widely used, dimensionless expression of H_{sv} (or NPSH). This parameter is known to be constant for similar flow and cavitation conditions in similar turbomachines, which means that it can be the same for machines of the same basic specific speed (although it does not necessarily have to be the same, as the same basic specific speed can be achieved by machines of dissimilar designs and flow conditions). It was thus natural to ask in which way σ_H would change with changing basic specific speed. This question implied a comparison between dissimilar turbomachines. It had always been empirically known that the value of σ_H required for satisfactory performance increases with increasing specific speed, but an analytical relation was not known.

A solution of this problem was obtained by the assumption that in the field of low and medium

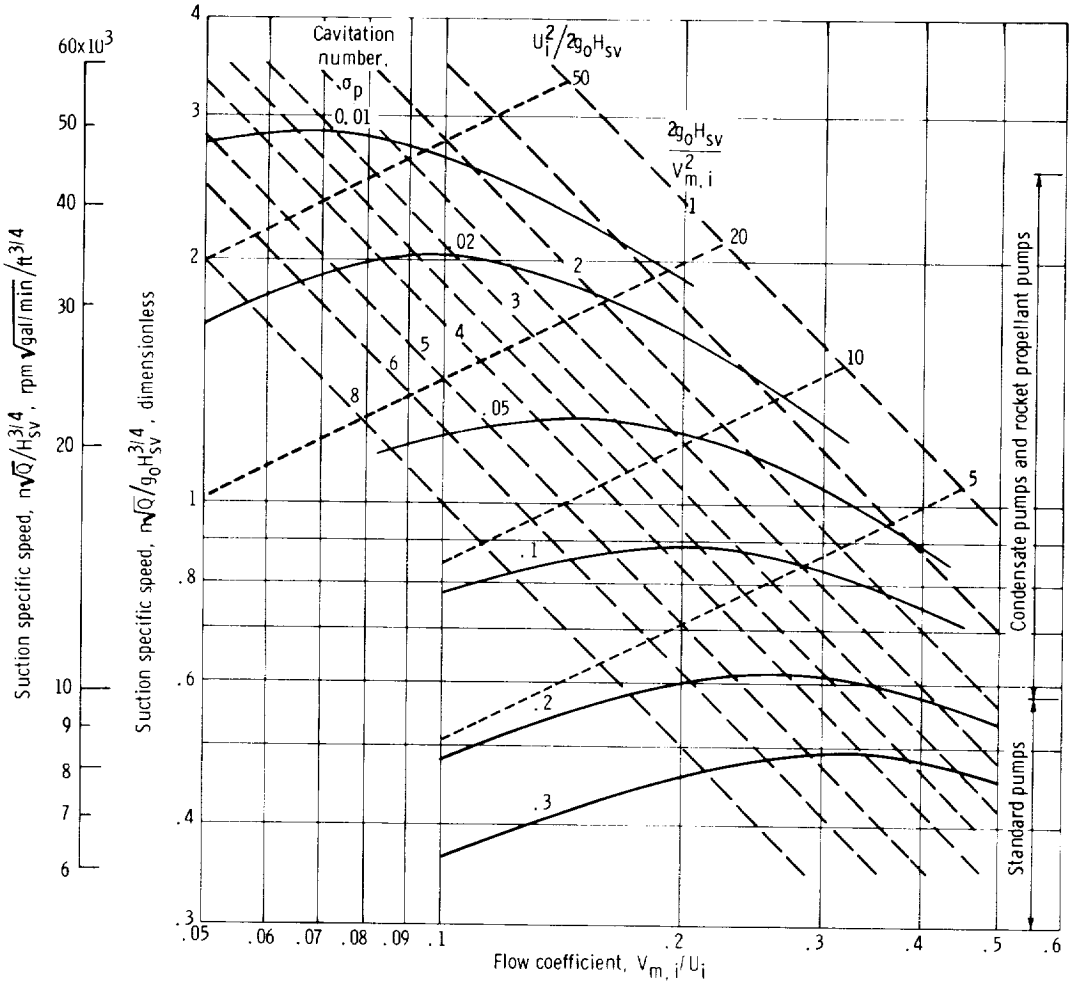

Figure 1-18.—Relations among cavitation parameters of turbomachinery. Meridional velocity, $V_{m,i}$; relative velocity, w_i; rotor velocity at periphery of low-pressure passage of rotor, U_i (peripheral fluid velocity at this point is zero); curves of constant cavitation number σ_p derived from $H_{sv} = C_1(V_{m,i}^2/2g_o) + \sigma_p(w_i^2/2g_o)$ with $C_1 = 1.1$.

specific speeds the low-pressure and high-pressure sides of the machine, particularly of its rotor, can be considered and changed independently of each other and that the head H is determined primarily by the high-pressure side and H_{sv} primarily by the low-pressure side. If this is true, H can be changed without changing the required H_{sv}. Thus H_{sv} is independent of H when the basic specific speed is changed by changing only the high-pressure side of the rotor (say, its outside diameter).

The unknown functional relation between σ_H and n_s was hypothetically written in the form

$$\sigma_H = \text{constant} \times n_s^{\chi}$$

where χ is an unknown exponent. Explicitly

$$\frac{H_{sv}}{H} = \text{constant} \times \left[\frac{n\sqrt{Q}}{(g_oH)^{3/4}}\right]^{\chi}$$

Hence

$$H_{sv} = \text{constant} \times H\left[\frac{n\sqrt{Q}}{(g_oH)^{3/4}}\right]^{\chi} \qquad (1\text{-}51)$$

For H_{sv} not to change with H requires that H cancel out of this expression, which is possible only when $\chi = 4/3$. Then equation (1-51) assumes the form

$$H_{sv} = \text{constant} \times \frac{(n\sqrt{Q})^{4/3}}{g_o}$$

and, therefore,

$$\frac{(n\sqrt{Q})^{4/3}}{g_o H_{sv}} = \text{constant}$$

which is readily recognized as the 4/3 power of the suction specific speed (eq. (1-36)).

A test of the general validity of this reasoning was obtained by plotting the σ_H values of commercial pumps with satisfactory performance with respect to cavitation against the basic specific speed (fig. 1-19). This plot shows remarkably good agreement between the data points and the direction of the lines for constant suction specific speed S. This agreement even persists into the field of high specific speeds, where the previously mentioned separation between the high-pressure and low-pressure parts of the rotor cannot be generally accepted. On the basis of this empirical evidence, it has become customary to regard the suction specific speed S as independent of the basic specific speed n_s. This particular view of S cannot generally be valid, however, because dimensionless expressions of operating conditions, such as S, should be functions of the specific speed, that is, of the general design form of the machine concerned.

According to figure 1-19, the suction specific speeds of commercial pumps are limited to values below 0.7 (12 000 in dimensional form). This is not generally true, as condensate pumps are regularly used up to $S = 1.75$ (30 000), which permits considerable local cavitation. Rocket propellant pumps with special inducers are used up to about $S = 2.5$ (43 000), and for liquid hydrogen much higher values have been achieved. Again, such pumps operate with considerable local cavitation but without excessive detrimental effects on their efficiency. However, one cannot assume that the points plotted in figure 1-19 represent truly cavitation-free performance. Most points for suction specific speeds over 0.4 (7000) represent operation with some local cavitation but without significant detrimental effects on hydrodynamic performance (efficiency). Nevertheless the existence of local cavitation can be important with respect to cavitation damage.

In this compendium, the suction specific speed S, like the basic specific speed n_s, is derived and used in dimensionless form, with n measured in rps, Q in cubic feet per second, and H in feet, and with H

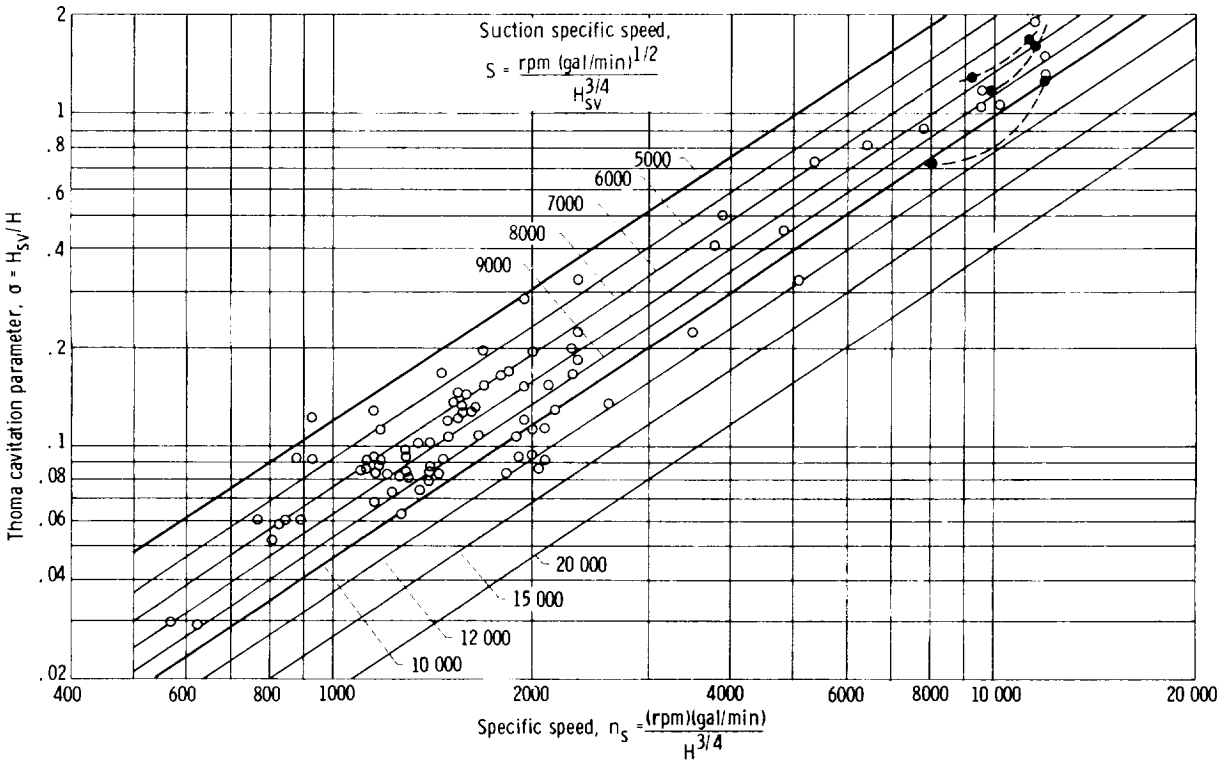

Figure 1-19.—Points of acceptable pump performance with respect to cavitation. For total pump head H for multistage pumps, only first stage is considered; total inlet head H_{sv} above vapor pressure of fluid pumped is referred to centerline of impeller; for double suction pumps, one-half of total capacity of pump is used for calculating n_s and S.

multiplied by $g_o = 32.2$ feet per second squared. Any other consistent system of units gives the same values for S. The relation of the conventional suction specific speed to the dimensionless S is, of course, the same as that given by equation (1-21) for the basic specific speed:

$$\frac{n(\text{rpm})[Q(\text{gal/min})]^{1/2}}{[H_{sv}(\text{ft})]^{3/4}} = 17\,200\,S \qquad (1\text{-}52)$$

1.2.3 General Relations Between Dimensionless Operating Conditions and Design Parameters

In the preceding sections 1.2.1 and 1.2.2, dimensionless expressions of the operating conditions n, Q, H, and H_{sv} are derived in the form of the basic specific speed $n_s = nQ^{1/2}/(g_o H)^{3/4}$ and the suction specific speed $S = nQ^{1/2}/(g_o H_{sv})^{3/4}$. These dimensionless operating conditions are related to combinations of dimensionless flow and design parameters (eqs. (1-24) to (1-31) and (1-43) to (1-50c)).

Certainly n, Q, H, and H_{sv} are not sufficient to describe the operating conditions of turbomachines in general. Additional variables are required to describe the operating conditions relative to compressibility, viscosity, stresses in the solid parts, accelerations of the entire machine (such as gravitational acceleration), vibrations of the machine, and probably others.

There are various ways in which these additional variables can be taken into account. One way, analogous to forming the Thoma cavitation parameter ($\sigma_H = H_{sv}/H$), is to form dimensionless ratios of the variables describing the additional phenomena to one of the variables already used in similarity relations, such as the head of the machine H. For example, similarity with respect to compressibility would be satisfied if the head H of the machine had a constant ratio to an enthalpy difference expressing the compressibility of the gas. An expression of this type, corresponding to the Thoma cavitation parameter $\sigma_H = H_{sv}/H$, is

$$\frac{a^2}{g_o H} = \text{constant} \qquad (1\text{-}53)$$

where a is the velocity of sound at some point in the machine. Of course, other forms of this expression can serve as well, for example, one in terms of a head Mach number $\sqrt{g_o H}/a$.

Instead of proceeding in this manner, this presentation uses the principle involved in forming the suction specific speed. With respect to compressibility, one can form a compressibility specific speed $n_a = nQ^{1/2}/a^{3/2}$, since $nQ^{1/2}$ is already recognized as the 3/2 power of a velocity representing the rate of rotation as well as the rate of flow of the machine. The compressibility specific speed can also be derived in the same manner as the basic specific speed by eliminating the linear dimension D, that is, by combining Q/nD^3 = constant with a suitable dimensionless ratio involving the new variable to be considered, such as a/nD or aD^2/Q. For instance,

$$\frac{Q}{nD^3}\frac{n^3D^3}{a^3} = \frac{n^2Q}{a^3}$$

or, written in the same form as other specific speeds,

$$n_a = \frac{nQ^{1/2}}{a^{3/2}} \qquad (1\text{-}53a)$$

The compressibility specific speed n_a is defined as that combination of operating conditions which, if held constant, permits similar flow of a compressible fluid in geometrically similar turbomachines provided that the specific speed is also held constant. Since the volume rate of flow Q changes for a compressible fluid within the machine, Q must obviously be measured in similarly located cross sections of the machines compared. It is customary to use the volume rate of flow on the low-pressure side of the machine (inlet for compressors, discharge for turbines) and to compute ρ for the stagnation conditions of this stream.

The speed $n_a^{2/3}$ may be written as a generalized Mach number of the form $(nQ^{1/2})^{2/3}/a$. Thus the equation n_a = constant is a generalization of the previously mentioned condition of similarity that the effects of compressibility are the same if the Mach number at geometrically similar locations has the same value. The condition n_a = constant has the advantage that n_a can be calculated before any specific information is available on the design of the machine.

Setting

$$n = \frac{U_o}{\pi D_o}$$

and

$$Q = V_{m,i}\frac{D_i^2\pi}{4}\left(1 - \frac{D_h^2}{D_i^2}\right)$$

one finds in the same manner as for the basic specific speed

$$n_a = \frac{nQ^{1/2}}{a^{3/2}} = \frac{1}{2\pi^{1/2}}\left(\frac{U_o}{a}\right)^{3/2}\left(\frac{D_i}{D_o}\right)^{3/2} \times \left(\frac{V_{m,i}}{U_i}\right)^{1/2}\left(1-\frac{D_h^2}{D_i^2}\right)^{1/2} \tag{1-54}$$

or, for the suction side of the rotor (inlet of compressor rotors),

$$n_a = \frac{1}{2\pi^{1/2}}\left(\frac{U_i}{a}\right)^{3/2}\left(\frac{V_{m,i}}{U_i}\right)^{1/2} \times \left(1-\frac{D_h^2}{D_i^2}\right)^{1/2} \tag{1-55}$$

Of course, a Mach number based on the fluid velocity may be used in the right side of equation (1-54) instead of one based on the peripheral velocity of the rotor. For example, when the meridional fluid velocity $V_{m,i}$ is used,

$$n_a = \frac{nQ^{1/2}}{a^{3/2}} = \frac{1}{2\pi^{1/2}}\left(\frac{V_{m,i}}{a}\right)^{3/2} \times \left(\frac{U_i}{V_{m,i}}\right)\left(1-\frac{D_h^2}{D_i^2}\right)^{1/2} \tag{1-56}$$

The Mach number usually considered critical is that of the relative fluid velocity w entering a rotor vane system. It is considered in this section with respect to a compressor or fan. The applicable relations are the same as those derived in section 1.2.2 for the suction specific speed. Specifically, equation (1-49) appears in the form

$$n_a = \frac{nQ^{1/2}}{a^{3/2}} = \frac{1}{2\pi^{1/2}}\left(\frac{w_i}{a}\right)^{3/2} \times \frac{(V_{m,i}/U_i)^{1/2}(1-D_h^2/D_i^2)^{1/2}}{\left[1-2(V_{U,i}/U_i)+V_{U,i}^2/U_i^2+V_{m,i}^2/U_i\right]^{3/4}} \tag{1-57}$$

where the notation is that given by figure 1-7.

For zero prerotation with $V_{U,i}=0$,

$$n_a = \frac{nQ^{1/2}}{a^{3/2}} = \frac{1}{2\pi^{1/2}}\left(\frac{w_i}{a}\right)^{3/2} \times \frac{(V_{m,i}/U_i)^{1/2}(1-D_h^2/D_i^2)^{1/2}}{(1+V_{m,i}^2/U_i^2)^{3/4}} \tag{1-58}$$

which corresponds to equation (1-49a).

Viscous forces can be introduced in the form of a viscous shear stress given by

$$\tau = \text{constant} \times \mu\frac{U}{D} = \text{constant} \times \mu\frac{nD}{D} = \text{constant} \times \mu n$$

Its ratio to inertial forces may be written in the form

$$\frac{\mu n}{\rho n^2 D^2} = \frac{\nu}{nD^2}$$

which is obviously the reciprocal of a Reynolds number. In such an expression, one might also use the head H of the machine to obtain the form

$$\frac{\mu n}{\rho g_o H} = \frac{n\nu}{g_o H}$$

which is the reciprocal of a head Reynolds number and is analogous to the Thoma parameter $\sigma_H = H_{sv}/H$ in the cavitation field.

One can also form a viscosity specific speed by eliminating D from ν/nD^2 and Q/nD^3:

$$n_\nu = \frac{n^{1/4}Q^{1/2}}{\nu^{3/4}} = \frac{nQ^{1/2}}{(n\nu)^{3/4}} \tag{1-59}$$

This equation is dimensionally correct because the kinematic viscosity ν has the dimensions L^2/T, so that $n\nu$ has the dimensions L^2/T^2, like $g_o H$.

A constant value of the viscosity specific speed n_ν permits similar flow of a viscous fluid in similar turbomachines provided that the basic specific speed n_s is also held constant.

The relation with flow and design parameters is obtained in exactly the same manner as those for other specific speeds:

$$n_\nu = \frac{nQ^{1/2}}{(n\nu)^{3/4}} = \frac{\pi^{1/4}}{2}\left(\frac{U_o D_o}{\nu}\right)^{3/4}\left(\frac{D_i}{D_o}\right)^{3/2} \times \left(\frac{V_{m,i}}{U_i}\right)^{1/2}\left(1-\frac{D_h^2}{D_i^2}\right)^{1/2} \tag{1-60}$$

or

$$n_\nu = \frac{\pi^{1/4}}{2}\left(\frac{U_i D_i}{\nu}\right)^{3/4}\left(\frac{V_{m,i}}{U_i}\right)^{1/2} \times\left(1-\frac{D_h^2}{D_i^2}\right)^{1/2} \qquad (1\text{-}61)$$

If it is more desirable to refer the Reynolds number to the meridional velocity $V_{m,i}$ than to the peripheral velocity U_o or U_i of the rotor, the viscosity specific speed may be related to flow and design parameters in the following manner:

$$n_\nu = \frac{nQ^{1/2}}{(n\nu)^{3/4}} = \frac{\pi^{1/4}}{2}\left(\frac{V_{m,i}D_i}{\nu}\right)^{3/4} \times\left(\frac{U_i}{V_{m,i}}\right)^{1/4}\left(1-\frac{D_h^2}{D_i^2}\right)^{1/2} \qquad (1\text{-}62)$$

The foregoing modifications of similarity relations cover the fluid-dynamic aspects of the problem. The basic operating conditions n, Q, and H are considered in terms of the basic specific speed and other similarity relations given in section 1.2.1. Also considered are departures from the basic flow conditions due to cavitation (in sec. 1.2.2) and due to compressibility and viscosity (in this section). In general, two conditions have to be satisfied by the operating conditions to have similar flow in similar machines, one with respect to the basic flow (n_s = constant) and another with respect to each of the departures from the ideal conditions (e.g., S = constant or σ_H = constant with respect to cavitation, n_a = constant or $\sqrt{g_o H}/a$ = constant with respect to compressibility, and n_ν = constant or $g_o H/\nu n$ = constant with respect to viscosity).

It is significant that the various conditions of similarity with respect to departures from the basic relation n_s = constant do not all have to be satisfied at the same time. Certainly the requirement of similarity with respect to cavitation (S = constant) does not have to be satisfied simultaneously with the requirement of similarity with respect to compressibility of gases (n_a = constant) as these generally apply to different kinds of fluids (the former to fluids capable of vaporization (liquids) and the latter to fluids subjected to major changes in volume (gases)). Thus only one, S = constant or n_a = constant, needs to be satisfied at a time.

Fortunately the viscosity of the fluid is rarely important with respect to turbomachinery, because the flow is usually fully turbulent, so that the shear forces (i.e., fluid friction forces) follow the same law as other inertial forces in the machine. Thus these forces can be included in the treatment of other hydrodynamic forces in the machine. Therefore it is usually not necessary to consider the condition n_ν = constant separately in similarity considerations on turbomachinery, and this condition is usually neglected.

In addition to fluid-dynamic relations, it is of equal importance to consider some purely mechanical relations, that is, relations involving the mechanics of the solid parts of the machine.

First consideration must be given to the mechanical steady-state stresses in the solid parts. For reasons of similarity, such stresses are proportional to the loads per unit area applied to the structure. Hence any stresses generated by the fluid in the solid parts of the machine are proportional to the fluid-dynamic pressure differences applied to these parts. For example, the bending stresses in turbomachinery blades are proportional to the fluid-dynamic pressure differences applied to these blades. (The distribution of these pressure differences does not change under similar flow conditions.)

This similarity of stresses in solid parts to pressure differences in the fluid goes farther than this. Centrifugal stresses σ_c are proportional to $\rho_s U^2$, where ρ_s is the mass per unit volume of the solid parts of the machine. It is shown in section 1.3.3 that the ratio $\sigma_c/\rho_s U^2$ depends primarily on the dimensionless geometric configuration of the rotating part. For example, $\sigma_c/\rho_s U^2 = 1$ applies to a thin freely rotating hoop. For a radial strut of constant cross section, the maximum stress at the axis of rotation is given by the ratio $\sigma_c/\rho_s U^2 = 0.5$. Thus all steady-state stresses in similar solid parts are (under similar flow conditions) proportional to the dynamic pressure differences in the machine, as they follow the same law, modified by the specific mass ratio between the structural material and the fluid:

$$\sigma_c = \text{constant} \times \left(\frac{\rho_s}{\rho_f}\right)\rho_f U^2$$

The structural stresses σ, insofar as they are generated by dynamic forces within the machine, could be made dimensionless. For example, the stress σ could be divided by the total-pressure rise

across the machine $\sigma/\rho_f g_o H$. However, one could also introduce a stress specific speed by eliminating D from a stress coefficient such as $\sigma/\rho n^2 D^2$ and from Q/nD^3 to obtain

$$\frac{Q}{nD^3}\left(\frac{\rho n^2 D^2}{\sigma}\right)^{3/2} = \frac{n^2 Q}{(\sigma/\rho)^{3/2}}$$

or

$$n_\sigma = \frac{nQ^{1/2}}{(\sigma/\rho)^{3/4}} \tag{1-63}$$

In these equations, ρ is the mass density of the fluid if the stresses considered are fluid-induced stresses σ_f, such as the bending stresses in blades or the casing stresses present if the so-called gage pressure on the low-pressure side of the machine is negligible, or ρ is the mass density of the solid rotating parts of the machine if the stresses considered are stresses generated by centrifugal forces σ_c.

Similar to other specific speeds, n_σ is that combination of operating and stress conditions which, if held constant, permits similar stress conditions in similar machines provided that the basic specific speed n_s is also held constant.

The specific speed n_σ may be related to design, stress, and flow parameters of the machine in exactly the same manner as done previously with respect to fluid-dynamic characteristics of the machine. One may write an equation analogous to equation (1-24):

$$n_\sigma = \frac{nQ^{1/2}}{(\sigma/\rho)^{3/4}} = \frac{1}{2^{1/4}\pi^{1/2}}\left(\frac{\rho U_o^2}{2\sigma}\right)^{3/4}\left(\frac{D_i}{D_o}\right)^{3/2} \times \left(\frac{V_{m,i}}{U_i}\right)^{1/2}\left(1-\frac{D_h^2}{D_i^2}\right)^{1/2} \tag{1-64}$$

This expression is probably most advantageous when centrifugal stresses σ_c are being considered, since $\rho_s U^2/2\sigma_c$ is useful in making the centrifugal stresses in rotating parts dimensionless (ρ_s being the mass density of the structural parts). This is discussed further in section 1.3.3.1.

For fluid-induced stresses σ_f, it may be more advantageous to make σ_f dimensionless by means of a fluid velocity, for example, $V_{m,i}$; this method leads to the expression

$$n_\sigma = \frac{nQ^{1/2}}{(\sigma_f/\rho_f)^{3/4}} = \frac{1}{2^{1/4}\pi^{1/2}}\left(\frac{\rho_f V_{m,i}^2}{2\sigma_f}\right)^{3/4}\frac{U_i}{V_{m,i}} \times \left(1-\frac{D_h^2}{D_i^2}\right)^{1/2} \tag{1-65}$$

If, instead, it is deemed desirable to make σ_f dimensionless by means of the relative velocity w_i at the low-pressure side of the rotor, one can derive the following expression in exactly the same manner as equation (1-49):

$$n_\sigma = \frac{nQ^{1/2}}{(\sigma_f/\rho_f)^{3/4}} = \frac{1}{2^{1/4}\pi^{1/2}}\left(\frac{\rho_f w_i^2}{2\sigma_f}\right)^{3/4} \times \frac{(V_{m,i}/U_i)^{1/2}(1-D_h^2/D_i^2)^{1/2}}{\left|1-2(V_{U,i}/U_i)+V_{U,i}^2/U_i^2+V_{m,i}^2/U_i^2\right|^{3/4}} \tag{1-66}$$

This equation is easy to simplify for zero rotation of the absolute flow by setting $V_{U,i}=0$.

It should be noted that steady elastic deformations δ are proportional to steady stresses, specifically that $\delta/D = \text{constant} \times (\sigma/E)$, where E is the modulus of elasticity. Steady elastic deformations are, therefore, included in the foregoing similarity considerations, but other deformations (e.g., thermal deformations) are not.

The second mechanical effect that is treated in the same manner as the previously discussed flow and stress phenomena is the effect of the acceleration of the system as a whole (e.g., the effect of gravitational acceleration). Generally this effect is considerable only for very large machines. For example, the gravitational static-pressure difference between the highest and the lowest points of a large hydrodynamic machine with a horizontal shaft may well be sufficient to require consideration in connection with cavitation. Gravitational deformation of helicopter blades is very common and requires careful attention. Even in machines of moderate size the effects of a large general acceleration can be considerable, as, for example, during the launch of rockets or missiles. A turbojet engine at the tip of a helicopter blade may be subjected to exceedingly high centrifugal and Coriolis accelerations.

The force due to acceleration of the system as a whole is obviously proportional to $g\rho D^3$, where g is the general acceleration of the system as a whole and, for a machine at sea level on Earth without any acceleration of the entire system, is equal to 32.2 feet per second squared. Generally speaking, g is a variable, equal to the true gravitational acceleration added vectorially to the kinematic acceleration of the system as a whole.

On dividing the inertial forces by the force due to a general acceleration g, one obtains the square of the familiar Froude number in the form

$$\frac{\rho(n^2D^2)D^2}{\rho gD^3} = \frac{n^2D}{g} = \frac{n^2D^2}{gD} \tag{1-67}$$

Combining this expression with Q/nD^3, one can eliminate the linear dimension D and obtain the following:

$$\left(\frac{n^2D}{g}\right)^3 \frac{Q}{nD^3} = \frac{n^5Q}{g^3}$$

or

$$\frac{n^{5/2}Q^{1/2}}{g^{3/2}} = \frac{nQ^{1/2}}{(g/n)^{3/2}} = n_g \tag{1-68}$$

which is named in this compendium the gravity specific speed, where the word gravity refers to any general acceleration of the system as a whole.

The gravity specific speed is that combination of the operating conditions n, Q, and g which, if held constant, permits similar conditions in similar machines provided that the basic specific speed n_s is also held constant.

As previously the inertial forces can be expressed by the head H of the machine in the form $\rho_f g_o HD^2$. Dividing by the force of the general acceleration ρgD^3 leads to

$$\frac{\rho_f g_o HD^2}{\rho gD^3} = \frac{\rho_f}{\rho}\frac{g_o}{g}\frac{H}{D} = \text{constant} \tag{1-69}$$

as the condition of similarity for turbomachines under the general acceleration g. If forces in the fluid (pressures) are being considered, the general density ρ is set equal to ρ_f, so that the condition of similarity reduces to $g_oH/gD = \text{constant}$ and for $g = g_o$ reduces to $H/D = \text{constant}$. That is, the head must change proportionally to the linear dimensions of the system. This is a form of Froude's law of similarity, which is well known in the field of large hydraulic turbines.

If the forces in the solid parts of the machine are being considered, the effective density is $\rho = \rho_s - \rho_f$ or $\rho = \rho_s$, depending on whether the solid parts considered are submerged in the fluid of density ρ_f or not.

Similar to the previously discussed specific speeds, n_g has the advantage over the ratio $\rho_f g_o H/\rho gD$ that it can be calculated before the size D of the machine is known. Furthermore n_g can be related to design and flow parameters of the machine in the same manner as the other specific speeds:

$$n_g = \frac{nQ^{1/2}}{(g/n)^{3/2}} = \frac{1}{2\pi^2} \times \left(\frac{U_o^2}{gD_o}\right)^{3/2}\left(\frac{D_i}{D_o}\right)^{3/2}\left(\frac{V_{m,i}}{U_i}\right)^{1/2} \times \left(1 - \frac{D_h^2}{D_i^2}\right)^{1/2} \tag{1-70}$$

or

$$n_g = \frac{nQ^{1/2}}{(g/n)^{3/2}} = \frac{1}{2\pi^2} \times \left(\frac{U_i^2}{gD_i}\right)^{3/2}\left(\frac{V_{m,i}}{U_i}\right)^{1/2} \times \left(1 - \frac{D_h^2}{D_i^2}\right)^{1/2} \tag{1-71}$$

or

$$n_g = \frac{1}{2\pi^2}\left(\frac{V_{m,i}^2}{gD_i}\right)^{3/2}\left(\frac{U_i}{V_{m,i}}\right)^{5/2} \times \left(1 - \frac{D_h^2}{D_i^2}\right)^{1/2} \tag{1-72}$$

Which form is used depends on which form of the Froude number (U^2/gD or V^2/gD) on the right side turns out to be most convenient for the design procedure chosen. These expressions for n_g do not, of course, exhaust the many ways in which n_g can be related to flow and design parameters.

The last mechanical relation to be considered is

that of mechanical oscillations or vibrations. The most obvious relation is that of the so-called critical speed n_{cr} of the machine to the speed of rotation n. This relation can also be brought into the form previously used.

It is generally known that for the same material the natural frequency of similar vibrating structures is inversely proportional to their linear dimensions. This relation may be derived as follows:

The weight W of a structure is obviously $W = \text{constant} \times g_o \rho_s D^3$, where D is any representative linear dimension of the structure or machine. Its deformations are $\delta_g = \text{constant} \times \sigma_g D/E$, where E is the modulus of elasticity, and the stress produced by the weight of the structure is $\sigma_g = \text{constant} \times W/D^2 = \text{constant} \times g_o \rho_s D$. Thus the deformation of the structure under its own weight is

$$\delta_g = \text{constant} \times \frac{g_o \rho_s D^2}{E} \tag{1-73}$$

The natural frequency f of a simple structure (a mass on a spring) is known to be

$$f = \text{constant} \times \sqrt{\frac{g_o}{\delta_g}} \tag{1-74}$$

Therefore, according to equation (1-73),

$$f = \text{constant} \times \sqrt{\frac{E}{\rho_s}} \frac{1}{D} \tag{1-75}$$

which proves the statement that the natural frequencies of similar structures are inversely proportional to the linear dimensions D of the system.

The fluid-mechanical frequency of a turbomachine is obviously proportional to its speed of rotation n. For example, its blade passing frequency is nN, where N is the number of blades. The relation of the fluid-mechanical frequency to the natural frequency of the same system treated as a vibrating solid structure is obviously expressed by the ratio

$$\frac{n}{f} = \text{constant} \times \frac{nD}{\sqrt{E/\rho_s}} \tag{1-76}$$

where ρ_s is some average mass density of the machine or of the part of the machine considered in this section (e.g., its rotor).

According to the kinematic condition of similarity,

$$\frac{Q}{nD^3} = \text{constant}$$

or

$$D = \text{constant} \times \frac{Q^{1/3}}{n^{1/3}}$$

Substituting this into equation (1-76) gives

$$\frac{n}{f} = \text{constant} \times \frac{nQ^{1/3}}{n^{1/3}\sqrt{E/\rho_s}}$$

$$= \text{constant} \times \frac{n^{2/3}Q^{1/3}}{(E/\rho_s)^{1/2}} \tag{1-77}$$

This equation can be written in the form of a specific speed by being raised to the 3/2 power:

$$\left(\frac{n}{f}\right)^{3/2} = \text{constant} \times \frac{nQ^{1/2}}{(E/\rho_s)^{3/4}} \tag{1-78}$$

The specific speed $n_v = nQ^{1/2}/(E/\rho_s)^{3/4}$ is named in this compendium the vibration specific speed. The equation $n_v = \text{constant}$ describes all combinations of operating conditions and mechanical properties of the machine permitting similar vibration behavior of the machines compared (e.g., a constant ratio of the speed of rotation to the critical speed) provided that the basic specific speed is also held constant.

With

$$n = \frac{U}{D\pi}$$

and

$$Q = V_{m,i} \frac{D_i^2 \pi}{4} \left(1 - \frac{D_h^2}{D_i^2}\right)$$

one finds

$$nQ^{1/2} = \frac{U}{\pi D} \frac{V_{m,i}^{1/2} \pi^{1/2} D_i}{2} \left(1 - \frac{D_h^2}{D_i^2}\right)^{1/2}$$

$$= \frac{1}{2\pi^{1/2}} U^{3/2} \left(\frac{V_{m,i}}{U_i}\right)^{1/2} \left(\frac{D_i}{D}\right)^{3/2} \left(1 - \frac{D_h^2}{D_i^2}\right)^{1/2}$$

Therefore

$$n_v = \frac{nQ^{1/2}}{(E/\rho_s)^{3/4}} = \frac{1}{2^{1/4}\pi^{1/2}} \times \left(\frac{\rho_s U^2}{2E}\right)^{3/4} \left(\frac{V_{m,i}}{U_i}\right)^{1/2} \left(\frac{D_i}{D}\right)^{3/2} \left(1 - \frac{D_h^2}{D_i^2}\right)^{1/2} \tag{1-79}$$

By analogy to the cavitation parameter σ_H, the similarity relation $n_v = \text{constant}$ can also be expressed by the ratio

$$\frac{E/\rho_s}{g_o H} = \frac{E}{\rho_s g_o H} = \text{constant} \tag{1-80}$$

that is, by the ratio of the modulus of elasticity to a pressure proportional to the head of the machine, which is a constant. Evidently

$$n_v = n_s \left(\frac{\rho_s g_o H}{E}\right)^{3/4} \tag{1-81}$$

The ratio $\rho_s U^2/2E$ in equation (1-79) has, of course, the equally simple meaning of a velocity pressure $\rho_s U^2/2$ of the mechanical velocity U divided by the modulus of elasticity E.

If, according to equation (1-75), E/ρ_s is replaced by constant $\times (Df)^2$, the vibration specific speed (eq. (1-79)) may be written in the form

$$n_v = \frac{nQ^{1/2}}{(E/\rho)^{3/4}} = \frac{\text{constant}}{2\pi^{1/2}} \left(\frac{U}{Df}\right)^{3/2} \times \left(\frac{V_{m,i}}{U}\right)^{1/2} \frac{D_i}{D} \left(1 - \frac{D_h^2}{D_i^2}\right)^{1/2} \tag{1-82}$$

where U/Df is obviously a Strouhal number of the machine.

The specific speeds described in this section and their most important relations to design parameters are listed in table 1-I. It is evident that all specific speeds and their relations to design parameters follow essentially the same scheme.

As stated previously, the specific speed, or any variation with respect to the force considered, is the 3/2 power of a velocity ratio, that is, the kinematic velocity $(nQ^{1/2})^{2/3}$ divided by a velocity representing the force action to be considered. For an ideal fluid, this velocity is $(g_o H)^{1/2}$, which represents inertial forces and leads to the basic specific speed n_s; with respect to cavitation, this velocity is $(g_o H_{sv})^{1/2}$, which represents inertial forces connected with cavitation and, thus, leads to the suction specific speed S; and so on. Only in the case of the acoustic specific speed is this representative velocity a physically existing velocity, namely, the velocity of sound a.

With all these force-representing velocities designated by (v) (with v always written in parentheses) all specific speeds can be written in the form

$$n_{(v)} = \frac{nQ^{1/2}}{(v)^{3/2}}$$

Their various relations to flow and design characteristics are given in table 1-II, and the various meanings of the force-representing general velocity (v) are given in table 1-III. The derivations of the various expressions in table 1-II are the same as those given in sections 1.2.1 and 1.2.2 and in the present section. Thus tables 1-I to 1-III constitute a summary of these three sections.

1.3 Dimensionless Design Forms as Functions of Design Parameters

1.3.1 Introduction

Section 1.2 establishes relations between dimensionless operating conditions of turbomachinery, the specific speeds, and a number of design parameters. These design parameters are a number of flow coefficients (ratios of fluid velocities V to peripheral velocities of the solid rotating parts of the machine U), a number of head coefficients of the general form $2g_o H/U^2$ or $2g_o H/V^2$, certain stress coefficients of the form $\rho U^2/2\sigma$, Mach numbers, Reynolds numbers, Froude numbers, Strouhal numbers, and a number of ratios of linear dimensions.

The next step obviously consists in establishing relations between these parameters and the design of the machine. This is clearly the general design problem of turbomachinery and, therefore, constitutes the general problem to be solved by this entire compendium as well as by other publications

TABLE 1-I. - SPECIFIC SPEEDS

Basic specific speed

$$n_s = \frac{nQ^{1/2}}{(g_o H)^{3/4}} = \frac{1}{2^{1/4}\pi^{1/2}} \left(\frac{U_o^2}{2g_o H}\right)^{3/4} \left(\frac{V_{m,i}}{U_i}\right)^{1/2} \left(\frac{D_i}{D_o}\right)^{3/2} \left(1 - \frac{D_h^2}{D_i^2}\right)^{1/2}$$

Suction specific speed

$$S = \frac{nQ^{1/2}}{(g_o H_{sv})^{3/4}} = \frac{1}{2^{1/4}\pi^{1/2}} \left(\frac{V_{m,i}^2}{2g_o H_{sv}}\right)^{3/4} \frac{U_i}{V_{m,i}} \left(1 - \frac{D_h^2}{D_i^2}\right)^{1/2}$$

Compressibility specific speed

$$n_a = \frac{nQ^{1/2}}{a^{3/2}} = \frac{1}{2\pi^{1/2}} \left(\frac{w_i}{a}\right)^{3/2} \frac{\left(\frac{V_{m,i}}{U_i}\right)^{1/2}}{\left(1 - 2\frac{V_{U,i}}{U_i} + \frac{V_{U,i}^2}{U_i^2} + \frac{V_{m,i}^2}{U_i^2}\right)^{3/4}} \left(1 - \frac{D_h^2}{D_i^2}\right)^{1/2}$$

Viscosity specific speed

$$n_\nu = \frac{nQ^{1/2}}{(n\nu)^{3/4}} = \frac{\pi^{1/4}}{2} \left(\frac{U_o D_o}{\nu}\right)^{3/4} \left(\frac{D_i}{D_o}\right)^{3/2} \left(\frac{V_{m,i}}{U_i}\right)^{1/2} \left(1 - \frac{D_h^2}{D_i^2}\right)^{1/2}$$

Stress specific speed

$$n_\sigma = \frac{nQ^{1/2}}{\left(\frac{\sigma}{\rho}\right)^{3/4}} = \frac{1}{2^{1/4}\pi^{1/2}} \left(\frac{\rho U_o^2}{2\sigma}\right)^{3/4} \left(\frac{D_i}{D_o}\right)^{3/2} \left(\frac{V_{m,i}}{U_i}\right)^{1/2} \left(1 - \frac{D_h^2}{D_i^2}\right)^{1/2}$$

Gravity specific speed

$$n_g = \frac{nQ^{1/2}}{\left(\frac{g}{n}\right)^{3/2}} = \frac{1}{2\pi^2} \left(\frac{U_o^2}{gD_o}\right)^{3/2} \left(\frac{D_i}{D_o}\right)^{3/2} \left(\frac{V_{m,i}}{U_i}\right)^{1/2} \left(1 - \frac{D_h^2}{D_i^2}\right)^{1/2}$$

Vibration specific speed

$$n_v = \frac{nQ^{1/2}}{\left(\frac{E}{\rho_s}\right)^{3/4}} = \frac{1}{2^{1/4}\pi^{1/2}} \left(\frac{\rho_s U_o^2}{2E}\right)^{3/4} \left(\frac{D_i}{D_o}\right)^{3/2} \left(\frac{V_{m,i}}{U_i}\right)^{1/2} \left(1 - \frac{D_h^2}{D_i^2}\right)^{1/2}$$

on the design of turbomachinery. In this chapter one can, at best, outline the solution of this broad problem in order to obtain a general picture of the relation between operating conditions and design.

This outline is presented in the order of the level of knowledge available in the various fields concerned: first, the fluid-mechanical design of axial-flow vane systems and machinery; second, the

fluid-mechanical design of radial- and mixed-flow machinery; third, the stress-determined mechanical design of turbomachinery; and fourth, the general influence of gravity and of vibrations on the design of turbomachinery (as yet poorly understood).

The treatment of the first two subjects of this outline can be reasonably definite, because the basic specific speed and the suction specific speed are regularly used in the design of turbomachinery, particularly hydrodynamic machinery. Stress considerations are extensively applied to the design of turbomachinery, but not as yet in terms of a stress specific speed. The treatment of the influence of gravity and vibrations on the design of turbomachinery becomes increasingly vague, because a general correlation between operating conditions and the weight or vibration parameters of a machine has never been attempted in the same sense as correlations involving the basic specific speed and the suction specific speed. The gravity specific speed and the vibration specific speed have never been used and may never be used.

1.3.2 Flow-Determined Design Forms of Turbomachines

1.3.2.1 *Axial-flow turbomachines.*—This section describes the design forms of axial-flow vane systems as determined by flow coefficients,

TABLE 1-II. - RELATIONS OF FORCE-REPRESENTING VELOCITIES[a] TO FLOW AND DESIGN CHARACTERISTICS

$$\frac{nQ^{1/2}}{(v)^{3/2}} = \frac{1}{2\pi^{1/2}} \left[\frac{U_o}{(v)}\right]^{3/2} \left(\frac{D_i}{D_o}\right)^{3/2} \left(\frac{V_{m,i}}{U_i}\right)^{1/2} \left(1 - \frac{D_h^2}{D_i^2}\right)^{1/2}$$

$$\frac{nQ^{1/2}}{(v)^{3/2}} = \frac{1}{2\pi^{1/2}} \left[\frac{U_i}{(v)}\right]^{3/2} \left(\frac{V_{m,i}}{U_i}\right)^{1/2} \left(1 - \frac{D_h^2}{D_i^2}\right)^{1/2}$$

$$\frac{nQ^{1/2}}{(v)^{3/2}} = \frac{1}{2\pi^{1/2}} \left[\frac{V_{m,i}}{(v)}\right]^{3/2} \left(\frac{U_i}{V_{m,i}}\right) \left(1 - \frac{D_h^2}{D_i^2}\right)^{1/2}$$

$$\frac{nQ^{1/2}}{(v)^{3/2}} = \frac{1}{2\pi^{1/2}} \left[\frac{w_i}{(v)}\right]^{3/2} \frac{\left(\frac{V_{m,i}}{U_i}\right)^{1/2}}{\left(1 - 2\frac{V_{U,i}}{U_i} + \frac{V_{U,i}^2}{U_i^2} + \frac{V_{m,i}^2}{U_i^2}\right)^{3/4}} \left(1 - \frac{D_h^2}{D_i^2}\right)^{1/2}$$

$$\frac{nQ^{1/2}}{(v)^{3/2}} = \frac{1}{\pi^{1/2}} \left[\frac{U_o}{(v)}\right]^{3/2} \left(\frac{V_{m,o}}{U_o}\right)^{1/2} \left(\frac{b_o}{D_o}\right)^{1/2}$$

$$\frac{nQ^{1/2}}{(v)^{3/2}} = \frac{1}{\pi} \left[\frac{U_o}{(v)}\right]^{3/2} \left(\frac{V_{U,o}}{U_o}\right)^{1/2} \left(\frac{D_o}{D_{th}}\right)^{1/2} \frac{A_{th}^{1/2}}{D_o} N^{1/2}$$

[a]The general velocity (v) may be compared with the head of the machine in the form $(v)^2/g_oH$, as given in table 1-III.

TABLE 1-III. - DEFINITIONS OF FORCE-REPRESENTING VELOCITIES

For the basic specific speed
$(v) = (g_o H)^{1/2}$
With respect to cavitation
$(v) = (g_o H_{sv})^{1/2}$
With respect to compressibility
(v) = a = velocity of sound
With respect to viscosity
$(v) = (n\nu)^{1/2} = (U\nu/\pi D)^{1/2}$
With respect to centrifugal stresses
$(v) = \left(\frac{\sigma_c}{\rho_s}\right)^{1/2}$
With respect to fluid-induced stresses
$(v) = \left(\frac{\sigma_f}{\rho_f}\right)^{1/2}$
With respect to any general acceleration g of the system as a whole
$(v) = \frac{g}{n} = \frac{g\pi D}{U}$
With respect to vibrations of the machine at a frequency f
$(v) = \left(\frac{E}{\rho}\right)^{1/2}$

head coefficients, and ratios of linear dimensions.

For axial-flow machines, these parameters are related to the basic specific speed in section 1.2.1 by the following equations:

$$n_s = \frac{nQ^{1/2}}{(g_o H)^{3/4}} = \frac{1}{2^{1/4}\pi^{1/2}}\left(\frac{U_i^2}{2g_o H}\right)^{3/4} \times \left(\frac{V_{m,1}}{U_i}\right)^{1/2}\left(1 - \frac{D_{h,1}^2}{D_i^2}\right)^{1/2} \qquad (1\text{-}25a)$$

and

$$n_s = \frac{1}{2^{1/4}\pi^{1/2}}\left(\frac{U_{h,2}^2}{2g_o H}\right)^{3/4}\left(\frac{D_i}{D_{h,2}}\right)^{3/2} \times \left(\frac{V_{m,1}}{U_i}\right)^{1/2}\left(1 - \frac{D_{h,1}^2}{D_i^2}\right)^{1/2} \qquad (1\text{-}26)$$

where the subscript 1 refers to the inlet side and the subscript 2 to the discharge side of a pump (or compressor) rotor, as shown in figure 1-20. For turbine rotors, the through flow is usually in the opposite direction; that is, it enters on the side of the maximum hub diameter. Equation (1-26) has the advantage that $\psi_{h,2} = 2g_o H/U_{h,2}^2$ usually has fairly well-known limiting values, about 1 for standard pump and compressor rotors and up to about 4 for turbine rotors and some exceptional pump rotors.

Since equation (1-26) is derived from equation (1-25) by using the relation $U_h = U_i(D_h/D_i)$, these equations are not independent and constitute only one relation. Therefore they are not sufficient to determine $V_{m,1}/U_i$ and $D_{h,2}/D_i$ even if $2g_o H/U_{h,2}^2$ is assumed to be given by its empirically determined upper limits. For liquids, the additional required relation is usually given by the suction specific speed in the form

$$S = \frac{nQ^{1/2}}{(g_o H_{sv})^{3/4}} = \frac{1}{2^{1/4}\pi^{1/2}}\left(\frac{V_{m,1}^2}{2g_o H_{sv}}\right)^{3/4} \times \frac{U_i}{V_{m,1}}\left(1 - \frac{D_{h,1}^2}{D_i^2}\right)^{1/2} \qquad (1\text{-}46a)$$

with the subscript 1 defined as previously (fig. 1-20). According to figure 1-18, the optimum values of $2g_o H_{sv}/V_{m,1}^2$ cover a very narrow band around 3.5, so that this coefficient can usually be considered as given. A value for $D_{h,1}/D_i$ is assumed (which is not very critical as the square of this ratio is usually less than 1/4). Equation (1-46a) or the equivalent figure 1-18 then determines the flow coefficient $V_{m,1}/U_i$, which in turn determines $D_{h,2}/D_i$ from equation (1-26) and, thus, completes the right side of this equation.

For compressible fluids, one would use in place of equation (1-46a) an equivalent expression of the compressibility specific speed, for example,

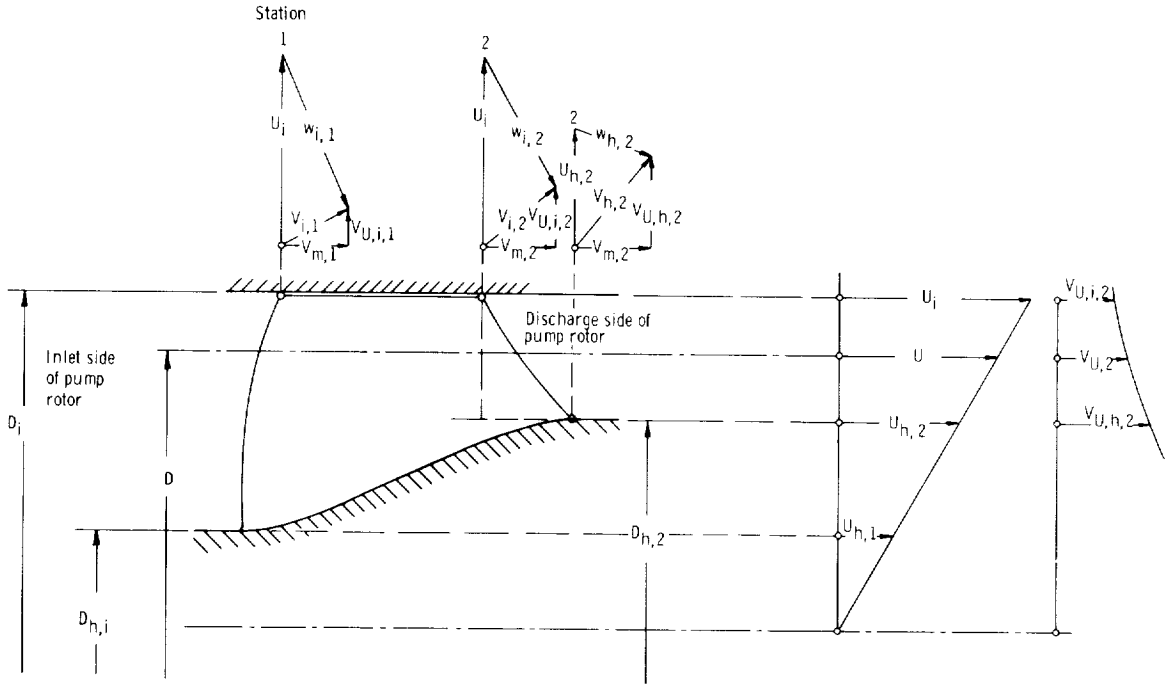

Figure 1-20.—Axial-flow pump rotor profile defining notation.

$$n_a = \frac{nQ^{1/2}}{a^{3/2}} = \frac{1}{2\pi^{1/2}}\left(\frac{w_{i,1}}{a}\right)^{3/2} \times \frac{(V_{m,1}/U_i)(1-D_{h,1}^2/D_i^2)^{1/2}}{[1-2(V_{U,i}/U_i)+V_{U,i}^2/U_i^2+V_{m,1}^2/U_i^2]^{3/4}} \tag{1-57a}$$

where the Mach number $w_{i,1}/a$ of the relative flow at the blade inlet tip in a compressor rotor is usually given from experience. The prerotation of the fluid $V_{U,i}$ would have to be known. Under these assumptions, equation (1-57a) permits the calculation of $V_{m,1}/U_i$.

It is evident that the suction specific speed S or the compressibilty specific speed n_a determines the flow coefficient $V_{m,1}/U_i$. With it the basic specific speed determines $2g_oH/U_i^2$, and with an assumed (limiting) value of $2g_oH/U_{h,2}^2$, also $D_{h,2}/D_i$.

On the basis of mechanical considerations of shaft diameter, it is fairly easy to make the required assumption of the hub diameter ratio $D_{h,1}/D_i$ at the low-pressure side of the rotor. If there is any rotation of the absolute flow $V_{U,i,1}$ at the low-pressure side of the rotor, this must be prescribed.

According to Euler's turbomachinery equation presented in chapter 2, section 2.3, the head coefficient for pumps is

$$\psi = 2\eta_h \frac{\Delta V_U}{U} \tag{1-11}$$

while for turbines η_h is replaced by $1/\eta_h$. Here $\Delta V_U = V_{U,2} - V_{U,1}$ and ψ may be applied to any diameter by affixing the appropriate subscripts i; $h,2$; or others to ψ, U, and ΔV_U.

The flow and head coefficients determined in this way establish the velocity diagrams at stations 1 and 2 at the diameters D_i and $D_{h,2}$ under the assumption that $V_{m,1}$ = constant over the entire radial extent of the inlet or low-pressure area (station 1). This assumption is used in the derivation of equations (1-25), (1-26), (1-46), and (1-58) by use of the continuity relation

$$Q = V_{m,1}\frac{D_i^2\pi}{4}\left(1-\frac{D_{h,1}^2}{D_i^2}\right)$$

What needs to be known is the rotation of the absolute flow V_U at one side of the rotor, usually the low-pressure side, where $V_U = V_{U,1}$.

Figure 1-21 shows three typical velocity vector diagrams for pump or compressor rotors (for which

usually $\Delta V_U < U$) for the following three conditions: $V_{U,1} = 0$ (fig. 1-21(a)); $V_{U,1} > 0$ (i.e., $V_{U,1}$ has the same direction as the rotor motion U) (fig. 1-21(b)); and $V_{U,1} < 0$ (i.e., the absolute rotation of the fluid at the inlet side of the pump rotor is directed against the rotation of the rotor)(fig. 1-21(c)).

To illustrate different possibilities, $V_{m,1} = V_{m,2}$ (i.e., $D_{h,1} = D_{h,2}$) is assumed for figures 1-21(a) and (c), $V_{m,1} < V_{m,2}$ (i.e., $D_{h,1} < D_{h,2}$) is assumed for figure 1-21(b). It is of interest to note that the absolute velocity vectors V_1 and V_2 also describe the flow leaving and entering stationary vane systems, with V_2 being the inlet and V_1 the discharge velocities of these systems, if the vane systems in front of and behind the rotor system have the same discharge velocity diagrams.

The velocity vector diagrams are shown without the subscript i or h,2, as they may apply to either D_i or $D_{h,2}$, or indeed to any other diameter D. Therefore, it is important to examine briefly the change in the flow and head parameters and the resulting changes in the velocity diagrams as a function of the diameter D.

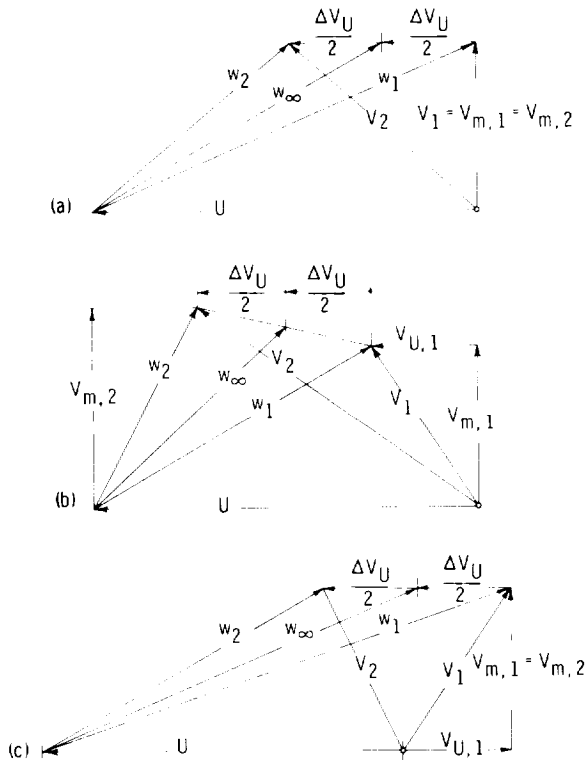

(*a*) $V_{U,1} = 0$; $V_{m,1} = V_{m,2}$.
(*b*) $V_{U,1} > 0$; $V_{m,1} < V_{m,2}$.
(*c*) $V_{U,1} < 0$; $V_{m,1} = V_{m,2}$.

Figure 1-21.—Typical velocity vector diagrams for axial-flow pump rotors.

As mentioned previously, in this chapter V_m is assumed constant with respect to the diameter or the distance from the axis of rotation. Other assumptions are possible and are discussed in chapter 2 but are too complicated to be considered in this outline.

The basic law to be considered in this section regarding the circumferential component V_U of absolute velocities is called the law of constant angular momentum:

$$V_U D = \text{constant} \tag{1-83}$$

with respect to changes in D, that is, changes in the distance from the axis of rotation. This law is assumed to hold at the inlet and the discharge planes of a rotor. Figure 1-20 shows at its right side the radial distribution of $V_{U,2}$ obeying this law. Since ΔV_U is the difference between two values of V_U, it must follow the same law. Only by the application of circumferential forces, as between the inlet (station 1) and the discharge (station 2) of a vane system, can the product $V_U D$ be changed.

Obviously the circumferential velocities U of solid rotating parts of the machine increase proportionally to D, so that

$$\frac{U}{D} = \text{constant} \tag{1-84}$$

This distribution of U is also shown in figure 1-20.

Therefore, with $V_m = \text{constant}$ in any one flow cross section and by use of equations (1-83) and (1-84), it is possible to derive from the velocity inlet and discharge diagrams in any one cylindrical section (such as that shown in fig. 1-21) the corresponding velocity diagrams in any other cylindrical section.

According to equation (1-84) and $V_m = \text{constant}$, the flow coefficient varies as follows:

$$\varphi = \frac{V_m}{U} = \frac{V_m}{U_i}\,\frac{U_i}{U} = \frac{V_m}{U_i}\,\frac{D_i}{D} \tag{1-85}$$

The head coefficient varies as follows:

$$\left.\begin{aligned} \psi &= \frac{2g_oH}{U^2} = \frac{2g_oH}{U_i^2}\frac{U_i^2}{U^2} = \frac{2g_oH}{U_i^2}\frac{D_i^2}{D^2} \\ \text{or} \\ \psi\frac{2g_oH}{U^2} &= \frac{2g_oH}{U_{h,2}^2}\frac{U_{h,2}^2}{U^2} = \frac{2g_oH}{U_{h,2}^2}\frac{D_{h,2}^2}{D^2} \end{aligned}\right\} \quad (1\text{-}86)$$

where D is any diameter between D_i and $D_{h,2}$. The head coefficient ψ can be evaluated in terms of the change in the peripheral velocity components ΔV_U according to equation (1-11), and the tangential velocities obey equation (1-83).

The inlet and discharge velocity vector diagrams are, therefore, available in all cylindrical sections if they are given by equations (1-11) and (1-26), (1-46a), or (1-58) for any one cylindrical section.

A few words are necessary to justify the terms axial-flow surfaces, cylindrical-flow surfaces, and cylindrical-flow sections in connection with a vane system profile such as that shown in figure 1-20. The existence of a noncylindrical hub (or a slightly noncylindrical outside contour) obviously forces departures from cylindrical flow for nearly all the flow through such a system. Section 3.3.3 in chapter 3 shows that a small departure from cylindrical flow can be treated by dividing the flow into a cylindrical and a radial component. However, this refinement should not be considered in the present broad outline of this design problem. It is obvious from figure 1-20 that completely cylindrical sections can be used only between $D=D_i$ and $D=D_{h,2}$, although partially (or fictitiously) cylindrical vane sections can be used very well at diameters between $D_{h,2}$ and $D_{h,1}$.

With the velocity vector diagrams at any point of the inlet and discharge vane edges determined by the design parameters and, thus, by the dimensionless operating condititions n_s and either S or n_a, one step remains to be accomplished, which is the most essential step in this design process, the design of the cylindrical vane sections from the inlet and discharge velocity vector diagrams.

The theory of this design process is given in chapter 2, and the design process itself is described in chapter 3. For the present outline, it is sufficient to indicate the existence of such a process.

The simplest approximation, called one-dimensional, obviously consists simply in drawing a smoothly curved centerline of the vane profile tangent to the relative velocity vectors at the inlet and the discharge. In reality one has to depart from this approximation by giving the vanes more curvature than prescribed by the one-dimensional approximation. This is shown for pump blades in figure 1-22, where at the inlet $\beta_1 > \beta_{w,1}$ and at the discharge $\beta_2 < \beta_{w,2}$. The magnitudes of these departures are given by the theory of axial-flow vane design in chapters 2 and 3.

Figure 1-22 also shows that the direction of the blade ends so determined does not prescribe the entire blade shape uniquely. Changing the curvature between the inlet and the discharge portions of the blades allows the locations of these two portions relative to each other to be varied substantially. Such changes affect the distribution of the pressure difference along the blades. For example, reduced curvature of the vane near its leading edge reduces the vane pressure difference over the leading portion of the vane, which is beneficial for good cavitation characteristics or good Mach number characteristics of the vane. However, far more definite methods of relating the shape of the profile centerline (called the mean camber line) to the vane pressure distribution are available. One such method is presented in detail in chapters 2 and 3. The same method also gives a systematic relation between the blade thickness distribution and the pressure and velocity distribution within the vane system.

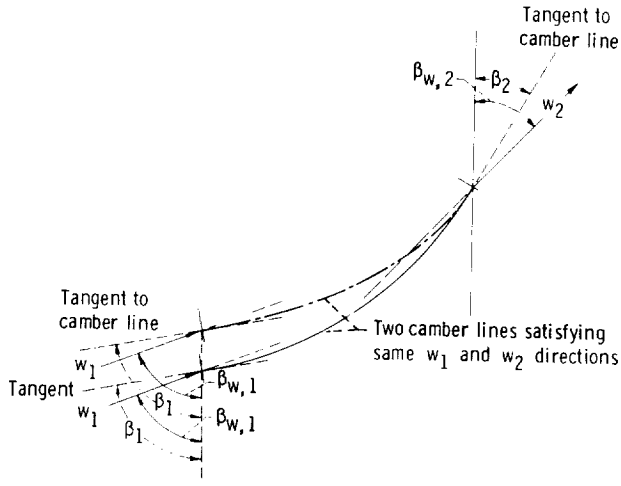

Figure 1-22.—Relation between vane camber line and velocity vectors.

Thus the inlet and discharge velocity vector diagrams together with the vane pressure distribution determine the vane shape within the accuracy of the available theory and design methods for such vanes. It is reasonable to assume that this determination of vane shape will become entirely definite and unique as the methods of design are further developed and perfected, although it is not certain that this degree of perfection is really justified from a practical point of view.

Figure 1-23 illustates diagrammatically the resulting relation between the design form of straight systems of parallel vanes and the flow and head coefficients which determine the velocity diagrams. In this figure, the velocity diagrams are shown for pump (or compressor) operation with the exception of the system for $\psi = 2$ and $\varphi = 0.25$; for the latter system, pump operation is not possible since it would require an excessive retardation of the relative flow, as discussed later in this section. All other configurations shown would be made usable for pump as well as turbine operation merely by reversing the direction of the axial velocity and interchanging the leading and trailing edges of the vanes, although the configurations for $\psi = 2$ and particularly $\psi = 4$ are used for pump operation only in exceptional cases. For example, with $\psi = 4$ no change in static pressure takes place in the rotor vane system, which accomplishes merely a change in the kinetic energy of the absolute flow. (The static pressure changes only in the stationary passages of such a machine.)

The relation between the vane system design form and the design parameters thus represents (at least) a three-dimensional theoretically infinite family of such vane systems. Two dimensions are the flow coefficient and the head coefficient, and the third

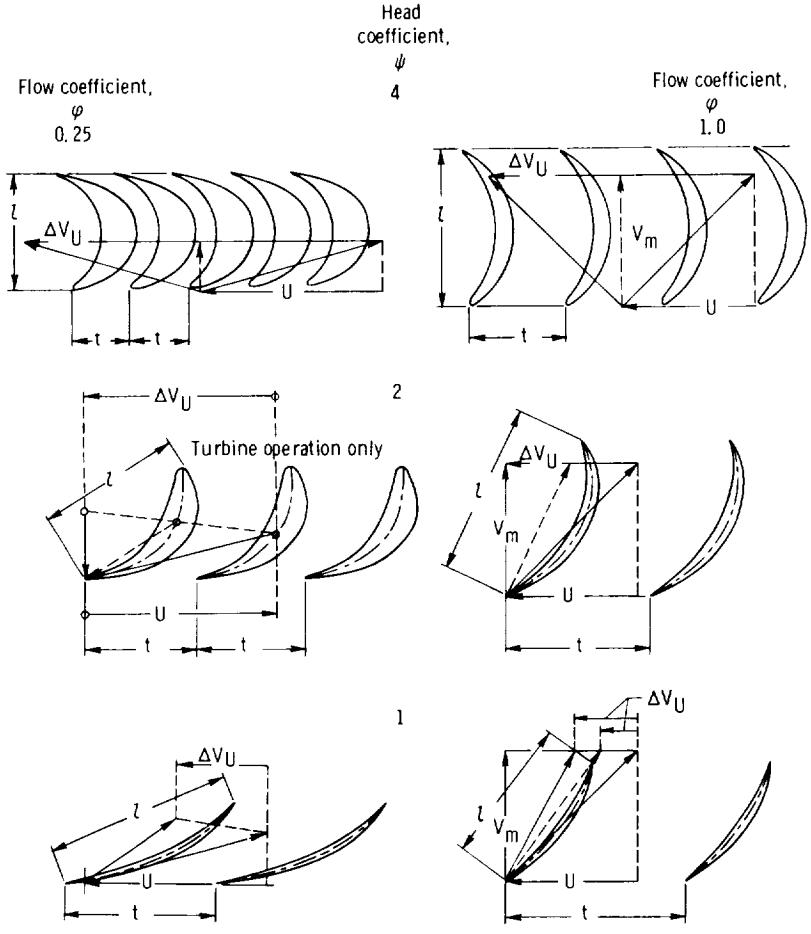

Figure 1-23.—Vane system design forms as function of flow coefficient and head coefficient.

dimension is the vane pressure distribution, based on the hypothetical assumption that the variations in this pressure can be represented adequately by a single variable.

The number of dimensions or variables increases if the axial velocity component V_m changes from the inlet to the discharge, either because of a change in width normal to the sections shown in figure 1-23 or because of compressibility effects. In the latter case, this additional variable is clearly related to the Mach number of the flow.

A circumferential velocity component of the absolute flow on both sides of the vane system changes the relation between the head coefficient ψ and the shape of the system, but does not otherwise constitute a new variable, as it is only the flow relative to the system which determines its design form.

It is doubtful whether the family of vane system forms shown in figure 1-23 can be represented as a group in the mathematical sense of this word, although it would be interesting to explore this possibility. The conditions, if any, under which this would be possible might be of practical interest.

Limitations in the flow through axial-flow vane systems are discussed up to this point only with respect to the field of cavitation or Mach number limitations. Yet additional limitations are strongly implied by the fact that the vanes in the systems illustrated diagrammatically in figure 1-23 show limited magnitudes of vane spacing t, whereas preceding considerations are concerned only with the vane shape. It is obvious that the vane spacing must not exceed certain upper limits so that the vane loading stays within practically acceptable bounds. On the other hand, the vane spacing should not be unnecessarily close to avoid excessive skin friction losses.

The loading of turbomachinery vanes can be expressed in dimensionless form by a lift coefficient C_L defined in the same manner as the lift coefficient for a single vane or airfoil represented in section 1.1.1 by equation (1-1). The lift coefficient of any one vane of an infinitely long system of straight and parallel vanes is

$$C_L = 2 \frac{\Delta V_U}{w_\infty} \frac{t}{l} \qquad (1\text{-}87)$$

where w_∞ is the vectorial mean of the relative inlet and discharge velocities w_1 and w_2 (fig. 1-21), t is the circumferential vane spacing, and l is the vane length measured normal to the resultant vane force (fig. 1-23).

For a single vane or airfoil, C_L has an upper limit of approximately 1.5. For straight systems of parallel vanes, the upper limit for C_L lies between 1.5 and 2.0 provided that the relative inlet and discharge velocities w_1 and w_2 have about the same magnitude. If $|w_2| < |w_1|$, the upper limit of C_L is lower than this range; if $|w_2| > |w_1|$, the upper limit of C_L is higher (see ch. 2, sec. 2.5.4.3).

It should be obvious that, for any velocity vector diagram giving the ratio $\Delta V_U / w_\infty$, a limiting value of C_L determines a lower limit for the so-called solidity l/t of the vane system by means of equation (1-87).

The previously mentioned retardation of the relative flow ($w_2 < w_1$) through a vane system constitutes an important limitation of the velocity vector diagrams which can be generated by any vane system. It has been found expermientally that $w_2/w_1 = 0.6$ constitutes an approximate lower limit for the discharge velocity of any rotating vane system, whereas $V_2/V_1 = 0.6$ expresses the same limit with respect to stationary vane systems. The theoretical and empirical background of this limitation is discussed in chapter 2, section 2.5.4.3.

It is apparent that the previously presented relation between flow coefficient, head coefficient, and vane pressure distribution on one hand and the design form of the vane system profile on the other has some important limitations. The solidity l/t must be sufficiently high to keep the lift coefficient below certain limiting values (eq. (1-87)), and the discharge velocity relative to the system (w_2 or V_2) cannot be less than approximately 0.6 of the corresponding inlet velocity (w_1 or V_1), which excludes an entire region from the field of possible velocity vector diagrams and corresponding design forms. This excluded region of excessive deceleration is most easily shown in a velocity vector diagram made dimensionless with respect to w_1 or V_1. Figure 1-24 shows such a diagram for rotors, and the region inside a semicircle with radius 0.6 w_1 is the excluded region for pump rotors. Also shown is a standard pump or compressor velocity diagram which satisfies the retardation criterion ($w_2/w_1 > 0.6$). The dimensionless velocities of this diagram can easily be transformed into the familiar ratios with respect to U. In the example given in figure 1-24, $U/w_1 = 1.32$; thus

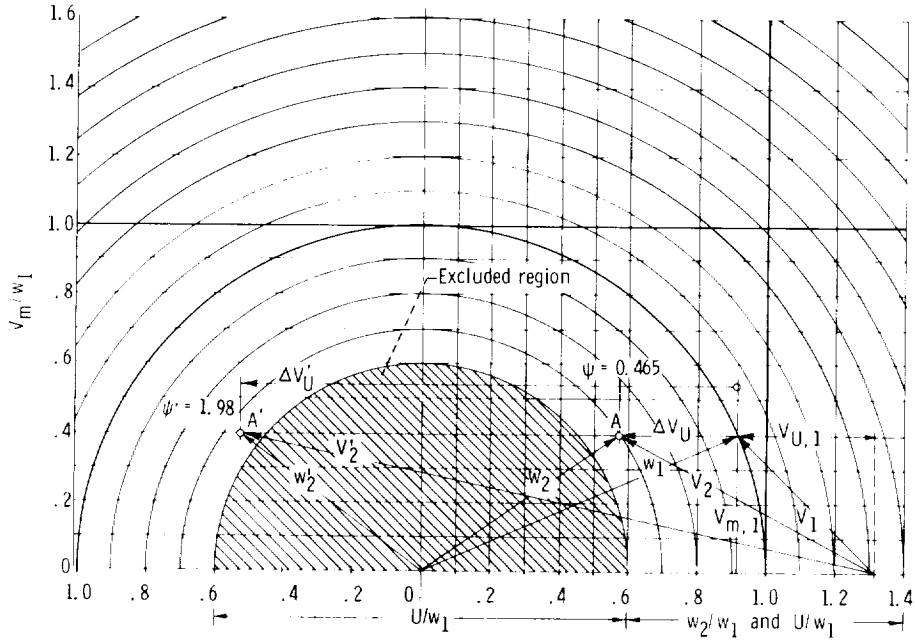

Figure 1-24.—Diagram showing limitation in retardation of relative flow of axial-flow rotors. For stationary vane system, absolute velocities V_1 and V_2 should be used in place of relative velocities w_1 and w_2.

$$\frac{\Delta V_U}{U} = \frac{\Delta V_U}{w_1}\,\frac{w_1}{U} = \frac{0.34}{1.32} = 0.258$$

and

$$\frac{V_{m,1}}{U} = \frac{V_{m,1}}{w_1}\,\frac{w_1}{U} = \frac{0.40}{1.32} = 0.303$$

For the particular flow coefficient and prerotation $V_{U,1}$ used in this example, $\Delta V_U/w_1$ can be increased to 0.465, and, therefore, $\Delta V_U/U$ to $0.465/1.32 = 0.353$, before point A enters the forbidden region inside the circle $w_2 = 0.6w_1$. Then one can choose a much higher ΔV_U value on the other side of the forbidden region; that is, one can turn the relative velocity vector past the axial direction until w_2 is again larger than $0.6\ w_1$. This second velocity vector diagram is also shown in figure 1-24. It should be obvious that this diagram permits the determination of the retardation limits for any flow coefficient, and that there is no such limit beyond $V_{m,1}/w_1 = 0.6$.

The foregoing considerations establish as many coaxial cylindrical sections through an axial-flow vane system as desired. However, these sections can be shifted relative to each other in the axial as well as the circumferential direction. Thus the entire three-dimensional vane shape is not uniquely determined by its cylindrical-flow sections.

Usually this uncertainty is removed by a geometric process called fairing, by which vane sections normal to the axis of rotation (or radial vane sections containing the axis of rotation) are made to show the vane contours as smooth flat curves with as few irregularities as possible. This process, described in chapter 3, determines the entire vane surface almost uniquely on the basis of geometric continuity and simplicity.

The simplest geometric condition for this fairing process is that vane sections normal to the axis of rotation show contours which are approximately radial. This condition is a mechanical necessity if centrifugal blade stresses are important. Under other circumstances, there may be reasons for departing from this simple form. (The resulting fluid-mechanics problems are discussed in chs. 2 and 3, and the mechanical problems in ch. 5.) In any event, with a sufficient number of conditions prescribed (number of specific speeds) and increasing knowledge of the theoretical background, it should eventually be possible to determine the optimum vane shape in three dimensions completely and uniquely from the

dimensionless operating conditions (the specific speeds) and the limiting conditions imposed.

While the relative flow in cylindrical sections through rotating vane systems is the same as the absolute flow in cylindrical sections through stationary vane systems, this resemblance between rotating and stationary vane sections does not apply to entire vane systems comprising many cylindrical sections of different diameters. In rotating sytems, the circumferential component of the relative flow usually increases with increasing diameter because of the increasing circumferential velocity U of the solid rotating parts. However, the circumferential component of the absolute flow usually diminishes with increasing diameter, in agreement with the law of constant angular momentum (eq. (1–83)). These effects generally give rotating vane systems fundamentally different three-dimensional design forms from those of stationary vane systems.

In review, then, the flow and head coefficients which are related to the dimensionless operating conditions (the specific speeds) do not determine the vane shape directly, but rather the velocity vector diagrams at the inlet and discharge edges of various coaxial cylindrical sections through the vanes. The velocity diagrams and the vane pressure distribution determine the cylindrical vane sections within the accuracy of available design methods.

The resulting family of cylindrical sections through the vanes of axial-flow turbomachinery is not unlimited. The circumferential vane spacing t has an upper limit imposed by the vane lift coefficient $C_L = 2(\Delta V_U / w_\infty)(t/l)$. Furthermore the velocity vector diagrams which determine the shape of cylindrical vane sections are limited by the condition that the ratio of the discharge to the inlet velocity of any flow section through the vane system (w_2/w_1 or V_2/V_1) should not be less than 0.6, since at lower values the active flow separates from the vanes.

The cylindrical vane sections so determined can be made to form a satisfactory three-dimensional surface by a geometric process called fairing. By this process, the vane contours as seen in plane sections normal to the axis of rotation are made to form smooth curves of limited curvature, which are usually not strongly inclined against the radial direction.

1.3.2.2 *Radial- and mixed-flow turbomachines.*—This section outlines the relation between the design forms of radial- and mixed-flow vane systems and the flow coefficients, head coefficients, and ratios of linear dimensions which are determined by various specific speeds. This outline is quite analogous to that given in the preceding section 1.3.2.1 with respect to axial-flow vane systems, except for the fact that the present subject is more complex and this outline is, therefore, less complete.

The design of radial- and mixed-flow vane systems is described in chapter 4. The flow in such systems is usually assumed to proceed along coaxial, curved stream surfaces of revolution, as indicated in figures 1–7 and 1–25. The flow departs from axial flow and plane radial flow sufficiently to make the flow and the design problem truly three-dimensional. Portions of this flow are frequently described by developing straight conical flow sections approximating local regions of the curved stream surfaces into planes (see section Y-Y in figs. 1–25 and 1–26). A more complete method of describing the three-dimensional design of such systems geometrically is given in chapter 4. The difference between rotating and stationary vane systems, briefly mentioned at the end of the section 1.3.2.1, is more fundamental for radial-flow systems, where the flow in the individual flow sections is quite different in stationary and in rotating systems.

The relations between the operating conditions n,

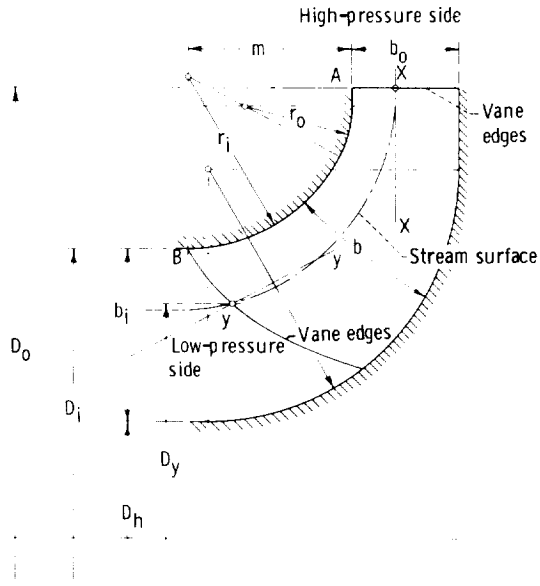

Figure 1–25.—Radial-flow rotor profile.

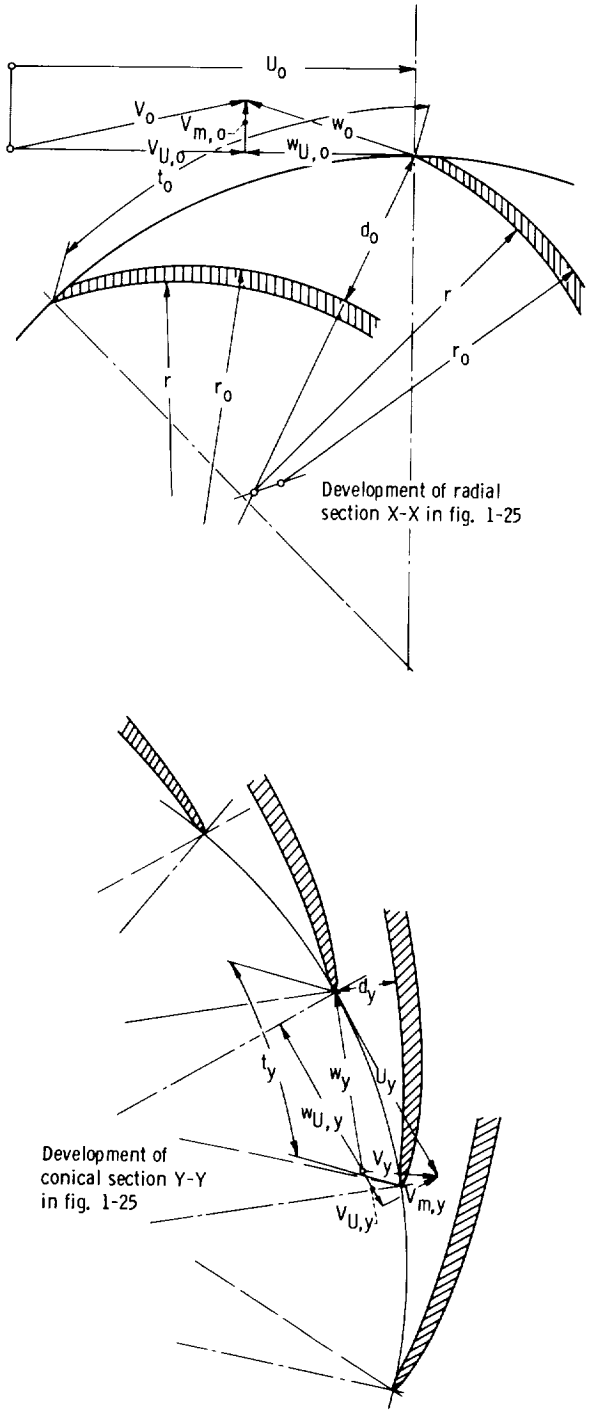

Figure 1-26.—Vane ends of radial- or mixed-flow rotor vane systems.

Q, and H and certain design parameters of radial- and mixed-flow rotors are given in section 1.2.1 in the form of various equations between the basic specific speed of one stage and the rotor design parameters, for example,

$$n_s = \frac{nQ^{1/2}}{(g_o H)^{3/4}} = \frac{1}{2^{1/4}\pi^{1/2}} \left(\frac{U_o^2}{2g_o H}\right)^{3/4} \times \left(\frac{V_{m,i}}{U_i}\right)^{1/2} \left(\frac{D_i}{D_o}\right)^{3/2} \left(1 - \frac{D_h^2}{D_i^2}\right)^{1/2} \tag{1-24a}$$

or

$$n_s = \frac{2^{3/4}}{\pi^{1/2}} \left(\frac{U_o^2}{2g_o H}\right)^{3/4} \times \left(\frac{V_{m,o}}{U_o}\right)^{1/2} \left(\frac{b_o}{D_o}\right)^{1/2} \tag{1-28}$$

where equation (1-24a) is derived from equation (1-24) by using the geometric and aerodynamic parameters shown in figures 1-7 and 1-25.

Another equation (eq. (1-31)) relates the basic specific speed to the stationary flow passages outside the rotor. For the present, only the relation between specific speed and the rotor design form is considered.

Equations (1-24) and (1-28) are used in section 1.2.1 to derive the relation between rotor form and basic specific speed given in figure 1-8. This relation is explored in somewhat greater detail in this section.

Equations (1-24) and (1-28) relate six dimensionless design parameters, $V_{m,i}/U_i$, $V_{m,o}/U_o$, $2g_oH/U_o^2$, D_i/D_o, D_h/D_i, and b_o/D_o, to the basic specific speed. As for axial-flow machines, additional relations are needed to narrow down the design choices, since the number of design parameters is much greater than the number of equations available so far.

For liquids under conditions involving the danger of cavitation, such an additional relation is available in terms of the suction specific speed, used in the form

$$S = \frac{nQ^{1/2}}{(g_o H_{sv})^{3/4}} = \frac{1}{2^{1/4}\pi^{1/2}} \left(\frac{V_{m,i}^2}{2g_o H_{sv}}\right)^{3/4} \times \frac{U_i}{V_{m,i}} \left(1 - \frac{D_h^2}{D_i^2}\right)^{1/2} \tag{1-46}$$

This form has the advantage that, according to figure 1-18, $2g_oH_{sv}/V_{m,i}^2$ is practically a constant (about 3.5) for optimum suction conditions with

respect to cavitation. This relation and figure 1-18 are the same as for axial-flow machines and permit the determination of the flow coefficient $V_{m,i}/U_i$ if one uses D_h^2/D_i^2 as given by mechanical design considerations.

For compressible fluids at velocities where compressibility is important, one may use the compressibility specific speed, as done for axial-flow machines, in the form of any equation from (1-54) to (1-58) to determine $V_{m,i}/U_i$ for a given or assumed value of the Mach number appearing in the equation. Again D_h/D_i has to be determined from other, usually mechanical, considerations.

With $V_{m,i}/U_i$ so determined by cavitation or Mach number considerations, equation (1-24) gives the diameter ratio D_i/D_o if the head coefficient $\psi = 2g_oH/U_o^2$ is given. This is true with particular reference to its maximum value $2g_oH/U_{o,min}^2$ at $D_{o,min}$. This is similar to the case of axial-flow rotors, where $2g_oH/U_{h,2}^2$ is assumed to have a known limiting value. For example, centrifugal pump rotors with backward-bent vanes usually have a maximum head coefficient $2g_oH/U_{o,min}^2 = 1$ or slightly more. Radial-flow rotors with straight radial vanes have $2g_oH/U_{o,min}^2$ values of approximately 1.5 for pumps or compressors and approximately 2 for turbines. Further information on the head coefficient ψ is given in chapters 2 and 4.

With respect to the flow coefficient $V_{m,o}/U_o$ and the rotor width ratio b_o/D_o at the outside diameter (fig. 1-7), equation (1-28) gives the value of the product $(V_{m,o}/U_o)(b_o/D_o)$ without any input from another specific speed, so that the two ratios forming this product must be determined by trial and error. The ratio b_o/D_o may also be determined by considerations of mechanical strength (see sec. 1.3.3.1 or 1.3.3.2). The fact that neither b_o/D_o nor $V_{m,o}/U_o$ (nor the change in meridional velocity $V_{m,o}/V_{m,i}$) is determined hydrodynamically is of major significance for the design of the vane systems of turbomachines and is discussed later in this section. The head coefficient $2g_oH/U_o^2$ in equation (1-28) is, of course, the same as that discussed in the previous paragraph with respect to equation (1-24).

The head coefficient determines the change in the peripheral components V_U of the absolute fluid velocities. For pumps,

$$\psi = \frac{2g_oH}{U_o^2} = 2\eta_h\left(\frac{V_{U,o}}{U_o} - \frac{V_{U,i}U_i}{U_o^2}\right) \qquad (1\text{-}88)$$

For turbines, the hydraulic efficiency η_h is replaced by $1/\eta_h$. The derivation of equation (1-88) is given in chapter 2, section 2.3.

With the aid of equation (1-88) the right sides of the specific speed equations (eqs. (1-24), (1-28), (1-46), and (1-54) to (1-58)) determine the velocity vector diagrams at any diameter to which these equations are applied. As in the preceding section 1.3.2.1, a continuous variation of the velocity diagrams as a function of the diameter D is obtained by using relations such as $V_m = \text{constant}$, $V_U D = \text{constant}$ and $U/D = \text{constant}$ for the same cross section of the merdional flow. The special conditions $V_m = \text{constant}$ and $V_U D = \text{constant}$ are replaced in chapters 2 and 4 by relations that are more general, but nevertheless continuous. Thus the velocity diagrams are determined for any point (coaxial circle) along the inlet and discharge vane edges. This situation is exactly the same as that described in section 1.3.2.1 with respect to axial-flow vane systems.

Figure 1-27 represents this situation. It shows points, representing coaxial circles, and lines, for $D = \text{constant}$, which are located relative to each other according to the ratios D_i/D_o, D_h/D_i, and b_o/D_o appearing in the specific speed equations. Every diameter determined by these equations is associated (by the head and flow coefficients) with a definite velocity vector diagram. Figure 1-27, therefore, represents all the information about the design of the rotor that can be derived from flow-determined specific speeds. Still needed is some rational estimate of the ratio $D_{o,max}/D_{o,min}$ and of the direction of the meridional velocity at the high-pressure side. For pumps, the ratio $D_{o,max}/D_{o,min}$ is often determined by the limits of retardation of the relative flow along the outer shroud (see ch. 2, sec. 2.5.4.3).

For radial- and mixed-flow machines, the next step is the essential process of design, that is, the derivation of the rotor profile and vane shape from the information represented in figure 1-27.

For axial-flow rotors, the determination of the rotor profile as shown in figure 1-20 is almost trivial with the exception of the determination of

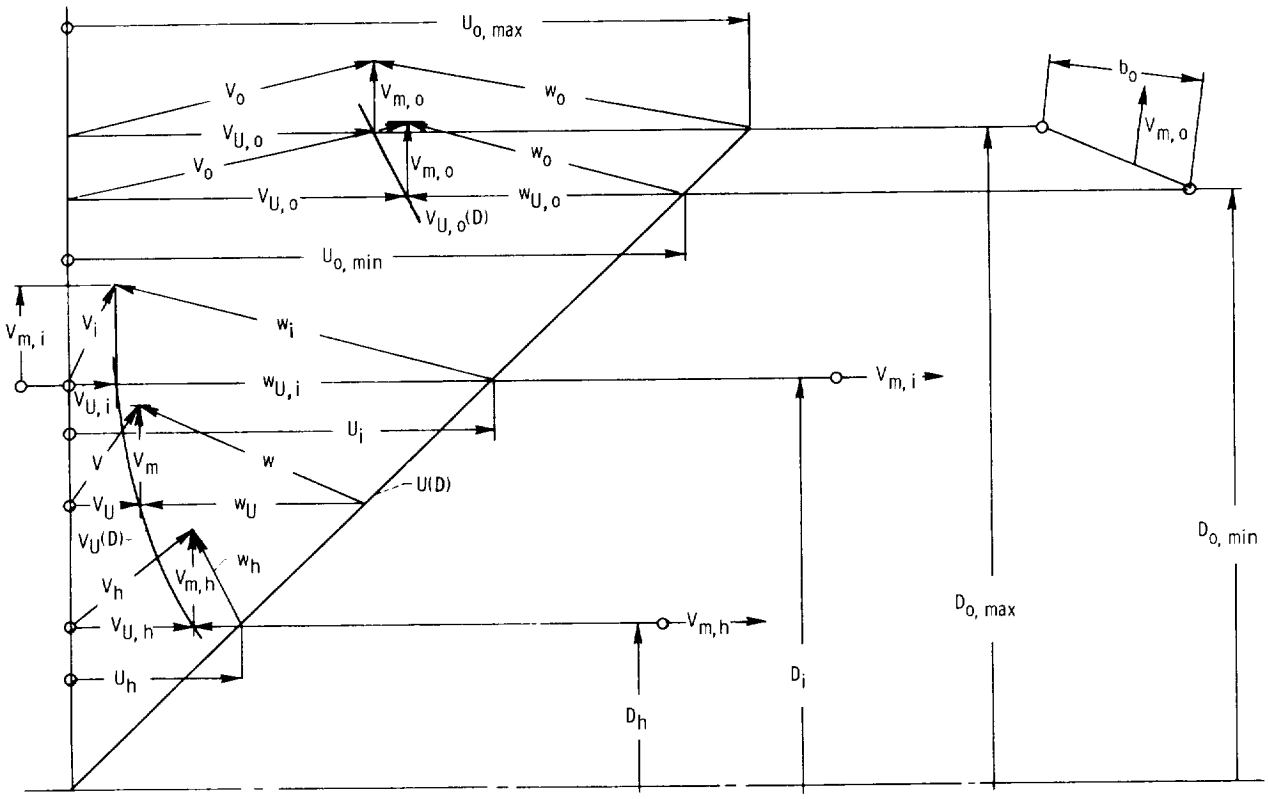

Figure 1-27.—Information on design of radial- and mixed-flow rotors derived from flow-determined specific speeds.

the axial rotor length, which requires considerations of mechanical strength. For radial- or mixed-flow rotors, the determination of the rotor profile (fig. 1-25) is not at all trivial as it involves the deflection of the meridional flow from the axial to the radial or conical direction. Unfortunately, there is no definite rule available for the hydrodynamic design of this profile. This is due to the fact that the meridional velocity component V_m of the flow relative to the vane system is generally smaller than the peripheral component w_U. Thus most flow considerations (e.g., those concerned with flow retardation within the blade row) are determined by the relative rather than the meridional flow. Furthermore, in many cases, the vanes exert an important influence on the meridional velocity distribution, which is, for radial- or mixed-flow rotors, not the same as that of a purely meridional flow in a vaneless space of revolution. The shape of the rotor profile, within the confines of the dimensions given in figure 1-27, must, therefore, be determined by rules of geometric continuity and other considerations which are not very well defined. For example, the outer contour AB of the profile shown in figure 1-25 is constructed from two circular arcs, with the radius of curvature r_i at point B equal to $b_i = (D_i - D_h)/2$ and the radius of curvature r_o just below point A equal to b_o. These relations may be generalized to $r \geqq b$ at any point of the outer contour AB. In principle this method can also be applied to the inner contour of the profile, except that there the radius r is always substantially larger than b. Clearly such a rule has some rational foundation based on the flow in stationary curved passages and is, therefore, useful as a general guide. However, such a rule has no rigid general validity and may well be violated for sufficient reasons. For example, the axial length m of the outer contour may well be limited for mechanical reasons (e.g., critical speed considerations) or for reasons of overall arrangement, size, and cost. It is, therefore, not possible as yet to relate the rotor profile uniquely to the dimensions given in figure 1-27. Additional considerations are presented in chapter 4.

The determination of the vane shape from the velocity vector diagrams is also less definite for

radial- and mixed-flow machines than for axial-flow machines. The velocity vector diagrams, which can be determined from the specific speeds for any point of the leading and trailing vane edges, permit the design of the vane ends on the basis of the one-dimensional assumption that the relative flow is essentially parallel to the vanes. Since vane angles are not very well defined (because of the vane thickness and the rapid changes of these angles in the leading and trailing portions of the vanes), this writer and others prefer to use the normal distance between the vanes d_o and d_y in figure 1-26. The one-dimensional approximation would suggest that $d_y/t_y = V_{m,y}/w_y$ and $d_o/t_o = V_{m,o}/w_o$. Departures from this approximation are discussed in chapter 4. These departures are substantial only at the discharge (outer) vane ends of centrifugal pump or compressor impellers, where d_o/t_o is greater than $V_{m,o}/w_o$ by a substantial amount (about 30 to 60 percent, see ch. 4).

The connections between the leading and trailing portions of the vanes can be designed on the basis of geometric continuity and to some extent by hydrodynamic considerations. The geometric requirements include a continuous simple change in the cross-sectional area between the vanes from the inlet to the discharge. Since this cross-sectional area is proportional to the normal distance between the vanes (d in fig. 1-26) times the normal distance between the shrouds (b in fig. 1-25), vane shape and profile shape are interconnected. Furthermore, since the velocity diagrams at the low-pressure vane edges change rapidly along the vane edge as a function of D_y in figure 1-25 (see also fig. 1-27), the vane ends as shown in section Y-Y of figure 1-26 change their shape substantially along that vane edge from the outer to the inner shroud. Thus the vane is strongly warped within the curved and axial part of the vane profile. The vane shape is, therefore, three-dimensional, and it is a function not only of the velocity diagrams and diameters but also of the profile shape of the system (fig. 1-25).

As mentioned previously, cylindrical sections through axial-flow vane systems can be represented as a family of systematically related vane sections diagrammatically shown in figure 1-23. Chapter 4 shows that the three-dimensionality of radial- or mixed-flow vane sections may not constitute an insurmountable obstacle to this type of representation. However, the number of independent variables of such a family of vane sections would certainly be greater than that for axial-flow vanes. The greatest difficulty would probably result from the deep interrelation between the profile shape and the vane shape, which might not permit the separation of the profile design from the vane flow section design that is so successfully employed in the axial-flow field. Thus there are real reasons why the design of radial- and mixed-flow vane systems is as yet more of a special problem in every individual case than the design of axial-flow vane systems.

Just as for axial-flow vane systems, consideration must be given to the possiblity of separation or stall in radial- or mixed-flow vane systems. While there are theoretical reasons why the resulting limitations in flow and design may be different in rotating radial-flow systems from those in axial-flow systems, these differences are not as yet known with sufficient accuracy to be considered for purposes of design. Thus there is no other approach open than to adopt the same limitations for radial- and mixed-flow as for axial-flow systems (i.e., the existence of a lower limit of the ratio of flow retardation and a dependence of the allowable lift coefficient on this ratio of retardation). (The fact that the ratio of flow retardation has the same significance for radial-flow as for axial-flow systems is not self-evident, but can be proven to be true within the limits of the present considerations.) Whether the lower limit of V_2/V_1 or w_2/w_1 is lower or higher for radial-flow systems than the 0.6 quoted in the previous section for axial-flow systems cannot be stated definitely. The relatively poorer knowledge about the flow in radial-flow systems suggests the use of more conservative (higher) ratios of V_2/V_1 or w_2/w_1 than 0.6 for radial-flow systems.

The second limit to be considered is that of the lift coefficient, which for radial- and mixed-flow sytems is

$$C_L = 2\,\frac{V_{U,o} - V_{U,i}D_i/D_o}{w_\infty}\,\frac{t_o}{l} \qquad (1\text{-}89)$$

where t_o is the circumferential vane spacing at the same outside diameter D_o where $V_{U,o}$ is measured and defined and l is the vane length. There is no rational reason for departing from the rules given in the preceding section 1.3.2.1 for limiting values of C_L. Thus equation (1-89) gives an upper limit of t_o/l (the reciprocal of the solidity) as a function of

the velocity vector diagrams and assumed limits of C_L.

From the foregoing considerations on radial- and mixed-flow machines, as well as those on axial-flow machines, it can be concluded that one obtains the most essential dimensional relations of the rotor profile and the velocity vector diagrams at the inlet and discharge edges of the rotor vane system from the dimensional ratios, velocity ratios, and head ratios derived from the specific speeds pertaining to the flow conditions. By appropriate rules of design, the dimensional ratios determine the profile of the rotor, while the velocity vector diagrams determine to a large extent the shape of the vane ends. The degree to which the flow specific speeds determine the hydrodynamic design form of the rotor depends on the state of knowledge available for the design of the machine concerned. It is reasonable to assume that for a hypothetical very high state of knowledge the relation between the specific speeds and the fluid-dynamic design of the machine would be just as complete as the degree to which the fluid-dynamic operating conditions are prescribed. (Sec. 1.3.3 demonstrates the fact that purely mechanical considerations, e.g., limitations of the stresses in the solid parts of the machine, also have a very decisive effect on the design of the rotor.)

As mentioned previously, the specific speeds which are concerned with flow conditions do not determine the design of the vane systems of the machine uniquely. To do so, it is necessary to make certain design decisions, for example, the choice of axial, radial, or mixed flow and the choice of the number of stages to be used. These decisions are dictated partly by mechanical considerations and partly by the existence of lower limits of the basic specific speed given by efficiency considerations.

The rotor design alone does not determine the design of the entire machine. The flow conditions on the inlet and discharge side of the rotor have a strong influence on the design of the stationary vane systems and passages adjacent to the rotor. Equation (1-31) describes the effect of the basic specific speed on the stationary passages outside a radial- or mixed-flow rotor. Yet these vane systems or passages are also decisively influenced by other considerations, particularly by the required form of guidance of the flow to and from the rotor. Of primary importance is whether the flow is to be guided to or from the outside of the machine or whether the flow is to be guided to or from another stage. Figure 1-28 gives three examples of these alternative possibilities. In all three examples, the specific speed for one stage is assumed to be the same, as expressed by the similarity of the rotors. The difference between examples A and B is dictated primarily by considerations of mechanical strength with respect to the inside pressure. In both cases, the flow is ducted away from the pump, or to the turbine, in a plane normal to the axis of rotation. For multistage machines, as shown by example C, the flow enters the next stage and must, therefore, leave the preceding stage in the direction of the axis of rotation; this flow pattern demands a completely different form of the stationary vane systems. Design forms A and B can also be used for multistage machines by turning the pipeline between the stages at least 180°; design C can be

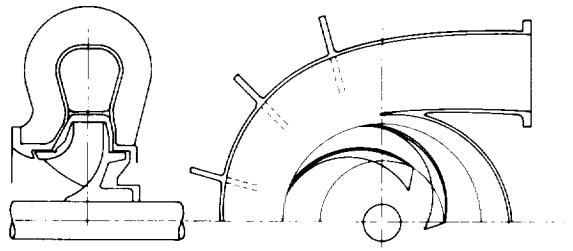

Example A: Open volute pump (or turbine)

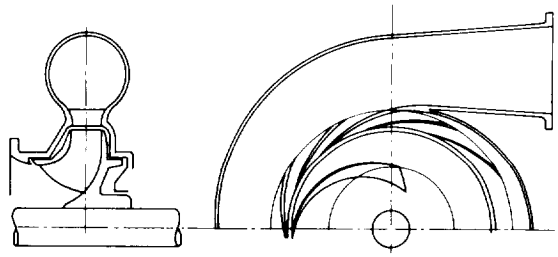

Example B: Volute pump or turbine with vane diffuser or nozzle ring

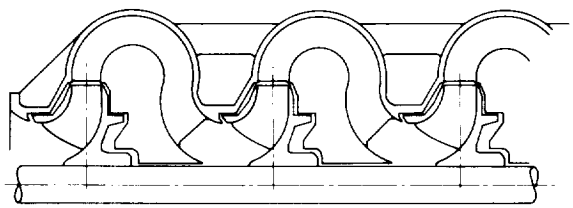

Example C: Multistage pump with vane diffusers (see also figs. 4-61 to 4-63 in ch. 4)

Figure 1-28.—Various design forms of radial-flow machines having same basic specific speed per stage.

used for single-stage machines if a discharge (for turbines, an inlet) coaxial with the axis of rotation is desired.

The design of all three examples given in figure 1-28 is described in chapter 4. The design of the diffuser vane systems of example C follows in principle similar lines outlined previously for radial-flow rotors in connection with figures 1-25 to 1-27 and in chapter 4 in connection with figures 4-59 to 4-62.

1.3.3 Stress-Determined Design Forms of Turbomachines

1.3.3.1 Centrifugal-stress-determined design forms.—In section 1.2.3, the stress specific speed is related to various design parameters in the following manner:

$$n_\sigma = \frac{nQ^{1/2}}{(\sigma/\rho)^{3/4}} = \frac{1}{2^{1/4}\pi^{1/2}}\left(\frac{\rho U_o^2}{2\sigma}\right)^{3/4}\left(\frac{D_i}{D_o}\right)^{3/2} \cdot \times\left(\frac{V_{m,i}}{U_i}\right)^{1/2}\left(1-\frac{D_h^2}{D_i^2}\right)^{1/2} \qquad (1\text{-}64)$$

The stress coefficient can be used in the form $2\sigma/\rho U_o^2$ as well as in the reciprocal form $\rho U_o^2/2\sigma$, which has a slightly different physical significance. The first form $2\sigma/\rho U_o^2$ makes the stress in solid parts σ dimensionless by means of the velocity pressure of U_o (which accounts for the factor 2). In its reciprocal form $\rho U_o^2/2\sigma$, this coefficient increases with the quality of the structural design form to resist applied forces with a given allowable stress, that is, for a given quality of the structural material (stress-density ratio). In this compendium, the stress coefficient is usually used in its reciprocal form.

If the stress σ is generated by fluid forces, then ρ is the mass density of the fluid. If the stress is generated by the rotation of the solid parts, then ρ is the mass density of the solid parts, as explained in the next paragraph.

In the present section, the stress σ is considered as generated by centrifugal forces ($\sigma = \sigma_c$), and therefore, ρ is principally the mass density of the solid rotating parts of the machine ρ_s. However, if these parts are completely submerged in a fluid rotating at the same angular velocity as the solid parts, their effective mass density is equal to the difference in mass density between the solid parts and the fluid (i.e., the effective mass density is $\rho = \rho_s - \rho_f$). Since centrifugal stresses are usually of major importance only when relatively light fluids (gases or liquid hydrogen) are used, ρ_f is neglected and ρ in equation (1-64) is considered equal to ρ_s.

The objective of this section is to explore the meaning of the right side of equation (1-64) with respect to the design form of the rotating parts, particularly the effect of the centrifugal stress coefficient $\rho_s U_o^2/2\sigma_c$ on the design form.

First consideration is given to straight radial members. Such members include, for example, axial-flow blades that form so-called straight helical surfaces (i.e., when their generating line is straight, radial, and normal to the axis of rotation). Such surfaces are also used with radial- and mixed-flow compressors and liquid-hydrogen pumps because their peripheral velocities are sufficiently high to demand straight radial elements for their rotating parts (see fig. 1-29). The mechanical element to be examined is a straight radial strut rotating about the zero radius point of its radial extent.

Figure 1-30 shows an element of a radial strut. The centrifugal force acting on this element is

$$dF_c = r\omega^2\rho_s a\,dr = \sigma a - (a+da)(\sigma+d\sigma) = -\sigma\,da - a\,d\sigma \qquad (1\text{-}90)$$

where a is an area extending in the circumferential and axial directions. For a strut of constant cross section a, $da = 0$. Hence

$$\rho_s\omega^2\int_r^{r_o} r\,dr = -\int_r^{r_o} d\sigma$$

$$\frac{\rho_s\omega^2}{2}(r_o^2 - r^2) = \frac{\rho_s U_o^2}{2}\left(1-\frac{r^2}{r_o^2}\right) = \sigma_r - \sigma_o \qquad (1\text{-}91)$$

where the subscript o refers to the maximum distance from the center of rotation and the subscript r refers to the variable distance r from the center of rotation.

For $\sigma_o = 0$ (zero stress at the outer tip), one finds the maximum stress at $r = 0$ to be

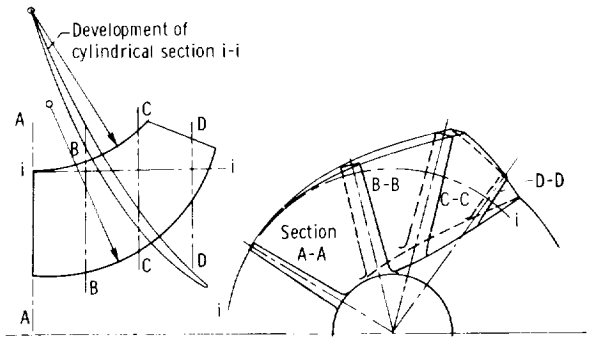

Figure 1-29.—Mixed-flow rotor with radial vane elements (according to F. Lawaczeck (ref. 3) and R. Birman).

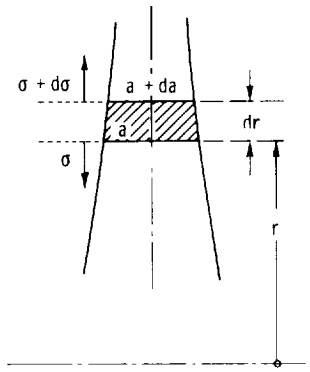

Figure 1-30.—Element of radial rotating strut.

$$\left.\begin{aligned} &\frac{\rho_s U_o^2}{2} = \sigma_{(r=0)} \\ &\text{or} \\ &\frac{\rho_s U_o^2}{2\sigma_{(r=0)}} = 1 \end{aligned}\right\} \qquad (1\text{-}92)$$

which is an example of a definite numerical value for the centrifugal stress coefficient appearing in equation (1-64).

For a radial strut with variable cross section but dimensioned in such a fashion that $\sigma_c = \text{constant}$ and $d\sigma_c = 0$, one finds

$$\rho_s \omega^2 a r\, dr = -\sigma_c\, da \qquad (1\text{-}93)$$

$$\rho_s \omega^2 \int_r^{r_1} r\, dr = -\sigma_c \int_r^{r_1} \frac{da}{a}$$

$$\frac{\rho_s}{2}\omega^2 (r_1^2 - r^2) = \frac{\sigma_s U_1^2}{2}\left(1 - \frac{r^2}{r_1^2}\right) = \sigma_c \ln \frac{a}{a_1}$$

$$\left.\begin{aligned} &\frac{\rho_s U_1^2}{2\sigma_c}\left(1 - \frac{r^2}{r_1^2}\right) = \ln \frac{a}{a_1} \\ &\text{or} \\ &\frac{a}{a_1} = exp\left[\frac{\rho_s U_1^2}{2\sigma_c}\left(1 - \frac{r^2}{r_1^2}\right)\right] \end{aligned}\right\} \qquad (1\text{-}94)$$

where the centrifugal stress σ_c is constant radially (i.e., it exists also in the outermost cross section a_1 at radius r_1).

Figure 1-31 shows a/a_1 as a function of r/r_1 and $\rho_s U_1^2/2\sigma_c$. It is shown later in this section that exactly the same relation as equation (1-94) holds also for the thickness distribution of a rotating disk having a uniform stress distribution and, therefore, a radial (and circumferential) stress σ_c at the outer perimeter (at the radius r_1).

Since the radial strut treated in this section has (so far) the tensile stress $\sigma_c = \sigma_1$ at its outer cross section a_1 and the radius r_1, such a strut must actually be extended radially beyond $r = r_1$ so as to physically generate (by its centrifugal force) the stress $\sigma_c = \sigma_1$ at $r = r_1$. For the special form with uniform cross section ($a = a(r) = a_1$) between r_1 and a larger, maximum radius r_o, the radius ratio r_1/r_o follows from equation (1-91) for the case of zero stress ($\sigma_o = 0$) at $r = r_o$. Figure 1-32 shows the distribution of the cross section of this strut with uniform stress from $r = 0$ to $r = r_1$ and radially diminishing stress from σ_1 at $r = r_1$ to $\sigma_c = 0$ at the maximum radius $r = r_o$ derived from equation

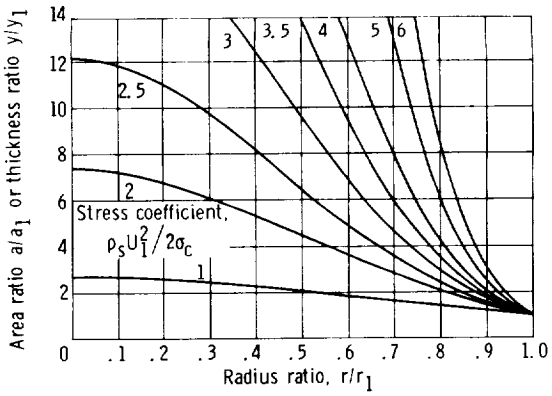

Figure 1-31.—Area distribution of radial strut and thickness distribution of rotating disk, both with uniformly distributed centrifugal stress. (Subscript 1 denotes stressed outer perimeter.)

(1-91) and the following equation:

$$\left.\begin{aligned} 1-\frac{r_1^2}{r_o^2} &= \frac{2\sigma_1}{\rho_s U_o^2} \\ \text{or} \\ \frac{r_1^2}{r_o^2} &= 1-\frac{2\sigma_1}{\rho_s U_o^2} \end{aligned}\right\} \qquad (1\text{-}95)$$

Evidently

$$\frac{\rho_s U_1^2}{\sigma} = \frac{\rho_s U_o^2}{\sigma}\frac{U_1^2}{U_o^2} = \frac{\rho_s U_o^2}{\sigma}\frac{r_1^2}{r_o^2}$$

so that equation (1-94), when referred to r_o and U_o rather than to r_1 and U_1, may be rewritten

$$\frac{\rho_s U_o^2}{2\sigma_1}\frac{r_1^2}{r_o^2}\left(1-\frac{r^2}{r_o^2}\frac{r_o^2}{r_1^2}\right) = \ln\frac{a}{a_1} \qquad (1\text{-}96)$$

The solution of this equation is represented graphically in figure 1-32. This figure represents the rotating strut with zero stress at its outer end ($r=r_o$) and shows the extent of the cylindrical outer portion of the strut ($a=a_o=a_1$) for $r_1 \leqq r \leqq r_o$ and the portion of constant stress and varying cross section a/a_1 for $r<r_1$.

Thus the centrifugal stress coefficient $\rho_s U_o^2/2\sigma_c$ gives the radial distribution of cylindrical coaxial cross sections for straight radial rotating members such as blades with radial blade elements. The stress specific speed and the stress coefficient so determined, therefore, supplement the information presented in section 1.3.2.1 regarding the design of axial-flow vane systems. However, according to the relations just derived, the stress specific speed and the centrifugal stress coefficient apply also to radial and mixed-flow rotor blades with radial blade elements (fig. 1-29). It is shown later in this section that the same stress coefficient can be applied also to rotor vanes of more general shapes.

The second form of rotating members to be considered is a relatively thin hoop or cylinder of the mean radius r. (For somewhat complex radial cross sections of the hoop, r may be the distance of the center of gravity of the cross section from the axis of rotation.)

It is well known that the centrifugal circumferential tensile stress in a thin rotating hoop or cylinder is

$$\sigma_c = \rho_s U^2$$

so that the centrifugal stress coefficient is

$$\frac{\rho_s U^2}{2\sigma_c} = 0.5 \qquad (1\text{-}97)$$

This stress coefficient is the lowest appearing in rotating elements subjected to simple tension. (Elements subjected to bending can have much lower coefficients $\rho_s U^2/2\sigma_c$.) While a freely rotating thin hoop, or a radially thin cylinder, is not very frequently used in turbomachinery, it is a good reference shape to be considered, because it appears as wearing rings, as outer shrouds, occasionally as hubs of axial-flow rotors, and so on. If the stress coefficient in the stress specific speed is as low as or lower than 0.5, ring-shaped rotating elements are acceptable, whereas for higher stress coefficients members extending radially toward the axis of rotation are required.

The next form of rotating element to be considered is a disk normal to the axis of rotation. The theoretically simplest rotating disk is the disk of constant stress. It is a disk without a central hole, so that it has to be fastened to its shaft by means of coaxial flanges. Its thickness distribution as a function of the distance r from the axis of rotation is

$$\frac{y(r)}{y_1} = \exp\left[\frac{\rho_s U_1^2}{2\sigma_c}\left(1-\frac{r^2}{r_1^2}\right)\right]$$

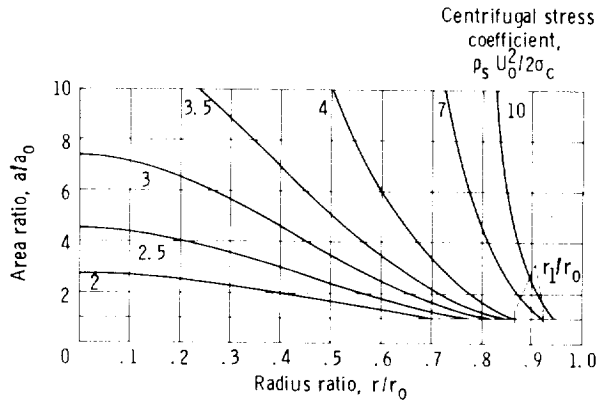

Figure 1-32.—Cross-sectional area distribution of rotating radial strut having uniform stress distribution for $r \leqq r_1$, zero stress at $r=r_o$, and diminishing stress from r_1 to r_o.

or

$$\frac{\rho_s U_1^2}{2\sigma_c}\left(1-\frac{r^2}{r_1^2}\right)=\ln\frac{y(r)}{y_1} \qquad (1\text{-}98)$$

where the subscript 1 refers to the outer circumference, which has a uniform radial and circumferential stress σ_c. The thickness ratio $y(r)/y_1$ safisfies exactly the same equation as the area ratio of a radial strut of constant stress (eq. (1-94)). Therefore figure 1-31 applies also to the thickness y of a disk of constant stress, with the thickness evenly distributed on both sides of a plane of symmetry which is normal to the axis of rotation (see also fig. 1-33). The dimensionless shape of the rotating disk of constant stress is uniquely determined by the value of its centrifugal stress coefficient $\rho_s U_1^2/2\sigma_c$.

Rotating disks of different shapes have, of course, different nonuniform stress distributions as long as their behavior is completely elastic. Thus, a flat disk of constant thickness with no hole has its maximum elastic stress in the center, while a disk with a central hole has its maximum stress at the periphery of the hole. The latter stress is tangential to the hole and is at least twice the stress of a disk with no hole. Fortunately the actual stress distribution is much more uniform if the disk is made of a reasonably ductile material because the regions of maximum stress yield and thus relieve the stress concentration. As a consequence, the so-called average stress (an assumed uniform circumferential stress) is of greater practical significance than an exactly computed elastic stress distribution. Chapter 5 describes the calculation of the average stress and of the corresponding centrifugal stress coefficient. For example, the average stress coefficient of a flat disk with no central bore, or only a very small central bore, is approximately $\rho_s U^2/2\sigma_c = 1.5$.

The last form of turbomachinery structure to be investigated in this section has elements, usually rotor blades, extending axially from one or between two disk-shaped shrouds, so that the centrifugal force acting on such elements has to be carried in bending.

Figure 1-34 depicts a vane of a radial-flow rotor which is overhung from a shroud on one side of the vane, that is, an element of an open radial- or mixed-flow rotor.

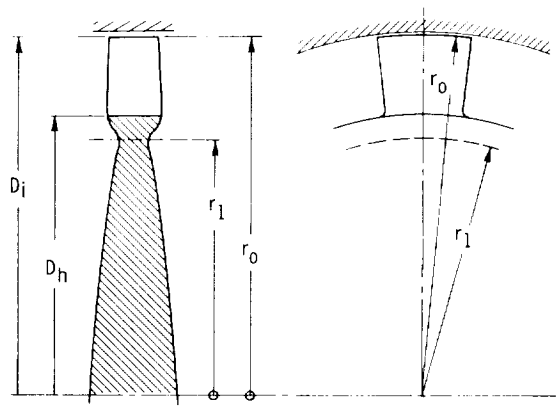

Figure 1-33.—Sketch of axial-flow rotor showing relation of r_o, r_1, D_i, and D_h.

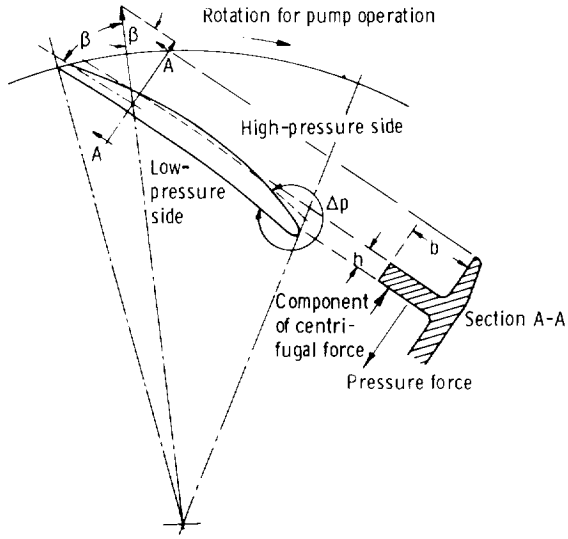

Figure 1-34.—Axially overhung vane of radial-flow rotor.

It is nearly obvious (and it is stated in standard handbooks) that the maximum bending moment at the root of the blade per unit length of the blade is

$$M_{max}=\frac{wb^2}{2} \qquad (1\text{-}99)$$

where w, the load per unit area, is

$$w = h\rho_s r\omega^2 \sin\beta$$

in which the angle is defined, as in figure 1-34, as the direction of a tangent to the mean camber line. Therefore

$$M_{max} = \frac{b^2}{2} h\rho_s r\omega^2 \sin\beta$$

The resulting centrifugal bending stress is

$$\sigma_c = \frac{M_{max}}{m_{s,1}}$$

where $m_{s,1}$ is the section modulus of the vane (moment of inertia divided by the maximum distance from the neutral axis) per unit of length of the vane. Hence the centrifugal bending stress is

$$\sigma_c = \frac{b^2 h\rho_s r\omega^2 \sin\beta}{2m_{s,1}}$$

and with $r\omega = U$, the centrifugal stress coefficient is

$$\frac{\rho_s U^2}{2\sigma_c} = \frac{rm_{s,1}}{b^2 h \sin\beta} \qquad (1\text{-}100)$$

Approximating the section modulus per unit length of the vane by $m_{s,1} = h^2/6$ gives

$$\frac{\rho_s U^2}{2\sigma_c} = \frac{hr}{6b^2 \sin\beta} \qquad (1\text{-}100a)$$

If the vane is strongly curved, $m_{s,1} = h^2/6$ is, of course, not a valid approximation of the section modulus per unit length. Then one uses equation (1-100) with

$$m_{s,1} = \frac{\text{total section modulus}}{\text{total vane length}}$$

If the vane is inclined against the axial direction, as shown in figure 1-35, equations (1-100) and (1-100a) assume the form

$$\frac{\rho_s U^2}{2\sigma_c} = \frac{rm_{s,1}}{b^2 h \sin\beta\cos\alpha} = \frac{hr}{6b^2 \sin\beta\cos\alpha} \qquad (1\text{-}101)$$

where the last expression applies to $m_{s,1} = h^2/6$.

It should be recognized that this relation neglects the uniform tensile stress in the blade. Therefore, for $\alpha = 90°$, the stress coefficient $\rho_s U^2/2\sigma_c$ obeys the relation given previously for radial struts (eq. (1-96) and fig. 1-32).

Vanes extending axially between two shrouds of the rotor, but not consisting of straight radial elements, can be treated as beams in bending

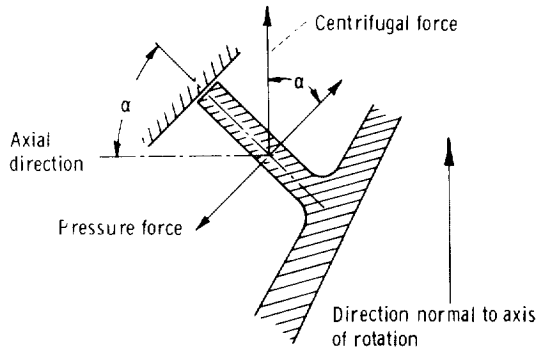

Figure 1-35.—Radial section through axially overhung vane inclined against axial direction.

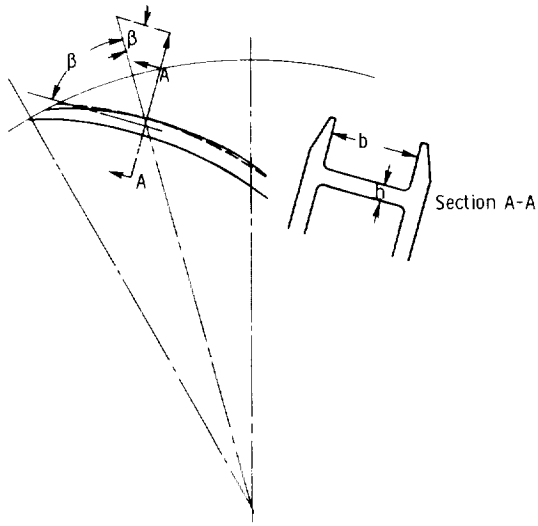

Figure 1-36.—Axially extending nonradial vane supported at both axial ends by shrouds.

between two end supports (see fig. 1-36). The maximum bending moment is in this case

$$M_{max} = \frac{wb^2}{q} \qquad (1\text{-}102)$$

where q varies from 8 for end supports without any bending stiffness to values between about 12 and 25 for more or less rigid end supports. For such supports, the mechanical complexity makes it necessary to assume a reasonable q value, presumably about 15.

All other relations are exactly the same as for the axially overhung blade. Thus, with the notation given in figure 1-36

$$\frac{\rho_s U^2}{2\sigma_c} = \frac{q}{12}\frac{h}{b}\frac{r}{b}\frac{1}{\sin\beta} \qquad (1\text{-}103)$$

Of course, blade inclination against the axial direction is also possible for rotors with two shrouds. Then the stress coefficient is given by a relation analogous to equation (1-101):

$$\frac{\rho_s U^2}{2\sigma_c} = \frac{q}{12}\frac{h}{b}\frac{r}{b\cos\alpha\sin\beta} \tag{1-104}$$

In this section, U is the peripheral velocity at the part of the vane considered, which is often, but not always, the outside velocity of the rotor U_o. If U is not U_o, the stress coefficient can easily be converted to the stress coefficient at the outer periphery by the relation

$$\frac{\rho_s U_o^2}{\sigma} = \frac{\rho_s U^2}{\sigma}\frac{r_o^2}{r^2} \tag{1-105}$$

If the outermost vane tips are thinner than the rest of the blade, it is advisable to use an average blade thickness h over a reasonably long part of the outer vane portion, because the thicker parts of the blades can help to support the thinner parts. This average vane thickness h is indicated in figures 1-34 and 1-36.

The foregoing considerations permit rather far reaching conclusions regarding the design of turbomachinery.

It is evident from figure 1-31 that stress coefficients $\rho_s U_1^2/2\sigma_c > 2$ lead to excessive disk thicknesses at the center ($r/r_1 = 0$) if one does not permit yielding in the central regions. Even if such yielding is permitted, the disk cannot have a constant thickness for which the average stress coefficient is 1.5. Therefore $\rho_s U_1^2/2\sigma_c = 2$ requires the disk to be substantially thicker in the central region than at $r = r_1$. However, r_1 is often not the maximum radius of the rotor. Then, according to equation (1-105), the stress coefficient referred to the maximum radius r_o is

$$\frac{\rho_s U_o^2}{2\sigma_c} = \frac{\rho_s U_1^2}{2\sigma_c}\frac{r_o^2}{r_1^2}$$

which is, for example, 4 for $\rho_s U_1^2/2\sigma_c = 2$ and $r_o/r_1 = \sqrt{2}$.

Accordingly, if the hub-tip ratio $D_h/D_i = r/r_o$ of the blades is assumed to be 0.75 (see fig. 1-33 for an explanation of $D_h/D_i > r_1 r_o = 1/\sqrt{2}$), one can read from figure 1-32 with $\rho_s U_o^2/2\sigma_c = 4$ that the area ratio a/a_o for straight radial blades is about 2.5. This value is a rather severe requirement for the blade design. Thus, by considerations of this type, one can reach a conclusion about a practical upper limit for the centrifugal stress coefficient $\rho_s U_o^2/2\sigma_c$, which, as mentioned previously, is approximately 4. (Usually somewhat lower limits are desirable.)

As a second example, consider a standard centrifugal pump impeller with backward-bent vanes extending axially between two shrouds. Assuming in equation (1-103) the vane thickness to span ratio $h/b = 1/4$ and $r/b = D_o/2b_o = 4.2$, which corresponds to the profile shown in figure 1-25, and letting $q = 15$ and $\beta = 60°$, one obtains

$$\frac{\rho_s U_o^2}{2\sigma_c} = \frac{15}{12}\frac{4.2}{4\times 0.866} = 1.52$$

This equation shows that the vanes of such a rotor are substantially stronger against centrifugal forces than a freely rotating thin hoop. This fact should give the design engineer some hint regarding the construction of the side shrouds.

Finally one can draw from the results just presented some conclusions regarding the magnitude of the stress specific speed $n_{\sigma,c}$ in relation to the basic specific speed. Evidently

$$\frac{n_{\sigma,c}}{n_s} = \left(\frac{g_o H}{\sigma_c/\rho_s}\right)^{3/4} = \left(\frac{2g_o H}{U_o^2}\frac{\rho_s U_o^2}{2\sigma_c}\right)^{3/4} \tag{1-106}$$

Considering the first of the foregoing examples and assuming that the rotor is a standard axial-flow compressor rotor, one can estimate that $2g_o H/U_o^2 = 0.56$ (for $D_h/D_i = 0.75$, and with $2g_o H/U_h^2 = 1$ at the hub). With $\rho_s U_o^2/2\sigma_c = 4$, which is the maximum stress coefficient previously estimated, one finds

$$\frac{n_{\sigma,c}}{n_s} = (0.56\times 4)^{3/4} = 1.83$$

It is, of course, just as easy to calculate the stress specific speed directly from equation (1-64) by using an axial-flow rotor with $D_o = D_i$ and assuming a value of the flow coefficient $V_{m,i}/U_i$. The hub-tip diameter ratio D_h/D_i is assumed to be 0.75, and with $V_{m,i}/U_i$ assumed to be 0.3, the result is $n_{\sigma,c} = 0.3217$.

The second of the foregoing examples leads, with $2g_o H/U_o^2 = 1$, to the conclusion $n_{\sigma,c}/n_s = 1.36$. In this example, the stress specific speed is most advantageously related to the basic specific speed in the form

$$n_s = \frac{nQ^{1/2}}{(g_o H)^{3/4}} = \frac{2^{3/4}}{\pi^{1/2}} \left(\frac{U_o^2}{2g_o H} \right)^{3/4} \times \left(\frac{V_{m,o}}{U_o} \right)^{1/2} \left(\frac{b_o}{D_o} \right)^{1/2} \quad (1\text{-}28)$$

Using $V_{m,o}/U_o = 0.12$ (see fig. 1-27), $b_o/D_o = 1/8.4$ (as previously), and $U_o^2/2g_o H = 1$, one finds $n_s = 0.1134$ (1950 is dimensional form). Therefore $n_{\sigma,c} = 0.1134 \times 1.36 = 0.1542$.

The fact that this stress specific speed is only about one-half of the corresponding value for the axial compressor impeller previously considered reflects correctly the fact that the axial compressor impeller represents a nearly optimum form of design relative to centrifugal stresses, whereas a standard centrifugal pump impeller with backward-bent vanes certainly does not represent such an optimum.

1.3.3.2 *Fluid dynamically generated stresses.*—Consider the stress specific speed represented by equation (1-64) (sec. 1.2.3). If the mass density ρ in this equation is given the value of the mass density of the fluid ρ_f, then $\rho_f U^2$ is obviously a dynamic fluid pressure and σ is, therefore, a stress generated by such fluid pressures σ_f. In order to relate this stress properly to the specific speeds, it is necessary to limit the stress-producing fluid pressures to pressure differences generated by inertial forces within the machine. Therefore this section is limited to stresses generated by this type of pressure difference.

The most obvious stress generated in this manner is the bending stress in a turbomachinery vane or blade, produced by the dynamic pressure difference between the two sides of the blade. This pressure difference is known to be $\Delta p = C_L \rho_f w^2/2$ when averaged over the chord length of the blade. Quite often the lift coefficient C_L is varied spanwise in such a manner that this pressure difference is approximately constant. With Δp considered to be the distributed load acting on the blade as a beam in bending, the maximum bending moment at the root of a blade held on only one spanwise end is

$$M_{max} = \frac{\Delta p b^2 l}{2} \quad (1\text{-}107)$$

where b, as previously, is the spanwise width of the blade (radial width for axial-flow blading) and l is an average chord length. (See figs. 1-34 and 1-35 for radial-flow blade configurations.) The bending stress is

$$\sigma_f = \frac{M_{max}}{m_s} = \frac{\Delta p b^2 l}{2m_s} \quad (1\text{-}108)$$

where m_s is the section modulus of the root section of the blade. For a twisted blade, the bending force may not be exactly normal to the neutral axis for the minimum section modulus of the root section. However, this discrepancy is not sufficient to be considered in this section.

As mentioned previously,

$$\Delta p = \frac{C_L \rho_f w^2}{2} \quad (1\text{-}109)$$

so that equation (1-108) may be written in the form

$$\sigma_f = C_L \frac{\rho_f w^2}{2} \frac{1}{2} \frac{b^2 l}{m_s}$$

or

$$\frac{\rho_f w^2}{2\sigma_f} = \frac{2}{C_L} \frac{m_s}{b^2 l} \quad (1\text{-}110)$$

where C_L must be determined from the velocity diagram which is related to the basic specific speed and to the particular vane under investigation. For axial-flow vane systems, it is quite satisfactory to refer C_L and w to the velocity diagram of the tip section.

The stress specific speed as expressed by equation (1-64) contains the familiar stress coefficient $\rho_f U_o^2/2\sigma_f$. Evidently this coefficient is related to the coefficient appearing in equation (1-110) as follows:

$$\frac{\rho_f w^2}{2\sigma_f} = \frac{\rho_f U_o^2}{2\sigma_f} \frac{w^2}{U_o^2}$$

so that equation (1-110) may be written in the form

$$\frac{\rho_f U_o^2}{2\sigma_f} = 2 \left(\frac{U_o^2}{C_{L,o} w^2} \right) \frac{m_s}{b^2 l} \quad (1\text{-}111)$$

where $U_o^2/C_{L,o} w^2$ must be derived from the velocity diagram applying to the vanes under consideration.

If the vane is held on both ends, the only difference is that

$$M_{max} = \frac{\Delta p b^2 l}{q} \tag{1-112}$$

where q varies from 8 for completely flexible supports to 25 for completely rigid supports. In section 1.3.3.1, a value of $q = 15$ is suggested as a suitable average value.

With equations (1-112), (1-109), and (1-108), one finds

$$\frac{\rho_f w^2}{2\sigma_f} = \frac{q}{C_L} \frac{m_s}{b^2 l} \tag{1-113}$$

and

$$\frac{\rho_f U_o^2}{2\sigma_f} = q \frac{U_o^2}{C_L w^2} \frac{m_s}{b^2 l} \tag{1-114}$$

It is of interest to compare the last expression with the corresponding expression for centrifugal stresses. For axial-flow rotors, the blade elements are radial and in pure tension (approximately). For example, for a radial blade element of constant cross section, one derives from equation (1-91) for $\sigma_o = 0$

$$\frac{\rho_s U_o^2}{2\sigma_c} = \frac{1}{1 - r_h^2/r_o^2} \tag{1-115}$$

Dividing this by equation (1-114) yields

$$\frac{\rho_s U_o^2/2\sigma_c}{\rho_f U_o^2/2\sigma_f} = \frac{\rho_s \sigma_f}{\rho_f \sigma_c} = \frac{C_L w^2 b^2 l}{q(1 - r_h^2/r_o^2) U_o^2 m_s} \tag{1-116}$$

which gives a comparison between the centrifugal tensile stress in a straight radial strut of uniform cross section with a mass density ρ_s and the bending stress in a straight helical blade with a radial span $b = (D_i - D_h)/2$, a chord length l, and a root section modulus m_s. Usually $b^2 l >> m_s$.

Equation (1-116) written in the form

$$\frac{\sigma_f}{\sigma_c} = \frac{\rho_f}{\rho_s} \frac{C_L w^2}{q(1 - r_h^2/r_o^2) U_o^2} \frac{b^2 l}{m_s} \tag{1-117}$$

permits a comparison between the aerodynamic or hydrodynamic stresses σ_f and the centrifugal stresses σ_c in axial-flow rotor blades with radial blade elements. Evidently $C_L w^2/q(1 - r_h^2/r_o^2)U_o^2$ is of the order of 1. Hence, for gases, where $\rho_f << \rho_s$, one finds $\sigma_f < \sigma_c$, unless $b^2 l/m_s$ is of the same order as ρ_s/ρ_f; this may be true for the radially long and slender blades used in the initial stages of aircraft compressors and for fans of aircraft fan engines. In such machinery, σ_f may be of the same order as σ_c. In all other machinery handling gases, such as axial-flow compressors with fairly short blades and radial- or mixed-flow compressor rotors with radial blade elements (see fig. 1-29), $b^2 l/m_s$ is of a lower order than ρ_s/ρ_f, so that according to equation (1-117) $\sigma_f < \sigma_c$. For liquid hydrogen, ρ_s/ρ_f may be of the same order as $b^2 l/m_s$, so that σ_f/σ_c may be of the order of 1. For fairly heavy liquids like water or liquid oxygen, ρ_s is only two to eight times greater than ρ_f, so that $b^2 l/m_s$ is nearly always larger than ρ_s/ρ_f, and, therefore, $\sigma_f > \sigma_c$. In other words, for heavy liquids the fluid-induced bending stresses dominate over centrifugal tensile stresses in radial blade elements.

The same comparison can be made between centrifugal bending stresses in axially extending vanes and the aerodynamically or hydrodynamically induced bending stresses. This comparison is furnished by equations (1-103) and (1-114). Since in the former equation the root section modulus m_s per unit length of the blade is set equal to $h^2/6$, one substitutes in equation (1-103) m_s/l for $h^2/6$. Hence, for axially extending blades,

$$\frac{\rho_s U_o^2/2\sigma_c}{\rho_f U_o^2/2\sigma_f} = \frac{\rho_s \sigma_f}{\rho_f \sigma_c} = \frac{q m_s r}{2hlb^2 \sin\beta} \frac{C_L w^2 b^2 l}{q U_o^2 m_s}$$

which simplifies to

$$\frac{\sigma_f}{\sigma_c} = \frac{\rho_f}{\rho_s} \frac{r}{2h} \frac{C_L w^2}{U_o^2 \sin\beta} \tag{1-118}$$

As q cancels out, this equation evidently holds for axially overhanging blades as well as blades held on both axial ends by rotating shrouds. The ratio $C_L w^2/U_o^2 \sin\beta$ is obviously of the order of 1. Hence the comparison is to be made between ρ_s/ρ_f and $r/2h$. For geometric reasons, $r >> 2h$, but this inequality is usually not as strong as the inequality $b^2 l >> m_s$ in equation (1-117) (except for strongly curved vanes). Nevertheless the comparison between fluid-induced and centrifugal stresses is quite similar to that made previously in connection with equation (1-117), although centrifugal stresses dominate in the present case over a somewhat wider range than in the former case.

Thus similarity considerations on stresses are quite comparable for fluid dynamic stresses σ_f and centrifugal stresses σ_c. The stress specific speeds for these two origins of stresses are related to each other as follows:

$$\frac{nQ^{1/2}/(\sigma_c/\rho_s)^{3/4}}{nQ^{1/2}/(\sigma_f/\rho_f)^{3/4}} = \left(\frac{\sigma_f}{\sigma_c}\frac{\rho_s}{\rho_f}\right)^{3/4} \tag{1-119}$$

The stress specific speed related to centrifugal stresses is of primary importance for gas-handling machines, and the stress specific speed related to fluid-dynamic stresses is of primary importance for machines handling fairly heavy liquids. For machines handling liquid hydrogen, both specific speeds may be of equal significance.

Instead of using the stress specific speeds, one can, of course, consider the pressure-stress ratios $\rho_s g_o H/\sigma_c$ and $\rho_f g_o H/\sigma_f$. These ratios may at times have practical advantages, as, for example, in considering the hydrodynamic thrust of a turbomachinery rotor, in which the pressure difference generating this thrust is (approximately) $\rho_f g_o H$, the pressure difference generated or used in the machine. However, the stresses that are critical with respect to the end thrust are usually those in a ball or roller thrust bearing, which do not fall within the scope of this section.

The ratios $\rho_s g_o H/\sigma_c$ or $\rho_f g_o H/\sigma_f$ may be readily related to the stress coefficients $\rho_s U_o^2/2\sigma_c$ and $\rho_s U_o^2/2\sigma_f$ by considering the head coefficient $\psi_o = 2g_o H/U_o^2$. Evidently

$$\frac{\rho_f g_o H}{\sigma_f} = \psi_o \frac{\rho_f U_o^2}{2\sigma_f} \tag{1-120}$$

There is a corresponding expression for centrifugal stresses, which, however, is not likely to be used very often.

1.3.3.3 *Gage-pressure-determined design forms (casing forms).*—The term gage pressure is commonly used to express a pressure in the machine in relation to the atmospheric pressure. By expressing the amount by which the internal pressure exceeds the ambient pressure, the gage pressure represents the pressure difference to which the casing is subjected.

Generally the gage pressure $p_g = p - p_a$ is not accessible by similarity relations, since the inlet pressure of a pump or compressor, or the discharge pressure of a turbine, is determined by external conditions which may not have any relation to the action of the machine. For example, a turbomachine may be one of several machines operating in series, and the pressure level in any one of these machines depends only partly on the head of that particular machine and to a large extent on the action of the other machines. Therefore it is not generally possible to describe the pressure-stress conditions in the casing of a turbomachine in terms of the stress coefficient used in the preceding sections. The gage pressure of a machine is, thus, an independent operating condition, not generally related to the operating conditions expressed by various specific speeds or equivalent similarity parameters.

Nevertheless a given gage pressure p_g inside the casing can be made dimensionless from a mechanical design point of view by division by a characteristic or allowable stress σ in the casing walls. The resulting pressure-stress coefficient p_g/σ can be related to certain dimensionless form characteristics of the casing.

For example, a fairly thin cylindrical casing has, without effects of its end covers, a pressure-stress coefficient given by

$$\frac{p_g}{\sigma} = \frac{t}{r} \tag{1-121}$$

where σ is an average stress over the wall thickness t of the cylinder and r is the inner (or average) radius of the cylinder. (For fairly thick cylinders, this average stress σ has a practical significance quite similar to that of the average stress in a rotating disk, which is mentioned in sec. 1.3.3.1, i.e., that local yielding tends to level out the uneven stress distribution.)

For a spherical casing,

$$\frac{p_g}{\sigma} = \frac{2t}{r} \tag{1-121a}$$

which is, of course, rarely used in its exact form, although an approximation of a spherical shape has been used successfully in connection with volute pumps, as is further described in chapter 5. Spherical walls are advantageously used as parts of casings or casing covers. Naturally, when only approximations or parts of a spherical shell are used, the pressure-stress coefficient must be reduced below the value given by equation (1-121a).

The stress in a conical casing wall or cover can be approximated by a coaxial conical section normal

to the conical wall. With the notation given in figure 1-37, the pressure-stress coefficient for a conical wall becomes

$$\frac{p_g}{\sigma} = \frac{t}{r_n} = \frac{t \cos \alpha}{r} \tag{1-122}$$

This solution can, of course, be checked by recognizing that section OA is a conic section, so that its radius of curvature at A can be determined accurately as a function of r and α. Another method is a consideration of surface curvature at point A.

For flat plates, the pressure-stress coefficient is approximately

$$\frac{p_g}{\sigma} = q\frac{t^2}{r^2} \tag{1-123}$$

where $q = 1.33$ to 1.5 if the outer rim is flexibly supported and $q = 2$ if the outer rim can be regarded as rigidly clamped. These values apply to ductile materials (mild steel). For cast iron, q is approximately 1. Flat side plates or casing covers can be effectively strengthened by double-wall construction with radial shear ribs, as is discussed further in chapter 5, section 5.3.3.

The foregoing equations permit making an estimate of the volume of the solid casing walls as compared with the fluid volume in the casing. It is evident that this ratio increases in first approximation proportionally to the ratio of the fluid gage pressure to the allowable stress in the casing walls whenever this allowable stress is reached. This consideration may be helpful in connection with the section 1.3.4.

If the gage pressure at the low-pressure end of the machine is quite low compared with the gage pressure at the high-pressure end, the maximum gage pressure in the casing can be approximated by $p_g = \rho_f g_o H$, that is, by the total pressure rise in the machine.

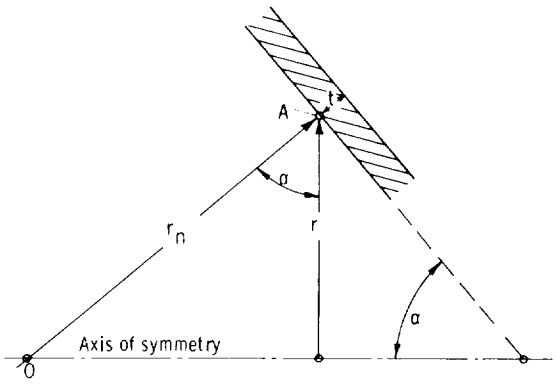

Figure 1-37.—Conical casing wall.

1.3.4 Gravity- and Vibration-Determined Design Forms

In section 1.2.3, the so-called gravity specific speed

$$n_g = \frac{nQ^{1/2}}{(g/n)^{3/2}} = \frac{1}{2\pi^2} \times \left(\frac{U_o^2}{gD_o}\right)^{3/2} \left(\frac{D_i}{D_o}\right)^{3/2} \left(\frac{V_{m,i}}{U_i}\right)^{1/2} \times \left(1 - \frac{D_h^2}{D_i^2}\right)^{1/2} \tag{1-70}$$

and the vibration specific speed

$$n_v = \frac{nQ^{1/2}}{(E/\rho_s)^{3/4}} = \frac{1}{2^{1/4}\pi^{1/2}} \times \left(\frac{\rho_s U^2}{2E}\right)^{3/4} \left(\frac{V_{m,i}}{U}\right)^{1/2} \frac{D_i}{D} \left(1 - \frac{D_h^2}{D_i^2}\right)^{1/2} \tag{1-79}$$

are related to various design parameters by these equations. This section relates the design parameters appearing on the right sides of these equations to some elementary design form characteristics of the machines considered, specifically the square of the Froude number U_o^2/gD_o and the vibration or critical speed number $\rho_s U^2/2E$. The latter is transformed in section 1.2.3 into the square of the Strouhal number $(U/fD)^2$, which involves an unknown constant. The relations of these design parameters to design forms are far less definite than relations considered previously, for example, with respect to the stress specific speed.

The relations of the gravity specific speed and of the vibration specific speed to design forms are treated together because of a deeply rooted connection between these specific speeds (i.e., between considerations relative to gravity (acceleration of the system as a whole) and to elastic deformations and vibrations of the system). This connection should be apparent from the relation

between the natural frequency f of an elastic system and the deformation δ_g under the general acceleration g of the system, which is

$$f = \frac{1}{2\pi}\sqrt{\frac{g}{\delta_g}} \tag{1-124}$$

where δ_g/g is obviously the steady-state deformation of the system under the unit of acceleration. Equation (1-124) applies directly only to a point mass on a massless spring, but can be applied to more complicated systems by changing the constant of proportionality $(1/2\pi)$.

The relation between the square of the Froude number U^2/gD_o (where U may be any velocity of dynamic significance) and the design form is not obvious and not generally established. Its underlying law is obviously the so-called square-cube law between surface and gravitational forces, which is that surface forces (pressures or stresses) are proportional to the square of linear dimensions and mass forces are proportional to the cube of linear dimensions. With respect to hydrodynamic and other dynamic forces, this relation is expressed by the well-known Froude law of similarity:

$$\left.\begin{aligned} &\frac{U}{\sqrt{gD}} = \text{constant} \\ &\text{or} \\ &\frac{V}{\sqrt{gD}} = \text{constant} \end{aligned}\right\} \tag{1-125}$$

where D may be any convenient linear dimension of the system.

The lower the Froude number $U/\sqrt{gD}$ or $V/\sqrt{gD}$, the greater the influence of gravitational relative to dynamic forces $g\rho D^3/V^2\rho D^2 = gD/V^2$.

True gravitational effects are those that result from the action of gravitational or body forces. An example of this type of effect is the difference in pressure observed at a point on a blade when that blade is observed at its highest and at its lowest position (e.g., a blade on a marine propeller or on a large hydraulic turbine or pump with a horizontal shaft). The similarity relation is obviously

$$\frac{\text{force preventing cavitation}}{\text{force due to gravity}} = \frac{H_{sv}g\rho_f D^2}{g\rho_f D^3} = \frac{H_{sv}}{D} = \text{constant} \tag{1-126}$$

This relation demands that not only H_{sv} but also all dynamic head differences be proportional to the vertical linear dimensions of the system, as all pressure differences due to gravity are proportional to these distances. This law of similarity is frequently used with respect to large hydraulic turbines and quite generally in marine engineering.

Similarity with respect to elastic deformations δ_g under the influence of gravity obviously demands that these deformations are proportional to the linear dimensions of the system (i.e., that $\delta_g/D = \text{constant}$). Evidently

$$\delta_g = \text{constant} \times \frac{\sigma}{E} D$$

and the stress is

$$\sigma = \text{constant} \times \frac{g\rho D^3}{D^2} = \text{constant} \times g\rho D$$

The requirement of similarity with respect to deformations is, therefore,

$$\frac{\delta_g}{D} = \text{constant} \times \frac{\sigma}{E} = \text{constant} \times \frac{\rho g D}{E} = \text{constant} \tag{1-127}$$

The well-known deformation of helicopter blades at a standstill is an example of this type of deflection.

The ratio E/ρ is encountered later in considerations relative to vibrations and may be described as a stiffness-density ratio.

Similarity with respect to stresses produced by gravitational forces obviously demands that

$$\frac{\text{gravitational forces}}{\text{internal or stress forces}} = \frac{g\rho D^3}{\sigma D^2} = \frac{g\rho D}{\sigma} = \text{constant} \tag{1-128}$$

This expresses the well-known fact that the structural stresses due to gravity increase for similar structures proportionally to the linear dimensions of the structure, or that the strength-weight ratio of the material $\sigma/g\rho$ must increase proportionally to the linear dimension.

According to equations (1-127) and (1-128), an increase in the size D of the machine leads to an increase in the relative deformation δ_g/D and in the stress σ. To avoid this increase in deformation and stress, one must depart from the structural similarity or change the structural material. For increasing D, this departure from similarity must constitute an improvement (refinement) in the structural form of the machine. This requirement is well known in connection with increases in the size of weight-limited structures such as airplanes and aircraft engines. In turbomachines, this refinement usually assumes the form of replacing a solid structural element (e.g., a blade or a shaft) with a hollow element. An apparently different kind of structural refinement of turbomachines consists in increasing only the diameters of axial-flow vane systems without increasing their axial extent, while keeping the solidity constant and, thus, increasing the number of blades proportionally to the diameters D. This increases the aspect ratio (span-chord ratio) of the vanes and requires either true structural refinement or acceptance of greater flexibility of the vanes.

As mentioned previously, the departures from structural similarity suggested by the similarity equations (1-127) and (1-128) are exactly the kind of refinements which are required whenever a weight-limited machine is to be increased in size, since it is usually not acceptable to increase the weight of the machine by the cube of its linear dimensions. It is really not the weight but the mass of the machine that needs to be limited, as the mass is significant under any acceleration, be it gravitational acceleration, the acceleration of a spacecraft in a weightless frame of reference, or a combination of both.

Under these circumstances, the mass of a given volume of solid material must be minimized for a stated strength or load-carrying capacity of the structure involved. Obviously this means that the strength-mass and stiffness-mass ratios of the material must be maximized. For the problem of form design, these properties of the material must be assumed to be given, as the task is to find the optimum form for given properties of the structural material. Therefore E/ρ and σ/ρ, where σ is an allowable stress, are assumed to be fixed. To minimize the mass of a machine, it is obviously necessary to minimize the volume of the structural material without reducing its structural strength or stiffness. The required structural refinement is discussed previously.

Without such refinement, the overall volume of the machine is approximately proportional to the volume of fluid in the machine. The volume of fluid passing through the machine per unit of time is Q. Let the unit of time be the time of one revolution. The volume passed through the machine per revolution is Q/n, which may very well be proportional to the volume of the machine, which is, in turn, proportional to D^3. The familiar similarity parameter Q/nD^3 is, therefore, the reciprocal of a meaningful dimensionless volume of the machine.

Dividing the basic specific speed by the dynamic parameter $(U_o^2/2g_oH)^{3/4}$ leads to

$$\left(\frac{Q}{nD_o^3}\right)^{1/2} = \frac{\pi}{2}\left(\frac{V_{m,i}}{U_i}\right)^{1/2}\left(\frac{D_i}{D_o}\right)^{3/2} \times\left(1-\frac{D_h^2}{D_i^2}\right)^{1/2} \tag{1-129}$$

which can, of course, be derived also on fundamental grounds, that is, on the basis of

$$n = \frac{U_i}{\pi D_i}$$

and

$$Q = V_{m,i}\frac{D_i^2\pi}{4}\left(1-\frac{D_h^2}{D_i^2}\right)$$

Overall weight considerations (i.e., volume considerations), therefore, do not lead to any new relations, except that Q/nD_o^3 should be maximized. This coefficient is easily calculated from equation (1-129) for any given definition of D_o and D_i. Evidently

$$\frac{Q}{nD_o^3} = \frac{Q}{nD_i^3}\left(\frac{D_i}{D_o}\right)^3 \tag{1-130}$$

where, according to equation (1-129),

$$\frac{Q}{nD_i^3} = \frac{\pi^2}{4}\frac{V_{m,i}}{U_i}\left(1-\frac{D_h^2}{D_i^2}\right) \tag{1-131}$$

According to figure 1-18, $V_{m,i}/U_i$ diminishes with increasing suction specific speed, but there is no reason why it should change with the basic specific speed. Therefore, for $S=\text{constant}$, Q/nD_o^3 increases primarily with $(D_i/D_o)^3$; that is, Q/nD_o^3 increases with the basic specific speed, as is evident from the reduction in the size of a machine with increasing n_s shown in figure 1-8.

The vibration specific speed, equation (1-79), contains the term $(\rho_s U^2/2E)^{3/4}$ on the right side. Usually the peripheral velocity U is the velocity U_o at the outer diameter D_o of the rotor. As stated previously, the parameter $\rho_s U_o^2/2E$ should be related to the design form of the machine, particularly its rotor. For simple configurations, this turns out to be somewhat easier than in the previously discussed correlation with the Froude number.

The natural frequency f of a prismatic bar in bending is

$$f=\text{constant}\times\sqrt{\frac{E}{\rho_s}}\sqrt{\frac{I}{A}}\frac{1}{l^2} \tag{1-132}$$

where I is the moment of inertia, A the area of the cross section, and l the length of the bar. The constant is 0.56 for the first natural frequency of a rigidly clamped cantilever and $\pi/2$ for the first form of vibration of a bar supported on both ends but not clamped. In the latter arrangement, the second natural frequency is obviously four times as high as the first, since the length between nodal points is $l/2$.

For a rectangular cross section with height h and width b, $I=h^3b/12$ and $A=hb$, so that $I/A=h^2/12$ and, therefore,

$$f=\frac{\text{constant}}{\sqrt{12}}\sqrt{\frac{E}{\rho_s}}\frac{h}{l^2} \tag{1-133}$$

where the constant is the same as that used previously.

For a circular cross section with shaft diameter D_s, $I/A=D_s^2/16$ and

$$f=\frac{\text{constant}}{4}\sqrt{\frac{E}{\rho_s}}\frac{D_s}{l^2} \tag{1-134}$$

For a hollow shaft with an inside diameter d_s,

$$f=\frac{\text{constant}}{4}\sqrt{\frac{E}{\rho_s}}\frac{D_s}{l^2}\left(1+\frac{d_s^2}{D_s^2}\right)^{1/2} \tag{1-135}$$

According to equation (1-132), a more general expression is

$$f=\text{constant}\times\sqrt{\frac{E}{\rho_s}}\frac{r}{l^2} \tag{1-136}$$

where the radius of gyration of the cross section $r=\sqrt{I/A}$ is equal to $h/\sqrt{12}$ for the rectangular cross section and $D/4$ for the circular cross section.

All expressions of natural frequency contain the factor $\sqrt{E/\rho_s}$, which appears also in the vibration specific speed in the form $U_o/\sqrt{E/\rho_s}$. Setting $U_o=\pi D_o n$ and writing equation (1-136) in the form

$$\sqrt{\frac{E}{\rho_s}}=\frac{fl}{\text{constant}}\frac{l}{r}$$

one finds

$$\frac{U_o}{\sqrt{E/\rho_s}}=\text{constant}\times\pi\frac{n}{f}\frac{D_o}{r}\frac{r^2}{l^2} \tag{1-137}$$

where the constant has the same value as in equations (1-132) to (1-136). Thus $U_o/\sqrt{E/\rho_s}$ has a fairly clear meaning regarding the form and frequency of structural members in bending. (Other forms of vibration, such as torsional vibrations, can be treated in a similar manner.)

While it is relatively simple to extend the foregoing relations to a variety of different arrangements by changing the constant of proportionality, there are other variations which are not covered by equations (1-132) to (1-136). One important variation of this type is the introduction of elasticity into the supports of the vibrating member. For example, it is well known that the elasticity of shaft bearings, particularly rolling-contact bearings, is important in calculating the natural frequencies (critical speeds) of turbomachinery rotors. The actual behavior of a rotor in an elastically supported casing is, of course, still more complex. In such complex situations, it would be of interest to explore how far the following

generalization of equation (1-137) would be applicable:

$$\frac{U_o}{\sqrt{E/\rho_s}} = \text{constant} \times \frac{Nn}{f} \times \text{function of form parameters} \qquad (1\text{-}138)$$

where Nn is the exciting frequency and f (as previously) is a significant natural frequency (critical speed) of the system. The exciting frequency Nn is usually a multiple N of the speed of rotation n, for example, a blade-passing frequency, where in the simplest case N is the number of vanes in one vane system. A relation such as equation (1-138) is useful as long as the most important natural frequencies f of the system can be determined. This is possible in a wide variety of cases if one accepts approximate solutions and includes solutions by numerical or graphical methods. This writer has used for the determination of the critical speed of shafts the graphical method described in section 92 of the well-known book by Stodola (ref. 2) (beginning on p. 446 of its English translation).

1.3.5 Design Choices in Turbomachinery

In the preceding sections, dimensionless operating conditions (the specific speeds) are related to design parameters (ratios) and these to certain elementary design form characteristics. However, these relations are not unique.

Certainly there is usually a considerable difference in design between turbomachines handling liquids and those handling gases. There is another difference between pumps or compressors on one hand and turbines on the other. Distinctions or choices of this type have to be made before the design process can begin and are called design choices, although they are usually not made by the design engineer but rather by the customer or by the circumstances under which the development of the machine is undertaken.

However, even regarding the design of a machine for a prescribed purpose (liquid or gas, pump or turbine), certain choices have to be made before one can start with any specific design considerations. For example, figures 1-8 and 1-9 show that essentially the same range of basic specific speeds can be covered either by axial-flow machines alone (fig. 1-9) or by both radial and axial-flow machines, with the latter used at the higher basic specific speeds. In fact, figure 1-38 shows that the entire field can be covered also by radial- and mixed-flow machines, although the flow becomes axial at the higher specific speeds. Thus the designer has the choice of a radial-flow machine, an axial-flow machine, or a combination of both types. While influenced by the basic specific speed, this choice is not uniquely determined by this specific speed but is also dependent on matters of general arrangement, preferred direction of the flow entering or leaving the machine, requirements of performance over a range of operation, and so on.

A related choice may have to be made between a single-stage radial-flow machine and a multistage axial-flow machine. This choice is depicted in figure 1-39 and has been debated a great deal in the field of rocket propellant pumps. Both types of machine have about the same volume and weight (or mass) and for basic specific speeds between 0.1 and 0.2 about the same efficiency. (For basic specific speeds below 0.09, the multistage axial-flow machine can have the higher efficiency because the number of stages can be increased. The radial-flow pump presently has a wider range of stable operation (at constant speed). The axial-flow pump has a mechanically much better casing with respect to high internal pressures and, by its large number of vanes and vane systems, can be made to have a much lower amplitude of pressure fluctuations at its discharge. In the field of aircraft gas turbines and compressors, the lower frontal area and the higher efficiency of the axial-flow compressor for high pressure ratios were decisive for the choice in favor of the axial-flow design.

This consideration leads to the more general design choice regarding the number of stages. Figure 1-12 (sect. 1.2.1) shows the estimated stage efficiencies of pumps as a function of the basic specific speed per stage for radial-flow stages at speeds below $n_s = 0.3$. At basic specific speeds below 0.1, a design choice has to be made between the loss in efficiency of a single-stage unit and the complication and loss in efficiency of two-stage or multiple-stage arrangements. For multiple-stage machines, the axial-flow stages permit, of course, a much simpler and usually more efficient arrangement than radial stages, which has led to the exclusive adoption of axial-flow stages for multistage steam and gas turbines. For commercial pumps and compressors, multistage radial-flow

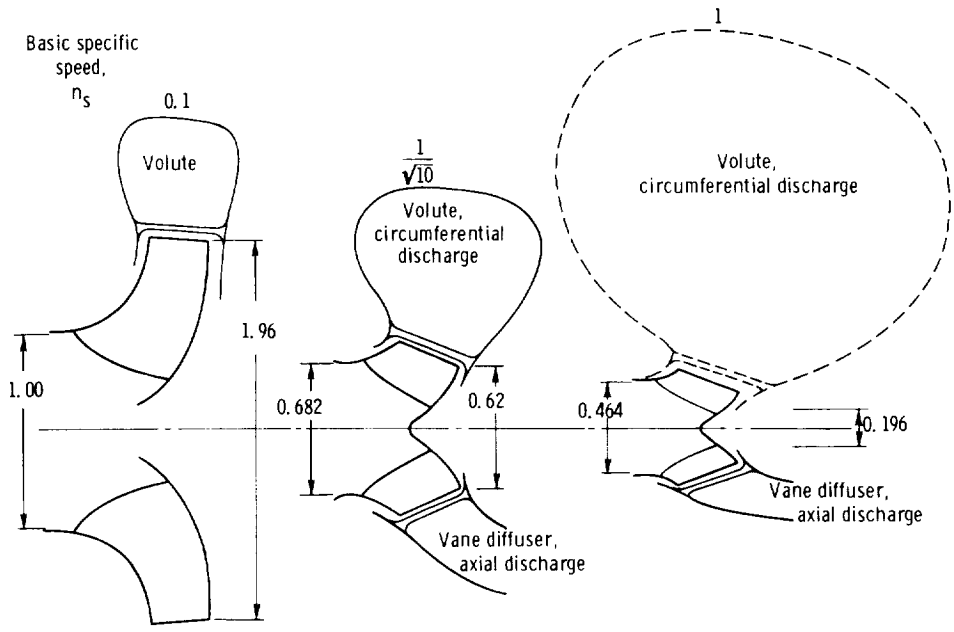

Figure 1-38.—Radial- and mixed-flow pump profiles as function of basic specific speed.

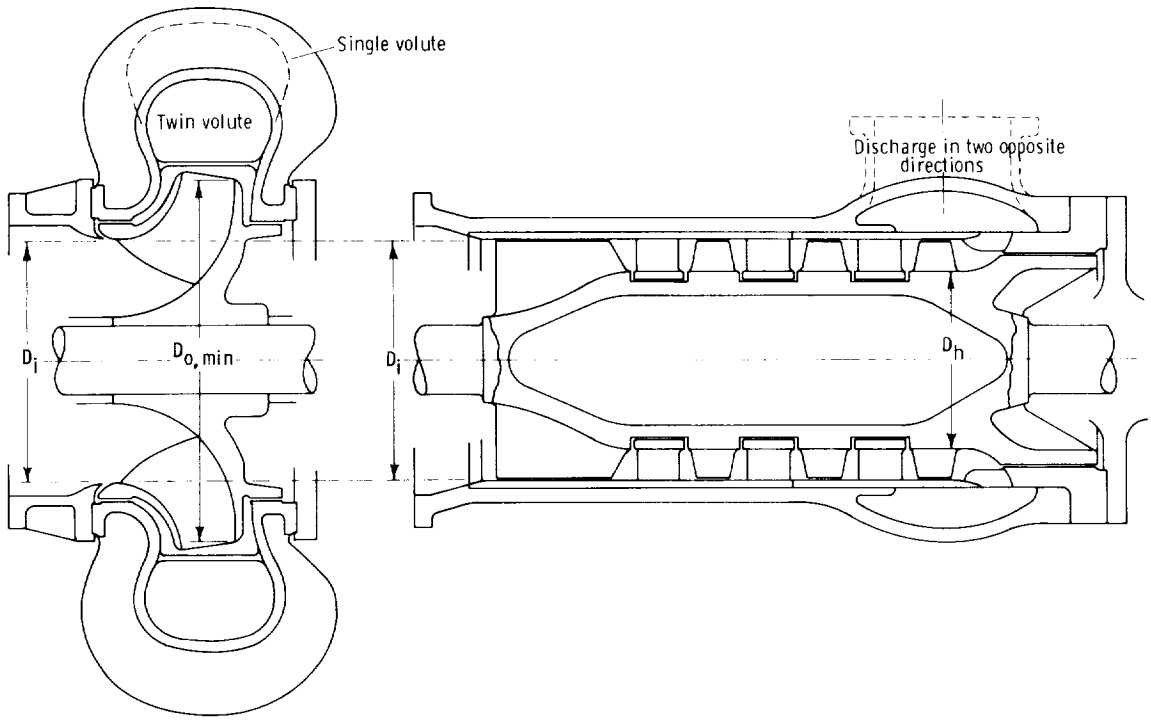

Figure 1-39.—Design choice between single-stage radial-flow and multistage axial-flow turbomachines.

machines have been used extensively because of the wider stable operating range of radial-flow pumps and compressors at constant speed.

The velocity vector diagrams and, therefore, the vane shapes cannot be determined before another

design choice has been made regarding the existence or absence of positive or negative rotation on one side of the rotor, usually the low-pressure side. This design choice is made on the basis of considerations of cavitation or Mach number, the magnitude and in particular the retardation of the relative flow, and the overall aerodynamics or hydrodynamics of multistage machines, particularly axial-flow machines. The exact magnitude of the rotation of the fluid cannot be termed a design choice as it is a continuous function of other flow conditions in the machine.

Another design choice is often to be made between single-suction and double-suction turbomachines, depicted in figure 1-40, usually having radial-flow rotors. (For turbines, the choice is between single and double discharge.) On the basis of fluid mechanics, one would probably elect the double-suction arrangement, as its peripheral velocity at the pump impeller inlet is lower for the same rate of flow Q and the same speed of rotation. This is advantageous with respect to cavitation as well as with respect to compressibility (Mach number) characteristics. Yet, because of the complication of the general arrangement and inlet ducting, double-suction rotors have nearly disappeared from the compressor field, although the British first radial-flow aricraft compressors were of the double-suction type. Double-suction pumps are widely used in the commercial field, but have seen only limited application in the liquid-rocket pump field. Double-discharge hydraulic turbines were used more than 50 years ago for horizontal-shaft turbines, but have almost disappeared since vertical-shaft turbines have become standard. Double discharge has been used widely in large axial-flow steam turbines to handle the very large volumes of flow discharged at high speeds of rotation (3600 rpm).

Figure 1-40 depicts still another design choice, the choice between the so-called horizontally split and vertically split casing constructions. This conventional terminology is not very accurate. Vertically split denotes the existence of mechanically separable joints along planes normal to the axis of rotation, whereas horizontally split denotes the existence of such a mechanical joint along a plane parallel to, and usually coinciding with, the axis of rotation. In this compendium, these terms are used with their conventional meanings.

Figure 1-40 illustrates this distinction for a single-stage centrifugal pump or blower. Figure 1-41 shows a horizontally split casing for a multistage pump or compessor, and figure 1-42 a vertically split casing for a multistage high-pressure pump. Large pumps and hydraulic turbines with vertical shafts are, by the conventional definition, vertically split, as their casing joints are normal to the axis of rotation, although these joints are actually in a horizontal position.

The vertically split construction has the advantage of permitting much simpler and more reliable joints and casing parts which are relatively simple and more or less axially symmetric. This construction is, therefore, used for pressures over 1000 pounds per square inch and in applications where general reliability and freedom from leakage are of paramount importance. The vertically split construction is, therefore, used for high-pressure boiler feed pumps, aircraft gas turbines and

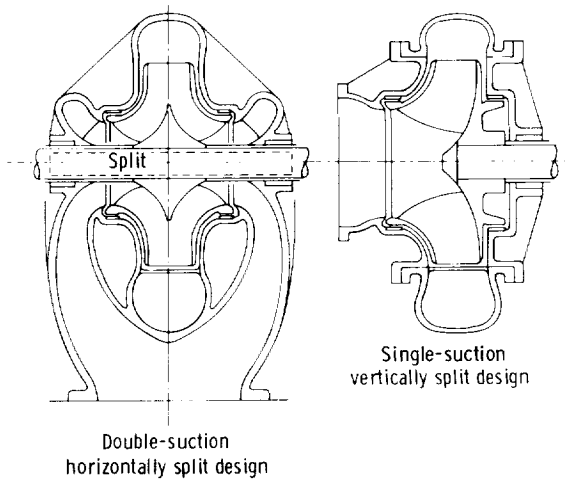

Figure 1-40.—Design choices between double-suction and single-suction machines and between horizontally split and vertically split casings.

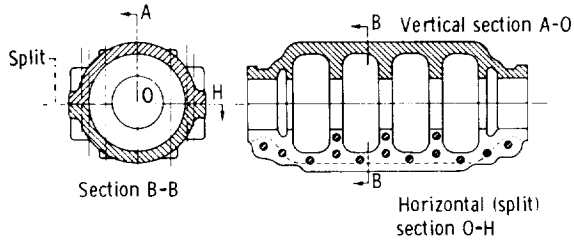

Figure 1-41.—Horizontally split casing of multistage pump.

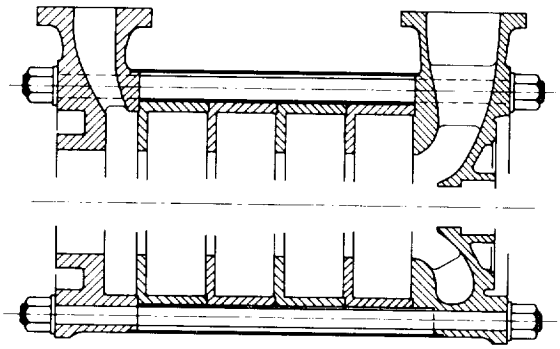

Figure 1-42.—Vertically split casing of multistage high-pressure centrifugal pump.

compressors, rocket propellant pumps and turbines, and pumps handling highly corrosive or toxic liquids and liquid metals.

Horizontally split machines, particularly multistage machines, have the great advantage of being much easier to assemble or dismantle than vertically split machines. This construction is, therefore, regularly used for commercial multistage pumps and compressors at pressures up to at least 1000 pounds per square inch, as well as for large multistage steam turbines. The horizontal split demands great care and often ingenuity in design to prevent leakage.

Thus the design choice between the vertically and horizontally split constructions is not directly related to the operating conditions expressed by the various specific speeds. This choice is made on the basis of absolute pressure, existing practice and experience, demands of the application of the machine, reliability considerations, and, too often, personal judgment and opinion. This choice is a good example of the fact that the design of turbomachines is not determined entirely by rational analysis.

The last design choice to be discussed in some detail is that between shrouded and unshrouded rotor vane systems. In axial-flow rotors, the shroud is simply a cylindrical ring around the outside of the vane system. In radial-flow rotors, the vane system has either one disk-shaped shroud on one side or two such shrouds, one on each side of the vane system (see fig. 1-46, sec. 1.4). The former arrangement is called open or single-shrouded, and the latter is called closed or double-shrouded. Open double-suction rotors have one shroud in an axially central plane, and closed double-suction rotors have two side shrouds and one central shroud, which may or may not extend to the outside diameter of the rotor (see left part of fig. 1-40).

To some extent, the design choice about shrouding of the rotor vanes can be made on the basis of the centrifugal stress specific speed, in particular the centrifugal stress coefficient $\rho_s U_o^2/2\sigma_c$ connected with that specific speed. There probably is an upper limit of this stress coefficient beyond which shrouding (or double shrouding) is not mechanically feasible, but such a limit has not yet been determined. This limit is doubtlessly higher for radial-flow than for axial-flow rotors, where the outer shroud by itself is essentially a thin hoop. This thin hoop has a very low stress coefficient, so that such a shroud usually depends for its mechanical integrity on the holding action of the blades, and the blades are loaded more than they would be without a shroud. Therefore, a shrouded axial-flow rotor always has a lower centrifugal stress coefficient $\rho_s U_o^2/2\sigma_c$ than any otherwise similar unshrouded axial-flow rotor. This statement is true also for radial-flow rotors with radial vanes.

Shrouds are beneficial with respect to blade vibrations. On this basis, it may be possible to determine the necessity of a shroud from the vibration specific speed (eq. (1-79), sec. 1.2.3).

However, while the choice between shrouded and unshrouded (or single- and double-shrouded) rotor vane systems can be made partly on the basis of the centrifugal stress specific speed (and the vibration specific speed), this choice is influenced by other important considerations. A single- or double-shrouded rotor is certainly more difficult and costly to manufacture than an open rotor. This means that, under certain conditions (e.g., cost limitations) and for certain materials or processes, the shrouded constructions are ruled out for manufacturing reasons. In other cases, for example, where axial-flow rotors with very low head coefficients ($\psi_o = 2g_o H/U_o^2$) are used, usually in machines or stages with very high basic specific speed, the use of an outer shroud would entail unacceptable losses in efficiency. Thus this choice is influenced by the basic specific speed, but not uniquely determined by it.

There are still many other design choices to be made, for example, those discussed in section 1.3.2 and illustrated in figure 1-28. However, the design choices just discussed are probably sufficient to illustrate this concept.

While the design choices depend to some extent on the dimensionless operating conditions (the specific speeds), there is one clear distinction between these choices and the previously described relations between the specific speeds and the design parameters appearing on the right sides of the specific speed equations (see tables 1-I and 1-II, sec. 1.2.3).

The design parameters and the corresponding design forms are, at least for each section of the machine, continuous functions of the specific speeds. With the exception of a few discontinuities that may exist in these relations, small changes in the dimensionless operating conditions (the specific speeds) in principle produce correspondingly small changes in the design parameters and the resulting design forms.

In contrast, design choices are usually made between two distinct possibilities (or among, at the most, a small number of possibilities), for example, between single and multistages, single and double suction, vertically and horizontally split construction, and so on. Design choices are not continuous functions of the conditions that influence these choices. This distinction between design parameters and design forms on one side and design choices and the resulting changes in design form on the other side may well serve as part of the definition of design choices.

It might be assumed that under idealized conditions of knowledge there would exist a definite relation between the dimensionless operating conditions (the specific speeds) and the corresponding design forms. It is now evident that even for completely given conditions this relation would not be unique, that there would be more than one set of optimum design forms and more than one optimum overall design. The multivalued results of the relation between dimensionless operating conditions and design forms are selected by the discrete design choices described in this section.

1.4 Representation of Relations Between Dimensionless Operating Conditions and Design Form

1.4.1 Introduction

The survey presented in this chapter begins with the dimensionless representation of the operating conditions in turbomachinery in the well-known form of the basic specific speed. Also presented in this form, in addition to the speed of rotation, are the volume flow rate; the head; and the effects of cavitation, compressibility, viscosity, stresses in solid parts, gravity, and vibration. (Of course, there may be other operating conditions that should be considered.)

The operating conditions presented in this form are related to certain design parameters appearing on the right sides of the various specific speed equations listed in tables 1-I and 1-II. Besides the flow coefficient V_m/U and certain ratios of linear dimensions appearing in all these equations in one form or another, there is one parameter in each equation whereby the equation is distinguished from all the other specific speed equations. These distinguishing parameters are a head coefficient, a suction head coefficient (cavitation number), a Mach number, a Reynolds number, a stress number, a Froude number, and a vibration number (principally a Strouhal number).

The ratios of linear dimensions appearing in the specific speed equations have, of course, a very direct influence on the form of the profile of the machine, particularly the rotor. The flow coefficients together with the head coefficients determine to a large extent the velocity vector diagrams, once the rotation of the fluid on one side of the rotor (usually the low-pressure side) has been determined by design choice or other considerations. The velocity vector diagrams determine certain elementary characteristics of the vane or casing shape as well as the ratio of vane length to spacing on the basis of the lift coefficient. The stress coefficient $\rho_s U^2/2\sigma$ determines certain structural characteristics of rotating elements and vanes, and the vibration number $U^2/\sqrt{E/\rho_s}$ other structural characteristics of rotors or vanes. (This writer has not been able to correlate design form characteristics in a definite manner with the Froude number, but such relations may well be established in the future.)

At this point, it seems appropriate to call attention to the process of establishing the overall three-dimensional design form of the entire machine. Certainly this process is made possible or aided by the previously acquired ratios of certain dimensions and elementary design form characteristics. Yet considerable knowledge, experience,

and skill are required to combine these bits of design information effectively into a geometrically and mechanically harmonious and logically consistent whole. (Most of the other chapters of this compendium are devoted to the foundations and execution of this process.)

It is hoped that the foregoing description is sufficient to distinguish the overall design form of the entire machine (or of a major part, like an impeller) from the elementary design forms or form characteristics derived from the design parameters such as the flow, head, and stress coefficients. A sharper distinction may not be desirable as the elementary design forms are likely to be extended by the development of design methods so as to cover progressively increasing portions of the overall design of the machine. (Sections through entire vane systems such as those shown in figure 1-23 are an example of this growth.)

The relation between the dimensionless operating conditions, the design parameters, and certain elementary design forms is not unique in itself and certainly not sufficient to determine uniquely the overall design of the machine, not even under the most idealized assumptions regarding the state of knowledge and experience. The design form of an entire machine depends also on a number of design choices such as those between gases and liquids, pumps and turbines, axial and radial flow, and so on. Only after such choices have been made can one hope to establish a definite relation between the dimensionless operating conditions and the overall design form of the machine. In other words, the multivalued nature of the relation between dimensionless operating conditions and design forms requires decisions regarding the pertinent design choices in order to make this relation as unique as possible under the existing state of knowledge and experience.

1.4.2 Space of Dimensionless Operating Conditions and Relation to Its Design Parameters

The last step in this presentation of turbomachinery design is the construction of a mental picture or scheme representing what is stated previously.

The field of all possible dimensionless operating conditions, presented as a number of specific speeds (the left sides of the equations in tables 1-I and 1-II), is imagined as a multidimensional space, each coordinate being one of the dimensionless continuously variable operating conditions (one of the specific speeds). A point in this space represents one complete set of dimensionless operating conditions.

As mentioned previously, every specific speed can be related to a number of design parameters as expressed by the right sides of the equations in tables 1-I and 1-II. This relation is multivalued, every particular solution depending on a number of design choices. However, after all pertinent design choices have been made, one can imagine that every point in the space of dimensionless operating conditions can be associated with a set of numerical values of the design parameters appearing on the right sides of the specific speed equations. Accordingly one can draw, in the multidimensional space of operating conditions, the loci of constant values of the design parameters concerned (lines, surfaces, etc.).

It is somewhat difficult to demonstrate the construction of these loci not only because the space of dimensionless operating conditions is multidimensional, but also because the design information available for most of the specific speeds is as yet far too incomplete to permit such a demonstration in definite terms. However, if we choose a highly simplified case, involving only a very limited number of variables, such a demonstration seems possible.

Only two specific speeds are considered variable. The best design information available today falls in the hydrodynamic field, represented by the basic specific speed and the suction specific speed. These two specific speeds are, therefore, the variable operating conditions considered in this demonstration, with all other specific speeds having fixed values in ranges where sufficient design information is available. One may consider this example as a plane section through the multidimensional space of operating conditions which is parallel to the n_s- and S-axes and normal to all other coordinate axes of this space.

The next step is that of making the necessary design choices. These choices are the following:

(a) The machine is a pump (not a turbine).

(b) The fluid is a liquid of low kinematic viscosity; this determines a sufficiently low value of the compressibility specific speed and a sufficiently high value of the viscosity specific speed so that

changes in compressibility and changes in viscosity (and size) have only negligible effects.

(c) The peripheral velocities are sufficiently low and the strength-weight ratio of the structural material is sufficiently high to practically eliminate stress considerations; specifically, the centrifugal stress specific speed is well below 0.1.

(d) The gravity specific speed is sufficiently high and the vibration specific speed sufficiently low to practically eliminate gravity and vibration effects from the design considerations.

(e) The rotor design form is single suction and varies continuously so that flow changes from radial (outward) for low basic specific speeds to axial for high basic specific speeds.

(f) Only single-stage pumps are considered.

This demonstration is concerned only with the impeller design. Consequently, no design choices need to be made regarding the casing construction, such as between vertical and horizontal splitting of the casing, or concerning the locations and directions of the casing inlet and discharge openings.

The foregoing design choices are not sufficient to solve the basic specific speed and the suction specific speed equations for the design parameters. However, certain design parameters can be chosen on theoretical and empirical grounds.

The inlet hub-tip diameter ratio D_h/D_i can be chosen on empirical grounds. A value of $D_h/D_i = 0.25$ is large enough to cover most mechanical requirements of shaft diameter for single-stage pumps. Yet, if for overhanging impellers, $D_h/D_i = 0$, the factor $(1 - D_h^2/D_i^2)^{1/2}$ in the specific speed equation changes only from 0.968 to 1, that is, by less than 3.5 percent. On the other hand, if D_h/D_i is larger than 0.25, say 0.35, then $(1 - D_h^2/D_i^2)^{1/2} = 0.9375$, only about 3 percent less than the value corresponding to the assumed diameter ratio of 0.25. This value is, therefore, a good mean value to assume, and departures from it within the range expected for single-stage pumps can have only minor effects.

Another parameter that is easy to estimate is the inlet head-velocity ratio $2g_oH_{sv}/V_{m,i}^2$. According to the cavitation parameter diagram shown in figure 1-18 (sec. 1.2.2), the suction specific speed reaches a maximum for practical values of blade cavitation number $C_p = \sigma_p$ when $2g_oH_{sv}/V_{m,i}^2$ is close to 3.5.

The same diagram and equation (1-46) indicates that under the assumptions of this demonstration, the equation for the suction specific speed is reduced to

$$S = \frac{1}{5.571}\frac{U_i}{V_{m,i}} \tag{1-139}$$

With the flow coefficient $V_{m,i}/U_i$ so determined by the suction specific speed alone, the basic specific speed equation can be solved for D_i/D_o if one can make a rational assumption about the head coefficient. It is assumed empirically that the maximum value of this head coefficient which exists at the minimum discharge diameter $D_{o,min}$ is $2g_oH/U_{o,min}^2 = 1$. Using this assumption and that of $D_h/D_i = 0.25$ together with equations (1-139) and (1-24), one finds

$$n_s = 0.4594\left(\frac{V_{m,i}}{U_i}\right)^{1/2}\left(\frac{D_i}{D_{o,min}}\right)^{3/2}$$

$$= \frac{0.4594}{(5.571\,S)^{1/2}}\left(\frac{D_i}{D_{o,min}}\right)^{3/2} \tag{1-140}$$

Figure 1-43 shows a graphical evaluation of equation (1-140), which is, in fact, the previously mentioned section through the multidimensional space of operating conditions. In this section appear two systems of lines, lines of constant values of the inlet flow coefficient $V_{m,i}/U_i$ and lines of constant values of the diameter ratio $D_i/D_{o,min}$. Logarithmic scales are, quite properly, used for the dimensionless coordinates and give this section the qualities of a computation chart. Thus this initially somewhat abstract concept of a section through the space of dimensionless operating conditions appears in a concrete and useful form.

The diameter ratio $D_i/D_{o,min}$ and the flow coefficient $V_{m,i}/U_i$ are, of course, not the only design parameters that are of interest and can be related to the specific speeds. Of particular significance is the maximum outside diameter $D_{o,max}$. Often this diameter must be larger than $D_{o,min}$ because of the previously mentioned limit of the retardation of the relative flow. A simple solution can be found by assuming that the circumferential component w_U of the relative flow should not be retarded more than indicated by $w_{U,o}/w_{U,i} \geq 0.65$.

Using Euler's turbomachinery momentum equation as well as $w_{U,i} = -U_i$ (for zero rotation of the absolute flow at the impeller inlet) and $2g_oH/U_{o,min}^2 = 1$, one obtains

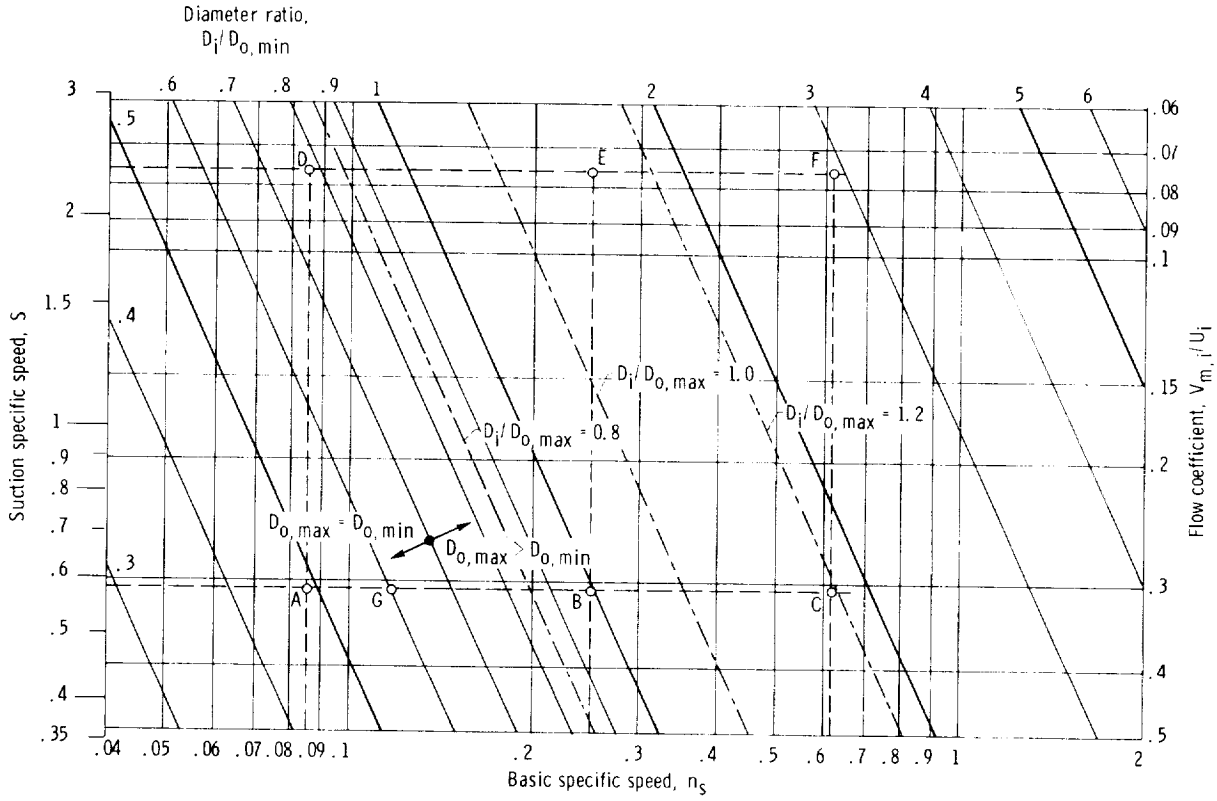

Figure 1-43.—Design parameters as functions of basic and suction specific speeds for head coefficient of 1.

$$\frac{D_{o,max}}{D_i} \geq \left[\frac{1}{2\eta_h}\left(\frac{D_{o,min}}{D_i}\right)^2 + 0.325^2\right]^{1/2} + 0.325 \qquad (1\text{-}141)$$

which is derived in appendix 1-A. In this equation, η_h is the so-called hydraulic efficiency of the machine, which accounts only for head losses, not for leakage or parasite torque increases. Figure 1-44 shows the evaluation of equation (1-141) under the assumption that $\eta_h = 0.90$, and with only the equality sign, so that $D_{o,max}/D_i$ has its minimum value. Instead of using this minimum value, one usually employs a larger value $D_o^* = D_i$ for all cases where $D_{o,max} < D_i$. The corresponding shifts of the curves representing $D_{o,max}$ are indicated in figure 1-44 by dashed arrows.

Evidently it would be possible to enter this information into the section through the space of operating conditions (fig. 1-43). This is done for $D_i/D_{o,max} = 0.8$, 1.0, and 1.2 to indicate this family of lines diagrammatically. Since, according to equation (1-141), the lines $D_i/D_{o,max} = \text{constant}$ are parallel to the lines $D_i/D_{o,min} = \text{constant}$, it would be difficult to distinguish the $D_i/D_{o,max}$ family of lines from the $D_i/D_{o,min}$ family. However, only this practical consideration of visibility prevents one from showing a multiplicity of parameters such as $D_i/D_{o,max}$ or $2g_oH/U^2_{o,max}$ in the section (fig. 1-43). The minimum head coefficient $2g_oH/U^2_{o,max}$ is derived easily from the assumed value of the maximum head coefficient $2g_oH/U^2_{o,min} = 1$ by the relation

$$\frac{2g_oH}{U^2_{o,max}} = \frac{2g_oH}{U^2_{o,min}} \frac{D^2_{o,min}}{D^2_{o,max}} \qquad (1\text{-}142)$$

with $D_{o,max}/D_{o,min}$ given in figure 1-44. This equation, of course, assumes equal energy addition in all stream surfaces.

Additional design parameters can easily be calculated. For example, the rotor width ratio $b_o/D_{o,min}$ (see fig. 1-7 or 1-25) is readily derived from the condition of continuity. Form characteristics of stationary passages adjacent to the rotor are obtained on the same basis and by the law of

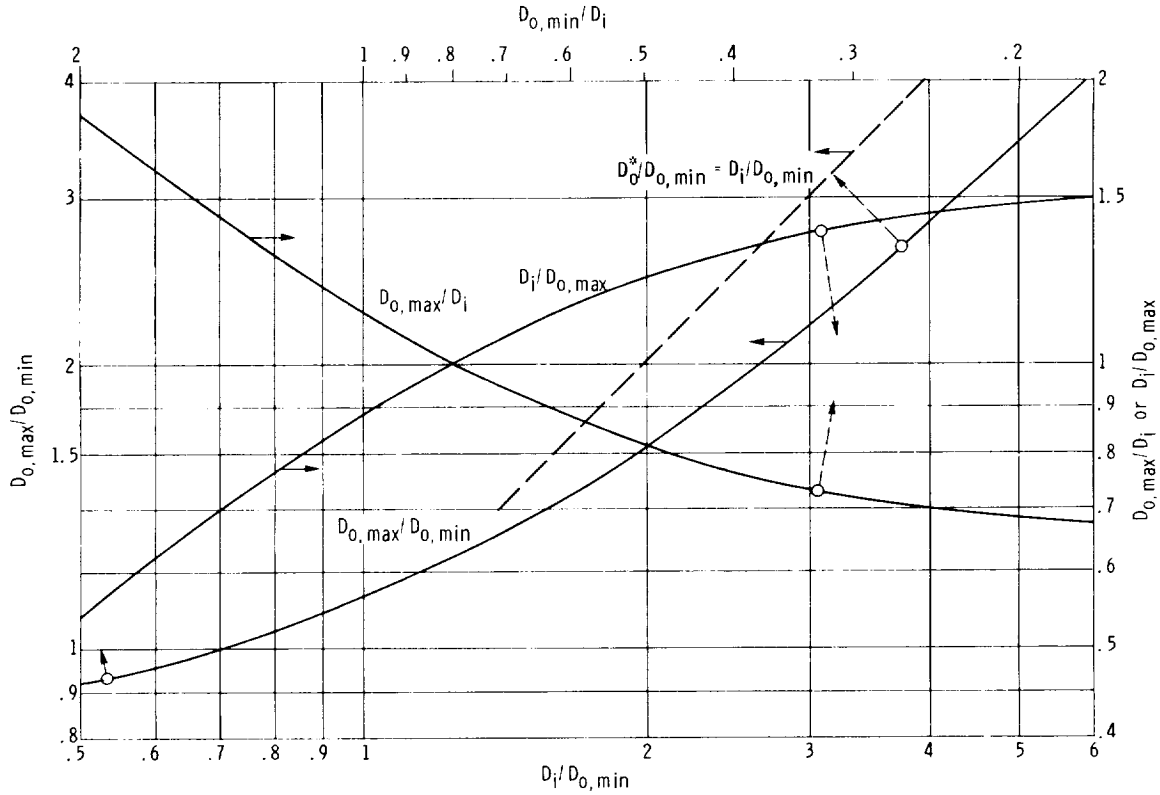

Figure 1-44.—Maximum pump discharge diameters $D_{o,max}$ and D_o^* as functions of $D_i/D_{o,min}$.

constant angular momentum. Every point in the section shown in figure 1-43, therefore, represents in principle the whole set of dimensionless design parameters, which is as complete as permitted by the state of knowledge available. Figure 1-27 depicts the type of information represented by every point in this section, in this demonstration with respect to the design form of the impeller only.

It is desirable to illustrate the last step, that is, the establishment of a complete design form from the design parameters. At present, this step can be demonstrated (under many simplifying assumptions) only for the relatively well-established field of hydrodynamic rotors and is represented in a space of only two dimensions, which are the operating conditions n_s and S.

Ideally every point in this space or section should be associated with a complete design form. This is demonstrated for a very limited number of points (A to F) in figure 1-43. Figure 1-45 illustrates diagrammatically the corresponding design forms by showing the impeller profiles. The various profiles are correlated with the six points in figure 1-43 by the same letters, as well as by the values of the basic specific speed n_s and the suction specific speed S.

Since the impeller design forms include the actual vane shapes derived from the velocity diagrams (shown in fig. 1-27), this last step is a very major step, demanding all the knowledge, experience, and skill available in the pump design field. It is the core of the design process. Hopefully the foregoing discussion shows this process in its proper position within the overall design procedure.

Since $D_{o,max}/D_i$ given by figure 1-44 is a minimum value of this ratio, it is permissible, even desirable, to show in figure 1-45 the larger ratio D_o^*/D_i whenever $D_{o,max} < D_i$.

1.4.3 Extension of Example to Three Dimensions With Particular Attention to Stress Specific Speed

We now return to the original, multidimensional picture of the space of dimensionless operating conditions. To aid the imagination, consider at one time the interaction of the n_s, S-section (shown in fig. 1-43) with only one of the other coordinates (specific speeds) of this space. This other coordinate

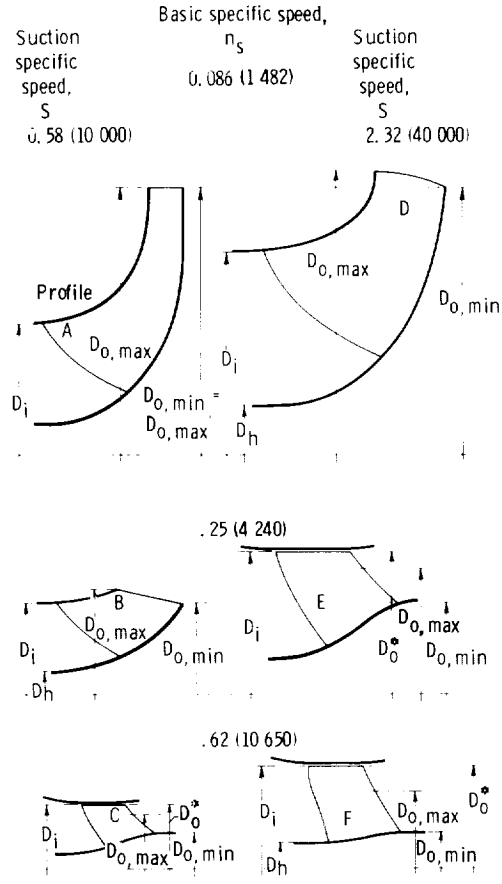

Figure 1-45.—Rotor profiles as function of basic specific speed and suction specific speed. Profile designations correspond to points in figure 1-43. (Values in parentheses are dimensional specific speeds.)

axis is, of course, normal to the n_s, S-plane, so that a three-dimensional picture of the interaction with a third specific speed is obtained.

The lines in figure 1–43 represent in this picture surfaces intersecting the n_s, S-plane. Among the design choices in the previous section are stipulations that small changes in compressibility, viscosity, stress, gravity, and vibration characteristics have only negligible effects. This means that within the range of validity of these stipulations the surfaces represented by the lines of constant $D_i/D_{o,min}$ and $V_{m,i}/U_i$ in figure 1–43 intersect the n_s, S-planes at right angles provided that the third specific speed considered is concerned with one of the characteristics just mentioned. Therefore, as intended, the set of design choices eliminates the multidimensional character of the space of dimensionless operating conditions within this limited range, which leaves n_s and S as the only independent variables.

As soon as one extends considerations to large changes in compressibility, viscosity, stress, gravity, and vibration characteristics, the picture becomes quite different. The surfaces, represented in the n_s, S-planes by the lines $D_i/D_{o,min}$ = constant and $V_{m,i}/U_i$ = constant, curve in planes normal to the n_s, S-planes. For example, at low viscosity specific speeds (low Reynolds numbers) the lines in the n_s,S-planes have different positions, and the surfaces they represent intersect the n_s, S-planes at angles substantially different from 90°. This is the statement in geometric terms that the viscosity of the fluid as well as the viscosity specific speed, and changes therein, have substantial effects on the design parameters of the machine if the viscosity specific speed is low.

Similar statements can be made for other specific speeds used as the third coordinate, for example, the stress specific speed. At high stress specific speeds, the surfaces of constant design parameters, such as $D_i/D_{o,min}$ or $V_{m,i}/U_i$, intersect n_s, S-planes not at right angles and not at the same places as for the low stress specific speed assumed previously. To describe this three-dimensional space of the three operating conditions n_s, S, and n_σ, one could investigate relations in planes normal to the n_s, S-plane, for example, in several n_σ, n_s-planes at different constant values of S. A series of diagrams analogous to figure 1–43, representing n_σ,n_s-, n_σ,S-, and n_s,S-planes at different constant values of S, n_s, and n_σ, respectively, would describe the field of single-suction centrifugal- and axial-flow pump design forms rather completely and would be of great practical value, particularly for preliminary design. Unfortunately, presently available information on the design of such pumps is not sufficient for arriving at an even approximately unique answer for such a representation.

In order to avoid the impression that the mental pictures discussed in this section are merely abstract speculations, figure 1–46 is presented to give a somewhat qualitative picture of the final results that might be obtained from a step in the direction of the $n_{\sigma,c}$-axis at constant values of n_s and S. The step is taken from a centrifugal stress specific speed $n_{\sigma,c} < 0.1$ (point G in fig. 1–43) to a value between $n_{\sigma,c} = 0.2$ and $n_{\sigma,c} = 0.3$. (It would require a fairly detailed stress analysis to arrive at more definite figures.) To accomplish this increase in the centrifugal stress specific speed, it is obviously

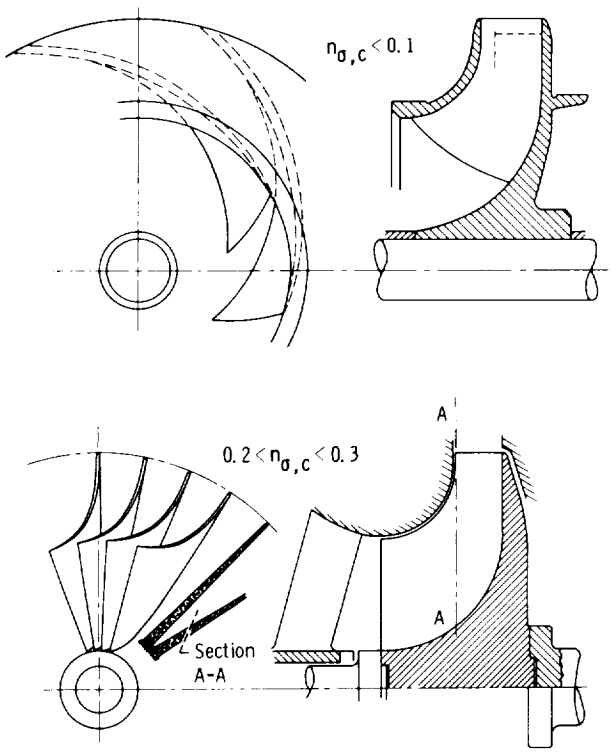

Figure 1-46.—Radial-flow rotor design as function of stress specific speed $n_{\sigma,c}$. Basic specific speed n_s, 0.117 (2000).

necessary to increase the stress coefficient $\rho_s U_o^2/2\sigma_c$. This is done by replacing design elements having relatively low stress coefficients by elements having relatively high stress coefficients. In section 1.3.3.1, it is stated that blades inclined so as to introduce bending stresses (under the influence of centrifugal forces) have relatively low stress coefficients. The rotor shown in figure 1-46 with $n_{\sigma,c} = 0.1$ has such blades (strongly inclined against the radial direction). Another element having a low stress coefficient is the outer shroud (sec. 1.3.3.1); the coefficient is low partly because the shroud is hoop-shaped and partly because it tends to increase the stresses in blades that are favorable with respect to stress (nearly radial blades).

The natural ways to increase $\rho_s U_o^2/2\sigma_c$ and $n_{\sigma,c}$ are, therefore, to change the blades so as to have nearly radial blade elements (see, e.g., fig. 1-29) and to eliminate the outer shroud of the rotor. The rotor design shown in figure 1-46 for stress specific speeds between 0.2 and 0.3 shows these changes in design. Note also the elimination of the central bore through the back shroud of the rotor.

Will this change in blade design have a harmful effect on the hydrodynamic performance? There is no compelling reason why it should directly harm the cavitation performance (nor the related performance with respect to compressibility). However, the efficiency and the stability of performance are likely to suffer if the relative flow in the rotor is excessively retarded. This can easily happen in pumps (or compressiors), because radial blade elements in connection with radial discharge of the meridional flow (as shown in fig. 1-46) lead to radial discharge relative to the rotating impeller and thereby to a minimum of the relative discharge velocity. To minimize this contingency, a stationary inlet guide vane system may be used (fig. 1-46). When the flow entering a pump rotor in this way is given a strong rotation in the direction of the rotor motion, the relative inlet velocity is reduced and excessive retardation of the relative flow from inlet to discharge is thus avoided. It must be noted, however, that this solution of the retardation problem may have an adverse effect on the cavitation performance of the machine.

As mentioned previously with respect to hydrodynamic design, all the available knowledge, experience, and skill in mechanical and hydrodynamic design, and perhaps more, are needed to make a reasonably useful attack on the design problems of the n_s, S, and $n_{\sigma,c}$ space. This situation can hardly be better in the n_s, n_a, and $n_{\sigma,c}$ space of gas-dynamic machines, and it is much worse when the viscosity, gravity, and vibration specific speeds are involved.

1.4.4 Inclined Sections Through Spaces of Turbomachinery Operating Conditions and Design Forms

In the preceding sections, the multidimensional space of operating conditions is described and used by means of plane sections through this space. Specifically a very limited number of dimensionless operating conditions, usually two, are considered variable, and all other operating conditions are considered fixed. This means that these sections are chosen to be parallel to two axes of this space and normal to all other axes. This discussion cannot be closed without calling attention to the fact that this selection of the sections considered is not the only selection possible. The section chosen might be inclined against the coordinate axes, which means that within such a section more than two of the dimensionless operating conditions might vary. However, these variations could not be independent

of each other because, if they were, the section would become a space of as many dimensions as there are independent variables.

Variations in the dimensionless operating conditions which are dependent on each other may be of considerable practical significance in some cases. For example, the stress specific speed and the compressibility specific speed of gas turbines or compressors may very well be interrelated for practical reasons. The effect of a particular structural material (a particular strength-density ratio) on the design form, in connection with given characteristics of the gas, can perhaps be described effectively by an inclined, conceivably curved, section through a space with the basic specific speed, compressibility specific speed, and stress specific speed as the principal variables. In other words, it may be of practical interest to limit the freedom of design variations in a prescribed fashion. Inclined or curved sections through the space of dimensionless operating conditions may be a convenient way of representing such a situation.

1.4.5 Review

The field of turbomachinery design is first represented by a number of analytical relations between various dimensionless operating conditions, the specific speeds, and a number of dimensionless design parameters, such as ratios of important linear dimensions, flow and head coefficients, and so on. Every set of operating conditions is associated with a corresponding set of design parameters which can be reasonably unique only after certain design choices have been made regarding the nature of the fluid, the purpose and type of the machine, and so on.

This situation can be represented as a space of dimensionless operating conditions, every coordinate representing one of these operating conditions (i.e., one specific speed). Every point in this space represents a complete set of dimensionless operating conditions, as complete as possible under the present state of knowledge.

After all pertinent design choices have been made, every point in this space can be associated with a corresponding set of design parameters, so that one can locate in this space the loci of constant values of all design parameters appropriate for the design choices made. A two-dimensional section through this space shows these loci as lines of constant values of a design parameter (fig. 1-43). Such a section may, thus, be a chart from which one can read values of the design parameters appearing therein. Modern means of computation may extend this possibility beyond the format of a two-dimensional graph.

The design parameters are either ratios of important dimensions or coefficients which determine directly or indirectly certain elementary design form characteristics. Thus each point in the space of dimensionless operating conditions represents a complete set of such ratios of dimensions and elementary design form characteristics; that is, each point represents all the design information that can be derived from the dimensionless operating conditions by the elementary means employed in this chapter.

The core of the form design process consists in associating with points in this space (with complete sets of ratios of dimensions and elementary design form characteristics) corresponding design forms of the entire machine (see figs. 1–45 and 1–46). This process requires all the knowledge, experience, and skill available in the field of design. This process is not described in this chapter, only summarized in relation to other aspects of the design process.

Appendix 1-A—Effect of Limit of Retardation of Relative Flow

Assume a ratio of retardation of the relative flow $w_{U,o}/w_{U,i}=0.65$. With no rotation of the absolute flow at the inlet,

$$w_{U,i}=-U_i=|U_i|$$

At the discharge,

$$w_{U,o}=U_o-V_{U,o}=U_o\left(1-\frac{V_{U,o}}{U_o}\right)$$

where U_o corresponds to $D_{o,max}$. From Euler's equation,

$$g_oH=\eta_h V_{U,o}U_o$$

and

$$\frac{g_oH}{\eta_h U_o^2}=\frac{V_{U,o}}{U_o}$$

Hence

$$w_{U,o}=U_o\left(1-\frac{g_oH}{\eta_h U_o^2}\right)$$

$$=U_o\left[1-\left(\frac{g_oH}{\eta_h U_{o,min}^2}\right)\frac{D_{o,min}^2}{D_{o,max}^2}\right]$$

Assume

$$\frac{g_oH}{U_{o,min}^2}=\frac{1}{2}$$

Hence

$$\frac{w_{U,o}}{U_o}=1-\frac{1}{2\eta_h}\frac{D_{o,min}^2}{D_{o,max}^2}$$

$$\frac{w_{U,o}}{w_{U,i}}=0.65=\frac{w_{U,o}}{U_i}=\frac{w_{U,o}}{U_o}\frac{U_o}{U_i}$$

$$=\left(1-\frac{1}{2\eta_h}\frac{D_{o,min}^2}{D_{o,max}^2}\right)\frac{D_{o,max}}{D_i}$$

$$0.65=\frac{D_{o,max}}{D_i}-\frac{1}{2\eta_h}\frac{D_{o,min}}{D_{o,max}}\frac{D_{o,min}}{D_i}$$

$$0.65=\frac{D_{o,max}}{D_i}-\frac{1}{2\eta_h}\frac{D_i}{D_{o,max}}\frac{D_{o,min}^2}{D_i^2}$$

$$\frac{D_{o,max}^2}{D_i^2}-0.65\frac{D_{o,max}}{D_i}=\frac{1}{2\eta_h}\frac{D_{o,min}^2}{D_i^2}$$

$$\frac{D_{o,max}^2}{D_i^2}-2\times0.325\frac{D_{o,max}}{D_i}+0.325^2$$

$$=\frac{1}{2\eta_h}\frac{D_{o,min}^2}{D_i^2}+0.325^2$$

$$\left(\frac{D_{o,max}}{D_i}-0.325\right)^2=\frac{1}{2\eta_h}\frac{D_{o,min}^2}{D_i^2}+0.325^2$$

$$\frac{D_{o,max}}{D_i}=\left(\frac{1}{2\eta_h}\frac{D_{o,min}^2}{D_i^2}+0.325^2\right)^{1/2}+0.325$$

Chapter 2

Theoretical Principles of the Hydrodynamic Design of Turbomachinery

2.1 Introduction

The theory of flow in turbomachinery relates the flow to the design form of the machine. It is based on the general laws of fluid mechanics. The most important of these laws are assumed to be known.

In this chapter, the theory of flow in turbomachinery is considered separately from the similarity considerations treated in chapter 1. The theory of flow attempts to approximate the actual flow conditions in some useful fashion. Similarity considerations merely compare flow conditions with each other while treating them either as unknown or as given by some other information.

As mentioned in chapter 1, flow conditions in turbomachines are exceedingly complex; they are three-dimensional and unsteady. The theory of flow attempts to approximate these flow conditions as closely as possible. This theory is as broad a field as general fluid mechanics, since there are indeed very few aspects of fluid mechanics that do not apply to turbomachinery.

In the design of turbomachinery, however, it is prudent to pay attention primarily to the simplest and most fundamental aspects of the flow, because the design process demands the solution of the so-called indirect problem, that is, the problem of finding the form of the flow boundaries required to generate a prescribed flow, or at least certain characteristics of that flow. This indirect problem is usually much more difficult to solve than the so-called direct problem, that is, the problem of finding the form of the flow for a given form of the flow boundaries. Generally the indirect problem (design problem) can be solved only for relatively simple approximations of the flow to be generated. The theory of flow as applied to the design of turbomachinery is, therefore, concerned primarily with approximations that are sufficiently simple to solve the indirect flow problem. Since the flow boundaries to be determined are usually expected to be strongly three-dimensional, the requirement for simplicity of the theoretical approximations to be used is even greater in the field of turbomachinery than in most other fields of hydrodynamic or aerodynamic design.

The presentation of the theory of flow in turbomachinery given in this chapter will impress many experts in this field as unduly elementary, since it contains only those aspects of the theory which are applied in the following chapters to the design of turbomachinery. This elementary character is pronounced particularly because the approach to the design problem that is used later proceeds in nearly all cases from the simplest approximation to more refined solutions. The theoretical background of the design process given in this chapter follows this scheme and pays primary attention to the broad theoretical principles on which the design of turbomachinery can be based.

The theoretical principles may well be called hydrodynamic, because the effects of compressibility of the fluid are treated separately as departures from the principles of incompressible flow. Only where compressibility does not affect the theoretical principles is it included from the beginning as, for example, in the derivation of Euler's turbomachinery momentum equation.

2.2 Meridional Flow in a Space of Revolution

The flow in a turbomachine proceeds in a space of revolution, a space bounded by two coaxial surfaces of revolution. There are exceptions to this rule, for example, the flow in a volute (or spiral) casing.

For the purely axial-flow machine, the flow proceeds between two coaxial, cylindrical surfaces. For a purely radial-flow machine, it proceeds between two planes normal to the axis of rotation. For the so-called mixed-flow or conical-flow machines, the flow may proceed between two coaxial, conical surfaces; however, in the most general case the flow proceeds between two coaxial, doubly curved surfaces of revolution and therefore changes its direction from generally axial to more or less radial. This description pertains primarily to the flow without its circumferential component, that is, to the flow component in radial planes containing the axis of revolution, which is called the meridional component. The flow in a space of revolution is thus divided into its circumferential and meridional components.

Usually the description of this flow is simplified by assuming that the meridional and circumferential components are both uniform along any circle coaxial with the flow boundaries. By this assumption, called the assumption of axial symmetry, it is also assumed that the flow proceeds generally along coaxial surfaces of revolution, and these surfaces are the stream surfaces of the meridional flow. This hypothesis of coaxial stream surfaces of revolution is usually maintained even if the circumferential velocity component and the meridional velocity component are not completely uniform along coaxial circles. It is by this hypothesis that one can divide the flow in a space of revolution into two separate parts, circumferential and meridional flow, which can be determined and treated independently of each other. In section 2.7 this independence is shown to break down as soon as the flow has vorticity. However, even in this case it is customary to adhere to the hypothesis of coaxial stream surfaces of revolution for the meridional flow, although this hypothesis is not strictly justified under these conditions.

The rest of this section describes the relation between the meridional flow and the boundaries of the space of revolution.

The simplest approximation of the meridional flow in a space of revolution is obviously the one-dimensional approximation, obtained by dividing the rate of volume flow by the cross sections of the space of revolution A_m, which are normal to the meridional flow (see fig. 2-1). Each cross section is the area of a surface of revolution, coaxial with and normal to the boundaries of the space of revolution considered. With the notations used in figure 2-1, one finds

$$A_m = b 2\pi r_b = 2\pi \int_A^B r\, db \tag{2-1}$$

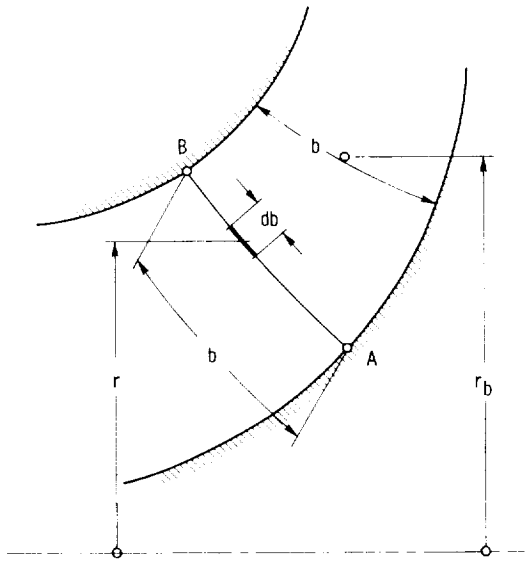

Figure 2-1. – Flow cross sections in space of revolution.

The condition of continuity defining the meridional velocity V_m in its one-dimensional meaning is

$$V_m = \frac{Q}{A_m} \tag{2-2}$$

Under the one-dimensional assumption that V_m = constant over any cross section A_m, one can determine the normal spacing d between successive meridional streamlines or stream surfaces, according to figure 2-2, by

$$\left.\begin{array}{l} 2\pi r d = \text{constant} \\ \text{or} \\ r d = \text{constant} \end{array}\right\} \tag{2-3}$$

since these products are constant along any cross section of the meridional flow, but not in the direc-

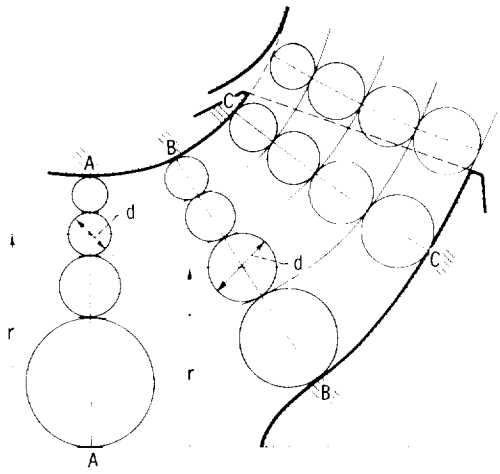

Figure 2-2. – Geometric construction of meridional streamlines.

tion of this flow. This means that the volume flow ΔQ is the same between successive stream surfaces.

The assumption that V_m is constant over the cross sections of this flow is in many cases a better approximation than might be expected on theoretical grounds. Nevertheless, departures from this assumption must be considered on a rational basis.

For a so-called potential velocity distribution of the meridional flow, that is, a distribution of uniform total energy (of an incompressible fluid), the equation for the V_m distribution across the stream is

$$\frac{\partial V_m}{\partial b} + \frac{V_m}{R} = 0 \tag{2-4}$$

where R is the radius of curvature of the meridional streamline, and b is the coordinate normal to V_m in radial planes (see fig. 2-3(a)). The coordinate b is assumed to increase in the direction away from the centers of curvature of the meridional streamlines. Figure 2-3(b) shows the curve of V_m against b constructed from the direction of its tangents $\partial V_m/\partial b = -V_m/R$. The magnitude of V_m at the point where this construction (i.e., the integration of eq. (2-4)) is started may first be chosen arbitrarily and then be determined by the condition of continuity:

$$Q = 2\pi \int_A^B r V_m \, db \tag{2-5}$$

The volume flow rate Q is, of course, constant for incompressible fluids. Its variations (along the meridional flow) for compressible fluids are

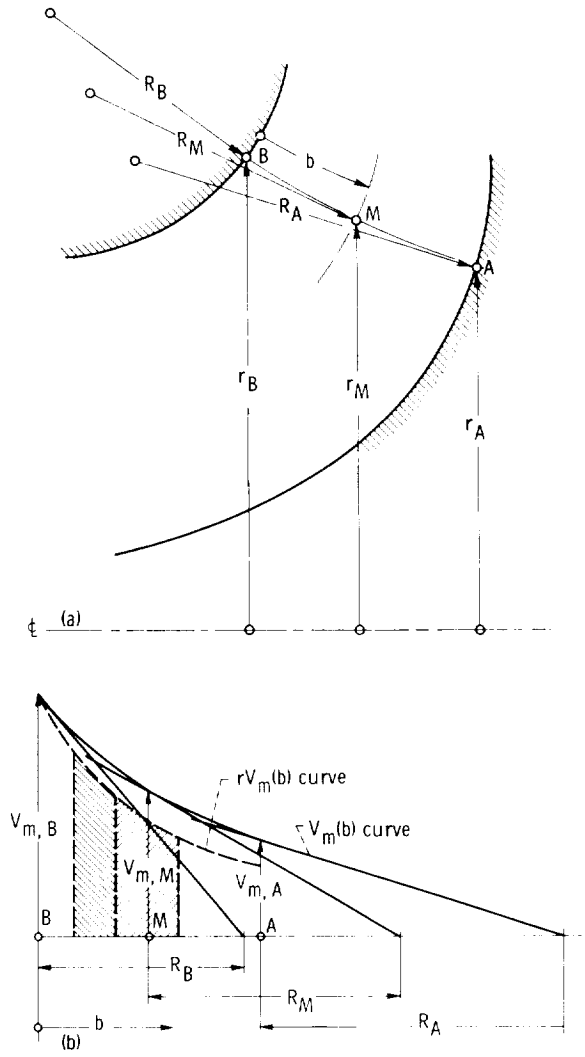

(a) Meridional flow configuration.
(b) Velocity and flow distribution in section B-A.
Figure 2-3. – Meridional velocity distribution for $\partial V_m/\partial b + V_m/R = 0$.

determined by a process of iteration, as described in section 2.4. Equation (2-5) is easily evaluated by the area under a rV_m curve (see fig. 2-3(b)). The intersections of the meridional streamlines (or surfaces) with the cross section AB are determined by dividing the area under the rV_m curve into a number of equal parts, as shown in figure 2-3(b).

Departures from equation (2-4) (i.e., departures from a meridional flow of uniform total energy in the sense of Bernoulli's equation) are expressed by the so-called vorticity ζ_U of the meridional flow. The meaning and determination of ζ_U are given in section 2.6.3.1, appendix 2-A, and section 2.7. The equation controlling the meridional velocity

distribution across a stream with the vorticity ζ_U is

$$\left.\begin{aligned} &\frac{\partial V_m}{\partial b} + \frac{V_m}{R} = \zeta_U \\ &\text{or} \\ &\frac{\partial V_m}{\partial b} = \zeta_U - \frac{V_m}{R} \end{aligned}\right\} \qquad (2\text{-}6)$$

The vorticity ζ_U is positive if it has the same direction of rotation as V_m/R.

The construction of the V_m against b curve for flow with vorticity ζ_U is shown in figure 2-4. However, in this case it is important to start the integration of equation (2-6) at approximately the correct value of V_m, because the condition of continuity cannot be satisfied by simply scaling the resulting V_m curve up or down by any desired ratio. The construction of the V_m curve should this time start at some midpoint M, presumably the area center of the cross section considered, where $V_{m,M}$ can be assumed to have the average value of the cross section as determined by the condition of continuity (eq. (2-2)). If a subsequent determination of the rate of flow by equation (2-5) shows a (small) discrepancy, this can be corrected by shifting and scaling the V_m curve up or down and using a curve between that obtained by a parallel shift and by scaling. One can, of course, also change the initial $V_{m,M}$ value according to the discrepancy and repeat the construction of the V_m curve.

2.3 Circumferential Flow in a Space of Revolution

The circumferential component of the flow in a space of revolution is determined by the condition that any torque or moment about the axis of rotation applied to the fluid is equal to the change in moment of momentum of the mass flow per unit of time passing through the space. This law is expressed by Euler's turbomachinery momentum equation, which is derived in this section.

The moment of momentum passing through an element $dA_{m,1}$ of the cross section $A_{m,1}$ of a space of revolution (fig. 2-5) is

$$dM_1 = \rho_1 V_{m,1}\, dA_{m,1} V_{U,1} r_1 \qquad (2\text{-}7)$$

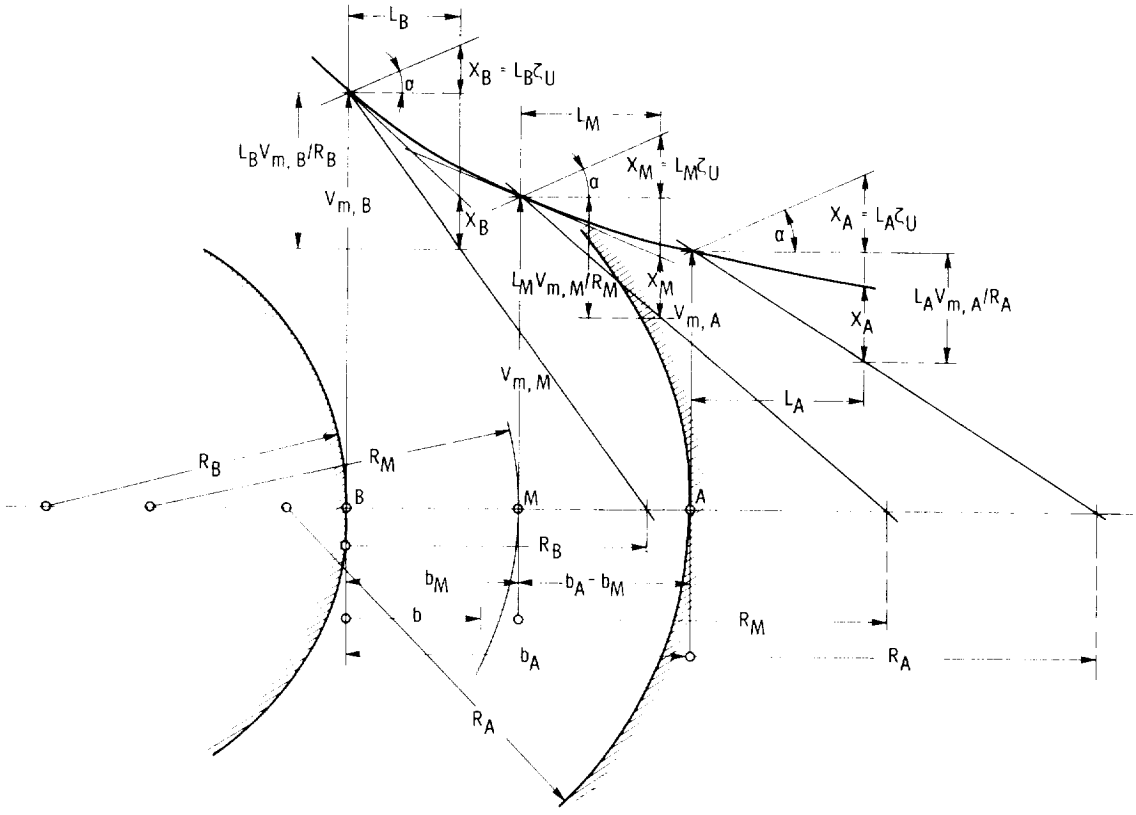

Figure 2-4. – Velocity distribution with vorticity ζ_U in curved duct (L is arbitrary length associated with points A, M, and B).

The corresponding moment of momentum passing through the element $dA_{m,2}$ of a second cross section $A_{m,2}$ is

$$dM_2 = \rho_2 V_{m,2}\, dA_{m,2} V_{U,2} r_2 \tag{2-8}$$

If the flow is assumed to enter through the cross section $A_{m,1}$ and leave through the cross section $A_{m,2}$, the moment applied to the fluid by vane and friction forces between sections $A_{m,1}$ and $A_{m,2}$ is

$$M = \int^{A_{m,2}} \rho_2 V_{m,2} V_{U,2} r_2\, dA_{m,2} - \int^{A_{m,1}} \rho_1 V_{m,1} V_{U,1} r_1\, dA_{m,1} \tag{2-9}$$

This is Euler's turbomachinery momentum equation in its most general form. It is rigorously correct if the moment M comprises all moments applied to the fluid within this part of the space of revolution, including circumferential friction forces on the boundaries of the space. In this form, Euler's turbomachinery equation does not depend on any assumption about the form of the flow; that is, it is independent of such assumptions as that of axial symmetry. However, for the same reason, Euler's turbomachinery equation is difficult to evaluate in this general form (eq. (2-9)).

To ease evaluation in several respects, one uses first the assumption that the flow proceeds through the system along stream surfaces of revolution coaxial to the boundaries of the space of revolution considered. Under this assumption, one can examine the flow along a coaxial stream surface S-S. For an infinitesimal region around this stream surface, Euler's turbomachinery equation (2-9) can be written in the form

$$dM = \rho_2 r_2^2\, db_2 \int_0^{2\pi} V_{m,2} V_{U,2}\, d\theta - \rho_1 r_1^2\, db_1 \int_0^{2\pi} V_{m,1} V_{U,1}\, d\theta \tag{2-10}$$

where θ is the angle about the axis of rotation (in radians).

Defining circumferentially averaged values of V_m and V_U by

$$2\pi \overline{V_m V_U} = \int_0^{2\pi} V_m V_U\, d\theta \tag{2-11}$$

one may write the last form of Euler's turbomachinery equation (eq. (2-10)) in the form

$$dM = \rho_2 2\pi r_2^2\, db_2 \overline{V_{m,2} V_{U,2}} - \rho_1 2\pi r_1^2\, db_1 \overline{V_{m,1} V_{U,1}} \tag{2-12}$$

However,

$$\rho_2 2\pi r_2\, db_2\, \overline{V_{m,2}} = \rho_1 2\pi r_1\, db_1 \overline{V_{m,1}} = d\dot{m} \tag{2-13}$$

which is the rate of mass flow entering and leaving the infinitesimal space of revolution around the stream surface S-S. This rate of mass flow is, of course, equal at inlet and discharge by definition of the stream surfaces of revolution adjacent to the stream surface S-S and also by definition of db_1 and db_2. With the approximation

$$\overline{V_m V_U} = \overline{V_m}\,\overline{V_U} \tag{2-14}$$

which can be exact if the average value $\overline{V_U}$ is defined in accordance with equation (2-12), Euler's turbomachinery equation can be written in the form

$$dM = d\dot{m}(r_2 \overline{V_{U,2}} - r_1 \overline{V_{U,1}}) \tag{2-15}$$

If no torque is applied between stations 1 and 2 (i.e., if $dM = 0$),

$$r_2 \overline{V_{U,2}} = r_1 \overline{V_{U,1}} \tag{2-16}$$

where the averaging applies in connection with equations (2-13) and (2-14) to the circumference of circles with radii r_2 and r_1, respectively.

Equation (2-16) expresses the well-known law of constant angular momentum, which controls all curved fluid motions of uniform total energy of the circumferential flow component. Euler's turbomachinery equation supplements this law for the case where torque or circumferential forces are applied to the flow.

If the moment dM in equation (2-15) is applied by a vane system rotating at the angular velocity ω, the work transmitted to the fluid per unit of time is obviously $\omega\, dM$. The mass involved per unit of time is $\rho\, dQ$, where dQ is the volume rate of flow passing along the narrow space of revolution of the widths db_1 and db_2 and following the meridional stream surface S-S (fig. 2-5). With these substitutions, equation (2-15) appears in the form

$$\omega\, dM = \omega\rho\, dQ(r_2 V_{U,2} - r_1 V_{U,1}) \tag{2-17}$$

If one divides the work per unit of time ωM by the mass flow per unit of time ρQ, one finds $\omega M/\rho Q$ has the dimensions of a velocity squared.

Instead of dividing by the mass flow ρQ, one customarily divides the work per unit of time ωM by the weight flow per unit of time $g_o \rho Q$. The resulting ratio $\omega M/g_o \rho Q$ has the dimensions foot-pounds per pound (ft-lb/lb); $\omega M/g_o \rho Q$ is a length (ft) which is called the rotor head of the machine. It is the height to which the work per unit of time ωM can raise the mass flow per unit of time ρQ against the (standard) gravitational field at sea level on Earth.

When this reasoning is applied to compressible fluids, it is often advisable to maintain the complete set of units, foot-pounds per pound. With this approach, equation (2-17) appears in the form

$$\frac{\omega\, dM}{g_o \rho\, dQ} = H_r = \frac{U_2 V_{U,2} - U_1 V_{U,1}}{g_o} \tag{2-18}$$

where the peripheral velocity U has been substituted for ωr.

For a gas the rotor head H_r is the change in total (stagnation) enthalpy. For incompressible fluids H_r is related to the total head H measured between inlet and discharge of the machine by $H = \eta_h H_r$ for pumps and $H = (1/\eta_h)\mathrm{H_r}$ for turbines, η_h being the hydraulic efficiency introduced in section 1.1 and equation (1-10a).

It is the last form of Euler's turbomachinery equation (eq. (2-18)) which permits the solution of the entire flow problem across the field of flow considered here and shown diagrammatically in figure 2-5. If it is desired, as usual, to exchange the same amount of energy per pound of fluid between the rotor and the fluid in every part of the flow, $U_2 V_{U,2} - U_1 V_{U,1} = \text{constant}$ and

$$H_r = \frac{U_2 V_{U,2} - U_1 V_{U,1}}{g_o} = \text{constant} \tag{2-19}$$

across the entire stream passing through the space of revolution and the rotor vane system contained in it. If equation (2-19) is not satisfied in the sense that the energy exchange per pound H is not constant across the entire stream, the flow contains vorticity on at least one side of the rotor vane system, since $rV_U = \text{constant}$ is the condition for the vortex-free or irrotational circumferential flow in a space of revolution. The laws of fluid motion applying to departures from this case are discussed in section 2.7. In most practical cases, equation (2-19) is satisfied across the stream passing through a turbomachinery rotor.

2.4 Effects of Compressibility on Flow in Turbomachinery

The flow of compressible fluids in turbomachinery and other fields of fluids engineering constitutes a very broad area of fluid mechanics, combining thermodynamics with fluid mechanics. This broad field is not covered in this section. Instead, an attempt is made to describe as simply as possible those aspects in which the mechanics of compressible fluids differ from the mechanics of incompressible fluids when applied to turbomachinery. Only major effects of compressibility are considered, and only to the extent that these effects influence the design of turbomachines in a fundamental fashion.

The basic effect of compressibility is obviously the change in the density ρ or in the specific volume v (volume per unit of weight) of the fluid in the machine. Thus, if the specific volume $v = 1/g_o \rho$ of the fluid can be determined as a function of the fluid velocity and the pressure or head in the machine, the problem of compressibility effects is solved in principle, although this solution might require a process of successive approximations or iteration.

The solution suggested here is based essentially on two principles:

(1) Bernoulli's equation for compressible fluids, which, when differences in elevation are neglected, may be written in the form

$$\frac{V_1^2}{2g_o} + h_1 = \frac{V_2^2}{2g_o} + h_2 \tag{2-20}$$

where h designates the enthalpy of the fluid expressed in mechanical units such as foot-pounds per pound. Bernoulli's equation in the generalized form (2-20) has the advantage of being independent of the fluid-mechanical losses in the flow, since such losses are converted into heat and therefore contribute to the enthalpy of the fluid. The enthalpy h is known to be (in mechanical units) equal to $h = u + pv$, where u is the internal energy (capability of doing work by expansion) and $v = 1/g_o \rho$, so that pv is the familiar pressure term in Bernoulli's equation for incompressible fluids. The internal energy u is obviously the term by which a compressible fluid differs from an incompressible fluid.

(2) The enthalpy h and the internal energy u are related to the pressure and the specific volume (or density), so that Bernoulli's equation (2-20) establishes a definite relation between changes in

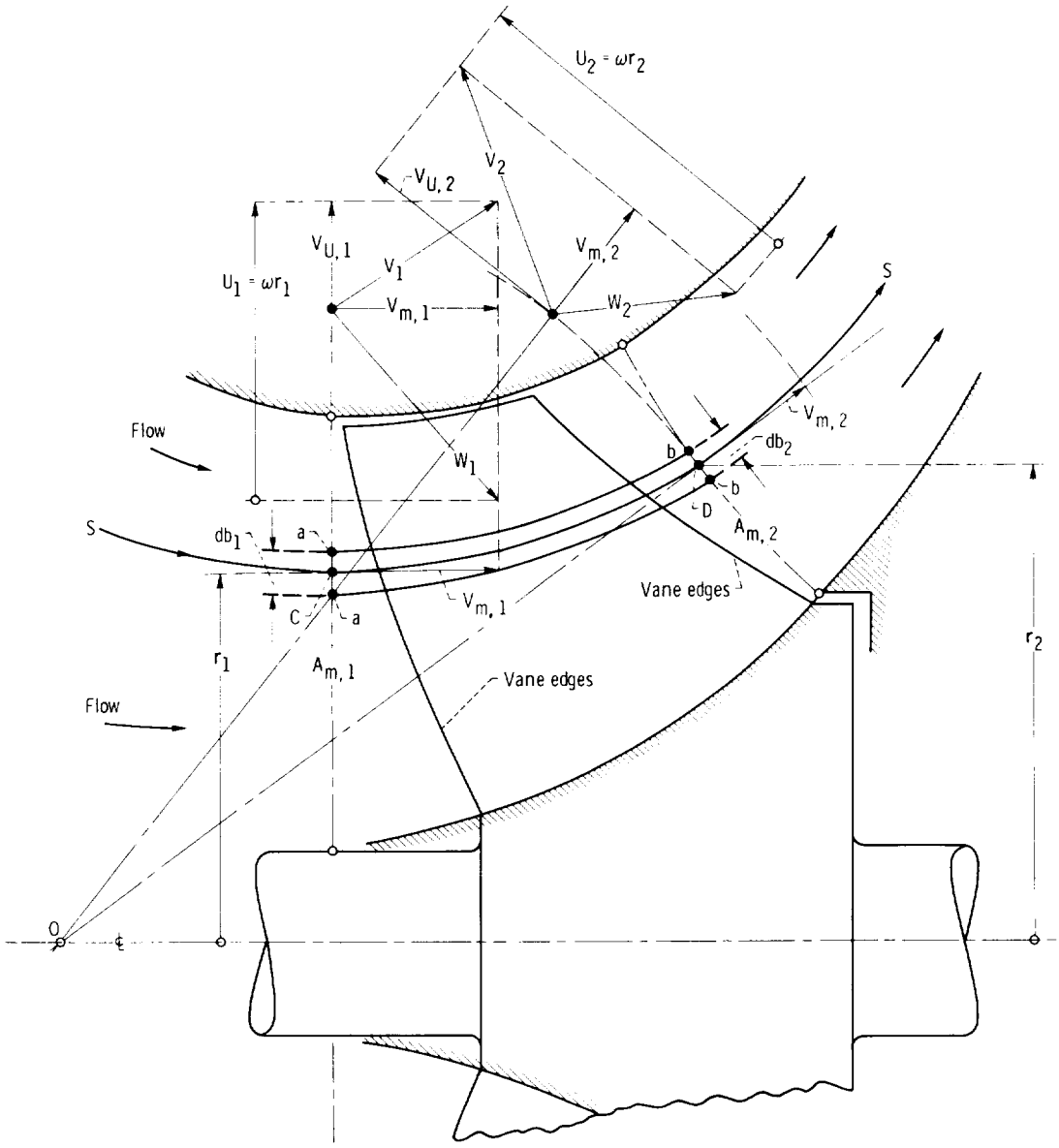

Figure 2-5. – Momentum change in turbomachine rotor.

the velocity V of the fluid and the corresponding changes in the properties of the fluid, in particular its volume v per unit weight.

If the zero points of the enthalpy and internal energy are placed fictitiously at zero absolute temperature ($T=0$), without considering any change in phase, the velocity obtained by (fictitious) expansion to zero pressure and temperature is

$$V_o = \sqrt{2gh_o} \tag{2-21}$$

which is a constant for any fixed value of the stagnation (zero velocity) enthalpy h_o. The properties of a compressible fluid may therefore be plotted in dimensionless form as a function of the dimensionless velocity V/V_o, as was done over 40 years ago by Busemann (refs. 4 and 5). Figure 2-6 shows various properties of air at temperatures below 700° R, where $\gamma = C_p/C_v$ and C_p are constant, so that by the definition of the zero point just given $h = C_pT$. Figure 2-7 presents an enlarged view of the specific volume ratio v/v_o as a function

C-2

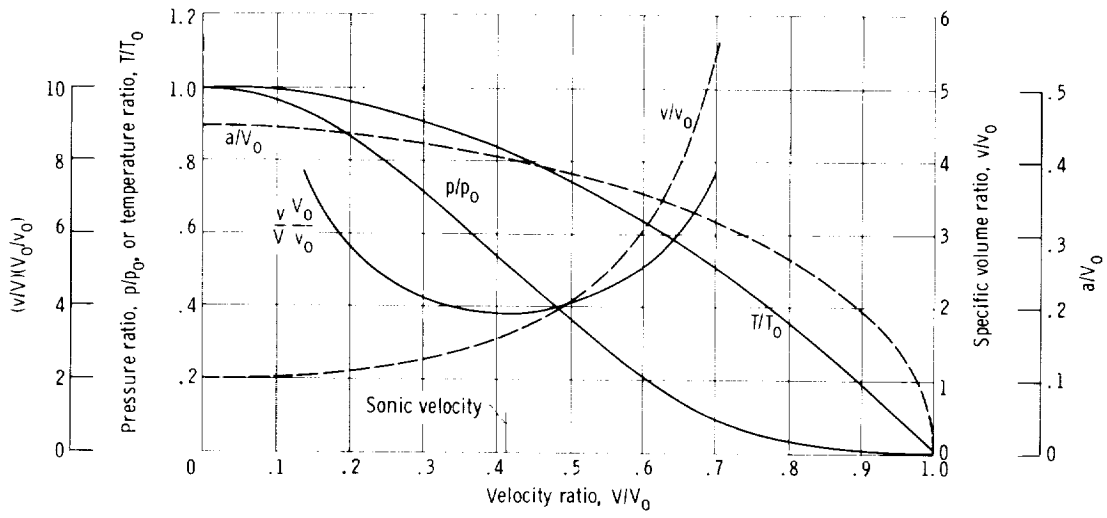

Figure 2-6. – Properties of air as functions of flow velocity. Subscript o refers to stagnation condition, and $V_o = \sqrt{2gh_o}$.

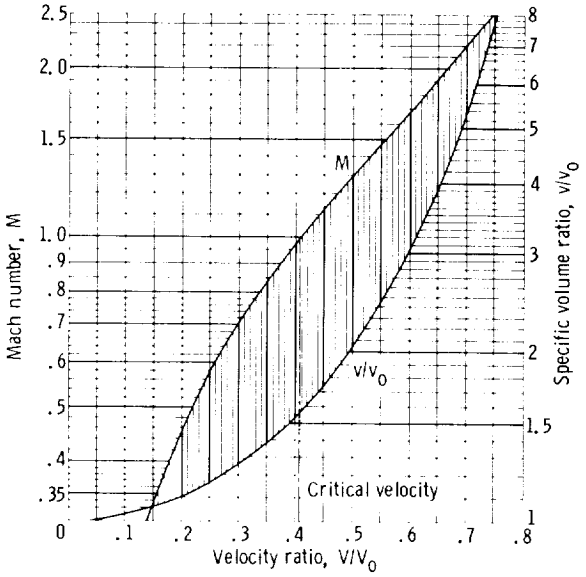

Figure 2-7. – Specific volume ratio of air as function of velocity and Mach number.

of V/V_o and also the familiar Mach number M. For any ideal gas, the velocity and property relations are

$$\frac{V}{V_o} = \sqrt{1 - \frac{h}{h_o}} = \sqrt{1 - \frac{T}{T_o}} \tag{2-22}$$

$$\frac{v}{v_o} = \left(\frac{T_o}{T}\right)^{1/(\gamma-1)} \tag{2-23}$$

$$\frac{p}{p_o} = \left(\frac{T}{T_o}\right)^{\gamma/(\gamma-1)} \tag{2-24}$$

and the acoustic velocity relation is

$$\frac{a}{V_o} = \sqrt{\frac{\gamma-1}{2}}\sqrt{\frac{T}{T_o}} \tag{2-25}$$

The subscript 0 refers to the $V=0$ or stagnation conditions, except in V_o, where it refers to equation (2-21). The product $(v/V)(V_o/v_o)$ is easily shown to be the cross-sectional ratio of the flow.

The critical velocity, defined as $V_{cr} = a$, is

$$V_{cr} = V_o\sqrt{\frac{\gamma-1}{\gamma+1}} \tag{2-26}$$

which is 0.4082 V_o for air, with $\gamma = 1.4$.

The relations used in deriving equations (2-22) to (2-26) are, of course, Bernoulli's equation (2-20) and the equation of state of an ideal gas

$$pv = RT \tag{2-27}$$

The gas constant R is equal to the difference between the specific heat at constant pressure C_p and the specific heat at constant volume C_v; that is, $R = C_p - C_v$.

Also used are the relations for isentropic changes:

$$pv^{\gamma} = \text{constant} \tag{2-28}$$

$$v^{(\gamma-1)}T = \text{constant} \tag{2-29}$$

$$\frac{T^{\gamma/(\gamma-1)}}{p} = \text{constant} \tag{2-30}$$

The plots shown in figures 2-6 and 2-7 can be drawn not only for ideal gases but also for other gases, for example, for air at high temperatures (where γ and C_p are not constant); of course, different operating conditions such as different initial temperatures or other initial properties will lead to different curves. In any event, at least an approximate relation between a dimensionless flow velocity and the specific volume ratio v/v_o is usually obtainable.

The stagnation enthalpy (h_o for $V=0$) is given by the inlet conditions to the machine and by the changes in stagnation enthalpy, which are equal to the rotor head H_r introduced in section 2.3 in connection with Euler's turbomachinery equation (2-18). If the properties of the gas are given as functions of its enthalpy (as, for example, by Keenan's well-known tables for air and steam) the stagnation conditions are known throughout the machine; from these, the properties of the flowing gas are also known as a function of dimensionless velocity in the form V/V_o or of Mach number. This means that, for a given mass or weight flow rate, the volume flow rate Q can be determined for any place in the machine with the same accuracy to which the fluid velocity is known or defined. For a given geometry of the machine this determination requires a process of iteration, since, for a given cross-section, the velocity V and volume flow rate Q are related by the condition of continuity in addition to the previously mentioned thermodynamic relation. Thus one must first estimate the specific volume v and the volume flow Q, then calculate the velocity V from the condition of continuity, then determine thermodynamically the previously estimated variables v and Q, and continue until consistent results are obtained. This process converges except near the critical flow conditions ($V=a$).

Less iteration is required for the solution of the indirect problem, that is, the design problem. In this case the velocity is usually prescribed by the head, the head coefficient, and the flow coefficient. The specific volume is then given by the foregoing considerations (for air at moderate temperatures by figs. 2-6 and 2-7). The specific volume v determines the volume flow rate for a given mass or weight flow rate. In this respect, the design can still be dimensionless, since, for the same velocity ratio V/V_o or the same Mach number, the rate of volume flow at any one cross section of the machine (say, inlet or discharge) still changes with the square of the linear dimensions. However, changes in the dimensionless velocities V/V_o (or in the Mach number) lead to changes in the required design form because of the resulting changes in the specific volume ratios. It should be evident that a change in velocities also changes the rotor head H_r and thereby the variations in enthalpy, specific volume, and volume flow rate from inlet to discharge of the machine. This result obviously requires a change in design form, which is merely a restatement of the well-known general fact that changes in the dimensionless velocities of a compressible fluid (changes in Mach numbers) lead to changes in the form of the flow and, therefore, to changes in aerodynamic design or changes in (dimensionless) performance characteristics, or both.

The effects of compressibility described previously cover primarily the one-dimensional aspects of this flow problem. This is sufficient for most practical considerations, particularly for the overall design form of the machine. However, the same approach also gives some qualitative information about the effects of compressibility on details of design, for example, vane systems.

Consider, for example, two-dimensional, plane flow pictures. With incompressible fluids the spacing between adjacent streamlines is inversely proportional to the local velocity simply for reasons of continuity of flow. This means, of course, that high-velocity regions, such as the region near a convex flow boundary, are characterized by relatively close spacing of the streamlines. Inversely the low-velocity region near a concave boundary has wider than average spacing between streamlines (see, e.g., fig. 2-8). It is easy to see that this must lead to a fairly rapid change in streamline curvature when moving away from the curved flow boundary into the interior of the flow field.

Compressibility reduces the effect of velocity differences in streamline spacing. While an increase in velocity primarily reduces this spacing, the accompanying increases in specific volume and in local volume flow rate tend to increase the streamline spacing. At the critical flow condition

($V=a$), these two tendencies just cancel each other and lead to approximately parallel streamlines with a corresponding extension of streamline curvature far into the flow field. This simple reasoning does not apply beyond critical flow into the supersonic regime, because the flow velocity is higher than the cross-stream propagation of flow deflections, so that the deflecting effects of curved flow boundaries are moved downstream.

The result of this consideration is that the deflecting effect of boundaries of given curvature is increased by the effect of compressibility with increasing velocity up to the critical or sonic flow velocity. Inversely, if a given flow deflection is desired, the curvatures of the boundaries should be decreased as the sonic velocity is approached from below; that is, for increasing subsonic velocities, deflecting vanes should become thinner and less curved than for incompressible flow.

For single airfoils in a widely extended stream, this reasoning is applied in an approximate, quantitative manner by the Prandtl-Glauert theory. This theory has not yet been applied to vane systems of turbomachines and is therefore not presented here. A principally one-dimensional solution of this problem for an axial-flow vane system is outlined in section 3.27 of chapter 3.

The supersonic flow through vane systems of turbomachines has been extensively explored both theoretically and experimentally. However, no theory of this flow except its one-dimensional approximation can be described as a simple extension or modification of the hydrodynamic theory of the flow of incompressible fluids, which is the principle of the present treatment of the flow of compressible fluids in turbomachines. Therefore only an approximate one-dimensional design method for subsonic and low supersonic flow in axial-flow vane systems is outlined in section 3.27. An example of high supersonic flow through an axial-flow vane system is given in section 2.5.6 by using the two-dimensional Prandtl-Meyer method of characteristics.

2.5 Theoretical Background of Hydrodynamic Design of Axial-Flow Turbomachinery

2.5.1 Introduction

The flow in axial-flow turbomachines has been treated extensively, primarily because of the importance of axial-flow compressors in the field of aircraft propulsion. A complete presentation of the theoretical and experimental principles of axial-flow compressors is given in reference 6 and in numerous NACA reports referenced herein. The reader is referred to this important group of references for a comprehensive study of this field. In accordance with the scheme stated in section 2.1, the presentation in this section pertains only to those theoretical principles and experimental data which have direct applications to the design of axial-flow vane systems.

Axial-flow vane systems are defined here as vane systems in which the flow can be assumed to proceed along cylindrical stream surfaces coaxial with the rotation and with the space of revolution confining the flow. Therefore the development of such a stream surface of a rotor has relative to the adjacent parts of the machine only a straight and uniform motion at the constant velocity U, that is, a nonaccelerated (translatory) motion in its own plane. Hence the flow relative to such a system is the same as the corresponding flow relative to a stationary system. For this reason, axial-flow vane systems are easier to treat theoretically than vane systems with a radial component of the meridional flow.

The simplest approach to the design, the one-dimensional approach, is also the oldest approach (for axial- as well as radial- or mixed-flow machines). It assumes that the entire flow along the meridional stream surfaces enters and leaves the vane system parallel to the respective vane ends. It is intuitively evident that this approach cannot be correct, because the mean flow between vanes is certainly less deflected than the flow in the immediate vicinity of the vanes. Figure 2-8 shows the development of a cylindrical section through an axial-flow vane system with the departures of the flow from the direction of the vanes. These departures are shown at approximately the correct magnitude and are considerable. The angular departures $\Delta\beta_1$ and $\Delta\beta_2$ are each approximately one-half of the angular deflection θ of the mean flow generated by the vane system, and the actual change of the circumferential flow component ΔV_U is less than three-fourths of the change $\Delta V_{U,v}$ which would result from the assumption that the entire flow leaves the system parallel to the discharge direction of the vanes. These departures of the mean flow from the direction of the vanes must be expected to increase with increasing vane spacing t, more exactly with decreasing solidity of the vane

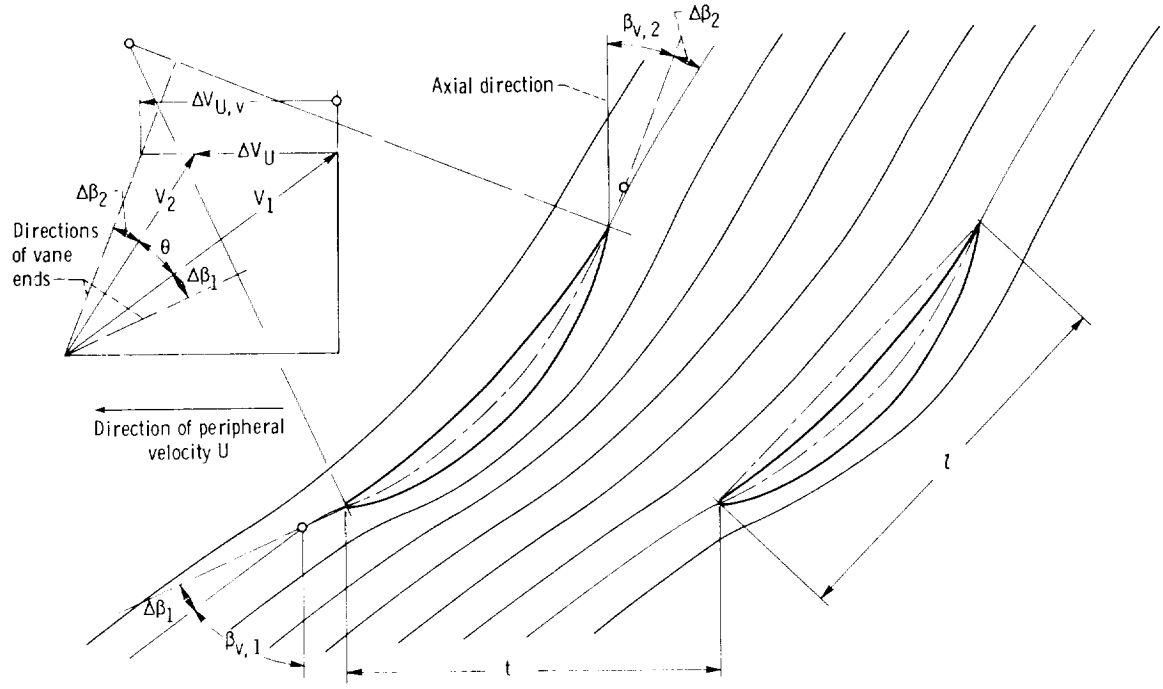

Figure 2-8. – Development of cylindrical section through axial-flow vane and streamline system.

system l/t. Since axial-flow vane systems sometimes have even lower solidities than that shown in figure 2-8, it can be concluded that a one-dimensional approach alone is not sufficient for vane systems of this type; the departures of the mean flow from the vane direction (particularly $\Delta\beta_2$) must be determined on some rational basis.

Departures from the one-dimensional theory obviously cannot be determined on the basis of strictly one-dimensional considerations, but require at least a two-dimensional approach. It is natural that the approach used in the aeronautical field for a single vane or airfoil in an infinitely extended stream was used first to solve this problem. Later it was found that this approach alone was not sufficient to treat the axial-flow turbomachinery problem except in cases of extremely low solidities, as in aircraft propellers. However, the principal concept used in solving the problem of a single airfoil in an infinitely extended stream, the concept of circulation, is applicable to all types of turbomachines and is indeed one of the most useful concepts of this field.

2.5.2 Airfoil Theory of Axial-Flow Turbomachinery

The term airfoil theory denotes the theory of turbomachinery which is based on the same concepts as the theory of a single airfoil in an infinitely extended flow field. The term is applicable irrespective of whether or not the flow sections through the vanes have airfoil shape. In fact, the best vane section forms developed during the last decades differ very markedly from conventional airfoil shapes. Yet the theoretical approach described in this section applies. This approach has little or nothing to do with the shape of the vane flow sections.

As mentioned in the last section, the principal concept of this theory is that circulation is a means of describing the deflection of a fluid stream by a vane or airfoil.

The usual definition of the circulation Γ is the contour integral of the velocity component V_s in the direction of a closed contour s about the deflecting body:

$$\Gamma = \oint V_s \, ds \tag{2-31}$$

The laws of fluid mechanics state that the circulation so defined is independent of the size and shape of the contour as long as the flow between the various contours compared is irrotational in the sense of equation (2-4) if applied to all velocity components.

The circulation thus describes a circulating fluid motion around the deflecting body, vane, or airfoil

with the understanding that this circulatory flow is only part of the total flow. Thus the existence of circulation does not mean that fluid particles actually travel on closed paths around the deflecting body.

The circulation is related to the force action between the deflecting body and the mean flow past the body by the law of Kutta and Joukowski:

$$F_l = \rho V_\infty \Gamma \tag{2-32}$$

where F_l is the force per unit span or unit distance normal to the plane of F_l and V_∞. The latter is the velocity of flow past the deflecting body at a sufficient distance to make the circulatory velocity V_s negligible compared with V_∞. The force F_l is normal to the velocity vector V_∞.

The law of Kutta and Joukowski can be derived with respect to the development of cylindrical sections through axial-flow vane systems. As can be seen from figure 2-9, the change in circumferential momentum per unit width (normal to the plane of flow) produces a circumferential force on the vane:

$$F_U = \rho w_a t (w_{U,1} - w_{U,2}) \tag{2-33}$$

The axial component of the force acting on the unit width of the vane is for the case of no change in axial momentum

$$F_a = t(p_2 - p_1) = t\frac{\rho}{2}(w_1^2 - w_2^2) \tag{2-34}$$

With $w_a = V_a = \text{constant}$, one finds

$$w_1^2 - w_2^2 = w_{U,1}^2 - w_{U,2}^2 = (w_{U,1} + w_{U,2})(w_{U,1} - w_{U,2}) \tag{2-35}$$

Hence,

$$F_a = t\frac{\rho}{2}(w_{U,1} + w_{U,2})(w_{U,1} - w_{U,2}) \tag{2-36}$$

and when equation (2-36) is divided by equation (2-33),

$$\frac{F_a}{F_U} = \frac{(w_{U,1} + w_{U,2})/2}{w_a} = \tan \beta_F \tag{2-37}$$

From figure 2-10, it is evident that $(w_{U,1} + w_{U,2})/2$ and w_a are the components of the vectorial mean

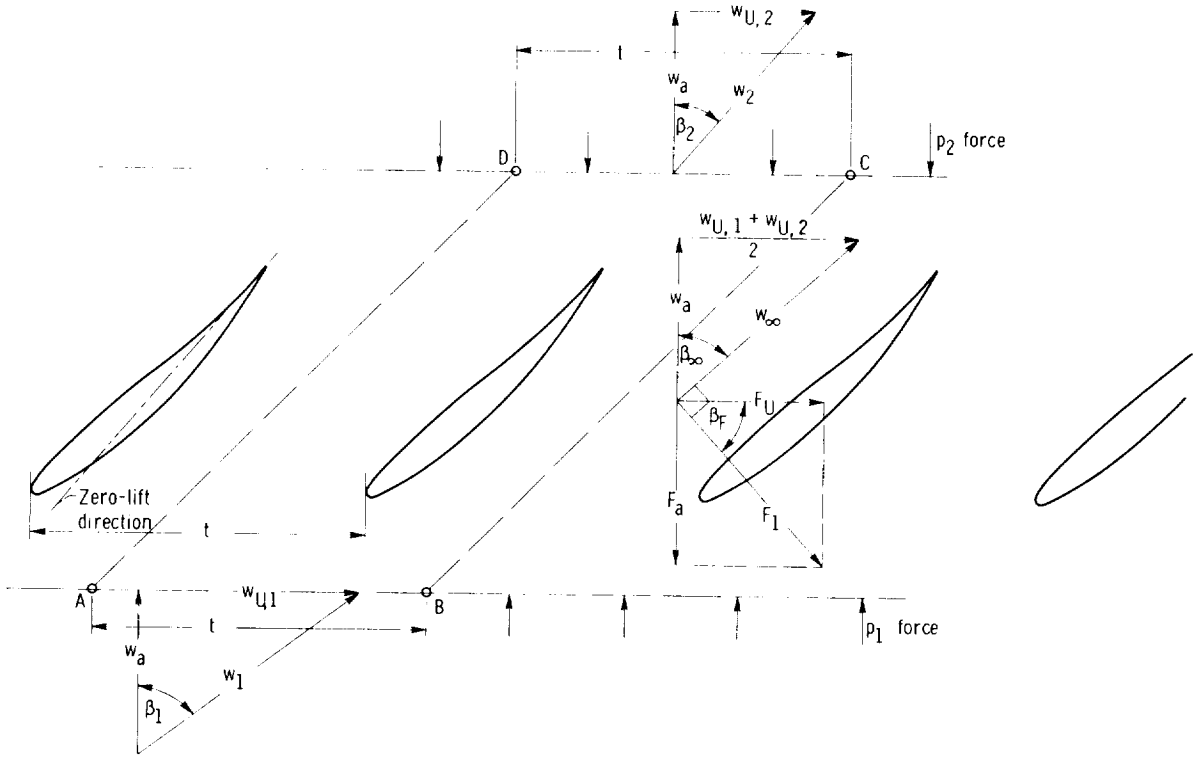

Figure 2-9. – Velocity and force vector diagrams in straight system of parallel vanes.

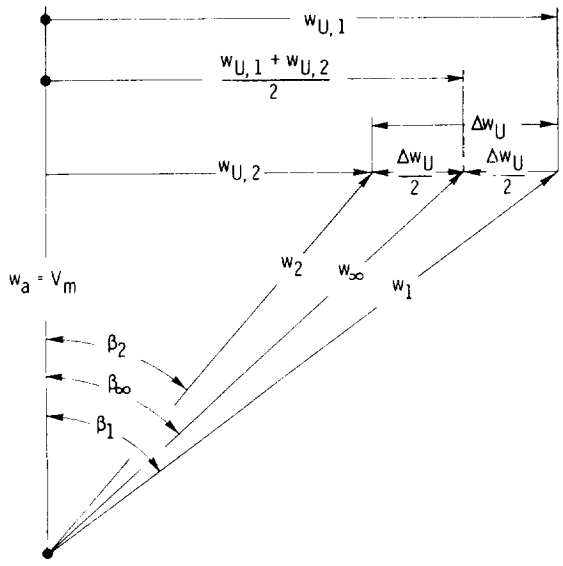

Figure 2-10. – Superposition of velocity vector diagrams for straight system of parallel vanes.

relative velocity of w_1 and w_2, which is designated w_∞ for reasons that become evident later. The angle of w_∞ with the axial direction is designated $\beta_\infty = \beta_F$, and equation (2-37) shows that the resultant vane force F, with components F_a and F_U, is normal to w_∞.

To determine the circulation Γ, one draws a contour of convenient form around one vane of the system. The parallelogram ABCD in figure 2-9 is such a contour if the sides AD and BC have the same location relative to the vanes and the sides AB and DC are far enough in front of and behind the vanes to consider the velocities along AB and DC as uniform.

The circulation about this contour is

$$\Gamma = \oint_{ABCD} w_s\, ds = \int_A^B w_s\, ds + \int_B^C w_s\, ds + \int_C^D w_s\, ds + \int_D^A w_s\, ds \qquad (2\text{-}38)$$

For periodically repeating, equal flow fields between the vanes,

$$\int_B^C w_s\, ds = -\int_D^A w_s\, ds \qquad (2\text{-}39)$$

Furthermore, for sufficient distance of AB and CD from the vanes,

$$\left.\begin{aligned} \int_A^B w_s\, ds &= w_{U,1} t \\ \int_C^D w_s\, ds &= -w_{U,2} t \end{aligned}\right\} \qquad (2\text{-}40)$$

By substituting equations (2-39) and (2-40) into equation (2-38), one obtains

$$\Gamma = (w_{U,1} - w_{U,2}) t \qquad (2\text{-}41)$$

Substituting this expression into equation (2-36) leads to the relation

$$F_a = \rho \frac{w_{U,1} + w_{U,2}}{2} \Gamma \qquad (2\text{-}42)$$

or into equation (2-33) leads to

$$F_U = \rho w_a \Gamma \qquad (2\text{-}43)$$

From figure 2-9, one can immediately read the geometric relations

$$\frac{(w_{U,1} + w_{U,2})/2}{w_\infty} = \sin \beta_\infty = \sin \beta_F = \frac{F_a}{F_1}$$

and

$$\frac{w_a}{w_\infty} = \cos \beta_\infty = \cos \beta_F = \frac{F_U}{F_1}$$

By these relations, either equation (2-42) or (2-43) can be converted into the equation

$$F_1 = \rho w_\infty \Gamma \qquad (2\text{-}44)$$

where the subscript 1 reminds one of the fact that all forces considered here apply to a unit width normal to the plane of flow.

Equation (2-44) has the very same form as the law by Kutta and Joukowski (see eq. (2-32)); this proves that the law applies to straight systems of parallel vanes provided the velocity appearing in the law is the vectorial mean of the velocity w_1 far in front of the system and the velocity w_2 far behind the system. Since, for an infinitely long, straight system of vanes, w_2 is generally not equal to w_1, there is not one velocity at infinity as for a single airfoil in an infinitely extended flow field. Therefore the velocity in the law by Kutta and Joukowski must be defined for an infinitely long, straight vane system, that is, the development of a cylindrical section

through an axial-flow system. The foregoing derivation provides this definition.

The velocity w_∞ in the law by Kutta and Joukowski is defined here only for the case where the axial velocity component $V_a = w_a$ is constant everywhere in front of, within, and behind the vane system. This assumption is generally not satisfied, but this writer does not know of any simple derivation of the law by Kutta and Joukowski for vane systems which does not use this assumption.

In this compendium the definition of w_∞ as the vectorial mean of w_1 and w_2 far in front of and far behind the vane system is used even in cases where the axial velocity component is known to change in the axial direction. This universal use of the foregoing definition of w_∞ is not likely to lead to serious errors as long as the components F_a and F_U of the blade force F_1 are determined by considerations that are independent of this definition, for example, if F_U is determined by Euler's turbomachinery momentum equation. In cases where F_a is of major importance (as in connection with propellers), considerations of the axial momentum far in front of and far behind the system lead to equally dependable results.

The foregoing considerations relate the forces on a straight system of parallel vanes (development of a cylindrical section through an axial-flow vane system) to the change of the flow through this system of vanes. This relation is quite similar to the principles of Euler's turbomachinery momentum equation (see sec. 2.3), but extends these considerations to include the concept of circulation, which is essential for the treatment of flow through vane systems where one-dimensional approximations are not sufficient.

Two steps are required to relate the foregoing considerations adequately to the design of turbomachinery:

(1) Properly relate the concept of circulation to the overall flow in the machine as controlled by the condition of continuity (see sec. 2.2), and more particularly by Euler's turbomachinery momentum equation (see sec. 2.3).

(2) Relate the vane circulation, that is, the deflection of the flow shown in figures 2-8 and 2-9, to the form of the vane sections appearing in the cylindrical sections through the system shown in these illustrations.

These steps are discussed next.

Consider a cylindrical section AB through an axial-flow rotor (fig. 2-11). The circulation around every vane profile appearing in this section is designated Γ_v. It is easy to show (see appendix 2-A) that the circulation about a contour containing several vanes with several circulations Γ_v is equal to the sum of all circulations contained within the outer contour. The total circulation of the developed section AB is, therefore,

$$\Gamma = N\Gamma_v \tag{2-45}$$

where N is the number of vanes.

The contour along which the total circulation Γ is measured consists of two coaxial circles A and B before and after the system and an arbitrary cut ab running more or less axially between two vanes. The axial distance d of the circles A and B from the system is large enough so that variations in the fluid velocities along these circles may be disregarded. The circulation about the developed section AB containing N vane profiles is

$$\Gamma = 2\pi r V_{U,2} + \int_b^a V_s\, ds - 2\pi r V_{U,1} + \int_a^b V_s\, ds \tag{2-46}$$

where the direction of integration, as given in figure 2-11, determines the signs of the terms $2\pi r V_{U,2}$ and $2\pi r V_{U,1}$. However,

$$\int_b^a V_s\, ds = -\int_a^b V_s\, ds$$

because these integrations are taken along two identical lines (namely, the cut) in opposite directions. Hence these integrals cancel out of equation (2-46), and we obtain

$$\Gamma = 2\pi r V_{U,2} - 2\pi r V_{U,1} \tag{2-47}$$

However, $rV_{U,2} - rV_{U,1}$ is the change in angular momentum of the flow through the system, on which the theory of hydrodynamic rotors is based (see sec. 2.3). This change in angular momentum, according to equations (2-46) and (2-47), is related to the vane circulation Γ_v by the equation

$$rV_{U,2} - rV_{U,1} = \frac{N\Gamma_v}{2\pi} \tag{2-48}$$

This relation was first established in this form by D. Thoma (ref. 7). He also pointed out that

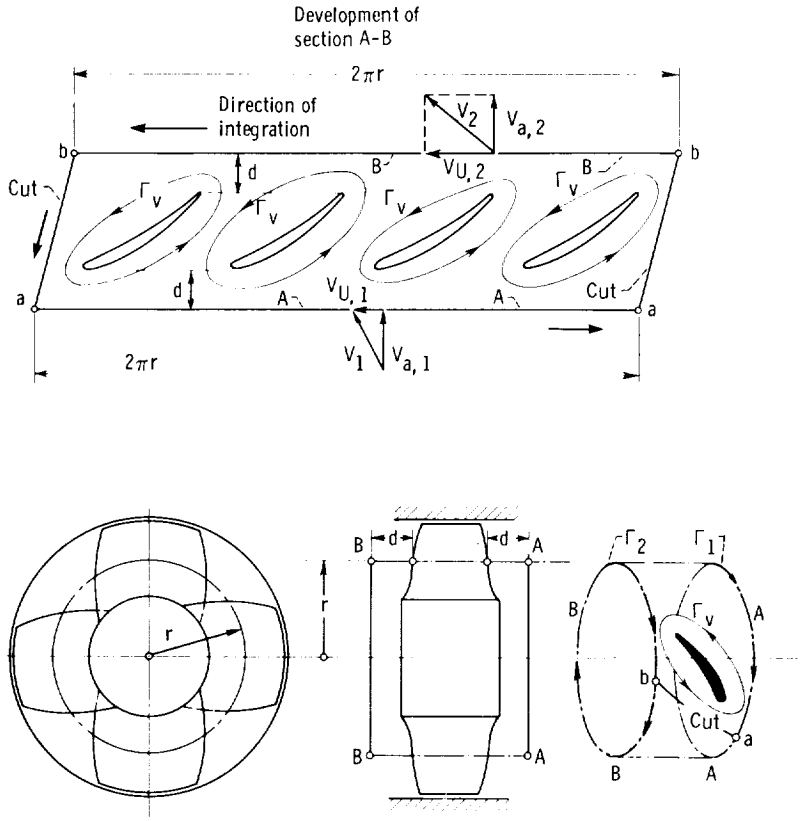

Figure 2-11. – Circulations of axial-flow rotor.

$$\left.\begin{aligned} 2\pi r V_{U,1} &= \Gamma_1 \\ \text{and} \\ 2\pi r V_{U,2} &= \Gamma_2 \end{aligned}\right\} \qquad (2\text{-}49)$$

where Γ_1 and Γ_2 are the circulations before and after the system measured along the circles A and B. By these equations, the vane circulation Γ_v measured in the cylindrical sections or generally in the stream surfaces of the meridional flow becomes related to the circulations before and after the vane system measured in sections normal to the axis of the machine. According to equations (2-48) and (2-49), this relation is simply

$$N\Gamma_v = \Gamma_2 - \Gamma_1 \qquad (2\text{-}50)$$

It indicates an increase in circulation in the direction of the flow ($\Gamma_2 > \Gamma_1$) for positive vane circulation Γ_v. This condition is satisfied for pump rotors. For turbine rotors, one may either consider Γ_v as negative or change the definitions so as to obtain equation (2-50) in the form

$$N\Gamma_v = \Gamma_1 - \Gamma_2$$

To relate the vane circulation Γ_v to the form of the vane section in the cylindrical stream surface, we return to consideration of the flow relative to the vane system. It should be recognized that the vane circulation Γ_v is the same for the relative and absolute flows through axial-flow rotors, because these two flows differ from each other by a uniform velocity U of that section. The difference in circulation between the relative and absolute flows is, therefore, the contour integral $\oint U_s\, ds$, which can be shown to be zero, since U is constant in magnitude and direction. The circulations Γ_1 and Γ_2 about the axis of the rotor differ between the absolute and relative flows by $2\pi r U = \text{constant}$. Therefore, their difference $\Gamma_2 - \Gamma_1 = N\Gamma_v$ is the same for the absolute and relative flows; this

agreement also proves the foregoing statement regarding the invariance of Γ_v.

The relation between the circulation Γ_v around a single vane and the vane shape is obtained by expressing the vane force per unit width first in terms of the lift coefficient $C_{L,\infty}$,

$$F_l = C_{L,\infty} \frac{\rho w_\infty^2}{2} l \tag{2-51}$$

and second by the law of Kutta and Joukowski, as expressed by equation (2-44) in the form

$$F_l = \rho w_\infty \Gamma_v$$

Equating these two expressions of the vane force F_l leads to

$$\rho w_\infty \Gamma_v = C_{L,\infty} \frac{\rho w_\infty^2}{2} l$$

and thereby

$$C_{L,\infty} = 2 \frac{\Gamma_v}{w_\infty l} \tag{2-52}$$

From equations (2-49) and (2-50), it follows immediately that

$$\Gamma_v = \frac{2\pi r}{N} (V_{U,2} - V_{U,1}) = t\, \Delta V_U \tag{2-53}$$

where $2\pi r/N$ is obviously the circumferential vane spacing t, and the change in the peripheral component of the flow $V_{U,2} - V_{U,1}$ is denoted by $\Delta V_U = -\Delta w_U$. By substituting equation (2-53) into equation (2-52), one finds

$$C_{L,\infty} = 2 \frac{\Delta V_U}{w_\infty} \frac{t}{l} \tag{2-54}$$

The lift coefficient is related to the shape and position of the vane by the angle of attack α. This relation is particularly simple if the angle of attack is measured from the zero-lift direction as shown in figure 2-12. Then, the lift coefficient of an airfoil in an infinitely extended stream is closely approximated by

$$C_{L,\infty} = 2\pi \sin \alpha_o \tag{2-55}$$

where for real fluids the lift coefficient has a limited maximum value of about 1.5. For higher angles of attack (higher than approximately 14°), the lift force does not increase with increasing α_o and often falls off slowly and irregularly. This so-called stall limit of a vane or airfoil may be much lower than $C_L = 1.5$ for unfavorable airfoil shapes and can be somewhat higher than $C_L = 1.5$ for exceptionally favorable configurations. The stall limits of the vanes of turbomachines may differ appreciably from $C_L = 1.5$; they are discussed in some detail in section 2.5.4.

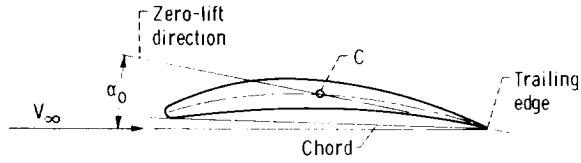

Figure 2-12. – Angle of attack referred to zero-lift direction.

The zero-lift direction in relation to the vane shape can be approximated by a line through point C and the trailing edge (see fig. 2-12), point C being located along the mean camber line about halfway between the leading and trailing edges. This is only a first approximation for an airfoil in an infinitely extended stream. For a closer approximation, see section 2.5.5, particularly figure 2-28.

Generally there is no assurance that vanes in a turbomachine, or any other system of several vanes, follow the same law (eq. (2-55)) as a single airfoil in an infinitely extended stream. Therefore equation (2-55) is used here for turbomachinery vanes in a slightly modified form:

$$C_{L,\infty} = 2\pi K \sin \alpha_o \tag{2-56}$$

where K is a correction factor intended to account for the effect of the arrangement of a vane in a system of vanes rather than in an infinitely extended flow field.

With equation (2-54) relating the lift coefficient to the change in the peripheral component of the flow and to the solidity of the vane system and with equation (2-56) relating the lift coefficient to the angle of attack with the zero-lift direction of the vanes, the desired connection between the flow and the most essential geometric characteristics of the vane system is established. (Note the relation between vane shape and the zero-lift direction stated previously and illustrated in fig. 2-12.) The most important uncertainty in this chain of relations is the correction factor K in equation (2-56). The fact that departures of this factor from

unity are essential to avoid contradictions can be demonstrated by the following reasoning:

Equation (2-54) indicates that for a fixed value of $C_{L,\infty}$ the deflection of the flow expressed by ΔV_U approaches infinity (if w_∞ remains finite) as the vane spacing t approaches zero. However, the approach to $t=0$ is obviously an approach to one-dimensional flow conditions. Certainly ΔV_U approaching infinity cannot be in agreement with the one-dimensional theory for fixed inlet flow conditions. To avoid this conflict, one must assume that $C_{L,\infty}$ and therefore (according to eq. (2-56)) the correction factor K are functions of the solidity of the system l/t and approach zero as t/l approaches zero. Thus one must investigate the one-dimensional approximation of K for the limiting case $t/l \to 0$.

Equations (2-55) and (2-56) imply that for the flow of a frictionless fluid one has replaced the curved vanes of the system by infinitely thin, straight-line vanes set at the zero-lift direction of the curved vanes. Therefore, as t/l approaches zero, the discharge velocity w_2 must approach its one-dimensional limit, the direction of the vane, which in this case is the zero-lift direction. Figure 2-13 shows this limiting velocity diagram. (See also fig. 2-9 for the relation between the zero-lift direction and the vane in a system.)

Equating the expressions for $C_{L,\infty}$ given by equations (2-54) and (2-56), one finds

$$\frac{\Delta V_U}{w_\infty}\frac{t}{l} = \pi K \sin \alpha_o$$

or

$$K = \frac{\Delta V_U}{\pi w_\infty \sin \alpha_o}\frac{t}{l} \tag{2-57}$$

From figure 2-13, one can read

$$w_\infty \sin \alpha_o = \frac{\Delta V_U}{2} \cos \beta_v$$

Substituting this into equation (2-57) (for t/l approaching 0) leads to

$$K = \frac{2}{\pi \cos \beta_v}\frac{t}{l} \tag{2-58}$$

Figure 2-14 shows this one-dimensional approximation of K as a function of t/l with β_v as a parameter.

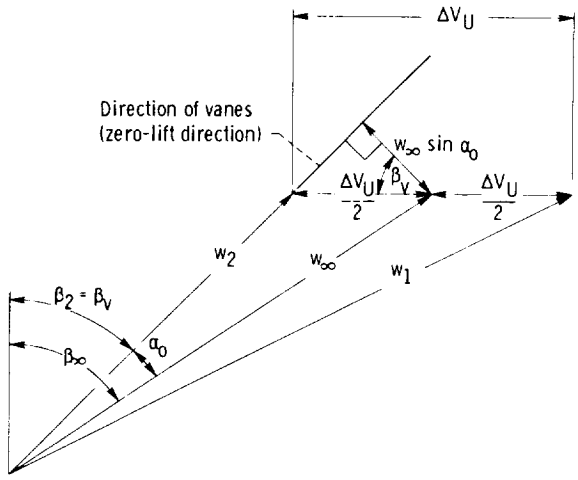

Figure 2-13. – Velocity diagram of straight system of straight, frictionless vanes for limit $t/l \to 0$.

On the other hand, it should be clear from equations (2-55) and (2-56) that for very large values of t/l the factor K must approach unity (i.e., the value which applies to a single vane in an infinitely extended flow field). The foregoing considerations and figure 2-14, therefore, give the tangents at $t/l=0$ and $t/l=\infty$ for the curves describing the variations of K as a function of t/l and of β_v.

It is plausible and can be proven that, under the well-known Kutta condition of smooth flow at the trailing edge, the deflection of the flow by the vanes can never be greater than that prescribed by the one-dimensional approximation. This means that the inclined K lines describing the one-dimensional

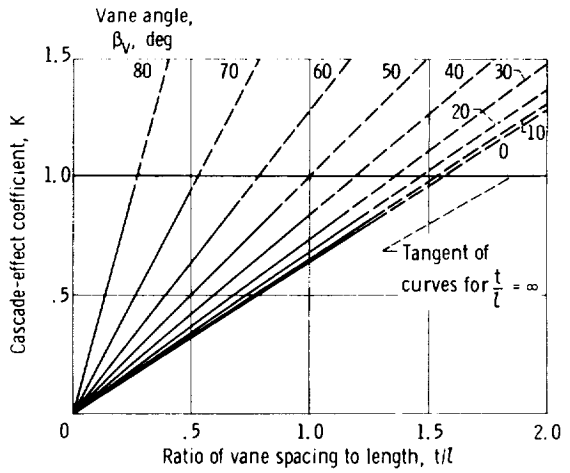

Figure 2-14. – One-dimensional approximation of cascade-effect coefficient K for $t/l \to 0$ and $t/l \to \infty$.

values of K are upper limit lines of K for the given values of the vane angle β_v (the angle between the zero-lift direction and the axial direction). This statement is, of course, only true for a straight system of straight and parallel vanes. For curved vanes, the discharging flow would, in the limit $t/l = 0$, be tangent to the trailing edge of the curved camber line of the vanes. This limiting condition could be obtained by using the angle $\beta_{v,2}$ of the discharge vane end in equation (2-58) in place of the angle β_v of the zero-lift direction. However, since this solution could be a useful approximation only in the immediate vicinity of $t/l = 0$, it is not of significant practical value. (In sec. 2.5.3 the straight lines in fig. 2-14, which represent eq. (2-58), are shown to be fair approximations of the actual K curves for a restricted but practically significant range.)

Since K can never be greater than prescribed by equation (2-58) and by the corresponding inclined lines in figure 2-14, the actual curves of K plotted against t/l must approach these inclined lines from below as t/l approaches zero. On the other end of the diagram, the actual K curves approach $K = 1$ as t/l approaches infinity. This approach may be from above or from below, since K, because of the interaction between adjacent vanes in the system, might be larger or smaller than 1.

Whereas this description restricts severely and constructively the curves of K against t/l, it does not exclude major variations in K curves that might be constructed within the bounds set by its limiting value for $t/l \to 0$ and $t/l \to \infty$. A rational, mathematical analysis of this situation is, therefore, urgently needed. The results of such an analysis are presented in the next section, together with a summary of the design theory resulting from this analysis in connection with the foregoing considerations.

2.5.3 Results and Application of Theoretical Analysis by Weinig of Straight Systems of Straight and Parallel Vanes

The theoretical approach presented in the previous section is in a somewhat indefinite state, because the relation between the correction factor K and the most essential parameters of an axial-flow vane system (as seen in the development of any cylindrical flow section) is not definitely established.

Recall that K corrects the relation between the lift coefficient and the configuration of a deflecting vane from a single vane in an infinitely extended stream ($K = 1$, eq. (2-55)) to the corresponding relation for a vane as part of an infinitely long, straight system of parallel vanes (eq. 2-56)). Replacing every curved vane section in this developed system of vanes by a straight line having the zero-lift direction of the curved vanes, one arrives at the previously mentioned straight system of straight and parallel vanes shown in figure 2-15. The vane shape shown in dotted lines might be a physical interpretation of this diagram, but it is not included in the following considerations.

This infinitely long system of straight vanes can be treated by the theory of incompressible, invicid flow in a reasonably simple and straightforward manner. This was done by F. Weinig (ref. 8). His derivation is not presented here, but his results applying the flow through straight systems of parallel vanes are quoted and represented in graphical form.

From the preceding section, it is evident that the most important result of an analysis such as Weinig's would be the exact determination of the cascade-effect coefficient K, defined previously by equation (2-56). Weinig's results, which can be regarded as exact for the flow of an invicid fluid through a system or cascade of straight vanes (fig. 2-15), are presented in figure 2-16. Although this diagram does not show zero regions of both coordinates, one can estimate that all its curves converge to $K = 0$ at $t/l = 0$. Furthermore all curves appear to approach $K = 1$ asymptotically as t/l increases. These were the conditions for the curves of K against t/l derived in the previous section for $t/l \to 0$ and $t/l \to \infty$.

A more accurate comparison between Weinig's exact curves and the approximations (or limiting conditions) derived in the previous section is presented in figure 2-17 for $\beta_v = 70°$ and $\beta_v = 20°$, that is, for a very substantial inclination of the vanes against the axial direction (normal to the

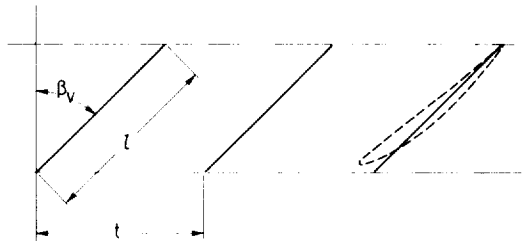

Figure 2-15. – Straight system of straight and parallel vanes.

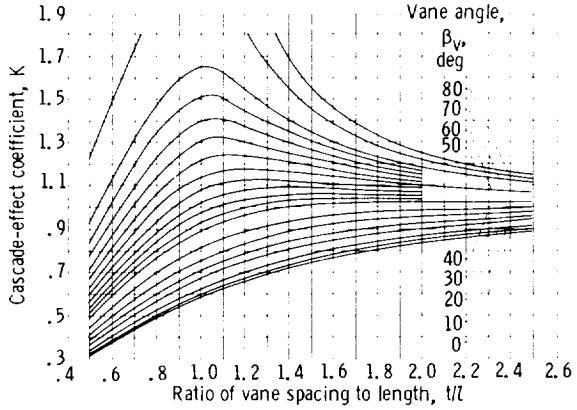

Figure 2-16. – Cascade-effect coefficient for straight systems of straight and parallel vanes (from Weinig, ref. 8).

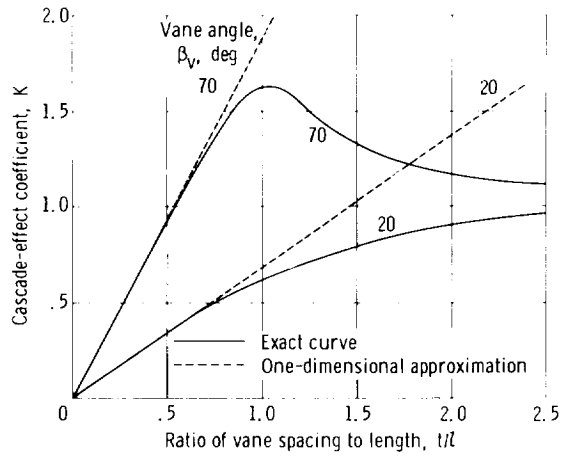

Figure 2-17. – Exact cascade-effect curves and approximations.

system) and for a small deviation of the vanes from the axial direction. In addition to the previously mentioned general agreement between the theoretically derived curves and the straight-line approximation, it is now apparent that the one-dimensional approximations are indeed upper-limit lines for K as the theoretical curves approach the one-dimensional limit lines from below with diminishing values of t/l. The general agreement between the theoretical curves and their asymptotes for $t/l=0$ and $t/l=\infty$ derived by independent considerations is, therefore, a reassuring confirmation of Weinig's results and the reasoning presented in the preceding section.

Figure 2-17 suggests a comparison between the theoretical solution by Weinig and the one-dimensional solution, which assumes that the flow leaves the vane system parallel to its straight vanes. This comparison is presented in figure 2-18 in terms of the head coefficient $C_H=\Delta V_U/\Delta V_U^*$, where ΔV_U^* is a fictitious change in the circumferential velocity component corresponding to the one-dimensional assumption that the entire flow leaves the vane system exactly in the direction of its (straight) vanes. Figure 2-19, the velocity diagram of the system, defines ΔV_U and ΔV_U^*.

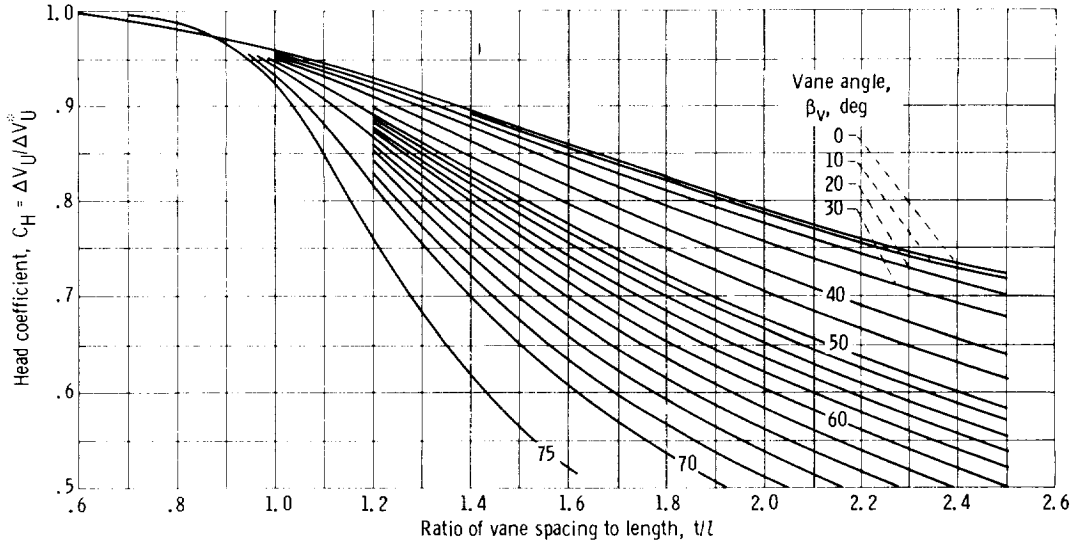

Figure 2-18. – Head coefficient, ratio of deflection of perfect flow ΔV_U to one-dimensional approximation ΔV_U^*, for straight system of straight, parallel vanes.

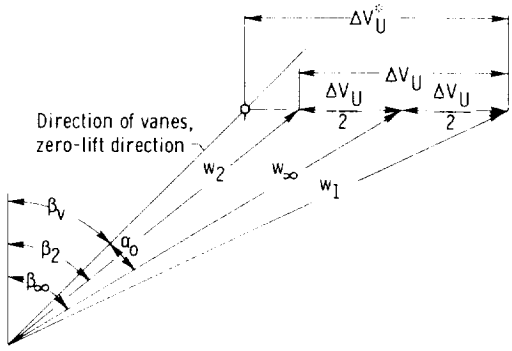

Figure 2-19. – Velocity diagram of straight system of parallel vanes compared with zero-lift direction.

Figure 2-18 indicates that the departure of the flow from its one-dimensional direction is negligibly small for $t/l<0.7$. This departure (in terms of $\Delta V_U/\Delta V_U^*$) is about 4 to 7 percent at $t/l=1$ and increases rapidly for $t/l>1$ (i.e., as the circumferential vane spacing exceeds the vane length).

The curves in figures 2-16 and 2-18 can also be used for curved vanes with small but finite thickness if the vane angle β_v is interpreted as the angle between the zero-lift direction and the axial direction. While these curves thereby lose their rigorous meaning with respect to the flow of a perfect fluid, at the same time they gain practical meaning with respect to the flow of real fluids through straight systems of moderately curved and fairly thin vanes. This meaning of the Weinig curves in figures 2-16 and 2-18 is further explored in section 2.5.5 by comparison with cascade test results.

2.5.4 Limitations of Flow in Vane Systems of Turbomachinery

The limitations of the flow in the vane systems of turbomachines are treated in this section. However, since the principles of such limitations are the same in all types of turbomachinery vane systems, the application of the principles presented here is not limited to axial-flow vane systems.

The flow in turbomachinery (and, in fact, in many other systems) is limited by three independent flow phenomena:

(1) With respect to liquids, by cavitation
(2) With respect to gases, by compressibility effects
(3) With respect to all real fluids, by separation or stall

The first two items are treated also in other sections of this compendium and are therefore only briefly discussed here. The third item is introduced in this section and is therefore fully discussed as far as is justified with respect to the design of turbomachinery.

2.5.4.1 Limitation by cavitation. – Limitation of flow by cavitation is discussed in section 1.2.2 on the basis of similarity considerations. The relation of this limit to design parameters of the machine is summarized in figure 1-18. Besides the flow coefficient $V_{m,i}/U_i$ and the important suction head coefficient $2g_oH_{sv}/V_{m,i}^2$, this diagram also relates the suction specific speed to the vane pressure reduction coefficient (eq. (1-37) expressed in terms of the relative velocity)

$$\sigma_p=\frac{p_i-p_v}{\rho w_i^2/2}$$

which appears in the important equation

$$H_{sv}=C_1\frac{V_i^2}{2g_o}+\sigma_p\frac{w_i^2}{2g_o} \qquad (1\text{-}42)$$

According to figures 1-7 and 1-20, the subscript i refers to the maximum diameter D_i of the rotor opening at the low-pressure side of the rotor and is, therefore, equivalent for pumps to the subscript 1 as used in the foregoing sections with respect to the development of a cylindrical section through the vane system, when this section is taken at the diameter D_i.

Figure 1-18 indicates that the blade pressure reduction coefficient $C_{p,min}=\sigma_p$ should not exceed 0.25 in order to achieve a commercially acceptable value of the suction specific speed S. Much lower values of σ_p are required to reach the S values in the vicinity of unity or higher which are demanded in the rocket or condensate pump fields. It is, therefore, prudent to examine the relation of the pressure reduction coefficient $C_{p,min}=\sigma_p$ to other characteristics of the vane system.

Figure 2-20 shows a typical pressure distribution over the vane of an axial-flow pump rotor. The mean static pressure in the flow approaching the rotor is designated p_1. With this notation, the coefficient of the minimum vane pressure is obtained by expressing equation (1-37) in terms of the relative velocity w_1 and the minimum pressure $p_{min}=p_v$ (vapor pressure):

$$\sigma_p=C_{p,min}=\frac{p_1-p_{min}}{\rho w_1^2/2}$$

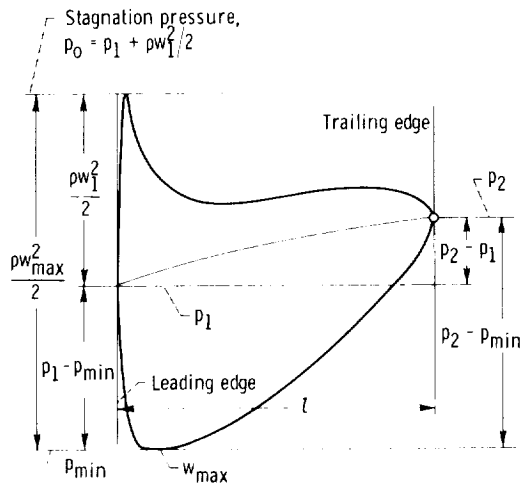

Figure 2-20. – Vane pressure distribution in pump.

It is plausible to compare the pressure reduction $p_1 - p_{min}$ with the average vane pressure difference Δp_{av}. The definition of the lift coefficient of the vane leads to the relation

$$C_{L,\infty} = \frac{\Delta p_{av}}{\rho w_\infty^2/2} \tag{2-59}$$

The lift coefficient could also be referred to the relative inlet velocity w_1 instead of the (vectorial) mean relative velocity w_∞, to arrive at another lift coefficient:

$$C_{L,1} = \frac{\Delta p_{av}}{\rho w_1^2/2} = C_{L,\infty} \frac{w_\infty^2}{w_1^2} \tag{2-60}$$

The comparison between the vane pressure reduction and the average vane pressure difference now assumes the form

$$\frac{p_1 - p_{min}}{\Delta p_{av}} = \frac{C_{p,min}}{C_{L,1}} = \frac{\sigma_p}{C_{L,1}} = q \tag{2-61}$$

Figure 2-20 suggests that the pressure ratio q may not be too far from unity, which would mean that the rectangular area $(p_1 - p_{min})l$ is not too far from the area inside the vane pressure curve. Thus $C_{L,1}$ cannot be much greater than $C_{p,min}$ previously found to be limited to values below 0.25 if good cavitation performance is required. However, since $w_\infty < w_1$ for retarding (pump) vane systems, equation (2-60) shows that $C_{L,\infty} > C_{L,1}$, that is, that the resulting limitation of $C_{L,\infty}$ is not quite as severe as the limitation of $C_{L,1}$. Nevertheless it is evident that cavitation limits the lift coefficient $C_{L,\infty}$, which is then likely to be considerably lower than unity (i.e., lower than the stall limit of the lift coefficient of a single airfoil in an infinitely extended stream, which, as stated in sec. 2.5.2, is about 1.5). While it is shown in section 2.5.4.3 that the limits of lift coefficient for retarding vane systems are lower than those for a single vane in an infinitely extended flow field (because of this retardation), it nevertheless must be concluded that cavitation alone places an additional limitation on the lift coefficient of axial-flow vane systems. Equation (2-54) shows that this limitation leads, for given deflections $\Delta V_U/w_\infty$ to low values of t/l (i.e., to higher solidities of axial-flow vane systems than would be used without the need for good cavitation performance). While this conclusion may impress us today as obvious, it is a historic fact that, in the early years of axial-flow turbomachinery development, this conclusion was often not recognized, and the result was very unsatisfactory cavitation performance.

Also apparent from figure 1-18 are other theoretical conclusions, in particular, the fact that, for any suction specific speed, there is one optimum flow coefficient $V_{m,i}/U_i$. Furthermore there is a possible flow regime in the field of fully developed cavitation, as shown in figure 2-21. This rotor flow problem can probably be approximated in any one stream surface by one-dimensional reasoning. A two-dimensional, theoretical solution is given in reference 9. Significant are the three-dimensional flow problems in a space of revolution (the liquid moves radially outward, while the gas accumulates in the center) and the flow problems of the stationary passages after the rotor (which alternately receive liquid and gas flow). Figure 2-22 shows an estimate of the three-dimensional flow through an impulse rotor with fully developed cavitation.

2.5.4.2 Limitation by compressibility effects. – In the beginning of the development of axial-flow compressors, there was reason to believe that the velocity of sound was an upper limit of the relative velocity approaching an axial-flow vane system. This belief was founded to a large extent on the fact that cascade tunnel test results showed a rapid deterioration of the cascade flow characteristics before the tunnel velocity in front of the vane system reached its critical or sonic value. Apparently the tunnel flow was choking under these conditions.

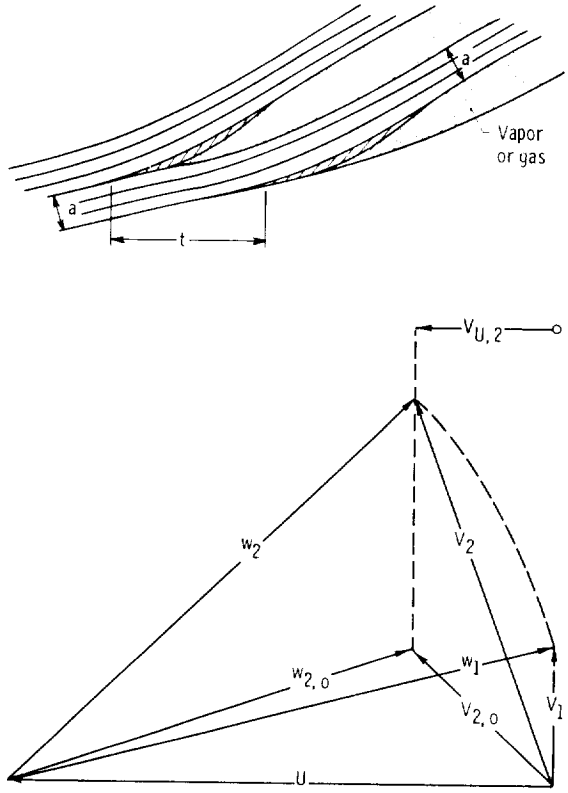

Figure 2-21. – Axial-flow vane action with fully developed cavitation.

The foregoing test results were misleading. Rotors with sonic and supersonic relative inlet flow have been operated successfully. The explanation used by this writer was that the rotor flow (or any flow in an annular cascade) is circumferentially infinite. Therefore the actual flow w_∞ or V_∞ with a substantial angle against the axial direction has a freedom of adjustment by changing its (subsonic) axial component. The principles outlined in section 2.4 are sufficient to explain this process on a quasi-one-dimensional basis sufficiently to avoid any major contradictions.

The flow of compressible fluids along cylindrical sections through axial-flow vane systems is outlined in section 2.5.6.

At present, it appears that the flow through axial-flow (and other) vane systems of turbomachinery is not limited by compressibility effects in any absolute manner. Problems of convergence of numerical or graphical solutions are likely to exist when the meridional component of the flow reaches the sonic velocity, but there is no reason why these problems cannot be overcome. It must be remembered that De Laval used high supersonic flow in axial-flow impulse-turbine vane systems as early as the turn of this century.

While there does not appear to exist any absolute limit of velocities or Mach numbers due to compressibility effects, there is a reason why supersonic flow in vane systems (or any closed passages) may lead to losses in efficiency. Supersonic flow in closed passages has a tendency to change to subsonic flow by a normal shock (or perhaps several oblique shocks). This abrupt reduction in velocity by a compression shock is connected with an increase in entropy, which constitutes a loss in the usual sense of efficiency. Flow at high supersonic velocities, therefore, cannot be accepted without some reservations regarding efficiency.

2.5.4.3 Limitation by separation or stall. – Separation or stall is a phenomenon occurring almost independently of the nature of the fluid except for its dependence on the Reynolds number (the ratio of inertial forces to viscosity forces).

The phenomenon of separation or stall is described very briefly in the later parts of section 2.5.2 in connection with the limits of the lift coefficient C_L and the angle of attack α_o on airfoils. Beyond certain angles of attack the lift does not increase with increasing angle of attack, but either remains constant or falls off in an irregular fashion, in contrast to the regular behavior indicated by equation (2-55). The reason for this phenomenon is the fact that at increasing angles of attack the pressure difference between the minimum pressure and the free-stream pressure near the trailing edge increases for constant free-stream velocity. As a consequence, the boundary layer of the flow cannot negotiate this pressure rise; it breaks away from the wall of the deflecting vane and forms a fairly wide region filled with fluid in irregular motion (see fig. 2-23).

There are at least three reasons why the stall phenomenon in axial-flow vane systems is likely to be different from that on a single vane in an infinitely extended stream:

(1) The vane boundary layers in axial-flow vane systems are not plane and two-dimensional, as a single vane in an infinitely extended stream, but are skewed and subject to crosswise flow, called secondary motions (discussed in sec. 2.5.7). No quantitative predictions of the effect of secondary motions on stall have yet been made, and only a qualitative description of one particular effect of such motions on stall can be suggested; it is given in section 2.5.7.

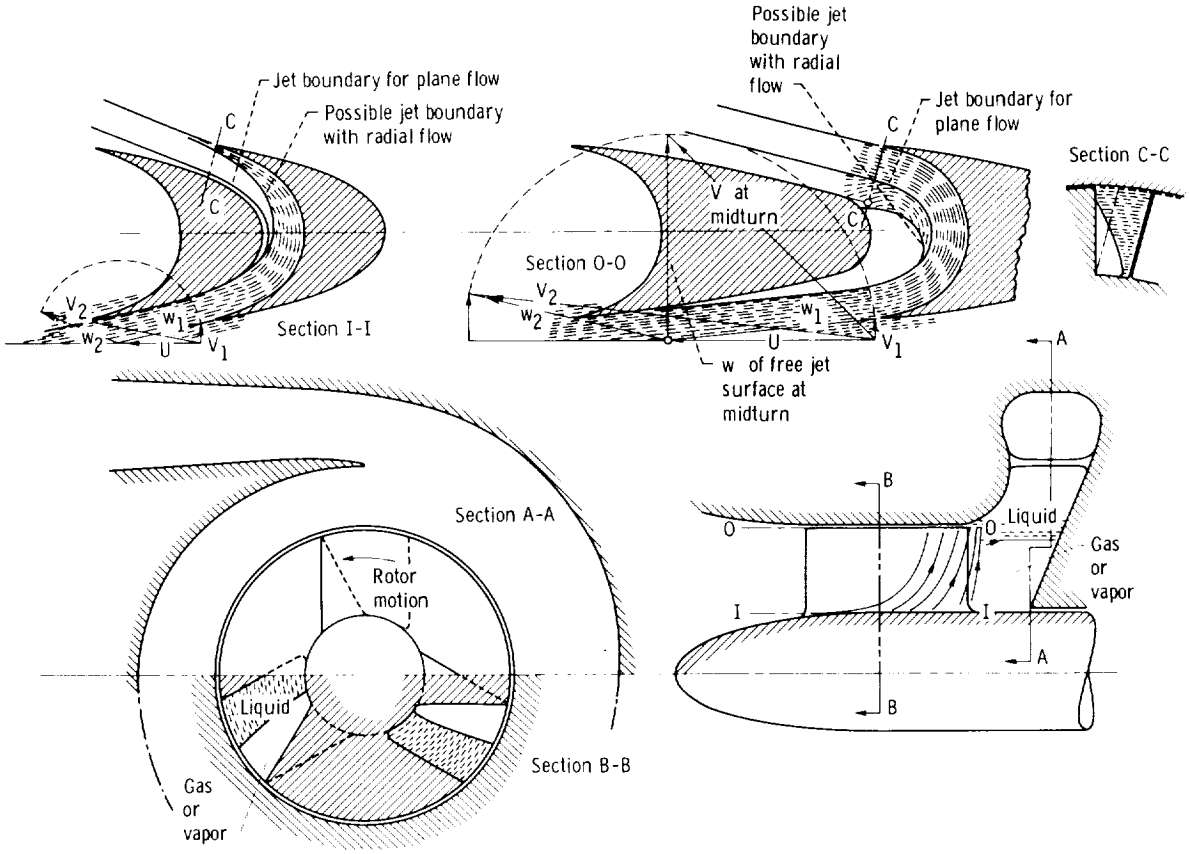

Figure 2-22. – Estimate of three-dimensional flow in impulse pump rotor with fully developed cavitation.

(2) In vane systems, the separation region shown in figure 2-23 is limited in width by the pressure face of the following vane. This may limit the hydrodynamic effect of stall in vane systems. Reference 9 describes the earliest attempt known to this writer to approximate this limitation by theoretical means. Applications of this theory are so far limited to flow with fully developed cavitation, mentioned in section 2.5.4.1.

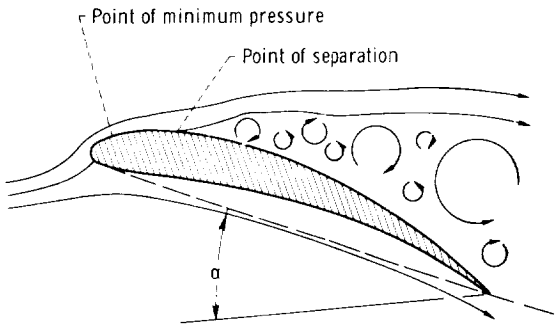

Figure 2-23. – Separation or stall on flow-deflecting vane.

(3) There is a difference in stall characteristics between a single vane and a vane in a system if there is a change in static pressure through the system. This difference can be approximated theoretically and by generalizations of test results in a manner that is sufficiently simple to permit application to the early phases of the design process of axial-flow vane systems. Separation or stall is caused by an excessive pressure rise along a solid flow boundary. The pressure rise that may lead to separation on any vane within the vane system of a turbomachine is the value $p_2 - p_{min}$, shown in figure 2-20, that exists just before the onset of separation. The effect of the general system configuration on this pressure rise is shown in figure 2-24, in particular its dependence on p_2/p_1 and w_2/w_1. The kinetic energy available to climb the pressure hill $p_2 - p_{min}$ is evidently that which exists at the point of minimum pressure and maximum relative velocity $\rho w_{max}^2/2 = p_o - p_{min}$. Thus the equation

$$K_A = \frac{p_2 - p_{min}}{\rho w_{max}^2/2} = \frac{p_2 - p_{min}}{p_o - p_{min}} \qquad (2\text{-}62)$$

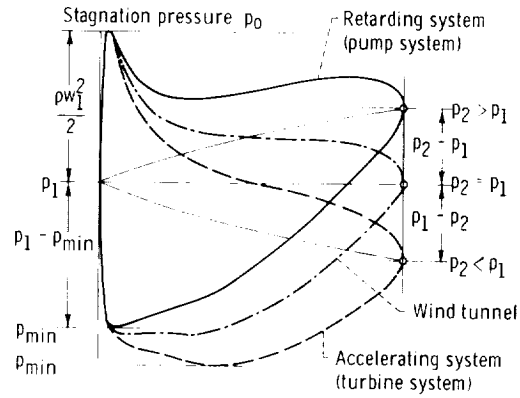

Figure 2-24. – Vane pressure distribution in different systems.

may well be expected to be a valid criterion for the danger of separation or stall. Ackeret told this writer that he used this criterion as early as 1928, but it was apparently not published before 1942 (ref. 10). He stated that the maximum value of the ratio $(p_2 - p_{min})/(p_o - p_{min})$ would be 0.8. He added, "Of course it cannot be quite that simple, but it is amazing how well this criterion works."

In 1955, NACA used the same criterion in the form $(w_{max}^2 - w_2^2)/w_{max}^2$ (ref. 11). However, Lieblein (refs. 12 and 13) replaced this pressure ratio by a velocity ratio which may be referred to as the local diffusion factor:

$$D_{loc} = \frac{w_{max} - w_2}{w_{max}} \tag{2-63}$$

Plotting the wake momentum thickness (divided by the blade chord) against D_{loc} shows that at $D_{loc} = 0.4$ the momentum thickness is about twice that at the lowest D_{loc} values tested (0.15 to 0.20), and for $D_{loc} > 0.5$, the momentum thickness increases so rapidly as to suggest separation. Considering that

$$K_A = \frac{w_{max}^2 - w_2^2}{w_{max}^2} = \frac{w_{max} - w_2}{w_{max}} \frac{w_{max} + w_2}{w_{max}}$$

$$= D_{loc} \frac{w_{max} + w_2}{w_{max}} \tag{2-64}$$

and that for a number of cascades investigated w_2/w_{max} ranges from about 0.46 to about 0.66 (see sec. 2.5.5), one obtains a mean value of $K_A = 1.56\, D_{loc}$. For $D_{loc} = 0.5$, one finds $K_A = 0.78$, which is as close to Ackeret's limit of 0.8 as could be expected.

The foregoing consideration and the resulting separation coefficient K_A and D_{loc} have the practical disadvantage that neither the minimum pressure p_{min} nor the corresponding maximum velocity w_{max} is generally known, since vane system designs are usually based on the velocity diagrams in front of and behind the vane system. This statement also applies to the apparently intermediate velocity diagram in figure 2-9 containing w_∞, because this diagram is obtained by averaging between the inlet and discharge velocity diagrams and, thus, is not independently established.

The foregoing considerations on limitations due to cavitation do involve the minimum pressure in the vane system p_{min} in a significant manner. However, this pressure was related to the average pressure difference across the vanes Δp_{av} and the lift coefficients $C_{L,1}$ and $C_{L,\infty}$ in the manner indicated by equations (2-60) and (2-61) by introducing the pressure ratio $q = (p_1 - p_{min})/\Delta p_{av}$. It is the relation quoted last which is used here to connect the parameters K_A (eq. 2-62) and D_{loc} (eq. 2-63) to the known flow conditions on the inlet and discharge sides of the system.

The first attempt in this respect was made by this writer in 1934 as part of his Ph.D. thesis at the California Institute of Technology (see ref. 14, secs. 64 and 111). The principles of this attempt are as follows:

The pressure rise $p_2 - p_{min}$ is divided into two parts:

$$p_2 - p_{min} = (p_2 - p_1) + (p_1 - p_{min}) \tag{2-65}$$

For cylindrical sections through axial-flow vane systems, we use the usually close approximation

$$p_2 - p_1 = \rho \frac{w_1^2 - w_2^2}{2} \tag{2-66}$$

The second part of equation (2-65) is related to the lift coefficient $C_{L,\infty}$ by equations (2-59), (2-60), and (2-61) as follows:

$$\frac{p_1 - p_{min}}{\rho w_\infty^2/2} = \frac{p_1 - p_{min}}{\Delta p_{av}} \frac{\Delta p_{av}}{\rho w_\infty^2/2} = q C_{L,\infty} \tag{2-67}$$

It is now natural to make all terms of equation (2-65) dimensionless by dividing by the velocity pressure of the vectorial mean velocity $\rho w_\infty^2/2$. Thus equation (2-65) appears in normalized form as follows:

$$K_\infty = \frac{p_2 - p_{min}}{\rho w_\infty^2/2} = \frac{p_2 - p_1}{\rho w_\infty^2/2} + qC_{L,\infty} \tag{2-68}$$

Obviously

$$p_2 - p_1 = \frac{\rho}{2}(w_1^2 - w_2^2) = \frac{\rho}{2}(w_1 + w_2)(w_1 - w_2)$$

When the approximation $w_\infty = (w_1 + w_2)/2$ is used, equation (2-68) can be written in the form

$$K_\infty = 4\frac{1 - w_2/w_1}{1 + w_2/w_1} + qC_{L,\infty} \tag{2-69}$$

since, according to equation (2-54)

$$C_{L,\infty} = 2\frac{\Delta V_U}{w_\infty}\frac{t}{l} \tag{2-54}$$

$$\approx 4\frac{\Delta V_U}{w_1 + w_2}\frac{t}{l}$$

equation (2-69) does indeed express a separation criterion entirely in terms of the flow conditions in front of and behind the vane system considered.

The first experimental test of this approach to the problem of separation in turbomachinery vane systems came through the important paper by Howell (ref. 15). Figures 2-25(a) to (c) are taken directly from Howell's paper. Howell concluded from these data that neither the angle of deflection, nor the lift coefficient, nor the pressure recovery coefficient $(p_2 - p_1)/(\rho w_1^2/2)$ is an adequate criterion for the occurrence of separation or stall in such vane systems. However, when the same data are plotted in the form of the separation coefficient K_∞ under the assumption $q = 1$ (fig. 2-25 (d)), they collapse to a rather narrow bundle of nearly horizontal curves, which suggest that K_∞ lies between 1.5 and 1.7.

In 1953, Lieblein, Schwenk, and Broderick (ref. 12) also worked to establish a separation criterion

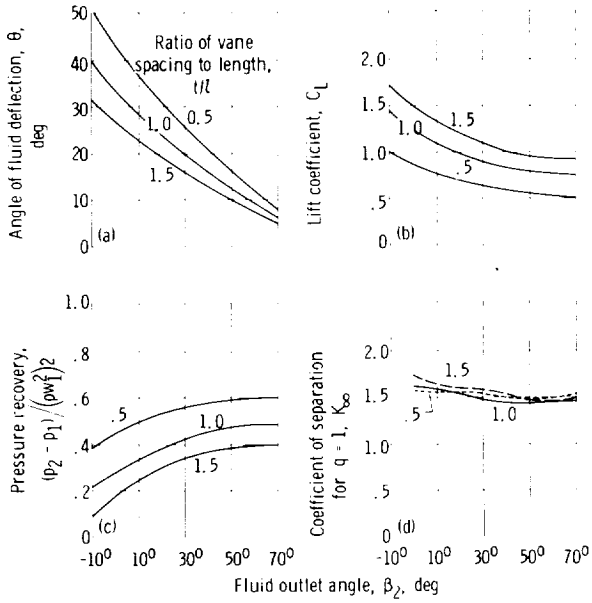

(a) Flow deflection angle. (b) Lift coefficient. (c) Pressure recovery. (d) Separation coefficient.

Figure 2-25. – Aerodynamic limits of axial-flow compressor operation according to Howell (ref. 15).

that could be calculated from the inlet and discharge conditions alone (i.e., without direct knowledge of p_{min}); this effort led to the now widely used diffusion factor

$$D = 1 - \frac{w_2}{w_1} + \frac{\Delta V_U}{2w_1}\frac{t}{l} \tag{2-70}$$

According to equation (2-54), this diffusion factor can also be expressed in terms of the lift coefficient $C_{L,\infty}$:

$$D = 1 - \frac{w_2}{w_1} + \frac{1}{4}C_{L,\infty}\frac{w_\infty}{w_1} \tag{2-71}$$

Again using the approximation $w_\infty = (w_1 + w_2)/2$, one finds

$$D = 1 - \frac{w_2}{w_1} + \frac{1}{8}C_{L,\infty}\left(1 + \frac{w_2}{w_1}\right) \tag{2-72}$$

While different from the separation coefficient K_∞ (eq. (2-69)), both separation criteria can be expressed in terms of the lift coefficient $C_{L,\infty}$ and the ratio of retardation (or acceleration) of the relative flow w_2/w_1.

As in the case of the local diffusion factor D_{loc}, the wake momentum thickness was plotted against the diffusion factor D. A rapid rise in the

momentum thickness beginning at $D=0.60$ indicated the beginning of separation at that D value. At about $D=0.4$, the momentum thickness increased to about twice its minimum value.

The comparison between various criteria of separation, or stall, is completed by expressing the Ackeret pressure ratio

$$K_A = \frac{p_2 - p_{min}}{\rho w_{max}^2/2} = \frac{p_2 - p_{min}}{p_o - p_{min}} \tag{2-62}$$

in a form not depending directly on a knowledge of p_{min}. Evidently, according to equations (2-66), (2-60), and (2-61) and figure 2-20,

$$K_A = \frac{p_2 - p_{min}}{p_o - p_{min}} = \frac{p_2 - p_1 + p_1 - p_{min}}{p_o - p_1 + p_1 - p_{min}}$$

$$= \frac{w_1^2 - w_2^2 + qC_{L,1}w_1^2}{w_1^2 + qC_{L,1}w_1^2} \tag{2-73}$$

Considering that (approximately)

$$C_{L,1} = C_{L,\infty}\frac{w_\infty^2}{w_1^2} = C_{L,\infty}\frac{(1 + w_2/w_1)^2}{4} \tag{2-74}$$

and with $(w_1^2 - w_2^2)/w_1^2 = (1 + w_2/w_1)(1 - w_2/w_1)$, one obtains

$$K_A \equiv \frac{p_2 - p_{min}}{p_o - p_{min}}$$

$$= \frac{(1 + w_2/w_1)(1 - w_2/w_1) + qC_{L,\infty}(1 + w_2/w_1)^2/4}{1 + qC_{L,\infty}(1 + w_2/w_1)^2/4}$$

$$K_A = \frac{(1 - w_2/w_1) + qC_{L,\infty}(1 + w_2/w_1)/4}{1/(1 + w_2/w_1) + qC_{L,\infty}(1 + w_2/w_1)/4} \tag{2-75}$$

which establishes K_A as a function of $qC_{L,\infty}$ and of the retardation (or acceleration) ratio w_2/w_1, like K_∞ according to equation (2-69) and the diffusion factor D according to equation (2-72). (This result and fig. 2-26 depend on the assumption that $w_\infty = (w_1 + w_2)/2$, which is not true for systems with small angle β_v, e.g., many diffuser and impulse vane systems.)

A comparison among the various separation criteria or diffusion factors presented by equations (2-62) or (2-75), (2-69), and (2-70) or (2-72) is given by figure 2-26, where these diffusion coefficients are plotted as functions of the retardation (or

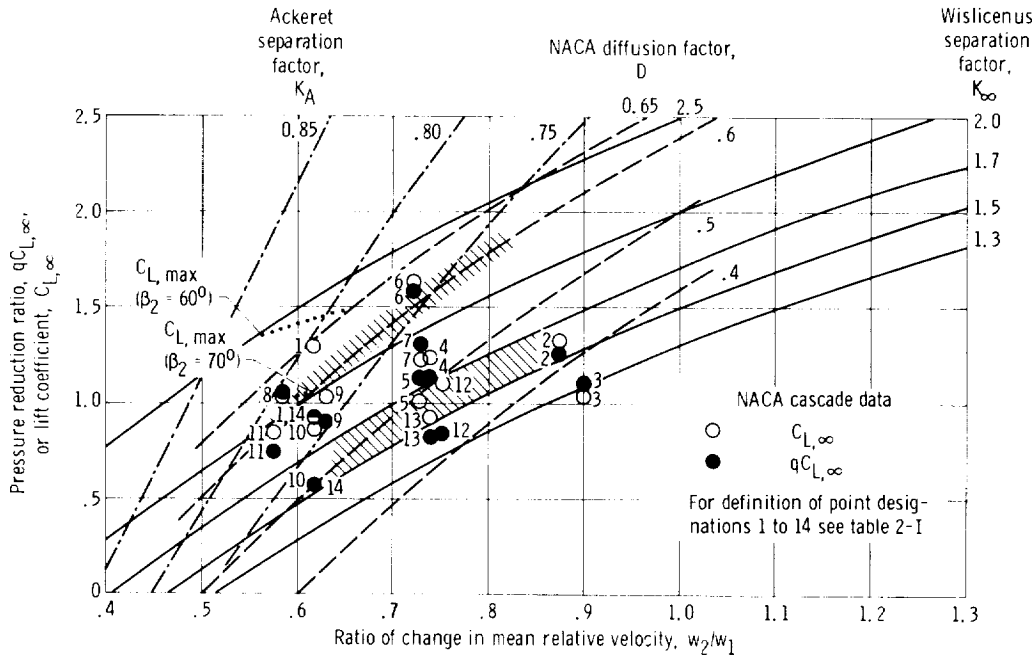

Figure 2-26. – Separation limits of straight systems of parallel, staggered vanes. (Data from ref. 16.)

acceleration) ratio w_2/w_1 and of the pressure reduction ratio $qC_{L,\infty}$. The scale for $qC_{L,\infty}$ serves also as a scale for the lift coefficient $C_{L,\infty}$ with respect to the diffusion factor D, with respect to the NACA cascade data (ref. 16)(open symbols), and with respect to the dotted curves representing maximum values of $C_{L,\infty}$ according to the same NACA data (ref. 16).

The numbers given with every test point plotted are associated with definite vane-system characteristics by table 2-I. The point coordinates are taken from the cascade information presented in reference 16 and section 2.5.5 and represent cascade operating conditions at or near optimum cascade performance. The points plotted, therefore, do not mark maximum $C_{L,\infty}$ and $qC_{L,\infty}$ values, but rather conditions that may be used as design values.

The shaded area between the curves $K_\infty = 1.5$ and $K_\infty = 1.7$ represents Howell's data from figure 2-25. The w_2/w_1 range of this area was estimated from figure 2-25(d).

The shaded region on the $D = 0.60$ curve marks the beginning of a very rapid increase in the blade-wake momentum thickness observed by NACA. It may well represent the beginning of separation and thereby an upper limit of $C_{L,\infty}$, although a few test points fall above this region. No information is available about the w_2/w_1 range of this region. Since a marked increase in wake momentum thickness was already observed at $D = 0.4$, the entire region between the $D = 0.4$ and $D = 0.6$ curves may be considered for design purposes.

TABLE 2-I. - POINT DESIGNATIONS IN FIGURE 2-26 AND CORRESPONDING ILLUSTRATIONS

[Data from ref. 16.]

Point	Vane	Inlet flow angle, β_1, deg	Solidity, ℓ/t	Vane shown in figure 2-27 -
1	NACA 65-(18)-10	60	1.0	(a)
2	NACA 65-(18)-10	30	1.0	(b)
3	NACA 65-(18)-10	30	1.5	(c)
4	NACA 65-(18)-10	45	1.0	(d)
5	NACA 65-(18)-10	45	1.5	(e)
6	NACA 65-(24)-10	45	1.0	(f)
7	NACA 65-(24)-10	45	1.5	(g)
8	NACA 65-(18)-10	60	1.5	(h)
9	NACA 65-(12)-10	70	1.0	(i)
10	NACA 65-(12)-10	70	1.25	(j)
11	NACA 65-(12)-10	70	1.5	(k)
12	NACA 65-(18 A_2 I_{sb})-10	45	1.0	(l)
13	NACA 65-(18 A_2 I_{sb})-10	45	1.5	(m)
14	NACA 65-(18 A_2 I_{sb})-10	60	1.5	(n)

As stated by Ackeret, his limit curve $K_A = 0.8$ marks an upper limit of boundary-layer retardation. This limit line cannot be used for moderate retardations of the mean relative flow, say above $w_2/w_1 = 0.8$, because it would lead to unreasonably high values of $qC_{L,\infty}$. The Ackeret curve sets a lower limit for w_2/w_1 rather than an upper limit for $qC_{L,\infty}$.

It is also doubtful whether the D=constant curves can be used for $w_2/w_1 > 0.9$, because of the very high $C_{L,\infty}$ values resulting from such application of the $D = 0.6$ curve. On the other hand, for $w_2/w_1 = 0.6$ and $D = 0.6$, one obtains $C_{L,\infty} = 1.0$, which seems reasonable in view of the available test data.

Since the K_∞=constant curves are the flattest curves of separation criteria, perhaps they can be applied in the regime of accelerated mean flow ($w_2/w_1 > 1$). The K_∞ parameter was originally intended to be limited to values between 1.5 and 1.7, as these limits correspond to the limits of the lift coefficient for a single vane in an infinitely extended stream. The condition $w_2/w_1 = 1$ is supposed to correspond to this case, and equation (2-69) shows that $qC_{L,\infty} = K_\infty$ for $w_2/w_1 = 1$. However, for stronger retardation of the mean flow, say for $w_2/w_1 < 0.7$, it seems that $1.5 \leq K_\infty \leq 1.7$ is rather conservative; in this region, $1.7 \leq K_\infty \leq 2.0$ (or 2.2) is more reasonable. Thus the arrangement of vanes in a straight cascade has some beneficial effects with respect to separation, if the mean pressure changes are taken into account.

No conclusion is drawn here regarding the relative merits of the three separation criteria or coefficients considered (K_A, D, and K_∞). Accurate separation limits cannot be established in terms of any one of these coefficients any more than a definite separation or stall limit can be defined for the lift coefficient of a single airfoil in an infinitely extended stream. However, consideration of these separation coefficients throws considerable light on the fundamentals of separation or stall in turbomachinery. One is tempted to draw the plausible conclusion that the adverse pressure gradient on the low-pressure side of the vanes, while important (if properly normalized), is not the only criterion of separation. The curvature of the flow as well as secondary fluid motions may offer additional criteria of separation. However, so far only the dimensionless pressure gradient has led to criteria which are sufficiently simple to be used by the designer.

Inspection of figure 2-26 may lead to the general conclusion that, for vane systems with retarded mean relative flow, the lift coefficient $C_{L,\infty}$ at design conditions should be between 1.0 and 1.5 and should diminish with diminishing ratio of retardation w_2/w_1. Furthermore the ratio of retardation w_2/w_1 has a lower limit near $w_2/w_1 = 0.6$.

With accelerated mean relative flow ($w_2/w_1 > 1$), the lift coefficient $C_{L,\infty}$ can progressively be increased with increasing ratio of acceleration w_2/w_1, but upper limits of $C_{L,\infty}$ for these conditions are not yet established.

2.5.5 Analysis of Cascade Test Results and Mean Streamline Method

It should be clear from the preceding section that a great deal of experimental work on flow through axial-flow cascades (i.e., cylindrical sections through axial-flow vane systems) was done. Initially Great Britain led in this work. Today the work of NACA supplies us with most of the information on flow through straight systems of staggered, parallel vanes (refs. 16 to 18). An interesting summary of these findings has been presented as a series of related graphs called carpet plots (ref. 16). Good correlations have been found between the flow observed in straight cascades in cascade tunnels (the cascade of vanes being stationary) and the flow in equivalent rotating systems in a space of revolution (refs. 19 and 20) (with the possible exception of flow at high Mach numbers).

The vast amount of experimental information and its theoretical interpretation cannot be covered here. Instead an attempt is made to extract from some of the data such information as may eventually be used for design purposes.

Figures 2-27(a) to (n) show vane systems selected from reference 16, and figure 2-27(o) shows one from reference 17. All pressure distributions are taken from NACA test results, but are plotted against the axial extent of the vane system for reasons that become apparent later.

All parameters from the vane systems of reference 16 used in this presentation of the theory and in the design of axial-flow vane systems (ch. 3) are evaluated and listed in table 2-II. These parameters are

(1) The lift coeficient referred to the inlet velocity, determined from the area inside the pressure distribution curve on the basis of

$$C_{L,1} = \frac{\Delta p_{av}}{\rho w_1^2/2} \tag{2-60}$$

where $\Delta p_{av} = (1/y_v) \int_o^{y_v} \Delta p \, dy$, y_v being the axial extent of the vane.

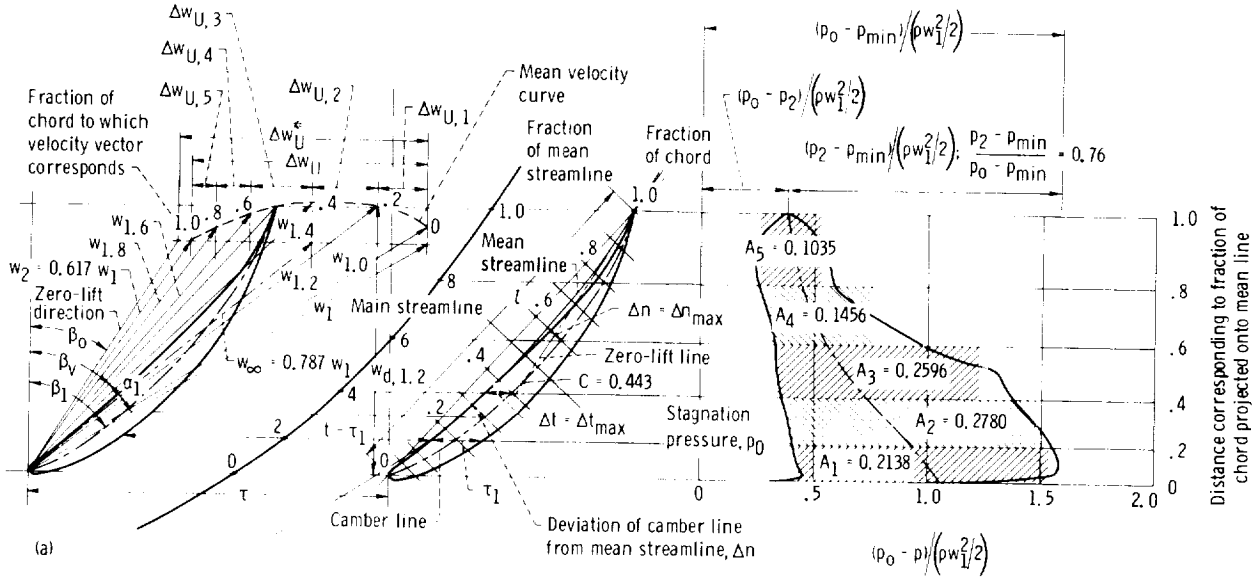

(a) Vane, NACA 65-(18)-10; inlet flow angle β_1, 60°; solidity l/t, 1.0; vane angle β_v, 42.2°; inlet angle of attack against baseline α_1, 17.5°; angle of deflection θ, 25.2°.

Figure 2-27. – Characteristics of cascade of vanes. (See table 2-II for cascade parameters.) Mean static-pressure curve is obtained from local mean velocity w_i and static pressure $p_{av,i}$ corresponding to that velocity (i.e., $(p_o - p_{av,i})/(\rho w_i^2/2) = constant$).

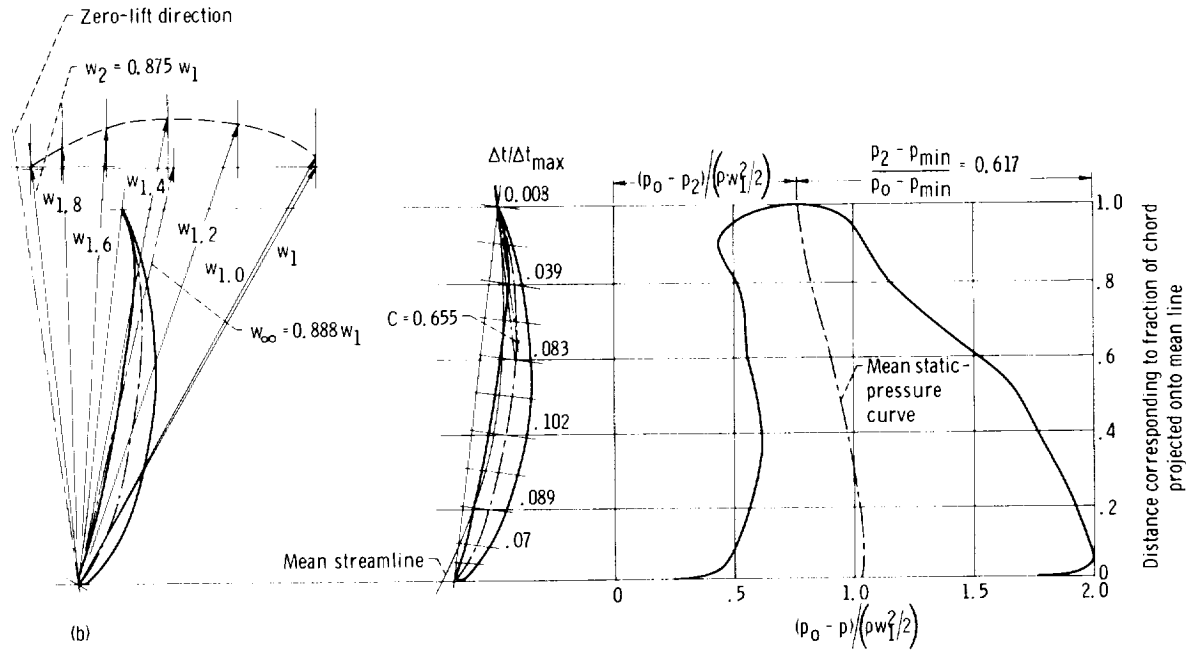

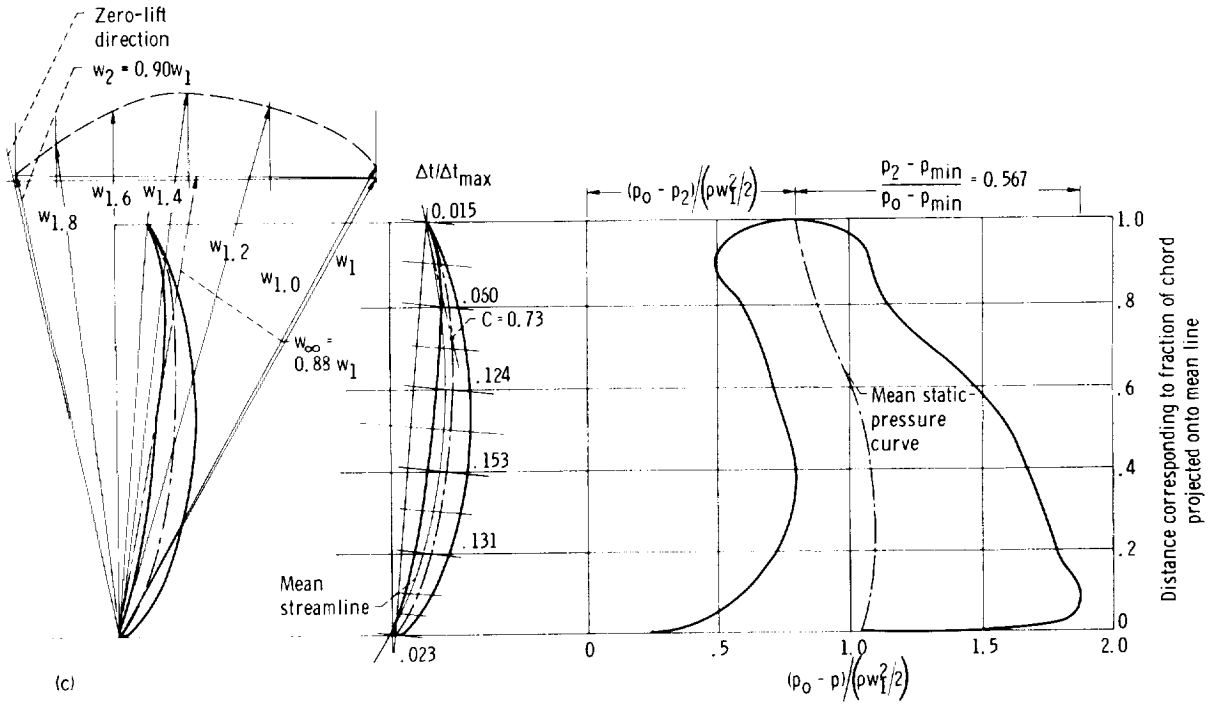

(b) Vane, NACA 65-(18)-10; inlet flow angle β_1, 30°; solidity l/t, 1.0; vane angle β_v, 7°; inlet angle of attack against baseline α_1, 23°; angle of deflection θ, 36°.

(c) Vane, NACA 65-(18)-10; inlet flow angle β_1, 30°; solidity l/t, 1.5; vane angle β_v, 5°; inlet angle of attack against baseline α_1, 25°; angle of deflection θ, 41.6°.

Figure 2-27. – Continued.

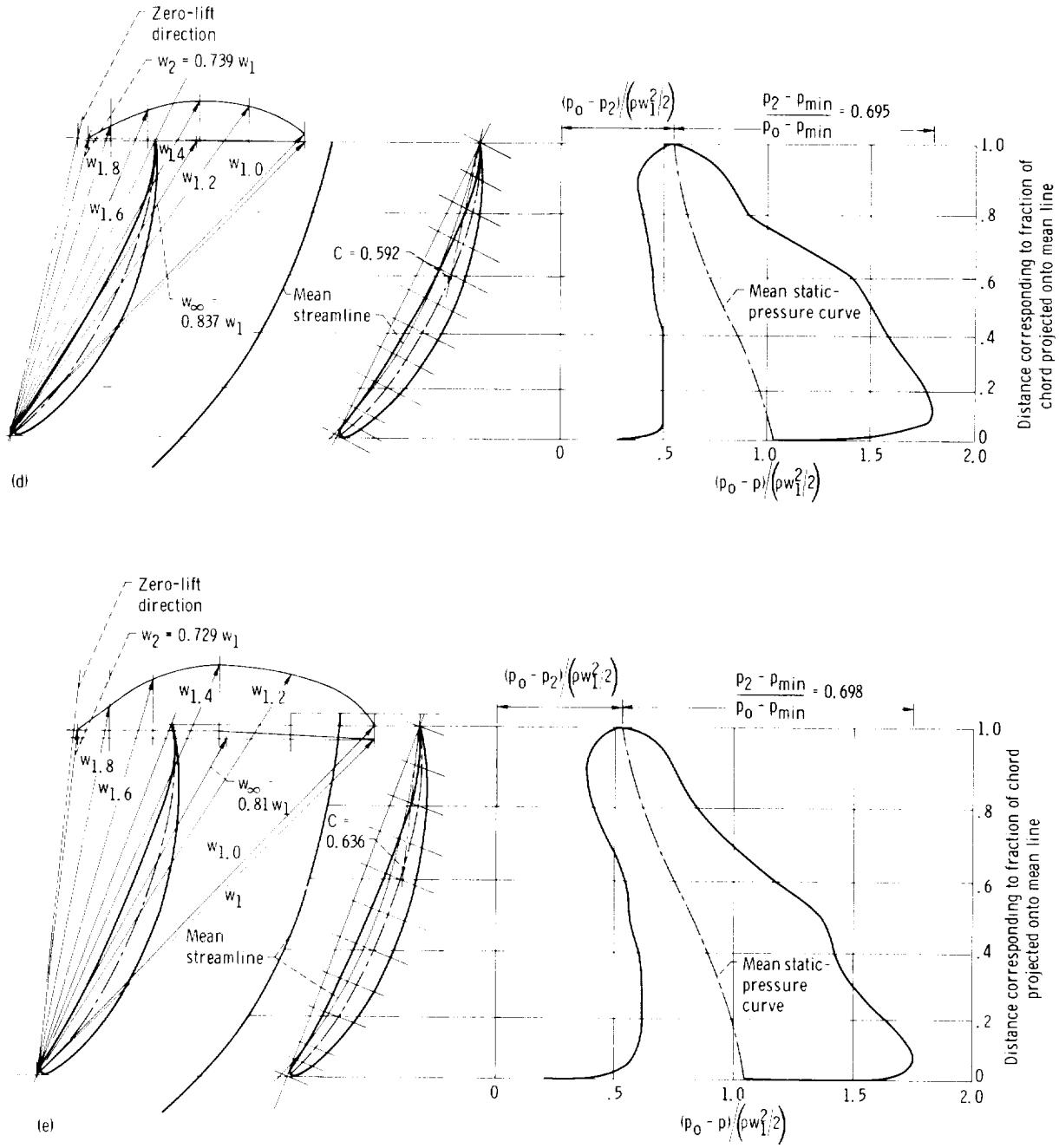

(d) Vane, NACA 65-(18)-10; inlet flow angle β_1, 45°; solidity l/t, 1.0; vane angle β_t, 26°; inlet angle of attack against baseline α_1, 19°; angle of deflection θ, 30°.

(e) Vane, NACA 65-(18)-10; inlet flow angle β_1, 45°; solidity l/t, 1.5; vane angle β_t, 21°; inlet angle of attack against baseline α_1, 24°; angle of deflection θ, 38.4°.

Figure 2-27. – Continued.

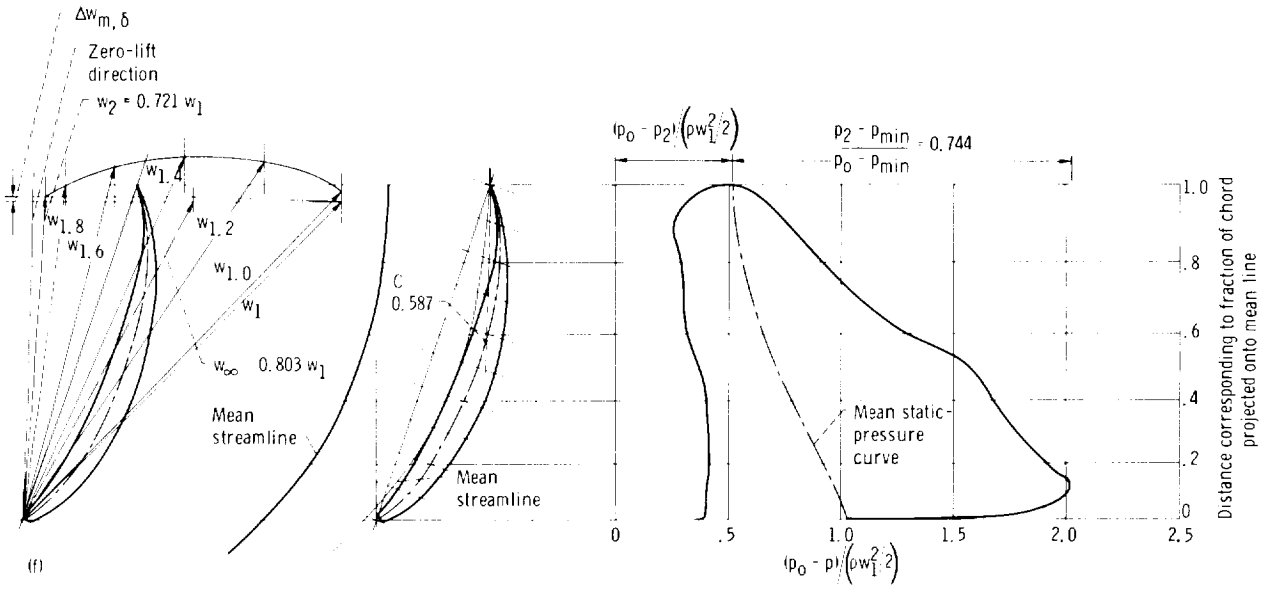

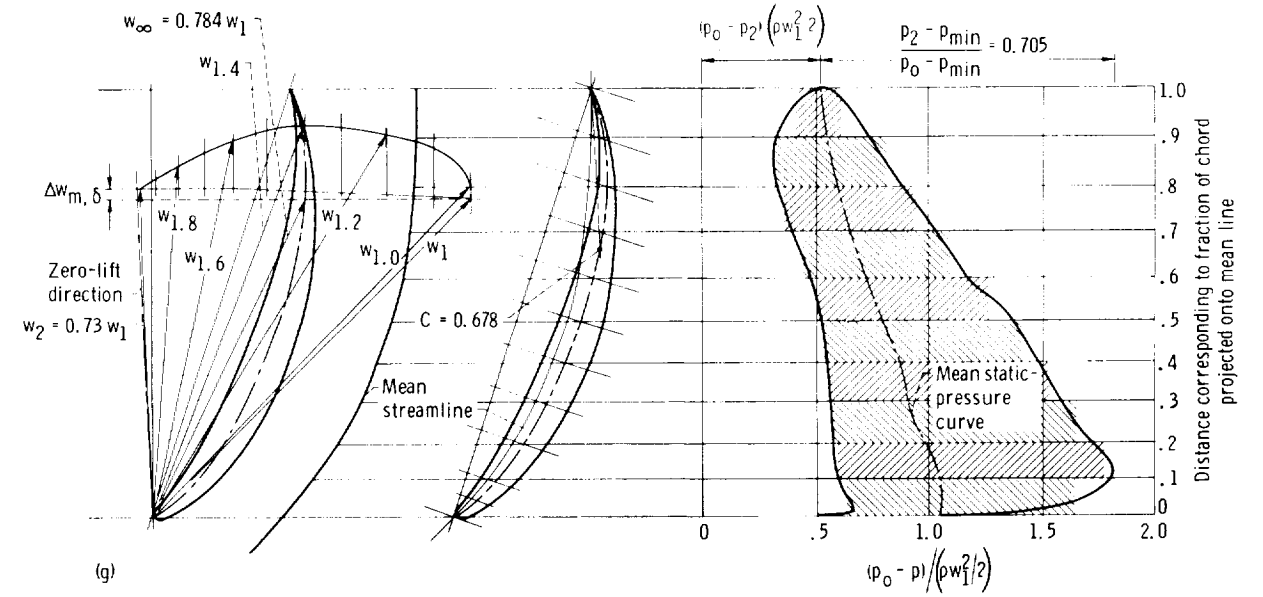

(f) Vane, NACA 65-(24)-10; inlet flow angle β_1, 45°; solidity l/t, 1.0; vane angle β_t, 19°; inlet angle of attack against baseline α_1, 26°; angle of deflection θ, 40.9°.

(g) Vane, NACA 65-(24)-10; inlet flow angle β_1, 45°; solidity l/t, 1.5; vane angle β_t, 18°; inlet angle of attack against baseline α_1, 27°; angle of deflection θ, 46.9°.

Figure 2-27. – Continued.

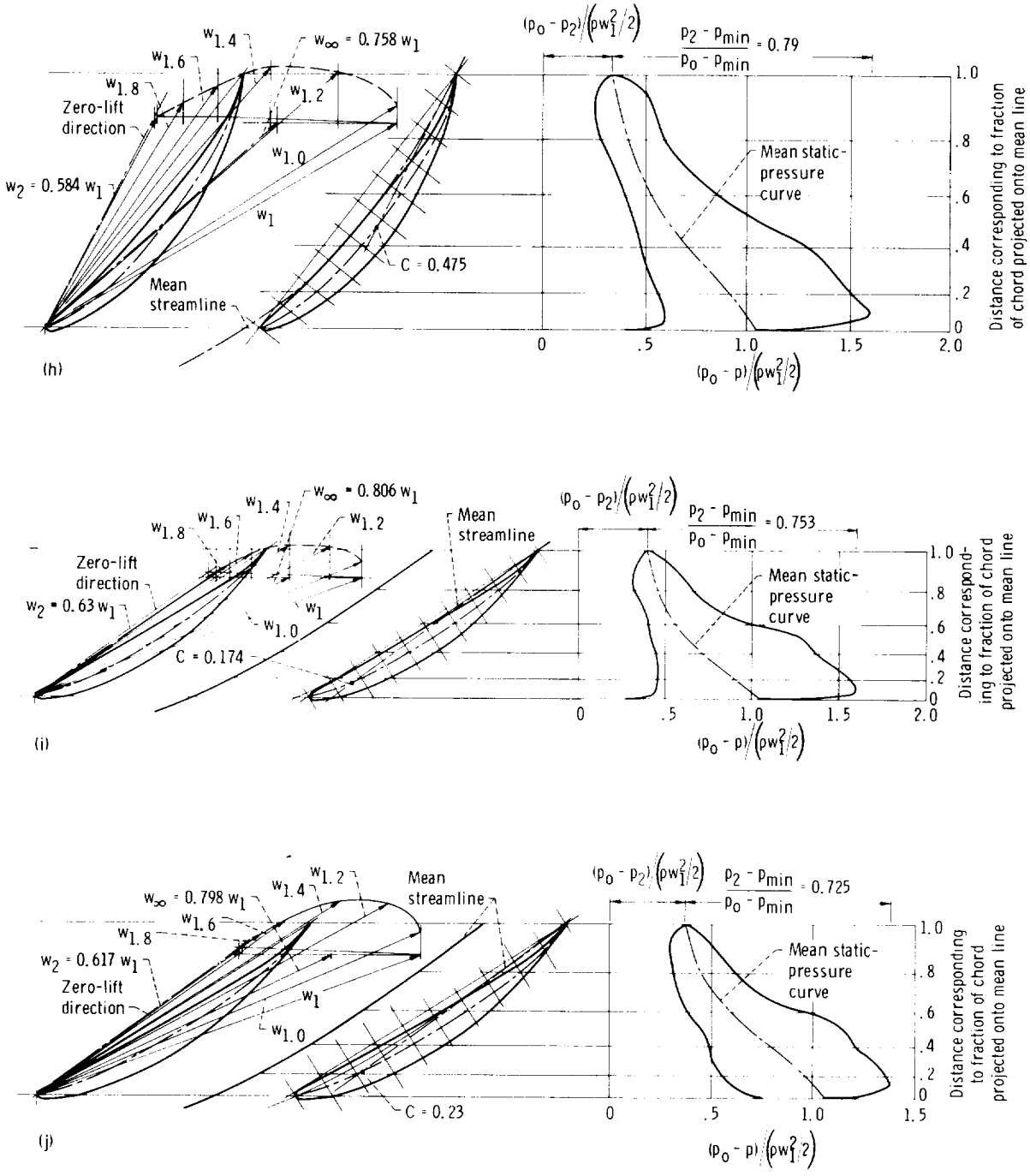

(h) Vane, NACA 65-(18)-10; inlet flow angle β_1, 60°; solidity l/t, 1.5; vane angle β_v, 38°; inlet angle of attack against baseline α_1, 22°; angle of deflection θ, 31.9°.

(i) Vane, NACA 65-(12)-10; inlet flow angle β_1, 70°; solidity l/t, 1.0; vane angle β_v, 57.2°; inlet angle of attack against baseline α_1, 12.6°; angle of deflection θ, 14.4°.

(j) Vane, NACA 65-(12)-10; inlet flow angle β_1, 70°; solidity l/t, 1.25; vane angle β_v, 57.8°; inlet angle of attack against baseline α_1, 12.1°; angle of deflection θ, 15.6°.

Figure 2-27. – Continued.

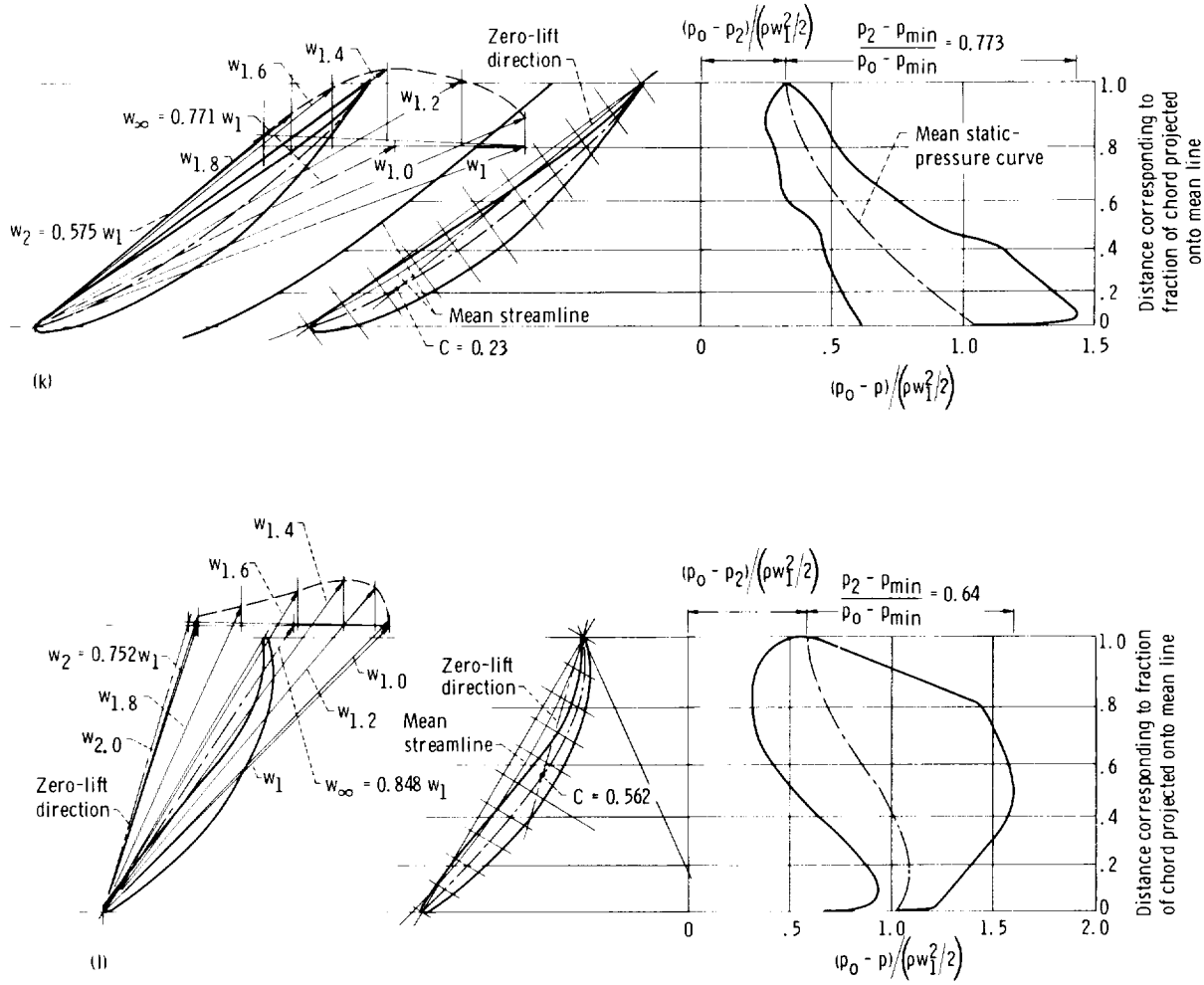

(k) Vane, NACA 65-(12)-10; inlet flow angle β_1, 70°; solidity l/t, 1.5; vane angle β_v, 54°; inlet angle of attack against baseline α_1, 16.1°; angle of deflection θ, 19.7°.

(l) Vane, NACA 65-($18A_2I_{8b}$)10; inlet flow angle β_1, 45°; solidity l/t, 1.0; vane angle β_v, 30.5°; inlet angle of attack against baseline α_1, 14.3°; angle of deflection θ, 26.7°.

Figure 2-27. – Continued.

(2) The lift coefficient referred to the mean relative velocity w_∞ calculated independently from

$$C_{L,\infty} = C_{L,1} \frac{w_1^2}{w_\infty^2} \tag{2-60}$$

and from equation (2-54) expressed in terms of the turning of the relative velocity

$$C_{L,\infty} = 2 \frac{\Delta w_U}{w_\infty} \frac{t}{l} \tag{2-54a}$$

The relatively good agreements between the two values of $C_{L,\infty}$ are quite reassuring.

(3) The pressure reduction ratio

$$q = \frac{p_1 - p_{min}}{\Delta p_{av}} = \frac{C_{p,min}}{C_{L,1}} \tag{2-61}$$

where

$$C_{p,min} = \frac{p_1 - p_{min}}{\rho w_1^2/2}$$

(4) The pressure reduction coefficient $qC_{L,\infty}$, which is plotted in figure 2-26. The value of $C_{L,\infty}$ used in figure 2-27 is the average of the two values determined from equations (2-60) and (2-54a).

(5) The velocity ratios w_∞/w_1 and w_2/w_1, by scaling from the velocity diagram, and

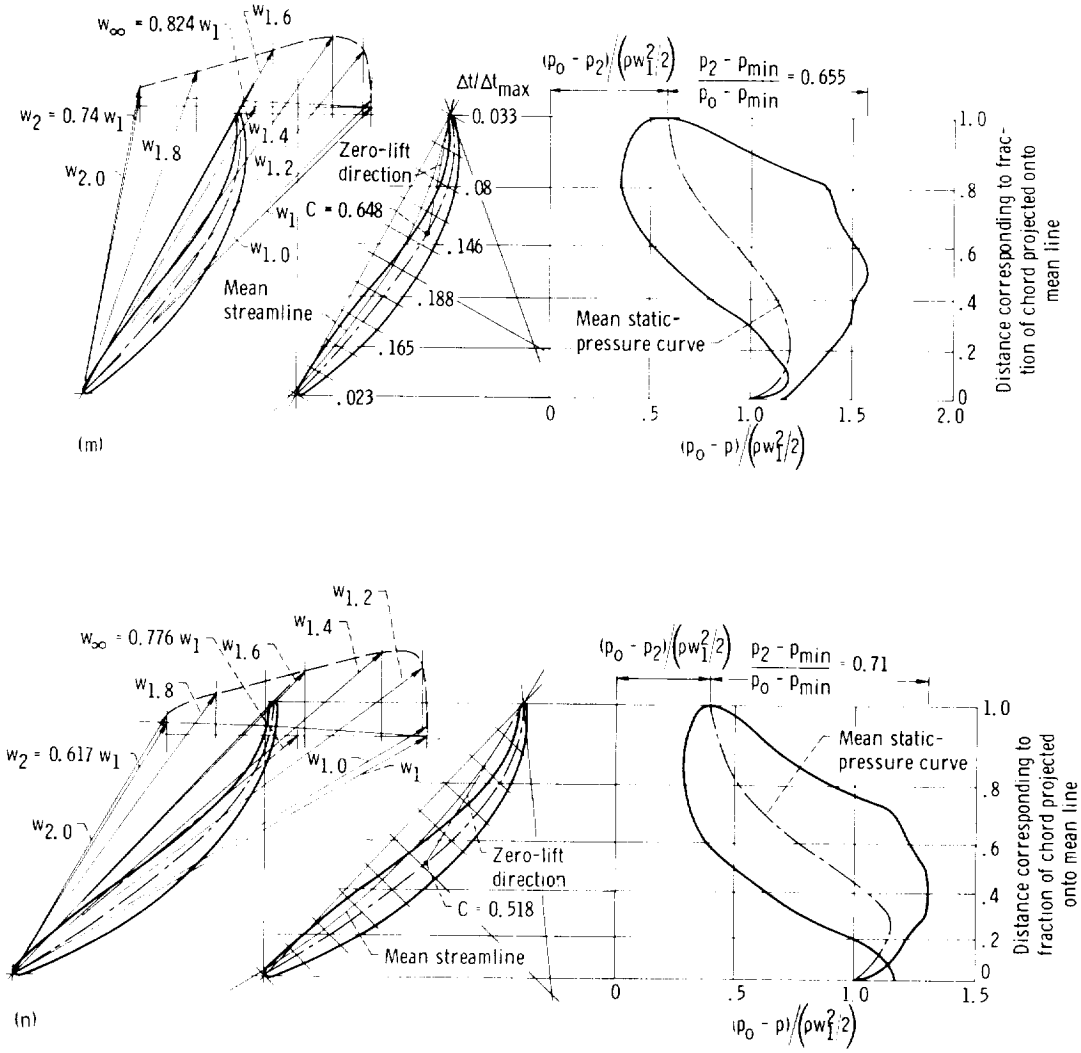

(m) Vane, NACA 65-(18A_2I_{8b})10; inlet flow angle β_1, 45°; solidity l/t, 1.5; vane angle β_t, 28.5°; inlet angle of attack against baseline α_1, 16.3°; angle of deflection θ, 34.1°.

(n) Vane, NACA 65-(18A_2I_{8b})10; inlet flow angle β_1, 60°; solidity l/t, 1.5; vane angle β_t, 43.5°; inlet angle of attack against baseline α_1, 16.4°; angle of deflection θ, 28.7°.

Figure 2-27. – Continued.

$$\frac{w_{max}}{w_1} = \sqrt{\frac{p_o - p_{min}}{\rho w_1^2/2}}$$

$$\frac{w_{max}}{w_\infty} = \left(\frac{w_{max}}{w_1}\right)\left(\frac{w_1}{w_\infty}\right)$$

the last of which is used in section 2.5.4 to compare the separation limit $D_{loc} = 0.5$ with the Ackeret limit of $K_A = 0.8$.

(6) The separation coefficients

$$K_A = \frac{p_2 - p_{min}}{p_o - p_{min}} \tag{2-62}$$

$$D_{loc} = \frac{w_{max} - w_2}{w_{max}} = 1 - \frac{w_2}{w_{max}} \tag{2-63}$$

$$K_\infty = 4\,\frac{1 - w_2/w_1}{1 + w_2/w_1} + qC_{L,\infty} \tag{2-69}$$

$$D = 1 - \frac{w_2}{w_1} + \frac{1}{8}C_{L,\infty}\left(1 + \frac{w_2}{w_1}\right) \tag{2-72}$$

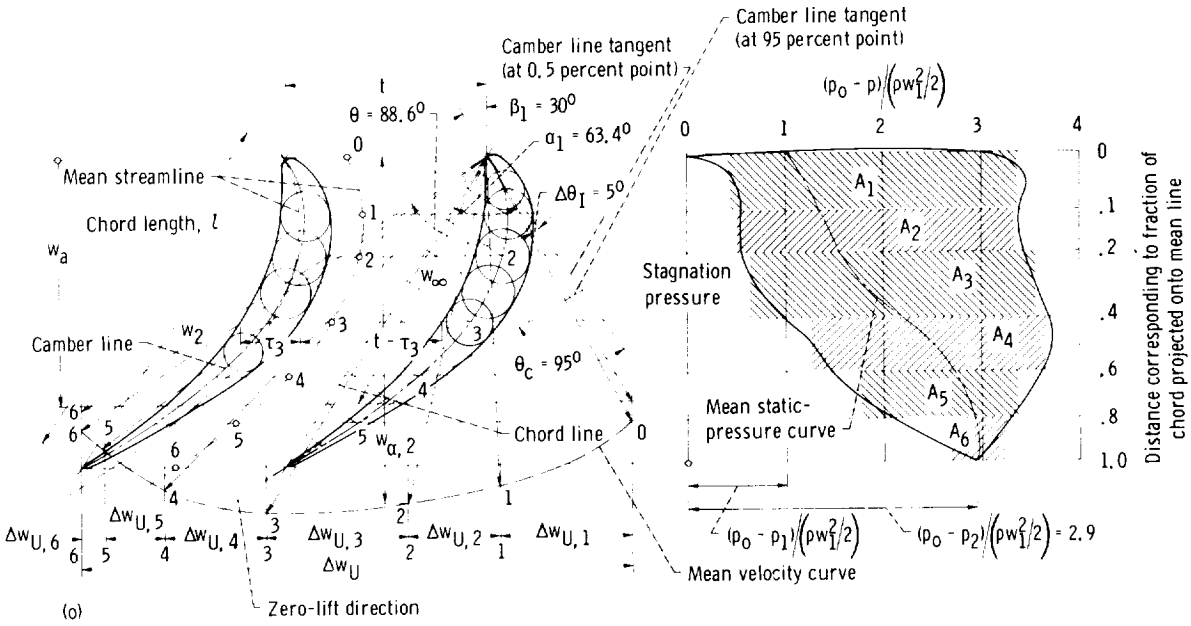

(o) Vane, NACA A_3K_7; inlet flow angle β_1, 30°; solidity l/t, 1.8; vane angle β_v, 34°; inlet angle of attack against baseline α_1, 63.40°; angle of deflection θ, 88.6°; camber angle θ_c, 95°.

Figure 2-27. – Concluded.

(7) The Weinig head coefficient (see sec. 2.5.3)

$$C_H = \frac{\Delta w_U}{\Delta w_U^*}$$

which is taken from figure 2-18 and permits the determination of the zero-lift direction in relation to the vane profile. A line drawn in this direction through the trailing edge of the vane intersects the mean camber line of the vane profile at point C. The location of this point of intersection is plotted in figure 2-28 as a function of the vane angle. Since the angle between the zero-lift line and the camber line is quite small, the scatter of these points does not represent a serious uncertainty about the direction of the zero-lift line. Figure 2-28 replaces the previously cited rule (based on the ideal-flow characteristics of single airfoils with circular-arc camber lines) that the zero-lift line intersects the mean camber line at the halfway point between the leading and trailing edges.

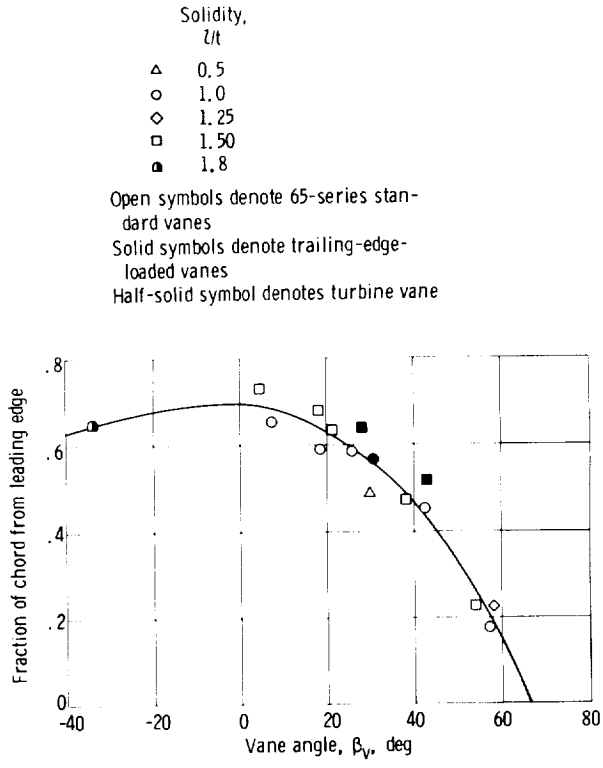

Figure 2-28. – Location of intersection C between zero-lift and camber lines.

It is hoped that the foregoing considerations in connection with figures 2-27 and 2-28 give the reader a reasonably vivid picture of the relation between certain physical parameters and the shape

TABLE 2-II. - CASCADE PARAMETERS

Parameters apply to figure 2-27 -	$C_{L,1} = \frac{\Delta p_{av}}{\frac{\rho w_1^2}{2}}$	$C_{L,\infty} = C_{L,1}\frac{w_1^2}{w_\infty^2}$	$C_{L,\infty} = 2\frac{\Delta w_U}{w_\infty}\frac{t}{\ell}$	$q = \frac{p_1 - p_{min}}{\Delta p_{av}} = \frac{C_{p,min}}{C_{L,1}}$	$qC_{L,\infty}$	$C_{p,min} = \frac{p_1 - p_{min}}{\frac{\rho w_1^2}{2}}$	$\frac{w_{max}}{w_1} = \sqrt{\frac{p_o - p_{min}}{\frac{\rho w_1^2}{2}}} = \sqrt{1 + C_{p,min}}$	$\frac{w_\infty}{w_1}$	$\frac{w_2}{w_1}$	$\frac{w_{max}}{w_\infty} = \frac{w_{max}}{w_1}\frac{w_1}{w_\infty}$	$\frac{w_2}{w_{max}} = \frac{w_2}{w_1}\frac{w_1}{w_{max}}$	$K_A = \frac{p_2 - p_{min}}{p_o - p_{min}}$	$K_\infty = 4\frac{1 - \frac{w_2}{w_1}}{1 + \frac{w_2}{w_1}} + qC_{L,\infty}$	$D_{loc} = 1 - \frac{w_2}{w_{max}}$	$D = 1 - \frac{w_2}{w_1} + \frac{1}{8}C_{L,\infty} \times \left(1 + \frac{w_2}{w_1}\right)$	$C_H = \frac{\Delta w_U}{\Delta w_U^*}$
(a)	0.79	1.28	1.31	0.728	0.94	0.58	1.257	0.787	0.617	1.598	0.491	0.76	1.89	0.509	0.646	0.95
(b)	1.05	1.33	1.342	.953	1.273	1.00	1.415	.888	.875	1.595	.618	.617	1.54	.382	.438	.956
(c)	.822	.985	1.035	1.06	1.07	.872	1.369	.88	.90	1.555	.6575	.567	1.28	.3425	.34	.99
(d)	.87	1.24	1.25	.92	1.145	.80	1.343	.837	.739	1.604	.55	.695	1.75	.45	.532	.954
(e)	.668	1.02	1.026	1.123	1.148	.75	1.323	.81	.729	1.634	.551	.698	1.775	.45	.492	.989
(f)	1.045	1.62	1.65	.978	1.599	1.022	1.423	.803	.721	1.772	.507	.744	2.248	.493	.631	.956
(g)	.755	1.225	1.240	1.066	1.315	.805	1.345	.784	.73	1.716	.543	.705	1.940	.457	.538	.989
(h)	.585	1.02	1.038	1.026	1.055	.60	1.265	.758	.584	1.67	.462	.79	2.108	.538	.620	.992
(i)	.68	1.04	1.04	.883	.918	.60	1.265	.806	.63	1.57	.498	.753	1.826	.502	.58	.949
(j)	.555	.87	.88	.675	.59	.375	1.173	.798	.617	1.469	.526	.725	1.538	.474	.560	.984
(k)	.505	.85	.865	.877	.752	.443	1.202	.771	.575	1.559	.4785	.773	1.832	.5215	.594	.995
(l)	.795	1.104	1.113	.761	.844	.605	1.267	.848	.752	1.495	.594	.64	1.410	.406	.491	.955
(m)	.652	.96	.92	.867	.815	.565	1.251	.824	.74	1.519	.592	.655	1.413	.408	.464	.99
(n)	.57	.945	.936	.54	.508	.308	1.144	.776	.617	1.475	.539	.71	1.456	.461	.573	.995

*Value scaled from velocity diagram of figure.

and form of flow in straight systems of parallel, staggered vanes. Such a picture is certainly needed for an attack on the problem of designing such a vane system for given flow conditions (i.e., given inlet and discharge velocity diagrams). However, the information given is not sufficient for a solution of the design problem.

One method of attack would be to select from the large number of cascade configurations that have been investigated the configuration which meets the prescribed operating (or flow) conditions. Such an attack would be possible if one could interpolate between the discrete vane system configurations that have been investigated. Reference 16 provides the means for this type of an attack on the design problem, namely the vane shapes and systems investigated by NACA.

In spite of the merits of the approach described in references 16 to 18, the method is still limited to the basic blade shapes used in these investigations and thereby to some common characteristics of their performance. The most significant shortcoming of the 65-series vanes affecting their use in pumps (or compressors) is probably the fairly large pressure reduction (and velocity increase) on the suction side of the vanes. According to section 2.5.4 and figure 1-18, the coefficient of minimum pressure $C_{p,min} = (p_1 - p_{min})/(\rho w_1^2/2)$ should not be greater than 0.3 to obtain acceptable cavitation performance. The NACA 65-series vane systems presented in figures 2-27(a) to (n) have in only one case a $C_{p,min}$ value as low as 0.308. The next lowest is 0.375, the next is 0.443, and all others are above 0.5. Cavitation-free performance, therefore, cannot be ensured by selection of a desirable 65-series system configuration; instead it is necessary to develop new configurations with more favorable pressure and velocity distributions. The same seems to be necessary for compressor vane systems.

A method of designing cascades of parallel, staggered vanes for prescribed vane pressure distributions is presented in chapter 3, specifically in sections 3.2.4 and 3.2.6 to 3.2.8. In this section only the basis of this design method is outlined; it is in the form of a particular method for the analysis of cascade test data, which may be called the first phase of the mean streamline method. This method relates the vane pressure distribution to the vane shape by means of the mean or average path of the plane flow through the vane system, which is called the mean streamline. These relations can be established definitely for vane systems which have been subjected to complete cascade tests, so that the vane pressure distribution is empirically known for given cascade and vane geometries and for known inlet and discharge velocity diagrams. The relations between vane pressure distribution and cascade and flow geometry, so established, are presented in dimensionless and otherwise generalized forms. It is reasonable to assume that they represent useful approximations of the corresponding relations for vane systems with geometries different from those which were investigated experimentally. The generalized relations between flow and cascade design characteristics are the basis for the mean streamline method of cascade design which is presented in chapter 3.

The construction of the mean streamline is based on the simple idea that the progressive changes in the circumferential component of the mean (or average) flow through a vane system can be related to the pressure distribution along the vanes, that is, to the distribution of the circumferential forces applied by the vanes to the flow. Furthermore the changes of the meridional (axial) component of the mean flow are related by the condition of continuity to the blockage effect of vanes with finite thickness and to the changes of the passage width normal to the plane of the cascade flow (actually a cylindrical surface). For compressible fluids, changes in the fluid density enter into this relation.

In principle, the method is quite old. This writer found it first in the initial edition (1924) of Pfleiderer's well-known book Die Kreiselpumpen (ref. 21) under the term point by point calculated vanes. In Pfleiderer's book, it is not the peripheral component and the meridional component of the velocity that are changed, but rather the magnitude of the relative velocity that is changed progressively from w_1 to w_2. (It is quite possible that the principles of this method were known before this application by Pfleiderer.)

The mean streamline method as outlined in this section is most directly described by Ackeret in reference 10, except for the fact that Ackeret obtained the relation between the mean streamline and the mean camber line of the vanes by theoretical means, whereas in the present treatment this relation is obtained on the basis of the NACA tests of 65-series vane systems.

The change in the meridional velocity component V_m is illustrated in figure 2-29. Evidently

$$\Delta Q = V_m \, \Delta b (t - \tau) N = V_m \, \Delta b \, tN \left(1 - \frac{\tau}{t}\right) \qquad (2\text{-}76)$$

where ΔQ is the volume flow rate passing through the annulus with the extent Δb in the meridional plane and normal to the meridional flow, and N is the number of vanes in any one system. The circumferential vane thickness τ should include an estimate of the displacement thickness of the vane boundary layers.

For incompressible fluids, ΔQ = constant. For compressible fluids, its changes have to be determined on the basis of the information given in section 2.4; these changes are discussed further in section 2.5.6.

It is evident that equation (2-76) is nothing but the condition of continuity between two meridional stream surfaces in a space of revolution. Under the one-dimensional assumption of uniform meridional velocity distribution over the entire cross section B-B in figure 2-29, one can substitute the total flow rate Q for ΔQ and the total width b for Δb. However, the following considerations are independent of this simplifying assumption.

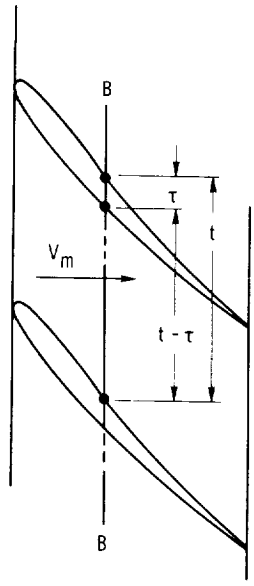

Development of section A-A

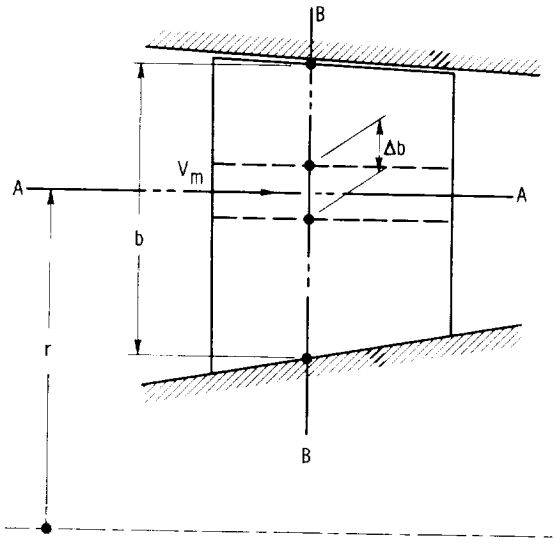

Figure 2-29. – Change in axial velocity component V_m.

The change in the peripheral velocity component w_U is determined by the equality of the change in circumferential momentum and the same component of the blade force (see fig. 2-30). This relation is, of course, essentially the same as that of Euler's turbomachinery equations (2-9 and 2-12). For the elementary step Δy in the axial direction, this relation assumes the form

$$\frac{\rho \, \Delta Q}{N} \frac{\partial w_U}{\partial y} \, \Delta y = \Delta F \cos \beta = \Delta p \, \Delta b \, \Delta l \cos \beta \qquad (2\text{-}77)$$

where N is the number of vanes.

By the condition of continuity, $\rho \, \Delta Q/N$ = constant. Furthermore $\Delta l \cos \beta = \Delta y$. Hence equation (2-77) appears in the form

$$\frac{\partial w_U}{\partial y} \, \Delta y = \Delta w_U = \text{constant} \times \Delta b \, \Delta p \, \Delta y \qquad (2\text{-}78)$$

Thus Δw_U is proportional to the elemental strip of the vane pressure diagram $\Delta p \, \Delta y$ if the vane pressure is plotted against the axial extent y of the vane system. This is the reason for this arrangement of plotting in figures 2-27, 2-30, and 2-31.

The schematic for the mean streamline method is illustrated in figure 2-31; the method may be described as follows: Determine the steps $\Delta w_{U,x}$ of the peripheral velocity component according to equation (2-78) in the form

$$\frac{\Delta w_{U,x}}{\Delta w_{U,tot}} = \frac{\Delta p_x \, \Delta y_x \, \Delta b_x}{\sum_a^f \Delta p_x \, \Delta y_x \, \Delta b_x} \qquad (2\text{-}79)$$

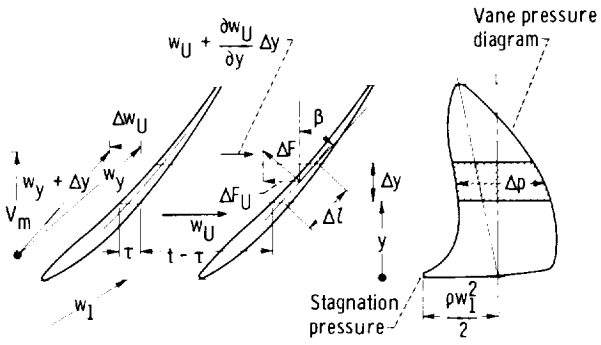

Figure 2-30. – Change in peripheral velocity component w_U in retarding vane system.

where the subscript x may designate any of the stations a to f along the mean flow path through the system. The sum $\sum_a^f \Delta p_x \, \Delta y_x \, \Delta b_x$ can be approximated by the area of the vane pressure diagram, plotted against the axial extent y, by

$$\sum_a^f \Delta p_x \, \Delta y_x \, \Delta b_x = \left(\sum_a^f \Delta p_x \, \Delta y_x \right) \Delta b_{av} \qquad (2\text{-}80)$$

For relatively large variations in Δb_x, the summation $\sum_a^f \Delta p_x \, \Delta y_x \, \Delta b_x$ must be carried out numerically, by using the local values of Δb_x.

The corresponding changes in the axial (meridional) velocity component V_m are determined according to the condition of continuity (eq. (2-76)). For incompressible fluids, $\Delta Q = \text{constant}$, and therefore

$$V_{m,1} t \, \Delta b_1 = V_{m,x} (t - \tau_x) \Delta b_x$$

or

$$\frac{V_{m,x}}{V_{m,1}} = \frac{t \, \Delta b_1}{(t - \tau_x) \Delta b_x} \qquad (2\text{-}81)$$

where the index x denotes stations a to f in figure 2-31, and Δb_1 and $V_{m,1}$ are measured in front of the vane system. Of course, one could also refer to $V_{m,2}$ and Δb_2 behind the vane system. For strictly axial-flow systems, obviously

$$t = t_1 = t_x = t_2 = \text{constant}$$

It has already been mentioned that τ_x should include an estimate of the displacement thickness of the vane boundary layers and will therefore not go

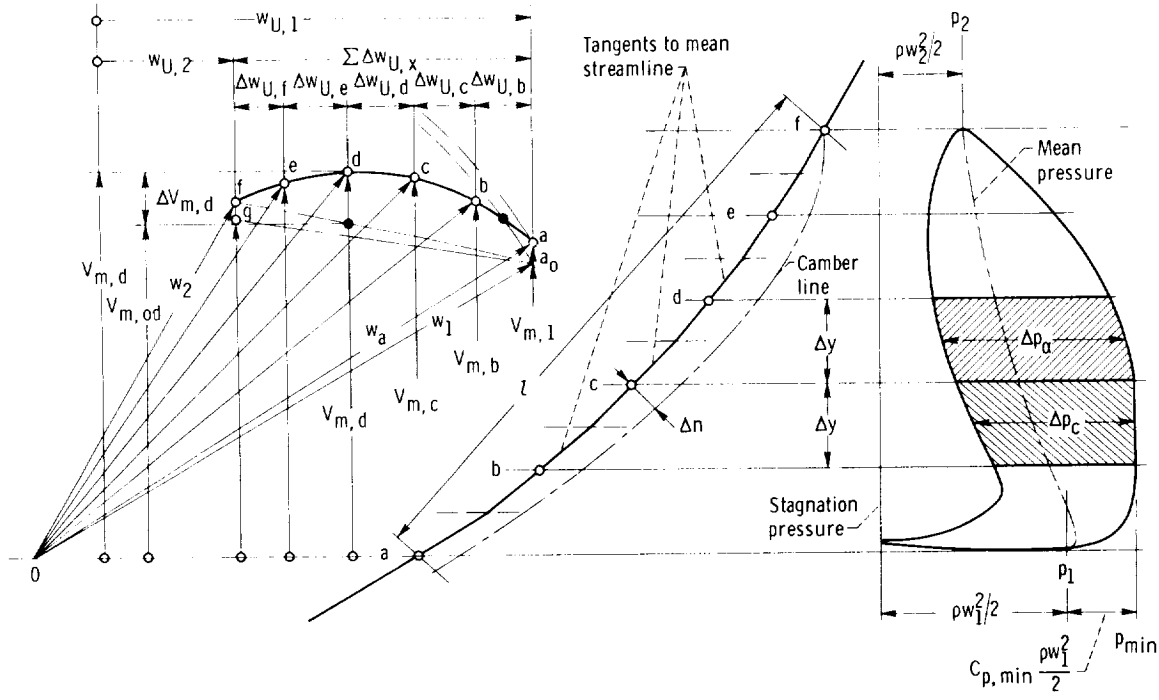

Figure 2-31. – Schematic for mean streamline method.

to zero behind the vane system. Figure 2-27 gives some indications of this effect. The boundary layers on the casing and hub walls can be considered by an appropriate (estimated) reduction of Δb or by an increased allowance for the displacement thickness of the vane boundary layers.

Often it is advantageous to account for boundary-layer growth and blade thickness separately by drawing a smooth curve (nearly straight line) a_0f in figure 2-31 from the end of the inlet velocity vector w_1 to the end of the discharge velocity vector w_2; this line includes an axial addition gf, allowing for boundary-layer effects on the meridional velocity component. The latter can include estimates of all boundary-layer effects. If so, the effect of blockage by the vane thickness τ alone (without boundary-layer effects) can be expressed as follows:

$$V_{m,o,x}t = (V_{m,o,x} + \Delta V_{m,x})(t - \tau_x)$$

The subscript o is defined in figure 2-31 as an example in connection with the station $x = d$. The foregoing equation can easily be converted into the form

$$\frac{\Delta V_{m,x}}{V_{m,o,x}} = \frac{\tau_x/t}{1 - \tau_x/t} \qquad (2\text{-}82)$$

If, as suggested previously, $V_{m,o,x}$ takes boundary-layer effects into account by being drawn to the line a_0f, then τ_x in equation (2-82) should not include the displacement thickness of the vane boundary layer, since all boundary-layer effects are considered in locating point f and thereby the line a_0f. This constitutes a substantial, practical simplification. The nonlinear growth of the boundary layer along the vane can be taken into account (qualitatively) by giving the line a_0f a slightly convex shape when seen from the top, that is, by letting the vertical distance between the line a_0g (the frictionless flow variation line) and the line a_0f increase slightly faster in the beginning (near a_0) than toward the end (near f).

With the points a, b, c, d, e, and f in the velocity vector diagram of figure 2-31 located according to equations (2-79) and (2-81) or (2-82), one can draw the intermediate mean velocity vectors from point 0 to the points a, b, c, d, e, and f along the curve af in the velocity vector diagram (in fig. 2-31) and construct the mean streamline by drawing its tangents at stations a, b, c, d, e, and f parallel to the corresponding mean velocity vectors. This construction defines the mean streamline.

From the analysis of existing cascade data the vane shape generating the vane pressure difference Δp_x and the corresponding changes in velocity from w_1 to w_2 are known. This vane shape, particularly its curvature, may now be characterized by the normal distance Δn between the mean streamline and the mean camber line (see figs. 2-31 and 2-27(a)); the location of these two lines relative to each other can be found by drawing the mean streamline through the trailing edge of the vane. Evidently the distance Δn describes the departure of the actual vane from its one-dimensional approximation, which is the mean streamline.

The normal distance Δn between the mean streamline and the camber line may, of course, be normalized by dividing it by the chord length l of the vane. The distance Δn can be further generalized by the assumption that it changes proportionately to the lift coefficient $C_{L,\infty}$ of the vane. This proportionality follows for a vane in a straight-line stream from geometric reasoning illustrated in figure 2-32, which shows two camber

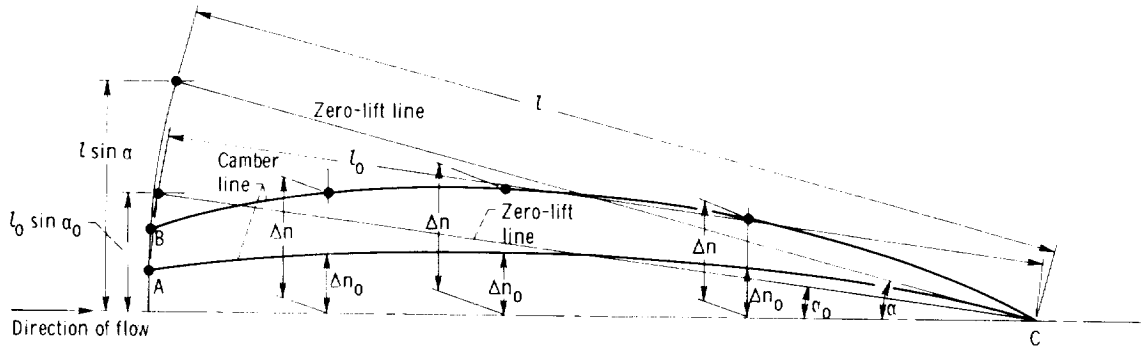

Figure 2-32. – Relation between departure Δn of mean camber line from direction of flow and lift coefficient expressed by angle of attack α between zero-lift line and direction of flow.

lines, one characterized by the subscript o and the other by symbols without subscripts. If the camber ratio $\Delta n/\Delta n_o$ is assumed constant along the vane and the small changes in the vane length l with changes in the camber are neglected, the sine of the angle attack α against the zero-lift line varies proportionally with Δn (at any one location). Since the lift coefficient $C_{L,\infty}$ is proportional to the sine of the angle of attack α measured from the zero-lift direction, it follows that Δn changes proportionally with $C_{L,\infty}$ in a straight stream. The application of this proportionality to the flow in a cascade of vanes, where the mean streamline describes the direction of the mean flow, confirms this theory. It is, therefore, permissible to define a standard, normal distance Δn_1 between the camber line and the mean streamline by $C_{L,\infty} = 1$, which leads to the relation

$$\Delta n_1 = \frac{\Delta n}{C_{L,\infty}} \tag{2-83}$$

In this manner, the deviations of the standard 65-series cascades represented in figures 2-27(a) to (k) could be brought into a reasonable relation to each other. Figure 2-33 shows as a heavy solid curve the maximum deviation $(\Delta n_1/l)_{max}$ for a unit of lift coefficient and for solidities from $l/t = 1.0$ to 1.5. For lower solidities, only one point (the diamond) was obtained from the configuration NACA 65-(18)-10, $\beta_1 = 45°$, $l/t = 0.5$ (ref. 16). It is natural that this configuration led to a higher $(\Delta n_1/l)_{max}$ than higher solidities, since zero solidity ($l/t = 0$) can easily be estimated to lead to a still higher value of approximately $\Delta n_1/l = 0.8$.

Figure 2-33 also shows as open double lines the maximum circumferential deviations $(\Delta t_1/l)$ between the mean streamline and the mean camber line. This representation of the deviation is far less advantageous than the normal deviation $(\Delta n_1/l)$, since $(\Delta t_1/l)_{max}$ forms two separate curves for $l/t = 1.0$ and $l/t = 1.5$ which are much steeper than the $(\Delta n_1/l)_{max}$ curve.

The distribution of the normal deviation Δn along the vane is shown in figure 2-34 in terms of the ratio $\Delta n/\Delta n_{max}$, where in all cases Δn_{max} has the value given by the heavy solid curve in figure 2-33. The shaded area in figure 2-34 covers the range of deviation distributions of the standard 65-series cascades shown in figures 2-27(a) to (k). The density of the shading represents qualitatively the frequency of deviation; that is, most deviations fall within the region bounded by two solid curves. The width of the shaded region around maximum

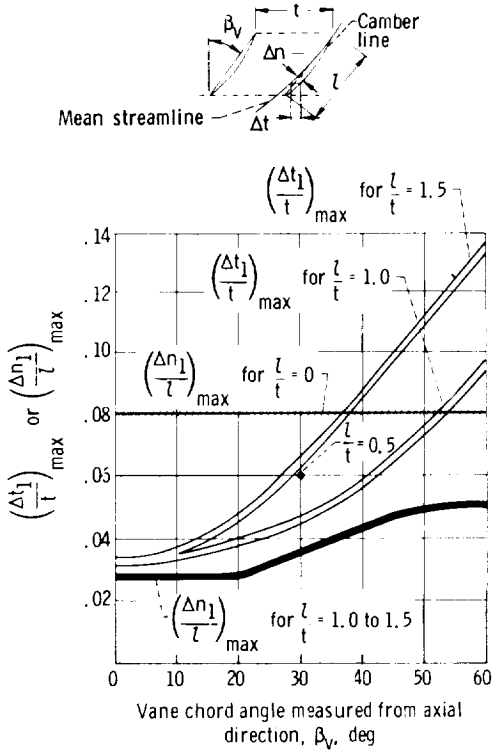

Figure 2-33. – Maximum deviation of camber line from mean streamline.

deviation represents the scatter of Δn_{max} around the solid curve shown in figure 2-33. The fact that this scatter is quite small for most cascades investigated (i.e., between the solid curves in fig. 2-34) demonstrates the validity of applying equation (2-83) to cascades of vanes, the accuracy being indicated by this scatter.

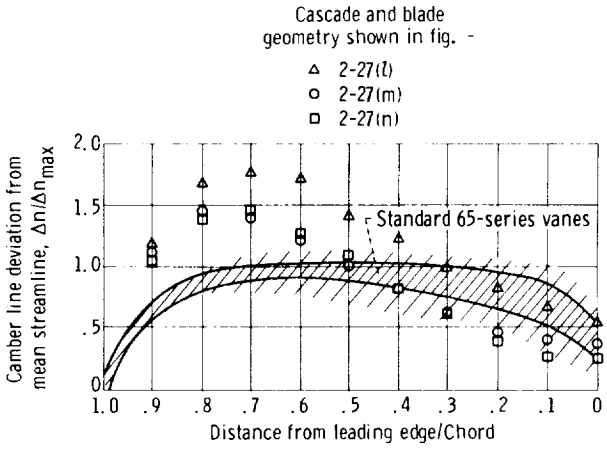

Figure 2-34. – Distribution of camber line deviation from mean streamline for cascade of vanes NACA 65-($18A_2I_{8b}$)10.

Also shown in figure 2-34 is the chordwise distribution of deviation for the trailing-edge-loaded vane profiles shown in figures 2-27(l) to (n), referred to the same Δn_{max} as shown by the heavy, solid curve in figure 2-33. The maximum deviation from the mean streamline for trailing-edge-loaded profiles is 40 to 70 percent larger than that for the standard 65-series profiles. Chapter 3 shows that the trailing-edge-loaded profiles are of particular importance for pump or compressor vane systems.

Assume that the deviations of the camber line from the mean streamline shown in figures 2-33 and 2-34 not only apply to the cascade forms from which these deviations were derived, but also are useful approximations for the same deviations of other cascade forms. Under this assumption the foregoing empirical derivation establishes a general relation between the vane pressure distribution and the form of the vane profiles. This relation is, of course, not as general as a relation based on theoretical considerations, for example, the method of Ackeret described in reference 10. The foregoing empirical derivation has, on the other hand, the advantage that it includes the effects of fluid friction on the overall flow, which would be difficult to achieve by theoretical means.

A relation between the vane pressure distribution and the form of the vane profile, as derived here, is reversible; that is, it can be used for the construction of the vane shape from a given or assumed vane pressure distribution. This process is described in chapter 3.

2.5.6 Effects of Compressibility on Flow Relative to Axial-Flow Vane Systems

The most important effects of compressibility on the flow in turbomachines, outlined in section 2.4, are applied in this section to the relative flow in axial-flow vane systems. The intent is not to present a complete description of this flow, but rather to characterize only some major effects of compressibility on this flow and to divide the flow conditions roughly into those of completely subsonic flow, completely supersonic flow, and flow with transition from supersonic to subsonic. As in section 2.5.5, only flow considerations forming the basis for the design of such vane systems (i.e., plane-flow cascades) are discussed, while the design problem itself is considered in chapter 3 (sec. 3.2.7).

The principles of subsonic flow (outlined in sec. 2.4) are essentially one-dimensional, and these principles alone are not sufficient to explain the general characteristics of supersonic flow and those of flow with transition from supersonic to subsonic. In this respect, the following outline is based on the methods established many years ago by Prandtl and Busemann (see refs. 22 (ch. IV), 4, 5, and 14 (ch. 19)). The considerations which follow may not be understandable without some knowledge of the philosophy of Prandtl and Busemann in dealing with the flow of compressible fluids.

The relation between the flow velocity and the pressure and density of a compressible fluid is described in section 2.4 on the basis of Bernoulli's flow-energy equation. As shown in section 2.5.1, this equation applies also to the relative flow in axial-flow vane systems, because the motion of the vane system appears in the development of cylindrical stream surfaces as a translatory or nonaccelerated, motion. Such a motion of the system has no influence on the laws of mechanics in the system, such as Bernoulli's equation. Therefore the velocity of the relative flow determines the specific volume and thereby the volume flow rate Q anywhere else in the system on the basis of its total enthalpy and the specific volume v at the system inlet.

In accordance with the principles outlined in section 2.5.5, the condition of continuity is used primarily with respect to sections parallel to the planes containing the leading and trailing edges of the vane system (see fig. 2-29) and involving the meridional velocity component V_m. As outlined in section 2.4, the determination of V_m from the geometry of the system requires a process of iteration, which converges as long as V_m does not approach sonic velocity. For given or assumed velocities, no iteration is required to determine the system geometry, unless the prescribed velocities lead to zero or negative vane thickness.

To obtain a first approximation of the flow entering and leaving an axial-flow vane system at any one cylindrical stream surface, assume that the width of the flow (b or Δb in fig. 2-29) normal to the cylindrical stream surface is constant. Furthermore assume that the thicknesses of the vanes and of the boundary layers have only negligible effects on the flow entering and leaving the system. Under these assumptions, figure 2-35

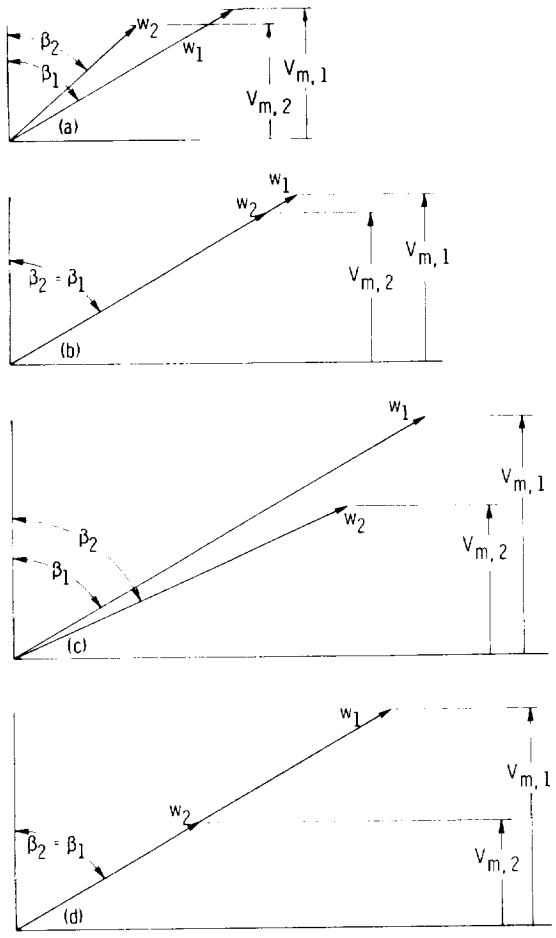

(*a*) *Completely subsonic flow.*
(*b*) *Sonic flow.*
(*c*) *Completely supersonic flow.*
(*d*) *Supersonic to subsonic flow entirely by normal shock.*

Figure 2-35. – Velocity diagrams for compressible flow in axial-flow cascades of constant width.

shows the relative inlet and discharge velocity vectors for four conditions:

(1) Subsonic inlet and discharge velocities relative to the system (cascade)
(2) Slightly supersonic inlet and slightly subsonic discharge velocities, that is, essentially sonic flow relative to the system
(3) Supersonic inlet and discharge velocities relative to the system
(4) Supersonic inlet and subsonic discharge velocities relative to the system, the change in velocity being entirely due to a normal shock in the system

Section 2.4 and references 22 and 14 show that (1) in subsonic flow the specific volume and thereby the volume flow rate change less than the flow velocity, (2) at sonic velocity the specific volume and volume flow rate change proportionally to the flow velocity and thus call for a constant cross section of the flow, and (3) in supersonic flow the specific volume and volume flow rate change faster than the flow velocity. With these statements and the fact that the axial velocity component V_m is proportional to the specific volume v and Q, the flow configurations in figures 2-35(a) to (c) become self-evident, considering that the velocity vectors shown represent average velocities along the vane system (in the circumferential direction).

Furthermore it should be evident that flow across a normal shock must be a flow of constant cross section, since the shock front is so thin as to prohibit any change in cross section of the flow normal to the shock front. This explains the flow configuration shown in figure 2-35(d), where any growth in boundary-layer thickness has been ignored.

Figure 2-35 indicates that subsonic cascade flow of constant width is curved in the same direction as but somewhat less than incompressible flow, sonic cascade flow of constant width has no net curvature (no change in direction from inlet to discharge), and completely supersonic relative flow curves in the opposite direction from incompressible flow. In the third flow, the convex side of the vanes faces the high-pressure side of the system. The fact that this does not involve any contradiction is demonstrated in figure 2-36 by means of the Prandtl-Meyer method of characteristics (see refs. 22 and 14).

The principle of this method is illustrated in figure 2-37. The flow changes direction only across Mach lines, which are inclined against the flow by the Mach angle α, for which $\sin \alpha = a/V =$ the reciprocal of the local Mach number. The law of momentum dictates that there cannot be any change in the velocity component parallel to the Mach line. The change in velocity and momentum normal to the Mach line must be small, a change from a small velocity difference below the local velocity of sound a to an equally small velocity difference above the velocity of sound. Thus the mean velocity normal to the Mach line is the velocity of sound a as has been evident by the Mach angle α. With the flow direction and the changes in the flow direction dictated by the direction of the flow boundary, these definitions permit the construction of a flow field from its boundaries by using the changes in the direction of the boundary in small, finite steps ($d\theta$, in fig. 2-37).

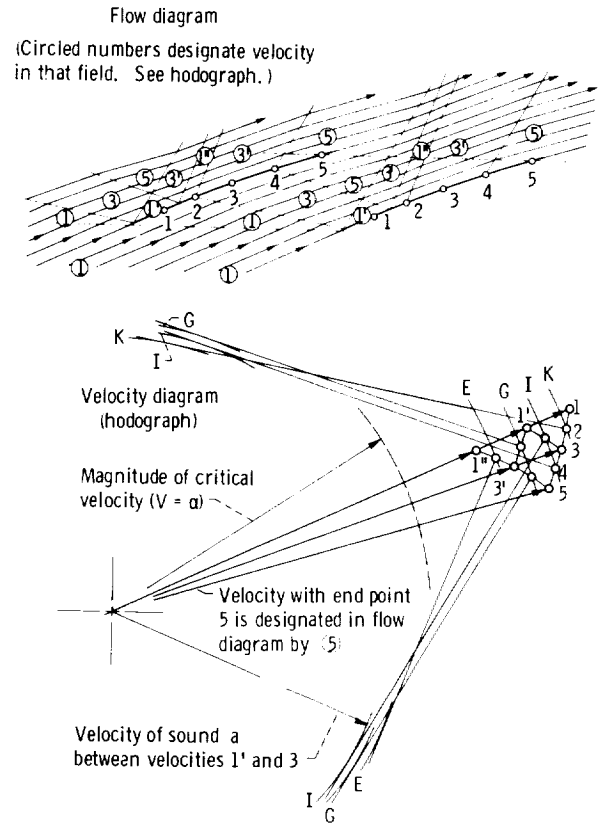

Figure 2-36. – Completely supersonic flow through system of parallel vanes.

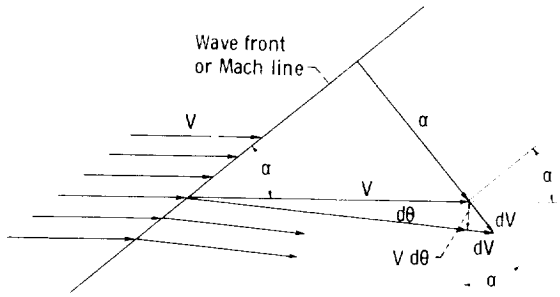

Figure 2-37. – Supersonic velocity change across Mach line.

A repeated use of this principle leads to the solution expressed by the velocity diagram (hodograph) in figure 2-36. The local acoustic velocities are correlated in the velocity diagram with corresponding flow velocities by the letters E to K. The numbers 1 to 5 denote the same velocities in the flow field and in the velocity diagram. Consider, for example, the flow field ③ on the concave side of the vane, which is opposite the flow field ③′ on the convex side of the vane. The velocity diagram gives the corresponding velocity vectors drawn to their end points 3 and 3′ and shows that $V_3 > V_{3'}$. Hence, according to Bernoulli's equation and the gas laws, $p_3 < p_{3'}$; that is, pressure on the convex side of the vane (field ③′) is higher than that on the adjacent concave side (field ③).

This discussion shows that the curvature of (thin) vanes in a system with completely supersonic flow does not constitute a contradiction regarding the pressure differences across the vanes and the entire system. Figure 2-36 actually established the theoretical feasibility of completely supersonic axial-flow compressors in the early days of this development.

Generally supersonic inlet flow into a vane system does not continue to be supersonic, but changes to subsonic flow by way of a normal shock within the system. However, the entire change in velocity does not have to take place in the shock, as assumed in connection with figure 2-35(d). First the flow may be retarded supersonically, then the normal shock takes place before the velocity drops to sonic, and after the shock the flow may be further retarded subsonically, but only slightly, because the shock causes a very rapid increase in boundary-layer thickness. The total flow resulting from supersonic inlet flow and subsonic discharge flow is, therefore, usually a successive combination of the flows described diagrammatically in figures 2-35(c), (d), and (a).

As mentioned previously, the foregoing considerations are based on the assumption of constant width b or Δb (fig. 2-29) normal to the flow section considered. This assumption may be negated for two reasons:

(1) The physical walls of the space of revolution in which this flow takes place may be changed so as to influence the axial velocity component V_m substantially. For example, the normal or radial width b might be changed proportionally to the specific volume v in order to keep the meridional (axial) velocity V_m constant. The shape of cylindrical flow sections through the system would then be (approximately) the same as that for an incompressible fluid with the same flow coefficient $V_{m,1}/U$ and the same circumferential deflection $\Delta w_U/U$. Additional corrections for compressibility pertaining to the local flow conditions are considered later.

(2) For radially deep vane systems, say for $D_h/D_o \leq 0.5$, one may encounter quasi-transonic flow conditions, supersonic relative inflow at the tip, and subsonic relative inflow near the hub. In such cases there may exist a radial interaction between coaxial stream surfaces of different diameters; that is, coaxial stream surfaces between the supersonic, sonic, and subsonic flow regimes may not be cylindrical. Early experiments with axial-flow rotors of this type showed this interaction to be favorable. Nevertheless it is evident that departures from flow between coaxial, cylindrical stream surfaces are of practical importance, although these departures are often difficult to predict.

Figure 2-35(a) indicates clearly that (at least in the subsonic flow regime) the ratio of retardation w_2/w_1 diminishes for fixed inlet and discharge angles β_1 and β_2 with increasing reduction in the fluid volume, that is, with diminishing ratio of the axial velocities $V_{m,2}/V_{m,1}$. Thus an increasing inlet Mach number w_1/a_1 leads to increasing flow changes in a given vane system and to an increasing rotor head coefficient $2gH_r/U^2$ until the limit of flow retardation w_2/w_1 is reached. Stall due to increasing Mach number is probably caused to a large extent, but not entirely, by this reduction in the relative velocity ratio w_2/w_1.

A few words should be said about the local effect of increasing Mach number of the inlet relative flow w_1/a_1 with particular reference to the previously mentioned case where the normal (radial) width of the flow is changed proportionally to the change in specific volume v, so that the average axial velocity component V_m as well as the inlet and discharge flow angles β_1 and β_2 can remain the same as for incompressible flow.

As indicated previously, the curvature of the flow of an incompressible fluid decreases rapidly with increasing distance from the curved boundary (see, e.g., fig. 2-8), since the spacing between the streamlines is a minimum near a convex boundary (because of maximum local velocity), is a maximum near a concave boundary, and approaches an average value away from the curved boundaries. This change in streamline spacing diminishes with increasing Mach number and approaches zero at sonic flow velocity (see, e.g., figs. 4.37 and 4.38 in ref. 22). Thus the cross-stream extent of the effects of boundary curvature into the flow field increases with increasing Mach number and calls for diminished vane curvature and thickness at increased Mach numbers, particularly near the leading vane edges of a retarding vane system (compressor) and near the trailing edges of an accelerating vane system (turbine).

The natural conclusion from these facts must not be driven to the extreme of an impossibility (choking) at a Mach number of 1, since, contrary to early expectations, axial-flow vane systems with slender vane ends have been operated quite successfully with sonic relative flow at their inlet and/or discharge, probably because of three-dimensional effects and the unending extent of actual vane systems in the circumferential direction. Nevertheless, for high Mach numbers of the relative flow, one should observe rules similar to those observed for flow with low cavitation numbers, that is, for low minimum-vane-pressure coefficients:

$$C_{p,min} = \frac{p_1 - p_{min}}{\rho w_1^2/2} = \frac{w_{max}^2 - w_1^2}{w_1^2} = \frac{w_{max}^2}{w_1^2} - 1 \quad (2\text{-}84)$$

This coefficient is directly related to the ratio of the maximum velocity at the vane to the average inlet (or discharge) relative velocity. For accelerating vane systems, w_1 in equation (2-84) is, of course, to be replaced by w_2.

Obviously the local w_{max} must be kept as low as possible in order to reduce detrimental compressibility or Mach number effects; that is, $C_{p,min} = w_{max}^2/w_1^2 - 1$ must be kept as close to zero as possible in order to minimize the Mach number effects in the extended field over which the local increase in Mach number is noticeable in a flow with high average Mach number. As mentioned previously, the same considerations apply to accelerating vane systems (turbines), where the discharge velocity and pressure (subscript 2) take the place of the inlet velocity and pressure in retarding vane systems (subscript 1), because $w_2 > w_1$ and $p_2 < p_1$.

As indicated previously, in the high subsonic and probably in the low supersonic flow regimes, design practices useful in the field of low cavitation numbers (high suction specific speeds) apply also to vane systems with high Mach numbers of the relative flow. This writer has found this reasoning to be of considerable practical value, as long as changes in the average specific volume and the

resulting changes in the overall volume flow rate Q are properly taken into account. Thus the fields of hydrodynamic machinery design (with respect to cavitation) and gas-dynamic machinery design (with respect to Mach number effects) can clearly benefit from each other. The pertinent vane design considerations are presented in some detail in chapter 3.

2.5.7 Secondary Flow in Axial-Flow Vane Systems Generated by Boundary-Layer Effects

In the beginning of section 2.5 it is stated that the flow in axial-flow vane systems can be assumed to proceed along coaxial, cylindrical stream surfaces. However, there are several reasons why this assumption is not correct in all parts of the flow.

Flow departing from the coaxial stream surfaces of revolution prescribed by the meridional velocities, here cylindrical surfaces, or from the associated condition of continuity, is called secondary flow. The basic reason for such secondary flow is usually the existence of vorticity in the flow, that is, the existence of departures from the so-called potential or ideal flow pattern. The principles of flow with vorticity are outlined in section 2.6.3.1.

There are at least three reasons for the existence of vorticity in the relative flow of turbomachinery rotors:

(1) The relative flow in the rotor has in sections normal to the axis of rotation a vorticity $\zeta_{rel} = -2\omega$, where ω is the absolute angular velocity of the rotor. The existence of this vorticity is explained in section 2.6.3.2, where vorticity is of major importance, because at least a component of it is effective in the meridional stream surfaces of radial-flow rotors. However, in axial-flow rotors this vorticity does not affect the flow in cylindrical stream surfaces, because the vorticity vector $\vec{\zeta}_{rel}$ has axial direction and, therefore, has no component normal to the meridional stream surfaces. For this reason, the frictionless, relative flow along these surfaces can be treated as irrotational, as stated in section 2.5.1.

Furthermore it is shown in appendix 2-A that this vorticity does not generate secondary fluid motions, because its effect is fully covered by the circumferential component of the relative flow if the absolute flow is irrotational. Therefore the vorticity $\zeta_{rel} = -2\omega$ does not have to be considered in this section.

(2) Vane systems with radially nonuniform vane circulation shed a trailing vorticity into the stream which is parallel to the relative flow. This vorticity, along with its effect on secondary flow, is treated in section 2.7 and is, therefore, not considered here.

(3) The vorticity which is considered in this section is that generated by fluid friction on the vane surfaces and on the cylindrical (or nearly cylindrical) walls bounding the flow space of an axial-flow machine. The effects of vane boundary layers are described qualitatively according to figure 2-38 (see also ch. XV of ref. 6).

The effects of the boundary layers on the cylindrical casing and hub surfaces are outlined in accordance with the work by Leroy Smith, presented in reference 23. They are caused by a secondary fluid motion shown in figure 2-39, but their most important effect is a flow along the meridional stream surfaces at the spanwise ends of the vanes.

As yet, quantitative predictions of the boundary-layer effects described in this section have not reached the simplicity necessary for preliminary design. The qualitative descriptions given in the following discussion are all that can be offered to guide the design engineer.

Figure 2-38 represents diagrammatically the secondary motion which is due to the rotor blade boundary layers of axial-flow machines. In the boundary layer, the relative velocity w_L *is smaller than the relative velocity* w_o outside the boundary layer. For blades staggered in the usual manner of

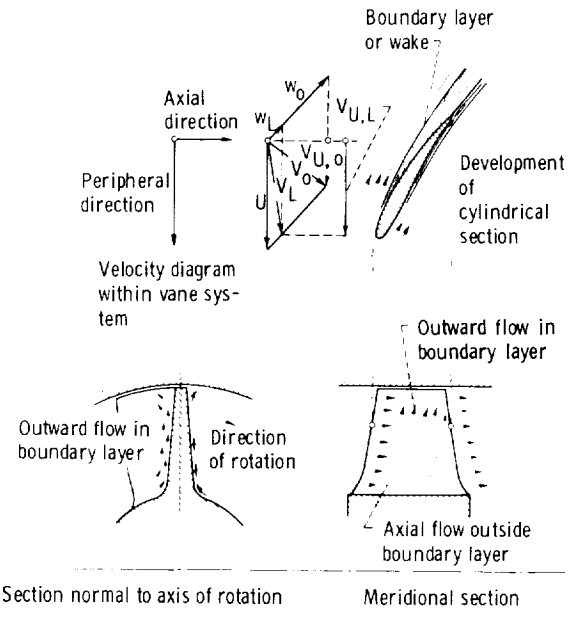

Figure 2-38. – Radial motion of blade boundary layer in axial-flow rotor.

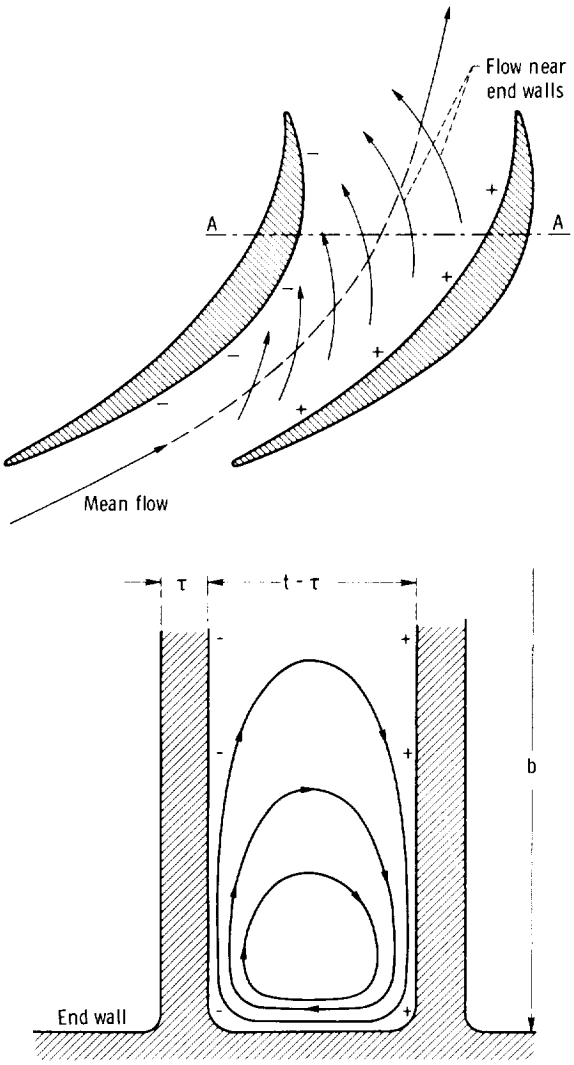

Figure 2-39. – Secondary end flow in axial-flow vane system.

axial-flow rotors, as shown in figure 2-38, the circumferential component of absolute velocity V_U is larger in the boundary layer than outside the boundary layer ($V_{U,L} > V_{U,o}$). The fluid is dragged along in the circumferential direction by the rotating blades. With the radial pressure gradient dictated by the circumferential component of the absolute flow outside the boundary layer ($V_{U,o}$), the faster rotating fluid in the boundary layer is centrifuged out, and the outward motion in the boundary layer indicated in figure 2-38 is generated.

This radial outward motion in the boundary layers of rotor blades causes a thickening of the blade boundary layers in the tip section. The tip section of the blade is, therefore, likely to stall earlier than would be expected without the radial motion of the boundary layer. For the same reason, the boundary layer of the root section of rotor blades is thinner than would be expected without this secondary motion. In fact, tip sections of rotor blades often stall earlier than the root section, although the root section usually has a higher lift coefficient $C_{L,\infty}$ and a more serious retardation (lower ratio of w_2/w_1) than the tip section and, therefore, should, according to figure 2-26, be more likely to stall than the tip section. The practical design consequence is that one must be much more conservative with respect to separation or stall at the tip section than at the root section of axial-flow rotor blades. However, no general quantitative information on this difference in stall characteristics between root and tip sections of axial-flow rotor blades is as yet available.

The first experimental observation known to this writer of this effect of the radial motion of rotor blade boundary layers was published in 1944 by Weske in reference 24.

A corresponding but opposite (radially inward) motion of the vane boundary layer exists in axial-flow stator vane systems if the flow through the system has a substantial circumferential component. Then the radial pressure gradient is generated by the circumferential component of the (absolute) velocity outside the boundary layer. Since the same velocity component inside the boundary layer is lower, the boundary layer cannot sustain the radial pressure gradient and is moved in the radial inward direction. As a consequence, the vane boundary layer is thickened at the root sections of the stator vane system and, therefore, tends more toward separation than it would if the radial motion did not exist. For the root section of stator systems, one should use separation criteria more conservative than those suggested by figure 2-26. Inversely one can be slightly more aggressive at the outer tip section of the stator, always under the assumption that the flow through the stator system has a substantial circumferential component.

Rotor or stator vane systems with substantially axial vane sections (see, e.g., figs. 2-27(b) and (c)) do not have significant radial motion of their vane boundary layers. Therefore information on separation or stall limits presented in section 2.5.4, particularly in figure 2-26, applies to these systems without modification.

There exists another type of secondary motion in axial-flow vane systems which should be briefly described, although its consideration in the design of such vane systems is even more difficult than that of radial boundary-layer motions along the blades. This additional secondary motion is generated by the boundary layers of the outer and inner cylindrical walls (shrouds). Together with the main flow, these boundary layers are turned (or deflected) by the vane system in the circumferential direction. It is well known that this kind of motion of a boundary layer (a layer of shear flow) leads to a secondary fluid motion, as shown diagrammatically in figure 2-39. This secondary motion can be explained in several ways. It is essentially the same motion as that existing in an ordinary pipe bend or elbow in the form of a pair of vortices with their axes in the direction of the main flow.

A simple, physical explanation of this secondary flow is as follows: The curved main stream between the curved vanes generates (by centrifugal forces) a pressure gradient across the stream (i.e., a pressure increase on the concave side and a pressure reduction on the convex side of the vanes). This pressure difference is determined by the flow outside the boundary layers of the end walls. Therefore the boundary-layer flow of reduced velocities cannot sustain this pressure difference without being curved more sharply than the main flow and thus deflected toward the low-pressure side of the channel. It is customary to describe this secondary motion as overturning of the end wall boundary layer. To satisfy the condition of continuity for this secondary motion, one must assume that the main flow outside the end wall boundary layers is displaced slightly toward the high-pressure (concave) wall of the channel, and thus the curvature (deflection) of the main flow is slightly reduced. In unshrouded pump rotors, this secondary motion is reduced by friction on the wall having the opposite motion relative to the system. This secondary motion is increased by the same wall friction effect in turbine rotors.

The same secondary motion has been explained in a more exacting manner by Hawthorne (ref. 25) on the basis of Helmholtz' vortex law that vorticity remains connected to the fluid. The vorticity representing the velocity gradient in the boundary layer is a vector normal to the boundary-layer flow in front of the vane system and parallel to the end walls. This vorticity vector remains connected to the fluid particles and, therefore, does not continue to be normal to the flow as the flow is turned by the vanes. If the vorticity vector is not normal to the flow, it has necessarily a component in the direction of the flow which describes the secondary motion. Hawthorne demonstrated the validity of this reasoning experimentally. (It should be understood that the first explanation given in this section and the more rigorous explanation by Hawthorne are not fundamentally different.)

Quantitative predictions about the effects of this secondary motion obviously depend on the thickness of the end wall boundary layer in relation to some other significant linear dimension of the system. Such a dimension may be the vane spacing t, $t-\tau$, or the width of the system b. Furthermore the boundary-layer thickness depends on the configuration of the passages ahead of the vane system in a somewhat complicated manner. The probability that quantitative predictions can be made for design purposes is, therefore, somewhat remote and is not considered further in this section.

It is somewhat improbable that δ would be proportioned to b, for multistage units. Under the natural assumption that greater end motion effects occur with larger δ/b, the condition that δ increases with t leads to the result that the aspect ratio b/t determines the effect of this end motion on performance and design. The larger the aspect ratio b/t, the smaller the end motion effect. However, even for $b/t \leq 1$, one usually ignores the end motion effects because of the present lack of knowledge on how this effect might be taken into account. It is even possible that the overturning in the end region might have a favorable effect on pump or compressor rotors by increasing the work input in the end region. If this reasoning were to some degree correct, it would imply that the same phenomenon should have an unfavorable effect on turbines, where it would increase the flow energy withdrawal from the end regions.

There is at least one other real flow effect causing local secondary motions; it is the leakage stream past the ends of unshrouded vanes. This stream often produces at its downstream side a significant vortex with its axis not quite parallel to the suction side of the vane tip section. Again no simple way has been suggested to predict the effect of this vortex on the performance or on the design of the vane system.

As mentioned previously, the secondary motions can also be produced in a frictionless fluid by spanwise nonuniform vane circulation, so that a trailing vorticity is shed into the main stream in accordance with Prandtl's wing theory. This type of

secondary motion is discussed in section 2.7, which includes a summary of all types of secondary motions.

2.6 Theoretical Background of Hydrodynamic Design of Radial-Flow Turbomachinery

2.6.1 Introduction

The term radial-flow turbomachinery, as used in this section, denotes turbomachinery in which the flow through the rotor has a substantial radial component. By this definition, the term is not limited to purely radial-flow machines, like that shown, for example, in figure 2-40, but also includes conical-flow machines (called mixed-flow machines), like that shown in figure 2-41, as well as machines where the meridional flow in the rotor changes from axial to more or less radial (see figs. 1-7 and 1-25).

Radial-flow rotors are hydrodynamically distinct from axial-flow rotors because coaxial stream surfaces composed of the meridional flow have changing radii (distances from the axis of rotation) and, therefore, the vane systems of such rotors have changing circumferential velocity $U(r)$ through the rotor. Thus analysis of the relative flow through such rotors must take account of the acceleration of this flow as a consequence of the change in radius. This acceleration exists regardless of the existence or absence of changes in the angular velocity of the system. Because of this acceleration, the relative flow along the stream surfaces of the meridional flow in radial- or mixed-flow rotors cannot be the same as the flow relative to the same system at rest, since an accelerated motion of the system changes

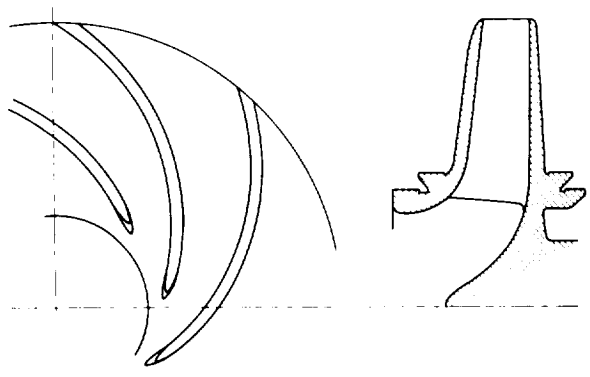

Figure 2-40. – Radial-flow centrifugal pump impeller.

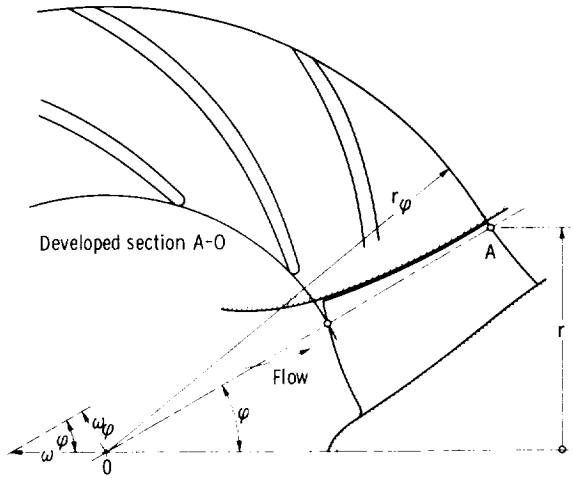

Figure 2-41. – Mixed-flow or conical-flow pump impeller.

the laws of mechanics for motions relative to the system. This change in flow is expressed most effectively by the so-called vorticity of the relative flow in rotating, radial-flow systems, as discussed in section 2.6.3.2.

It should be recognized that this situation is different from that described in section 2.5 for the flow within the cylindrical stream surfaces of an axial-flow rotor, where the motion of the vane system in the plane development of this surface is not accelerated (at uniform angular velocity of the rotor) and, therefore, follows the laws of mechanics of a stationary system. This difference between radial- and axial-flow vane systems is responsible for the fact that the relative flow within a cylindrical flow section through an axial-flow rotor can be simulated by tests with a stationary vane system (cascade tests), whereas the flow through rotating, radial-flow vane systems cannot. It should be noted that the flow in an axial-flow rotor as a whole is not the same as that for a corresponding stationary vane system, since the flow in different cylindrical sections has quite different relations from section to section for a rotating system than for a stationary system.

The distinction outlined here between radial- and axial-flow rotor vane systems is the only fundamental hydrodynamic difference between them. However, there are other important distinctions of a less fundamental nature that need to be considered in the theoretical background of radial-flow turbomachinery design.

Usually radial- and mixed-flow vane systems have a higher solidity (vane length-spacing ratio) than axial-flow vane systems. Furthermore the

aspect ratio (vane span-length ratio) is usually much lower in radial-flow than in axial-flow machines. Both distinctions lead to a greater influence of real-flow effects on the flow in radial-flow systems than in axial-flow systems. While this may increase the skin friction and resulting secondary flow losses in radial-flow machines, the useful action of a single, radial-flow rotor is usually larger in relation to the velocity head than that of a single-stage axial-flow rotor. It is apparently for this reason that single-stage, radial-flow machines have been developed to efficiencies as high as (or higher than) those of axial-flow machines.

Because of the increased importance of real-flow effects, the design of radial-flow machines depends more on empirical data than the design of axial-flow machines. This dependence is also due to the strongly three-dimensional flow in radial-flow rotors, which involves transition from axial to radial flow. Even under ideal flow conditions, this three-dimensional flow problem is not near a solution, nor are the complex real-flow effects under such three-dimensional flow conditions.

The resulting design problems of radial- and mixed-flow machines are discussed in chapter 4. This section presents only that part of the theoretical background that can be applied to the design of radial-flow machines in a simple and straightforward manner.

2.6.2 Flow and Design Principles of Stationary, Radial-Flow Vane Systems

Consider the flow in a stationary, radial-flow vane system, where the aforementioned problem resulting from the rotation of the system does not exist.

Stationary, radial-flow vane systems are usually used as diffusers around the outside of pump or compressor rotors (impellers) with radial outward flow, or as nozzle rings or guide-vane systems around the outside of turbine rotors with radial inward flow. In pumps and compressors, the guide vane system receives a flow with substantial angular momentum from the inside (i.e., from the impeller), and in turbines, a flow with or without angular momentum from the outside, which discharges with strong angular momentum.

The flow is considered frictionless, incompressible, and, as a first approximation, two-dimensional and plane, that is, as proceeding between two parallel walls normal to the axis of rotation.

Consider first a circumferentially and axially uniform flow in such a space of revolution without vanes. This flow may be regarded as the basic flow which is to be altered by the action of the vanes.

For the radial component V_r the condition of continuity demands that the volume flow rate be

$$Q = 2\pi r b V_r = \text{constant} \tag{2-85}$$

where b is the depth of the flow normal to the plane of the flow (i.e., in the direction of the axis of rotation) and is assumed to be constant. Hence

$$V_r = \frac{Q}{2\pi b}\frac{1}{r} = \frac{\text{constant}}{r} \tag{2-86}$$

In the absence of any circumferential force acting on the flow, this flow satisfies the law of constant angular momentum:

$$V_U = \frac{\text{constant}}{r} \tag{2-87}$$

The direction of a streamline of this flow, measured from the radial direction, is obviously

$$\tan\beta = \frac{V_U}{V_r} = \text{constant} \tag{2-88}$$

which characterizes the streamline as a logarithmic spiral (i.e., a spiral with constant inclination β against the radial direction). Its equation is

$$\varphi - \varphi_1 = \tan\beta \ln\frac{r}{r_1} \tag{2-89}$$

where φ is the angular coordinate, r is the distance from the center of the polar system, and φ_1 and r_1 are constants.

The rotating and radial outward flow between two parallel walls, having theoretically this form of streamlines, is called the flow of a vaneless diffuser or, hydrodynamically, the flow of a vortex source, and the corresponding inward flow that of a vortex sink. Except for real-flow effects discussed later, vanes are needed in such a system only if departures from the natural flow of constant angular momentum are desired.

The flow in stationary, radial-flow vane systems is closely related to the flow through straight systems of parallel vanes, which is discussed in section 2.5 in connection with the flow through axial-flow systems. In fact, one such flow can be transformed into the other by a process of conformal mapping, a transformation which preserves geometric similarity in infinitely small regions everywhere in the two pictures compared. If the orthogonal (Cartesian) coordinates of the

straight system of parallel vanes are designated x in the tangential direction and y in the axial direction and φ and r are the circumferential and radial coordinates of the radial-flow (polar-coordinate) system, the conformal transformation of one system into the other is described by

$$\left.\begin{aligned} x &= a\varphi + b \\ y &= a \ln r + c \end{aligned}\right\} \qquad (2\text{-}90)$$

It follows that

$$\left.\begin{aligned} dx &= a\,d\varphi \\ dy &= a\frac{dr}{r} \end{aligned}\right\} \qquad (2\text{-}91)$$

which show that the inclination of any line in one system is equal to the inclination of the corresponding line in the other system, since

$$\frac{dy}{dx} = \frac{dr}{r\,d\varphi} \qquad (2\text{-}92)$$

It can also be seen that an inclined, straight line in the Cartesian system described by the equation

$$y = mx + n \qquad (2\text{-}93)$$

and having an inclination against the x-direction of

$$\frac{dy}{dx} = m \qquad (2\text{-}94)$$

is transformed into a logarithmic spiral with the same inclination against the peripheral direction. Substituting equations (2-90) into equation (2-93) leads to

$$a \ln r + c = ma\varphi + mb + n$$

$$\frac{1}{m}\ln r = \varphi + \frac{mb + n - c}{ma} = \varphi + \text{constant} \qquad (2\text{-}95)$$

which is indeed a logarithmic spiral with the inclination $1/m$ against the radial direction or the inclination m against the peripheral direction. (The term inclination denotes here the tangent of the angle of inclination.)

An orthogonal network of lines $x = \text{constant}$ and $y = \text{constant}$ in the Cartesian system (straight system of parallel vanes) is transformed by equations (2-90) into an orthogonal network of lines $\varphi = \text{constant}$ and $r = \text{constant}$ in the polar (radial-flow) system. Constant spacing Δx of the $x = \text{constant}$ lines results, according to equation (2-91), in constant angular spacing $\Delta\varphi = \Delta x/a$ of the radial lines, and constant spacing Δy of the $y = \text{constant}$ lines results in a radial spacing Δr of the circles $r = \text{constant}$, which, according to equation (2-91), is proportional to r, that is,

$$\Delta r = \frac{\Delta y}{a} r = \text{constant} \times r \qquad (2\text{-}96)$$

A system of parallel curved vanes in the Cartesian system is transformed into an equivalent system of vanes in the radial-flow system simply by giving corresponding points along the vane contours the same locations relative to the two networks of orthogonal coordinate lines just derived. Figure 2-42 shows this transformation.

The laws of fluid mechanics state that a conformal transformation of a plane, irrotational

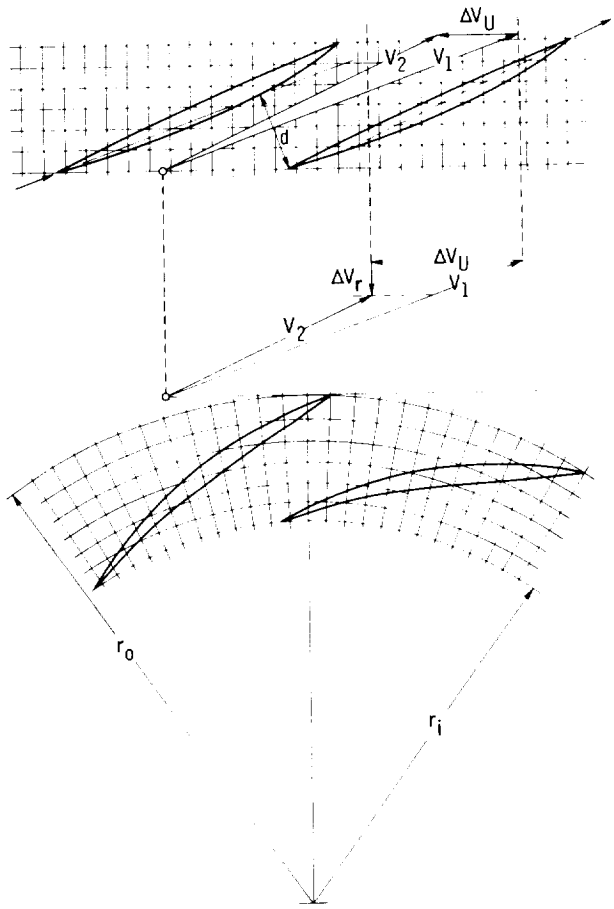

Figure 2-42. – Conformal relation between stationary, radial-flow vane system and straight cascade of vanes.

flow (see appendix 2-A) of a frictionless, incompressible fluid results in a flow obeying the same laws. This means that a plane, irrotational flow through the system of straight and parallel vanes is transformed into an equally valid flow through the radial flow vane systems, with all flow angles measured from the respective coordinate lines being the same in both systems. For example, with the inlet flow angle (measured from the axial and radial directions, respectively) the same in both systems, the discharge flow angles are also the same in both systems. The angular departures of the frictionless flow from the one-dimensional approximations are also the same, and all theoretical information available on the frictionless, incompressible flow through straight systems of parallel vanes (such as Weinig's results given in sec. 2.5) applies to the conformal, stationary, radial-flow system. (Weinig's results apply directly to a radial-flow system of thin vanes curved as logarithmic spirals, which may be regarded as the zero-lift direction of other radial-flow vane systems.)

The correspondence between the two flow pictures compared has so far been described only by the equality of flow angles relative to the two coordinate systems. However, the velocities in the two systems, while not equal, also have a very simple relation to each other. If the condition of continuity of an incompressible fluid in both systems is to be satisfied, the product of the velocity and any characteristic linear dimension of the system must stay the same, because in a plane, two-dimensional system a linear dimension is equivalent to an area, since the dimension normal to the plane is constant. Thus the velocities at corresponding points of the two systems are related by the local, linear scale ratio, which, according to equations (2-92) and (2-91), is

$$\frac{r\,d\varphi}{dx} = \frac{dr}{dy} = \frac{r}{a} \tag{2-97}$$

This is the local radial flow system scale divided by the scale of the straight system. When the velocities in the straight system are designated V_{str} and velocities at corresponding points of the radial system V_{rd}, the velocity ratio becomes

$$\frac{V_{rd}}{V_{str}} = \frac{a}{r} \tag{2-98}$$

The factor a is a constant scale ratio of the drawings compared. For example, if one sets the scale ratio equal to 1 at any particular radius r_1 of the radial system, so that $r_1/a = 1$ or $a = r_1$, then

$$\frac{V_{rd}}{V_{str}} = \frac{r_1}{r} \tag{2-99}$$

Velocities in the two systems are, therefore, definitely related by magnitude as well as direction.

There exists an extremely important limitation regarding the equivalence of flow pictures related by a conformal transformation.

As observed previously, all statements regarding conformal transformations of flow pictures pertain only to frictionless fluids. Therefore the equivalence between conformal flow pictures does not apply to any phenomena related to fluid friction, such as viscosity and turbulence. This can be demonstrated best in connection with the most important effect of fluid friction, namely, separation or stall.

In section 2.5.4, separation is related to the pressure rise along the low-pressure side of the vanes. There is no obvious reason why this criterion should not apply to stationary radial-flow vane systems, and it is so applied throughout this compendium. However, the specific results derived from this principle change as a result of a conformal transformation. This should be obvious from the fact that the pressure rise from the point of minimum pressure to the trailing end of the blade changes according to the difference in the square of the local scale ratio between these two points and produces an additional change in velocity and thereby an additional change in pressure.

A fairly exact consideration of this effect would probably be too complex for design purposes and hardly justified in view of the highly approximate character of all calculations regarding separation. However, a first approximation is very simple to achieve.

The ratio of discharge to inlet velocity is of major significance and is used as one of the principal variables. Assume that this ratio is $V_{2,str}/V_{1,str}$ in the straight system of parallel vanes. To simplify the consideration without any real loss in generality, one may assume that the local scale ratio is unity at either r_1 or r_2, say at r_1, so that $V_{1,str} = V_{1,rd}$. The ratio of velocity change in the radial system is then

$$\frac{V_{2,rd}}{V_{1,rd}} = \frac{V_{2,str}}{V_{1,str}} \frac{V_{2,rd}}{V_{2,str}} \frac{V_{1,str}}{V_{1,rd}}$$

From equation (2-99), $V_{2,rd}/V_{2,str}=r_1/r_2$. With $V_{1,str}=V_{1,rd}$, it follows that

$$\frac{V_{2,rd}}{V_{1,rd}}=\frac{V_{2,str}}{V_{1,str}}\frac{r_1}{r_2} \tag{2-100}$$

Assume, for example, that the radial-flow system is an outward flow system, so that $r_2>r_1$; then

$$\frac{V_{2,rd}}{V_{1,rd}}<\frac{V_{2,str}}{V_{1,str}}$$

which means that with retarded flow in the straight system ($V_{2,str}/V_{1,str}<1$) the retardation in the radial outward flow system is more severe than that in the straight system. For design purposes, one can set a lower limit for $V_{2,rd}/V_{1,rd}$ according to section 2.5.4 and figure 2-26 and then determine $V_{2,str}/V_{1,str}$ from equation (2-100) so that the limit of $V_{2,rd}/V_{1,rd}$ is not violated. In other words, separation limits must be considered in connection with the finally desired system and must be computed by means of equation (2-100) to establish the conformal system to be used to develop the final system.

In addition to the effects of fluid friction, there are other limitations on the use of conformal mapping, such as compressibility and nonuniformities in the axial width of the vane systems. Such departures from the ideal conditions can be handled by approximate corrections, which are discussed in chapter 4 in connection with the practical design of stationary, radial-flow vane systems. The same is true for the design of such systems by methods different from those of a conformal transformation from a straight system of parallel vanes.

2.6.3 Flow Through Rotating Radial-Flow Vane Systems

2.6.3.1 Summary of laws of incompressible, frictionless flow. – This section merely states the laws of incompressible, frictionless flow used in this and later sections. The derivations of these laws are presented in appendix 2-A, and the equation numbers are those used in the appendix. Particular attention is given to the laws of vorticity.

From section 2-A.1, with u and v denoting the velocity components in the Cartesian coordinate directions x and y, the condition of continuity is

$$\frac{\partial u}{\partial x}+\frac{\partial v}{\partial y}=0 \tag{2-A-1}$$

and the condition of irrotational flow is

$$\frac{\partial v}{\partial x}-\frac{\partial u}{\partial y}=0 \tag{2-A-16}$$

(The term irrotational is also used where the entire flow rotates about one center at radially uniform angular momentum, which satisfies eq. (2-A-16).)

Equations (2-A-1) and (2-A-16) together satisfy the general momentum equations by Euler for any plane, frictionless flow. Equation (2-A-16) expresses the fact that a fluid particle dx,dy does not rotate and that the circulation around this particle is zero.

The general momentum equations by Euler can also be satisfied by equation (2-A-1) and the condition that for any fluid particle

$$\frac{d\zeta(x,y)}{dt}=0 \tag{2-A-19}$$

where

$$\zeta(x,y)\equiv\frac{\partial v}{\partial x}-\frac{\partial u}{\partial y} \tag{2-A-17}$$

and is called the vorticity of the flow.

Equation (2-A-19) expresses the second vortex law by Helmholtz: The vorticity $\zeta=\partial v/\partial x-\partial u/\partial y$ of a particle of a frictionless fluid does not change with time; that is, the vorticity remains connected to the fluid. Consequently the vorticity is constant along the streamlines of such a fluid in steady motion.

The vorticity describes the rotation of a fluid particle according to the relation

$$\omega=\frac{1}{2}\zeta(x,y) \tag{2-A-23}$$

where ω is the average angular velocity of the fluid particle.

The circulation around a fluid particle dx,dy is

$$d\Gamma=\zeta(x,y)dx\,dy \tag{2-A-25}$$

that is, the circulation is equal to the vorticity of the particle times its area (or volume).

The circulation along a finite, singly connected, closed contour C is equal to the (algebraic) sum of all circulations inside the contour:

$$\Gamma_{around\ C} = \Sigma\Gamma_{within\ C} \tag{2-A-26}$$

As a consequence, the circulation about a finite contour is

$$\Gamma = \iint \zeta(x,y)dx\,dy \tag{2-A-27}$$

where the integrals cover the area inside the contour.

The vorticity in polar coordinates is

$$\zeta(r,\varphi) = \frac{V_U}{r} + \frac{\partial V_U}{\partial r} \tag{2-A-28}$$

where V_U is the circumferential velocity component. The vorticity is connected with the radial change in the angular momentum, or moment of momentum rV_U, as follows:

$$\zeta(r,\varphi) = \frac{1}{r}\frac{\partial(rV_U)}{\partial r} \tag{2-A-29}$$

Therefore a curved, irrotational flow ($\zeta(r\varphi) = 0$) is a flow with radially constant angular momentum (rV_U = constant) about the center of curvature.

From section 2-A.2, with u, v, and w denoting the velocity components in the directions of the Cartesian coordinates x, y, and z, the condition of continuity is

$$\frac{\partial u}{\partial x} + \frac{\partial v}{\partial y} + \frac{\partial w}{\partial z} = 0 \tag{2-A-30}$$

The vorticity is a vector normal to the plane of the vortex motion. Its three components are

$$\left.\begin{aligned} \zeta_x &= \frac{\partial w}{\partial y} - \frac{\partial v}{\partial z}\ (\text{in the } y,z-\text{plane}) \\ \zeta_y &= \frac{\partial u}{\partial z} - \frac{\partial w}{\partial x}\ (\text{in the } z,x\text{-plane}) \\ \zeta_z &= \frac{\partial v}{\partial x} - \frac{\partial u}{\partial y}\ (\text{in the } x,y\text{-plane}) \end{aligned}\right\} \tag{2-A-31}$$

The first vortex law by Helmholtz expresses the condition of continuity of the vorticity vector:

$$\frac{\partial \zeta_x}{\partial x} + \frac{\partial \zeta_y}{\partial y} + \frac{\partial \zeta_z}{\partial z} = 0 \tag{2-A-32}$$

If vortex lines are defined as having everywhere the direction of the local vorticity vector, the first vortex law by Helmholtz (eq. (2-A-32)) can be stated in the following form: vortex lines cannot end in a frictionless fluid.

The second vortex law by Helmholtz can be stated for three-dimensional flow in the following form: vortex lines and vorticity vectors remain connected to the fluid and move and are stretched (or shortened) with the fluid; that is,

$$\zeta_1 A_1 = \zeta_2 A_2 \tag{2-A-34}$$

(If the vortex lines are curved, the vorticity vectors must be drawn at a sufficiently small scale to coincide everywhere with the vortex lines.)

2.6.3.2 Vorticity of relative flow. – The flow entering a rotor without any rotation of its absolute flow (no prerotation) will rotate relative to the rotor at an angular velocity oppositely equal to the angular velocity ω of the rotor. Thus the vorticity of the flow entering and relative to the rotor is, according to equation (2-A-23),

$$\zeta_{rel,\varphi} = -2\omega \tag{2-101}$$

In the more general case, where the fluid at the inlet has a tangential component, the vorticity relation can be expressed as

$$\vec{\zeta}_{abs} - \vec{\zeta}_{rel} = 2\vec{\omega} \tag{2-101a}$$

From this expression, it is evident that, whenever the radial distribution of the inlet tangential velocity is such that $\zeta_{abs} = 0$, which implies that it must obey the law of constant angular momentum, equation (2-101a) reduces to equation (2-101).

If the rotor is a mixed-flow rotor (fig. 2-41), the vorticity of the incoming flow is determined by the angular velocity of the rotor, as shown in the development of a conical flow surface. This angular velocity is

$$\omega_\varphi = \omega \sin \varphi \tag{2-102}$$

where ω is the true angular velocity of the conical-flow rotor. The vorticity of the relative flow in the conical stream surface is, therefore,

$$\zeta_{rel,\varphi} = -2\omega_\varphi = -2\omega \sin \varphi \tag{2-103}$$

Evidently this vorticity goes to zero as the cone angle φ goes to zero, that is, as the system approaches axial flow. (Eq. (2-102) is most convincingly derived from the peripheral velocity at any point A: $U_A = r\omega = r_\varphi\omega_\varphi$; therefore $\omega_\varphi = \omega r/r_\varphi = \omega \sin \varphi$.)

For kinematic reasons (when flow is viewed from a rotating platform), the axial component of the vorticity of the relative flow must remain constant as long as the absolute flow continues to be irrotational. This vorticity cannot influence the relative flow under the one-dimensional assumption of an infinite number of frictionless vanes, since the form of the relative flow is uniquely prescribed. The vorticity of the relative flow, therefore, can influence only the departures of this flow from the one-dimensional assumption, that is, from the vane shape. If the absolute flow between the vanes (of finite spacing) is assumed to remain irrotational, the relative flow between the vanes should have vorticity with a constant axial component.

The vorticity of the relative flow in radial-flow rotors complicates its theoretical analysis considerably. As a result, only one approximate solution of the relative flow problem has been used extensively in the design of radial-flow rotors. This solution is described in section 2.6.3.5 and is compared with an exact solution of this flow problem obtained by investigating the absolute flow through radial-flow rotors. This comparison shows an amazingly good agreement between the exact solution and the approximate solution.

2.6.3.3 Static pressure, circulation, lift coefficient, and separation. – Since the relative flow in radial-flow rotors is not irrotational, the laws of relative fluid motions are expected to be substantially different from those of irrotational flow through the same passages at rest. The first relation to be investigated in this section is that between the static pressure and the relative velocities.

According to Euler's turbomachinery equation, the change in total head from inlet r_1 to discharge r_2 of the rotor is

$$H_r = \frac{U_2 V_{U,2} - U_1 V_{U,1}}{g_o} \tag{2-104}$$

For a frictionless fluid, if all head losses are neglected, the change in rotor head is also

$$H_r = h_{st,2} - h_{st,1} + \frac{V_2^2 - V_1^2}{2g_o} \tag{2-105}$$

where V denotes absolute fluid velocities, and h_{st} denotes the static head $h_{st} = p/g_o\rho$. The change in static head is, therefore,

$$h_{st,2} - h_{st,1} = \frac{U_2 V_{U,2} - U_1 V_{U,1}}{g_o} - \frac{V_2^2 - V_1^2}{2g_o} \tag{2-106}$$

In the following derivations up to equation (2-108), the subscript r denotes not only the strictly radial direction, but also the radial direction in the development of a conical flow section such as that shown in figure 2-41. With this definition, the meaning of these derivations is not restricted to flow along planes normal to the axis of rotation, but applies also to conical stream surfaces. Using the substitutions

$$V^2 = V_U^2 + V_r^2$$

$$V_U = U - w_U$$

$$V_U^2 = (U - w_U)^2 = U^2 + w_U^2 - 2Uw_U$$

one obtains

$$g_o(h_{st,2} - h_{st,1}) = U_2^2 - U_2 w_{U,2} - U_1^2 + U_1 w_{U,1}$$

$$- \frac{U_2^2}{2} - \frac{w_{U,2}^2}{2} + U_2 w_{U,2} - \frac{V_{r,2}^2}{2}$$

$$+ \frac{U_1^2}{2} + \frac{w_{U,1}^2}{2} - U_1 w_{U,1} + \frac{V_{r,1}^2}{2}$$

$$g_o(h_{st,2} - h_{st,1}) = \frac{U_2^2 - U_1^2 - w_{U,2}^2 + w_{U,1}^2 - V_{r,2}^2 + V_{r,1}^2}{2} \tag{2-107}$$

Considering that

$$w_{U,2}^2 + V_{r,2}^2 = w_2^2$$

$$w_{U,1}^2 + V_{r,1}^2 = w_1^2$$

one obtains

$$h_{st,2} - h_{st,1} = \frac{U_2^2 - U_1^2}{2g_o} + \frac{w_1^2 - w_2^2}{2g_o} \tag{2-108}$$

The term $(U_2^2 - U_1^2)/2g_o$ is the difference in static head between the radii r_2 and r_1 in a body of fluid rotating at uniform angular velocity ω, since $U_1 = r_1\omega$ and $U_2 = r_2\omega$. The term $(w_1^2 - w_2^2)/2g_o$ is the static head difference due to the change in relative velocity from w_1 to w_2, according to Bernoulli's equation.

The foregoing derivation is obviously based on the assumption of complete axial symmetry. Thus the results apply only to changes along the

streamline of the relative flow, since changes across the streamlines, specifically in the circumferential direction, are eliminated by the assumption of axial symmetry. Equation (2-108) and the subsequent paragraph can, therefore, be expressed by the following statement:

Differences in static head or pressure along any streamline of the relative flow in radial-flow rotors are obtained by adding the static head or pressure difference calculated from the relative flow according to Bernoulli's equation to the static head or pressure difference that would exist if the fluid within the rotor were rotating at the angular velocity of the rotor like a rigid body.

It should be noted that Bernoulli's equation cannot be valid along the streamlines of the absolute flow through any turbomachine rotor (radial or axial), because these streamlines are intersected (generally) by the rotor vanes in motion, that is, they are subject to moving forces and thereby to a head addition or subtraction which is on the average just equal to the rotor head H_r.

The static-pressure or head changes, according to equation (2-108), are partly due to the rotation of the fluid and partly due to the (radial) vane forces. A general derivation of these forces would be quite complex. However, the validity of the foregoing result can be demonstrated by cases where the radial vane force is zero.

First, consider a rotor with straight radial vanes (fig. 2-43). The flow is assumed to enter at such a velocity that $V_{U,1} = U_1$ and the circumferential component $w_{U,1} = 0$. According to the one-dimensional theory of the relative flow, w_U is zero everywhere. To simplify the reasoning, assume V_r = constant. Then, according to equation (2-107), the static head increase from r_1 to r_2 is

$$h_{st,2} - h_{st,1} = \frac{U_2^2 - U_1^2}{2g_o}$$

which is immediately seen to be valid since the absolute peripheral velocity within the rotor is indeed $V_U = U = r\omega$ and conforms to solid body rotation.

Second, consider flow in a fictitious vaneless rotor. It has the same meridional profile as the first rotor (fig. 2-43), but has no vanes, so that there are no vane forces. Hence the absolute flow must obey the law of constant angular momentum:

$$V_U = V_{U,1} \frac{r_1}{r} \tag{2-109}$$

Assume again that at radius r_1

$$V_{U,1} = U_1$$

so that

$$V_U = U_1 \frac{r_1}{r} \tag{2-110}$$

Since the pressure p is here a function of r only (axial symmetry), the equation of simple radial equilibrium appears in the form

$$\frac{dp}{dr} = \rho \frac{V_U^2}{r} \tag{2-111}$$

or

$$\int_1^2 dp = p_2 - p_1 = \rho \int_1^2 V_U^2 \frac{dr}{r}$$

Substituting equation (2-110) gives

$$p_2 - p_1 = \rho U_1^2 r_1^2 \int_1^2 \frac{dr}{r^3} = \frac{\rho U_1^2}{2} \left(1 - \frac{r_1^2}{r_2^2}\right) \tag{2-112}$$

This result, derived independently of the previous derivations of equations (2-107) and (2-108), can be compared with (2-107) and (2-108) to check their validity. Evidently, according to equation (2-110),

$$w_U = U - V_U = U - U_1 \frac{r_1}{r}$$

Hence

$$w_{U,1} = U_1 \left(1 - \frac{r_1}{r_1}\right) = 0 \tag{2-113}$$

$$w_{U,2} = U_2 - U_1 \frac{r_1}{r_2}$$

$$w_{U,2}^2 = U_2^2 + U_1^2 \frac{r_1^2}{r_2^2} - 2U_2 U_1 \frac{r_1}{r_2}$$

$$w_{U,2}^2 = U_2^2 \left(1 - 2\frac{r_1^2}{r_2^2}\right) + U_1^2 \frac{r_1^2}{r_2^2} \tag{2-114}$$

Substituting equations (2-113) and (2-114) and $V_{r,2} = V_{r,1}$ into equation (2-107) leads to

$$p_2 - p_1 = \rho g_o (h_{st,2} - h_{st,1})$$

$$= \rho \left[\frac{U_2^2}{2} - \frac{U_1^2}{2} - \frac{U_2^2}{2}\left(1 - 2\frac{r_1^2}{r_2^2}\right) - \frac{U_1^2}{2}\frac{r_1^2}{r_2^2} \right]$$

With $U_2/U_1 = r_2/r_1$,

$$p_2 - p_1 = \frac{\rho U_1^2}{2}\left(\frac{r_2^2}{r_1^2} - 1 - \frac{r_2^2}{r_1^2} + 2 - \frac{r_1^2}{r_2^2} \right)$$

$$p_2 - p_1 = \frac{\rho U_1^2}{2}\left(1 - \frac{r_1^2}{r_2^2}\right) \qquad (2\text{-}115)$$

which agrees with equation (2-112) and proves that, in the absence of vane forces, considerations of simple radial equilibrium give the same results as equations (2-107) and (2-108), derived from Euler's turbomachinery equation.

Finally, consider velocity and pressure changes across the relative flow in a rotating vane system which would have no such velocity or pressure changes if it were at rest. The velocity and pressure changes in such a system are entirely due to the rotation of the system.

Refer again to figure 2-43. The flow is again assumed to enter at the circumferential velocity $V_{U,1} = U_1$, so that $w_{U,1} = 0$. The condition $w_U = 0$ or $V_U = U$ is assumed to be satisfied throughout the system.

The change in angular momentum for an infinitesimal radial step dr is equated to the moment applied to the flow by the vane pressure difference Δp:

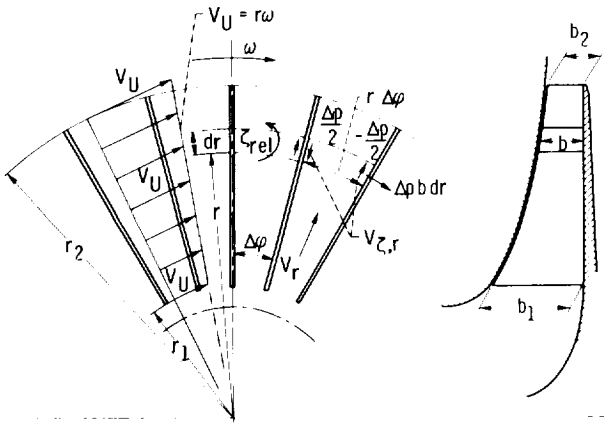

Figure 2-43. – Radial-flow rotor with straight radial vanes.

$$dM = \Delta p\, rb\, dr = \rho Q_1 \left[\left(U + \frac{\partial U}{\partial r} dr \right)(r + dr) - Ur \right] \qquad (2\text{-}116)$$

where Q_1 is the rate of volume flow per blade.

With $V_U = U = r\omega$, evidently $\partial U/\partial r = \omega$. Furthermore $Q_1 = r\,\Delta\varphi\, bV_r$. Hence

$$dM = \Delta p\, rb\, dr = \rho r\, \Delta\varphi\, bV_r (Ur + \omega r\, dr + U dr - Ur)$$

$$\Delta p\, r\, dr = \rho r\, \Delta\varphi\, V_r 2U\, dr$$

and thus

$$\Delta p = 2\rho\, \Delta\varphi\, UV_r = 2\rho\, \Delta\varphi\, r\omega V_r \qquad (2\text{-}117)$$

(which could be derived also from the Coriolis forces).

The circulation over the element by the vorticity of the relative flow ζ_{rel} is obtained by equating the differential form of the equation (2-31) to equation (2-A-25):

$$d\Gamma_{rel} = r\zeta_{rel}\, \Delta\varphi\, dr = 2V_{\zeta,r}\, dr \qquad (2\text{-}118)$$

where $V_{\zeta,r}$ is the velocity generated by the vorticity ζ_{rel}. (Since radially adjacent elements can be assumed to have the same flow within the limits of the equality of these flow fields, there is no significant contribution to $d\Gamma$ from the flow along the outer and inner sides of the element. An analysis of this problem has shown that any contributions of these sides to $d\Gamma$ must be of a lower order of magnitude than that expressed by eq. (2-119). This argument does not hold true in the radial end portions of the passage and is further investigated in sec. 2.6.3.5.)

By equation (2-118) and $\zeta_{rel} = -2\omega$,

$$V_{\zeta,r} = r\zeta_{rel}\frac{\Delta\varphi}{2} = -r\,\Delta\varphi\,\omega \qquad (2\text{-}119)$$

Accordingly equation (2-117) can be rewritten so that the vane pressure difference is

$$\Delta p = -2\rho V_r V_{\zeta,r} \qquad (2\text{-}120)$$

This vane pressure difference can also be computed by using the circulation $d\Gamma$ over the vane element of length dr. According to the law by Kutta and Joukowski (see eq. 2-32) and equation (2-31), the force on the blade element of the length dr is

$$dF_1 = \rho V_r \, d\Gamma_v = \rho V_r \, 2dr \; V_{\Gamma,v} = \Delta p \; dr$$

or

$$\Delta p = 2\rho V_r V_{\Gamma,v} \tag{2-121}$$

where $V_{\Gamma,v}$ is the velocity induced by the local vane circulation.

Note that in figure 2-43 the circulation $d\Gamma_{rel}$ about the fluid element ($r \, \Delta\varphi \, dr$) has the opposite direction from the circulation $d\Gamma_v$ about the vane element dr; this difference accounts for the difference in signs between equations (2-120) and (2-121). These two equations and figure 2-43 show that $V_{\zeta,r}$ and $V_{\Gamma,v}$ are actually identical.

Finally, one must consider the departure ΔV_B from the uniform radial velocity V_r which would exist if it were related by Bernoulli's equation to the vane pressure difference Δp determined by the change in angular momentum over the radial distance dr. With p denoting the mean pressure, Bernoulli's equation takes the form

$$p + \frac{\Delta p}{2} + \frac{\rho}{2}(V_r - \Delta V_B)^2 = p - \frac{\Delta p}{2} + \frac{\rho}{2}(V_r + \Delta V_B)^2$$

or

$$\Delta p = \frac{\rho}{2}(V_r^2 + \Delta V_B^2 + 2V_r \, \Delta V_B - V_r^2 - \Delta V_B^2 + 2V_r \, \Delta V_B)$$

Hence

$$\Delta p = 2\rho V_r \, \Delta V_B \tag{2-122}$$

Equations (2-117) and (2-119) to (2-122) show that, in a rotating system of straight, radial vanes, the departures $V_{\zeta,r}$ from the average radial velocity V_r due to the vorticity $\zeta_{rel} = -2\omega$ are identical to the departures $V_{\Gamma,v}$ from the average radial velocity caused by the local vane circulation according to the law by Kutta and Joukowski. Both departures $V_{\zeta,r}$ and $V_{\Gamma,v}$ are related to the vane pressure difference Δp (as determined from the radial change in angular momentum) by Bernoulli's equation. In a rotating system of straight, radial vanes, Bernoulli's equation, therefore, holds for the changes in relative (radial) velocities across the relative (radial) flow.

The vane circulation in rotating, radial-flow vane systems is determined from the absolute fluid velocities in the same manner as for axial-flow vane systems. As can be seen from figure 2-44, the contributions of the contour portions BC and DA to the circulation about the contour ABCD cancel out, since these lines can be chosen to be in identical positions relative to the blades. All that needs to be assumed is perfect periodicity of the flow picture from blade to blade. (It is also assumed that r_2 and r_1 as defined by fig. 2-44 are far enough from the vane system to justify the use of average values of $V_{U,2}$ and $V_{U,1}$ at these radii.) As a consequence, the vane circulation Γ_v is

$$\Gamma_v = V_{U,2} r_2 \, \Delta\varphi - V_{U,1} r_1 \, \Delta\varphi \tag{2-123}$$

where $\Delta\varphi$ is the angular spacing between the vanes.

The lift coefficient is derived by the same principle as for axial-flow vane systems (see sec. 2.5.2), by equating the vane force per unit span

$$F_1 = C_{L,\infty} \frac{\rho w_\infty^2}{2} l \tag{2-124}$$

(where $C_{L,\infty}$ is the lift coefficient) to the same vane force according to the law by Kutta and Joukowski:

$$F_1 = \rho w_\infty \Gamma_v \tag{2-125}$$

The mean velocity w_∞ of the flow relative to the blades of a rotating, radial-flow vane system is defined by equations (2-124) and (2-125). A separate investigation would be necessary to

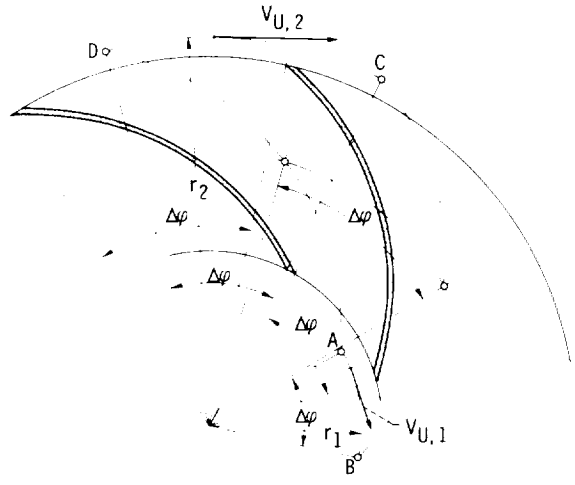

Figure 2-44. – Circulation about vane of radial-flow rotor. $\Delta\varphi = 2\pi/N = constant$.

determine how w_∞ is related to the relative velocities at the inlet and discharge of the system. In the absence of such an investigation, it may be assumed that

$$w_\infty = \frac{w_1 + w_2}{2} \tag{2-126}$$

Equations (2-124) and (2-125) obviously lead to the same relation as for single airfoils and for straight systems of parallel vanes:

$$C_{L,\infty} = \frac{2\Gamma_v}{w_\infty l} \tag{2-127}$$

With equation (2-123),

$$C_{L,\infty} = 2\,\Delta\varphi\,\frac{V_{U,2}r_2 - V_{U,1}r_1}{w_\infty l} \tag{2-128}$$

When the peripheral vane spacing at the radii r_2 and r_1

$$\left.\begin{aligned} t_2 &= r_2\,\Delta\varphi \\ t_1 &= r_1\,\Delta\varphi \end{aligned}\right\} \tag{2-129}$$

is introduced, equation (2-128) may be written in the form

$$C_{L,\infty} = 2\,\frac{V_{U,2}}{w_\infty}\,\frac{t_2}{l}\left(1 - \frac{V_{U,1}r_1}{V_{U,2}r_2}\right) \tag{2-130}$$

which applies primarily to pumps or compressors where $V_{U,2}r_2 > V_{U,1}r_1$, the subscript 2 applying to the rotor discharge and the subscript 1 to its inlet.

For turbines, where $V_{U,1}r_1 > V_{U,2}r_2$, one avoids negative values by defining the vane circulation by

$$\Gamma_v = V_{U,1}r_1\,\Delta\varphi - V_{U,2}r_2\,\Delta\varphi \tag{2-131}$$

so that

$$C_{L,\infty} = 2\,\Delta\varphi\,\frac{V_{U,1}r_1 - V_{U,2}r_2}{w_\infty l} \tag{2-132}$$

which leads to

$$C_{L,\infty} = 2\,\frac{V_{U,1}}{w_\infty}\,\frac{t_1}{l}\left(1 - \frac{V_{U,2}r_2}{V_{U,1}r_1}\right) \tag{2-133}$$

For zero angular momentum of the flow on the low-head side of the rotor ($V_{U,1} = 0$ for pumps; $V_{U,2} = 0$ for turbines), equations (2-130) and (2-133) assume the same form as equation (2-54), derived in section 2.5 for axial-flow vane systems.

In the field of axial-flow turbomachines, the lift coefficient can be used to obtain a first approximation of the vane shape, and in combination with figure 2-26, it constitutes a criterion for separation or stall.

The relation between the lift coefficient and the form of the vane (including its angle of attack) stems primarily from the comparison between the vanes of axial-flow turbomachines and single airfoils in an infinitely extended flow. This comparison is not directly applicable to design problems of radial-flow rotors, partly because of the vorticity of the relative flow and partly because of the predominant use of vane systems of high solidity. It is indicated in section 2.5 and becomes more apparent in chapter 3 that even the design of axial-flow vanes begins to differ very strongly from that of single airfoils whenever the solidity of the system approaches or exceeds unity. Therefore, it is safe to conclude that the lift coefficient generally cannot be related effectively to the shape of vanes in rotating, radial-flow (and some axial-flow) systems. Such a relation is, therefore, not further explored in this compendium.

The situation is somewhat different with respect to separation or stall. While it is true that the flow conditions in radial-flow rotors differ markedly from those in axial-flow vane systems, the lift coefficient, nevertheless, describes for both the ratio of the average vane pressure difference to the velocity pressure of the mean velocity relative to the blades. Since this velocity pressure (or energy) must be expected to be of major importance in negotiating the vane pressure variations without separation, it is reasonable to assume that the vane lift coefficient plays with respect to separation in radial-flow rotors a part similar to that in axial-flow machines, although this comparison is as yet purely qualitative.

Recall that, in addition to the lift coefficient, the retardation (or acceleration) of the general relative flow (the ratio w_2/w_1, in fig. 2-26) has an important

influence on separation in axial-flow vane systems. Pressure changes (gradients) of the mean relative flow should be expected to have a similar effect in radial-flow systems.

Many years ago von Karman called this writer's attention to the fact that pressure differences resulting from a centrifugal force field cannot have any effect on separation any more than a gravitational field can have such an influence, because the body force that produces this type of pressure gradient is identical to the body force acting on the fluid particles, and thus the effect is cancelled.

The static-pressure gradients in radial-flow rotors are described previously as being partly due to a centrifugal force field and partly due to changes in the relative flow velocities. With some reservations, one can say that only those pressures gradients that are due to changes in relative velocities should be taken into account with respect to separation in radial-flow rotors. This means that only the second term in equation (2-108)

$$\Delta h_{st,w} = \frac{w_1^2 - w_2^2}{2g_o} = \frac{w_1^2}{2g_o}\left(1 - \frac{w_2^2}{w_1^2}\right) \qquad (2\text{-}134)$$

contributes to the danger of separation. Accordingly the relative velocity ratio w_2/w_1, which is important for axial-flow vane systems, has conceivably the same significance for radial-flow rotors. (There is no reason why it should not be used in the same manner for stationary, radial-flow vane systems; it can be written with respect to the absolute velocities in the forms $(V_1^2 - V_2^2)/2g_o$, and V_2/V_1, as can be seen from eq. (2-106) with $U_1 = U_2 = 0$.)

Since the vane lift coefficient has with regard to separation at least qualitatively the same significance for radial- and axial-flow rotors, it can be concluded that in the absence of better information, figure 2-26 can be used also for radial-flow rotors (and radial-flow stator vane systems) with the understanding that the limiting values of various separation coefficients may be different for radial- and axial-flow systems, since no test points are available for radial-flow systems. Our relative ignorance of the flow in rotating radial-flow passages and certain theoretical and experimental results by Johnston, which are discussed briefly in section 2.6.3.8, strongly suggest that more conservative limits of C_L and w_2/w_1 be used for radial-flow rotors than for axial-flow vane systems.

On the other hand, radial-flow rotors with axial inlets and straight radial vanes in their discharge portions have been operated with reasonable success at ratios of relative flow retardation w_2/w_1 far below the lower limits indicated by figure 2-26. It is as yet not clear whether such rotors operate with a more or less separated form of flow. Overall pump or compressor efficiencies obtainable with such rotors may exceed 80 percent, but they have not yet reached the 90-percent level achieved reliably with radial-flow pumps with backward-bent rotor vanes, which permit the flow to stay within the w_2/w_1 limits indicated by figure 2-26.

2.6.3.4 Results of exact theoretical analysis of absolute frictionless flow. – The inward flow through radial-flow vane systems, usually used in hydraulic turbines, is fairly well described by the one-dimensional theory, partly because the relative flow in such systems is mostly accelerated and partly because departures of the discharging flow from the direction of the vanes are effective at the minimum diameter of the system, so that their effect is reduced.

The opposite is true for the outward flow in radial-flow systems used with centrifugal pumps and compressors. The departures from the one-dimensional theory in well-designed radial-flow pump rotors as measured by the change in angular momentum (the rotor head H_r) are about 20 percent.

Figure 2-45 shows the inlet and discharge velocity diagrams of a standard centrifugal pump rotor with

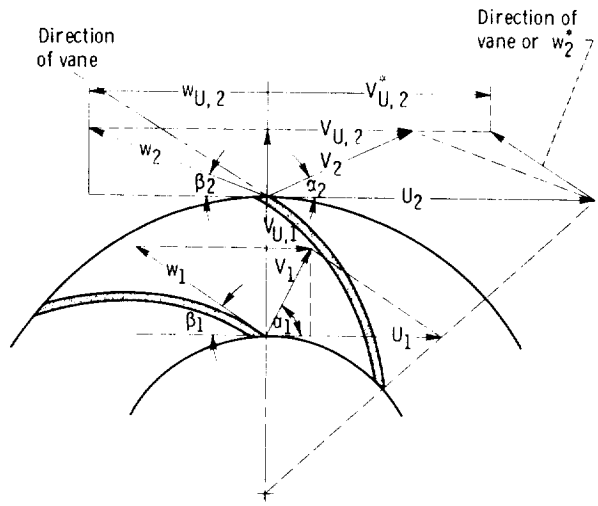

Figure 2-45. – Velocity diagrams of radial-flow pump rotor. Flow angles α and β are measured from peripheral direction, in agreement with Busemann's paper (ref. 30).

backward-bent vanes. The discharge diagram is shown in relation to the discharge direction of the vanes and to a fictitious relative discharge velocity w_2^*. The magnitude of this velocity is calculated by the condition of continuity from the volume flow rate Q and the cross-sectional area between, and normal to, the vanes at their discharge ends (d_2, as shown in fig. 2-46, times the average axial width of the impeller over the vane distance d_2). The fictitious velocity diagram obtained on this basis contains a fictitious absolute discharge velocity with a peripheral component $V_{U,2}^*$, which may be used in Euler's turbomachinery equation in the form

$$\frac{H}{\eta_h} = H_r = C_H \frac{V_{U,2}^* U_2 - V_{U,1} U_1}{g_o} \qquad (2\text{-}135)$$

(It should be understood that the inlet velocity $V_{U,1}$ is not part of the rotor problem but is determined by similar considerations from the inlet passages or guide vanes ahead of the rotor.)

As indicated previously, the head correction factor C_H is equal to or slightly less than 0.8 if w_2^* is determined from the discharge cross section between the vanes. This method of approximating the relative flow one dimensionally from the vane shape has the advantage of taking a fair portion of the vane shape into account and thus avoids the difficulty of defining a representative discharge vane angle for vanes with finite thickness and radially varying vane angle.

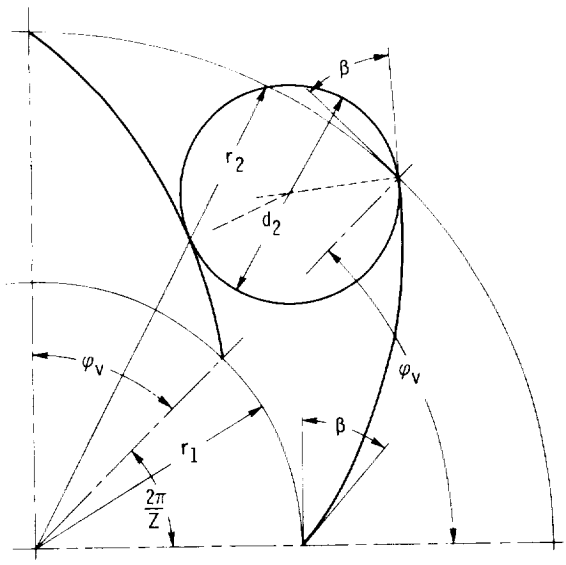

Figure 2-46. – Logarithmic spiral vanes with notation of figure 2-47.

Because of the substantial departures of C_H from unity, the two-dimensional outward flow through radial-flow rotors has received extensive attention in Europe during the second and third decades of this century in the form of a number of theoretical investigations (see refs. 26 to 30). The following presentation is based on the last of these investigations (ref. 30, by Busemann), because its results are given in a form readily applicable to the design of turbomachinery.

All investigations described in the references are based on the theory of plane, two-dimensional motions of an incompressible, frictionless fluid. Because of the vorticity of the relative flow through radial-flow rotors, the absolute flow is investigated.

In the investigation by Busemann (ref. 30), the vane system is approximated by a finite number of logarithmic spirals grouped symmetrically around the center of the system. All vanes of the system are transformed conformally into a single circle. The center of the system appears as a vortex source close to the circle representing the vanes, and infinity is transformed into infinity.

The flow through the system is divided into three parts:

(1) Through flow, that is, the absolute flow through the system at rest

(2) Displacement flow, that is, the absolute fluid motion produced by the rotation of the vane system at zero through flow

(3) Circulation flow, the flow about the vanes whereby the Kutta condition of smooth flow at the trailing vane edges is satisfied

If the circulation flow is divided into two parts, one satisfying the Kutta condition for the through flow alone and the other the condition for the displacement flow alone, the following statements can be made:

(1) The displacement flow with its part of the circulation describes the ideal-flow characteristics, particularly the ideal head H_r at zero through flow (shutoff conditions). According to the one-dimensional theory, $V_{U,2} = U_2$ and $V_{U,1} = 0$ under these conditions, so that the shutoff rotor head is

$$H_{o,1} = \frac{U_2^2}{g_o} \qquad (2\text{-}136)$$

where the head subscript o refers to $Q = 0$, and the subscript 1 refers to the one-dimensional theory.

Figure 2-47 shows the results by Busemann regarding the shutoff rotor head H_o under ideal, two-dimensional flow conditions by the ratio h_o of this head to its one-dimensional approximation.

Combining equation (2-136) and the results in figure 2-47 gives

$$H_o = h_o \frac{U_2^2}{g_o} \tag{2-137}$$

(2) The through flow, including its part of the circulation, is the flow through the vane system at rest and thereby accounts for the departures of the ideal-flow characteristics, particularly the head, from the ideal shutoff (zero-flow) conditions. By this definition, the velocities of this flow are obviously proportional to the volume flow rate through the machine.

From his theoretical work, Busemann was able to conclude from this situation that, at constant rotational speed, the relation between the ideal rotor head H_r and the flow rate Q can be represented by a straight line. This conclusion can be made plausible on the basis of Euler's turbomachinery equation (2-19) in the following manner. Evidently

$$V_{U,2} = U_2 - w_{U,2}$$

Therefore

$$H_r = \frac{U_2(U_2 - w_{U,2}) - U_1 V_{U,1}}{g_o}$$

$$= \frac{U_2^2 - (U_2 w_{U,2} + U_1 V_{U,1})}{g_o} \tag{2-138}$$

According to figure 2-45,

$$w_{U,2} = w_2 \cos \beta_2$$

$$V_{U,1} = V_1 \cos \alpha_1$$

so that

$$H_r = \frac{U_2^2 - (U_2 w_2 \cos \beta_2 + U_1 V_1 \cos \alpha_1)}{g_o} \tag{2-139}$$

where β_2 and α_1 are, in the notation of Busemann's paper, the flow angles measured from the circumferential direction.

From the condition of continuity, one can conclude that $w_2 = \text{constant}_2 \times Q$ and $V_1 = \text{constant}_1 \times Q$, since V_1 is controlled by a stationary guide-vane system in front of and inside the rotor inlet. Hence

$$H_r = \frac{U_2^2 - Q[U_2(\text{constant}_2 \times \cos \beta_2) + U_1(\text{constant}_1 \times \cos \alpha_1)]}{g_o} \tag{2-140}$$

This equation demonstrates the aforementioned straight-line relation between H_r and Q, since there is no reason to assume any variation in the flow angles α_1 and β_2 under ideal flow conditions.

For pump rotors with backward-bent vanes, that is, with the relative flow discharging backward, so that $V_{U,2} < U_2$, the ideal head-capacity (H_r, Q) curve is generally a straight line falling off in the direction of increasing capacity Q. With radial discharge relative to the rotor ($V_{U,2} = U_2$) and $V_{U,1} = 0$, the ideal head-capacity curve is a horizontal straight line. With forward-bent vanes ($V_{U,2} > U_2$), this curve is a straight line rising with increasing capacity. These results are nearly self-evident from the one-dimensional application of Euler's turbomachinery equation, but according to Busemann's analysis, are also valid for the two-dimensional flow of an ideal (frictionless and incompressible) fluid through pump rotors.

Busemann's h_o curves shown in figure 2-47 correspond to the point of intersection between the H_r,Q line and the $Q = 0$ axis for the one-dimensional approximation of this line. The same results also show that the two-dimensional line is approximately parallel to its one-dimensional approximation in the range where the h_o, r_1/r_2 curves are straight and horizontal, that is, where the discharge of a radial-flow pump rotor is not influenced by the inlet to the system. Thus in this range the head reduction

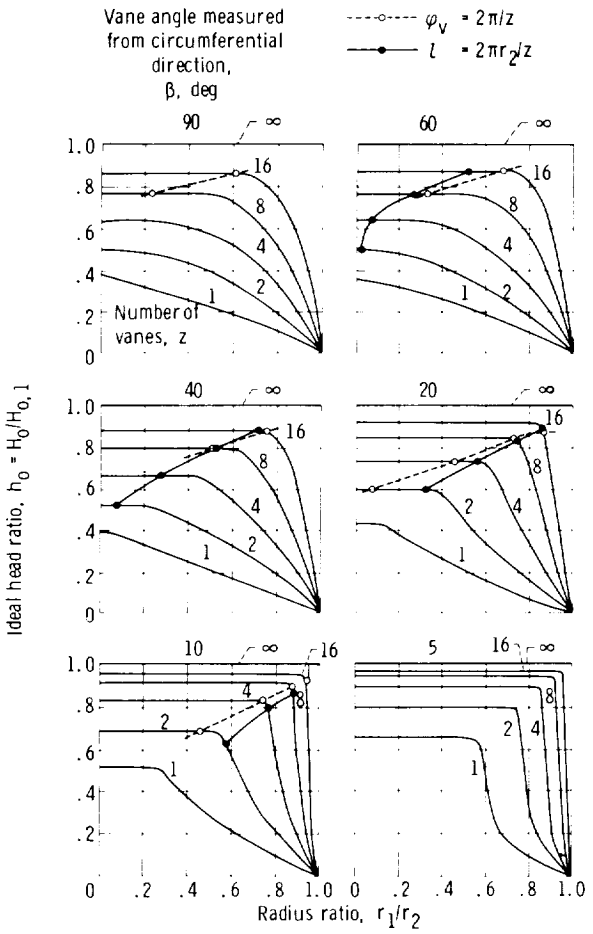

Figure 2-47. – Ideal head ratio at zero flow according to Busemann (ref. 30) for vane system of logarithmic spirals (see fig. 2-46).

$$H_1 - H = (1 - h_o)\frac{U_2^2}{g_o} \qquad (2\text{-}141)$$

is approximately constant at varying flow rates Q, where H_1 is the ideal shutoff head determined by the one-dimensional approximation.

In order to illustrate the physical meaning of the Busemann curves, this writer has drawn in figure 2-47 a few additional curves describing the solidity (or ratio of overlapping) of the vanes in the system. Here φ_v is the angular (or circumferential) extent of a vane (see fig. 2-46), and z is the number of vanes. Evidently $\varphi_v = 2\pi/z$ denotes the solidity where the end of one vane is radially in line with the beginning of the next vane. The vane angle β is measured from the circumferential direction (in contrast to the general practice of this compendium). Since the φ_v criterion of solidity does not apply to straight radial vanes, curves for the vane length $l = 2\pi r_2/z$ are also shown; this equation corresponds to the conventional definition of a solidity of 1 for the vane spacing at the outer periphery.

It is evident from figure 2-47 that the h_o curves depart from their straight, horizontal trend approximately when the solidity by either definition drops below 1. In other words, the inlet to the vane system ceases to have an overall effect on the discharging flow when the solidity of the system substantially exceeds 1. It is this range of overlapping vanes where the curves in figure 2-47 have their most definite practical meaning. This meaning is further discussed in the next section.

2.6.3.5 Semiempirical corrections of discharge velocity diagram. – Besides the exact solution of the ideal-flow problem of centrifugal pump impellers discussed in the preceding section, there exist a number of semiempirical solutions of the same problem that attempt to correct the one-dimensional discharge velocity diagram on some rational basis with support where possible by comparison with test results.

In this section, only one method of this type, that by Stodola (described at the end of his famous book on steam and gas turbines, ref. 2), is discussed in some detail, since it is by far the most rational and at the same time the simplest method of correction. It is compared with the exact solution by Busemann and is thereby found to be quite good within the limits of ideal (frictionless) flow considerations.

Another correction method of this general type was suggested by Pfleiderer in his well-known book on centrifugal pumps (ref. 21). It is shown here by a qualitative comparison with the results by Busemann that Pfleiderer's method does not apply in the important field of impellers with strongly overlapping vanes, in which its author intended it to be used.

The method by Stodola is based on the principal difference between radial- and axial-flow rotors, namely, the vorticity of the relative flow. Stodola actually investigated by the so-called soap film method the flow within the vane channel of radial-flow compressor impellers generated by the uniformly distributed vorticity of the relative flow. However, the practical value of the method stems from the ingenious, very simple way in which Stodola derived from this vorticity a correction of the one-dimensional discharge velocity diagram:

In figures 2-46 and 2-48, a circle (circular cylinder) is inscribed into the discharge opening of the vane channel. Its diameter d_2 is the normal distance between two adjacent vanes, measured from the discharge edge of the outer vane forming the channel. According to section 2.6.3.2, this cylinder may be considered as rotating relative to the channel at an angular velocity ω which is oppositely equal to the angular velocity of the rotor. The relative peripheral velocity of this cylinder w_{SA} is the Stodola correction of the one-dimensional discharge velocity diagram

$$w_{SA} = \omega \frac{d_2}{2} \tag{2-142}$$

which is assumed to exist at the outer periphery of the rotor in the circumferential direction opposite U_2. From previous statements, it is immediately evident that

$$w_{SA} = U_2 \frac{d_2}{D_2} \tag{2-143}$$

which illustrates the simplicity of this correction.

The extreme simplicity of the foregoing determination of the Stodola correction (highly desirable for design purposes), of course, raises the question of the accuracy of this correction. This question can be answered by comparing the Stodola correction with the exact results obtained by Busemann (sec. 2.6.3.4).

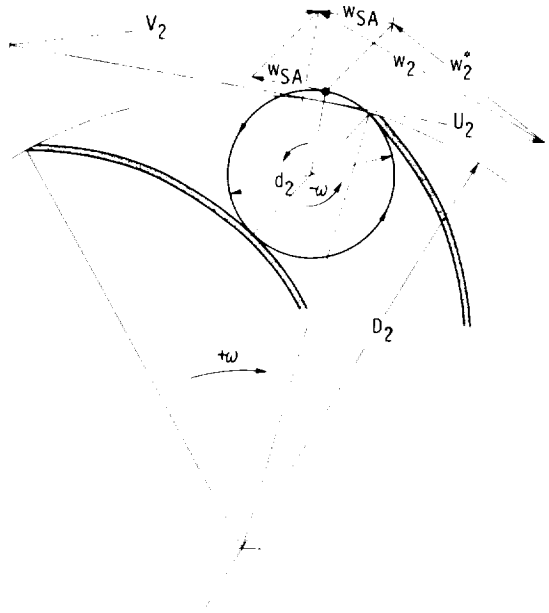

Figure 2-48. – Stodola correction of flow leaving centrifugal pump rotor.

The Stodola correction velocity w_{SA} is evidently independent of the rate of flow through the rotor. To permit easy comparison with Busemann's results as presented in figure 2-47, it is, therefore, desirable to apply the Stodola correction to the shutoff conditions ($Q = 0$). With the same notation as used in section 2.6.3.4 and with reference to Euler's turbomachinery equation (with $V_{U,1} = 0$ at $Q = 0$), one finds the shutoff head H_o to be

$$H_o = \frac{(U_2 - w_{SA})U_2}{g_o} \tag{2-144}$$

Hence, with the one-dimensional head $H_{o,1} = U_2^2/g_o$,

$$h_{SA} = \frac{H_o}{H_{o,1}} = \frac{U_2 - w_{SA}}{U_2} = 1 - \frac{w_{SA}}{U_2} \tag{2-145}$$

where the introduction of the symbol h_{SA} suggests comparison with the Busemann head ratio h_o.

Substitution of equation (2-143) into (2-145) yields

$$h_{SA} = 1 - \frac{d_2}{D_2} \tag{2-146}$$

which may be compared with the h_o values in figure 2-47.

The determination of the discharge opening ratio d_2/D_2 constitutes something of a problem. The general shape of the logarithmic-spiral vanes is determined from the equation of a logarithmic spiral in the form

$$\ln \frac{r_2}{r_1} = (\tan \beta)(\varphi_2 - \varphi_1) \tag{2-147}$$

where φ is the angle about the center of the system (see figs. 2-44 and 2-46), and β is the angle of the spiral against the circumferential direction as used by Busemann.

For small values of β (flat spirals), the ratio d_2/D_2 was approximated by the equation (see fig. 2-49)

$$d_2 = (r_2 - r_v)\cos \beta \tag{2-148}$$

where $r_2 - r_v$ is calculated from equation (2-147) for $\varphi_2 - \varphi_v = 2\pi/N$, with N being the number of vanes.

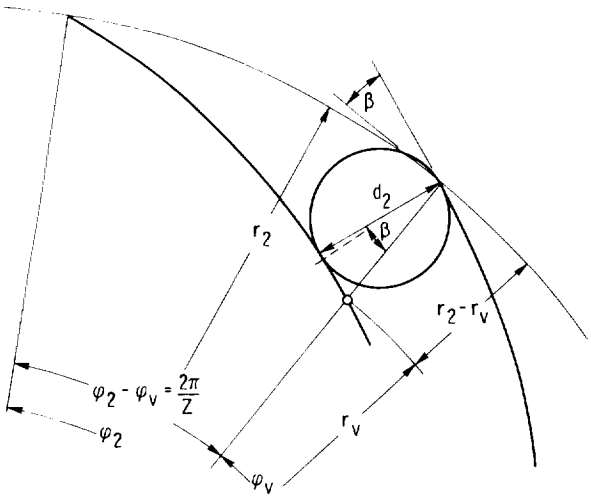

Figure 2-49. – Vane end configuration for flat vanes.

For $\beta > 10°$, the diameter of the circle (cylinder) inscribed in the discharge area of the vane system (radial-outward-flow system) is obtained graphically from the logarithmic spirals drawn according to equation (2-147) and the law of constant vane angle β. The results of this derivation are shown in figure 2-50.

The agreement indicated by figure 2-50 between the simple approximation by Stodola and the exact theory by Busemann is amazing. Within the practical range of the vane angle β and the number of vanes z or N, this agreement is within ±6 percent, far better than this writer would have expected. (These results correct an earlier statement by the same writer in sec. 53 (fig. 127) of ref. 14.) The simple Stodola correction may, therefore, be used under most practical conditions in place of the Busemann curves within the range that these curves are straight and horizontal, that is, for vane systems with solidities significantly larger than 1.

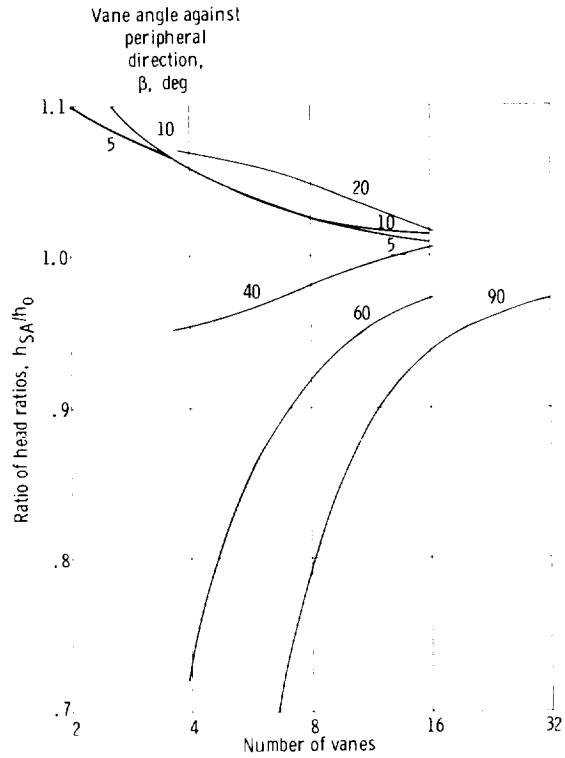

Figure 2-50. – Head ratios at zero flow with Stodola correction divided by same ratio according to exact solution by Busemann; ratio h_0 denotes ideal, two-dimensional head divided by head given by one-dimensional theory.

From the comparison with the Stodola correction, one can draw the conclusion that, for frictionless flow, the departures of the flow (at the discharge of pump rotors) from the one-dimensional theory at solidities substantially greater than 1 are primarily due to the vorticity of the relative flow. This conclusion is now used to evaluate the correction by Pfleiderer of the one-dimensional flow through radial-flow vane systems.

Pfleiderer uses the pressure difference between the two vane sides to derive a departure of the relative flow at the discharge of pump vane systems from the one-dimensional flow pattern. However, the foregoing conclusion indicates that the vane pressure difference is not the principal cause for departures of the discharging flow from the one-dimensional flow pattern in radial-flow vane systems of high solidity. This argument also agrees with the conclusions drawn in section 2.5 on axial-flow pumps, because the Pfleiderer correction should apply to axial-flow as well as radial-flow pumps. For axial-flow vane systems, the departure of the relative flow from the mean direction of the vane (the zero-lift direction) is negligibly small if the solidity of the vane system l/t substantially exceeds 1. This writer, therefore, does not recommend the application of the Pfleiderer correction, or of any other vane-pressure-based correction, to radial-flow vane systems with solidities substantially larger than 1. This contention is valid only as long as the one-dimensional theory and velocity diagrams are not based on the direction of the vane ends alone but on the average direction of a substantial part of the discharge portions of the vanes. A practical definition of this average vane direction is mentioned in section 2.6.3.4 and is further discussed in chapter 4.

2.6.3.6 Effect of fluid friction on flow leaving vane systems of high solidity. – This section discusses the effect of fluid friction on the performance of hydrodynamic rotors over and above the simple reduction in the net head due to skin friction or duct losses. Accordingly, Euler's turbomachinery equation is used, and the discussion is limited to the effects of fluid friction on the change in angular momentum in the rotor. Evidently one is concerned here with the effect of fluid friction on the circumferential velocity components of the flow leaving the rotor.

The circumferential component of the flow leaving the rotor is not likely to be affected significantly by friction-induced variations in the relative flow if the discharge ends of the vanes form radial and axial planes as shown, for example, in the lower part of figure 1-46, so that the discharging relative flow is very nearly radial. Therefore this section is concerned primarily with rotors discharging the fluid with an important circumferential component of the relative flow. While this component may have the same direction as the peripheral velocity of the rotor or the opposite direction, in turbopumps and related machinery, it usually has the opposite direction, associated with backward-bent vanes, as shown in figure 2-44. Hence this section deals primarily with this standard configuration of centrifugal pumps, but the principles described apply also to other arrangements as long as the discharging relative flow has a significant circumferential component.

The same considerations also apply in principle to the flow entering the rotor from a guide-vane system in front of the inlet to the rotor, which is particularly important for turbines. However, for the present, the flow entering the rotor, particularly its angular momentum under the influence of fluid friction, is considered as given and known.

The necessity of considering the effects of fluid friction on the performance of a rotor, particularly on the rotor head H_r, stems from the fact that the ideal flow considerations given in sections 2.6.3.4 and 2.6.3.5 have one result that is in conflict with practical experience, namely, that the rotor head should increase continuously with increasing number of vanes and approach asymptotically the head predicted for an infinite number of vanes. This is known to be not true for pump rotors with backward-bent vanes, not even for the rotor head H_r, which should not be affected by the increasing skin-friction losses.

It is assumed in the following that fluid friction does not affect the direction of the relative flow leaving the rotor. This assumption simplifies the problem of finding the effect of nonuniformities in the distribution of the relative velocities leaving the rotor. It is reasonable to assume that such nonuniformities in the magnitude of the relative velocities are the primary manifestation of fluid friction in the rotor, unless the fluid friction effects are very major, as in the case of separation.

Under this assumption, any nonuniformities in the relative velocity w_2 result in the same nonuniformities of any component of this velocity, in particular its circumferential component $w_{U,2}$.

The simplest way of representing the effect of fluid friction in the rotor passages is by the displacement thickness of the boundary layers in these passages. This merely means that, if, for example, the displacement thicknesses of these boundary layers would occupy 20 percent of the rotor passage cross section (at its discharge end), the relative discharge velocities w_2 and $w_{U,2}$ would be $1/0.80 = 1.25$ times higher than those calculated without taking fluid friction into account.

On this basis, the practical effect of fluid friction in a turbomachinery rotor is illustrated by the following: Consider a standard centrifugal pump impeller with a discharge velocity diagram like that shown in figure 2-45. To simplify the example, assume that $V_{U,1} = 0$. Then

$$\frac{H}{\eta_h} = H_r = C_H \frac{V^*_{U,2} U_2}{g_o} = \frac{V_{U,2} U_2}{g_o} \qquad (2\text{-}149)$$

where the asterisk indicates a velocity determined according to the one-dimensional theory without any consideration of fluid friction. The head coefficient is

$$C_H = \frac{V_{U,2}}{V^*_{U,2}} \qquad (2\text{-}150)$$

For standard, well-designed centrifugal pumps with specific speeds near 0.1 (1700), the head coefficient C_H has been found empirically to be equal to or slightly less than 0.8, depending somewhat on the way w_2^* is related to the vane shape.

In this example, C_H is assumed to be 0.78. From the velocity diagram shown in figure 2-51, it is evident that

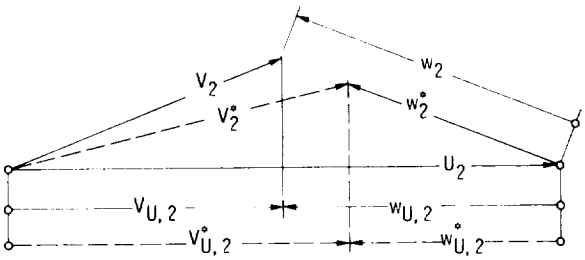

Figure 2-51.—Effect of skin friction in rotor passages on discharge velocity diagram.

$$\frac{w_2}{w_2^*} = \frac{w_{U,2}}{w^*_{U,2}} = \frac{U_2 - V_{U,2}}{U_2 - V^*_{U,2}} = \frac{1 - V_{U,2}/U_2}{1 - V^*_{U,2}V_{U,2}/V_{U,2}U_2}$$

$$= \frac{1 - V_{U,2}/U_2}{1 - (1/C_H)(V_{U,2}/U_2)} \qquad (2\text{-}151)$$

For standard centrifugal pumps of the type considered here, $V_{U,2}/U_2$ is slightly larger than 0.5. When it is assumed that $V_{U,2}/U_2 = 0.55$ and $C_H = 0.78$, equation (2-151) yields $w_2/w_2^* = 1.525$.

If this ratio between the actual (average) relative velocities and those determined from one-dimensional theory is assumed to be entirely due to fluid friction in the vane channels, the ratio of the channel discharge cross section reduced by the displacement thickness of its boundary layer A_f to the actual channel discharge cross section A is

$$\frac{A_f}{A} = \frac{1}{1.525} = 0.656 \qquad (2\text{-}152)$$

This figure would imply a very nonuniform relative velocity distribution. However, the foregoing assumption that the entire difference between the one-dimensional and the actual relative velocity is due to channel friction is somewhat unreasonable, since the finite vane spacing should lead to some reduction in head on the basis of frictionless flow, as discussed in sections 2.6.3.4 and 2.6.3.5. Assuming that approximately half of the difference between $w_{U,2}$ and $w^*_{U,2}$ is due to fluid friction, one arrives at the result

$$\frac{A_f}{A} = 0.82 \qquad (2\text{-}153)$$

which is reasonable as far as the friction-induced nonuniformities of the relative flow are concerned.

The suggestion that some of the departures from the one-dimensional, ideal-flow behavior are due to fluid friction and some are due to the two-dimensional characteristics of a frictionless flow is certainly reasonable and is not likely to lead to conflicts with experience. However, a theoretical prediction of the effect of channel friction on the rotor head is not possible on the basis of present knowledge. All that can be said is that fluid friction must be expected to have an effect on the rotor head, an effect over and above its effect on head losses by friction in the machine. An exception to this statement are rotors with axial, radial vanes on the discharge side, so that the relative flow has no substantial peripheral component, and its distribution, therefore, no significant effect on the rotor head.

The example just given leads to the conclusion that, with combined ideal-flow and fluid friction effects, the relative discharge flow has on the average about a 10-percent-thick displacement boundary-layer thickness all around the discharge end of the vane channel (but probably a much thicker boundary layer on the low-pressure side of the vanes than on the other channel walls). While this does not imply only minor effects of fluid friction, it contradicts any contention implying that even efficient centrifugal pump impellers might have very nonuniform relative velocity distributions, perhaps with separation. Again these conclusions cannot be drawn for rotors with straight radial (and axial) vanes at their discharge sides.

Thus, while the present considerations on the effects of fluid friction do not lead to any significant quantitative results, they do permit some fairly dependable qualitative conclusions which may be of value for the design engineer.

2.6.3.7 Effect of rotation on fluid friction.—The idea that rotation of a system should have an effect on real flow effects such as fluid friction and turbulence is fairly old. The thought of investigating such flows experimentally originated at least 50 years ago at Prandtl's institute for flow research in Goettingen, Germany. This writer is not aware of any major results of these early attempts to answer this problem.

The reason for interest in this field presumably stems from the fact that most real flow effects are intimately connected with vorticity, which must be expected to interact with the inherent vorticity or the relative flow in a rotating system. No doubt the potential importance of this interaction for the field of turbomachinery was recognized by early pioneers in this field. However, this writer is not acquainted with any publications on this particular subject prior to his own brief remarks in section 66 of reference 14, which cover only the intuitively

obvious aspects of this problem. More recently a number of investigations have been devoted to this problem. In reference 31, Johnston presents not only a review and an extensive bibliography of this subject, but also the results of his own theoretical and experimental investigations, which clarify the matter effectively and correct the earlier, over-simplified consideration by this writer (ref. 14).

In conformity with the general scheme of this compendium, the following presentation gives only those aspects of the problem which this writer has judged to be of value for the design engineer. The old concepts based on the relation between boundary-layer and relative flow vorticities are briefly reviewed, and then these concepts are corrected on the basis of Johnston's work (ref. 31). Some effects of rotation on separated flow and on secondary motions in radial-flow pump rotors are outlined. For a more complete study, the reader is referred to reference 31 and to some of the publications listed therein.

Figure 2-52, taken from reference 14, compares the direction of the vorticity in the boundary on the low-pressure side of the vanes with the vorticity of the relative flow. These two vorticities have opposite directions in the conventional configurations of the outward-flow pump (fig. 2-52(a)) and the inward-flow turbine (fig. 2-52(b)), whereas, in outward-flow turbines (used in torque converters and Ljungstroem turbines) (fig. 2-52(c)) and in inward-flow pumps (fig. 2-52(d)), these two vorticities have the same direction. From this comparison, the writer drew the premature conclusion that, in conventional pump and turbine rotors, the boundary layer on the low-pressure side of the vane may be reduced in thickness, with a corresponding reduction in the danger of separation, as compared with the boundary layer of a vane in a straight system of parallel vanes (axial-flow cascade). The opposite conclusion was drawn for the unconventional configurations (figs. 2-52(c) and (d)). In reference 14, it is shown that these conclusions can be confirmed analytically by considering the effect of turbulent velocity fluctuations under the influence of Coriolis forces in a rotating stream, if cross-stream velocity gradients in the relative flow are disregarded. This is, of course, a serious omission in considerations of boundary-layer flow.

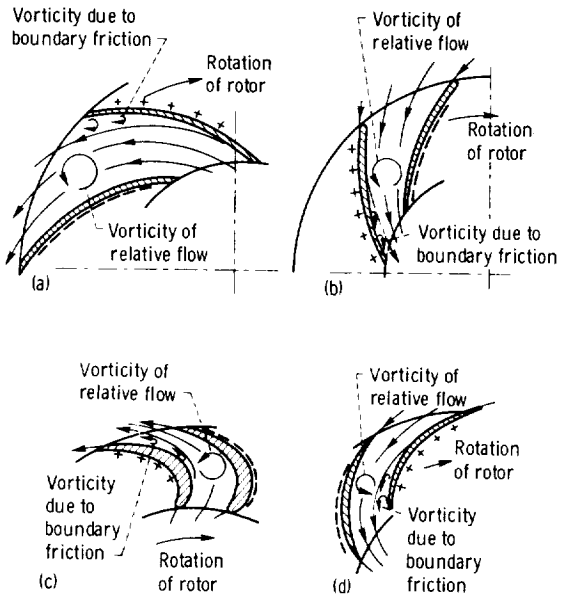

(a) Outward-flow pump rotor. (b) Inward-flow turbine rotor. (c) Outward-flow turbine rotor. (d) Inward-flow pump rotor.
Figure 2-52. – Relation between vorticity in boundary layer or separated region and vorticity of relative flow in radial-flow rotor.

The principal difference between the first considerations by this writer and those by Johnston is that the latter considers cross-stream velocity gradients in a rational stability analysis of the boundary layers; for normal boundary-layer flow, this method leads to conclusions opposite to those quoted from reference 14.

Before the principles of Johnston's analysis are described, another consideration deserves attention. In a private communication to this writer, Johnston pointed out that the vorticity in a reasonably orderly, turbulent boundary layer is by at least one order of magnitude greater than the distributed vorticity of the relative flow. Therefore the latter cannot be expected to have a significant influence on boundary-layer behavior. This correct remark leads this writer to apply figure 2-52 to the wake regions formed in connection with separation of the boundary layers, rather than to normal, thin boundary layers. The suction-side boundary layers are shown in figure 2-52 so thick as to suggest this interpretation. The average vorticity in a wake is, of course, much lower than in a normal boundary layer and may indeed be influenced by the vorticity of the relative flow. This reasoning can be further illustrated by using the very conventional, though highly idealized, way of representing the fluid motions in a separated flow region by a single, flat vortex, as shown diagrammatically in figures 2-53 and 2-54. The direction of the friction-induced

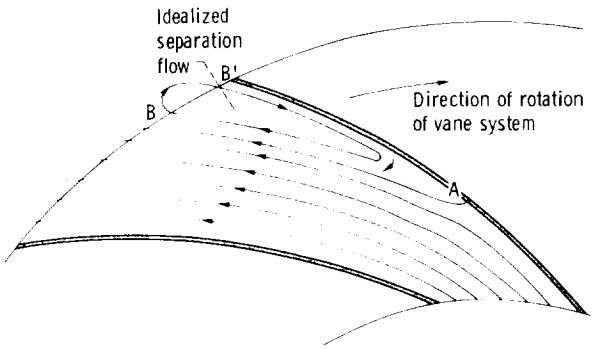

Figure 2-53. – Idealized separation in radial-flow rotor with backward-bent vanes.

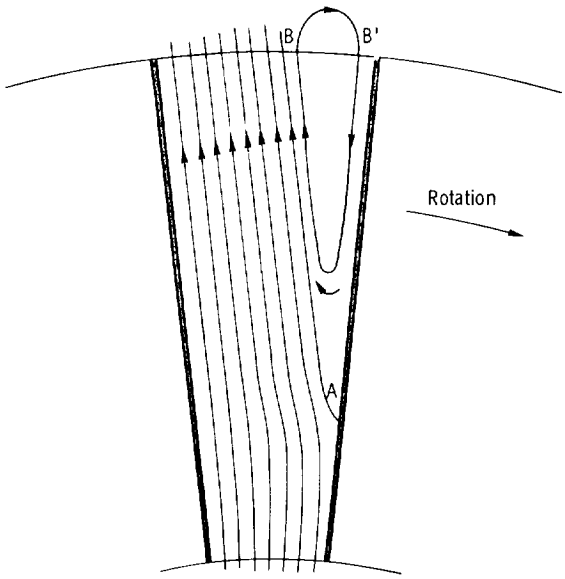

Figure 2-54. – Idealized separation in radial-flow rotor with straight radial vanes.

vortex is evidently opposite to that of the vorticity of the relative flow. Furthermore it is easy to show that the Coriolis forces tend to oppose the vortex motion in the separated region. This effect can be made plausible by referring to figure 2-53, in particular to the wake flow from point B′ toward point A. This flow evidently has a greater momentum in the direction of the rotation of the rotor than the wake flow from A to B or the flow outside the separated region. Such a momentum would require the application of a greater force in the direction of the rotor motion than existing normally in a separated region. The same argument could be used if the single vortex in the separated region were replaced by a row of vortices turning in the same direction as the single vortex shown in figure 2-53, and it applies also to a vortex in a rotor with radial blades, as shown in figure 2-54.

Alternatively one could, of course, consider the fluid in the separated region to be at rest relative to the rotor. In this case, the separated region could be in equilibrium with the adjacent active flow to approximately the same extent as a separated region on a stationary body, such as a stalled airfoil in a wind tunnel. Certainly no real equilibrium exists in the latter case, and with respect to any induced turbulent motions in this region of a rotating system, the Coriolis forces would have the same effect on individual vortices as described previously.

It can be concluded that the vorticity of the relative flow in radial-flow rotors must be expected to have a direct effect on the flow in separated regions. In figures 2-52(a) and (b), the relative-flow vorticity opposes the friction-induced vorticity in the separated region and probably destabilizes this region more than it is in connection with a stalled airfoil in a wind tunnel. The opposite should be true for figures 2-52(c) and (d). No statement can as yet be made regarding the resulting actual behavior of turbomachines.

We now return to the effect of rotation of the system on the behavior of boundary layers before separation. Although the following presentation is based on reference 31, this writer must assume full responsibility for the form of this presentation, which is not nearly as detailed as the Johnston paper because it serves a different purpose.

In a system rotating at a uniform angular velocity ω, a mass m moving radially relative to the system at a velocity w_r must exchange with its surroundings a so-called circumferential Coriolis force

$$C_U = 2m\omega w_r \tag{2-154}$$

Since this force produces the change in absolute moment of momentum connected with a radial motion in the rotating system, the force exerted by the surroundings on the mass m points in the direction of the circumferential motion of the system. The reaction to this force exerted by the mass on its surroundings is, thus, directed opposite to the circumferential motion of the system and, in the absence of constraints keeping the mass on a radial path relative to the system, causes a circumferential acceleration of the mass relative to the system in a direction opposite to the circumferential motion of the system.

In the same system, the same mass moving relative to the system at a circumferential velocity w_U exchanges with its surroundings a radial Coriolis force

$$C_r = 2m\omega w_U \tag{2-155}$$

Since this force is due to centrifugal forces, the body exerts a radial outward force on its surroundings if w_U is directed in the direction of the circumferential motion of the system and, in the absence of constraints keeping the mass at constant distance from the center of rotation, causes a radial outward acceleration of the mass relative to the system. If w_U is directed oppositely to the motion of the system, the force and resulting acceleration are radial and inward.

Equations (2-154) and (2-155) are now applied to the flow in radial-flow rotors of turbomachinery. Figure 2-55 shows the relative flow in a radial-flow pump rotor with straight radial vanes (the case primarily considered by Johnston). All relative velocities are radial, except turbulent fluctuations. All parts of the fluid encounter circumferential Coriolis forces in accordance with their nonuniform radial velocity w.

A fluid particle with mass m is displaced (by turbulence) in relation to its radial path from A to B (toward the vane) and carries its radial momentum and velocity w_A with it. (The very same conclusions would be reached by considering displacements in the opposite direction, i.e., away from the boundary.) At B it has a greater radial velocity than the average of the surrounding fluid by $\Delta w = w_A - w_B$. It, therefore, exerts on its surroundings a greater Coriolis force than the surrounding fluid by

$$\Delta C_U = 2m\omega\, \Delta w \tag{2-156}$$

where the subscript r is dropped because there are only radial relative velocities. Since this force is not in equilibrium with the forces (pressure differences) in its surroundings, the particle is accelerated in the direction of ΔC_U. Since Δw is positive for the assumed displacement toward the flow boundary (vane), ΔC_U and the resulting acceleration of the particle are directed against the direction of rotation. Figure 2-55 shows that this tends to return the particle to its original position at the trailing and low-pressure side of the vane and to remove it farther from its original position at the leading and high-pressure side. This means turbulence is suppressed, that is, the boundary-layer flow is stabilized at the trailing and low-pressure side and destabilized at the leading and high-pressure side. Since boundary-layer turbulence is essential for preventing separation, it follows that the danger of separation is increased by the Coriolis forces (system rotation), because separation can generally be expected only on the low-pressure side of the vane. Recall that this conclusion is just the opposite from that drawn by this writer from the relation between boundary-layer and relative-flow vorticity shown in figure 2-52. It is of interest to observe that the new conclusion was confirmed by Johnston experimentally by observing the reduction in turbulence on the low-pressure side of a rotating, radial channel.

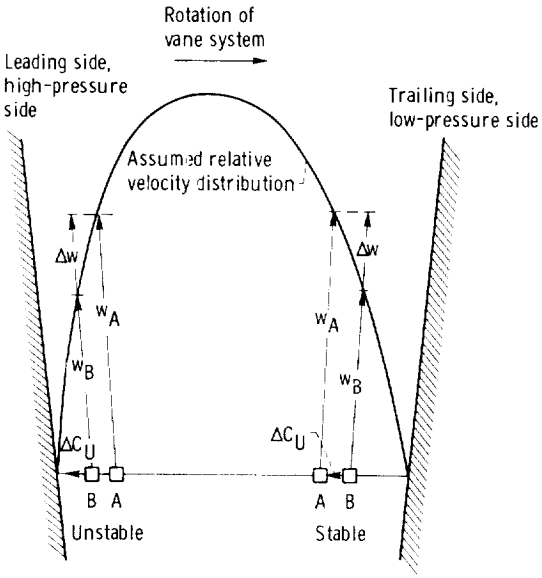

Figure 2-55. – Effect of rotation of radial-flow pump system with radial vanes on stability of vane boundary layers.

Figure 2-56 shows that the same conclusion can be reached with respect to the relative flow in a radial-flow pump rotor with backward-bent vanes. As in the previous case, turbulent fluctuations are assumed to displace the mass m from A to B, that is, toward the blade surface. The opposite assumption would lead to the same results.

In considering this figure, observe that the relative flow is directed against the rotation of the system. Hence the Coriolis forces resulting from the peripheral component Δw_U of the relative flow are directed radially inward; specifically these forces are those connected with the difference in relative velocity between position A and the perturbed

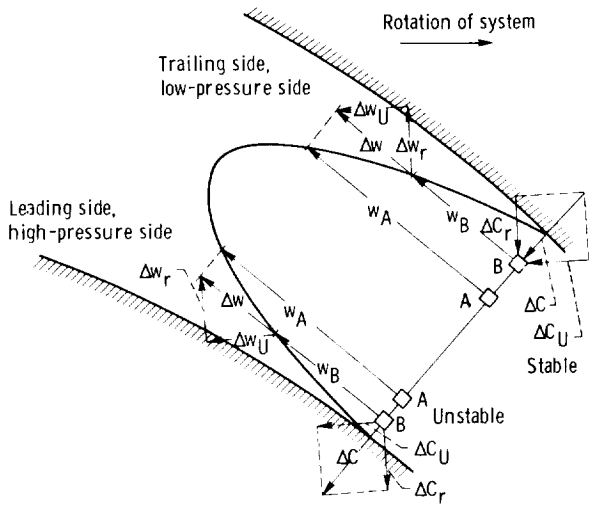

Figure 2-56. – Effect of rotation of radial-flow pump system with backward-bent vanes on stability of vane boundary layers.

position B and are associated with a local increase in the backward relative velocity Δw. Thus, in comparison with equation (2-155),

$$\Delta C_r = -2m\omega\,\Delta w_U \tag{2-157}$$

It should be noted that Δw_U is considered positive if it increases the magnitude of w_U in spite of the fact that w_U is here always negative.

The ΔC_U component points in the same direction as in figure 2-55. The ΔC vectors are plotted in figure 2-56 at a much larger scale than in figure 2-55, where no vectorial addition is required. This does not mean a difference in physical magnitude.

It is now desirable to extend the conclusion reached previously to other configurations. First convert the configuration shown in figure 2-55 to turbine operation simply by reversing the direction of the radial flow. The direction of rotation is kept the same, so that leading and trailing vane sides also remain the same. However, what was the low-pressure side becomes the high-pressure side and vice versa, since, as is obvious, in a turbine, the force acting on the vane (from the high- to the low-pressure side) must have the same direction as the motion of the rotor. (The opposite is necessarily true for pumps.) When the direction of the through flow alone (of w and Δw) is reversed, the direction of the Coriolis force difference must also be reversed. Thus increased stability (reduction in turbulence) remains connected with the (changed) low-pressure side, and the opposite is true for the (changed) high-pressure side.

Changing the system of figure 2-56 to turbine operation (according to fig. 2-52(b)) would require a reversal in direction of system rotation as well as a reversal of the relative flow w. Thus the Coriolis forces ΔC would retain their directions, and the stable and unstable sides would remain where they are; that is, the low-pressure side would continue to be the stable side with reduced turbulence, and the high-pressure side the unstable side with increased turbulence, since the low-pressure and high-pressure sides would remain the same (because of the reversal in the direction of rotation).

Next, in connection with figures 2-56 and 2-52(c), consider operation of an outward-flow turbine. The directions of relative flow and rotation would remain the same, and therefore, the stable and unstable sides also. However, high-pressure and low-pressure sides would be reversed, so that the boundary layer on the low-pressure side would be unstable (turbulence would be increased), a condition which is favorable for the prevention of separation, and the boundary layer on the high-pressure side would be stable (turbulence would be decreased). (High efficiencies should be obtainable with this configuration.)

Finally, in connection with figure 2-56, consider an inward-flow pump of the general arrangement shown in figure 2-52(d). In this case, the directions of relative flow and rotation would have to be reversed from those shown in figure 2-56, and the stable and unstable boundary layers would be left on the same sides as shown. However, since this is still pump operation with reversed direction of rotation, the high-pressure and low-pressure sides would be reversed from those shown, so that the unstable (high-turbulence) boundary layer would be placed on the low-pressure side (favorable for the prevention of separation), and the stable (low-turbulence) boundary layer would be placed on the high-pressure side (skin friction would be reduced). This configuration may lead to renewed consideration of the inward-flow pump in spite of its unfavorable overall stability of operation at reduced rates of flow.

In summary, then, the conventional outward-flow pump and inward-flow turbine are less desirable regarding boundary-layer growth and the onset of separation (stall) than the unconventional outward-flow turbine and inward-flow pump. However, after the onset of separation, conven-

tional outward-flow pumps and inward-flow turbines may be better than their unconventional counterparts. For example, if a highly efficient inward-flow pump could be developed, this pump might have exceedingly unfavorable stall characteristics.

2.6.3.8 Friction-induced secondary flow. – In closing the discussion on radial-flow rotors, we now consider briefly the secondary fluid motions in such rotors, just as done at the end of the section on axial-flow rotors (sec. 2.5.7). In agreement with the principle used there, only secondary motions produced by boundary layers are considered at this point, whereas secondary flows induced by vorticity in the main stream are discussed in section 2.7, together with the origin of the vorticity in the main stream.

Mixed- or conical-flow rotors with a strong axial-flow component have, of course, secondary flows quite similar to those of axial-flow machines, which are described in section 2.5.7 and are not further considered here. The present discussion is limited to secondary flows, which, because of the differences in geometric configuration, do not exist in axial-flow machines.

The secondary flow in the spanwise end boundary layers from the high-pressure toward the low-pressure side of the vane channel (shown for axial-flow systems in fig. 2-39) exists also in radial-flow rotors and can in principle be explained in the same manner as for axial-flow systems. For radial-flow systems, it is easier to explain this secondary motion by the Coriolis forces. Refer, for example, to figure 2-55; the circumferential Coriolis force in the end zone is lower than that in the midsections, because w is lower in the end zone. Since the circumferential pressure difference across the channel is dictated by the Coriolis forces in the midsections, the reduced Coriolis forces in the end zones cannot sustain this pressure difference without the fluid being accelerated from the high-pressure side toward the low-pressure side of the channel. This phenomenon may well be called overturning of the end-layer fluid, as it is for axial-flow machines. The same argument holds for radial inward flow in a turbine rotor.

Figure 2-57 shows the same secondary flow for a pump rotor with backward-bent vanes. The reasons for this flow are the same as for the flow between radial vanes except that components of both the relative flow and the Coriolis forces must be considered.

The outward motion of the boundary layer near the rotating end walls can, of course, be understood

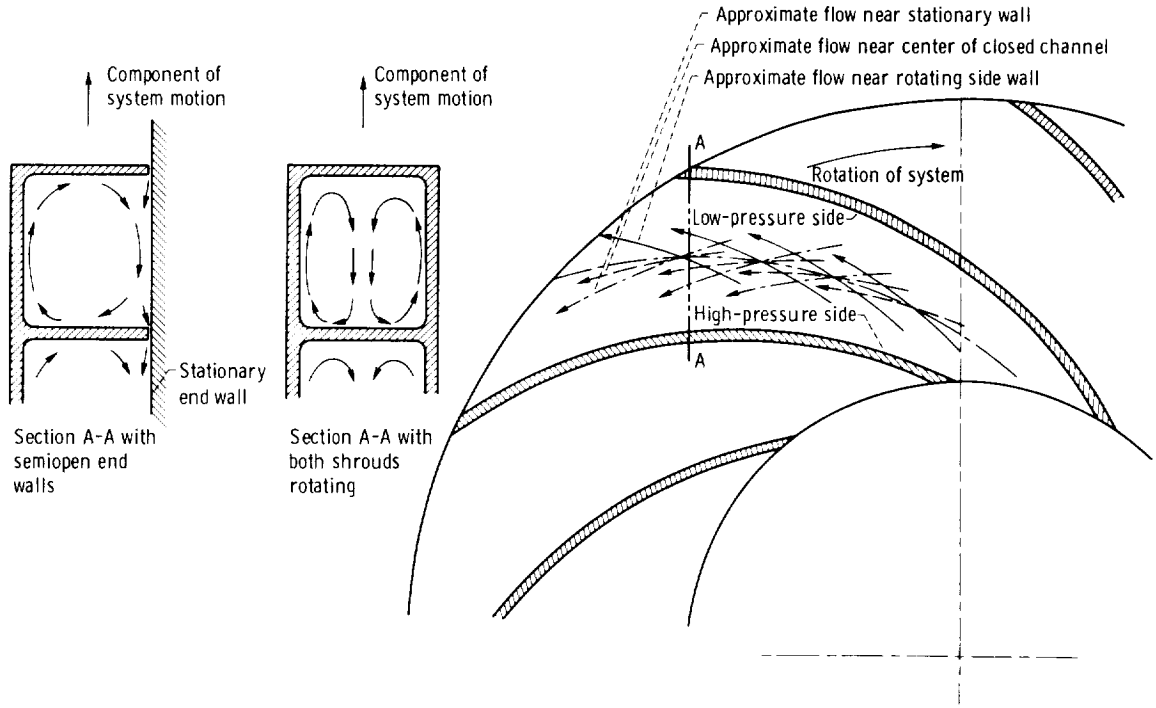

Figure 2-57. – Secondary flow in radial-flow pump rotors with backward-bent vanes. (Same type of flow exists also in rotors with straight radial vanes.)

here intuitively as centrifuge action on the fluid, which is dragged along by turbulent friction of the rotating shrouds. (This consideration is fundamentally not different from that viewing the Coriolis forces as resulting from the friction-induced boundary layer on the end walls.) The resulting secondary flow pattern in a closed vane channel (with both shrouds rotating) is principally not different from the familiar secondary flow in a curved duct or elbow relative to the high-pressure and low-pressure sides of the duct. It is reversed in direction relative to the concave and convex sides of the duct, and this change demonstrates the effect of rotation on the flow in this duct.

2.7 Three-Dimensional Flow Problems of Turbomachinery, Their Two-Dimensional Solutions, and Flow With Distributed Vorticity

2.7.1 Introduction

In sections 2.5 and 2.6, the inlet and discharge velocity diagrams are assumed to be given for every meridional stream surface considered. In other words, both the meridional and the circumferential velocity distributions at the inlet and discharge of the vane system considered are assumed to be known.

The only rational basis for the knowledge of these velocity distributions is a flow with uniform energy at the inlet to the first vane system and uniform changes of the energy (i.e., addition or subtraction of head which is uniform across the stream) in every rotating system of the machine. Under the assumption of frictionless flow for both the meridional and circumferential velocities, this reasoning leads to so-called irrotational velocity distributions. The meridional velocity distribution is determined by equation (2-4) of section 2.2 and may be found by the graphical construction shown in figure 2-3. The circumferential velocity follows the law of constant angular momentum (rV_U = constant) across the stream and changes in the rotating systems by constant steps in angular momentum according to Euler's turbomachinery equation in the form of equation (2-18). A flow of constant angular momentum can easily be shown to satisfy the same differential equation (eq. (2-4)) as the meridional flow.

Sections 2.2 and 2.3 mention that both flows may differ from the irrotational velocity distributions just discussed, but do not mention any general laws for such departures except that such departures are expressed for the meridional flow by its vorticity in the form of equation (2-6). Departures of the circumferential flow from the law of constant angular momentum can also be expressed by the vorticity of this flow, since

$$\zeta_z = \frac{\partial V_U}{\partial r} + \frac{V_U}{r} = \frac{1}{r}\frac{\partial (V_U r)}{\partial r} \tag{2-158}$$

so that

$$r\zeta_z = \frac{\partial (V_U r)}{\partial r} \tag{2-159}$$

which obviously describes the change in the angular momentum $V_U r$ as a function of the distance r from the axis of rotation. Appendix 2-A shows that the vorticity ζ is a vector normal to the plane of the vortex flow. This direction is here the axial direction and is designated by the coordinate z. The axial vorticity component ζ_z is a special case of the vorticity component ζ_m in the direction of the meridional flow, which is used in section 2.7.3.

A nonuniform angular momentum across the stream can be generated by any suitably designed vane system, since there is no general law prohibiting such a design. However, a circumferential flow with nonuniform angular momentum can easily be shown to have by itself a nonuniform energy distribution. If the vane system is assumed to be stationary and to receive an inflow with uniform energy distribution, it follows (for frictionless flow) that the discharging meridional flow cannot have a uniform energy distribution in connection with a circumferential flow of nonuniform energy, since the resultant, three-dimensional discharge flow must have the uniform energy distribution dictated by the incoming flow. This reasoning leads for the first time to a necessary interrelation between the circumferential and the meridional flow in a turbomachine, in contrast to the independence of these two flow components previously assumed. This interrelation constitutes the principal subject of this section and is shown to exist also if the flow of nonuniform angular momentum is generated by a rotating vane system.

There is one additional reason why the meridional flow may differ from the irrotational flow pattern: In the area swept by the rotor vanes or covered in a meridional section by the stator vanes

(where all points of these vanes are rotated into one meridional plane), there may very well be a component of the vane forces parallel to the planes of the meridional flow. In other words, vanes may not only exert circumferential forces on the flow according to their primary intent (Euler's turbomachinery eqs. (2-10) to (2-18)), but also forces lying in meridional planes, that is, in directions having no circumferential components. These forces exist only if the vanes are inclined against the radial and axial (meridional) planes and, for discrete vanes, would appear to be exerted by radial sections through the vanes (fig. 2-58). When the fiction of an infinite number of vanes is used for the meridional flow picture, this blade force on the meridional flow becomes distributed over the entire radial and axial planes of the meridional flow. This section shows that this vane action on the meridional flow can be evaluated as a distributed vorticity of this flow.

All considerations of this section are based on the assumption of frictionless flow with complete axial symmetry (infinite number of vanes), except where departures from this rule are explicitly indicated, as in the introductory part of section 2.7.2 and, of course, in section 2.7.5, on secondary fluid motions.

2.7.2 Effects of Spanwise Nonuniform Circulation

The effects of spanwise nonuniform circulation are demonstrated first on the basis of the particular

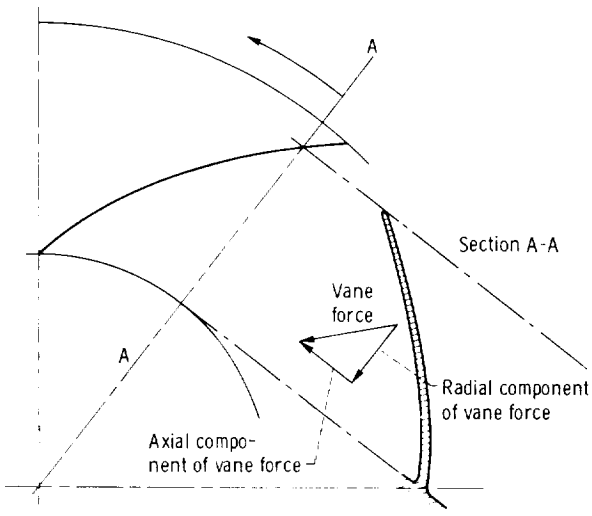

Figure 2-58. – Vane forces in meridional plane.

problem which, at least 35 years ago, gave rise to a rational investigation of the problems covered in this section. In the development of high-performance axial-flow compressors (for aircraft engines), it was obviously desirable to use the highest possible peripheral velocities of the rotor. At the same time, it was believed to be necessary to limit the relative inlet velocity to the rotor vane system to values below the acoustic velocity of the air under local conditions (a contention later contradicted by further developments, although it is still considered desirable to have only a limited excess of the acoustic velocity). In any event, it was desirable to minimize the relative velocity at the rotor inlet (which may also be true for hydrodynamic rotors for reasons of cavitation). It was natural to give the flow entering the rotor an initial rotation in the direction of the rotor motion and thus effectively reduce the relative inlet velocity. (Note that, in the absence of such prerotation, the peripheral component of the relative inlet velocity is $w_{U,1} = -U_1$, whereas, with prerotation, it is $w_{U,1} = -(U_1 - V_{U,1})$, where $V_{U,1}$ is the peripheral component of the absolute velocity entering the rotor.) Usually the peripheral component $w_{U,1}$ is the dominant component of the relative inlet velocity w_1, so that reductions in the latter are nearly proportional to reductions in $w_{U,1}$.

Assume that, for the purposes of reducing w_1, one chooses at the tip section $V_{U,1} = 0.25\ U$, so that $w_{U,1} = -0.75\ U_1$. Assume further that the inlet hub diameter is one-half of the maximum inlet diameter and that the blades of the axial-flow compressor start from this hub diameter. Thus $U_{1,h} = U_1/2$, and assuming for the prerotation the law of constant angular momentum gives

$$V_{U,1,h} = 2V_{U,1}$$

Therefore

$$\frac{V_{U,1,h}}{U_{1,h}} = \frac{0.50\ U_1}{0.50\ U_1} = 1$$

that is, the flow enters the hub section relative to the rotor axially, which gives this vane section an entirely forward turn and reduces static pressure. This is obviously undesirable for a machine intended to increase the static pressure of the medium.

If, instead, the pretotation could have (for example) the velocity distribution of a solid body rotation

$$\frac{V_{U,1,h}}{V_{U,1}} = \frac{U_{1,h}}{U_1} = \frac{r_h}{r_1} \qquad (2\text{-}160)$$

one would find (according to the previous assumption regarding $V_{U,1}/U_1$), instead of equation (2-160),

$$\frac{V_{U,1,h}}{U_{1,h}} = \frac{V_{U,1}}{U_1} = 0.25$$

which is quite acceptable for the design of the hub section. There is, therefore, a strong incentive to depart for the inlet guide vane system from the irrotational velocity distribution of constant angular momentum.

If it is assumed that the inlet guide vane system receives a flow of uniformly distributed energy and that the angular momentum of the oncoming flow is zero (very reasonable assumptions), the previously mentioned problem has to be solved for finding the meridional discharge velocity distribution, which, together with the assumed peripheral discharge velocity distribution (solid body rotation)

$$V_U = V_{U,o}\frac{r}{r_o} \qquad (2\text{-}161)$$

satisfies everywhere Bernoulli's equation. Here the subscript o refers to the outside, discharge diameter (or radius) of the inlet guide vane system, and the meridional flow at its discharge is assumed to be axial.

The problem can be solved on the basis of the so-called condition of radial equilibrium, which in its simplest form can be derived as illustrated in figure 2-59. The figure simply relates the radial change in static pressure to the centrifugal forces per unit area in a plane, rotating flow. This relation is

$$\left(p + \frac{\partial p}{\partial r}dr\right)(r+dr)\,d\alpha - p\,dr\,d\alpha - pr\,d\alpha = \rho r\,d\alpha\,dr\frac{V_U^2}{r}$$

which reduces to

$$\frac{\partial p}{\partial r} = \rho\frac{V_U^2}{r} \qquad (2\text{-}162)$$

When combined with Bernoulli's equation in a plane rotating flow, this equation simply leads to the familiar law of radially constant angular momentum $V_U r = \text{constant}$. Generally, for any prescribed relation between V_U and r, it will lead to a definite relation between the static pressure p and the distance r from the center (axis) of rotation.

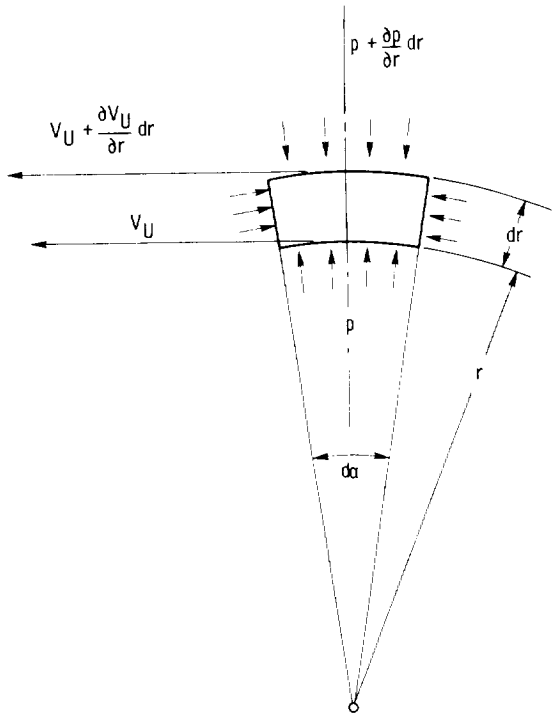

Figure 2-59. – Derivation of condition of simple radial equilibrium.

For the flow in a strictly axial-flow machine, where the radial velocity component is zero, the resulting velocity is $V = \sqrt{V_U^2 + V_z^2}$, where V_z is the axial velocity component. Hence, when the effects of differences in elevation are neglected, Bernoulli's equation appears in the form

$$p + \frac{\rho V^2}{2} = p + \frac{\rho}{2}\left(V_U^2 + V_z^2\right) = \text{constant} \qquad (2\text{-}163)$$

If, by a prescribed relation between V_U and r, equation (2-162) gives a relation between p and r, or p and V_U, the static pressure p can be replaced in equation (2-163) by a function of r or V_U. Since V_U is assumed to be a known function of r, equation (2-163) yields V_z as a function of r, that is, it gives the axial velocity distribution, which, together with the given V_U distribution, satisfies Bernoulli's equation.

In section 3.3.4.2 of chapter 3, this problem is solved for the case of solid-body rotation where V_U is proportional to r. The only general solution that can be suggested without a given relation between V_U and r is one based on the vortex laws by Helmholtz (see sec. 2.6.3.1 and appendix 2-A), particularly these laws in the form involving the concept of trailing vorticity, used by Prandtl to derive his famed wing theory. It becomes evident

later in this section that this solution also satisfies Bernoulli's equation.

Figure 2-60 shows one vane of an axial-flow vane system such as may be used at the inlet to a pump or compressor. For simplicity, it is assumed that the flow enters the system in the axial direction with uniform velocity and leaves the system with radially increasing circulation, so that $\Gamma_o > \Gamma > \Gamma_i$. According to the treatment by Thoma described in section 2.5.2 and figure 2-11 (which applies also to stationary vane systems), the vane circulation must also increase radially, since, with axial inlet flow, $\Gamma_o = N\Gamma_{v,o}$, $\Gamma = N\Gamma_v$ (at any radius), and $\Gamma_i = N\Gamma_{v,i}$.

According to Helmholtz' vortex laws and Prandtl's wing theory (appendix 2-A), between the section with circulation $\Gamma_{v,o}$ and the section with circulation Γ_v, the vane must shed a trailing vortex with circulation $\Delta\Gamma_o = \Gamma_{v,o} - \Gamma_v$, and this vortex vector must be parallel to the direction of the flow leaving the vane system. This means that the fluid motions or velocities representing the trailing vorticity (ζ in fig. 2-60) must be normal to the direction of the flow leaving the vane system. It is this fact on which the solution of this particular flow problem is based.

Figure 2-60 shows a second trailing vortex with circulation $\Delta\Gamma_i = \Gamma_v - \Gamma_{v,i}$, but in reality the vane circulation Γ_v and the circulation Γ in the flow downstream of the system change continuously from hub to tip, so that one should approximate this by a large number of trailing vortices, since actually each vane sheds a continuous vortex sheet.

Consider again the fiction of two trailing vortices per vane; the axial view of the entire trailing vortex system is shown in figure 2-61. Evidently

$$\left.\begin{aligned} \Gamma_o - \Gamma &= N\,\Delta\Gamma_o \\ \Gamma - \Gamma_i &= N\,\Delta\Gamma_i \end{aligned}\right\} \qquad (2\text{-}164)$$

since, according to section 2.5.2, the circulation about any contour (such as that formed by the outer circle with radius r_o and the middle circle with radius r) is equal to the sum of all circulations inside the contour.

Figures 2-60 and 2-61 imply that there exists a flow field with circumferential and radial motions between the trailing vortices. The corresponding flow field between two trailing vortex sheets is shown in figure 2-62, which may be regarded as a section normal to the vortex sheets (a slightly twisted surface) or as a section normal to the axis of

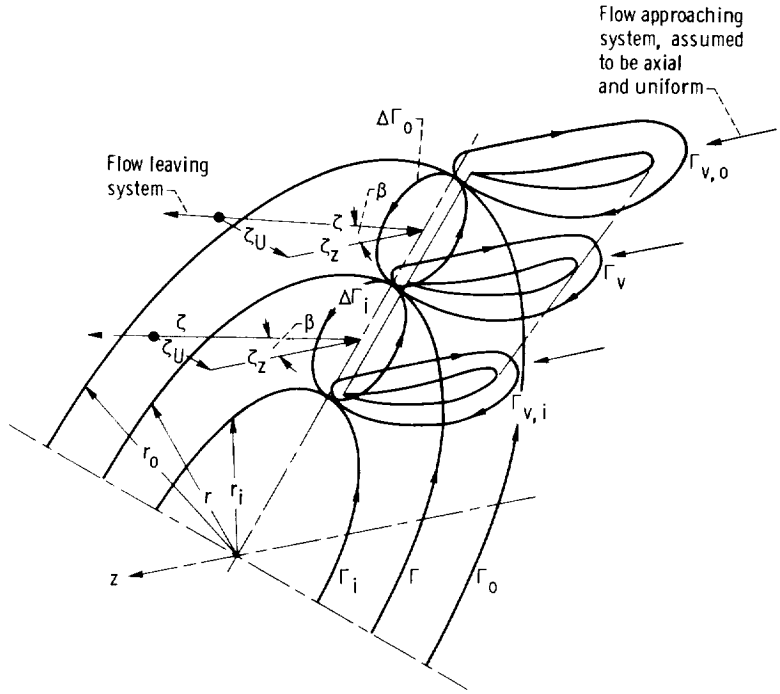

Figure 2-60. – Relation between vane circulations and circulation of flow leaving vane system. ($\Gamma_{v,o} > \Gamma_v > \Gamma_{v,i}$; $\Gamma_o > \Gamma > \Gamma_i$; $\Gamma = N\Gamma_v$; $\Delta\Gamma_o = \Gamma_{v,o} - \Gamma_v$; $\Delta\Gamma_i = \Gamma_v - \Gamma_{v,i}$.)

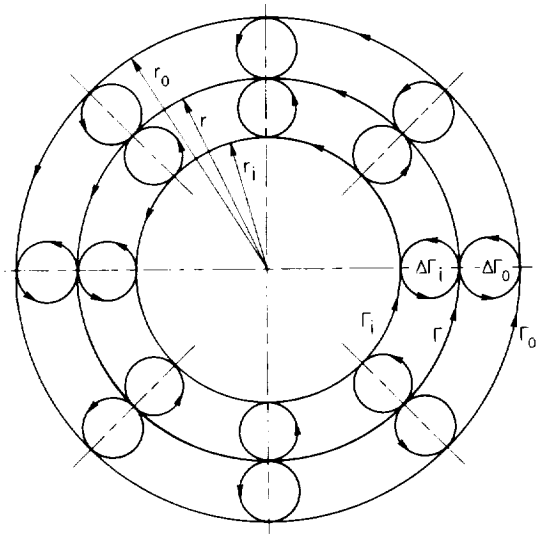

Figure 2-61. – Circulations in flow leaving vane system. ($\Gamma_o > \Gamma > \Gamma_i$; $N\,\Delta\Gamma_o = \Gamma_o - \Gamma$; $N\,\Delta\Gamma_i = \Gamma - \Gamma_i$.)

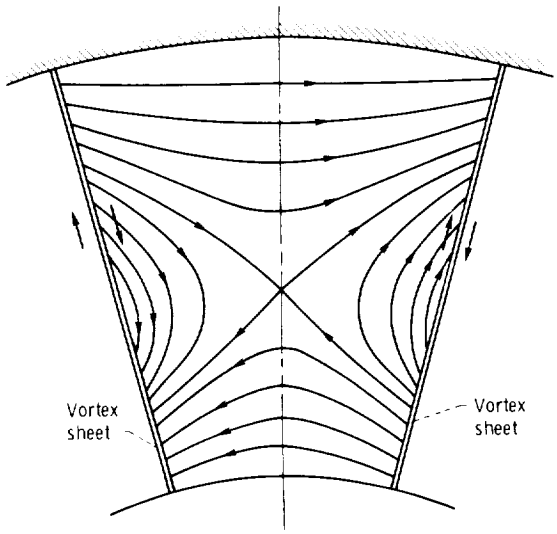

Figure 2-62. – Approximate flow with finite vane spacing induced by trailing vortex sheets.

rotation as in figure 2-61, or finally (with a slight distortion) as an axial and radial plane section showing the effect of the trailing vortex sheets on the meridional flow. These flow pictures must be superimposed onto the flow that would exist without any trailing vorticity, that is, the irrotational flow with radially constant vane circulation.

The flow shown in figure 2-62 is too complex to be used in the design of turbomachines. For this reason, one uses the familiar fiction of an infinite number of frictionless vanes. When this is done, the right and left parts of the flow field in figure 2-62 (close to the vortex sheets) with their radial velocity components vanish, the effect of the now continuously distributed axial vorticity ζ_z (fig. 2-60) is confined to the peripheral velocity component, and the effect of the (continously distributed) circumferential vorticity component ζ_U is confined to the axially symmetric meridional flow.

The distributed axial vorticity ζ_z can easily be calculated for any radial step, say from r to r_o, by the relation among circulation, vorticity, and area inside the contour of the circulation (eq. (2-A-26)):

$$\zeta_z = \frac{\Gamma_o - \Gamma}{\pi(r_o^2 - r^2)} \tag{2-165}$$

The vorticity of the meridional flow ζ_U is obtained from ζ_z by the condition that the total trailing vorticity is parallel to the flow leaving the vane system, so that

$$\frac{\zeta_U}{\zeta_z} = \frac{V_U}{V_z} \tag{2-166}$$

The meridional velocity V_z is first approximated by its average value according to the condition of continuity. Then the nonuniform distribution of V_z is determined from ζ_U by equation (2-6) and the construction shown in figure 2-4, which is, of course, particularly simple for axial-flow vane systems, where the radius of curvature R of the meridional streamlines is (in first approximation) infinite. The values of V_z so determined may then be substituted into equation (2-166) and the process repeated. The integration shown in figure 2-4 should start approximately in the area center of the duct, where one can assume V_z has its average value, used for the first approximation. After completing the V_z curve on this basis, one can correct it to comply more accurately with the condition of continuity as described briefly in section 2.2.

Fortunately there exists a simpler graphical method for deriving the V_z distribution for a given V_U distribution: Starting again approximately from the area center of the duct, approximate the discharge velocity diagram at that radius r_A by the average meridional velocity ($V_{z,av} = Q/A_m$, see sec. 2.2) and the prescribed local circumferential velocity V_U. The end point of the resultant velocity vector V is point A in figure 2-63. Then draw a new velocity diagram for a nearby radius r_B according to the assumption that the entire flow is irrotational, that is, that the circumferential velocity satisfies the law of constant angular momentum

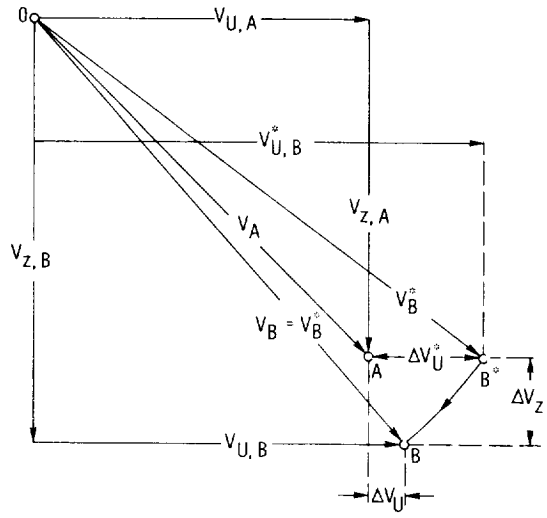

Figure 2-63. – Change in vane discharge velocity to account for trailing vorticity of axial-flow vane system where $V_m = V_z$.

$$\frac{V^*_{U,B}}{V_{U,A}} = \frac{r_A}{r_B} \tag{2-167}$$

where the asterisk signifies that this is not the true value of $V_{U,B}$, since a distribution departing from the law of constant angular momentum is prescribed. The fictitious meridional velocity at radius r_B is obtained in a similar manner for an irrotational meridional velocity distribution according to equation (2-4). For straight meridional streamlines, $V^*_{z,B} = V_{z,A}$. The end point of the new, fictitious velocity vector is marked B*.

The true peripheral velocity $V_{U,B}$ at radius r_B is prescribed. Also known is the fact that the velocity departures from the irrotational velocities (i.e., the velocities of the trailing vortex flow) are normal to the discharging flow in order to give the vorticity vector the same direction as the discharging flow. This is accomplished (for a small radial step) by swinging the velocity vector drawn to point B* about its origin O to a new point B where the circumferential velocity has the prescribed value $V_{U,B}$. This construction satisfies not only the vortex law but also Bernoulli's equation to the extent that the true static-pressure difference between r_A and r_B can be approximated by the pressure difference for irrotational flow, which is known to satisfy Bernoulli's equation. (Consider that the magnitude of the velocity is not changed in going from B* to B.)

Figure 2-64 shows a succession of these steps for the peripheral as well as the meridional velocity components. Every step requires, and is based on, a velocity diagram such as that shown in figure 2-63. This example solves the inlet vane system problem described previously.

The same method applies in principle also to rotating vane systems, except that the trailing

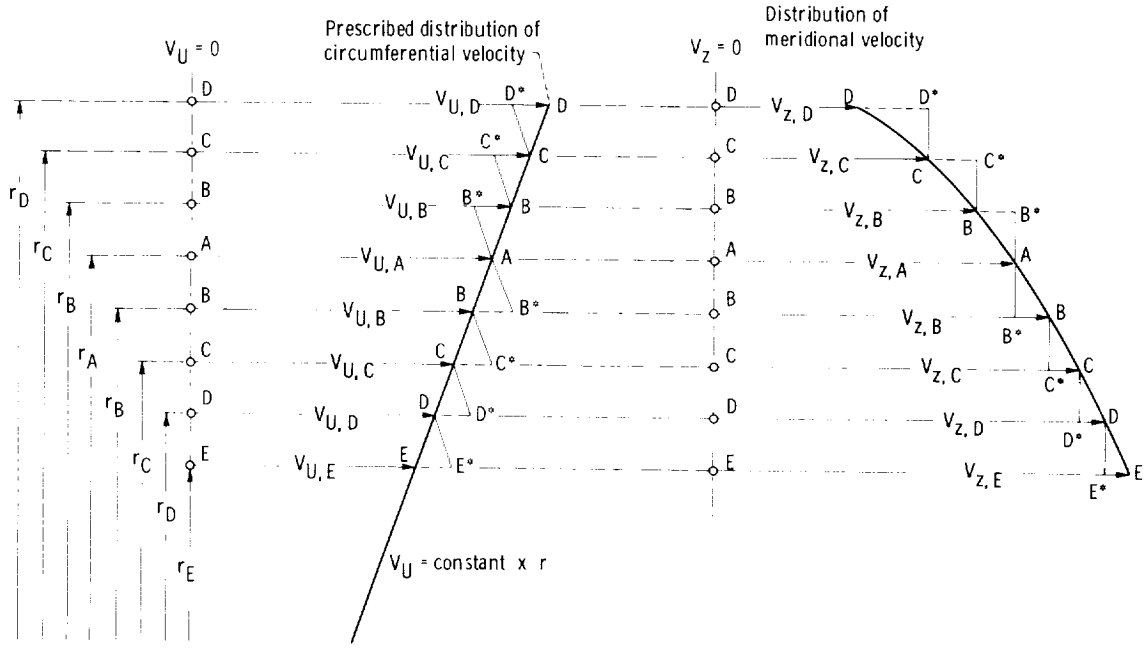

Figure 2-64. – Stepwise determination of meridional velocity of axial-flow vane system.

vorticity is parallel to the relative velocity leaving the vane system, so that, in place of equation (2-166), one must use

$$\frac{\zeta_U}{\zeta_z} = \frac{w_U}{w_z} \tag{2-168}$$

The principal reason for considering the foregoing graphical solution is the clarity with which it illustrates the effect of vorticity (the effect of departures from the potential velocity distribution) on the flow. For the practical solution of flow problems with vorticity, the graphical method should be used only for small changes in the distance from the axis of rotation. For appreciable changes in this distance, an analytical solution, presented in the next section, is better than the graphical solution, particularly if the meridional streamlines are curved. The practical execution of such a flow problem is described in chapter 4, section 4.4.1.

2.7.3 General Solution of Problem of Flow With Vorticity in Turbomachinery

The effectiveness of the concept of vorticity in permitting a relatively simple solution of the flow problem discussed in the preceding section leads one to attempt on the same basis a more general solution of the problem of flow with vorticity in turbomachinery.

For the present, the assumption of complete axial symmetry (i.e., of an infinite number of frictionless vanes) is maintained. However, the assumption of irrotational (vorticity-free) inlet flow to the vane system considered is dropped to permit the application of the results obtained to vane systems behind other systems which may put vorticity into the stream. This vorticity is, according to the assumption of complete axial symmetry, uniformly distributed in the circumferential direction.

The following presentation is based on a solution of this problem by Leroy H. Smith given in reference 32 and follows his presentation closely in principle and in some details.

The objective of the following presentation is not the solution of a specific problem of flow with vorticity through a vane system, but rather the derivation of general equations by which such problems can be solved in various ways. The following derivation differs from those given in references 14 (ch. 26) and 33 by the fact that it is based on kinematic considerations of flow with vorticity, which are basic to this problem, whereas the derivations in these references are based primarily on dynamic considerations of radial equilibrium.

The present derivation assumes that the inlet flow to the vane system is completely known, so that the inlet velocity and vorticity vectors w_1 and ζ_1 in figure 2-65 are given. The particular meridional stream surface to which the vector diagrams in figure 2-65 apply is chosen in such a manner that the meridional discharge velocity $w_{m,2} = V_{m,2}$ can be estimated or selected by the condition of continuity; that is, the chosen flow surface is located near the average radius of the discharge cross section. The change in the peripheral velocity component $\Delta w_U = \Delta V_U$ is usually given by the change in angular momentum required from the vane system considered, although this requirement is not precise, since, with vorticity, the angular momentum and its change are not uniform over the discharge cross section.

It remains to determine the discharge vorticity in accordance with the vortex laws by Helmholtz (see appendix 2-A), which may be called the practical objective of the following considerations.

The velocity and vorticity diagrams shown in figure 2-65 apply directly to the flow through a rotating vane system, as is evident from the relative velocities w_1 and w_2. The same diagrams apply in principle also to a stationary vane system when the relative velocity vectors w_1 and w_2 are replaced by the absolute velocity vectors V_1 and V_2.

For the derivations, Helmholtz's vortex laws are used in the following form:

(1) The vorticity vector of the flow entering the system remains connected with the fluid particles.

(2) The vorticity generated within the system has vectorially the same direction as the flow leaving the system (trailing vorticity).

(3) The flow through the system obviously satisfies the condition of continuity.

For incompressible or compressible flow, the first condition is satisfied by drawing the vorticity vector divided by the density of the fluid between two adjacent streamlines within the meridional stream surface considered (ref. 34). These vorticity vectors are shown in figure 2-65 between the point 0 and the line C_1B_1 at the inlet to the system and between the point 0 and the line C_2B_2 at the discharge from the system. The scale of ζ/ρ and the angular spacing $\Delta\theta$ are assumed to be so small that the local curvature of the streamlines considered can be ignored. For

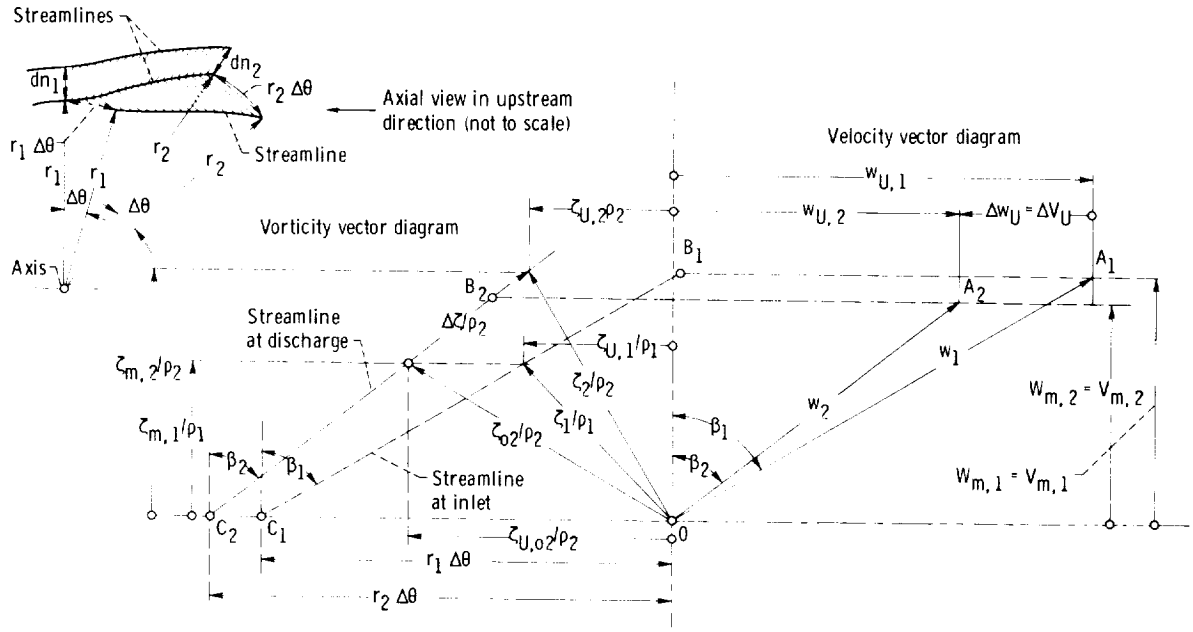

Figure 2-65. – Velocity and vorticity vector diagram for axially symmetric flow through vane system (according to L. H. Smith, ref. 32).

reasons of axial symmetry, the angular distance $\Delta\theta$ between two such adjacent streamlines is constant.

We are now in a position to describe the vorticity vector diagram shown in figure 2-65. While quite general in principle, it assumes the existence of a stationary vane system (such as that discussed in sec. 2.7.2) in front of the rotating vane system with the flow characteristics shown in figure 2-65. The inlet flow to this rotating vane system is, therefore, approximately that shown in figure 2-64, specifically that at an intermediate meridional stream surface, for example, that at radius r_A in figure 2-64.

It would be natural to think of a uniform energy input by the rotor to all stream surfaces, which means $\Delta(V_U r) = \text{constant}$ across the flow, that is, there is no change of the meridional vorticity component $\zeta_{m,1}$ within the rotor. The result obtained by this assumption is shown in figure 2-65 by the discharge vorticity vector ζ_{02} under the restriction $\rho_2 = \rho_1$. The aforementioned requirement that the vorticity vector remain between the same streamlines leads to an increase in the peripheral vorticity component from $\zeta_{U,1}$ to $\zeta_{U,02}$, which may not be acceptable, because this increase may lead to zero or negative meridional discharge velocities at the maximum discharge radius (see the $V_z = V_{m,2}$ distribution in fig. 2-64). This possibility is avoided by having the rotor add a vorticity $\Delta\zeta$ to the flow. This addition results at the discharge in a trailing vorticity $\Delta\zeta$, which has the direction of w_2 and of the streamline at the discharge of the system. It can be seen from figure 2-65 that the magnitude of $\Delta\zeta$ can be determined from the vorticity vector diagram, so that $|\zeta_{U,2}| \leq |\zeta_{U,1}|$, that is, the departure of the meridional discharge velocity from the irrotational distribution is not greater than that shown in figure 2-64 for the rotor inlet. (The same could be accomplished by an outward curvature of the meridional discharge flow, but this is not significant with respect to the present considerations.)

With the vorticity vectors in figure 2-65 determined by the foregoing or other equivalent considerations, the law of vortex flow through a rotating vane system can be derived from figure 2-65 as follows: To satisfy the condition of continuity, one can write

$$\rho_1 r_1 \, dn_1 \, w_{m,1} = \rho_2 r_2 \, dn_2 \, w_{m,2}$$

so that

$$\frac{r_1 w_{m,1}}{r_2 w_{m,2}} = \frac{\rho_2 \, dn_2}{\rho_1 \, dn_1} \tag{2-169}$$

where r_1 and r_2 are the distances from the axis of rotation at the inlet and discharge of the vane system.

It is clear that the ratio on the left side of equation (2-169) is the ratio of the areas of two parallelograms in figure 2-65, namely, $OA_1B_1C_1$ and $OA_2B_2C_2$.

The areas of the same parallelograms are also equal to the vector products of the velocity vectors and vorticity vectors w and ζ/ρ. The fact that the vorticity vector remains within the parallelogram described by two adjacent streamlines expresses the fact that the change in vorticity $\Delta\zeta$ within the vane system has the direction of the flow leaving the vane system w_2 and, therefore, does not change the vector product of the velocity and the vorticity. Thus the ratio of the areas of the two parallelograms $OA_1B_1C_1$ and $OA_2B_2C_2$ may be written in the form

$$\frac{r_1 w_{m,1}}{r_2 w_{m,2}} = \frac{|\overleftarrow{(\zeta_1/\rho_1)} \times \overleftarrow{w_1}|}{|\overleftarrow{(\zeta_2/\rho_2)} \times \overleftarrow{w_2}|} \tag{2-170}$$

If equation (2-170) is written in the form

$$\frac{|\overleftarrow{\zeta_1 \times w_1}|}{\rho_1 r_1 w_{m,1}} = \frac{|\overleftarrow{\zeta_2 \times w_2}|}{\rho_2 r_2 w_{m,2}} \tag{2-171}$$

it can be broken up into its components:

$$\frac{\zeta_{m,1} w_{U,1} - \zeta_{U,1} w_{m,1}}{\rho_1 r_1 w_{m,1}} = \frac{\zeta_{m,2} w_{U,2} - \zeta_{U,2} w_{m,2}}{\rho_2 r_2 w_{m,2}} \tag{2-172}$$

The subscript m denotes the meridional flow direction; that is, ζ_m is the vorticity of the circumferential flow in a section normal to the meridional flow. The component ζ_U is the vorticity of the meridional flow.

Finally, when the vorticity components are expressed in terms of velocities and velocity gradients, equation (2-172) assumes the form

$$\left[w_{U,1} \left(\frac{\partial V_U}{\partial n} + \frac{V_U}{r/\cos\varphi} \right)_1 + w_{m,1} \left(\frac{\partial V_m}{\partial n} \pm \frac{V_m}{R} \right)_1 \right] \frac{1}{\rho_1 r_1 w_{m,1}} = \left[w_{U,2} \left(\frac{\partial V_U}{\partial n} + \frac{V_U}{r/\cos\varphi} \right)_2 + w_{m,2} \left(\frac{\partial V_m}{\partial n} \pm \frac{V_m}{R} \right)_2 \right] \frac{1}{\rho_2 r_2 w_{m,2}} \tag{2-173}$$

where n is a coordinate normal to the meridional streamlines, increasing with increasing distance r from the axis of rotation, and φ is the angle between the meridional streamline and the axial direction, so that $r/\cos\varphi$ is the distance from the axis of rotation as seen in a conical section normal to the meridional flow (fig. 2-66). The radius of curvature of the meridional flow in the radial and axial planes is designated R. The plus sign in the second term applies to meridional stream surfaces concave toward the axis of rotation, so that the centrifugal forces of the meridional flow are additive to the centrifugal forces of the circumferential flow (fig. 2-66(a)). Meridional streamlines turning their convex sides toward the axis of rotation produce centrifugal forces opposed to those of the circumferential flow; thus the minus sign applies in this case (fig. 2-66(b)).

For stationary vane systems, one replaces the relative velocity w by the absolute velocity V, as mentioned previously. Thus

$$\frac{|\overleftarrow{\zeta_1 \times V_1}|}{\rho_1 r_1 V_{m,1}} = \frac{|\overleftarrow{\zeta_2 \times V_2}|}{\rho_2 r_2 V_{m,2}} \tag{2-174}$$

or, in components,

$$\frac{\zeta_{m,1} V_{U,1} - \zeta_{U,1} V_{m,1}}{\rho_1 r_1 V_{m,1}} = \frac{\zeta_{m,2} V_{U,2} - \zeta_{U,2} V_{m,2}}{\rho_2 r_2 V_{m,2}} \tag{2-175}$$

$$\left[V_{U,1} \left(\frac{\partial V_U}{\partial n} + \frac{V_U}{r/\cos\varphi} \right)_1 + V_{m,1} \left(\frac{\partial V_m}{\partial n} \pm \frac{V_m}{R} \right)_1 \right] \frac{1}{\rho_1 r_1 V_{m,1}} = \left[V_{U,2} \left(\frac{\partial V_U}{\partial n} + \frac{V_U}{r/\cos\varphi} \right)_2 + V_{m,2} \left(\frac{\partial V_m}{\partial n} \pm \frac{V_m}{R} \right)_2 \right] \frac{1}{\rho_2 r_2 V_{m,2}} \tag{2-176}$$

where it should be remembered that $w_m = V_m$.

In all equations stated so far in this section, the subscript 1 applies to one side, say the inlet side of the vane system considered, and the subscript 2 to the other side, say the discharge side of the same vane system.

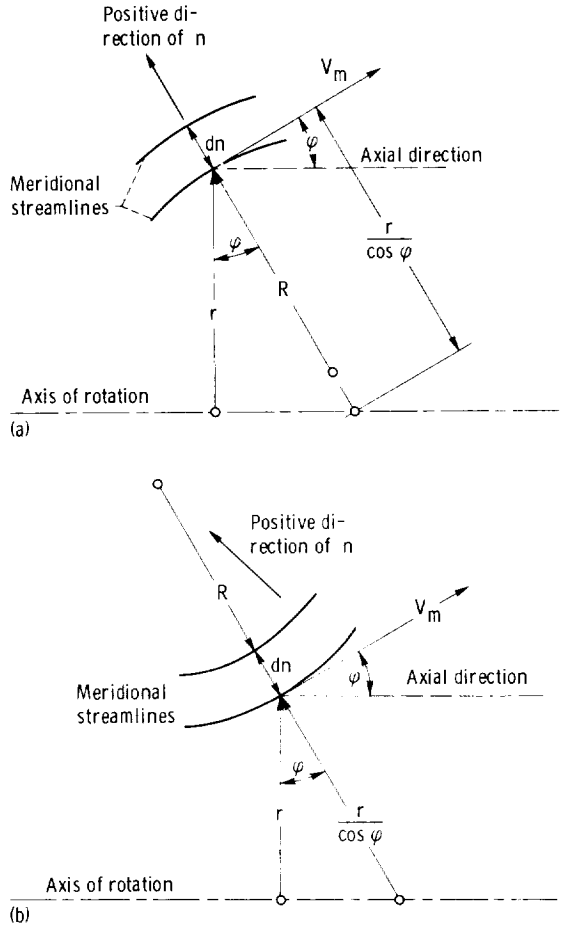

(a) Concave when viewed from axis.
(b) Convex when viewed from axis.
Figure 2-66. – Curvature of meridional streamlines.

It is well to remember that the fundamental equations (2-171) and (2-174) and, therefore, all equations derived from them express primarily the facts that any vorticity added by a vane system must have at the discharge the same (or opposite) direction as the discharging flow and that the incoming vorticity remains between corresponding streamlines, as shown in figure 2-65.

The meridional component of the vorticity added by the vane system $\Delta\zeta_m$ is usually given by a prescribed change in angular momentum. Sometimes, as in the case of a rotor following an inlet guide vane system, discussed in section 2.7.2, the vorticity change of the meridional flow is prescribed in order to achieve a reasonable meridional discharge velocity distribution. In any event, there are given restrictions on the vorticity and velocity distribution at the discharge of the vane system considered in addition to the restrictions expressed by equations (2-171) to (2-176) as well as figure 2-65.

Furthermore the inlet velocity and vorticity distribution (i.e., one side of all eqs. (2-171) to (2-176)) must be given to establish a definite problem, so that the inlet velocity and vorticity vectors in figure 2-65 are prescribed. With respect to the expanded equations (2-173) and (2-176), not only is one side given, but also, on the other side, one component of the velocities, either V_U or V_m, is prescribed. This reduces the solution of the problem to the determination of the other velocity component by its vorticity, either

$$\zeta_m = \frac{\partial V_U}{\partial n} + \frac{V_U}{r/\cos\varphi} \tag{2-177}$$

or

$$-\zeta_U = \frac{\partial V_m}{\partial n} + \frac{V_m}{R} \tag{2-178}$$

A graphical solution of this problem is presented in section 2.2 in connection with figure 2-4. The solution starts from some suitably chosen midpoint M, where the velocity components V_U, w_U, and $V_m = w_m$ are given or calculated from the condition of continuity.

Finally, it is also possible to solve many problems on the basis that the departures from the irrotational velocity distributions are normal to the resultant vorticity vector given by figure 2-65 and equations (2-171) and (2-174). This is the method described in the preceding section in connection with a particularly simple problem. Examples for the practical execution of these solutions are presented in chapters 3 and 4 in connection with definite design problems.

2.7.4 Determination of Off-Design Operating Characteristics

An important application of the principles of flow with vorticity in turbomachines is the determination of the off-design operating characteristics. Even for machines designed for vorticity-free operation at one particular volume flow rate or one particular flow coefficient V_m/U, the flow acquires vorticity if the flow coefficient departs from its design value. This is particularly true for pumps where the flow leaves the rotor at more than one diameter, as it does with axial-flow and mixed-flow rotors. For simplicity of reasoning, the

following considerations are confined to axial-flow rotors, but the principles employed apply to mixed-flow rotors as well.

Figure 2-67 shows the solution suggested. Figure 2-67(a) shows the (ideal) straight-line head-flow characteristics of three cylindrical sections O, M, and I through the discharge opening of an axial-flow rotor with radii r_o, r_M, and r_I. (All that must be assumed to understand this relation is the fact that the discharge relative velocity at any one section has a constant relation to the zero-lift direction of the vanes (C_H in sec. 2.5).)

The design point D is assumed to have irrotational flow, that is, constant head and angular momentum and constant V_m over the discharge cross section, and for simplicity the inlet angular momentum is assumed to be zero (or constant). Thus the head-flow lines must intersect at the design point D.

At a reduced flow rate, the three flow sections produce different head values. Wattendorf in reference 35 suggests averaging these head values at a constant value of V_m/U_o (where the subscript o refers to the outermost flow section). O'Brien and Folsom suggest the same in reference 36. This writer has suggested (in sec. 48 of ref. 14) drawing a horizontal line through point A (fig. 2-67(a)) and integrating the various rates of flow along this line.

A more dependable solution can be obtained in the following manner: Starting (as in sec. 2.7.2) from the irrotational solution H_r = constant under the fictitious assumption that the flow sections O and I have relative discharge directions different from their actual discharge directions, one arrives in figure 2-67(b) at the velocity end points B* and C* at the same head and meridional velocity as assumed for the midsection, marked point A. Since the rotor system does not permit these discharge directions, it generates a trailing vorticity which displaces the end points of the relative velocity vectors in sections O and I from B* to B and C* to C by the same construction as used in figure 2-63. The corresponding operating points are marked by B and C in the head-capacity diagram (fig. 2-67(a)). The true total rate of flow under the off-design operating condition must be obtained by a flow integration over the discharge cross section of the rotor

$$Q = 2\pi \int_{r_I}^{r_o} V_m r \, dr \tag{2-179}$$

The average head is determined by a similar weighted integration

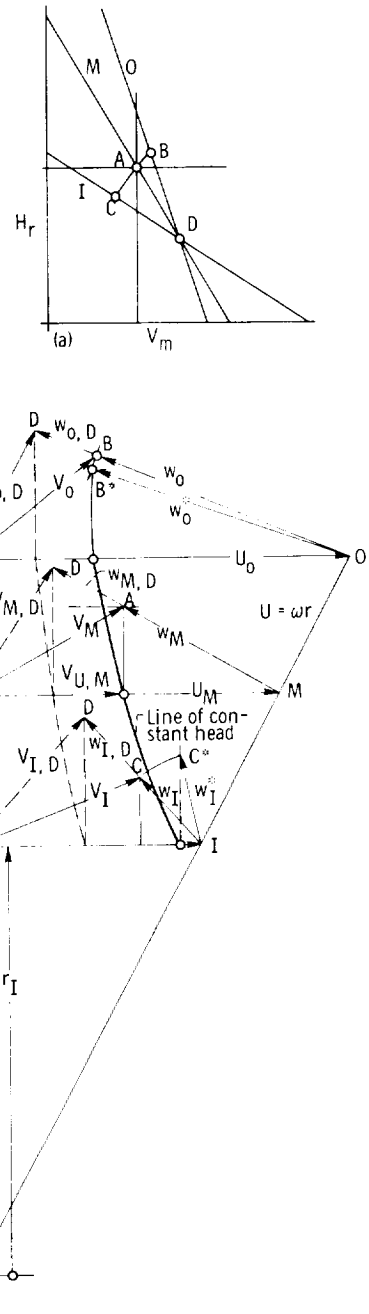

(a) Head-flow curves.
(b) Velocity diagrams at three discharge diameters.
Figure 2-67. – Determination of off-design conditions for axial-flow rotor.

$$H_{r,av} = \frac{2\pi}{Q} \int_{r_I}^{r_o} H_r V_m r \, dr \tag{2-180}$$

The mixing losses between parallel streams with different head values are not predictable in a general manner, but should be added to other head

losses in the machine connected with operation under off-design conditions.

In the example shown in figure 2-67, the radial step from r_M to r_I is a little large for the approximate step from the irrotational solution to the true solution. This is apparent from the fairly large angle between the fictitious relative velocity vector drawn to point C* and the true vector drawn to point C. One can avoid angles that large or larger by using more radial steps. The process is essentially the same as that described in section 2.7.2 in connection with figures 2-63 and 2-64 except that the final end point of the (relative) velocity vector (B or C) is not determined by one given component of this vector but by the direction of this vector given by the velocity diagram under the design conditions.

By using the process described here for two off-design conditions, preferably on opposite sides of the design point D, one can draw an $H_{r,av}$, $V_{m,av}$ (or Q) curve with sufficient accuracy for most practical purposes.

2.7.5 Secondary Flow in Turbomachinery

Secondary flow in turbomachinery is discussed previously in connection with boundary layers and the vorticity introduced into the flow by them. Specifically, section 2.5.7 discusses this problem with respect to axial-flow turbomachines; the problem is related to the radial motion or centrifuging of the rotor blade boundary layers (fig. 2-38), to the vane interaction with the casing boundary layers, leading to overturning, and to a secondary vortex in the spanwise end zones of axial-flow vane systems, as described graphically in figure 2-39.

In addition to (friction-induced) secondary flow, which exists also in mixed-flow (conical-flow) turbomachinery, radial-flow turbomachines have secondary flows due to other causes. These flows are described in section 2.6.3.8 and depicted for radial-flow pump rotors with backward-bent vanes in figure 2-57. The figure shows in the spanwise end regions of the passage a flow from the high-pressure to the low-pressure side of the passage, which is a phenomenon generally existing in axial-flow machines in the form shown in figure 2-39. An exception to this rule occurs in open impellers (and guide vane systems), where one end of the passage has a wall with a different motion inducing in pump rotors a flow from the low-pressure to the high-pressure side of the vane passage (see fig. 2-57).

Another friction-induced secondary flow exists in open impellers by virtue of the leakage stream between the vane ends and the adjacent casing wall. This flow has the same direction as the end wall motion in open pump rotors, whereas the leakage stream is opposite to the end wall motion in open turbine rotors.

This section introduces on the basis of frictionless-flow considerations an additional reason for secondary flow. Figures 2-60 to 2-62 depict the secondary flow induced by radial nonuniformities of the vane circulation into the main stream, discussed in section 2.7.2. An approximately radial vortex sheet induces on its two sides opposite, approximately radial velocities, which lead to the flow picture shown in figure 2-62. An experimental investigation by Leroy Smith (ref. 32) showed that, even under very dramatic changes in vane circulation (i.e., very intense trailing vorticity), the resulting secondary motions did not have truly significant effects on the overall performance of the vane system. The same author showed in reference 37 that certain aspects of secondary flow, such as the vortex in the end zones (fig. 2-39), can be approximated theoretically. It is of interest to observe that the secondary motion just mentioned is significant only in the spanwise end regions, where the vorticity of the flow entering the vane system is very intense because of the boundary layers on the casing or shroud walls.

The following is a partial listing of secondary fluid motions in turbomachinery:

(1) Radial motion of the boundary layer on the vanes of axial-flow turbomachines. Leads to an accumulation of fluid with reduced (relative) velocity in the outer tip region of rotors and in the hub region of stators (fig. 2-38) and increases the danger of separation in these regions.

(2) Secondary flow due to vorticity entering a vane system or generated within the system by skin friction on the end walls. Appears as a flow near the end walls from the high-pressure to the low-pressure side of the vane channel (overturning) and a more distributed flow of much lower velocity in the opposite direction in the rest of the channel (end vortex, see figs. 2-39 and 2-57).

(3) Secondary flow due to the trailing vortex sheet shed from every vane with spanwise nonuniform

circulation. Generates a spanwise velocity component near and behind the trailing edges in opposite directions on the two sides of the vanes and trailing vortex sheets. (The entire secondary flow field is shown in fig. 2-62.)

(4) Blade end leakage flow in open vane systems. Forms a trailing vortex near the low-pressure sides of the vanes (see fig. 2-68).

(5) Flow due to the relative motion of the end wall in an open vane sytem. In pumps, this flow opposes the secondary flow from the high-pressure toward the low-pressure side of the channel (item (2)), but increases the leakage stream through the gap. In turbines, it increases the secondary flow from the high-pressure toward the low-pressure side of the channel, but opposes the leakage stream.

(6) The vorticity $\zeta_{rel} = -2\omega$ of the relative flow in radial-flow rotors does not generate secondary flow motion, as shown in section 2-A.3 of the appendix.

2.7.6 Effect of Vane Forces on Meridional Flow

As mentioned in section 2.7.1, the fluid-connected vorticity (such as the trailing vorticity) considered so far is not the only reason for the departure of the meridional flow from the irrotational flow pattern. The vanes may very well exert on the flow not only circumferential forces but also forces parallel to the meridional planes. Under the familiar assumption of complete axial symmetry (an infinite number of frictionless vanes), the vanes exert continuously distributed forces on the meridional flow, which, therefore, cannot remain irrotational. The purpose of this section is to describe the action of the vanes on the meridional flow in a rational, quantitatively tractable manner.

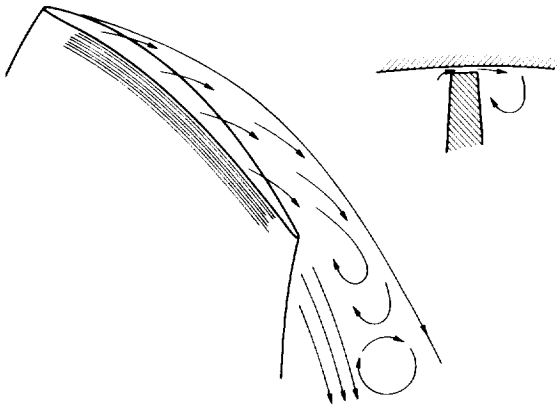

Figure 2-68. – Trailing vortex induced by vane-tip leakage stream.

The principles of vane action on the meridional flow were described first by Lorenz in reference 38. In reference 39, Bauersfeld pointed out how Francis turbines can be designed in such a manner as to avoid this effect of the vanes on the meridional flow. However, this vane action can indeed be favorable and, under additional restrictions of the vane design (e.g., by centrifugal stress considerations), may not be avoidable. The following considerations are based on reference 14. A few additional publications on this subject are collected in reference 40.

The vane action is represented by the familiar concept of bound vorticity, that is, the vorticity that must be connected with any deflecting vane or airfoil in order to deal with the circulation about such a body in a consistent manner. The relation between the change in angular momentum along the vanes of turbomachines and the bound vorticity of the vanes has in principle the same form as equation (2-159) except for the fact that the direction of the bound vane vorticity is axial only in strictly radial-flow vane systems (see fig. 2-40).

Figure 2-69 shows the construction of the lines or surfaces of constant angular momentum for a mixed-flow pump impeller. The vane shape of this rotor is assumed to be given from other considerations. (This example uses a vane shape with radial vane elements like that shown in fig. 1-29 of ch. 1.)

The meridional velocity distribution is first assumed to be irrotational and, thus, determined according to equation (2-4) and figure 2-3. Then the vane shape permits the construction of the velocity diagram for any point in the meridional flow field (a radial and axial section through the rotor) by using the one-dimensional assumption that the relative flow is parallel to the vanes except near the discharge vane edge, where it can be corrected by semiempirical rules. Figure 2-69 shows the two of these velocity diagrams that apply to the points A and B of a cylindrical section with radius $r = 0.9$. (The velocity diagrams are shown as appearing in planes tangential to the meridional stream surfaces through the points (circles) A and B.)

From a large number of velocity diagrams so constructed, one can determine the change in angular momentum along a number of cylindrical sections and determine the rV_U distribution diagram shown above the meridional rotor section in figure 2-69. Horizontal lines through this diagram determine the points of constant angular momentum, which can be brought back into the

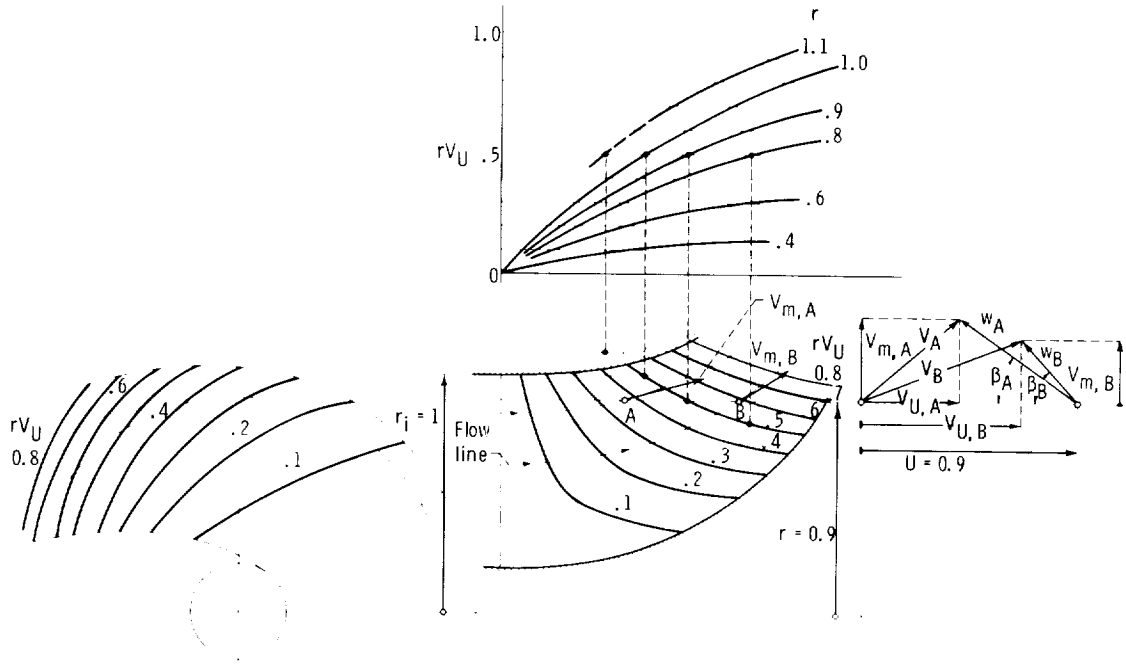

Figure 2-69. – Construction of lines of constant angular momentum and bound vortex lines for mixed-flow rotor.

rotor layout to determine directly the lines of constant angular momentum in the meridional (radial and axial) section and, by means of the vane layout (not shown), also the same lines in the axial end view of the rotor. The strong inclination of the lines mentioned last against the radial direction may lead one to the conclusion that there must be correspondingly strong action by the vanes on the meridional flow.

Figure 2-70 shows a way in which this action can be evaluated. The lines a and b are two successive lines of constant angular momentum (rV_U). One can imagine the corresponding bound vortex line to be halfway between the lines a and b. The bound vorticity vector of this vortex line has in the meridional section shown in figure 2-70 a value

$$\zeta_C = \frac{1}{r}\frac{\Delta(rV_U)}{\Delta n} \tag{2-181}$$

(according to eq. (2-159)) for a finite step, where n is measured normal to the direction of the bound vorticity vector ζ_C, that is, normal to the lines a and b. The relation of ζ_C to the axial component, that is, the z-component, of the same vorticity ζ_z is

$$\zeta_C = \frac{\zeta_z}{\cos\theta} \tag{2-182}$$

where θ is the local inclination of the lines of constant angular momentum against the axial direction. Since $\Delta n = \Delta r \cos\theta$, equation (2-181) can be immediately converted to

$$\zeta_z = \frac{1}{r}\frac{\Delta(rV_U)}{\Delta r} \tag{2-183}$$

which is in agreement with the definition of ζ_z (eq. (2-159)).

The effect of the vane action on the meridional flow results from the facts that the vorticity, representing the vane action at point A completely, must have the direction of the vane and that this direction is, in general, inclined against the meridional plane. This condition can be seen best in the development of a conical section BB containing the vorticity vector ζ_C. If the vane is, in this section, inclined against the meridional plane by an angle λ, it can be seen (in the development) that ζ_C is only one component of the total vane action represented by the vorticity ζ. This vorticity has a component ζ_U normal to the meridional plane, which, therefore, represents a vortex motion in the meridional plane and expresses the desired effect of the vane action on the meridional flow. Thus

$$\zeta_U = \zeta_C \tan\lambda = \zeta_z \tan\lambda' \tag{2-184}$$

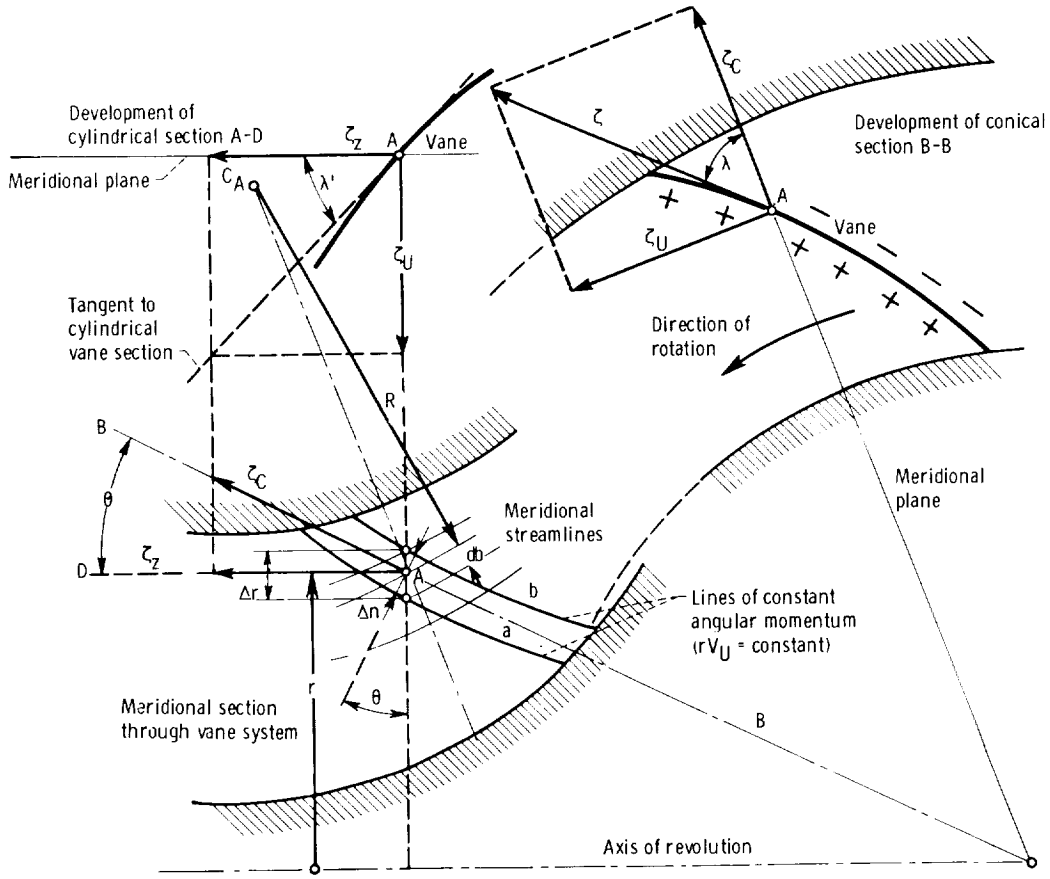

Figure 2-70. – Construction of vorticity of meridional flow from bound vorticity of vanes.

(For λ' see cylindrical section AD.)

The effect of this vorticity ζ_U on the meridional flow can be determined on the basis of equation (2-6) and figure 2-4 (in sec. 2.2 at the beginning of this chapter).

The meridional velocity distribution with vorticity ζ_U is now used to reconstruct the velocity diagrams, rV_U variations, and rV_U=constant curves in figures 2-69 and 2-70 by reiterating the whole process. Automatic convergence is not assured. To obtain convergence, the designer may have to start with an estimated, better approximation of V_m than the irrotational.

The direction of the vorticity can be found on the basis of the formal rules presented in appendix 2-A. However, it is desirable to have some simple, physical reasoning which can be applied at the end to check the validity of any theoretical results. Two criteria are presented.

The first one is based on the direction of the vane vorticity representing the increase in angular momentum. Assume, in agreement with figure 2-69, that the momentum along lines a and b in figure 2-70 is directed toward the observer and is (for a pump rotor) larger at b than at a. This means the vorticity represented by ζ_C is counterclockwise when one is looking in the direction of vector ζ_C, as shown. The development of the conical section B-B is viewed in figure 2-70 against the direction of the meridional flow, because this is consistent with the projection used. Since the resultant vane vorticity vector ζ must have the same meaning regarding direction of rotation as ζ_C, ζ denotes a reduction of the meridional (and relative) velocity at the high-pressure side of the vane (plus side), in agreement with the laws of fluid motion discussed in section 2.6.3.3. By the same definition, the vorticity of the meridional flow reduces the meridional velocity at the inside of the rotor passage (side closest to the axis of rotation) for the overall configuration shown in figures 2-69 and 2-70. This reduction in meridional velocity exists over and above that resulting from an irrotational meridional flow. (This effect of vorticity happens to be opposite to

that shown in fig. 2-4, where the meridional velocity gradient for flow with vorticity is less than that of the irrotational flow.)

The second physical criterion for the direction of the effect of vane forces on the meridional flow is still simpler. The vane forces reduce the meridional velocity on the side of the meridional flow passage that faces the high-pressure side of the vanes, as shown by a conical section coinciding (approximately) with the lines (or surfaces) of constant angular momentum. Applied to the case shown in figures 2-69 and 2-70, the result of this criterion agrees with that obtained on the basis of the direction of change in angular momentum and of the corresponding vorticity.

It is generally known that vanes of radial-flow or mixed-flow rotors with radial blade elements have an unfavorable effect on the meridional velocity distribution. The foregoing result is, thus, in agreement with experience in this field. On the other hand, if radial blade elements are not required, which is true for most liquid-handling machines (except those for liquid hydrogen), it is possible to design radial-flow rotor vanes in such a manner as to have a more uniform meridional velocity than would exist without any vane action. This could be accomplished by having the high-pressure side of the vanes face the rotor shroud whose convex side on a meridional section faces the flow. Similar considerations apply to double-curve guide vane passages.

The application of the principles outlined in sections 2.6 and 2.7 to the design of turbomachines is described in chapter 4.

2.8 Cavitation in Turbomachinery

2.8.1 Introduction

Cavitation is the local vaporization of a flowing liquid caused by local pressure reductions due to the dynamic action of the flow. By this definition, the subject is introduced in section 1.2.2 of chapter 1. According to the general subject of that chapter, cavitation is treated there entirely on the basis of similarity considerations. This treatment necessitates using the so-called classical assumption about cavitation: Cavitation takes place instantaneously whenever and wherever the local static pressure in the liquid drops to the vapor pressure of the liquid,

$$p = p_v \tag{2-185}$$

as given by its vapor tables, for example, the familiar steam tables for water.

Similarity relations of sufficient simplicity for design purposes are obtained by assuming that the vapor pressure in the region of cavitation is known, which means that the temperature of the liquid is everywhere equal to its average temperature, called here bulk temperature. In addition, it is tacitly assumed that the local pressure drop is due to inertial forces only; this assumption eliminates the local effects of viscosity and gravity (i.e., the effects of Reynolds number and Froude number). These assumptions are usually included in the classical assumptions on cavitation.

It is amazing how closely the foregoing assumptions are satisfied under most conditions of practical hydraulic pump and turbine operation, specifically operation with ordinary water at room temperatures. Under such conditions, the vapor pressure is usually so low as to make its local changes quite negligible, but there are other reasons why the classical assumption may not be valid. Furthermore liquids with high vapor pressures, such as high-temperature liquids or cryogenic liquids, pose a significant problem with respect to the local temperature and vapor pressure in the region of cavitation. This section is, therefore, primarily devoted to a discussion of departures from the classical assumption.

A brief remark is necessary regarding ideal-flow solutions for flow with fully developed cavitation. Problems involving plane, two-dimensional flow are amenable to theoretical solutions by the hodograph method described in reference 9 for systems of straight and parallel vanes. More general problems have not yet been solved rigorously. The nature of this type of turbomachinery flow problem is briefly indicated in section 2.5.4.1.

Symbol notations in section 2.8 are the same as those used and defined in section 1.2.2 except for new variables, whose symbols are explained at the place of their first introduction.

2.8.2 Flow Effects on Cavitation

2.8.2.1 Effects of local cavitation on flow. – With fully developed cavitation, there is obviously a major, overall effect of cavitation on the flow and the pressure distribution. However, even local cavitation generally has a local effect on the flow and usually reduces the local pressure. Figure 2-71(a) shows a case where the local pressure is reduced, and 2-71(b) one where it is not. In the

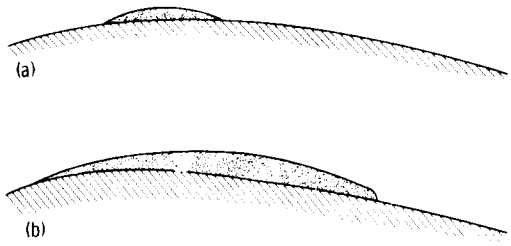

(*a*) *Void that reduces local pressure.*
(*b*) *Void that does not reduce local pressure.*
Figure 2-71. – Two possible forms of cavitation voids.

first case, the cavitation void reduces the minimum radius of curvature of the boundary; in the second case, it increases that radius. In the first case, the cavitation void grows until it is swept downstream and a new void is formed (unsteady cavitation); in the second case, cavitation may be steady or unsteady. If the cavitation void blocks a significant part of a confined flow passage, it further reduces the pressure, therefore, grows, and leads to unsteady cavitation, as in the first case.

On the basis of ideal-flow considerations, there is reason for questioning whether cavitation can ever be steady. The ideal (frictionless) flow picture of a void in a liquid involves necessarily a reentering jet (see fig. 2-72), because there must be a stagnation point behind the closing end of the void, which cannot be along the streamline bounding the void, since it cannot be on a line (or surface) of constant pressure like the boundary of a void. The reentering part of the flow eventually fills the void and causes it to be swept away and subsequently reestablished. This unsteady behavior of cavitation voids was experimentally observed by Knapp, although the actual region of closure seems to differ substantially from its ideal picture.

Thus it is questionable whether cavitation will ever be steady. If steady, such behavior of cavitation voids is an exception rather than a rule. Cavitation is sometimes steady at very small scales, where viscosity may have a dampening effect on unsteady pulsations. Large cavitation voids behind a body have also been observed to be steady.

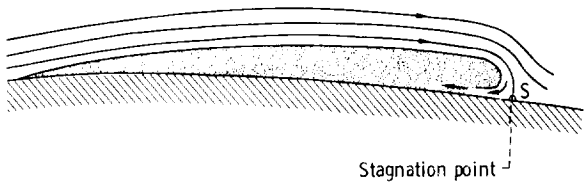

Figure 2-72. – Ideal closure flow of void and reentering jet.

The flow-disturbing effects of cavitation, just described, are the reason why cavitation has in most cases a detrimental effect on the performance of the machine. It is theoretically possible, but practically still uncertain, that a machine designed for operation with cavitation can reach the quality of performance achievable by a different design without cavitation.

2.8.2.2 Reynolds number effects. – It is natural to expect some effect of viscosity on cavitation (i.e., changes in Reynolds number), at least as much effect as on any other flow phenomenon and perhaps more because cavitation usually originates at the flow boundaries. Figure 2-73 shows the results of one of the earliest systematic investigations, carried out jointly by Parkin and Holl in the water tunnels of the California Institute of Technology and the Pennsylvania State University (see appendix A of ref. 41). (Ref. 41 also contains extensive information on other scale effects (departures from the classical assumptions) on incipient and desinent cavitation, particularly on Reynolds number effects.) Consistent results were obtained only when the disappearance (desinence) of cavitation was observed at increasing static pressures. The test objects were bodies of revolution (ogives), of different sizes, coaxial with the direction of the test stream. The material was polished stainless steel.

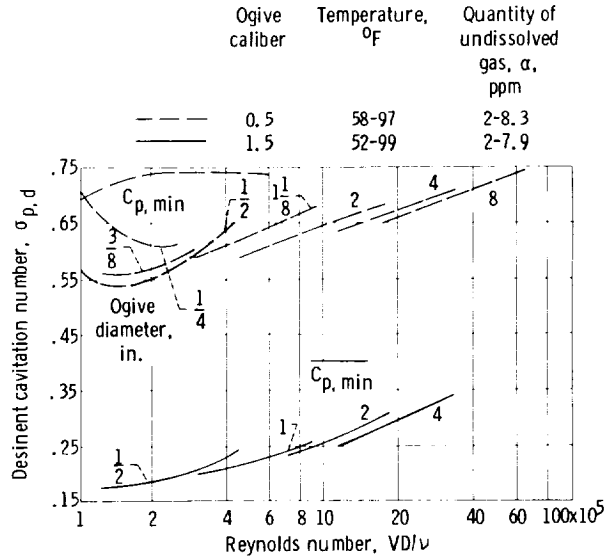

Figure 2-73. – Desinent cavitation number as function of Reynolds number for ogives. Tunnel diameter, 48 inches; data from reference 41.

Figure 2-73 shows that there is a significant Reynolds number effect on the desinent cavitation number $\sigma_{p,d}$. Nearly all cavitation numbers observed are lower than the calculated pressure coefficient at the point of minimum surface pressure $C_{p,min}$, for one ogive by as much as a factor of 2. No corresponding effects of Reynolds number changes have been reliably observed with hydraulic pumps or turbines, but it must be remembered that the scatter of pump test results is generally far greater than the scatter in a laboratory experiment with visual observation of cavitation and that no systematic cavitation tests of pumps as a function of Reynolds number only are known to this writer. To eliminate the important effects of manufacturing inaccuracies, such tests would have to be conducted with the same pump at different speeds and perhaps with different viscosities. Cavitation tests at different speeds have been conducted, but the range of speed has usually been fairly small. No consistent scale effects have been reported. Lately some apparent scale effects have been observed, but these effects run in the opposite direction from those shown in figure 2-73, that is, the cavitation performance was poorer (the cavitation number σ_p was higher) at reduced speeds and Reynolds number. It is difficult to explain this effect by anything but the influence of undissolved gas on cavitation. The effect of undissolved gas on performance under cavitating conditions is detrimental, because (1) undissolved gas forms voids in the stream at pressures higher than the vapor pressure (gaseous cavitation), (2) gas bubbles are nuclei of cavitation and, therefore, promote vaporization and the formation of cavitation voids, and (3) at reduced velocities, and, therefore, reduced pressures, at cavitation inception any given mass of gas occupies an increased volume, so that the effect of the undissolved gas on the flow is increased.

2.8.2.3 Froude number effects. – The effect of gravity on cavitation is mentioned here mainly for reasons of completeness, since it is of importance primarily in connection with very large hydrodynamic machinery, such as large ship propellers or hydraulic turbines. Froude's law of similarity needs to be considered only if the vertical dimensions of the rotor (primarily its suction side) constitute a significant part of the suction head above the vapor pressure H_{sv}. Besides the aforementioned cases of machines with large, vertical dimensions, this condition may exist in connection with propellant pumps for large liquid rockets at times of very high acceleration of the whole system, which usually coincides with a low free-liquid level in the propellant tank.

This writer is not aware of theoretical or experimental investigations regarding the effect of differences in H_{sv} within the cavitation region of a hydrodynamic machine. The most severe differences in H_{sv} are probably those that occur across the rotor in so-called horizontal shaft units, that is, units where the shaft is located at approximately right angles to the general acceleration of the entire system. This acceleration may be gravitational acceleration or any other acceleration of the entire system, such as the acceleration of a rocket or other vehicle. In this case, the rotor blades are subject to unsteady conditions with respect to cavitation. Considering the complexity of the cavitation phenomenon, there is but little hope for a theoretical solution of this problem. J. W. Holl, at the Pennsylvania State University, has observed and investigated a hysteresis effect of incipient cavitation, that is, on the onset of cavitation at timewise decreasing H_{sv}. His results would lead one to believe that incipient cavitation on a rotor blade is determined by the time average of H_{sv} (i.e., the H_{sv} value calculated for the elevation of the center of rotation of the blade).

While pressure differences in the entire suction pipe or reservoir system due to a general acceleration of the whole system (such as gravity) are easy to calculate by hydrostatic considerations, the effect of such pressure differences within the region of cavitation is not yet predictable. It is not likely to be major. In the absence of better knowledge, the H_{sv} of the unit should be calculated for the elevation of the center of the expected region of cavitation.

2.8.2.4 Compressibility effects. – Since cavitation starts from the liquid state, it may be surprising to find a section on compressibility effects on cavitation. There is indeed no significant effect of compressibility in essentially cavitation-free operation,including incipient (or desinent) cavitation. Water-hammer phenomena in the suction pipeline are an exception to this statement. This is a separate problem of the entire flow system, not of the turbomachine as such, and is not treated in this compendium.

As soon as there are significant cavitation voids, compressibility may become important. This possibility results from the fact that significant changes in pressure have been observed along so-called cavitation voids (see refs. 42 and 43); these

changes indicate that the voids may contain a mixture of the liquid and vapor phases of the fluid or a mixture of liquid and gas which may have come out of the solution.

Mixtures of liquids and gases (or vapors) have exceedingly low acoustic velocities if the mixture behaves approximately like a homogeneous fluid, because the mixture may have a compressibility (volume elasticity) comparable with that of the gas or vapor phase and a density comparable with that of the liquid phase. If the liquid-gas or liquid-vapor mixture becomes part of the active flow in the machine, this flow may well reach high (possibly supersonic) Mach numbers in terms of the low acoustic velocity of the mixture. These Mach numbers might lead to significant changes in the flow pattern as a function of the flow velocity. However, the actual flow pattern and density distribution in the region of cavitation are far too complex to permit any prediction of them that could be of direct value to the design engineer. All that can be done is to call attention to the possibility of compressibility effects on flow with cavitation in order to create a better understanding of the observed, extreme complexity of such flow.

2.8.2.5 Effects of small surface irregularities on incipient and desinent cavitation. – A good surface finish is important, since the effect of small surface irregularities on incipient and desinent cavitation can be quite substantial. Figure 2-74 represents a highly condensed and simplified summary of the most important results of an extensive investigation by Holl (ref. 41) on this subject. A sharp-edged roughness would, of course, have a very high cavitation number if exposed to the free-stream velocity. Small roughnesses are buried in the boundary layer and are, therefore, exposed to velocities lower than free-stream. Figure 2-74 shows the cavitation number σ_1 of the roughness alone (i.e., when placed on a flat plate parallel to the stream), referred to the free-stream velocity (see eq. (1-37)), as a function of the height of the roughness h divided by the local thickness δ of the boundary layer. This cavitation number drops from its nearly free-stream value of about 2 to 0.3 as the height of the roughness is reduced to about one-thirtieth of the boundary-layer thickness, in practice a very small roughness. Yet even this relatively low cavitation number of the roughness is quite significant.

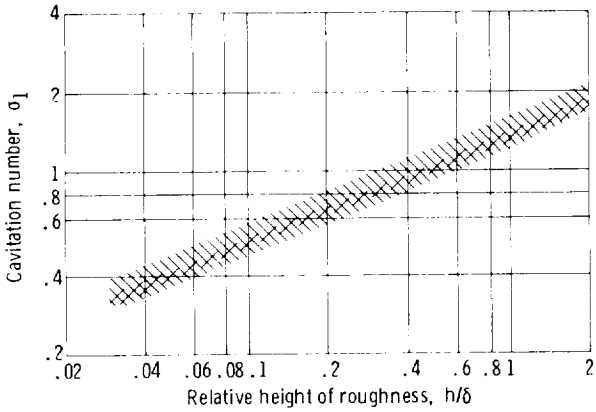

Figure 2-74. – Approximate cavitation numbers of sharp-edged surface irregularities. (Data from ref. 41.)

To be investigated is the effect of a single roughness on a point of an otherwise smooth body where the pressure-reduction coefficient without the roughness is

$$C_{p,o} = \frac{p_\infty - p_o}{\rho V_\infty^2/2} \tag{2-186}$$

The subscript o denotes conditions at that particular point of the parent body without the effect of the roughness.

Ignoring effects of the boundary layer at this point gives

$$p_\infty + \frac{\rho V_\infty^2}{2} = p_o + \frac{\rho V_o^2}{2} \tag{2-187}$$

so that

$$C_{p,o} = \frac{p_\infty - p_o}{\rho V_\infty^2/2} = \frac{V_o^2}{V_\infty^2} - 1$$

or

$$C_{p,o} + 1 = \frac{V_o^2}{V_\infty^2} \tag{2-188}$$

The cavitation number of the roughness alone, referred to the local flow conditions (subscript o), is

$$\sigma_1 = \frac{p_o - p_v}{\rho V_o^2/2} = \frac{p_o - p_v}{\rho V_\infty^2/2}\frac{V_\infty^2}{V_o^2} \tag{2-189}$$

Hence the resultant cavitation number σ_R of the roughness at the point on the parent body designated by the subscript o, referred to the free-stream velocity, is

$$\sigma_R = \frac{p_\infty - p_v}{\rho V_\infty^2/2} = \frac{p_\infty - p_o}{\rho V_\infty^2/2} + \frac{p_o - p_v}{\rho V_\infty^2/2}$$

$$= C_{p,o} + \frac{p_o - p_v}{\rho V_o^2/2}\frac{V_o^2}{V_\infty^2}$$

substitution from equations (2-188) and (2-189) yields

$$\sigma_R = C_{p,o} + \sigma_1(C_{p,o} + 1) \qquad (2\text{-}190)$$

If it is assumed, for example, that $C_{p,o} = 0.3$ and $\sigma_1 = 0.3$, then $\sigma_R = 0.3 + (1.3 \times 0.3) = 0.69$; that is, the resultant cavitation number of the body with roughness is more than twice that for a smooth body.

It is doubtful that the very local cavitation connected with a small roughness has a measurable effect on performance, but it may lead to premature cavitation damage and thereby increase the local roughness.

2.8.3 Microscopic Effects on Cavitation

2.8.3.1 Effects of tensile strength and surface tension of liquids on incipient and desinent cavitation. – The physicists tell us that a clean liquid should be capable of sustaining very high tensile stresses, that is, pressures considerably below the equilibrium vapor pressure, including negative pressures. (See ref. 44, particularly the Conclusions, which are very instructive.) In order to explain why vaporization or cavitation usually sets in promptly at the vapor pressure, one must assume weak spots in the liquid called nuclei of vaporization or cavitation.

If one assumes that cavitation starts from very small vapor or gas bubbles, one finds an additional problem connected with cavitation inception due to the substantial pressure difference between the inside and the outside of a small bubble resulting from its surface tension. Figure 2-75 gives this pressure difference for water as a function of the bubble radius. For a 10^{-3}-inch radius, the difference is about 1 pound per square inch; for a 10^{-4}-inch radius, the difference is 10 times higher. If the pressure inside such a bubble is the vapor pressure, the pressure in the liquid outside the bubble must be less than the vapor pressure by the amounts given in figure 2-75. While considerable tensions have been observed in water, for example, after subjecting the water to high pressures, tensions of several pounds per square inch are not regularly observed under ordinary conditions. One must, therefore, conclude that cavitation under ordinary conditions starts with bubbles larger than 10^{-3} inch.

How can small bubbles exist in a liquid? If they are vapor bubbles and the pressure inside the bubble is larger than the vapor pressure, the vapor condenses and the bubble disappears. If they are gas bubbles, the excess pressure inside the bubble (due to surface tension) forces the gas to dissolve into the liquid, and the bubble disappears.

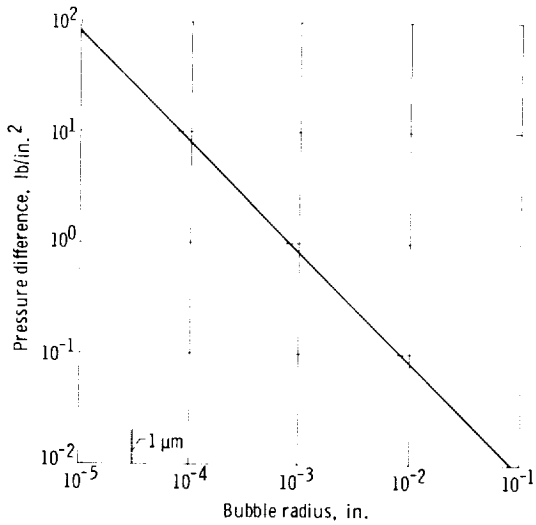

Figure 2-75. – Pressure difference between inside and outside of bubble in water.

If cavitation can start only from a gas or vapor bubble of finite size, one must assume what is usually referred to as the Harvey nucleus (fig. 2-76). Its important characteristic is a crack in a hydrophobic material, either in the solid flow boundaries or in small solid particles suspended in the liquid. Under such conditions, the liquid surface bounding the gas trapped in the crack is curved in such a manner that, under the influence of surface tension,

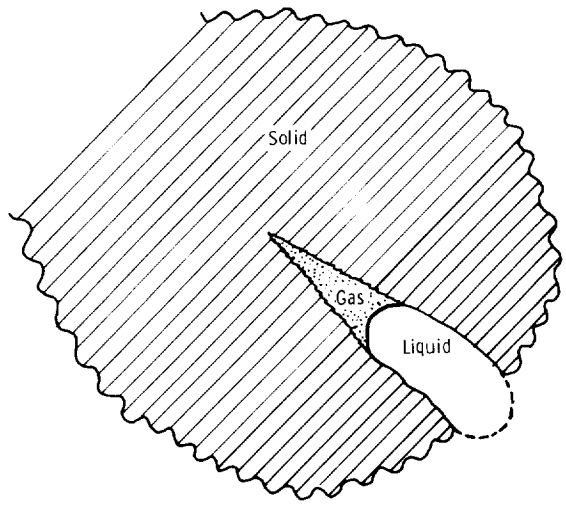

Figure 2-76. – Diagram of Harvey nucleus.

the pressure in the gas is lower than the pressure in the liquid.

The hypothesis of the Harvey nucleus is confirmed by the fact that ordinary tap water sustains tension (i.e., pressure below its vapor pressure) after it has been subjected to very high pressures. This can perhaps be explained by assuming that, under high pressure, most of the gas in the nucleus crack is absorbed, and so little is left that even under greatly reduced pressures (or tensions) the remaining gas does not flow out of the crack (i.e., does not reach the broken line in fig. 2-76), so that it does not become effective as a cavitation nucleus.

In a paper delivered in September 1970 at the Pennsylvania State University (ref. 45), Plesset stated that it is not necessary to assume the presence of undissolved gas to explain the onset of cavitation. The same is stated by Knapp, Daily, and Hammitt in their book on cavitation (ref. 46). A hydrophobic solid alone can serve as a nucleus of cavitation. This constitutes an appreciable broadening of the concept of cavitation nuclei, to include both hydrophobic particles without gas and hydrophobic particles with cracks harboring undissolved gas.

If one considers only cavitation nuclei suspended in the liquid, one is still confronted with the necessity of assuming that these particles are sufficiently large to keep the effects of surface tension below easily observable limits (see fig. 2-75) after the gas or vapor covers a significant part of the particle. However, particles of such size are easily removed by filtration or settle out under the influence of gravity or any other general acceleration of the system. In reference 44, Plesset draws the conclusion that particles kept in suspension in a streaming fluid reduce the tensile strength of the liquid to the order of tens of atmospheres. Even if he underestimates the size of the paricles suspended in a turbulent stream, a tensile strength of, say, 1 atmosphere (33 ft. of water) could never escape detection by the usual cavitation experiments and field observations with hydraulic pumps and turbines that have been carried out under varying conditions for over half a century. Such observations, which have been the basis of the classical assumptions on cavitation, usually involve tap water at about room temperature, with ordinary gas content, ordinary concentration of suspended solids, and mean pressures ranging from about 0.5 to 2 or 3 atmospheres on the low-pressure side of the machine. Apparently there is no evidence of tensions of 1 (or several) atmospheres under such conditions.

In response to the last statement, Holl, referring to work by Ripken (ref. 47), pointed out to this writer in a private conversation that, under such ordinary conditions, water probably contains, besides solid nuclei, gas bubbles, which may take a fairly long time to rise to the free surface or upper wall of the container.

In a private communication with this writer, Plesset pointed out that, under ordinary conditions, suspended solid particles may be substantially larger than he assumed in reference 44, and thus tensile strength of the liquid may be as low as a small fraction of an atmosphere.

These possibilities should be carefully explored, since they would make cavitation test results significantly dependent on the gas content of the test liquid, as well as on the time before the test during which the liquid was either quiescent or disturbed. To the best knowledge of this writer, no such dependencies have been reliably observed. Nevertheless the potential differences between cavitation under practical conditions of application and under laboratory test conditions demand careful attention, especially because there is a tendency, and sometimes a necessity, to keep the test liquid in the laboratory very free from undissolved gas and solid particles. The significance of such differences are further examined in the next section.

The foregoing comments on suspended particles focus attention on cavitation nuclei connected with the solid boundaries of the flow. If the boundary nuclei (cracks) were of major importance, these boundaries should have observable properties (such as crystallized rather than amorphous structures, hydrophobic rather than hydrophilic reactions, and various types of surface treatment). No observations of this type have become known to this writer, although Holl at the Pennsylvania State University has started investigations of this problem.

2.8.3.2 Effect of number of nuclei on incipient and desinent cavitation. – In 1950, Gilmore and Plesset (ref. 48) called attention to the fact that the finite number of nuclei in a liquid might produce a significant scale effect on incipient or desinent cavitation. The following brief outline of their thoughts is written from memory. This writer is, therefore, responsible for any incorrectness in this presentation.

Gilmore and Plesset distinguished between two hypothetical cases:

(1) That there is an abundance of nuclei, so that only a small fraction of the nuclei are actually involved in the inception of cavitation. If there are plenty of nuclei, even in connection with the smallest scale of cavitation experiment ever conducted, one cannot expect any effect of the number of nuclei on incipient cavitation. This case is, therefore, not considered any further.

(2) That there is a significantly limited number of nuclei in the liquid and that nearly all available nuclei are involved in the inception of cavitation. In this case, a change in the size (scale) of the flow should have an observable effect on cavitation inception. Only this case is considered in the following.

Let N be the number of cavitation nuclei per unit volume of the liquid. The average, linear spacing between nuclei is, therefore,

$$\Delta l = \frac{1}{\sqrt[3]{N}} \tag{2-191}$$

If Δt is the average interval of time between arrivals of nuclei at a small region of critical pressure (pressure sufficiently low to cause cavitation),

$$\Delta l = V\,\Delta t \tag{2-192}$$

where V is the average flow velocity.

Let L be representative linear dimension of the flow system considered. Then the simplest condition of similarity with respect to cavitation is

$$\left.\begin{aligned} &\frac{\Delta l}{L} = \frac{V\,\Delta t}{L} = \text{constant} \\ &\text{or, according to equation (2-191),} \\ &\frac{1}{L\sqrt[3]{N}} = \text{constant} \end{aligned}\right\} \tag{2-193}$$

For liquids with a constant, limited number N of nuclei per unit volume, the condition of similarity for incipient cavitation would be

$$L = \text{constant} \tag{2-194}$$

that is, a constant size (scale) would be required to maintain similarity of incipient cavitation with a limited number of nuclei in the liquid, if, of course, the surface of the cavitation body does not contribute to the nucleation of cavitation.

Since condition (2-194) is generally not a requirement for meaningful cavitation experiments (reduced-scale experiments are commonly used in the turbomachinery field), it must be concluded that either or both of the following are true:

(1) The number of nuclei in the liquid is usually larger than that required to sustain a certain degree or form of cavitation.

(2) The surface of the cavitating body contributes substantially to the nucleation of incipient cavitation.

It is also possible in the first case just mentioned that there is a lower limit of size where the number of nuclei is just sufficient to sustain a certain degree or form of cavitation and that further reduction in size destroys the similarity with respect to incipient cavitation. This lower limit in size of cavitation experiments is increased (according to eq. (2-193)) when the test fluid is filtered or otherwise kept very clean, since this reduces the number N of nuclei per unit volume (and increases their average spacing Δl).

The foregoing considerations may be of considerable practical importance. It is common practice to keep the test fluid rather clean for cavitation experiments where optical observations are desired. In some fields (particularly the field of nuclear power), high purity of the liquid is a necessity for other reasons. Cryogenic liquids, particularly liquid hydrogen used for propulsion, may have a low number of suspended cavitation nuclei. Thus it is entirely possible that in several important fields the number of cavitation nuclei in the liquid may have to be considered as an important test variable and that means have to be developed to measure and control this variable. Simply having the liquid as clean as possible may not be sufficient and may, in fact, be misleading, because very low numbers of nuclei increase the criticality of this problem. Whether a very low number of cavitation nuclei can be used to minimize cavitation in a practically dependable fashion is as yet quite uncertain, since a state of tension in the liquid may be unstable and could involve major problems of reliability.

2.8.4 Thermodynamic Effects on Cavitation

2.8.4.1 Introduction. – One of the classical assumptions on cavitation is that the vapor pressure in the region of cavitation is known. What is actually meant is that the combination of vapor and gas pressure within the cavitation void is known, considering that gas comes out of solution under the influence of the cavitation process.

If the partial pressure of the gas in the liquid is p_g, similarity with respect to gaseous cavitation is obviously

$$\left.\begin{aligned} &\frac{p_g}{p} = \text{constant} \\ &\text{or} \\ &\frac{p_g}{\rho V^2} = \text{constant} \end{aligned}\right\} \qquad (2\text{-}195)$$

where p is any representative pressure, and V is any representative velocity of the flow process involved.

Analogously the similarity condition with respect to the vapor pressure p_v is

$$\left.\begin{aligned} &\frac{p_v}{p} = \text{constant} \\ &\text{or} \\ &\frac{p_v}{\rho V^2} = \text{constant} \end{aligned}\right\} \qquad (2\text{-}196)$$

If, as in the case of cold water, p_v is negligibly small compared with p and ρV^2, the similarity relation (2-196) becomes insignificant. (The same is true for negligibly small partial gas pressures p_g with respect to eq. (2-195).)

No general relations are available for the case where the partial gas pressure p_g is not negligibly small compared with the liquid pressure p. However, if the vapor pressure is not negligibly small, as at high temperatures and pressures and for cryogenic liquids, a rational approach to the resulting problem of cavitation is possible on thermodynamic grounds. This approach was first pointed out by Stahl and Stepanoff in reference 49. The following presentation uses the data provided by Ruggeri and his associates given in references 42 and 43 and other NASA reports. A significant extension of the work was offered by Billet in reference 50. The form of the following presentation is similar to that of an older publication by Holl and this writer (ref. 51).

The simple principle of these publications and the following considerations is that the process of cavitation necessarily involves vaporization, which demands a heat flux from the liquid into the cavitating region. This heat flux is associated with a temperature drop in the liquid close to the surfaces of cavitation and vaporization in the liquid stream. The temperature drop, in turn, reduces the local vapor pressure below the vapor pressure corresponding to the bulk temperature of the liquid. It is this local drop in vapor pressure which constitutes the thermodynamic effect on cavitation; it is discussed in the next section.

2.8.4.2 Equations of thermal effects and their application. – Following the procedure used by Ruggeri (refs. 42 and 43), we start with a simple equation of heat balance: the mass of vapor times the latent heat of vaporization λ equals the mass of liquid involved times the specific heat of the liquid $C_{p,l}$ times the change in temperature ΔT of that mass of liquid; that is,

$$\rho_v V_v \lambda = \rho_l V_l C_{p,l} \Delta T \qquad (2\text{-}197)$$

where V_v is the volume of the vapor, and V_l is the volume of the liquid.

In accordance with Hollander (ref. 52), Ruggeri as well as Holl and Billet interpret equation (2-197) as a static equation, describing equilibrium between vapor and liquid in a heat-insulated cylinder and piston, the piston having been slowly withdrawn to generate the vapor volume.

In the opinion of this writer, this static interpretation does not do justice to the value of equation (2-197) in a flow system. When both sides of this equation are divided by the unit of time, the equation can be written in the form

$$\rho_v Q_v \lambda = \rho_l Q_l C_{p,l} \Delta T \qquad (2\text{-}198)$$

where Q_v is the volume of vapor carried away per unit of time from the cavitation void by entrainment at its downstream end, which has been observed and measured by Billet (ref. 50). The rate of liquid volume flow cooled (by vaporization) by ΔT is Q_l (see fig. 2-77).

The temperature reduction is

$$\Delta T_1 = -\frac{\rho_v Q_v \lambda}{\rho_l Q_l C_{p,l}} \qquad (2\text{-}199)$$

where the subscript 1 is introduced to distinguish the temperature drop from one calculated by different means, described later.

Evidently the ratio Q_v/Q_l is equivalent to the ratio of vapor to liquid volume B introduced by Stahl and Stepanoff in reference 49.

It should be understood that, in contrast to the usual interpretation of the basic equation (2-197), equations (2-198) and (2-199) can describe a completely convective mechanism of heat transfer from the liquid to the vapor phase: A liquid stream Q_l being cooled provides the heat required to generate a vapor stream Q_v.

Instead of assuming this purely convective mechanism, one can assume that the heat is supplied from the liquid to the vaporizing fluid by conduction. The flow of vapor from the cavitation void is described in the same manner as previously, so that

$$\rho_v Q_v \lambda = K \frac{\partial T}{\partial y} A_w \tag{2-200}$$

where K is the heat-transfer coefficient, and A_w is the heat-transfer area, presumably the wall area of the cavitation void. The coordinate y is measured normal to the wall of the cavitation void.

The temperature gradient is approximated by

$$\frac{\partial T}{\partial y} = \frac{\Delta T_2}{\Delta y} \tag{2-201}$$

where Δy is the (small) thickness of the thermal boundary layer adjacent to the cavitation void. Since the flow near this void is not a usual boundary-layer flow of known characteristics (the shear stress at the surface of the void is practically zero), there is no simple way to approximate Δy except by assuming that it is proportional to a representative, linear dimension L of the flow mechanism involved, say the length of the cavitation void. Under this crude assumption, the temperature drop ΔT_2 connected with the heat-transfer mechanism expressed by equation (2-200) is

$$\Delta T_2 = -\text{constant} \times \frac{\rho_v Q_v \lambda L}{K A_w} \tag{2-202}$$

A comparison with equation (2-199) yields

$$\frac{\Delta T_2}{\Delta T_1} = \text{constant} \times \frac{\rho_l Q_l C_{p,l} L}{K A_w} \tag{2-203}$$

The liquid flow is

$$Q_l = V_n A_w \tag{2-204}$$

where V_n is an average turbulent convection velocity of the liquid normal to cavity wall A_w, which, for completely turbulent flow, may be assumed to be proportional to the free-stream velocity V (i.e., $V_n = \text{constant} \times V$). Thus equation (2-203) can be written in the form

$$\frac{\Delta T_2}{\Delta T_1} = \text{constant} \times \frac{\rho_l C_{p,l}}{K} VL = \text{constant} \times Pe \tag{2-205}$$

where we introduce the Peclet number

$$Pe = \frac{\rho_l C_{p,l}}{K} VL \tag{2-206}$$

which describes the ratio of convective to conductive heat transfer.

The foregoing statement should be obvious because equation (2-199) can describe, according to equation (2-198), a purely convective heat-transfer process (in contrast with the usual interpretation of eq. (2-197)), whereas equation (2-202) uses a purely conductive process (according to eq. (2-200)) at the surface of the cavity while maintaining a purely convective process for the removal of the vapor at the downstream end of the cavity (see fig. 2-77).

Both equations (2-199) and (2-202) can be brought into the same form by using $\Delta T_2 = \text{constant} \times \Delta T_1 Pe$, so that with

$$Q_l = \text{constant} \times A_w V$$

and

$$Q_v = \text{constant} \times A_v V$$

(defining A_v)

$$\Delta T = -\text{constant} \times \frac{\rho_v}{\rho_l} \frac{A_v}{A_w} \frac{\lambda}{C_{p,l}} Pe^n \tag{2-207}$$

where the unknown exponent n varies from $n = 0$ for pure convection to $n = 1$ for pure conduction on the liquid side. It is reasonable to assume that the heat transfer on the liquid side is partly convective and partly conductive, so that the exponent n may be expected to lie between 0 and 1.

The temperature depression ΔT causes a local reduction in vapor pressure. For small temperature changes ΔT this reduction in vapor pressure can be approximated by

$$\Delta p_v = \frac{\partial p_v}{\partial T} \Delta T \tag{2-208}$$

Ruggeri as well as Billet and Holl use the Clausius-Clapeyron equation to approximate $\partial p_v / \partial T$.

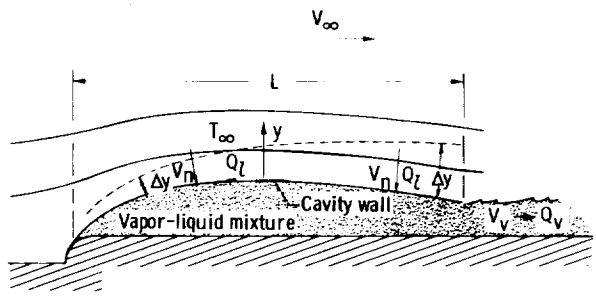

Figure 2-77. – Typical cavitation void.

However, if p_v is empirically known as a function of T (by the standard vapor tables), no approximation is necessary, and the physical meaning of the resulting equation remains quite clear. This equation is

$$\Delta p_v = -\text{constant} \times \frac{\partial p_v}{\partial T} \frac{\rho_v}{\rho_l} \frac{A_v}{A_w} \frac{\lambda}{C_{p,l}} Pe^n \qquad (2\text{-}209)$$

This equation was first presented in reference 51 as equation (12).

It would, of course, be desirable to give the reduction in vapor pressure in dimensionless form. In references 14 and 51, this is achieved by dividing Δp_v either by a representative system pressure p (e.g., by $\rho_l g_o H_{sv}$) or by a representative velocity pressure $\rho_l V^2$. The latter leads to clear similarity relations in terms of the linear dimensions L and the liquid velocities V of the system.

At present, this writer believes that division of Δp_v by the bulk vapor pressure p_v may lead to interesting and useful results. Applying this idea to the Freon test results by Ruggeri and by Billet leads to the conclusion that $\Delta p_v/p_v$ for developed cavitation in Freon lies between 0.1 and 0.2. Results by Billet with water indicate ratios between 0.04 and 0.1, but many other data would have to be evaluated before more general conclusions can be drawn.

The most significant departures from the classical cavitation behavior have been observed with liquid hydrogen. With this medium, pumps have been operated experimentally with practically zero *NPSH* (H_{sv}) referred to the vapor pressure corresponding to the bulk temperature of the liquid. The only known explanation of this behavior is the thermodynamic reduction in temperature ΔT and in vapor pressure $\Delta p_v = \rho_l g_o \Delta h_v$ discussed in this section. Figure 2-78 shows this reduction in vapor pressure in liquid hydrogen in dimensionless form: $\Delta p_v/p_v = \Delta h_v/h_v$, where h_v is the vapor pressure expressed in feet of liquid hydrogen. The data presented in figure 2-78 are taken from figure 1 of reference 43. The same reference gives in its figure 8 minimum cavity pressures corresponding to $\Delta p_v/p_v = 0.440$ to 0.533 at liquid-hydrogen velocities of about 150 feet per second. It is possible that such high values of the dimensionless reduction in vapor pressure are responsible for the strong departures from the classical behavior observed experimentally with pumps handling liquid hydrogen.

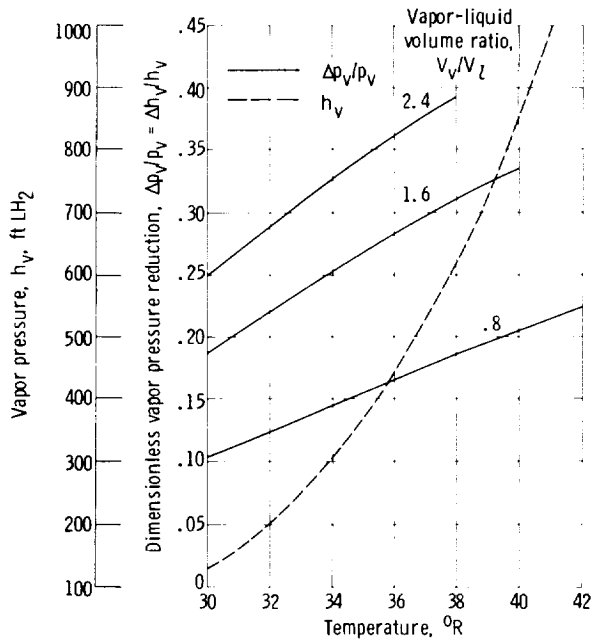

Figure 2-78. – Dimensionless vapor pressure reduction for liquid hydrogen and vapor pressure as a head.

The investigations by Ruggeri and his associates as well as by Billet and Holl cover additional aspects of developed cavitation, such as the pressure and temperature distribution along a cavitation void. Figure 2-79, from references 42 and 43, shows the pressure reduction distribution (in terms of head) along a cavitation void on the wall of a venturi-shaped test section of a research cavitation tunnel using Freon-114 as the test medium. The values of $\Delta p_v/p_v = (h_v - h_x)/h_v$ are added at the minimum-pressure points located at the leading edge of the cavitation void. These tests were carried out at a nearly constant liquid velocity of about 32 feet per second.

Other tests of the same series indicate that the pressure reduction $\Delta p_v = \rho_l g_o (h_v - h_x)$ increases with the velocity of flow, a change in velocity by a factor of about 1.4 giving a change in Δp_v by a factor of about 1.3. An increase in the length of the cavitation void produces a relatively smaller increase in Δp_v.

Equations (2-199), (2-202), (2-207), and (2-209), can be evaluated only by comparisons, because of the unknown constants of proportionality, other unknown ratios, and an unknown exponent n in these equations. Thus, only if the results ΔT or Δp_v are known experimentally for at least one case

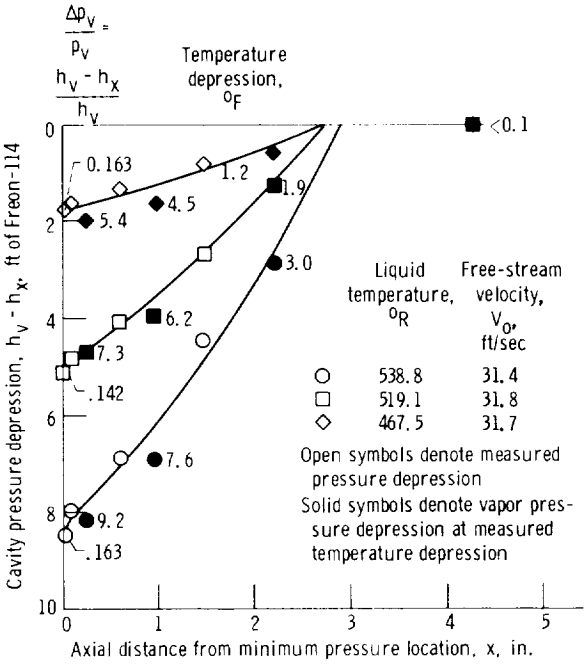

Figure 2-79. – Effect of free-stream liquid temperature on cavity pressure and temperature depressions. Freon-114; 1.0-scale venturi; nominal cavity length, 2¼ inches (from ref. 43).

under given geometric and flow conditions can one draw conclusions regarding the behavior (ΔT and Δp_v) of other geometrically and hydrodynamically similar systems operating at different temperatures, velocities, or linear dimensions with different fluids. Knowing ΔT and Δp_v permits the application of model experiments with more convenient fluids than the fluid used under the actual operating condition, as long as the model fluid maintains approximately certain characteristics of the operating fluid. In particular, the ratio of the bulk vapor pressure to a representative, hydrodynamic pressure should be of the same order of magnitude in both cases. For example, cold water is not usually an acceptable test fluid for studying thermodynamic effects on cavitation in cryogenic fluids because p_v of cold water is negligibly small compared with the hydrodynamic pressures under most practical test conditions.

Ruggeri and his associates have demonstrated the feasibility of this type of similarity consideration by numerous experiments reported in references 42, 43, and 53.

It has also been established by Ruggeri (refs. 42 and 43) that the usual cavitation number is (under hydrodynamically similar conditions) constant if it is referred not to the bulk vapor pressure of the liquid but to the minimum static pressure (minimum local vapor pressure) in the cavitation void; that is,

$$\sigma_{c,min} = \frac{p_\infty - p_{c,min}}{\rho V_\infty^2/2} = \text{constant} \tag{2-210}$$

where the minimum pressure in the cavitation void

$$p_{c,min} = p_{v,bulk} - \Delta p_v \tag{2-211}$$

is obviously determined by the same considerations as presented previously.

2.8.5 Review

The most important results of section 2.8 are summarized in table 2-III. This table is the same as the table on pages 596 and 597 of reference 14 except for some minor changes in notations and for the introduction of the ratio $\Delta p_v/p_v$ under item 7. The table was first presented in reference 51.

TABLE 2-III. - SIMILARITY RELATIONS REGARDING CAVITATION

Effect	Item	Forces and characteristics	General similarity requirements	Similarity requirements for some fluid properties	Probable effects on σ_p of changes in V and L only
Ideal flow	1	Inertial forces only (classical theory)	$\sigma_H \equiv \frac{H_{sv}}{H}$ constant or $\sigma_p \equiv \frac{p - p_v}{\rho V^2/2}$ constant	$H_{sv} \propto V^2$ $p - p_v \propto V^2$	No effects; $\sigma_p = C_{p,min}$ σ_p constant and σ_H constant
Hydrodynamic scale on fluid pressure	2	Viscosity and inertial forces	Reynolds' law of similarity $R \equiv \frac{VL}{\mu/\rho}$ constant	VL constant	$\sigma_p < C_{p,min}$; σ_p increases with VL as σ_p approaches $C_{p,min}$ from below
	3	Gravity and inertial forces	Froude's law of similarity $F_L \equiv V/\sqrt{gL}$ constant	$V/\sqrt{L}$ constant	Vertical differences in cavitation decrease with increasing $V/\sqrt{L}$
	4	Elastic and inertial forces (compressibility)	Law of constant Mach number $M = V/a$ constant, where a may be acoustic velocity of gas-liquid mixture	V constant	Not predictable; probably important only with extensive cavitation
	5	Effects of surface irregularities of height h, tending to increase C_p over $C_{p,min}$ calculated for smooth surface	h/δ constant, where δ is local thickness of boundary layer h/L constant for R constant	Geometric similarity of roughness: h, L constant and VL constant	$\sigma_p \approx C_{p,min}$ (except by item 2); σ_p decreases with decreasing relative roughness h/L and with decreasing L/V
Thermodynamic scale and gas content[a]	6	Effects of changes in vapor pressure Δp_v	$p_v - p$ constant or $p_v/\rho V^2$ constant	p constant V constant	Effects of local changes in p_v decrease with increasing V
	7	Effects of vaporization and heat transfer (vaporization reduces p_v; hence Δp_v is negative; heat transfer reduces local temperature drop, therefore, reduces absolute value of Δp_v)	$\frac{\Delta p_v}{p}$ constant $\propto \frac{1}{p}\frac{\partial p_v}{\partial T} \equiv \frac{p_v A_v A}{\rho_f A_w C_{p,f}} Pe^n$, where $Pe \equiv \frac{\rho_f C_{p,f}}{K} VL$ is Peclet number and $0 < n < 1$, $n = 0$ for pure convection, $n = 1$ for conduction $\frac{\Delta p_v}{p_v}$ constant $\propto \frac{1}{p_v}\frac{\partial p_v}{\partial T} \equiv \frac{p_v A_v A}{\rho_f A_w C_{p,f}} Pe^n$ $\frac{\Delta p_v}{\rho_f V^2}$ constant $\propto \frac{\partial p_v}{\partial T} \equiv \frac{A_v p_v}{A_w \rho_f^{2-n} C_{p,f}^{1-n} K^n V^{2-n}} \equiv \frac{L^n}{V^{2-n}}$	$\frac{L^n}{V^{2-n}}$ constant	$\sigma_{p,o}$ calculated on basis of bulk, steady-state vapor pressure decreases with increasing negative $\Delta p_v \propto \rho V^2$; hence $\sigma_{p,o}$ decreases with increasing $L^n V^{2-n} \sigma_{p,o}$ constant $\equiv \frac{\Delta p_v}{\rho V^2/2}$, where Δp_v is usually negative)
	8	Effect of gas content, probably for desinent cavitation only	$p_g - p$ constant or $p_g/\rho V^2$ constant	p constant V constant	p_g tends to increase $\sigma_{p,o}$; this effect decreases with increasing V
Molecular and other microscopic scale	9	Surface tension σ_s and inertial forces (surface tension tends to reduce σ_p)	Weber number constant $W \equiv \frac{\rho V^2 \Delta}{\sigma_s}$ constant, where Δ is size of nuclei $W \equiv \frac{\rho V^2 L}{\sigma_s}$ constant, if Δ/L constant	$V^2\Delta$ constant $V^2 L$ constant if Δ/L constant	σ_p increases with $V^2\Delta$ σ_p increases with $V^2 L$ if Δ/L constant
	10	Number of nuclei	$\frac{\Delta t V}{L}$ constant and $\frac{1}{\sqrt[3]{N}L}$ constant, where N is number per unit volume and Δt is average interval of time required for arrival of nucleus at point of critical pressure; important only if nearly all nuclei are centers of cavitation, no effect if nuclei are abundant (Plesset)	L constant	$\frac{\Delta t V}{L}$ decreases with increasing L; Δt decreases with increasing V (if N constant)

[a]May be neglected if $p_v - p$ is very small (e.g., for cold water) and or if $p_g - p$ is very small.

Appendix 2-A

Laws of Incompressible, Frictionless Flow

2-A.1 Laws of Plane, Two-Dimensional Flow of Incompressible, Frictionless Fluids

The local condition of continuity of plane, incompressible flow states that the same volume of fluid enters and leaves an infinitesimal region ABCD shown in figure 2-80. The rate of flow through side AD is $u\,dy$, through side AB is $v\,dx$, through side BC is $-[u+(\partial u/\partial x)\,dx]dy$, and through side CD is $-[v+(\partial v/\partial y)\,dy]dx$, where u is the velocity component in the x-direction, and v is the velocity component in the y-direction. Therefore

$$u\,dy + v\,dx - \left(u + \frac{\partial u}{\partial x}dx\right)dy - \left(v + \frac{\partial v}{\partial y}dy\right)dx = 0$$

Canceling oppositely equal terms and dividing by the area $dx\,dy$ of the region ABCD simplifies the condition of continuity to the form

$$\frac{\partial u}{\partial x} + \frac{\partial v}{\partial y} = 0 \qquad \text{(2-A-1)}$$

A relation between velocities and forces in the fluid (i.e., pressure differences) is readily obtained from Newton's law: force equals mass times acceleration. It must first be understood that the pressure differences considered here do not include those due to gravitational forces; differences in elevation are either negligible or may be considered to be eliminated by measuring all pressures at one elevation.

Consider a fluid particle such as that shown in figure 2-81. Its volume is $dx\,dy$ times 1; consequently its mass is $\rho\,dx\,dy$. The x-component of the local fluid velocity is again represented by u, and the y-component by v. The change in pressure, for a small step dx, in the x-direction only, is represented by $(\partial p/\partial x)dx$; for a corresponding step dy, the change is $(\partial p/\partial y)dy$. Pressure differences in the x-direction act on the area dy times 1, and those in the y-direction act on the area dx times 1. Then the equilibrium of forces in the x-direction is expressed by

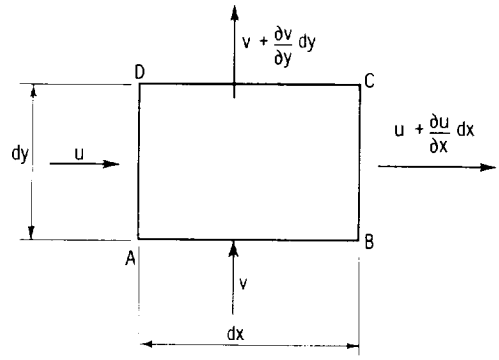

Figure 2-80. – Flow in and out of fluid region.

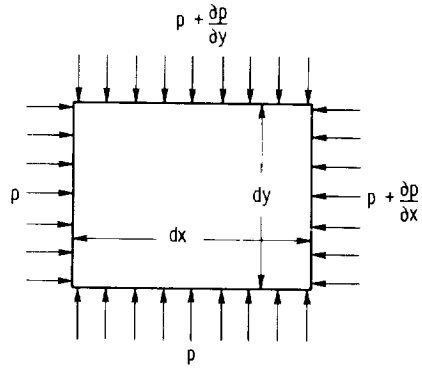

Figure 2-81. – Pressure forces acting on fluid particle.

$$\rho\,dx\,dy\frac{du}{dt} = p\,dy - dy\left(p + \frac{\partial p}{\partial x}dx\right)$$

that is,

mass times acceleration = forces due to pressure differences

Canceling $p\,dy$ and dividing by $dx\,dy$, we obtain the relation

$$\left.\begin{aligned}\frac{\rho\,du}{dt} &= -\frac{\partial p}{dx}\\ \frac{du}{dt} &= -\frac{1}{\rho}\frac{\partial p}{\partial x}\end{aligned}\right\} \qquad \text{(2-A-2)}$$

By precisely the same reasoning, one finds, for the equilibrium of forces in the y-direction,

$$\frac{dv}{dt} = -\frac{1}{\rho}\frac{\partial p}{\partial y} \qquad \text{(2-A-3)}$$

The total increase du of the x-component of the fluid velocity may be divided into three parts:

(1) The velocity increase due to the acceleration of the fluid as a whole, that is, a velocity increase at any fixed point in the field of fluid motion (no change of x and y) as a function of time only. This part is $(\partial u/\partial t)dt$.

(2) The velocity increase due to the fact that the fluid passes in the x-direction into a region of increased velocity. This is $(\partial u/\partial x)dx$.

(3) The velocity increase due to the fact that the fluid passes in the y-direction into a region of increased velocity. This is $(\partial u/\partial y)dy$.

When these three parts of the change in u are added and divided by dt, the following equation is obtained:

$$\frac{du}{dt} = \frac{\partial u}{\partial t} + \frac{\partial u}{\partial x}\frac{dx}{dt} + \frac{\partial u}{\partial y}\frac{dy}{dt} \tag{2-A-4}$$

For a fluid particle participating in the general motion of the fluid,

$$\left.\begin{aligned} \frac{dx}{dt} &= u \\ \frac{dy}{dt} &= v \end{aligned}\right\} \tag{2-A-5}$$

Hence

$$\frac{du}{dt} = \frac{\partial u}{\partial t} + u\frac{\partial u}{\partial x} + v\frac{\partial u}{\partial y} \tag{2-A-6}$$

Analogously, for the total increase of the y-component of the fluid velocities,

$$\frac{dv}{dt} = \frac{\partial v}{\partial t} + u\frac{\partial v}{\partial x} + v\frac{\partial v}{\partial y} \tag{2-A-7}$$

By substituting equations (2-A-6) and (2-A-7) into equations (2-A-2) and (2-A-3), we find that

$$\frac{\partial u}{\partial t} + u\frac{\partial u}{\partial x} + v\frac{\partial u}{\partial y} = -\frac{1}{\rho}\frac{\partial p}{\partial x} \tag{2-A-8}$$

and

$$\frac{\partial v}{\partial t} + u\frac{\partial v}{\partial x} + v\frac{\partial v}{\partial y} = -\frac{1}{\rho}\frac{\partial p}{\partial y} \tag{2-A-9}$$

These are Euler's equations for two-dimensional fluid motions; they express the equilibrium between inertial forces and pressure forces on a small fluid particle. Tangential, or friction (shear), forces are not included, and the gravitational forces and pressure differences have been eliminated, as stated previously.

Equations (2-A-8) and (2-A-9) may be simplified by limiting the present considerations to steady fluid motions, that is, fluid motions that do not change with time. Steady fluid motions are characterized by the condition

$$\frac{\partial u}{\partial t} = \frac{\partial v}{\partial t} = 0 \tag{2-A-10}$$

Under this assumption, equations (2-A-8) and (2-A-9) are reduced to

$$u\frac{\partial u}{\partial x} + v\frac{\partial u}{\partial y} = -\frac{1}{\rho}\frac{\partial p}{\partial x} \tag{2-A-11}$$

and

$$u\frac{\partial v}{\partial x} + v\frac{\partial v}{\partial y} = -\frac{1}{\rho}\frac{\partial p}{\partial y} \tag{2-A-12}$$

It is important to note that the fluid motions in hydrodynamic machines are not steady, since the rotor continuously changes its position relative to the stationary parts of the machine. The departure from steady-state flow, however, can be assumed to be small under normal flow conditions and must generally be neglected in order to permit a simple, theoretical attack on the flow problems involved.

Using equation (2-A-11) in the x-direction only and assuming that the flow is in the same direction, so that $v = 0$, lead to

$$u\frac{du}{dx} = -\frac{1}{\rho}\frac{dp}{dx} \tag{2-A-13}$$

The integration of this equation yields

$$\int_1^2 u\,du = -\frac{1}{\rho}\int_1^2 dp$$

and, therefore,

$$\frac{u_2^2 - u_1^2}{2} = -\frac{1}{\rho}(p_2 - p_1) \tag{2-A-14}$$

which is obviously Bernoulli's equation.

Thus equations (2-A-11) and (2-A-12) are equivalent to Bernoulli's equation for steady flow, and Bernoulli's equation holds true along the streamlines of any flow obeying equations (2-A-11) and (2-A-12), if the x-direction is locally adjusted to the direction of the streamlines.

One variable, conveniently the pressure p, can be eliminated from equations (2-A-11) and (2-A-12) by differentiating these equations with respect to y (eq. (2-A-11)) and with respect to x (eq. (2-A-12)). The resulting relations are

$$\frac{\partial u}{\partial y}\frac{\partial u}{\partial x}+u\frac{\partial^2 u}{\partial x\,\partial y}+\frac{\partial v}{\partial y}\frac{\partial u}{\partial y}+v\frac{\partial^2 u}{\partial y^2}=-\frac{1}{\rho}\frac{\partial^2 p}{\partial x\,\partial y}$$

and

$$\frac{\partial u}{\partial x}\frac{\partial v}{\partial x}+u\frac{\partial^2 v}{\partial x^2}+\frac{\partial v}{\partial x}\frac{\partial v}{\partial y}+v\frac{\partial^2 v}{\partial y\,\partial x}=-\frac{1}{\rho}\frac{\partial^2 p}{\partial x\,\partial y}$$

Subtracting the second equation from the first gives

$$\frac{\partial u}{\partial x}\frac{\partial u}{\partial y}-\frac{\partial u}{\partial x}\frac{\partial v}{\partial x}+\frac{\partial v}{\partial y}\frac{\partial u}{\partial y}-\frac{\partial v}{\partial x}\frac{\partial v}{\partial y}+u\frac{\partial^2 u}{\partial x\,\partial y}-u\frac{\partial^2 v}{\partial x^2}+v\frac{\partial^2 u}{\partial y^2}-v\frac{\partial^2 v}{\partial x\,\partial y}=0$$

$$\frac{\partial u}{\partial y}\left(\frac{\partial u}{\partial x}+\frac{\partial v}{\partial y}\right)-\frac{\partial v}{\partial x}\left(\frac{\partial u}{\partial x}+\frac{\partial v}{\partial y}\right)-u\frac{\partial}{\partial x}\left(\frac{\partial v}{\partial x}-\frac{\partial u}{\partial y}\right)-v\frac{\partial}{\partial y}\left(\frac{\partial v}{\partial x}-\frac{\partial u}{\partial y}\right)=0$$

According to the condition of continuity (2-A-1),

$$\frac{\partial u}{\partial x}+\frac{\partial v}{\partial y}=0$$

Consequently

$$u\frac{\partial}{\partial x}\left(\frac{\partial v}{\partial x}-\frac{\partial u}{\partial y}\right)+v\frac{\partial}{\partial y}\left(\frac{\partial v}{\partial x}-\frac{\partial u}{\partial y}\right)=0 \qquad (2\text{-A-}15)$$

Equation (2-A-15) is certainly satisfied if

$$\frac{\partial v}{\partial x}-\frac{\partial u}{\partial y}=0 \qquad (2\text{-A-}16)$$

It follows that any solution of the latter equation, together with equation (2-A-1), is also a solution of the Euler equations (2-A-11) and (2-A-12) for steady flow; that is to say, any velocity distribution or flow picture that satisfies equations (2-A-16) and (2-A-1) also satisfies equations (2-A-11) and (2-A-12). It should be noted that the elimination of the pressure is an important step that reduces the flow problem to a purely kinematic one. In other words, the dynamic conditions are automatically satisfied if the kinematic equations (2-A-1) and (2-A-16) are fulfilled.

Equation (2-A-16), however, is not the only way in which equation (2-A-15) can be satisfied. If we introduce a new function of x and y by the definition

$$\zeta(x,y)\equiv\frac{\partial v}{\partial x}-\frac{\partial u}{\partial y} \qquad (2\text{-A-}17)$$

equation (2-A-15) appears in the form

$$u\frac{\partial\zeta}{\partial x}+v\frac{\partial\zeta}{\partial y}=0 \qquad (2\text{-A-}18)$$

Since ζ is a function of x and y, and only of x and y, the total differential of ζ may be written in the form

$$d\zeta=\frac{\partial\zeta}{\partial x}dx+\frac{\partial\zeta}{\partial y}dy$$

When this is compared with equation (2-A-18),

$$\frac{d\zeta}{dt}=\frac{\partial\zeta}{\partial x}\frac{dx}{dt}+\frac{\partial\zeta}{\partial y}\frac{dy}{dt}=\frac{\partial\zeta}{\partial x}u+\frac{\partial\zeta}{\partial y}v=0$$

where the substitutions $dx/dt=u$ and $dy/dt=v$ indicate, as previously, that we are following in the field of fluid motion the paths of the fluid particles. Equation (2-A-18) and, consequently, equation (2-A-15) then express the fact that

$$\frac{d\zeta(x,y)}{dt}=0 \qquad (2\text{-A-}19)$$

that is, the newly introduced function ζ does not change with time along the paths of the fluid particles. This statement means that

$$\zeta=\text{constant} \qquad (2\text{-A-}20)$$

along the streamlines.

Before we proceed with the general derivations, we should consider the physical meanings of the derivatives appearing in the equations derived so far. The physical meaning of $\partial u/\partial x$ and $\partial v/\partial y$ (i.e., the derivative, or rate of change of each velocity component in its own direction) is illustrated by figure 2-82, which shows the flow in a converging conduit. Here $\partial u/\partial x$ is positive, since u increases in the x-direction. On the other hand, $\partial v/\partial y$ is

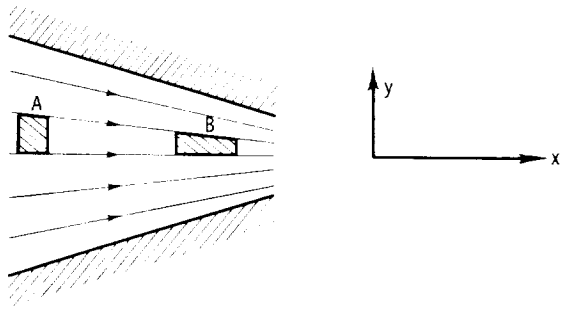

Figure 2-82. – Deformation of fluid particle demonstrating that $\partial u/\partial x=-\partial v/\partial y$.

negative, since the flow at the upper edge of the fluid particle shown has a greater downward component (greater negative v-component) than that at the lower edge of the fluid particle. The deformation of each fluid particle is shown by the successive positions A and B of a particle of the same volume. The fluid particle contracts laterally (in the y-direction) in the same ratio as it is elongated, and it is exactly this law of deformation which is expressed by the condition of continuity (2-A-1).

The meaning of $\partial u/\partial y$ (the rate of change of the x-component of the velocity with respect to the y-direction) is shown in figure 2-83. The flow is assumed to proceed in the x-direction with a velocity gradient, or change in velocity in the y-direction. This situation exists, for instance, in the vicinity of a fixed boundary under the influence of fluid friction. The velocity gradient $\partial u/\partial y$ is represented as the tangent of the angle β in this figure, and the deformation of the fluid under these conditions is shown by a fluid particle in two successive positions A and B. This deformation is a shear deformation and is simply due to the fact that the velocity at the upper streamline b is greater than that at the lower streamline a.

The simultaneous existence of a velocity gradient $\partial u/\partial y$ and gradient $\partial v/\partial x$ is illustrated in figure 2-84. The vertical velocity component at B is greater than that at A by $(\partial v/\partial x)dx$; after a time element dt, the point B has, therefore, moved, relative to A, by a vertical distance $BB' = (\partial v/\partial x)dx\,dt$. Correspondingly the point D moves during the same time, relative to A, by a horizontal distance $DD' = (\partial u/\partial y)dy\,dt$. The deformation of the fluid may be characterized by a rotation of the line AB by an angle $d\beta_x$ and of the line AD by a negative angle $d\beta_y$. For small angles, where the tangent is equal to the arc,

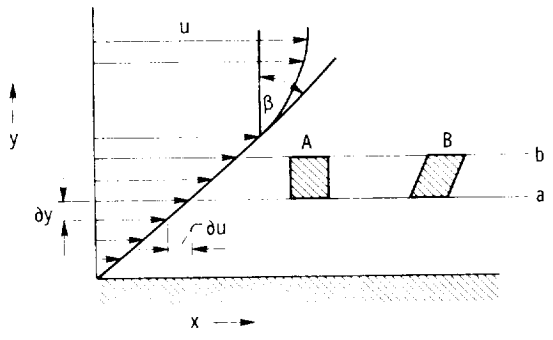

Figure 2-83. – View of shear flow illustrating $\partial u/\partial y$.

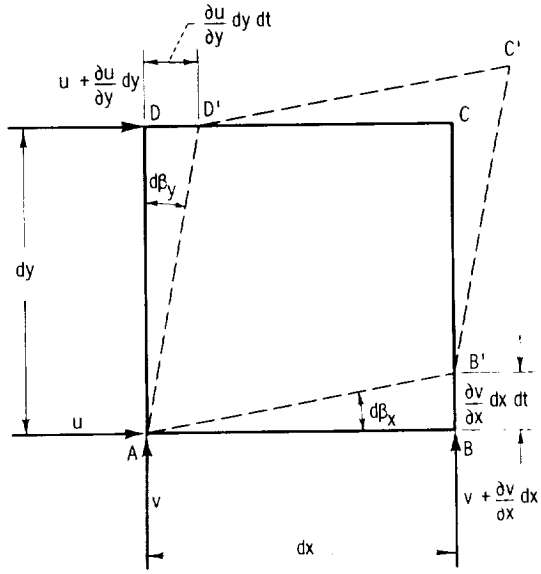

Figure 2-84. – Shear deformation of fluid particle.

$$d\beta_x\,dx = \frac{\partial v}{\partial x}dx\,dt$$

$$-d\beta_y\,dy = \frac{\partial u}{\partial y}dy\,dt$$

The angular velocities of the lines AB and AD are, therefore,

$$\left.\begin{aligned}\omega_x &= \frac{d\beta_x}{dt} = \frac{\partial v}{\partial x}\\ \omega_y &= \frac{d\beta_y}{dt} = -\frac{\partial u}{\partial y}\end{aligned}\right\} \qquad (2\text{-A-}21)$$

Figure 2-84 further demonstrates the kinematic significance of equation (2-A-16). If this equation is satisfied, the direction of each diagonal of the fluid particle remains unchanged, since, in this case,

$$\omega_x = -\omega_y \qquad (2\text{-A-}22)$$

The arithmetic mean of ω_x and ω_y, representing the average angular velocity of the fluid particle, is

$$\omega = \frac{\omega_x + \omega_y}{2} = \frac{1}{2}\left(\frac{\partial v}{\partial x} - \frac{\partial u}{\partial y}\right) = \frac{1}{2}\zeta(x,y) \qquad (2\text{-A-}23)$$

This equation shows that the function $\zeta(x,y)$, as introduced by equation (2-A-17), is the average angular velocity of the fluid at the point x,y multiplied by 2. This function is called the vorticity

of the fluid. With this terminology, equations (2-A-19) and (2-A-20) can be expressed as the so-called second Helmholtz law: The vorticity $\zeta = \partial v/\partial x - \partial u/\partial y$ of a particle of a frictionless fluid does not change with time. Consequently the vorticity is constant along the stream lines of such a fluid in steady motion.

The law leads to important conclusions when considered in connection with the previously derived fact that the total energy of a frictionless and steady flow is constant along the streamlines. Figure 2-85 shows a flow starting from a large body of fluid that is practically at rest. The total energy is constant in such a stationary body of fluid, and the vorticity is obviously zero. Every streamline of the flow, however, originates at A or B in this stationary body of fluid. With all streamlines coming from a region of constant energy and with the energy constant along the streamlines, it follows that the energy must be constant throughout the whole field of fluid motions. Thus Bernoulli's equation holds not only along each streamline, but also between any two points in the system. Inversely any flow with uniformly distributed energy can be assumed to come from a stationary body of fluid.

Furthermore if all streamlines originate in a region of zero velocity and, therefore, zero vorticity, it follows from the second Helmholtz law that the vorticity is zero throughout the field of fluid motions. In this connection, note that it has already been established that the condition (2-A-16) satisfies the Euler equations (2-A-11) and (2-A-12). Considering any flow of constant energy as coming from a stationary body of fluid, one can draw the important conclusion that the vorticity is zero for any steady fluid motion of constant energy. Such a fluid motion is called irrotational.

The circulation Γ has been defined as the line integral around any closed contour of the velocity component parallel to the contour times the linear elements of the contour. Applying this definition to the infinitesimal region ABCD shown in figure 2-86 leads to

$$d\Gamma = u\,dx + \left(v + \frac{\partial v}{\partial x}dx\right)dy - \left(u + \frac{\partial u}{\partial y}dy\right)dx - v\,dy$$

When oppositely equal terms are canceled, this reduces to

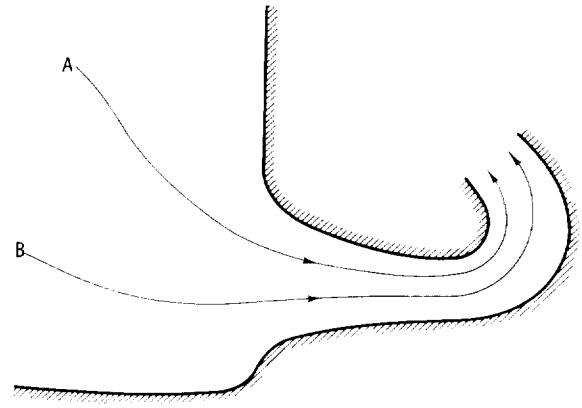

Figure 2-85. – Flow from infinitely extended region.

$$d\Gamma = \left(\frac{\partial v}{\partial x} - \frac{\partial u}{\partial y}\right)dx\,dy \qquad \text{(2-A-24)}$$

and, with the definition of the vorticity $\zeta(x,y)$ in a two-dimensional field given by equation (2-A-17),

$$d\Gamma = \zeta(x,y)dx\,dy \qquad \text{(2-A-25)}$$

that is, the circulation is equal to the vorticity in an elementary region times the area of the region.

Furthermore, if several regions like that shown in figure 2-86 are placed next to each other in chessboard fashion, it is easy to show that the circulation along a finite, singly connected, closed contour (c) is equal to the (alegbraic) sum of all circulations inside the contour:

$$\Gamma_{around\ C} = \Sigma\Gamma_{within\ C} \qquad \text{(2-A-26)}$$

As a consequence, the circulation about a finite contour can be written in the form

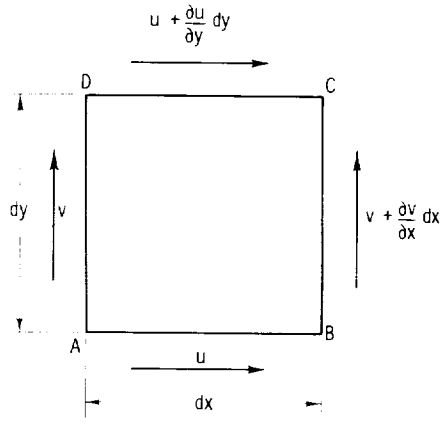

Figure 2-86. – Circulation about fluid element.

C - 3

$$\Gamma = \int\int \zeta(x,y)dx\,dy \qquad (2\text{-A-}27)$$

where the double integration covers the area inside the contour.

The transformation of vorticity from Cartesian to polar coordinates is illustrated by figure 2-87. Point A is the center of the Cartesian system (x,y), and 0 is the center of the polar system (r,φ). The peripheral velocity component in the polar system is V_U, which is equal to $-u$ at point A.

Furthermore figure 2-87 shows that

$$-dx = r\,d\varphi$$

$$dy = dr$$

$$-dv = V_U\,d\varphi$$

so that

$$\frac{\partial v}{\partial x} = \frac{V_U\,d\varphi}{r\,d\varphi} = \frac{V_U}{r}$$

$$\frac{\partial u}{\partial y} = -\frac{\partial V_U}{\partial r}$$

By substituting the last two equations into equation (2-A-17), one obtains the polar expression for the vorticity:

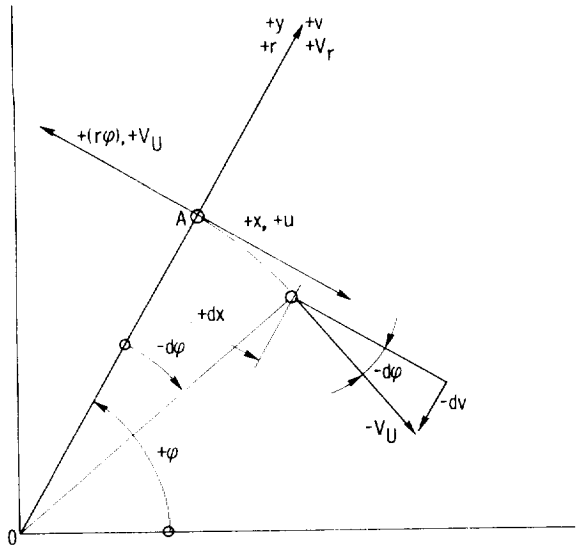

Figure 2-87. – Transformation of vorticity from Cartesian to polar coordinates. Positive directions of φ and V_U are counterclockwise.

$$\zeta(r,\varphi) = \frac{V_U}{r} + \frac{\partial V_U}{\partial r} \qquad (2\text{-A-}28)$$

The vorticity can readily be seen to be proportional to the radial gradient in angular momentum, since equation (2-A-28) can be written in the form

$$\zeta(r,\varphi) = \frac{1}{r}\frac{\partial(rV_U)}{\partial r} \qquad (2\text{-A-}29)$$

Therefore a curved, irrotational flow ($\zeta(r,\varphi)=0$) is a flow of radially constant angular momentum, because $\partial(rV_U)/\partial r = 0$ means that rV_U = constant with respect to r.

2-A.2 Laws of Three-Dimensional Motions of Incompressible, Frictionless Fluids

The condition of continuity is derived for three-dimension flow in exactly the same manner as equation (2-A-1) for plane, two-dimensional flow. The corresponding three-dimensional expression of continuity is

$$\frac{\partial u}{\partial x} + \frac{\partial v}{\partial y} + \frac{\partial w}{\partial z} = 0 \qquad (2\text{-A-}30)$$

where u, v, and w are the orthogonal velocity components in the direction of the Cartesian coordinates x, y, and z.

The vorticity is in three-dimensional flow a vector normal to the plane of the vortex motion. Its three components are

$$\left.\begin{aligned} \zeta_x &= \frac{\partial w}{\partial y} - \frac{\partial v}{\partial z} \text{ (in the } y,z\text{-plane)} \\ \zeta_y &= \frac{\partial u}{\partial z} - \frac{\partial w}{\partial x} \text{ (in the } z,x\text{-plane)} \\ \zeta_z &= \frac{\partial v}{\partial x} - \frac{\partial u}{\partial y} \text{ (in the } x,y\text{-plane)} \end{aligned}\right\} \qquad (2\text{-A-}31)$$

The first vortex law by Helmholtz expresses the condition of continuity for the vorticity vector field:

$$\frac{\partial \zeta_x}{\partial x} + \frac{\partial \zeta_y}{\partial y} + \frac{\partial \zeta_z}{\partial z} = 0 \qquad (2\text{-A-}32)$$

This law is proven by substituting the definitions of the vorticity components, ζ_x, ζ_y, and ζ_z from equations (2-A-31) into equation (2-A-32). This substitution leads to the following identity:

$$\frac{\partial^2 w}{\partial x\,\partial y} - \frac{\partial^2 v}{\partial x\,\partial z} + \frac{\partial^2 u}{\partial y\,\partial z} - \frac{\partial^2 w}{\partial y\,\partial x} + \frac{\partial^2 v}{\partial z\,\partial x} - \frac{\partial^2 u}{\partial z\,\partial y} \equiv 0 \quad \text{(2-A-33)}$$

which means that the vortex law of Helmholtz (eq. (2-A-32)) follows directly from the definition of vorticity given by equation (2-A-31).

If vortex lines are defined to have everywhere the direction of the local vorticity vector, then the first vortex law by Helmholtz (eq. (2-A-32)) can also be stated in the following form: vortex lines cannot end in a frictionless fluid.

The second vortex law by Helmholtz must be stated for three-dimensional flow differently from the previous statement for two-dimensional, plane flow. It is still true that vorticity remains connected with the fluid. However, in three-dimensional flow, the area of a fluid particle (of unchanging volume) normal to the vorticity vector does not remain constant if the particle is stretched (or shortened) in the direction of the vorticity vector. It is the circulation about the particle which remains constant, so that the vorticity changes according to equations (2-A-25) and (2-A-27) in inverse proportion to the area of the particle normal to the vorticity vector, or the vorticity vector changes its length in proportion to the length of the fluid particle in the same direction, that is,

$$\zeta_1 A_1 = \zeta_2 A_2 \qquad \text{(2-A-34)}$$

This changes the second vortex law by Helmholtz to the following statement: vortex lines and vorticity vectors remain connected to the fluid and move and are stretched (or shortened) with the fluid.

(The vorticity vectors must be drawn at a sufficiently small scale that the (changing) curvature of the vortex lines is negligible regarding the form of vorticity vectors.)

2-A.3 Circulation of Relative Flow

The circulation of the relative flow can be expressed, by using the parameters shown in figure 2-88, as

$$-\Gamma_w = w_{U,o}\, r_o\, \varphi - w_{U,i}\, r_i\, \varphi = (U_o - V_{U,o}) r_o\, \varphi - (U_i - V_{U,i}) r_i\, \varphi$$

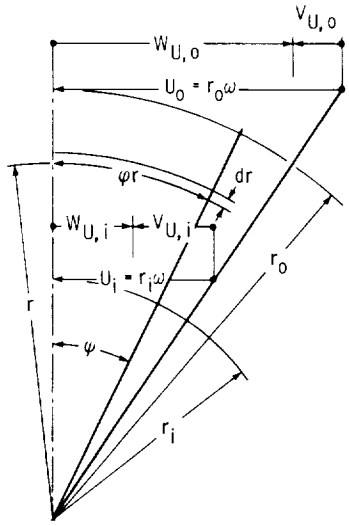

Figure 2-88. – Parameters for obtaining circulation of relative flow.

Assume $V_{U,o}\, r_o = V_{U,i}\, r_i$, that is, potential absolute flow; then

$$-\Gamma_w = (r_o\,\omega - V_{U,o}) r_o\,\varphi - \left(r_i\,\omega - V_{U,o}\frac{r_o}{r_i}\right) r_o\,\varphi\,\frac{r_i}{r_o}$$

$$-\Gamma_w = r_o\,\varphi\left(r_o\,\omega - V_{U,o} - \frac{r_i^2}{r_o}\omega + V_{U,o}\right)$$

$$= r_o\,\varphi\left(r_o\omega - \frac{r_i^2}{r_o}\omega\right)$$

$$-\Gamma_w = r_o^2\,\varphi\omega\left(1 - \frac{r_i^2}{r_o^2}\right)$$

The circulation due to the vorticity $\zeta = -2\omega$ of the relative flow is

$$\Gamma_\zeta = \int^a \zeta\, da = \zeta \int^a da$$

since ζ = constant. The elemental area da is given by

$$da = \varphi r\, dr$$

from which the total area is given by

$$\int^a da = \varphi \int_{r_i}^{r_o} r\, dr = \varphi\left(\frac{r^2}{2}\right)_{r_i}^{r_o} = \frac{\varphi}{2}(r_o^2 - r_i^2)$$

Therefore

$$\Gamma_\zeta = -2\omega \frac{\varphi}{2}(r_o^2 - r_i^2) = -\omega\varphi r_o^2 \left(1 - \frac{r_i^2}{r_o^2}\right)$$

$$\Gamma_\zeta = \Gamma_w$$

This means that there is no flow along the radial boundaries of the area a considered, that is, no secondary flow due to the vorticity $\zeta = -2\omega$ of the relative flow.

Chapter 3

Hydrodynamic and Gas-Dynamic Design of Axial-Flow Turbomachinery

3.1 Introduction

As stated in the preface, this compendium is intended to present in the simplest way possible principles and methods of the design of turbomachinery which are applicable to the preliminary phases of design, that is, to those phases where the basic form of the machine is yet to be determined. This intent is particularly important in the field of axial-flow turbomachinery, where the leading manufacturing companies have developed highly advanced methods of design (extensively computerized) which rapidly produce detailed answers to a large variety of design problems in a well-established, specific field. The most prominent example of this fact is obviously the field of aircraft turbine engines. This compendium cannot be expected to make significant contributions to this highly developed discipline. Instead this compendium presents principles and methods of design in a form applicable by the individual design engineer in the formative stages of a new design; it presents a rational approach to the selection or development of design forms prior to the establishment of computerized or otherwise highly developed design procedures.

According to the broad approach developed in chapter 1, the first step in the present procedure is to express the given operating conditions, including certain characteristics of the fluid and the structural materials, in the form of a number of specific speeds (i.e., a number of dimensionless expressions). Together with certain design choices, the specific speeds determine a number of design parameters, such as flow coefficients, head coefficients, and stress coefficients, as well as certain ratios of dimensions which, in turn, determine some general proportions of the machine to be designed. Figure 1-27 presents an example of the type of information obtained in this manner.

For chapter 3, one design choice is already made, the choice of axial-flow machines rather than radial-flow machines, both shown in figure 1-39. The number of stages is determined to a large extent by the basic specific speed of the entire unit compared with the specific speed per stage, whereas the design difference between the first stage and the higher stages, which obviously have very different inlet pressures, is prescribed by the suction specific speed (by eqs. (1-44), (1-46), and (1-48) as well as fig. 1-18). For single-stage units, the relation between the basic specific speed and the general design form of the rotor is shown in figure 1-9 for liquid-handling machines, and the corresponding analytical relations to various design parameters are expressed by equations (1-25) and (1-26) and others presented in chapter 1.

This chapter describes the process by which the actual design of the machine is developed on the basis of the aforementioned similarity relations and design choices. Involved are the relations between elementary design forms and design parameters presented in section 1.3 of chapter 1.

In this chapter, the flow is considered subsonic and incompressible except where the effects of compressibility are explicitly mentioned in the title of the section.

3.2 Design of Cylindrical Flow Sections Through Axial-Flow Vane Systems (Cascade Design)

3.2.1 Construction of Inlet and Discharge Velocity Diagrams and Some Principles of Cascade Design

The flow coefficient $\varphi = V_{m,i}/U_i$ (appearing in all specific speed equations listed in table 1-I), the head coefficient $\psi_i = 2g_o H/U_i^2$ (appearing in the basic specific speed equation (1-25)), and the ratio of prerotation $V_{U,i}/U_i$ (prescribed by the upstream vane or duct system) determine the inlet and discharge velocity diagrams of the outermost, cylindrical flow section with diameter $D_o = D_i$.

For any other cylindrical flow section with a diameter D, evidently $U = U_i D/D_i$. Furthermore, for irrotational flow, $V_{U,1} = V_{U,i} D_i/D$ and $V_{m,1} = V_{m,i} =$ constant. For flow with vorticity, the fluid velocity relations for flow between various cylindrical flow sections are given as outlined in section 2.7 of chapter 2. In such cases, the vorticity or velocity distribution of the oncoming flow as well as the radial distribution of the vane circulation (i.e., the radial gradient of the change ΔV_U in peripheral velocity across the vane system) must be given in order to have a completely determined design problem.

Thus the inlet and discharge velocities of the outermost flow section determine the corresponding velocities for all other coaxial, cylindrical flow sections through the vane system to the extent of the general determination of the flow problem.

The inlet and discharge velocity vector diagrams, in turn, determine the vane shape within that particular flow section to the extent of the available knowledge of axial-flow vane system design. This relation is outlined in section 1.3.2.1, particularly by figure 1-23. A more detailed description of the process of vane section (cascade) design is given in sections 3.2.2 to 3.2.6. Section 3.2.7 extends these methods to compressible fluids.

Design methods for straight cascades of parallel, staggered vanes (cylindrical sections through axial-flow vane systems) developed by the NACA and NASA are well documented in references 6 and 16 to 18. An excellent summary of this field of design consideration is given in reference 54. No attempt is made to cover the contents of these references in the present compendium, so the reader must study these references to obtain a reasonably complete picture of the entire field of cascade design.

Most existing methods of cascade design use so-called series of systematically varied vane section shapes arranged in cascades of different stagger angles and solidities. Reference 16 presents the characteristics of such a series useful in hydrodynamic design. In contrast, the following sections present the design of entire cascades as a function of the inlet and discharge velocity diagrams. The vane shape, stagger angle, and solidity are determined together, and one design characteristic of the cascade is not varied independently of the others.

3.2.2 First Approximation of Cylindrical Flow Section Design by One-Dimensional Considerations, Zero-Lift Direction, and Elementary Stress Considerations

The primary relation between the inlet and discharge velocities and the form of a straight cascade of parallel, staggered vanes is illustrated in figure 3-1 for an axial-flow pump or compressor vane system. This illustration applies to any coaxial, cylindrical flow section through the system where the inlet and discharge (relative) velocities are established as outlined in section 3.2.1. The procedure applies only with some reservations to turbine vane systems, because there might be a conflict between the zero-lift direction and the vane-distance consideration.

The leading part of the vane (lower part in fig. 3-1) is essentially parallel to the velocity vector w_1 of the incoming flow, but often has a very small, negative angle of attack. This alignment is important in avoiding major pressure reductions and velocity increases at the low-pressure side of the vanes near the leading edge, which are significant in

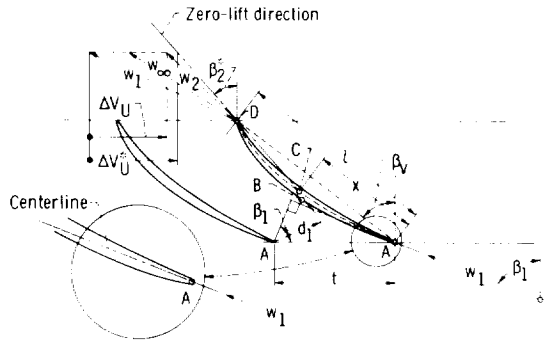

Figure 3-1. – First approximation of cylindrical vane section (cascade) design for axial-flow pump or compressor.

liquids with respect to cavitation, in gases with respect to locally supersonic flow, and in all fluids with respect to the static-pressure rise from inlet to discharge along the low-pressure side of the vanes (danger of stall, see section 2.5.4.3).

For vane systems with solidities l/t substantially larger than unity, the normal distance d_1 between the vanes at their inlet end must be sufficient to admit the flow without increase in average relative velocity. Thus the minimum distance between the vanes should satisfy the relation

$$d_1 \geqq t \cos \beta_1 \tag{3-1}$$

This requires that the low-pressure side of the vane be slightly curved (convex) between point B and the leading edge A.

Vane systems for exceedingly high suction specific speeds usually have a somewhat different inlet configuration than that described here; it is discussed in section 3.4.

The discharge portion of the vane section can be designed effectively by means of the zero-lift direction, a procedure which is introduced in section 2.5.2. The relation between the relative discharge velocity vector and the zero-lift direction is given by figure 2-19 and by the results of the theoretical work by Weinig expressed by figure 2-18. A straight line drawn through the trailing edge parallel to the zero-lift direction intersects the mean camber line of the vane at a distance x from the leading edge (fig. 3-1). The ratio of x to the vane length is given by figure 2-28 on the basis of NACA cascade test results.

The design of a pump vane section by means of the information just outlined and presented in section 2.5 is approximately that given by the following 12 steps:

(1) From the inlet and discharge velocity vector diagrams (such as shown, e.g., in fig. 1-21), determine the retardation ratio w_2/w_1.

If this ratio is smaller than (approximately) 0.6, the considerations that determined the velocity diagrams (sec. 3.2.1) must be changed by reducing the head coefficient $\psi = 2g_o H/U^2$, increasing the flow coefficient $\varphi = V_{m,1}/U$, or changing the prerotation ratio $V_{U,1}/U$ or by a combination of these measures.

If the retardation ratio w_2/w_1 is larger than 0.6, select a lift coefficient $C_{L,\infty}$ from the information presented in figure 2-26. Base this selection on certain values of the diffusion factor D (say $0.5 < D < 0.6$) or of the coefficient K_∞ (say $1.5 < K_\infty < 2.0$) and maintain certain limits of the lift coefficient $C_{L,\infty}$ (say $0.9 < C_{L,\infty} < 1.6$). For rotor tip sections, the choice should be more conservative than for rotor root sections because of the radial motion of the blade boundary layer.

There is another limitation on the blade lift coefficient which in many important cases overrides the limits set by flow separation or stall. This additional limit results from (lower) limitations of pressure or (upper) limitations of velocity at the vane surface set by cavitation or by compressibility effects. Since reductions in pressure and increases in local velocity are closely related by Bernoulli's equation it is sufficient to demonstrate this limitation with respect to the cavitation limits of liquid-handling machines. This demonstration is given in section 2.5.4.1. It points out in particular that the lift coefficient referred to the inlet (relative) velocity cannot be much higher than the minimum pressure coefficient $C_{p,min}$ referred to the same velocity. Physically this means that the average pressure difference across the vane cannot be much larger than the pressure reduction on the low-pressure side of the vanes. Thus, if the minimum pressure coefficient $C_{p,min} = \sigma_p$ is given by the required suction specific speed (eq. (1-48) and fig. 1-18), the blade lift coefficient referred to the relative inlet velocity $C_{L,1}$ may be limited by its relation to the minimum pressure coefficient $C_{p,min}$.

With

$$C_{L,\infty} = C_{L,1} \frac{w_1^2}{w_\infty^2} \tag{2-60}$$

the lift coefficient $C_{L,\infty}$ of turbomachinery vanes is also limited by the pressure reductions or velocity increases at the vane, set by cavitation or Mach number considerations, rather than by considerations of stall.

(2) From the lift coefficient

$$C_{L,\infty} = 2 \frac{\Delta V_U}{w_\infty} \frac{t}{l} \tag{3-2}$$

and the velocity vector diagrams (which determine ΔV_U and w_∞), establish the solidity l/t.

(3) Line up the inlet portion of the vane with the incoming flow w_1. A slightly negative angle of attack relative to the local vane centerline, with only slight curvature of the centerline, is desirable at the

leading edge to minimize pressure and velocity differences near that edge, as shown in figure 3-1. The thickness near the leading edge should be small, usually less than one-fifth of d_1 (fig. 3-1), which is the minimum vane distance normal to the direction of the incoming, relative velocity w_1.

(4) For vane systems with a solidity $l/t > 1$, the normal distance d_1 between vanes at their inlet edge must be sufficient to pass the flow without increase in average relative velocity. The resulting geometric requirements are stated previously and are apparent from figure 3-1. Estimate the blade thickness at B to be between 0.05 l and 0.10 l, and approximate the curvature of the mean camber line from the leading edge to the vicinity of point B accordingly. Disregard this step if the solidity $l/t < 1$.

(5) Establish in connection with item (4), or independently, a length representing the circumferential vane spacing t, and draw around the leading edge of the vane a circular arc with radius l determined by equation (3-2) and items (1) and (2) in terms of the solidity l/t. This arc is one locus for the trailing (discharge) edge of the vane.

(6) Establish the zero-lift direction in accordance with figures 2-18 and 2-19 as outlined previously.

(7) Shift a line having the zero-lift direction until it intersects an estimated mean camber line at a point approximately meeting the ratio of this intersection length x (measured from the leading edge) to the vane length l given by figure 2-28. As a first approximation, use $x/l = 1/2$ in figure 3-1, and make further approximations by means of figure 2-28. With the position of the zero-lift line so determined, its intersection with the arc about leading edge A with radius l determines the trailing edge D.

(8) The process just outlined determines the mean camber line by at least three points:

(a) The leading edge, point A (fig. 3-1)

(b) The trailing edge, point D (fig. 3-1), determined by the graphical procedure outlined in item (7)

(c) The point of intersection C between the zero-lift line (drawn through the trailing edge D) and the mean camber line, estimated from the inlet portion of the blade developed according to items (3) and (4) and figure 2-28

(d) For vane systems of high solidity ($l/t > 1$), a fourth point adjacent to point B in figure 3-1, based on an estimated blade thickness at this place

One draws the mean camber line as a smooth curve through the points so determined. One or two circular arcs may be sufficient. Consider that, for good cavitation or Mach number characteristics, the curvature along the leading portion of the blade must be small, and the angle of attack at the leading edge must be zero or small and negative (except for pumps operating with developed cavitation, e.g., inducers; see sec. 3.4).

(9) Around the mean camber line so determined, place a certain thickness distribution. To achieve good cavitation performance or high Mach number characteristics, place maximum thickness around or behind the midpoint of the vane section, and use a small leading-edge thickness, as indicated under item (3).

(10) The vane section derived according to items (1) to (9), and shown in figure 3-1, is dimensionless, since it is given by the solidity ratio l/t and the angles β_1 of the incoming flow, β_2^* of the zero-lift line, and β_v of the resulting chord line of the blades. Since the circumferential vane spacing is

$$t = \frac{\pi D}{N} \tag{3-3}$$

where N is the number of vanes (the same at all diameters), the geometry of the entire vane system is not determined because N is yet to be chosen. This choice is to be based on mechanical considerations briefly outlined in the following items and further described in section 3.3.1.

(11) For vane systems handling gases or liquid hydrogen, where centrifugal stresses dominate or are of the same order as bending stresses, the cross-sectional area of the vane must be determined for the root section and the tip section. Section 1.3.3.1, particularly figure 1-32, relates the cross-sectional area ratio a/a_o to the diameter or radius ratio r/r_o of the tip and root section and to the centrifugal stress coefficient $\rho_s U_o^2/2\sigma_c$, the latter being given in connection with the centrifugal stress specific speed (eq. (1-64)). The curves in figure 1-32 also give cross sections between the root and tip sections for radially constant tensile stress (except for the cylindrical outer portion of the blade, where $a/a_o = 1$).

The relation between the cross-sectional dimensions of various cylindrical sections at different diameters is given by equation (3-3) with N = constant. However, the absolute dimensions of the blade are not determined by centrifugal tensile stress considerations alone. For example, while a large number of blades with small cross sections may satisfy the centrifugal tensile stresses, bending stresses in, or deflections of, such blades could be intolerable.

A lower limit for the cross-sectional dimensions of the blades is usually set by the bending stresses or bending stiffness of the blades; this limit is briefly discussed in item (12) and further investigated in section 3.3.1. A theoretical lower limit is also given by a lower limit of the Reynolds number of the flow referred to the chord length l of the blade section. However, this limit is usually not reached before relative surface roughness and manufacturing accuracy have set the lower limit for the absolute dimensions of the blade cross sections.

(12) For liquids with densities of the order of that of water (e.g., liquid oxygen), blade bending stresses dominate over centrifugal tensile stresses, whereas for liquid hydrogen, bending stresses have about the same value as tensile stresses. The same may be true for gases if the cross section of the blade is minimized (the number of blades is maximized) in order to minimize the weight of the machine, as in the case of aircraft fan engines. Blade bending stresses are related to the blade form and to the operating conditions (the stress specific speed) in section 1.3.3.2 and are further related to the overall blade design in section 3.3.1.

In section 1.3.3.2, the equation (1-108) is established for blade bending stress generated by fluid-dynamic forces; this equation can be written

$$\sigma_f = \frac{\Delta p_{av} b^2 l}{2 m_s}$$

where $\Delta p_{av} = C_{L,1} \rho w_1^2/2 = C_{L,\infty} \rho w_\infty^2/2$ is the average pressure difference between the two sides of the blade, b is the blade span, l is the blade chord, and m_s is the section modulus of the root section of the blade with respect to an axis normal to the blade force. In most practical cases, m_s is close to the minimum section modulus of the root section. This section modulus can be expressed as follows:

$$m_s = \frac{C_m l t_m^2}{6} = \frac{C_m l^3}{6} \frac{t_m^2}{l^2} \qquad (3\text{-}4)$$

where t_m is an average thickness of the blade, and C_m is a coefficient expressing the effect of blade curvature on the section modulus; C_m increases with curvature and approaches its minimum value of approximately unity for zero curvature. Hence equation (1-108) assumes the form

$$\sigma_f = 3 \frac{\Delta p_{av}}{C_m} \frac{b^2}{l^2} \frac{l^2}{t_m^2} \qquad (3\text{-}5)$$

For a given shape of the blade cross section, C_m and the thickness-chord ratio t_m/l are constants, so that the bending stress is proportional to the pressure difference Δp_{av} and to the square of the aspect ratio b/l. Thus, for a given blade pressure difference Δp_{av}, the allowable bending stress σ_f sets an upper limit for the aspect ratio b/l and thereby a lower limit of the chord length l for a given blade span $b = (D_o - D_{root})/2$. This limit, of course, depends on the form of the blade section in terms of its form coefficient C_m (eq: (3-4)).

As mentioned previously, the effective section modulus m_s of the root section may be assumed to be the minimum section modulus of that section, approximated in most cases by determining the section moment of inertia with respect to a neutral axis parallel to the baseline (or chord line) AD of the root section (see fig. 3-1). If the resultant blade bending force is not approximately normal to this direction, one may use the component of the blade bending force which is normal to the baseline of the root section. The maximum tensile bending stress usually occurs at the leading and trailing edges of the root section.

The total steady-state tensile stress is obtained by adding the maximum tensile bending stress σ_f to the centrifugal stress σ_c. However, the most critical stresses are usually not the steady-state stresses but the alternating (vibratory) stresses. Because of the difficulty of determining the latter in a reliable manner, reference 55 suggests assuming that the vibratory stress is equal to the steady-state bending stress σ_f, as defined by equation (1-108). Thus the vibratory stress is assumed to be equal to the fluid-dynamic bending stress without any compensating centrifugal bending stress obtained by tilting the blade so that the centrifugal bending moment opposes the fluid-dynamic bending moment.

The vibratory and steady-state stresses are combined in a modified Goodman diagram as shown in figures 16 and 31 of reference 55. Inversely, the allowable steady-state stress is derived from the same diagram and thus furnishes the basis for the determination of the required area and section modulus of the root section according to equations (1-94), (1-108), (3-4), and (3-5).

3.2.3 Cascade Design by Consideration of Curvature of Relative Flow and Design of So-Called Impulse Vane Systems

The relation between the fluid-dynamic vane forces and the change in the relative velocity of flow

is derived in section 2.5.2. The change in the relative velocity is connected with a change in the direction of the relative flow except when changes in the width normal to the plane of the flow, or effects of compressibility near the critical velocity of a gas, cause variations in the peripheral and meridional (axial) velocity of flow which are proportional to each other so that no changes in the direction of the relative flow are involved. Nevertheless the curvature of the relative flow, whenever it exists, can be used for the analysis of the flow in axial-flow vane systems, particularly for systems with strong curvature. This process is illustrated in connection with a so-called impulse vane system, that is, a vane system which changes only the direction, not the magnitude, of the relative velocity. For vane systems between parallel end walls, this requires that the circumferential component of the relative flow changes from a certain inlet value to an equal but opposite value on the discharge side of the system.

Figure 3-2 shows what may be called the classical design of an axial-flow impulse vane system. The curved part of the vane channel is formed by two concentric circular arcs (circular cylindrical surfaces). The perpendicular distance between the surfaces of two successive vanes is constant, so that the mean velocity of flow is constant on the basis of a strictly one-dimensional consideration.

The two-dimensional velocity distribution of a frictionless fluid is easy to determine for the flow along and between two concentric, circular boundaries. It satisfies the law of constant angular momentum:

$$r_o w_o = rw = r_i w_i = \text{constant} \tag{3-6}$$

where r is the distance from the common center of curvature of the outer and inner flow boundaries, and the streamlines are approximated by circular arcs concentric with the outer and inner flow boundaries. This approximation obviously breaks down where the curved flow joins the straight approach and discharge flow, but should be fairly good at the midturn section $C_o C_i$. The velocity distribution at section $C_o C_i$ is derived from equation (3-6) and is shown in figure 3-2. Its relation to the average velocity $w_{av} = w_1 = w_2$ is given by

$$w_{av}(r_o - r_i) = \int_{r_i}^{r_o} w\, dr \tag{3-7}$$

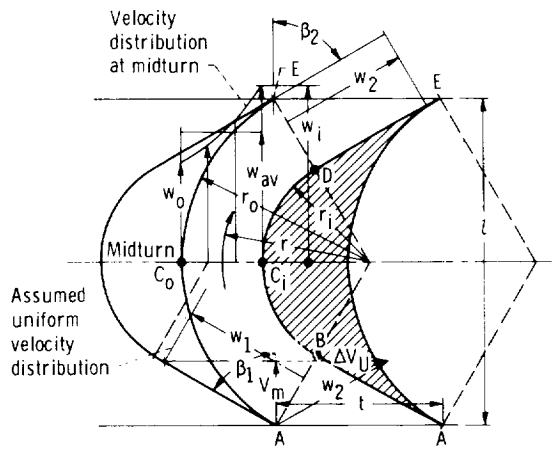

Figure 3-2. – Classical design of impulse axial-flow vane system.

and

$$w = w_i \frac{r_i}{r} \tag{3-8}$$

which lead to

$$w_{av}(r_o - r_i) = w_i r_i \int_{r_i}^{r_o} \frac{dr}{r} = w_i r_i \ln \frac{r_o}{r_i}$$

and hence

$$\frac{w_{av}}{w_i} = \frac{r_i}{r_o - r_i} \ln \frac{r_o}{r_i} \tag{3-9}$$

In the case shown in figure 3-2, the radius-of-curvature ratio $r_o/r_i = 1.764$ can be obtained from the geometry of the configuration, where $\beta_1 = \beta_2 = 60°$ and $l/t = 2$, which yield, together with $\Delta V_U/w_1 = 2 \sin 60° = 1.733$, a lift coefficient $C_L = 2 \times 1.733 \times 1/2 = 1.733$. (According to figure 2-26, this value is reasonable for $w_2/w_1 = 1$.) In this case, the velocity ratio w_{av}/w_i is $(1/0.764)\ln 1.764 = 0.741$. This ratio is also the ratio of retardation from C_i to D along the convex (low-pressure) side of the blade when, by one-dimensional reasoning, a uniform velocity distribution is assumed between D and E (as shown in fig. 3-2). When this assumption is dropped, retardation takes place between points C_i and E along the low-pressure side of the blade.

There is also a retardation of the flow along the high-pressure side of the blade between the leading

edge A and the outer midturn point C_o from w_1 to w_o. For the case shown in figure 3-2, this retardation is

$$\frac{w_o}{w_1} \approx \frac{w_o}{w_{av}} = \frac{w_o}{w_i}\frac{w_i}{w_{av}} = \frac{r_i}{r_o}\frac{w_i}{w_{av}}$$

$$= \frac{1}{1.77 \times 0.741} = 0.763 \qquad (3\text{-}10)$$

that is, the retardation along the concave (high-pressure) side is only slightly less severe than that along the convex (low-pressure) side, where $w_{av}/w_i = 0.741$. Intuitively one expects the danger of separation to be much less on the concave than on the convex side of the vane. This intuitive expectation can be confirmed by a simple stability consideration similar to that used by Johnston for rotating channels, which is outlined in section 2.6.3.7.

Figure 3-3 shows the principles of turbulent flow in the presence of a concave and a convex, curved flow boundary. The essential fact to be observed is that, adjacent to the concave boundary, the angular momentum of the flow decreases with increasing distance from the center of curvature. According to a stability criterion by Prandtl, the boundary layer adjacent to the concave wall is unstable, and the boundary layer adjacent to the convex wall is stable.

This statement can be proven qualitatively as follows: Assume a fluid particle is displaced by

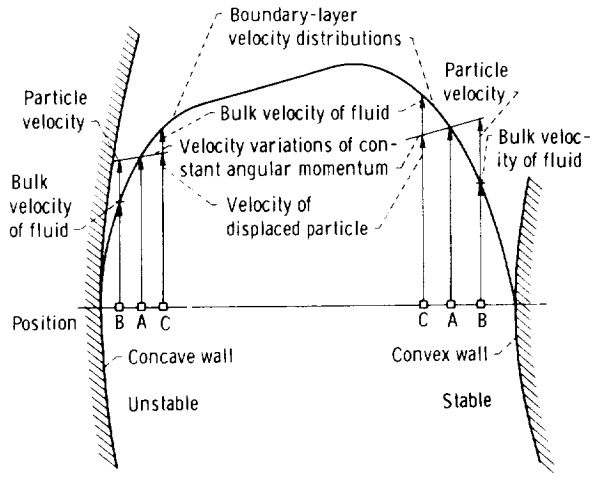

Figure 3-3. – Stability of boundary-layer flow along curved walls.

turbulent velocity fluctuations from its normal position A along its mean flow path to a position B closer to the solid boundary. One assumes (with Prandtl) that this fluid particle follows the law of constant angular momentum, although a slightly different assumption (such as displacement with unchanged velocity) would lead to the same conclusion. The particle has in its displaced position a higher velocity than the bulk velocity in the surrounding fluid. This higher velocity causes an acceleration of the displaced particle away from the center of curvature of the flow. Near the concave wall, this is an acceleration away from the original position A of the particle, and the flow is unstable. Near the convex wall, the same acceleration tends to return the particle to its original position, and the flow becomes stable. It is easy to show by analogous reasoning that a displacement to a position C farther away from the wall causes acceleration toward the center of curvature, that is, away from the original position A of the particle near the concave wall and toward the original position near the convex wall. Thus the result is the same as when displacement toward the wall is considered; that is, the flow near the concave wall is unstable, and that near the convex wall is stable. Unstable flow means increased turbulence, tending to prevent separation at the concave wall; stable flow means reduced turbulence, tending to promote separation at the convex wall.

The foregoing qualitative result has been confirmed experimentally by Wattendorf (ref. 56) and Eskinazi and Yeh (ref. 57), so that this reasoning can be considered well established. In particular, it is an experimental fact that the boundary layer along a stationary, convex wall is, under the same conditions, considerably thicker than the boundary layer along a concave wall. Unfortunately this writer is not aware of any quantitative conclusions regarding the difference among separation limits of concave, convex, and straight walls. Thus the design engineer can only use the fact that he can allow much less of an adverse pressure gradient along the convex side of a vane than along the concave side.

This qualitative result is now applied to the improvement of the impulse blade design shown in figure 3-2. Included in the revision of this design is a slight correction of the leading- and trailing-edge shape from a mechanical as well as a fluid dynamic point of view. The latter demands a slight difference between the direction of the leading and trailing edges and the direction of the mean flow

approaching and leaving the system, as shown in figure 2-8.

If all retardation along the convex (low-pressure) side of the blade were to be eliminated, the mean velocity, and thereby the local distance between the vanes, would have to be changed by the ratio $w_{av}/w_i = 0.741$, quoted in the text following equation (3-9). According to figure 3-2, an increase of the midturn distance by 1/0.741 (accomplished by an increase in r_i and perhaps a slight decrease in r_o) would not lead to any obvious inconsistencies. Thus it might be possible to design the convex (low-pressure) side of the vane so as to eliminate any retardation of this side of the vane.

However, the retardation along the concave (high-pressure) side of the vane would be more severe than before. If the same radius-of-curvature ratio were assumed as in figure 3-2, the high-pressure-side retardation from the leading edge A to the outer midturn point C_0 would be w_o/w_1 (from eq. (3-10)) times the suggested mean velocity reduction, that is,

$$\frac{w_o}{w_i} = 0.763 \times 0.741 = 0.565 \tag{3-11}$$

The question of whether this severe retardation would be acceptable is difficult to answer not only because the limit of retardation along a concave flow boundary is not known, but also because separation between A and C_0 (fig. 3-2) may not be of major detrimental consequence because of the expected reattachment of the accelerating flow from C_0 to the trailing edge E.

Under this situation, the design engineer is likely to accept a very slight retardation along the convex (low-pressure) side of the vane in order to reduce the likelihood of separation along the concave (high-pressure) side of the vane. Figure 3-4 shows the resulting vane layout under the assumption that the mean velocity at midturn is reduced to 0.77 w_i (on the basis of some preliminary geometric considerations), instead of 0.741 w_i as previously estimated for no retardation along the convex side of the blade. Furthermore the intended design preserves the circular-arc contour of the classical layout (fig. 3-2) on the concave (high-pressure) side in the hope that thereby the radii of curvature along the convex (low-pressure) side are increased over those of the classical layout.

Important is the transition from the approach and discharge portion of the blade to the midturn section. The straight-line and single-circular-arc low-pressure contour of the classical design is being replaced by five circular arcs over the entire extent from the leading edge A to the trailing edge E. A continuous change in curvature would at least be equally acceptable. Distinct radii of curvature are chosen in this case to illustrate the change in curvature along the convex side and to ease the construction of the ideal velocity distributions in the intermediate sections B_iB_o, C_iC_o (midturn), and D_iD_o by the tangents to the velocity curve as described by equation (2-4) and figure 2-3 of section 2.2. Of course, this method is here applied to plane, two-dimensional flow instead of the meridional flow in a space of revolution considered in section 2.2.

The construction of the velocity distribution curves is illustrated in figure 3-4 for the midturn section C_iC_o. The velocity distribution curve OI is constructed by the slopes of this curve at O and I, where according to equation (2-4),

$$\frac{dV}{dn} = -\frac{V}{r} \tag{3-12}$$

n being the normal coordinate across the stream from vane to vane. Equation (3-12) is satisfied by the equality of the angles $\alpha_i = \alpha_i'$ and $\alpha_o = \alpha_o'$ at the velocity points I and O in figure 3-4. The relation between w_i at I and w_o at O must be estimated from the tangents to the $w(n)$ curves at I and O. The curvature of the flow at a point between C_i and C_o would supply additional information, as explained further in section 3.2.5. In addition, the area under the velocity curve OI must satisfy the condition of continuity; that is, the area under this curve must be the same as that under the inlet and discharge velocity curves w_1d_1 if the width normal to the plane shown in figure 3-4 is constant and if the flow is incompressible.

It should be realized that the method described is primarily a method for finding the flow in a given vane passage. As a method of design, it requires a process of trial and error.

A gradual transition of flow from the uniform approach velocity w_1 to the midturn section and back to the discharge velocity $w_2 = w_1$ is obtained by making the sections B_iB_o and D_iD_o larger than the approach and discharge flow cross sections, but not as large as the midturn section C_iC_o. The radius of curvature at B_i and D_i is larger than at the midturn point C_i, so that the ideal velocity distribution in sections B_iB_o and D_iD_o is somewhat flatter than in the midturn section C_iC_o. By some geometric process of trial and error, a

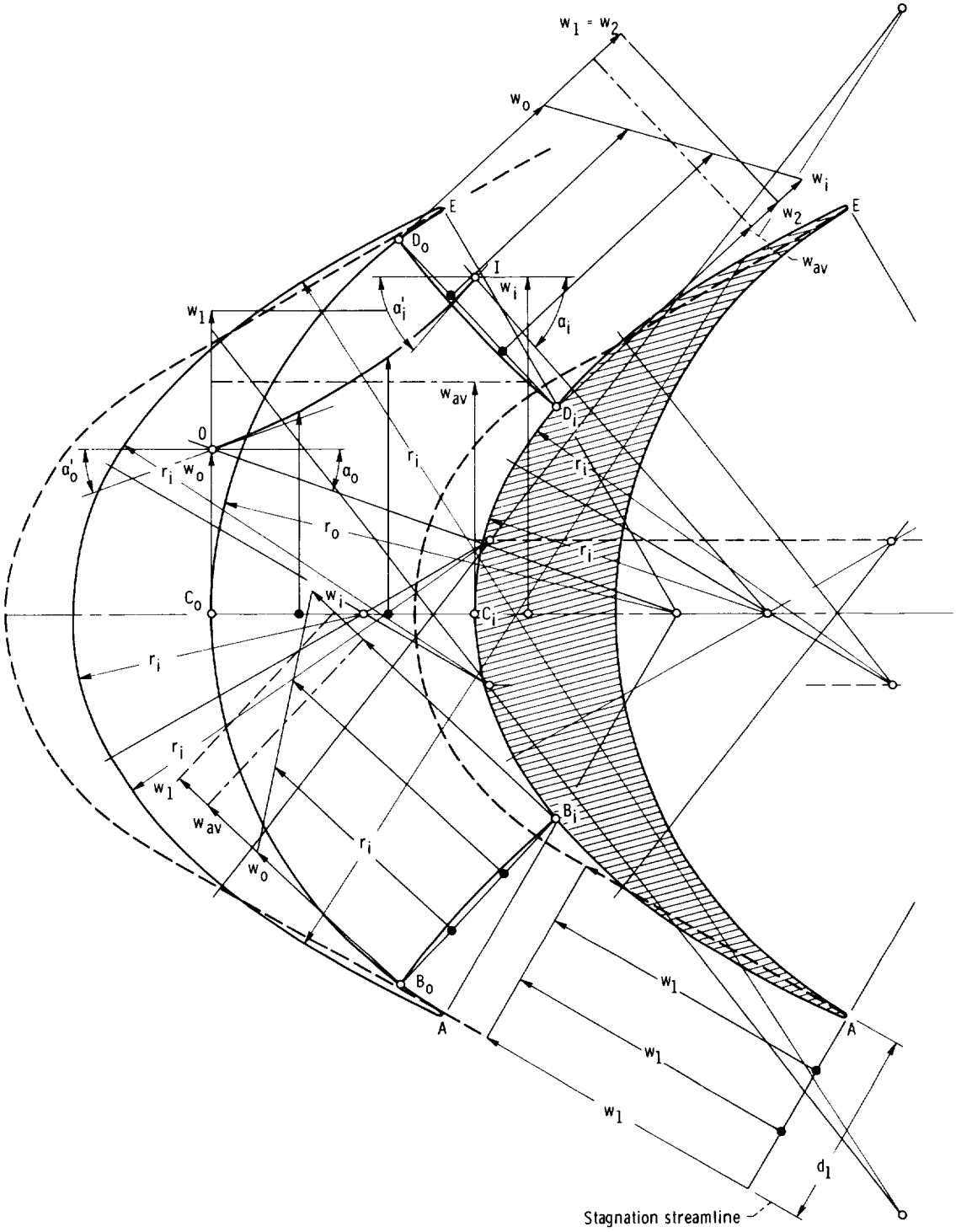

Figure 3-4. – Improved design of impulse axial-flow vane system. (Classical design shown in dashed lines.)

rather favorable velocity distribution along the convex blade side can be obtained. According to the graphical method employed, the velocity at B_i and D_i is $w_i = 1.1\ w_1$ and at C_i is $w_i = 1.11\ w_1$; that is, the ideal velocity along the convex contour from B_i to D_i is nearly uniform. The retardation from C_i to

the trailing edge E is $w_2/w_i = 0.90$ and from D_i to E is 0.91; that is, most of the retardation takes place along the only slightly curved contour from D_i to E. Furthermore the retardation is much less than that with the classic design, where w_2/w_i is 0.741. The improved design (fig. 3-4) may, therefore, be considered safe with respect to separation from the low-pressure side, provided the inlet velocity w_i has the direction assumed for this design.

The retardation along the concave (high-pressure) side of the vane from the leading edge A to B_o is $w_o/w_1 = 0.65$ and from A to C_o is $w_o/w_1 = 0.544$; that is, the retardation along the concave side is even slightly more severe than estimated earlier for no retardation along the convex wall. As mentioned previously, the information available does not permit assessment of the severity of this situation. It is reasonable to accept this situation because the stagnation point near the leading edge is likely to be located on the high-pressure side of the vane (see fig. 2-8), so that there may be little or no retardation of the flow between A and B_o. (A more dependable answer can be obtained by a detailed theoretical analysis of the velocity and pressure distributions over this vane, particularly near its leading edge.)

Design considerations based on the curvature of the vane contour and the channel width between successive vanes are, of course, not limited to impulse vane systems. For example, the design method of sections B_iB_o and D_iD_o of the impulse vane system shown in figure 3-4 is readily applicable to any inlet or discharge flow cross section of any vane system of high solidity, such as section AB in figure 3-1. If one desires to avoid at B velocities in excess of the approach velocity w_1 (the discharge velocity in an accelerating (turbine) vane system), one makes the distance d_1 between the vanes larger than $t \cos \beta_1$ and determines the velocity distribution between A and B (particularly near B) from the radius of curvature of the vane contour at B. This radius of curvature contributes significantly to the definition of the entire vane shape, which has to be developed, as mentioned previously, by a method of trial and error. The principles of design illustrated in connection with the impulse blading shown in figure 3-4 are indeed applicable to any vane system with sufficient solidity to form a well-defined vane channel, provided the vane contours are sufficiently curved to have a well-established relation to their radii of curvature. Further applications of the design principles illustrated in this section are presented in section 3.2.5. It can be seen that considerations of the curvature of the vane contours are particularly helpful for the analysis and improvement of vane systems developed initially by some other considerations.

3.2.4 Design of Cylindrical Flow Section of Axial-Flow Vane Systems by Mean Streamline Method Applied to Incompressible Fluids

As already mentioned, the mean streamline method described in section 2.5.5 is reversible; that is, the method not only can be applied to the analysis of existing cascade test results (as done in sec. 2.5.5) but also, on the basis of such test results, can be used for the development of new cascade configurations with flow characteristics which may be superior to those of the tested configurations. When the mean streamline method is introduced in section 2.5.5, it is pointed out that most standard cascade configurations (e.g., the NACA 65 series) have minimum pressure coefficients $C_{p,m} = (p_1 - p_{min})/(\rho w_1^2/2)$ which are well in excess of those permitted for satisfactory cavitation performance of pumps. For the same reason, the Mach number characteristics of the standard cascade configurations are not acceptable for modern axial-flow compressors and fans used for aircraft propulsion and similarly demanding applications.

The application of the mean streamline method to the design of axial-flow vane sections is illustrated by the example given in chapter 29 of reference 14. This section concentrates on the design of the cylindrical tip and root sections of the rotor. The three-dimensional overall design of this example is presented in section 3.3.

The example chosen here demonstrates the mean streamline method of design under rather demanding conditions, a combination of severe cavitation requirements with a rather high head coefficient for an axial-flow rotor with a 0.50 hub-tip ratio on its discharge side.

Specifically the suction specific speed is 0.70 (12 000) referred to zero hub diameter, $V_{m,i}/U_o = 0.25$, $U_o = U_i$, $2gH/U_o^2 = 0.357$, and the basic specific speed is $n_s = 0.498$ (8560). The profile of, or radial section through, the rotor is shown in figure 3-5; since the surfaces of revolution swept out by the leading and trailing vane edges are not yet

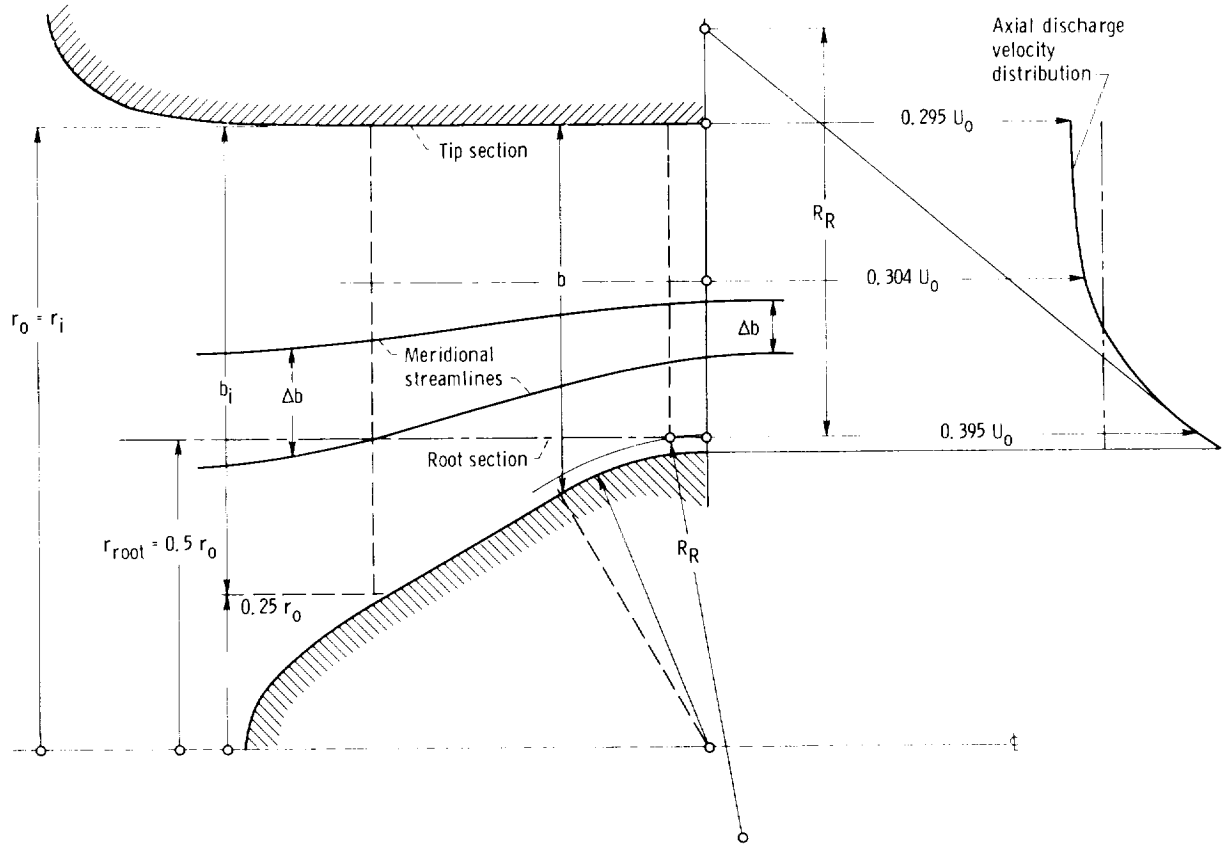

Figure 3-5. – Preliminary layout of impeller profile.

known, the dashed lines are a crude estimate of their location.

The layout of the blade tip section by the mean streamline method begins with an estimate of the vane pressure distribution. For a vane system with severe cavitation requirements, the minimum vane pressure coefficient or blade cavitation number σ_p defined by the equation

$$H_{sv} = C_1 \frac{V_i^2}{2g_o} + \sigma_p \frac{w_i^2}{2g_o} \qquad (1\text{-}42)$$

is of decisive importance. From equation (1-49) or figure 1-18, one can find for the specified suction specific speed and flow coefficient that $\sigma_p = 0.16$ and that the flow coefficient $V_{m,1}/U_o = 0.25$ is indeed the optimum for this S. The cavitation number $\sigma_p = 0.16$ is probably too low to permit completely cavitation-free operation because this value requires a very thin leading edge, which renders the blade very sensitive to minor changes in angle of attack. However, if one designs the blade for a somewhat lower minimum pressure coefficient, cavitation can be expected to be sufficiently localized to permit hydrodynamically satisfactory operation, that is, the actual pressure distribution, which must be expected to be more irregular than that assumed for the design, is likely to cause σ_p to exceed a value of 0.16 only over small portions of the blade length.

The minimum pressure coefficient assumed for this design was $C_{p,min} = 0.125$, which was the lowest value considered achievable in connection with a lift coefficient of reasonable magnitude in order to avoid the need for excessive solidity of the vane system. Figure 3-6 shows on the right end of the drawing a vane pressure distribution considered achievable with $C_{p,min} = 0.125$ (except for local departures). In accordance with the mean streamline method presented in section 2.5.5, this pressure distribution is plotted against the axial extent of the vane, and the minimum pressure coefficient of 0.125 is assumed to be constant over one-half of this extent. The discharge static pressure is given by the discharge relative velocity and, in the dimensionless scale used here, has the value

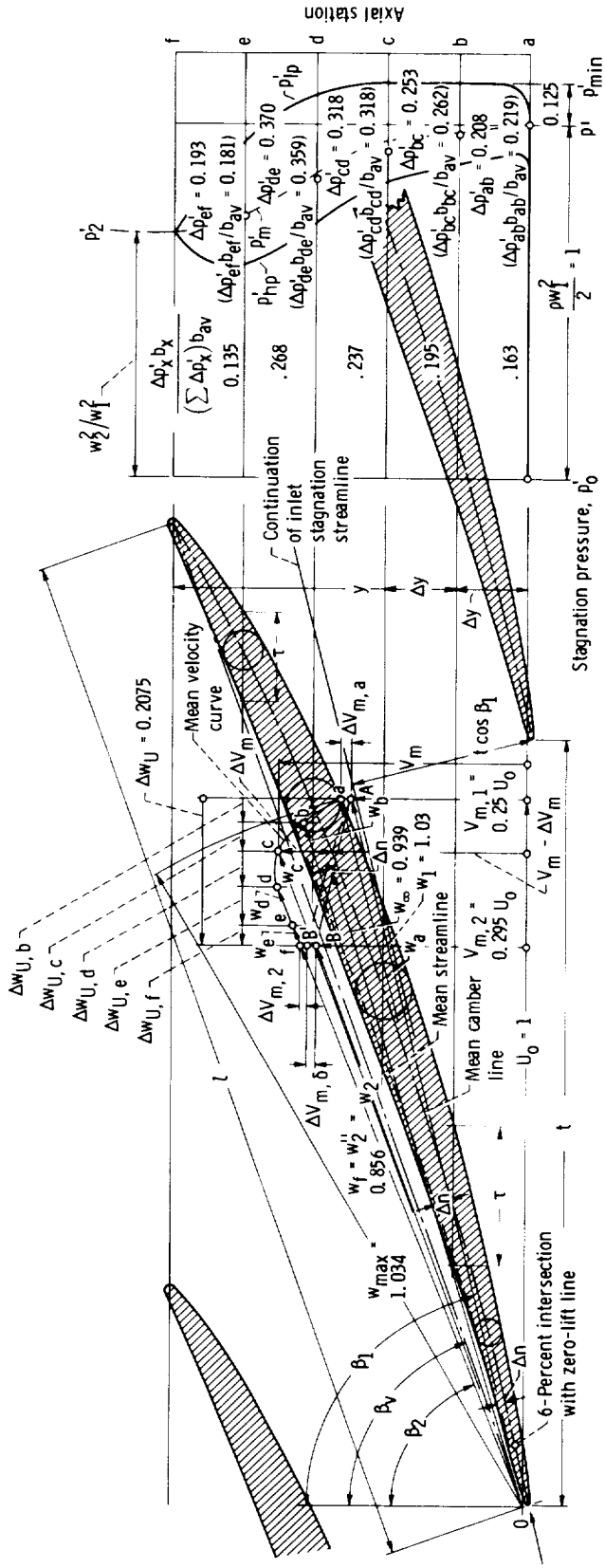

Figure 3-6. – Design of cylindrical tip vane section by mean streamline method for small deflection Δw_U and low $C_{p,min} = p_1 - p_{min}/(\rho w_1^2/2)$. Primed pressures are dimensionless by division by $\rho w_1^2/2$ $(p' = p/(\rho w_1^2/2))$; $C_{L,1} = \Delta p'_{av} = 0.269$; $C_{L,\infty} = C_{L,1} w_1^2/w_\infty^2 = 0.324$.

$(p_2-p_1)/(\rho w_1^2/2)=1-w_2^2/w_1^2$. The velocities at the tip section are shown in figure 3-6. The inlet velocity diagram is given (for zero prerotation) by $V_{m,1}/U_o=0.25$. The discharge diagram is determined by the change in circumferential velocity $\Delta w_U/U_o=g_oH/(U_o^2\eta_h)=0.2075$ (with $\eta_h=0.86$), by the meridional discharge velocity ratio $V_{m,2}/U_o=0.295$ at the tip (see fig. 3-5), and by two additions to the meridional discharge velocity, $\Delta V_{m,\delta}$ (due to the displacement thicknesses of the boundary layers) and $\Delta V_{m,2}$ (due to the trailing-edge thickness of the vane). From these velocity diagrams, shown in figure 3-6, one finds $w_1=1.03\ U_o$ and $w_2''=0.856\ U_o$, which include the effect of the boundary-layer displacement thickness $\Delta V_{m,\delta}$ and of the leading-and trailing-edge thicknesses $\Delta V_{m,a}$ and $\Delta V_{m,2}$.

The meridional discharge curve shown in figure 3-5 is determined by its tangent near the hub, which is given by the radius of curvature R_R in equation (2-4) plus the condition of continuity.

The design pressure distribution diagram may now be completed by first estimating the mean static-pressure p'_m curve between the inlet and discharge static pressures, shown by a dash-dot line in figure 3-6. The pressure along the low-pressure side p'_{lp} is approximated by a smooth curve between the end of the minimum pressure line $(p_1-p_{min})/(\rho w_1^2/2)=0.125$ and the discharge static pressure. The pressure along the high-pressure side of the vane p'_{hp} is approximated by the rule

$$p'_{hp}-p'_m=a_p(p'_m-p'_{lp}) \tag{3-13}$$

where the subscript *hp* denotes high pressure, and the subscript *lp* denotes low pressure. The factor a_p varies between about 0.6 in the central portion of the blade and about 0.75 in the end portions. This is a conservative estimate because

$$p'_{hp}+\frac{\rho(w-\Delta w)^2}{2}=p'_{lp}+\frac{\rho(w+\Delta w)^2}{2}$$

$$=p'_m+\frac{\rho w^2}{2} \tag{3-14}$$

which leads to

$$\frac{p'_{hp}-p'_m}{p'_m-p'_{lp}}=a_p=\frac{2-\Delta w/w}{2+\Delta w/w} \tag{3-15}$$

where Δw is the departure of relative velocity at the vane surface from the mean relative velocity w. For an infinitely thin vane in a uniform stream (w=constant) with uniform pressure differences $p'_{hp}-p'_m$=constant and $p'_m-p'_{lp}$=constant and with Δw=constant, one finds on the basis of the left side of equation (3-14) and from $p'_{hp}-p'_{lp}=C_L\rho w^2/2$

$$\frac{\Delta w}{w}=\frac{C_L}{4} \tag{3-16}$$

For the case shown in figure 3-6, one finds from equation (3-2) that $C_{L,\infty}=0.323$ and from equation (3-15) that $a_p=0.922$. Because of the finite blade thickness and the resulting blockage, a_p must be expected to be substantially lower, as can also be concluded from the cascade data presented in section 2.5.5. Such a reduced value of a_p is assumed in constructing the vane pressure diagram shown in figure 3-6. For a prescribed minimum pressure (i.e., a prescribed $p'_m-p'_{lp}$) this value of a_p leads to a reduced $p'_{hp}-p'_m$ (see eq. (3-13)) and thereby to a reduced $p'_{hp}-p'_{lp}$ and a reduced lift coefficient.

The next step is to divide the axial extent of the blade section into a number of equal parts, five in figure 3-6. The dimensionless, average vane pressure difference of each part

$$\Delta p'=\frac{p'_{hp}-p'_{lp}}{\rho w_1^2/2} \tag{3-17}$$

is estimated and recorded in the pressure diagram.

Evidently the arithmetic mean of these dimensionless pressure differences, that is, the area inside the dimensionless pressure curve (with $\rho w_1^2/2$ and the axial extent of the vane section being unity), is the lift coefficient referred to the inlet relative velocity (eq. (2-60)):

$$C_{L,1}=\frac{\Sigma\Delta p'}{N}=\frac{\Delta p_{av}}{\rho w_1^2/2}=0.269 \tag{3-18}$$

where N is the number of axial steps used (here five).

The lift coefficient referred to the vectorial mean between w_1 and w_2 (i.e., to w_∞) is from equation (2-59)

$$C_{L,\infty}=\frac{\Delta p_{av}}{\rho w_\infty^2/2}=C_{L,1}\frac{w_1^2}{w_\infty^2}=0.324 \tag{3-19}$$

where $w_\infty=0.939\ U_o$ is (arbitrarily) defined and determined without taking the meridional velocity

increases $\Delta V_{m,\delta}$ and $\Delta V_{m,2}$ into account. (It should be noted that there is no theoretical definition of w_∞ unless $V_{m,1} = V_m = V_{m,2}$ throughout the system.

The lift coefficient is evidently in this case very much lower than it could be according to any reasonable stall limit (see fig. 2-26). Thus the lift coefficient and solidity of the system are here completely determined by limitations of the pressure reduction $C_{p,min}$ along the blade. (Since this pressure reduction accompanies a local velocity increase, the same limitation exists in gases with respect to effects of compressibility. See sec. 3.2.7.)

The next step is obviously to relate the changes in the peripheral velocity component $-\Delta V_U = \Delta w_U$ to the circumferential blade force. The total change in the circumferential velocity component $\Delta w_{U,tot}$ is obviously proportional to the total blade force. Hence

$$\frac{\Delta w_{U,x}}{\Delta w_{U,tot}} = \frac{\Delta p_x' b_x \Delta y}{\Sigma(\Delta p_x' b_x \Delta y)} = \frac{\Delta p_x' b_x}{\Sigma(\Delta p_x' b_x)} \tag{3-20}$$

which is similar to equation (2-79). The axial step Δy is here equal to $1/N$, which is a constant equal to one-fifth of the axial extent of the vane (unity), and the index x denotes any one of the N steps taken (in this example, five). These steps are designated consecutively b (i.e., a to b) to f (i.e., e to f). The total (radial) width b is here used in place of the radial distance Δb between meridional streamlines, since the approximation that Δb is proportional to b is sufficiently accurate in view of the approximate character of the entire process (see fig. 3-5).

The values of $\Delta p_x' b_x / b_{av}$ are given in parentheses under the values of $\Delta p_x'$, and the values of $\Delta p_x' b_x / (\Sigma \Delta p_x') b_{av}$ are given to the left of the pressure distribution diagram.

The steps $\Delta w_{U,x} = -\Delta V_{U,x}$ are now determined by equation (3-20). The meridional velocities associated with the intermediate velocity diagrams between the inlet and discharge must be estimated. If V_m is the total meridional velocity including vane blockage,

$$(t - \tau) V_m = t(V_m - \Delta V_m)$$

or

$$1 - \frac{\tau}{t} = 1 - \frac{\Delta V_m}{V_m}$$

Hence

$$\frac{\tau}{t} = \frac{\Delta V_m}{V_m} \tag{3-21}$$

The notations are given by figures 2-29 to 2-31 and by figure 3-6.

The circumferential vane thickness τ and vane spacing t can be estimated as follows: The solidity of the vane system l/t is determined by $C_{L,\infty}$, equations (3-19) and (2-54), and the inlet and discharge velocity diagrams, including w_∞.

The vane length l can be calculated from the axial extent y of the vane, which is unity, and an estimate of the vane chord angle β_v, which is slightly larger than the discharge flow angle β_2 (see fig. 3-6):

$$l = \frac{\Sigma \Delta y}{\cos \beta_v} \tag{3-22}$$

The vane length and solidity l/t determine the circumferential vane spacing t.

The circumferential vane thickness τ is determined in the center of the vane from the normal vane thickness τ_n by the approximate relation

$$\tau \simeq \frac{\tau_n}{\cos \beta_v} \tag{3-23}$$

where τ_n is given by an estimate of the thickness-length ratio τ_n / l, which is assumed to be between 5 and 6 percent for the blade layout of figure 3-6.

The mean velocity curve (fig. 3-6) is drawn from

(1) The maximum value of $\Delta V_m / V_m = \tau / t$ (at the center of the vane) in the form $\Delta V_m / (V_m - \Delta V_m) = (\Delta V_m / V_m)/(1 - \Delta V_m / V_m)$, where $V_m - \Delta V_m$ is the height of the flat zero-thickness curve (slightly convex from the top) between A and B′. The distance of the zero-thickness curve from the zero-blockage line AB represents an estimate of the blockage by the blade boundary layers alone. This boundary layer blockage is about two to three times as large as that shown in figures 2-27 (a) to (o), because the spanwise end boundary layers were removed in the NACA tests represented by figure 2-27. This blockage effect may also be assumed to be proportional to the solidity l/t.

(2) Its starting point a, which lies $\Delta V_{m,a}$ above point A, with $\Delta V_{m,a}$ determined by equation (3-21) from a τ/t value very close to the leading edge.

(3) Its end point f, located $\Delta V_{m,2}$ above point B′, with $\Delta V_{m,2}$ determined by τ/t near the trailing edge in the same manner as $\Delta V_{m,a}$.

(4) The condition that the mean velocity curve should stay below a circular arc about O, drawn through the starting point a of the curve, with the relative velocity vector drawn to point a as the radius. Thus the mean relative velocity is nowhere higher than it is just after the flow has entered the system, and unnecessary acceleration and subsequent retardation of the mean flow are avoided.

Of course, the points and conditions stated in items (1) to (4) cannot determine the mean velocity curve uniquely. However, they permit drawing an estimated mean velocity curve satisfying all conditions known at this stage of the design process. It is entirely possible that the mean velocity curve so derived will later have to be corrected to obtain an acceptable vane shape.

The velocity vectors of the flow at stations b, c, d, and e between the inlet and the discharge may now be drawn to points b, c, d, and e along the mean velocity curve determined by the respective values of $\Delta w_{U,x}$ computed according to equation (3-20). Next one draws a sequence of tangents to the mean streamline, with every tangent parallel to the corresponding velocity vector as described in section 2.5.5 with the aid of figure 2-31. Note that the joining points of successive tangents must be about halfway between stations a, b, c, d, e, and f, which mark the points of tangency between the mean streamline and the sequence of tangents. For a flat vane like that shown in figure 3-6, the sequence of tangents and the mean streamline are practically indistinguishable.

The construction of the mean camber line of the blade from the mean streamline is now described under the assumption that the dimensionless form of the deviation between these two curves is the same for the vane to be designed as for the NACA vane systems described and analyzed in section 2.5.5 and represented by figures 2-33 and 2-34. It is also assumed that the magnitude of this deviation divided by the vane length is proportional to the lift coefficient $C_{L,\infty}$. Under these assumptions, the magnitude of the maximum deviation Δn of the mean camber line from the mean streamline can be determined from figure 2-33 and from $C_{L,\infty} = 0.324$. Furthermore the distribution of Δn along the blade is given approximately by figure 2-34. The pressure distribution shown in figure 3-6 clearly characterizes the new blade as trailing-edge loaded. Therefore the deviation curve used for this design must average the data points in figure 2-34. The solid curves in figure 3-7 do this. It should be remembered that the actual dimensions represented by the vertical coordinates in figures 2-34 and 3-7 are fairly small. For example, unity of the vertical scale in these figures corresponds to a value of Δn which, according to the solid curve in figure 2-33, is $0.05\ C_{L,\infty} l = 0.05 \times 0.324\ l$, or 1.62 percent of the length of the blade section. The maximum deviation of the camber line from the mean streamline is, according to the assumption represented by figure 3-7, $1.54 \times 0.0162 = 0.0248$, or about 2.5 percent of the chord length. In other cases, such as the root section, the maximum deviation might be greater, but rarely more than 5 to 8 percent of the chord length. Thus 10 percent of the deviations shown in figures 2-34 and 3-7 are of the order of 1/2 percent of the blade length and are, therefore, close to the practical limits of drafting and manufacturing accuracy. This reasoning agrees with the fact that one is concerned here only with the departures from the one-dimensional approximation represented by the mean streamline (including the effect of blade thickness).

The leading portion of the solid departure curve in figure 3-7 is represented by three different lines. This is justified because the NACA cascade tests showed that variations in the leading portion of the vane do not substantially affect the overall performance of the system. Thus the designer is free to vary the leading portion slightly to meet the inlet flow conditions in the most favorable fashion. The condition to be met particularly is the normal vane distance d_1 across from the leading edge (see fig. 3-1), which should not be smaller than the normal distance between two stagnation streamlines of the oncoming flow before it is influenced by the system.

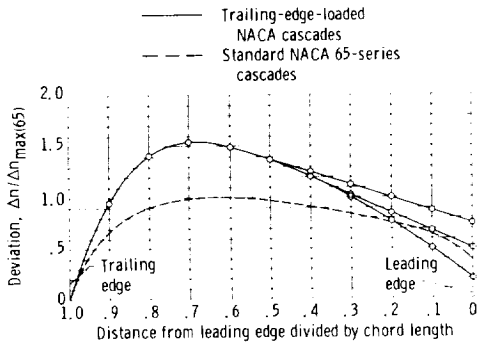

Figure 3-7. – Distribution of normal deviation of camber line from mean streamline. Unity deviation is average maximum deviation of standard NACA 65 series.

For the tip section, the lowest of the three leading branches of the departure curves in figure 3-7 meets the condition of vane distance and is, therefore, selected.

The last step in the design of the vane section according to the mean streamline method is placing an appropriate thickness distribution around the mean camber line derived from the mean streamline. This thickness distribution is, of course, already given by the mean velocity curve, that is, by ΔV_m, whereby this curve determines departure from the mean velocity distribution for zero blade thickness. The velocity ratio $\Delta V_m / V_m$ is related to τ/t by equation (3-21), so τ can be determined at the scale of the drawing expressed by t. The normal blade thickness τ_n is related to τ by equation (3-23), where the local vane angle β_v is given at any point (station) by the direction of the mean camber line. By drawing a circle with the radius $\tau_n/2$ (where τ_n is a local value different for every station) around any station point b to e along the mean camber line, one can construct low-pressure and high-pressure sides of the blade tangent to these circles and to some reasonable, streamlined contours around the leading and trailing edges. Note that the small thickness around both ends of the blade is given by $\Delta V_{m,a}$ and $\Delta V_{m,2}$ of the velocity vector diagram, and these velocities, according to equation (3-21), give a τ value and thereby a normal blade thickness τ_n near the leading and trailing edges.

It is important to note that the blade contours are determined only approximately by the conditions just outlined. Rather than drawing these contours exactly tangent to the circles with radii $\tau_n/2$ about the station points b to e, one must draw these curves at the minimum local curvature, that is, everywhere with a maximum radius of curvature, which varies continuously along the blade and satisfies the overall shape of the blade with fair, not exact, adherence to the thickness circles and end conditions mentioned previously.

The art of drawing good blade sections requires skill and experience. However, this experience cannot be derived from conventional airfoil shapes. The mean velocity curve is determined to a large extent by fluid-mechanics considerations and dictates, by the distribution of $\Delta V_m / V_m$, the major features of the thickness distribution. Usually it places the point of maximum blade thickness (for pump or compressor systems) behind the midpoint of the blade section, which is contrary to standard airfoil design practice. Furthermore a trailing-edge-loaded vane pressure distribution that is advantageous for good cavitation or Mach number characteristics of pump and compressor blades usually places the maximum curvature of the mean camber line behind the midpoint of the blade, which is also not in agreement with standard airfoil practice. Thus the design engineer has to develop a new sense of a good blade shape, particularly in the field of pumps and compressors.

The completed velocity vector diagram enables one to check the original assumption about the mean pressure variation from inlet to discharge represented by the dash-dot curve in the vane pressure diagram (fig. 3-6). The mean static pressure at any station from a to f is related to the corresponding relative velocities by Bernoulli's equation, which may be written in the form

$$p_{m,x} + \frac{\rho w_x^2}{2} = p_1 + \frac{\rho w_1^2}{2}$$

or

$$\frac{p_x - p_1}{\rho w_1^2/2} = 1 - \frac{w_x^2}{w_1^2} \tag{3-24}$$

The resulting p_x points at stations a to e are shown as circles in the vane pressure diagram (fig. 3-6). The agreement with the originally assumed dash-dot curve is quite acceptable, particularly since the actual mean static pressures are a little higher than assumed, so that the high pressure curve would be shifted slightly toward higher pressures. It must be remembered that the entire design process described here gives only a practical approximation to the real flow conditions, so that insistence on high accuracy in detail is not justified. Nevertheless careful execution of all steps described is a requirement.

Other cylindrical sections through the vane system can be developed in the same manner as described for the tip section, provided the flow proceeds through the rest of the system along straight, cylindrical flow surfaces. In this case, the inlet and discharge velocity diagrams are prescribed by the operating conditions in the form of the specific speeds, as indicated in section 3.2.1.

In the present design example, the meridional stream surfaces are intentionally assumed to depart from the strictly cylindrical shape in order to treat the general case, which must be treated in order to achieve satisfactory suction specific speeds as well as other advantages.

The great theoretical and empirical advantages of axial flow are retained by dividing the meridional flow through a rotor of this shape (see figs. 3-5 and 3-32) into a strictly axial and a (circumferentially uniform) radial component. The radial flow component does not need to be considered explicitly in this section. The effect it can have on the peripheral component of the absolute flow is derived in section 3.3.3.

The axial-flow component is first determined for the total inlet and discharge cross sections by the condition of continuity and by an estimated curvature of the meridional streamlines as indicated diagrammatically in figure 3-5. Between the inlet and discharge of every cylindrical section, the axial velocity component is assumed to vary in some simple fashion, for example, along the straight line between the points A and B in figure 3-6; this approximate assumption is used because a more accurate solution would complicate the design process in an undesirable manner. This approximate procedure has been used in the field of marine propulsion pumps for many years with good success and may, therefore, be considered empirically justified.

Because of the very slight curvature of the meridional streamlines in the inlet region of the impeller shown in figure 3-5, the meridional inlet velocity $V_{m,1}$ is here assumed to be radially uniform, so that the inlet flow coefficient $V_{m,1}/U$ changes in inverse proportion to the diameter of the cylindrical section considered. The small difference in magnitude between the axial and the meridional velocity components is neglected.

The axial discharge velocity $V_{m,2}$ is not assumed to be uniform and is approximated according to the curvature of the meridional flow near the hub shown in figure 3-5. With zero prerotation ($V_{U,1}=0$), the total step in peripheral velocity $\Delta w_U=\Sigma\Delta w_{U,x}$ changes radially in inverse proportion to the diameter of the cylindrical section under consideration.

Figure 3-8 shows the cylindrical vane section at half the tip radius. The tip velocity of the rotor is still considered unity for the velocity scale, so that for this section $U=0.500\ U_o$. With $V_{m,1}=0.25\ U_o$, the flow coefficient is $V_{m,1}/U=0.50$, and $\Delta w_U=\Sigma\Delta w_{U,x}=\Delta w_{U,tip}/0.5=0.415$ (see fig. 3-6 for Δw_U of the tip section). The axial discharge velocity is (according to fig. 3-5) $V_{m,2}=0.395\ U_o$ without the additions due to trailing-edge thickness and boundary-layer displacement thickness. When these

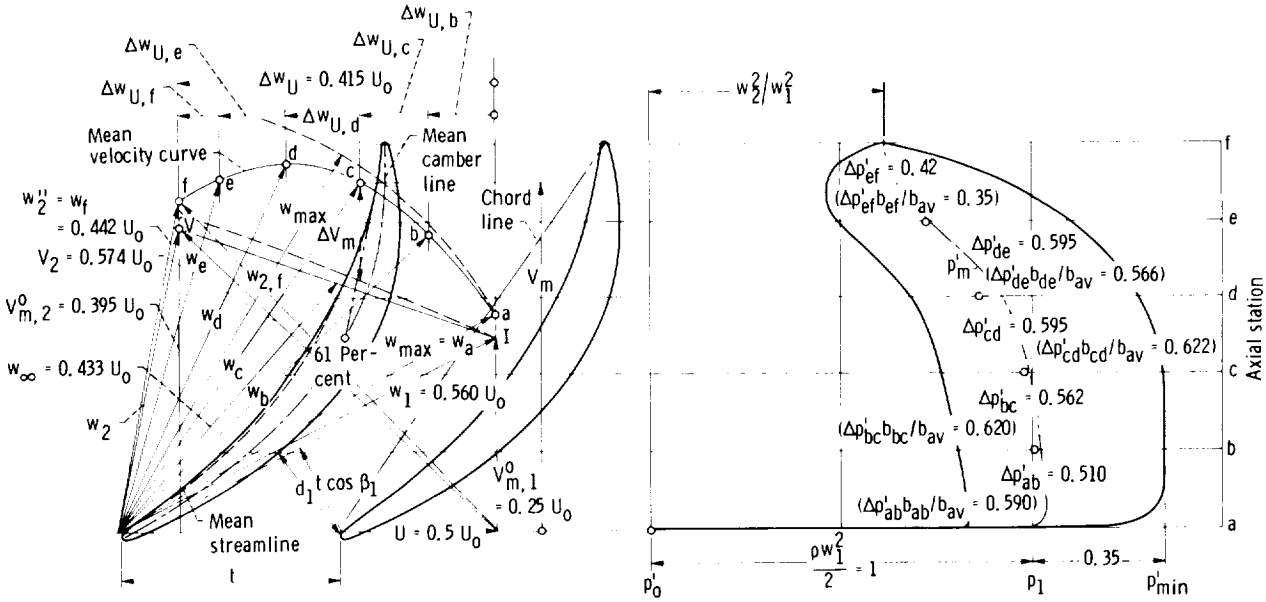

Figure 3-8.—Design of cylindrical root vane section by mean streamline method. $C_{L,1}=\Delta p'_{av}=0.537$; $C_{L,\infty}=C_{L,1}w_1^2/w_\infty^2=0.90$. ($p'=p/(\rho w_1^2/2)$.)

corrections are included, the relative discharge velocity w_2 is 0.442, and the ratio of retardation w_2/w_1 is $0.442/0.560 = 0.79$, which is conservative mainly because of increase in meridional velocity from inlet to discharge.

It is of interest to check the same ratio for an axial vane diffuser following this rotor. If the diffuser is placed between cylindical outer and inner boundaries, it has the same axial inlet and discharge velocities; that is, the vane diffuser should return the absolute discharge velocity of the rotor, $V_2 = 0.574$, to the axial velocity, $V_{m,2} = 0.395$, so that the diffuser retardation ratio is $0.395/0.574 = 0.688$. This is acceptable, but indicates that a further increase in ΔV_U in the half-diameter section (fig. 3-8) would be limited by the retardation in the stator rather than by that in the rotor vane system.

The pressure distribution again contains the coefficient of minimum pressure $C_{p,min}$ as an essential element. When the absolute minimum pressure is assumed to be the same at the half-diameter section and at the tip section,

$$C_{p,min,0.5} = C_{p,min,tip} \frac{w_{1,tip}^2}{w_{1,0.5}^2}$$

$$= 0.125 \frac{1.03^2}{0.56^2} = 0.422 \qquad (3\text{-}25)$$

A coefficient of minimum pressure of 0.35 is chosen in order to give the strongly deflecting half-diameter section an extra margin of safety against extensive cavitation. With this minimum pressure condition and the discharge static pressure determined by w_2, the vane pressure distribution is estimated by the principles explained in connection with figure 3-6. The circumferential velocity steps $\Delta w_{U,x}$ are determined by the same subdivision of the pressure diagram as used previously.

In this case, the required estimate of the vane blockage effect $\Delta V_{m,x}$ is somewhat more difficult to achieve than for the tip section. It requires a preliminary vane section layout like that described in section 3.2.2 (fig. 3-1). Mechanical requirements of strength, cross-sectional area, and section modulus must be considered at this point (see sec. 1.3.3). The mean velocity curve is then derived in the same manner as described in connection with figure 3-6. The velocity vectors drawn to the stations b to e along this curve determine the mean streamline by the method of tangents.

The area within the dimensionless vane pressure curve determines the lift coefficient referred to the inlet relative velocity w_1:

$$C_{L,1} = \frac{\Delta p_{av}}{\rho w_1^2/2} = \frac{\Sigma \Delta p'}{N} = 0.537 \qquad (3\text{-}26)$$

where N is the number of subdivisions (here five). From equation (3-26) and the vectorial mean w_∞ of the inlet and discharge velocities w_1 and w_2 (obtained by scaling from the vector diagrams), one finds

$$C_{L,\infty} = C_{L,1} \frac{w_1^2}{w_\infty^2} = 0.537 \frac{0.560^2}{0.433^2} = 0.90 \qquad (3\text{-}27)$$

This value is quite reasonable, perhaps conservative, for the retardation ratio $w_2/w_1 = 0.79$ determined previously (see fig. 2-26) and indicates that even for the half-diameter section the lift coefficient and the resulting solidity l/t are given primarily by limits in the dimensionless vane pressure distribution, dictated to a large extent by the coefficient of minimum pressure $(p_1 - p_{min})/(\rho w_1^2/2) = C_{p,min} = 0.35$.

The lift coefficient permits the determination of the departure of the mean camber line from the mean streamline by using figures 2-33 and 2-34. Since the vane pressure distribution characterizes this vane section as trailing-edge-loaded (like the tip section), the solid departure curves in figure 3-7 apply also to this vane section. In this case, the middle branch of the leading portion of the departure curves meets the inlet vane distance d_1 requirement most advantageously (for d_1 see fig. 3-8).

The thickness distribution in terms of τ/t and τ_n is again derived from ΔV_m under the mean velocity curve by using equations (3-21) and (3-23). Minimizing local curvature and ensuring continuity of local curvature of the vane contours again took precedence over exact adherence to the thickness distribution derived from ΔV_m. In this case, it becomes particularly apparent that the resulting vane shape does not conform to standard so-called good looking airfoil shapes.

The departure curves in figures 2-33, 2-34, and 3-7 were derived from NACA cascade data

obtained with standard cascade forms like those shown in figures 2-27(a) to (n). The application of these departure curves to cascade shapes that differ from standard forms as much as shown in figure 3-8 raises the question of validity of this degree of extrapolation.

At the Ordnance Research Laboratory of the Pennsylvania State University, some theoretical and experimental work is in progress to examine the validity of cascade shapes designed by the mean streamline method as described in connection with figures 3-6 and 3-8. With respect to cavitation characteristics, the validity of this method seems to be well confirmed by accurate observations of cavitation inception and desinence (the disappearance of cavitation at rising pressures). Overall performance of units designed in this manner generally agrees with expectations. However, results for the vane pressure distribution and the thickness of the vane boundary layers near the trailing edges can not yet be used to either confirm or correct the mean streamline method of cascade design.

For strongly curved vanes like that shown in figure 3-8, the stream-curvature method of analyzing the flow through cascades (sec. 3.2.3) offers a simple way of checking the validity of the cascade shapes obtained by the mean streamline method or any other method of design. This fact is demonstrated in the next section.

3.2.5 Further Applications and Refinements of Stream-Curvature Method

As mentioned previously, for vane systems departing from standard NACA cascades as strongly as that depicted by figure 3-8, it is prudent to check the validity of the mean streamline method by some other method of design or analysis. Theoretical methods available may be quite suitable for achieving this goal, particularly with the aid of computers. However, for the initial design phases, it is desirable to have a simpler method that can be carried out with hand calculator and drawing board. The stream-curvature technique, outlined in section 3.2.3, is such a method. Its application to the cascade form shown in figure 3-8 is illustrated in figures 3-9 and 3-10 and is described in this section.

The first step is to redraw the vane contour (except the leading and trailing edges) by means of circular arcs as shown in figure 3-9. The approximation achieved in this manner can be within drafting accuracy.

Furthermore one selects a number of cross-section lines, sections AB, CD, and EF, drawn without inflection and normal to the vane contours simply by making the curved section line at both ends tangential to radial lines intersecting the vane contours at the points A, B, C, D, E, and F. The centers of the circular arc contours are marked with

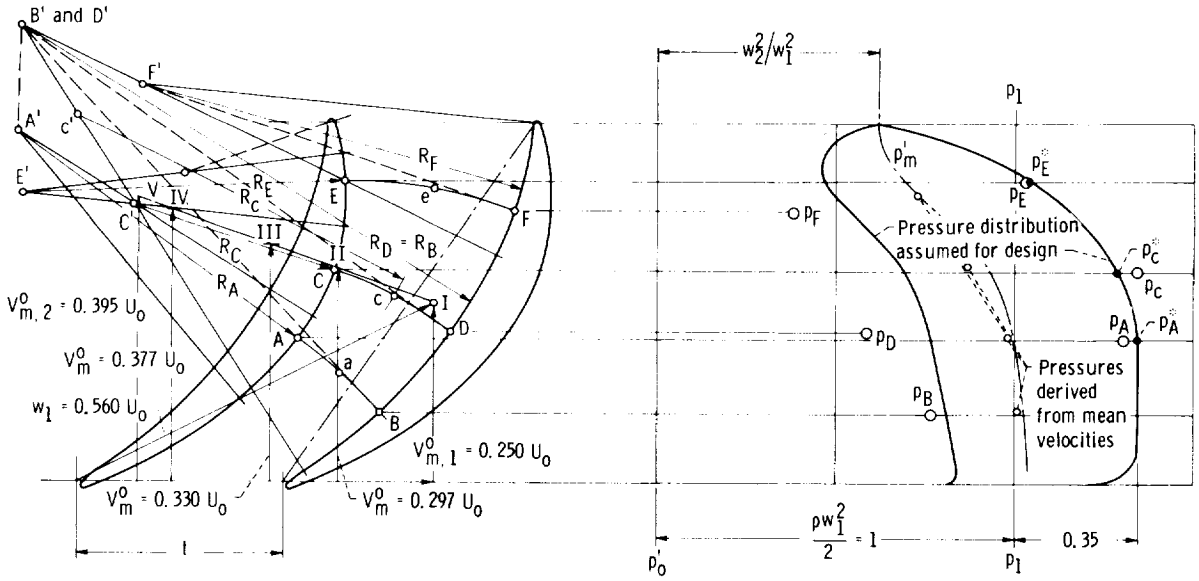

Figure 3-9.—Curvature analysis of pump blade section for strong deflection (vane system shown in fig. 3-8). ($p' = p/(\rho w_1^2/2)$.)

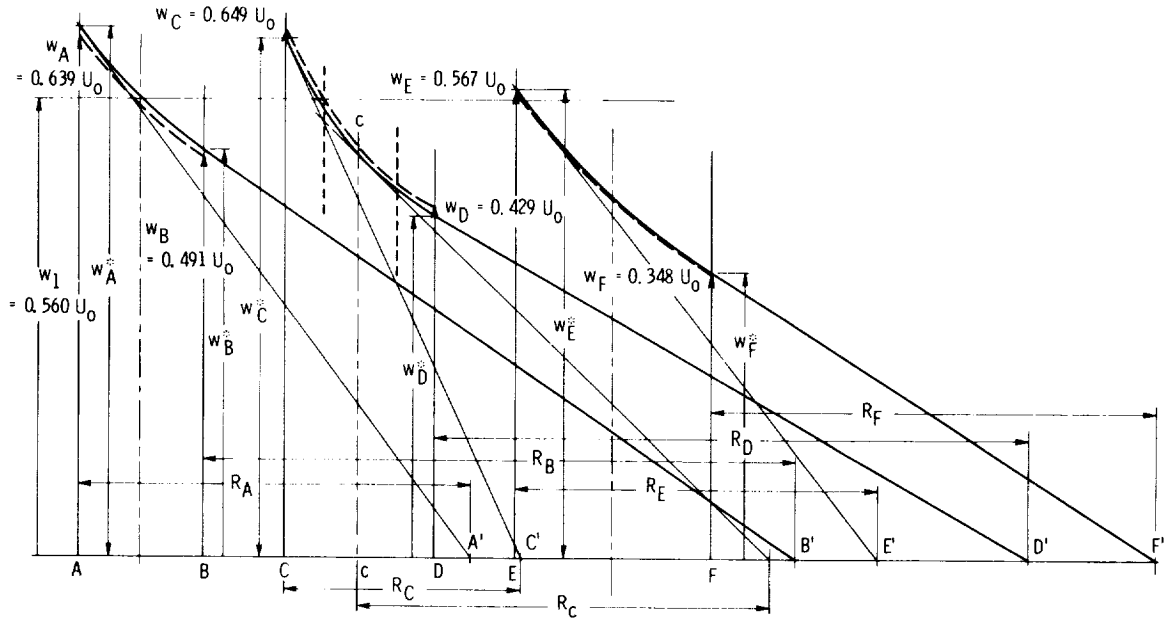

Figure 3-10. – Velocity distributions in three flow cross sections of vane system shown in figure 3-9.

the same letters as the section lines and with primes. The cross-section lines should be located well within the closed, curved passage between the blades, because at the ends of this passage the velocity distribution cannot be assumed to be determined by the curvature of the vanes and the passage.

One is now in a position to determine the velocity distribution in the sections AB, CD, and EF according to the method described in section 2.2 by means of equation (2-4) and figure 2-3. However, the sections AB, CD, and EF are here approximated as plane sections, so that the area under the velocity curve is equal to the rate of volume flow, and the dashed V,r curve used in figure 2-3(b) is eliminated. The plane flow in curved passages is described in section 3.2.3 in connection with equation (3-6) and figures 3-2 and 3-4. The resulting construction of the velocity curves for section AB, CD, and EF is given in figure 3-10, which shows these curves plotted over straight-line developments of the flow sections AB, CD, and EF.

It is stated in section 2.2 that the starting point for each velocity distribution can be chosen arbitrarily, since, for irrotational flow (eq. (2-4)), all velocities of one curve can be multiplied by a constant factor to meet the condition of continuity. This is also true here. However, in the present case one has for any one end point of each velocity curve a first approximation by the assumed vane pressure distribution curve shown in figure 3-8 and reproduced in figure 3-9. This assumed pressure p^* gives in relation to the pressure difference $p_o - p_1$ (stagnation minus inlet static pressure) the assumed blade surface velocity w^* by the relation

$$\frac{w^*}{w_1} = \sqrt{\frac{p_o - p^*}{p_o - p_1}} \tag{3-28}$$

The end points on the convex surface, A, C, and E, in the construction shown in figure 3-10, were (arbitrarily) chosen as starting points for the construction of the velocity curves. Thus

$$\left.\begin{aligned} w_A^* &= w_1 \sqrt{\frac{p_o - p_A^*}{p_o - p_1}} \\ w_C^* &= w_1 \sqrt{\frac{p_o - p_C^*}{p_o - p_1}} \\ w_E^* &= w_1 \sqrt{\frac{p_o - p_E^*}{p_o - p_1}} \end{aligned}\right\} \tag{3-29}$$

The rest of the construction follows equation (2-4) and figure 2-3. For example, for point A, the tangent to the velocity curve is drawn from the end point of w_A^* to point A′ in figure 3-10, the distance from A′ to A being the radius of curvature R_A at A.

The construction of the velocity curves is aided by assuming the radius of streamline curvature in the middle of each section to be the mean between the radii of curvature at the end points of the section. This mean value c for section CD is approximated graphically by the distance from the midpoint c of the section to the midpoint c′ between the centers of curvature C′ and D′ of the contours at the ends of this section. The tangents to the velocity curves at the starting point C, the midpoint c, and the end point D are drawn successively and brought to intersect each other at the two halfway stations between these three points (see the vertical short dashed lines in fig. 3-10). The velocity distribution curve is then drawn to touch these three tangents. Of course, this is not an accurate construction of the velocity distribution curves, but it serves practical requirements quite adequately. The method is capable of improvement by reiteration and other considerations, as outlined later in this section.

As mentioned previously, the areas under the velocity curves in figure 3-10, multiplied by a representative width normal to the flow cross-section lines AB, CD, and EF, should give the volume flow rate through each cross section in the (dimensionless) scale chosen. For incompressible fluids, the volume flow should be the same for successive sections of the same system. For a more or less arbitrary choice of the starting velocities w_A^*, w_C^*, and w_E^*, this equality is, of course, not to be expected with the first approximation.

For unit width, the inlet volume flow is $V_{m,1}t = 0.25\ U_o t$. Because of the actual change in (radial) width through the system (see fig. 3-5), V_m changes from 0.25 U_o at the inlet to 0.395 U_o at the discharge of the system. In the design of this system by the mean streamline method, it was assumed, without any consideration of fluid friction and vane blockage, that this variation in V_m takes place along a straight line in the velocity diagram in figure 3-8. (Some assumption of this type is necessary, since, at this stage of design, the axial extent of the vane in relation to a (tentatively assumed) rotor profile is not known.) In order to obtain a fair comparison between the results of the mean streamline and the curvature methods, one must use the same V_m variation for both methods. The straight line between the end point I of the relative inlet velocity vector w_1 and the end point V of the ideal discharge velocity vector is also shown in figure 3-9. The dimensionless values corresponding to the centers of the sections AB, CD, and EF are given below the points II, III, and IV along the straight line from I to V in figure 3-9, and they involve, of course, an approximate relation between axial location in the vane system and the change in w_U as given by the velocity diagram in figure 3-8.

Table 3-I gives the pertinent evaluations of the velocity curves in figure 3-10. The following explanations apply to the evaluations in the table:

(1) Symbols having the superscript * apply to solid curves in figure 3-10 derived by starting from the low-pressure points p_A^*, p_C^*, and p_E^* on the assumed pressure distribution curve in figure 3-9.

(2) The subscript x refers to points A, C, and E on the convex (low-pressure) side of the vanes, the subscript y to points B, D, and F on the concave

TABLE 3-I. - EVALUATIONS OF VELOCITY CURVES IN FIGURE 3-10

Point or section	$\frac{p_o - p_x^*}{p_o - p_1}$	$w_x^* = w_1\sqrt{\frac{p_o - p_x^*}{p_o - p_1}}$ (a)	w_y^* from w^* curves in fig. 3-10	w_{av}^* by integration of w^* curves	$\frac{S_{xy}}{t_1}$	$\frac{w_{av,xy}^*}{V_{m,xy}^o}$	$\frac{Q_{xy}^*}{Q} = \frac{S_{xy}w_{av,xy}}{t_1 V_{xy}^o}$	$\frac{w_x}{w_1} = \frac{w_x^*/w_1}{Q_{xy}^*/Q}$	$\frac{p_o - p_x}{p_o - p_1} = \left(\frac{w_x}{w_1}\right)^2$	$\frac{w_y}{w_1} = \frac{w_y^*/w_1}{Q_{xy}^*/Q}$	$\frac{p_o - p_y}{p_o - p_1} = \left(\frac{w_y}{w_1}\right)^2$
A	1.35	0.56×1.161 = 0.65	-----	------	-----	-----	-----	1.142	1.305	------	-----
B	-----	----------	0.50	------	-----	-----	-----	-----	-----	0.88	0.775
AB	-----	----------	-----	0.5655	0.535	1.905	1.018	-----	-----	------	-----
C	1.29	0.56×1.135 = 0.636	-----	------	-----	-----	-----	1.159	1.344	------	-----
D	-----	----------	0.42	------	-----	-----	-----	-----	-----	0.766	0.586
CD	-----	----------	-----	0.502	0.644	1.521	0.98	-----	-----	------	-----
E	1.045	0.56×1.022 = 0.571	-----	------	-----	-----	-----	1.015	1.03	------	-----
F	-----	----------	0.351	------	-----	-----	-----	-----	-----	0.6225	0.388
EF	-----	----------	-----	0.4484	0.847	1.190	1.007	-----	-----	------	-----

[a] $w_1 = 0.560\ U_o$.

(high-pressure) side of the vane, and the subscript xy to the flow cross sections AB, CD, and EF.

(3) S_{xy} is the length of the flow cross sections AB, CD, and EF from vane to vane, as shown in figure 3-9; b is the cross-sectional dimension normal to S and to the plane of figure 3-9; V_m is the meridional fluid velocity derived from the meridional inlet velocity $V_{m,1}$; V_m^* is the meridional fluid velocity derived from the area under the w^* curves; t is the circumferential vane spacing without blockage. The superscript o refers to zero blockage; hence V_m^o is the meridional velocity described by the (assumed) straight line from I to V in figures 3-8 and 3-9.

(4) By the condition of continuity for incompressible fluids, the rate of volume flow from the inlet (defining b_{xy}) is

$$Q = V_{m,1} t_1 b_1 = V^o_{m,xy} t_{xy} b_{xy} = \text{constant}$$

Hence

$$\frac{b_{xy}}{b_1} = \frac{V_{m,1}}{V^o_{m,xy}}$$

because $t_{xy} = t_1$ for $r = 0.5\ r_o = \text{constant}$. The rate of volume flow from the solid w^* curves in figure 3-10 is

$$Q^* = w^*_{av,xy}\ S_{xy}\ b_{xy}$$

$$\frac{Q^*}{Q} = \frac{w^*_{av,xy} S_{xy} b_{xy}}{V_{m,1} t_1 b_1}$$

$$= \frac{w^*_{av,xy} S_{xy} V_{m,1}}{V_{m,1} t_1 V^o_{m,xy}} = \frac{w^*_{av,xy} S_{xy}}{V^o_{m,xy} t_1}$$

(5) The velocity $V^o_{m,xy}$ is used only to approximate the normal (radial) passage width b_{xy} in the same manner as for the mean streamline method.

The velocity curves obtained after upward and downward adjustments to satisfy a constant volume flow rate are shown as long dashed lines. The departures of these velocity curves from the curves based on the minimum vane pressure curve originally assumed (solid curves) are quite small. However, in figure 3-9, the departure of the points p_B, p_D, and p_F from the assumed pressure curve along the high-pressure side of the vanes is substantial. To understand this, one must remember that the mean streamline method does take fluid friction effects into account, partly by assuming a greater increase in V_m through the system than would be obtained by using the frictionless, straight-line connection between the points I and V in the velocity vector diagram in figures 3-8 and 3-9 and partly by basing the departure between the mean streamline and the mean camber line used in the mean streamline method of design on test results with real fluids and thus taking fluid friction fully into account. On the other hand, the velocity curves shown in figure 3-10 are derived from a frictionless flow consideration of the curvature of the flow boundaries. This is particularly significant at the high-velocity end points A, C, and E, because there is a steep local gradient of the frictionless velocity curves at these points, so that even a thin boundary layer produces a significant velocity change. Since A, C, and E are the starting points for the construction of the velocity curves, this change causes a downward shift of the entire velocity curve derived from flow curvature and thereby of the end points B, D, and F. It is, therefore, quite reasonable that the vane pressure differences as well as the high pressures derived by frictionless considerations of the vane curvature effects are larger than those connected with the mean streamline method. Since the mean pressure points derived from the mean velocities shown in the velocity vector diagram in figure 3-8 are higher than the mean pressures originally assumed (dash-dot line) and since the ratios of the vane surface pressure drop and rise below and above the mean pressure are somewhat arbitrarily assumed, the agreement between the pressure points p_B, p_D, and p_F (derived from vane curvature) and the pressure distribution curve which led to this vane shape (by the mean streamline method) is somewhat better than expected by this writer. It constitutes a confirmation of both methods employed, since both methods involve a considerable number of approximations.

As previously mentioned, the simple method of determining the velocity distribution from the passage wall curvature used in figures 3-10 and 3-4 could be improved. Two methods of making improvements are briefly outlined here.

First, it is possible to derive by simple theoretical means the velocity distributions for various prescribed changes of the radius of streamline curvature across a curved passage.

The simplest of these cases is, of course, an increase in the radius of streamline curvature r from its minimum value r_i at the convex boundary to its maximum value r_o at the concave boundary proportional to distances n across (and normal to) the flow ($r = r_i + n$). For irrotational flow,

$$\frac{\partial V}{\partial n} = -\frac{V}{r} \tag{3-30}$$

This leads to the familiar velocity distribution of constant angular momentum:

$$Vr = \text{constant} \tag{3-31}$$

It is shown in figure 3-11 as the central curve for the case that the radius of curvature on the convex boundary is $r_i = d$, where d is the distance across the passage normal to the flow. This distribution is, of course, easily determined for any other ratio of passage width to radius of curvature. It applies approximately whenever $r_o \cong r_i + d$, where d is any total distance across the passage ($d = n_{max}$ of the cross section considered).

Equally easy to solve is the case where $r_o \cong r_i$, which can be approximated by assuming $r = \text{constant}$ across the stream. According to equation (3-30), this leads to

$$\ln V = -\frac{n}{r} + \text{constant} \tag{3-32}$$

The lower curve in figure 3-11 represents this relation.

Finally consider the case where $r_o = \infty$, that is, where the outer flow boundary is a straight line. This flow can be approximated by half the flow between two vortices with opposite directions of circulation. The velocity as well as the radius of streamline curvature distribution of this flow field are shown in figure 3-12, and its velocity distribution is also represented by the top curve in figure 3-11.

From the curves in figures 3-11 and 3-12, one can approximate velocity distributions for a wide variety of curved channel configurations characterized by the radius ratio r_o/r_i and the radius-width ratio r_i/d. For $r_o > r_i + d$, one can obtain an approximation by selecting along the r/d curve in figure 3-12 a portion of the horizontal width d such

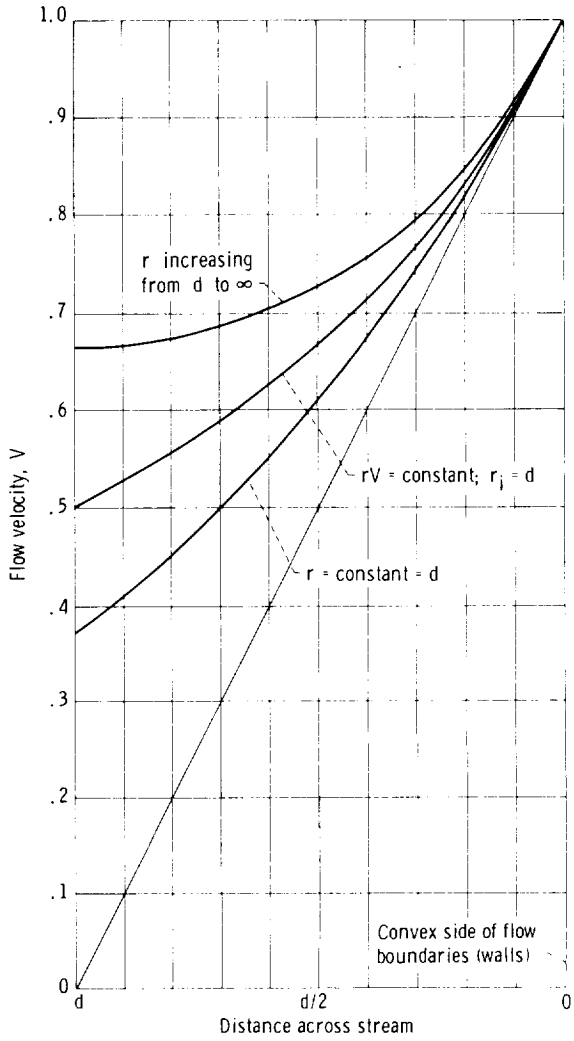

Figure 3-11. – Curved flow velocity distributions.

that this portion satisfies simultaneously the values of r_o/r_i and of d/r_i or d/r_o of the given curved passage. These conditions can be satisfied by a process of trial and error without using the analytical relations involved.

Second, it should be considered that all previously described methods of deriving the velocity distribution from the curvatures of the flow boundaries can be expected to yield reasonably good results only if the curvature of the passage does not change too rapidly in the direction of the flow. Whenever this condition is not satisfied, it is necessary to derive from the first approximations of the velocity distributions for a number of cross sections a (small) number of streamlines by dividing (for incompressible, plane flow) the areas under the velocity distribution curves into a corresponding

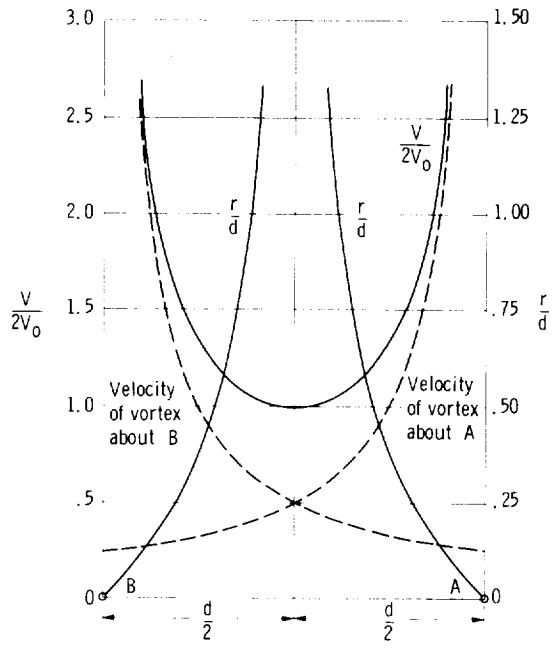

Figure 3-12. – Velocity and flow curvature distribution between two vortices.

number of equal areas. The places where the subareas meet each other mark the intersections of the streamlines and the cross-section lines. It is of practical importance to note that this process can be carried out (for irrotational, incompressible flow) before the velocity distribution curves of the various cross sections have been adjusted to represent the same volume flow rate.

For flow with major effects of compressibility, it is necessary to determine first a mean flow velocity by one-dimensional continuity considerations as outlined in section 2.4. This mean velocity is used as a starting point for the dimensionless velocity distribution curve V/V_o by beginning the first approximation of this distribution near the center of the channel and using the radii of wall curvature and of an estimated streamline curvature at the starting point. This approximate velocity distribution is converted into a curve of mass flow per unit area by plotting specific volume against V/V_o, as shown in figure 2-7. The area under the mass flow curve is divided into equal parts, and the division lines between these parts determine the first approximation of the intersections between the streamlines and the cross section considered.

Several cross sections so divided determine the streamlines. Their radii of curvature are determined preferably by graphical procedures like those indicated previously for the vane contour lines. These radii permit the construction of the velocity distribution curves from their tangents according to equation (3-30) for irrotational flow (or eq. (2-6) for flow with vorticity). This method avoids the more or less arbitrary estimates of the intermediate radii of curvature previously employed when considering the flow in any one cross section independently from that in other cross sections.

Figures 3-13 and 3-14 show the execution of this method of flow determination for a passage with rapidly changing curvature, which may be the passage between two turbine vanes changing the (relative) flow rapidly from the approximately axial direction to one which has a strong circumferential component.

The flow cross sections ab, cd, pq, ef, gh, and ij are assumed more or less arbitrarily and are normal to the flow boundaries. The first approximations of the velocity distributions over these sections are obtained largely as described previously. For section ab (fig. 3-14(a)), the flow between two vortices (fig. 3-12) is, of course, considered. Since this section meets the boundaries close to a rapid change in radius of curvature, an average value is used for this radius.

For sections cd and pq, figures 3-14 (b) and (c) give the results of three successive approximations. In section cd (fig. 3-14(b)), the changes in the division lines between the constant-area subdivisions of the area below the velocity curves are considerable; they are indicated in figure 3-13 also. The resulting changes in the streamline configuration caused a change in the flow cross section from cd to c′d and c″d, since all cross-section lines should be normal to the streamlines. The streamlines shown in figure 3-13 as solid lines are derived from the second approximation of the velocity distribution curves and lead by their curvature to the third approximations of the velocities. The velocity distribution in section lk is assumed to be uniform.

3.2.6 Design of Vane Sections for Multistage Axial-Flow Pumps

Multistage axial-flow turbomachines were introduced by Parsons into the field of steam turbines before the turn of the century. Apparently Parsons also considered the use of this type of turbomachine as a compressor.

Multistage axial-flow compressors were developed first by Brown Boveri in Switzerland around

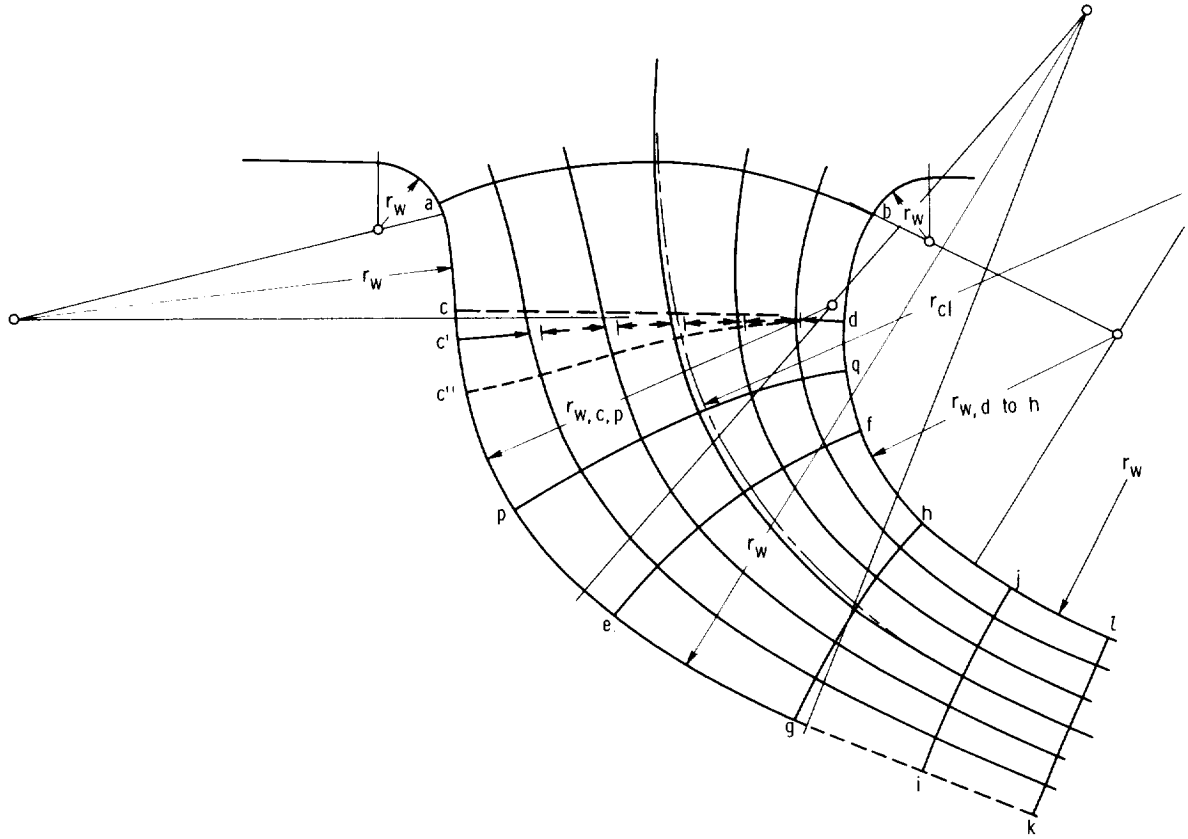

Figure 3-13. – Curved flow passage. The symbol r_w denotes radius of wall curvature and additional subscripts indicate places where curvature has this radius; r_{cl} denotes radius of centerline curvature.

1930. However, the decisive developments in this field took place in the forties and led to the almost exclusive use of axial-flow compressors in aircraft turbine engines (see ref. 6).

Multistage axial-flow pumps have been developed in a significant manner only recently as rocket propellant pumps for liquid hydrogen (ref. 55). However, there is no reason why multistage axial-flow pumps should not be used for any liquid as long as the flow rate does not have to vary over a wide range at constant speed of rotation, in other words, as long as the dimensionless flow rate Q/nD^3 is not varied widely for pumps of any one fixed design form.

Figure 1-39 shows a typical multistage axial-flow pump in comparison with a single-stage radial-flow pump of the same overall basic specific speed. For liquid hydrogen, the basic specific speed is usually very low (because of the high pump head compared with the inlet head); the low speed leads to inefficient single-stage radial-flow pumps (see fig. 1-12), whereas the resulting increase in the number of stages of a multistage axial-flow pump does not necessarily lead to a reduced efficiency. It is quite possible that this reasoning has led to the use of multistage axial-flow pumps for liquid hydrogen; this practice is sound as long as it is not interpreted as a limitation of the use of axial-flow pumps.

Figure 1-39 shows an inducer-type first-stage impeller, which is necessary to achieve generally acceptable suction (cavitation) performance. This type of impeller is discussed in section 3.4, except for considerations, presented here, which are necessary to determine the design characteristics of the higher stages with a large hub-tip diameter ratio. These higher stages, the principal subject of the present section, are axial stages between essentially cylindrical outer and inner walls leading to an approximately constant flow coefficient V_m/U.

To determine the flow coefficient of the higher stages, one derives first the inlet flow coefficient of the inducer stage from its prescribed suction specific speed (see fig. 1-18). From the condition of

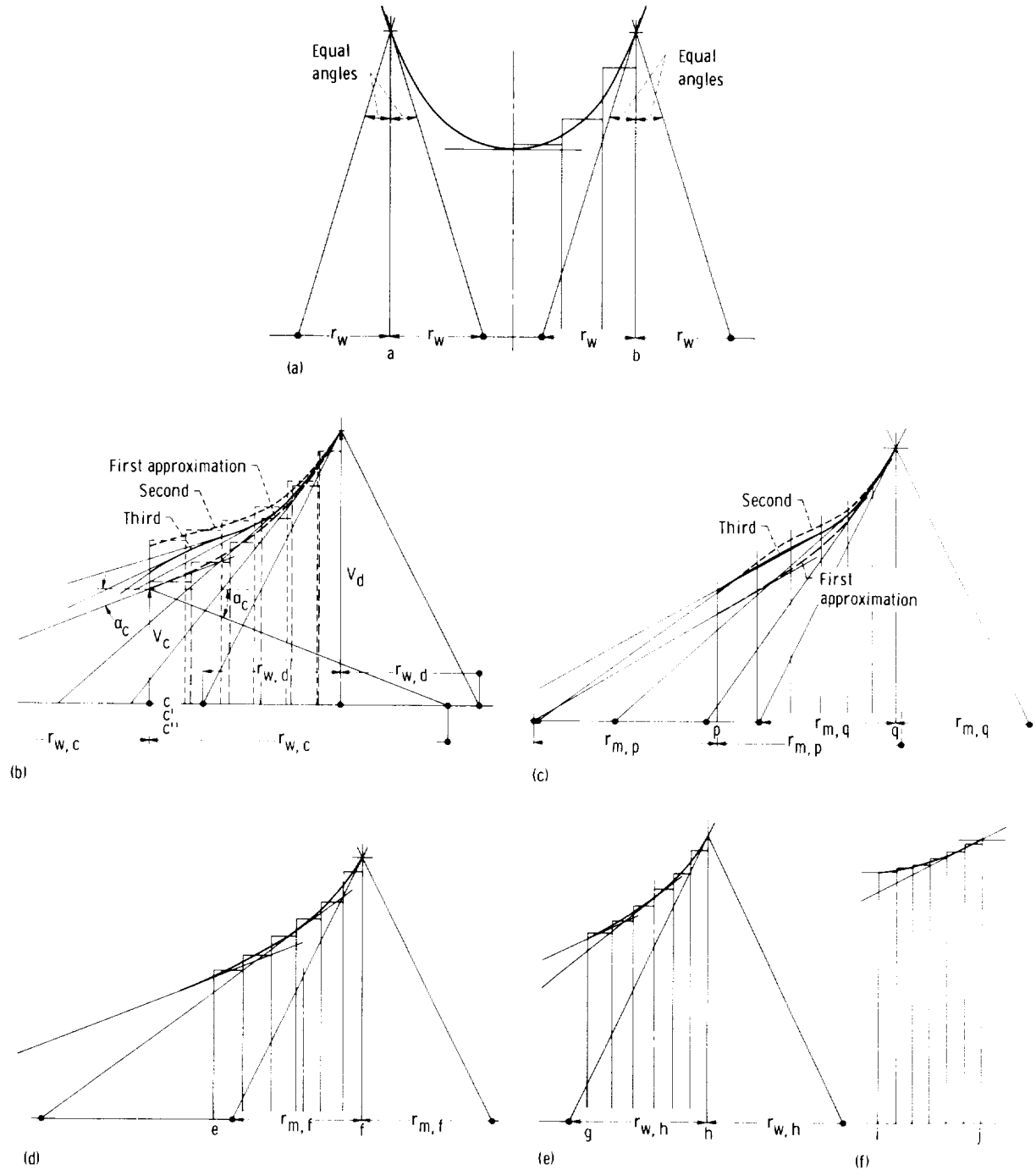

(*a*) *Section ab.*
(*b*) *Section cd.* (*c*) *Section pq.*
(*d*) *Section ef.* (*e*) *Section gh.* (*f*) *Section ij.*

Figure 3-14. – Velocity distributions in sections of curved flow passage (fig. 3-13). Tangents to curve are determined as illustrated in figure 3-10.

continuity (with the slight compressibility of the liquid neglected for the present), one finds

$$V_{m,2}(D_i^2 - D_{h,2}^2) = V_{m,1}(D_i^2 - D_{h,1}^2) \tag{3-33}$$

(see fig. 1-20 for notations). Hence

$$\frac{V_{m,2}}{U_i} = \frac{V_{m,1}}{U_i} \frac{1 - D_{h,1}^2/D_i^2}{1 - D_{h,2}^2/D_i^2} \tag{3-34}$$

This equation applies to the tip sections of all stages, which are here assumed to have a constant diameter D_i.

Generally one is more interested in the flow condition of the hub section, because the retardation of the flow and the lift coefficient there are usually more critical than at the tip section. From equation 3-34, one obtains

$$\frac{V_{m,2}}{U_{h,2}} = \frac{V_{m,1}}{U_i} \frac{D_i}{D_{h,2}} \frac{1 - D_{h,1}^2/D_i^2}{1 - D_{h,2}^2/D_i^2} \tag{3-35}$$

Assuming $V_{m,1}/U_i = 0.10$ (for higher suction specific speeds of the inducer) and $D_{h,1}/D_i = 0.20$, one finds

$$\frac{V_{m,2}}{U_{h,2}} = 0.096 \frac{D_i/D_{h,2}}{1 - D_{h,2}^2/D_i^2} \tag{3-36}$$

which gives the following values: for $D_{h,2}/D_i = 0.80$, 0.85, and 0.90, $V_{m,2}/U_{h,2} = 0.333$, 0.407, and 0.562, respectively.

On this basis, the following flow section considerations of the higher stages are carried out for three constant flow coefficients:

$$\frac{V_m}{U} = 0.333, 0.40, \text{ and } 0.50 \tag{3-37}$$

The subscript denoting the section diameter can now be dropped, since the following considerations do not apply only to the root sections of the higher stages. They are usually used for a section between the root section and the midspan section

---

It is obviously of practical interest to develop as much head per stage for a given peripheral rotor velocity U as possible. After some preliminary investigations pertaining mainly to the retardation of the relative flow, it was found that the change in peripheral velocity ΔV_U should not be greater than 0.50 U at the flow section considered. Hence the ratio $\Delta V_U/U = 0.50$ and the flow coefficients given by equation (3-37) are the basis for the following investigations of flow sections for multistage axial-flow pumps.

Figure 3-15 shows some typical velocity vector diagrams with $\Delta V_U/U = 0.5$ and $V_m/U = 0.5$. One may regard the vectors shown by solid lines as relative velocity vectors and those shown by dashed lines as absolute velocity vectors; this arrangement leads to more or less conventional flow configurations. Under this assumption the rotor velocity vector U points from right to left. However, the diagrams are equally valid if the solid lines denote absolute velocities and the dashed lines relative velocities. Then the rotor velocity vector U points from left to right. The vectors shown by dash-dot

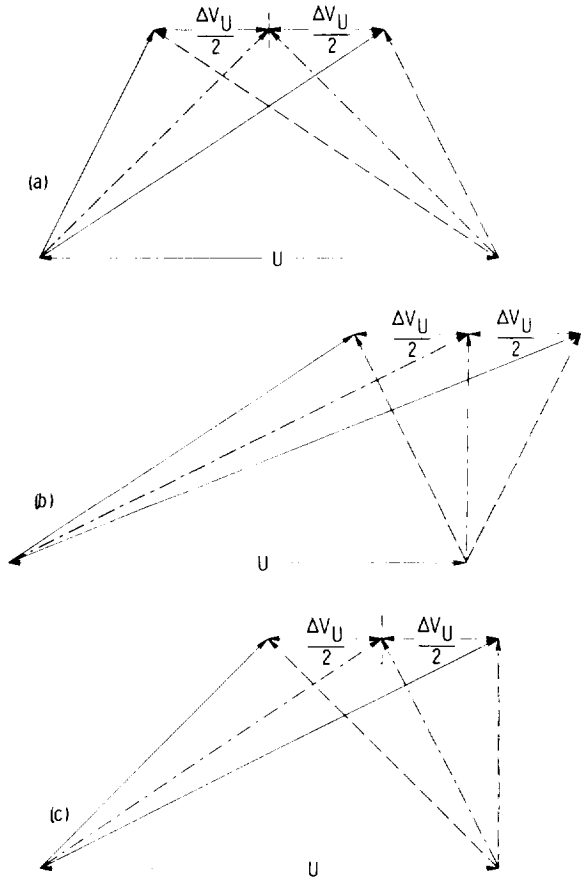

(*a*) *Symmetrical diagram.*
(*b*) *Strongly nonsymmetrical diagram.*
(*c*) *Intermediate diagram.*

Figure 3-15. – Typical velocity diagrams for multistage axial-flow pumps.

lines are the vectorial mean values of the inlet and discharge velocities, V_∞ and w_∞, respectively.

The velocity configurations presented in figure 3-15 apply to pumps as long as the change in peripheral velocity ΔV_U is in the same direction as the velocity U of the system. If ΔV_U and U are in opposite directions, the diagrams apply to turbine operation. In this section, only pump operation is considered.

Figure 3-15(a) shows the so-called symmetrical velocity arrangement, described in reference 55 as the one used in the past with multistage pumps for liquid hydrogen. The relative and absolute vector diagrams are equal to each other. Both end points of the velocity change ΔV_U can be shifted in the circumferential direction to arrive at different possibilities. Figure 3-15(b) shows an extreme of nonsymmetrical arrangement. The flow depicted by one diagram is retarded, while the flow depicted by the other changes its peripheral component from positive to negative (or vice versa), but the magnitude of the velocity through the system is not changed (impulse system). It is of interest to observe that the velocity reduction ratio in the retarding vane system is in this case not worse (is, in fact, better) than that in the symmetrical system, where both the rotor and the stator have retarded flow.

Figure 3-15(c) shows an intermediate arrangement, which may be the most commonly used configuration with commercial (usually single-stage) axial-flow pumps, provided the dashed-line arrows are interpreted to designate the absolute flow which enters the rotor system axially. The rotor gives the absolute flow a circumferential component. The stator vanes return this flow to the axial direction. Although not customary, it is quite possible to use the rotor to turn the flow to the axial direction (relative to itself).

The most important limiting variables to be considered with the diagrams depicted in figure 3-15 are the ratios of flow retardation V_2/V_1 and w_2/w_1. Figure 3-16 shows the variations of these ratios for the complete spectrum of velocity diagrams with $\Delta V_U/U=0.5$ and $V_m/U=0.333$, 0.40, and 0.50 from pure impulse in the stator system ($V_2 = V_1$), to the symmetrical stage, to pure impulse in the rotor system ($w_2 = w_1$). The ratios V_2/V_1 and w_2/w_1 are plotted against the circumferential location of the center of ΔV_U (or Δw_U) in order to show the symmetry regarding relative and absolute flows. The results are interesting.

The symmetrical arrangement gives very nearly the minimum for V_2/V_1 and w_2/w_1; it is in this respect close to the least favorable arrangement. On the other hand, the extremes of pure impulse in the stator (right in fig. 3-16) or rotor (left) are optimum regarding retardation, except for accelerating vane systems which would lie outside these extremes. Accelerating systems are rarely used in pumps or compressors, although accelerating stator systems discharging into the rotor against the direction of rotation were used successfully by Brown Boveri in early multistage compressors.

Besides indicating the existence of a lower limit for the ratio of retardation, figure 2-26 relates the value of this ratio in a somewhat indefinite, empirical fashion to the lift coefficient $C_{L,\infty}$. From figure 2-26, the writer has, for design purposes, drawn a single curve relating $C_{L,\infty}$ to V_2/V_1 or w_2/w_1. This curve is shown in figure 3-17. Figure 2-26 shows clearly the highly approximate character of this curve. Nevertheless the curve permits a systematic approach to the design of vane systems corresponding to various velocity vector diagrams and their ratios of flow retardation as shown, for example, in figure 3-16.

Figure 3-18 shows a vane layout of a symmetrical vane system for $\Delta V_U/U=0.5$ and $V_m/U=0.5$. From figure 3-16, one finds V_2/V_1 or $w_2/w_1 = 0.62$, and from figure 3-17, one can select a corresponding lift coefficient $C_{L,\infty}=0.95$. The velocity vector diagram gives $\Delta V_U/w_\infty$, and with it equation (2-54) gives the solidity of the system:

$$\frac{l}{t} = \frac{2}{C_{L,\infty}} \frac{\Delta V_U}{w_\infty} \tag{3-38}$$

In this case, there is probably no severe cavitation requirement because of the head produced by the inducer stage. Assuming the inducer produces as much head as the higher stage to be designed, one can merely estimate that the maximum vane pressure reduction should not be greater than the stage pressure rise, a requirement easily met by this design. It is, therefore, not necessary to start with an assumed vane pressure distribution. Rather one can begin with dividing the total change in peripheral velocity Δw_U into a suitable number of steps (here five) by starting near the leading edge with steps somewhat larger than the average step and tapering the size of the steps down toward the

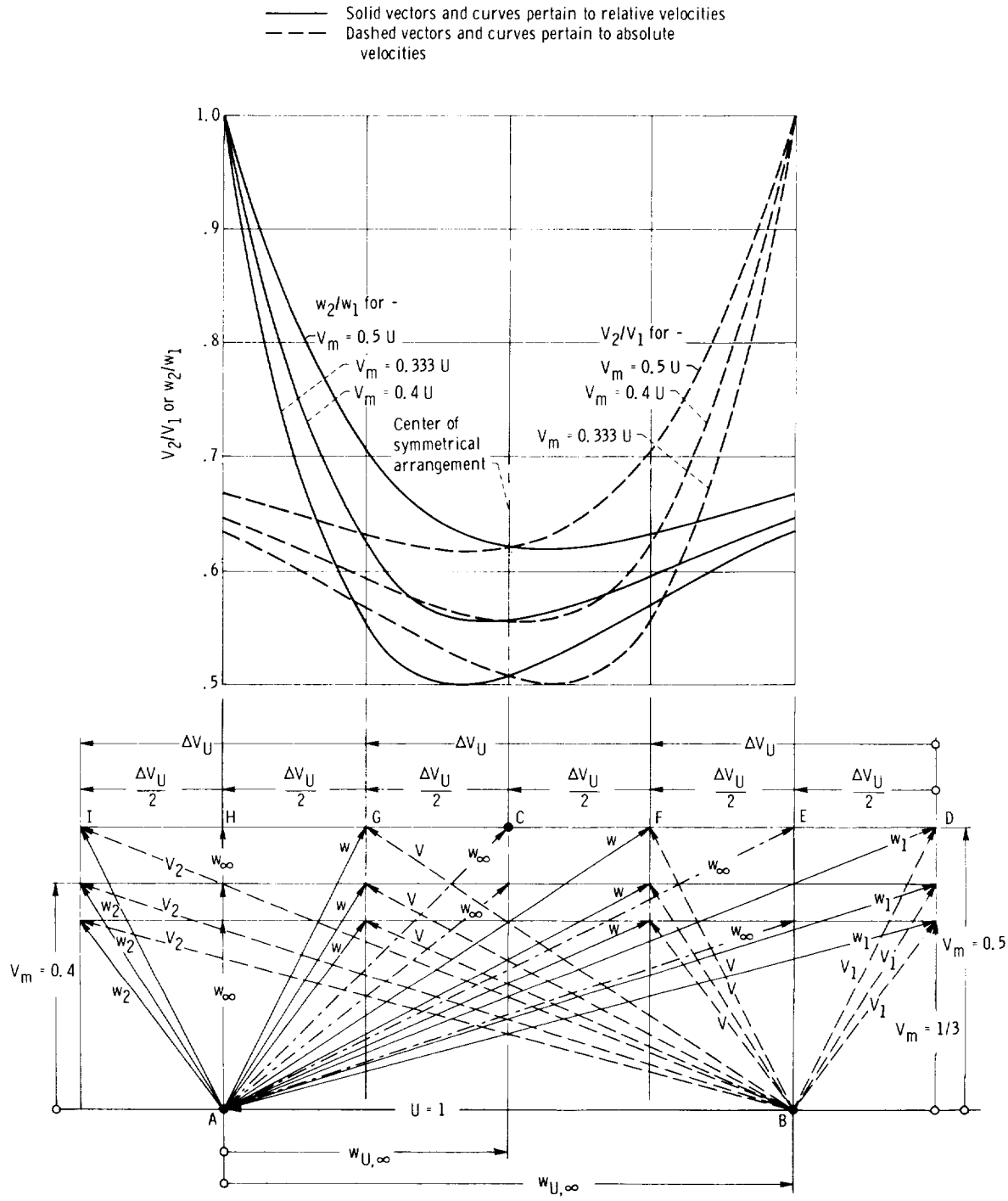

Figure 3-16. – Variations of axial-flow velocity diagrams.

trailing edge. Estimating the mean velocity curve to account for vane thickness, one is ready to draw the intermediate mean velocity vectors and from them the mean streamline by its tangents. The deviation of the mean camber line from the mean streamline is taken from the deviation curve in figure 3-7 by using its middle branch near the leading edge, which is satisfactory regarding the normal vane spacing d_1 near the leading edge. The thickness distribution is derived from the mean velocity curve according to

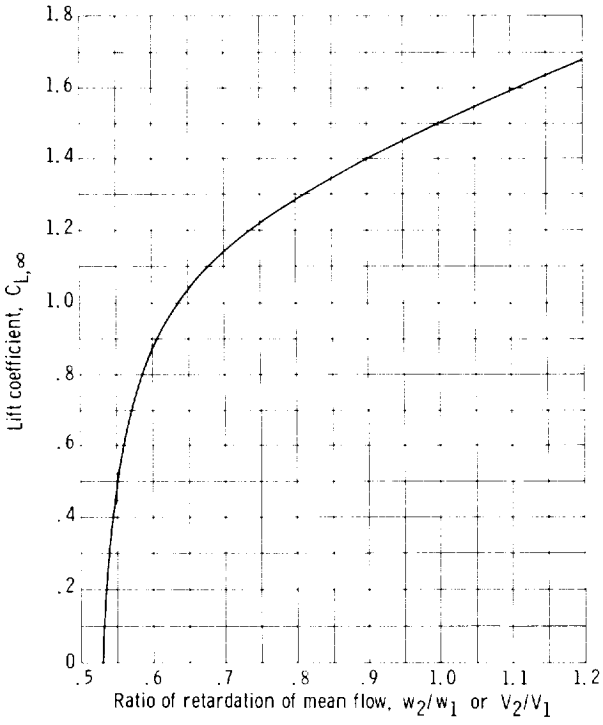

Figure 3-17. – Lift coefficient as function of retardation.

equation (3-21). In this case, some correction of the mean velocity curve is necessary before a satisfactory thickness distribution is obtained. An uncorrected part of this curve is shown as a dashed line between points c and f in figure 3-18.

As a check on various assumptions made, the vane pressure distribution is derived from the velocity vector diagram. First the mean pressure is derived from the mean (relative) velocities according to equation (3-24), where the index x may run from a through f in figure 3-18. The vane pressure difference is calculated from the average vane pressure difference of the entire vane

$$\Delta p_{av} = \frac{C_{L,1}\rho w_1^2}{2} \tag{3-39}$$

where

$$C_{L,1} = \frac{C_{L,\infty} w_\infty^2}{w_1^2} \tag{3-40}$$

and $C_{L,\infty} = 0.95$ according to figure 3-17. Then, according to equation (3-20), and with $\Delta w_U = \Delta w_{U,b} + \Delta w_{U,c} + \Delta w_{U,d} + \Delta w_{U,e} + \Delta w_{U,f}$,

$$\frac{\Delta p_b}{\Sigma \Delta p} = \frac{\Delta p_b}{N \Delta p_{av}} = \frac{\Delta w_{U,b}}{\Delta w_U}$$

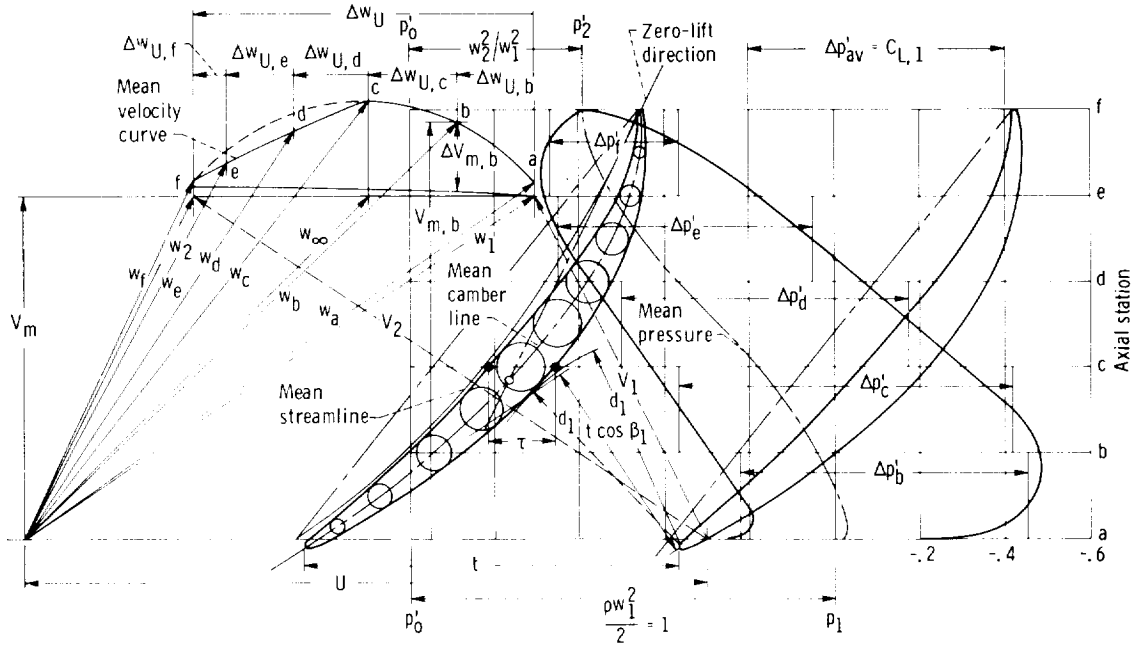

Figure 3-18. – Vanes for symmetrical stage with $V_m/U = 0.5$ and $\Delta w_U/U = 0.5$; $p_1 = 0$. $(p' = p/(\rho w_1^2/2))$.

or

$$\frac{\Delta p_b}{\Delta p_{av}} = \frac{N \Delta w_{U,b}}{\Delta w_U}$$

$$\frac{\Delta p_c}{\Delta p_{av}} = \frac{N \Delta w_{U,c}}{\Delta w_U}$$

where N is the number of equal, axial steps through the system, five in figure 3-18. The pressure differences Δp_b, Δp_c, Δp_d, Δp_e, and Δp_f are placed in the pressure diagram according to some reasonable rule, for example, that the pressure drop below the mean pressure shall be twice the pressure rise above the mean pressure. The pressure distribution curves can be drawn through the local, mean surface pressures of the steps ab, bc, cd, de, and ef as shown in figure 3-18.

It should be evident that the stator vanes of the symmetrical stage have exactly the same shape and characteristics as the rotor blades for the diameter considered. For other diameters, the stage is usually not symmetrical.

A somewhat unusual vane system for multistage axial-flow pumps is the impulse system, to be used with the right and left extremes of the spectrum of velocity diagrams shown in figure 3-16. Such a vane system is shown in figure 3-19 for the same operating conditions as used in figure 3-16, that is, for $V_m/U = 0.5$ and $\Delta V_U/U = 0.5$. Figure 3-19 uses symbols for absolute velocity V, which correspond to the assumption that the system shown is a stator vane system, but it should be clear that the same system could be used also as a rotor vane system.

Since for an impulse system $V_2/V_1 = 1$, one can select according to figure 3-17 a lift coefficient $C_{L,\infty} = 1.5$, although it should be recognized that this is not the only choice possible.

The subdivisions of ΔV_U are chosen to be somewhat similar but not exactly equal to those in figure 3-18. These steps start at the leading vane end with 0.25 ΔV_U and taper off gradually to 0.13 ΔV_U.

In its central portion, the mean velocity curve is drawn slightly below the circular arc representing a constant mean velocity in order to achieve a reduction in this velocity as suggested in section 3.2.3 in connection with figure 3-4. However, as a consequence of this purpose, the mean velocity curve is very flat, that is, it rises very little above the

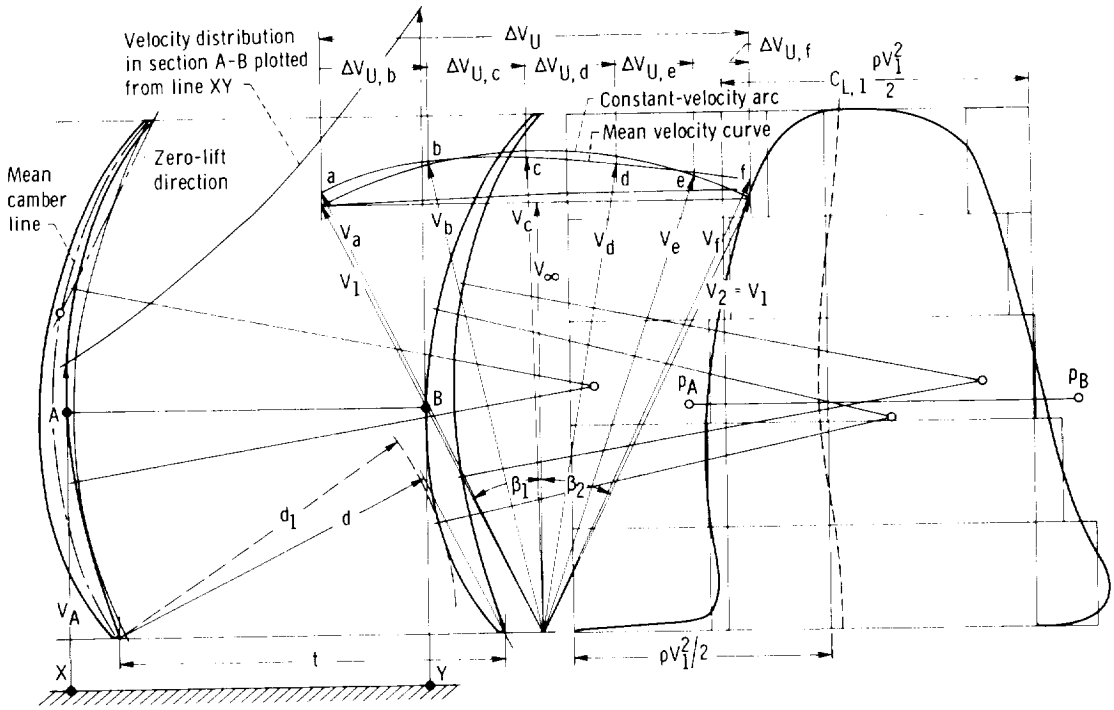

Figure 3-19. – Impulse vane system for $V_m/U = 0.5$ and $\Delta V_U/U = 0.5$.

zero-thickness curve, so that the resulting vane is necessarily quite thin (about 6.67 percent). It may, nevertheless, have the required stiffness because the camber is greater than that of the 9.4-percent-thick blade in figure 3-18.

The vane channel shown in figure 3-19 permits the application of the stream-curvature method. The velocity distribution in section AB is plotted from the baseline XY at the same scale as the velocities in the vector diagram. It can be seen that the maximum velocity in section AB is substantially higher than the inlet and discharge velocities $V_1 = V_2$. The corresponding vane surface pressures p_A and p_B are plotted in the pressure distribution diagram, which is derived in the same manner as described in connection with figure 3-18, with p_A and p_B determined by equation (3-24) from the minimum and maximum velocities in section AB.

The fact that the vane system shown in figure 3-19 has a less favorable velocity distribution and smaller vane thickness than the vane system shown in figure 3-4 is obviously due to the fact that in figure 3-19 the inclination of the incoming and discharging flow against the axial direction (angles β_1 and β_2) is very much smaller than in figure 3-4. However, figure 3-16 shows that, for the right and left extremes of this spectrum, the retardation ratio of the blade row having retarded flow is above the lower limit of about 0.6, even at the minimum flow coefficient (0.333) considered in the present investigation. Therefore an impulse vane system is developed for $V_m/U = 0.333$ and $\Delta V_U/U = 0.5$ (not changed); it is shown in figure 3-20. The lift coefficient $C_{L,\infty}$ used in this figure and the subdivisions of ΔV_U are the same as those in figure 3-19, while $C_{L,1}$ is, of course, reduced according to the changed ratio of V_∞ to V_1.

In figure 3-20, an attempt is made to use the increased flow angles β_1 and β_2 to increase the vane thickness and to reduce the mean velocity and thereby the maximum velocity in the midturn flow section AB between the vanes. This is successful, since the maximum velocity at midturn (point B) exceeds V_1 and V_2 by only 27 percent as compared with 40 percent for the vane system shown in figure 3-19. Correspondingly, the minimum pressure p_B is substantially increased. The vane thickness is increased from 6.2 to 7.2 percent.

The impulse vane systems in figures 3-19 and 3-20 differ substantially in form from the design shown in figure 3-4. Since this difference is greater than can be explained by the differences in the flow angles, it is desirable to compare the results obtained by the mean streamline method with those obtained by the stream-curvature method for the same flow angles. This is done in figure 3-21 for the flow angles used in figure 3-20.

The vane contour shown in figure 3-21 by short- and long-dash lines was obtained in the same manner as the so-called improved vane shape in figure 3-4, by starting with the classical design (fig. 3-2), shown in figure 3-21 entirely in long-dash lines. The design form developed in figure 3-20 by means of the mean streamline method is shown by solid lines.

The difference between these vane forms is small at the inlet and quite substantial at the discharge side. This should not be surprising, since the so-called improved design shown in short- and long-dash lines really corresponds to a design derived by the mean streamline method without any deviation of the mean camber line from the mean streamline. In this respect, the vane shape developed by the mean streamline method with deviation (solid lines) represents a higher degree of approximation than the short- and long-dash-line contour developed by stream-curvature considerations, which degenerate into one-dimensional considerations at the vane ends.

The complete equality of the inlet and discharge portions of the vane developed on the basis of stream curvature alone reveals another shortcoming of this method, namely, that the inlet vane distance d_1 was made equal to that corresponding to the velocity V_1, whereas it should be larger in order to avoid excessive velocities at the convex side of this section. This consideration does not apply to the discharge vane distance d_2, because the flow leaving the trailing edge is not the same as that approaching the leading edge. Thus one must conclude that the trailing end of impulse vanes should have a vane angle $\beta_{v,2}$ against the axial direction larger than that at the leading vane end and also larger than the discharge flow angle β_2. The vanes developed by the mean streamline method (solid lines) do have this characteristic.

On the other hand, the vanes developed by the mean streamline method have a discharge vane distance d_2' which is smaller than that corresponding to the one-dimensional condition of continuity with respect to the discharge velocity V_2. A similar but somewhat milder conflict with the condition of continuity is found in the NACA vane

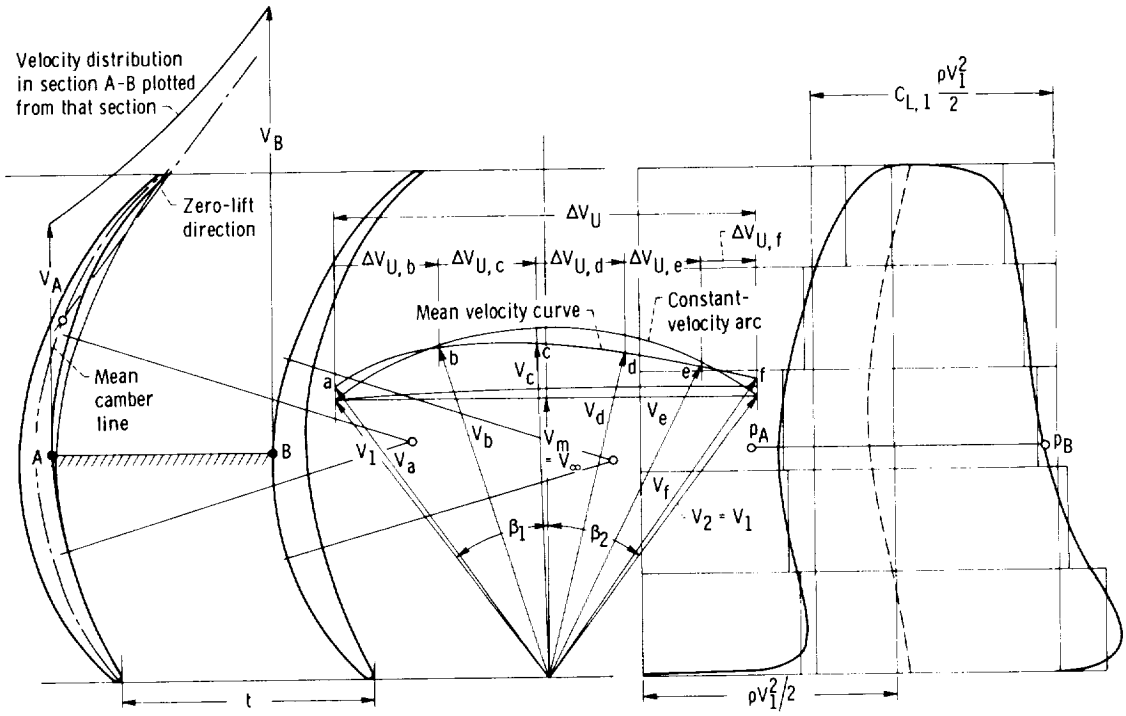

Figure 3-20. – Impulse vane system for $V_m/U = 0.333$ and $\Delta V_U/U = 0.5$.

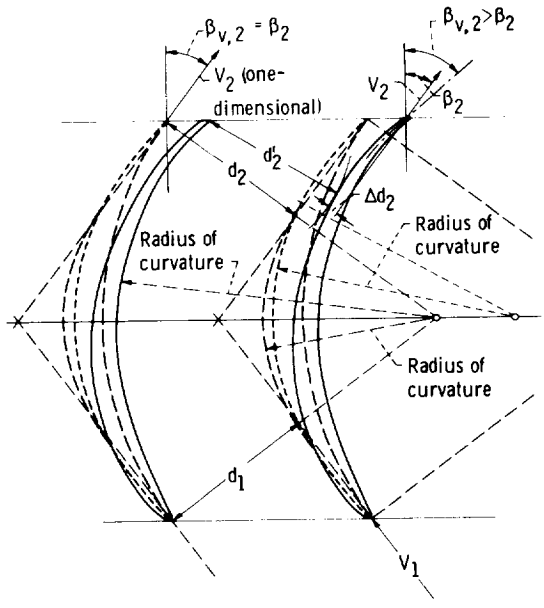

Figure 3-21. – Comparison between impulse vane systems developed by mean streamline and one-dimensional methods.

system shown in figures 2-27(b) and (c) and may exist in most cases where the flow is deflected past the axial direction. This indicates that the one-dimensional condition of continuity does not have to be satisfied strictly at the discharge end of vane systems with β_2 close to zero. Nevertheless one must conclude that steep vane systems of this type, if developed by the mean streamline method, must be checked regarding the normal vane distance not only at their inlet but also at their discharge ends.

For the vane system shown in figures 3-20 and 3-21, one may use a vane system and vane shape somewhere between the two designs compared in figure 3-21 and aim to satisfy the one-dimensional condition of continuity approximately with respect to the mean velocity at the discharge as well as the inlet. This can be accomplished with the mean streamline method by selecting a somewhat flatter deviation curve than that shown in figure 3-7. The vane shapes shown in figures 3-19 and 3-20 were derived by using the dashed curve in figure 3-7 representing the standard NACA 65-series cascades. By flattening the deviation curve further near the trailing edge, one can reduce the discrepancy Δd_2 between the actual vane distance d_2' and the distance corresponding to the one-dimensional condition of continuity (fig. 3-21).

These considerations lead to the general conclusion that none of the methods of cascade design presented in this compendium are self-sufficient. Any simple check, be it by the one-dimensional condition of continuity, by the zero-lift direction (see Weinig's results, sec. 2.5.3), or by any other simple and rational consideration, is highly desirable.

A preliminary layout of the retarding vane system to be used in connection with the impulse vane system in figure 3-20 is shown in figure 3-22. According to figure 3-16, the ratio of retardation in this system is $w_2/w_1 = 0.635$, which by figure 3-17, suggests a lift coefficient $C_{L,\infty} = 1.0$. The subdivision of Δw_U into five steps is chosen to be the same as in figure 3-18, as is the dimensionless curve for the deviation of the mean camber line from the mean streamline, which is the central branch of the solid curve in figure 3-7. The mean velocity curve and the vane thickness are derived by successive approximations. The last correction of the vane thickness distribution is shown on the trailing part of the blade by the step from the dashed-line contour to the solid contour. No corresponding correction of the velocity diagram and the mean streamline is necessary, since the resulting change would be insignificant. The maximum thickness of the final blade profile is about 6 percent.

As a check on the design forms presented here, the zero-lift direction is shown in every vane layout (figs. 3-18, 3-19, 3-20, and 3-22) as a dash-dot line through the trailing edge. The intersection of this line with the mean camber line is marked, and the location of this point is compared with the empirical curve shown in figure 2-28. The comparison is fairly satisfactory with the exception of the blade shown in figure 3-22, which should be steepened (i.e., the stagger angle measured from the axial direction should be reduced) by about 2° to satisfy this requirement, provided one accepts an extrapolation of the curve in figure 2-28 to a vane stagger angle β_v of about 66½°.

The departure of the vane system design shown in figure 3-22 from its usual relation to the zero-lift direction and the abnormally rapid increase in vane curvature toward the trailing end make it desirable to attempt a modification of this design form. Within the design rules adopted here, the only way of overcoming the previously mentioned shortcomings of this design is a modification of the curve describing the deviation of the vane camber line from the mean streamline. An attempt to do this is shown in figure 3-23. The deviation curves given in figure 3-7 are shown as dashed lines. To accomplish the desired modification, one must increase the deviation at the leading edge by a factor of 2 over that used previously. Furthermore, one must reduce the curvature of the deviation curve over the trailing half of the vane. With these two requirements

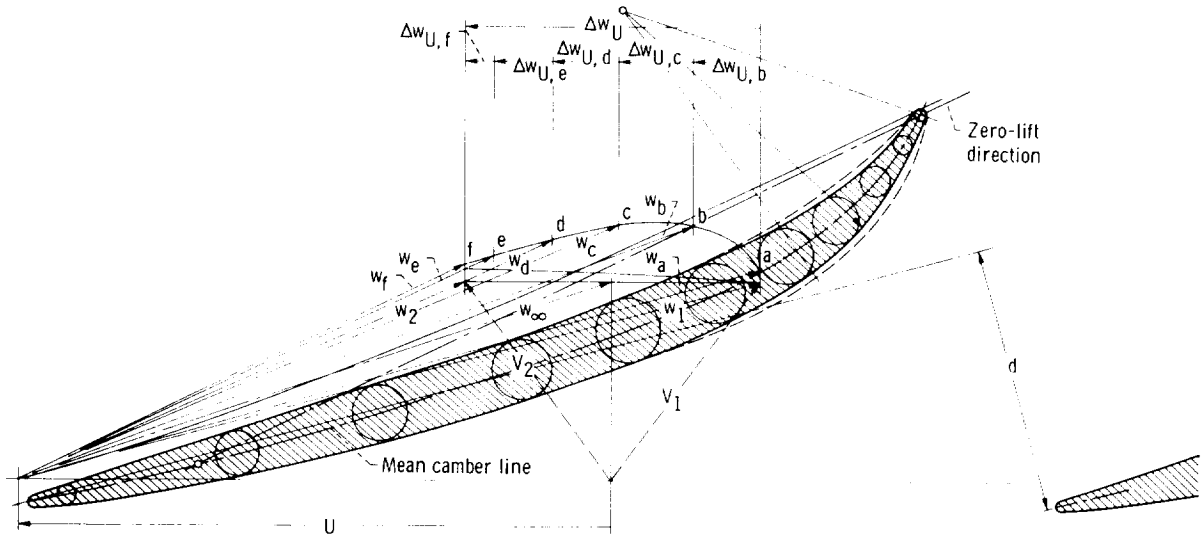

Figure 3-22. – Retarding vane system for $V_m/U = 0.333$ and $\Delta w_U/U = 0.5$.

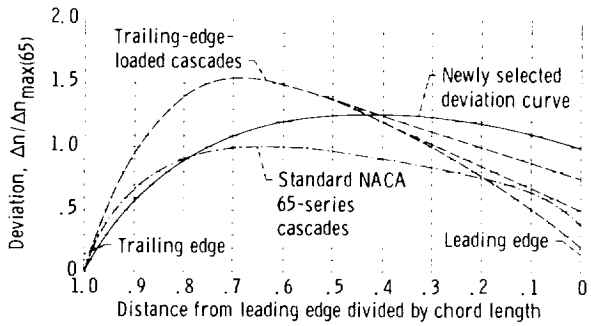

Figure 3-23. – Revised deviation of camber line from mean streamline. (See also fig. 3-7.)

satisfied, it is not difficult to arrive at the newly selected deviation curve shown in figure 3-23 as a solid line.

The subdivisions of ΔV_U are assumed to be the same as previously used for the impulse systems shown in figures 3-19 and 3-20, beginning at the leading end with 0.25 ΔV_U and ending at the trailing end with 0.13 ΔV_U. The mean velocity curve was selected to conform in the leading half of the vane to that used for figure 3-22 and somewhat reduce the height of the old curve in the trailing part of the vane.

The vane shape resulting from these steps, shown in figure 3-24, corrects the shortcomings of the previous design. The zero-lift line intersects the mean camber line practically at the leading edge, as demanded by an extrapolation of the curve in figure 2-28, and the curvature over the trailing part of the vane is greatly reduced.

Thus, it is evident that, by a reasonable change in the deviation curve, significant improvements in vane shape can be achieved. The spread of the deviations originally derived from NACA cascade forms and tests, which is shown diagrammatically in figure 2-34, indicates that the solid deviation curve presented in figure 3-23 can be considered reasonable.

One arrives at the same conclusion as stated previously at the end of the design considerations for impulse vane systems, namely, that a single design procedure such as the mean streamline method is by itself not sufficient for arriving at a good design form in all cases. Additional considerations must be employed to improve the probability of finding a successful solution.

As mentioned previously, the use of the vane systems shown in figures 3-19, 3-20 and 3-24 as stator and rotor systems can be reversed. This means that the impulse systems in figures 3-19 and 3-20 could be used as rotor vane systems, with the system in figure 3-24 becoming the stator system and feeding to the impulse rotor a stream with substantial, positive prerotation. It can be shown that this reversal in the parts played by these systems does not change the slope of the ideal head-capacity curve; that is, an impulse rotor system operating in a stream having the same average

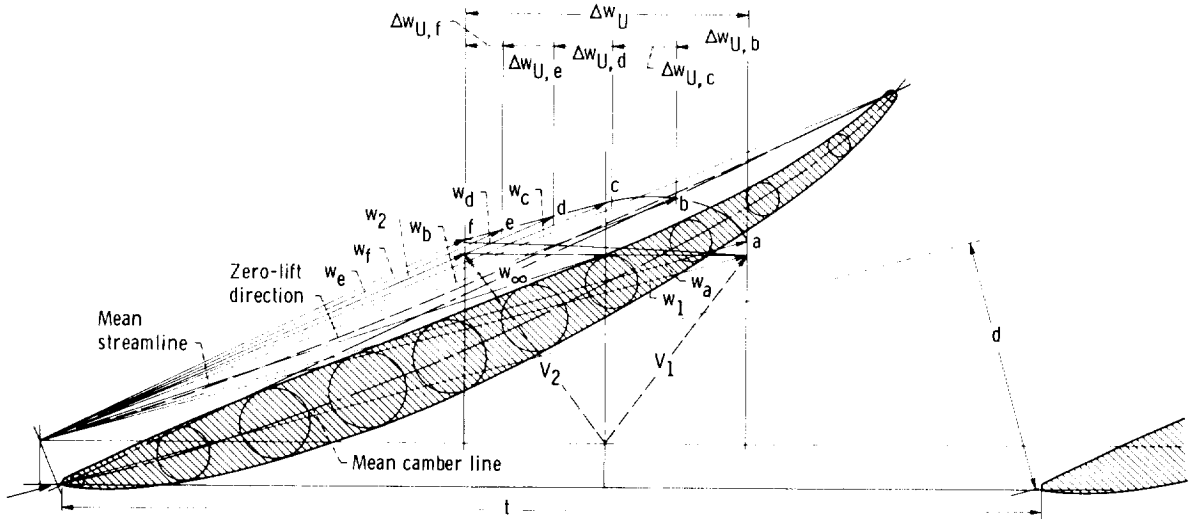

Figure 3-24. – Revised design of retarding vane system for $V_m/U=0.333$ and $\Delta w_U/U=0.5$.

peripheral velocity as the rotor still has the same falling head-capacity characteristic as a rotor with the vanes shown in figure 3-24. Only the flow in the first (inducer) stage and the discharge from the last stage change substantially.

With impulse rotors in the higher stages, the inducer has to develop many times the head it would develop with impulse stators in the higher stages; therefore the flow in the inducer may pose a major problem of relative flow retardation, because the absolute flow must be accelerated circumferentially to (approximately) the peripheral velocity of the rotor.

At the discharge, there is the problem of converting a flow having essentially the peripheral velocity of the rotor into static pressure. This problem may not be too difficult if the flow is collected circumferentially by a single- or multiple-volute casing (see sec. 4.5.2) discharging through one or more tangential passages. In this case, a high peripheral flow component may be advantageous. A volute casing is a very efficient flow passage, and the higher the peripheral flow components, the smaller the volute casing. The velocity head of the flow leaving the volute casing can be converted efficiently into static pressure by tangential, diffusing passages.

Thus the use of impulse rotor systems poses some flow problems at the inlet, but the flow can probably be handled efficiently at the discharge. An impulse rotor has the advantage that the blade system does not exert any axial thrust, so that the required diameter of a hydrostatic balancing device is reduced (see sec. 5.4). Considering that the drag moment of a rotating disk increases with the fourth power of its diameter, a reduction of this diameter is a matter of importance.

In the present section only the symmetrical stage and the right and left extremes of the spectrum illustrated in figure 3-16 are considered. It should be evident that these cases do not exhaust the design possibilities of multistage axial-flow machines. The examples presented should be sufficient to guide the reader in the design of other arrangements within the spectrum outlined in figure 3-16. Even solutions outside this spectrum, that is, with accelerated flow in one of the vane systems (stator or rotor), should be considered.

3.2.7 Cascade Design for Compressible Fluids

In this section, the methods of cascade design described in the preceding sections are shown to be applicable also to compressible fluids. The method of this application is that described in section 2.4, particularly the use of the change in specific volume v/v_o as a function of the dimensionless fluid velocity V/V_o, given for isentropic changes in air (at moderate temperatures) in figure 2-7 (derived from eqs. (2-21) to (2-23) and (2-25)). For axial-flow vane systems, these relations apply also to the relative flow through moving vane systems; that is, w/w_o can be substituted for V/V_o in figure 2-7, where w_o is related to the stagnation enthalpy h_o of the relative flow by equation (2-21).

The design of axial-flow cascades is described first for a compressor cascade with an inlet flow coefficient of 0.68 (with zero absolute prerotation assumed) and an inlet relative Mach number w_1/a of 0.93. The flow changes through the system are assumed to be as high as is safely compatible with the retardation of the mean relative flow.

The first step is to determine the relative velocity diagram, which differs for compressible fluids from that for incompressible fluids because the meridional velocity component varies with the specific volume v. The following demonstration is simplified by assuming that the width of the flow field normal to the plane of flow is constant. Under this assumption, the axial component V_m is proportional to the specific volume, that is,

$$\frac{V_m}{V_{m,1}} = \frac{v/v_o}{v_1/v_o} = \frac{v}{v_1} \tag{3-41}$$

The curve ABD in figure 3-25 is derived under this assumption, by using figure 2-7 with $V/V_o = w_1/w_o = 0.38$. Point B of this curve, marking the end of retardation under the assumption of no blockage of any type, is determined by a lower limit for w_2/w_1, which is here assumed to be 0.66. The horizontal distance between A and B is the circumferential deflection Δw_U that can be achieved under the assumptions $w_2/w_1 = 0.66$ and $w_1/w_o = 0.38$, equivalent to a relative inlet Mach number $M_{1,rel} = 0.93$.

It is evident that, for the same retardation w_2/w_1, a substantially higher circumferential deflection $\Delta w_{U,C}$ could be achieved with an incompressible fluid, where the end point C of the deflection is determined by $V_{m,2} = V_{m,1}$. Inversely, under the assumption of the deflection $\Delta w_{U,C}$

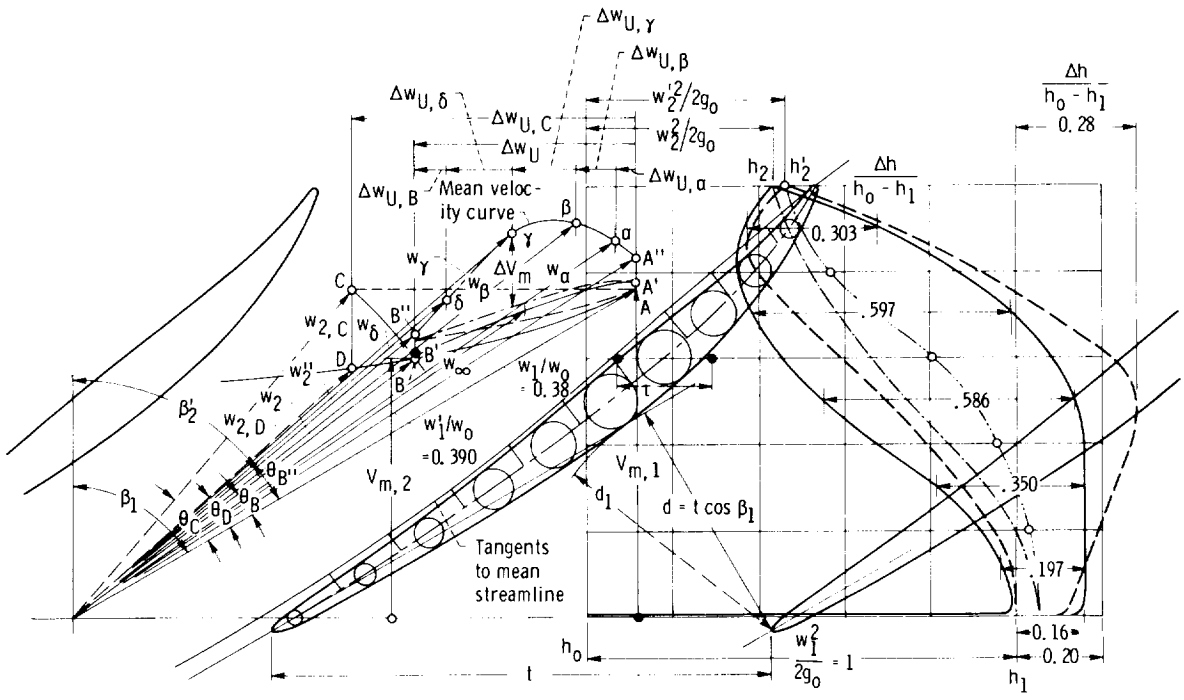

Figure 3-25. – Design of axial-flow cascade for inlet Mach number of 0.93, equivalent to $w_1/w_0 = 0.38$. $C_{L,1} = 0.407$; $C_{L,\infty} = 0.582$.

achievable with incompressible flow, the retardation $w_{2,D}/w_1$ has a much lower value than for incompressible flow, which leads to the probability of stall under the influence of increased compressibility. Furthermore the deflection angle θ in figure 3-25 diminishes under the influence of compressibility: $\theta_C > \theta_D > \theta_B$.

The end point B may be shifted under the influence of blockage by vane thickness and fluid friction to point B″, the end point of the discharge vector w_2''. This discharge vector w_2'' and the inlet vector w_1 permit the construction of an approximate vane shape according to the method presented in section 3.2.2 and figure 3-1, except for the fact that the point of intersection between the zero-lift direction (determined by incompressible flow considerations) and the mean camber line cannot be expected to have the location suggested by figure 2-28. (Apparently compressibility shifts this point toward or beyond the leading edge.) However, the rule suggested by equation (3-1) regarding the vane distance d_1 gains in importance for inlet flow approaching the critical (acoustic) velocity. Choking in the vane passage can be prevented by making the normal, inlet vane distance d larger than suggested by the flow in front of the system, that is, for $d = t \cos \beta_1$,

$$d_1 > d \tag{3-42}$$

where d_1 is the minimum normal distance between the vanes. This rule is obviously to be modified if the channel width normal to the plane of flow shown in figures 3-1 and 3-25 is not constant, since only flow cross-section areas, not vane distances as such, are of importance in this one-dimensional consideration.

The mean streamline method should be expected to offer, and does offer, a better approximation for the design of cascades for compressible fluids than the first approximation presented in section 3.2.2. The vane design shown in figure 3-25 is carried out by the mean streamline method, by using figure 2-7 for compressibility effects.

The assumed vane pressure distribution diagram is shown in solid lines on the right side in figure 3-25; the pressures are replaced by the local enthalpy of the gas in order to obtain the same simple relation between this diagram and the velocities as used for incompressible fluids (Bernoulli's eq. (2-20)). Since this vane layout is intended for a fairly high, subsonic inlet Mach

number ($w_1/w_o = 0.38$, $M_1 = 0.93$), one is interested in minimizing the local enthalpy reduction and the corresponding velocity increase at the low-pressure side of the vanes. For the assumed enthalpy distribution diagram, $2g_o(h_1 - h_{min})/w_1^2$ is chosen to be 0.16, which corresponds to approximately sonic flow at the vane surface. (It is, of course, recognized that the actual maximum velocity is somewhat higher.) The mean enthalpy change (dash-dot curve) is drawn by eye from its minimum value $h_o - (w_1')^2/2g_o$ to its maximum value $h_2 = h_o - w_2^2/2g_o$, where $w_1'/w_o = 0.39$ takes into account an estimated vane blockage effect at the leading edges of the vanes (point A″ of the velocity diagram). The enthalpy distribution along the low-pressure side is approximated by a smooth (solid) curve from its assumed minimum value to the discharge enthalpy h_2. On the high-pressure side, the enthalpy is assumed to rise above the mean stream value half as much as the enthalpy drops on the low-pressure side, the value for the latter being given by the distance between the dash-dot mean enthalpy curve and the solid enthalpy curve along the low-pressure side.

The enthalpy distribution over the vane should now be converted into a pressure distribution in order to obtain the vane force distribution which determines the steps in the change in the peripheral velocity that are needed to find the intermediate mean velocity vectors and thereby the mean streamline. The relation between the enthalpy (as defined in sec. 2.4) and the pressure is (for constant specific heat C_p and isentropic conditions)

$$h_o - h = C_p T_o \left[1 - \left(\frac{p}{p_o} \right)^{1 - 1/\gamma} \right] \tag{3-43}$$

where γ is the familiar ratio of specific heats. (For air at or below room temperatures, γ is 1.40, and it drops only to 1.38 at 1000° R.) The subscript o refers to the stagnation conditions except in connection with the velocity w_o, where it is defined by equation (2-21).

With the definitions for the enthalpy h introduced in section 2.4, equation (3-43) can be converted to the form

$$\left(\frac{h}{h_o} \right)^{\gamma/(\gamma - 1)} = \frac{p}{p_o}$$

and with $\Delta h = h_o - h$ and $\Delta p = p_o - p$,

$$\left(1 - \frac{\Delta h}{h_o} \right)^{\gamma/(\gamma - 1)} = 1 - \frac{\Delta p}{p_o} \tag{3-44}$$

For subsonic and sonic relative inflow velocities, $\Delta h/h_o$ lies below 0.2, which suggests expansion of the left side into a power series. Neglecting powers of $\Delta h/h_o$ in excess of 2, one finds with $\gamma = 1.4$ and, therefore, $\gamma/(\gamma - 1) = 3.5$

$$\left(1 - \frac{\Delta p}{p_o} \right) = 1 - 3.5 \frac{\Delta h}{h_o} + 4.37 \left(\frac{\Delta h}{h_o} \right)^2$$

$$= 1 - 3.5 \frac{\Delta h}{h_o} \left(1 - 1.25 \frac{\Delta h}{h_o} \right)$$

Hence

$$\frac{\Delta p}{p_o} = 3.5 \frac{\Delta h}{h_o} \left(1 - 1.25 \frac{\Delta h}{h_o} \right) \tag{3-45}$$

For the conditions shown in figure 3-25, the factor $1 - 1.25\ \Delta h/h_o$ does not vary by more than about 10 percent due to the enthalpy differences across the blades. For cases of this type (subsonic up to sonic inflow and velocity changes within the rule $w_2/w_1 \geq 0.6$), one can, therefore, calculate the steps in the peripheral velocity changes under the assumption that

$$\frac{\Delta p}{p_o} = \text{constant} \times \frac{\Delta h}{h_o} \tag{3-46}$$

so that the conversion of the enthalpy distribution into a pressure distribution is unnecessary; that is, the steps in velocity can be derived from the dimensionless enthalpy differences across the blade ($\Delta h/(h_o - h_1) = 0.197$, 0.350, 0.586, 0.597, and 0.303) rather than from corresponding pressure differences. The steps so determined do not depart more than about ±5 percent from the steps derived from a pressure distribution; this agreement is well within the accuracy of procedure justified for the mean streamline method. The sum of all velocity steps is, of course, adjusted so as to agree with the prescribed total change Δw_U in peripheral velocity.

The mean velocity curve in the velocity vector diagram is somewhat more difficult to estimate for

compressible fluids than for incompressible fluids.

One must consider that the deviation of the mean velocity curve from the baseline AB (which applies to zero blockage of any kind) involves not only the blockage effect by the boundary layers (dashed) and by the vane thickness but also an increase in V_m due to further expansion of the gas resulting from the increase in velocity caused by the blockage. The estimate of at least the maximum height of the mean velocity curve above the no-blockage line should include this effect; that is, it should be based on the specific volume derived by figure 2-7 from the w/w_o value of a velocity vector drawn to the (estimated) mean velocity curve. This effect on V_m of an increase in specific volume is to be added to the familiar effects of blockage by the boundary layer and vane thickness.

Figure 3-25 can show, of course, only the final result of this reiterative process. The final zero-blockage line A′B′ is based on the specific volumes derived by figure 2-7 from the velocity vectors drawn to the mean velocity curve, $w/w_o = 0.390$, 0.386, 0.372, 0.341, 0.287, and 0.259. One adds to these zero-blockage V_m values (curve A′B′) a V_m allowance for boundary-layer displacement thickness, which leads to the dash-dot curve. The remaining distance ΔV_m between that curve and the mean velocity curve represents the effect of vane thickness alone and is, therefore, used to determine the vane thickness after the mean camber line is determined.

The mean velocity curve so estimated and the steps in peripheral velocity derived from the (estimated) enthalpy distribution along the vanes determine the end points of the mean velocity vectors of the flow through the system. The mean streamline is then drawn from its tangents which are parallel to the mean velocity vectors.

To determine the deviation of the mean camber line from the mean streamline, one must, of course, know the vane lift coefficient. The lift coefficient $C_{L,1}$ (referred to the inlet velocity w_1) is derived from the area inside the dimensionless enthalpy curve along the vane surface and calculated as the arithmetic mean of the enthalpy differences across the vane. This may be regarded as a new definition of the lift coefficient for compressible fluids. However, this definition is practically identical with the conventional force definition, since it uses the previously derived relation between enthalpy and pressure differences in the system. The agreement regarding the lift coefficient should be closer than that obtained between the local enthalpy and corresponding pressure differences, since the lift coefficient is concerned only with the average pressure and enthalpy difference across the vane. (The error involves only the departures of local enthalpy or pressure differences from the average enthalpy or pressure difference.)

In the case shown in figure 3-25, the average of the enthalpy differences across the vanes is $C_{L,1} = 0.407$, and the corresponding $C_{L,\infty}$ is $C_{L,1}\, w_1^2/w_\infty^2 = 0.582$. From it, one calculates the deviation of the mean camber line from the mean streamline. According to figure 2-33, for vane stagger angles $\beta_v > 50$ and for unity lift coefficient one finds $\Delta n_1/l = 0.05$, and, therefore, with $C_{L,\infty} = 0.582$, $\Delta n/l = 0.0291$. These values apply to the maximum deviation of the standard NACA 65-series cascades (fig. 2-34). For the trailing-edge-loaded vane considered here, one uses the upper (solid) distribution curve of deviation in figure 3-7. The maximum deviation is, thus, $\Delta n_{max}/l = 0.0291 \times 1.54 = 0.0449$.

The question arises of whether the dimensionless deviations derived from cascade tests with practically incompressible fluids apply to cascade flow of compressible fluids. Considerations given in section 2.4 lead one to believe that these deviations should diminish with increasing compressibility; however, no simple way of predicting the reduction in deviation from the mean streamline is as yet available.

In the absence of any rule that compares in simplicity with the concepts underlying the mean streamline method, the design shown in figure 3-25 uses the solid-line deviations given in figure 3-7, which may lead for the inlet Mach number considered here ($M_1 = 0.93$) to a slightly greater deflection than intended. This deflection involves, of course, the danger of greater retardation and stall. A reduction in deviation by some unknown factor (say 0.6) would reduce this danger, but, as mentioned previously, there is as yet no simple way of approximating such a correction.

The choice between the leading branches of the upper deviation curve in figure 3-7 is to be made by considering the normal vane distance between the vanes at the inlet to the system. The uppermost of these three branches has to be selected before the minimum normal distance d_1 between the vanes is larger than the normal distance d between two successive stagnation streamlines ahead of the system.

The circumferential vane thickness is $\tau/t = \Delta V_m/V_m$, as described previously. This

thickness is shown at a place where a certain departure from τ was permitted in order to obtain a smooth vane contour.

The dash-double-dot line in the enthalpy distribution diagram at the right side in figure 3-25 describes the mean enthalpy as derived by Bernoulli's equation for compressible fluids (eq. (2-20)) from the mean velocities given in the velocity vector diagram of the same figure. The dashed curves, describing the vane surface enthalpy, are derived from the dash-double-dot mean enthalpy line by using the same enthalpy differences as previously. The enthalpy drop on the low-pressure side of the vanes below the inlet free-stream enthalpy ($0.28\ w_1^2/2g_o$) is greater than originally assumed, and the extent of the supersonic flow regime along the low-pressure side can be estimated from the dashed enthalpy curve.

Compressor cascades with supersonic inlet velocities can be shown, by the same method as applied previously, to have in the supersonic regime, and in the absence of blockage, a mean streamline curvature opposite in direction to that in the subsonic regime. The zero-blockage curve 12345 for an inlet Mach number $M_1 = 1.43$ is shown in figure 3-26 and corresponds to line ABD in figure 3-25. The zero-blockage curve dips well below the inlet velocity vector in the supersonic regime, which indicates an increase in flow angle β with diminishing velocity of the (relative) flow.

Actually supersonic flow is hardly ever retarded continuously to the local velocity of sound a, but changes abruptly from some supersonic velocity to a corresponding subsonic velocity. The velocity change across this so-called normal shock obeys the law

$$ww^* = a^2 \tag{3-47}$$

derived in many publications on gas dynamics, for example, reference 14 (ch. 19). In equation (3-47), w is the velocity before and normal to the shock, and w^* is the velocity after and normal to the shock.

For example, if the incoming velocity w_1 changes by a normal shock to the correpsonding subsonic velocity w_1^*, the end point of the velocity vector changes abruptly from 1 to 1* in figure 3-26. If the flow is first retarded supersonically to a velocity vector with end point 2, a normal shock at this condition changes the velocity abruptly to a velocity vector with end point 2*, and so on. In the subsonic flow regime behind such a normal shock, the velocity changes and design procedures are the same as described in connection with figure 3-25. Figure 3-27 shows a possible vane and flow configuration with some supersonic compression in the inlet of the system followed by a normal shock and some subsonic retardation similar to the flow described

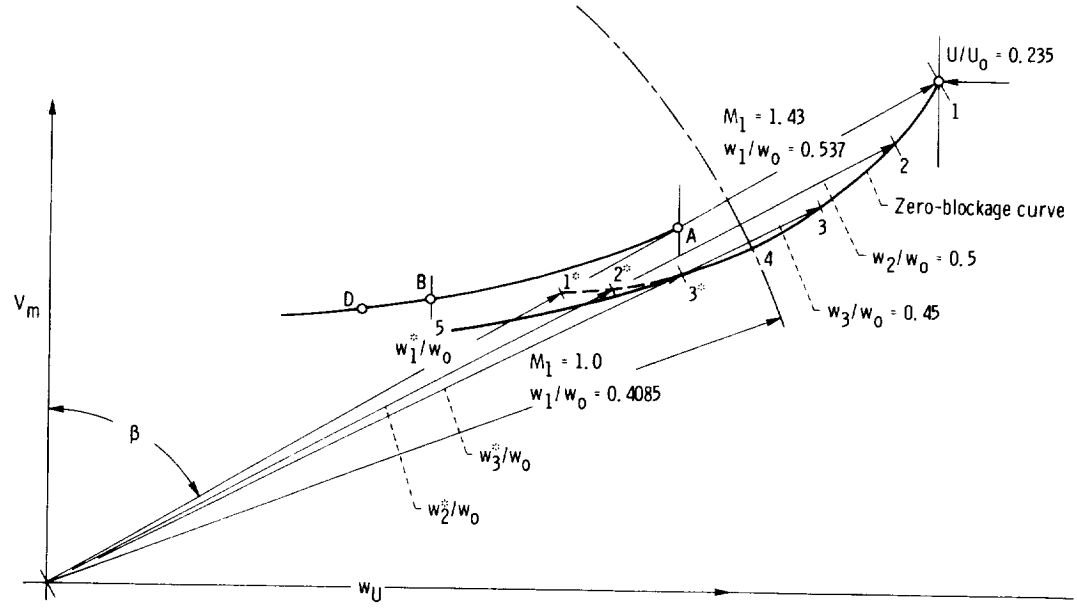

Figure 3-26. – Velocity variations at inclined supersonic and subsonic inlet to cascade.

by figure 3-25. It should be observed that the low-pressure vane surface between the leading edge and the normal shock is slightly concave, in contrast to subsonic vane shapes but in agreement with the vane system for completely supersonic flow shown in figure 2-36. Nevertheless the vane shapes shown in figures 3-25 and 3-27 are not radically different from each other, so that there is hope that a vane system designed primarily for high subsonic inlet Mach numbers might be usable also for supersonic inflow, particularly if designed with a very thin and almost uncambered leading portion.

Configurations such as that shown in figure 3-27 invite the question of what minimum flow retardation ratios w_2/w_1 can be accepted if part of this retardation takes place in a normal shock. Two considerations apply to this question:

First, it has been proven that a normal shock is necessarily connected with some losses (increases in entropy), which have the practical effect that the pressure rise through a shock is always less than if the change in velocity and pressure takes place isentropically (without losses). Figure 3-28 shows this shock pressure ratio as a function of the Mach number and of the dimensionless velocity V/V_o or w/w_o immediately in front of the shock. For Mach numbers that are likely to occur in compressor vane systems in front of a shock (say $M \leqq 1.45$), this pressure loss does not exceed 5 percent and is, therefore, usually not serious. For a Mach number of 1.3, this loss is less than 2 percent. Thus one is tempted to regard a normal shock at moderate supersonic Mach numbers as an efficient form of gas compression.

Second, a normal shock, however, produces an abrupt increase in boundary-layer thickness at the place where the shock meets the wall, particularly if the wall boundary layer is already thickened by a

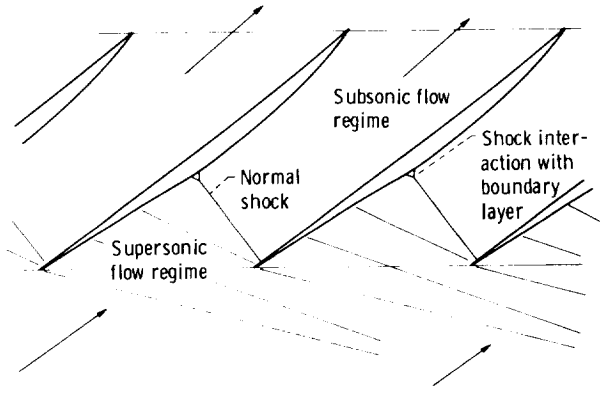

Figure 3-27. – Vane system with supersonic inlet.

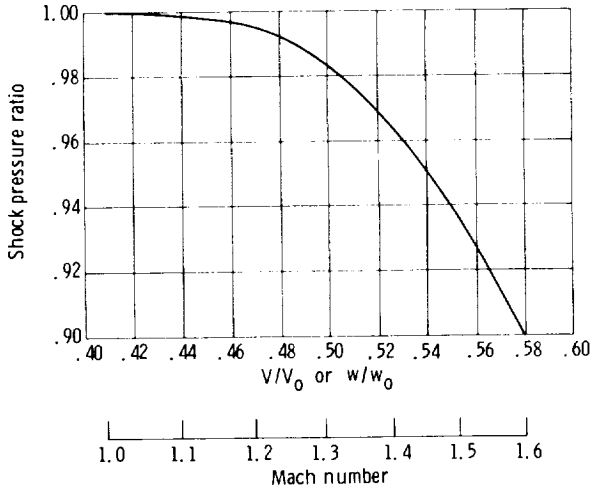

Figure 3-28. – Ratio of pressure change across normal shock to pressure change by isentropic compression.

supersonic retardation in front of the shock, as shown in figure 3-27. As a consequence, further retardation after a shock is either impossible or must take place very gradually if separation is to be avoided. In any event, the retardation through a normal shock must be considered when deciding on additional retardations before and particularly after the shock. Unfortunately sufficient test data are not available to predict the allowable total retardation ratio w_2/w_1 in the presence of a shock, while the retardation ratio w/w^* through the normal shock is, of course, given by equation (3-47) if the dimensionless velocity w/w_o in front of the shock is known.

Two final observations are in order in this section:

(1) The relation between the mean camber line and the zero-lift line drawn through the trailing edge given by figure 2-28 does not hold for the vane system developed in figure 3-25. A casual examination of this figure indicates that this fact is not entirely due to the effects of compressibility, but is also due to a rather generous allowance for boundary-layer thickness made in this design. Furthermore the blade thickness chosen (about 7.5 percent) is perhaps a little larger than justified for a blade of such small camber, the latter being indeed due to compressibility effects. The comparison with the zero-lift direction may lead one to the conclusion that the vanes in figure 3-25 are a little

too steep for the discharge flow requirements, that is, the vanes may generate a somewhat greater deflection (angle θ) than intended. Only test results obtained with the design inlet Mach number can answer this question. It must be considered that compressibility takes this design method still farther away from the NACA test data from which the empirical elements of this method were derived, particularly the deviation of the camber line from the mean streamline.

(2) Compressibility effects are small for vane systems with small changes of the mean flow velocity. Impulse vane systems are systems of this type. Even for the determination of the velocity distribution across strongly curved flow passages, compressibility is not of primary importance, because the law of constant angular momentum is primarily kinematic and, therefore, does not depend on changes in fluid density. Even supersonic flow on the inside of a curved passage does not lead to difficulties until the local Mach number is sufficiently high to generate a strong normal shock as the local flow is retarded toward subsonic velocities.

Only if one desires to obtain streamlines is it necessary to derive a curve of mass flow per unit area from the velocity distribution curve by means of figure 2-7. The area under the mass flow curve is divided into equal parts to determine the points of intersection of the streamlines with the flow cross section considered, as described previously in section 3.2.5.

It is of practical interest that the design of impulse or near-impulse vane systems is actually aided by the effects of compressibility. Recall that it is desirable to have at midturn a larger flow cross section and lower mean velocity than at inlet and/or discharge in order to minimize the velocity excess on the convex wall. Also recall that this arrangement is in conflict with vane thickness requirements. However, at high subsonic Mach numbers, a fairly small increase in cross-sectional area leads to a fairly substantial reduction in mean velocity because of the velocity effect on the specific volume (fig. 2-7), and the previously mentioned design problem is eased considerably.

3.2.8 Summary of Cascade Design

The following items summarize the foregoing considerations on the fluid mechanics of vane system or cascade design. These considerations deal with the flow within given cylindrical sections through axial-flow turbomachines for prescribed inlet and discharge velocity diagrams. The main emphasis is placed on the design of pump and compressor vane systems. However, the principles of designing axial-flow turbine vane systems on the same basis are included. Considerations determining the inlet and discharge velocity diagrams are presented in section 3.3.

(1) The methods of cascade design outlined in section 3.2 deal with the design of an entire cascade as a unit (vane shape, solidity, and stagger) from the inlet and discharge velocity diagrams, in contrast to the more conventional methods of composing cascades out of vane sections of various given shapes (see refs. 6, 16 to 18, and 54).

(2) The solidity l/t, the lift coefficient $C_{L,\infty}$, and the given velocities are related by equation (2-54), and the maximum lift coefficient is given approximately by the ratio of retardation V_2/V_1 or w_2/w_1, as shown in figures 2-26 and 3-17.

(3) A first approximation of pump or compressor cascade design is obtained according to figure 3-1, where the inlet portion of the vane is approximately parallel to the inlet velocity vector w_1; the discharge portion of the vane is related to the zero-lift direction as shown by figures 3-1 and 2-28. The zero-lift direction is related to the discharge velocity w_2 according to figures 2-18, 2-19, and 3-1, and the minimum normal vane distance is $d_1 \geq t\cos\beta_1$.

(4) Strongly curved vane systems of high solidity can be developed or improved through the stream-curvature method, by determining the velocity distribution in the curved passage in the first approximation from the radii of curvature of the passage walls according to the law of constant angular momentum (eqs. (3-30) and (3-31) and figs. 3-4, 3-9, and 3-10). A better approximation can be obtained by considering also the curvature of intermediate streamlines according to figures 3-11 to 3-14.

(5) The shape of the mean camber line can be determined by the mean streamline method as follows:

(a) The mean streamline is derived from an assumed distribution of vane pressure difference and an assumed distribution of vane and boundary-layer blockage. The former determines progressive changes of the mean peripheral relative velocity, and the latter progressive changes of the mean meridional velocity through the system (see figs. 2-31, 3-6, 3-8, and others). The vane pressure distribution is estimated from the prescribed minimum pressure or maximum velocity along the

vane and from the discharge (relative) velocity w_2 and pressure p_2. The lift coefficient is derived from the area inside the vane pressure distribution curve so determined, and from it the solidity of the vane system (eq. (2-54)) is found. Instead of using this procedure, one can determine the lift coefficient from the ratio of retardation (figs. 2-26 and 3-17) and from it the vane pressure diagram, by assuming the distribution of the pressure difference.

(b) The dimensionless normal deviations Δn of the mean camber line from the mean streamline are derived from NACA cascade test results and are represented in figures 2-33, 2-34, and 3-7. The dimensionless deviation $(\Delta n_1/l)_{max}$ in figure 2-33 refers to unity lift coefficient ($C_{L,\infty} = 1$) and to the maximum deviation of the standard NACA 65-series cascades. The general deviation $\Delta n/l$ is proportional to $C_{L,\infty}$.

Cascade shapes of high solidity derived by the mean streamline method should be checked by means of the zero-lift direction (figs. 2-18, 2-19, and 2-28) and the one-dimensional condition of continuity relative to the inlet and discharge normal vane distances d_1 and d_2 and the corresponding relative velocities w_1 and w_2. These conditions need to be satisfied only approximately.

(6) The design of the higher stages of multistage axial-flow pumps (fig. 1-39) must consider rotor and stator vane systems together. The primary criterion of the velocity diagrams is the retardation ratio V_2/V_1 and w_2/w_1 of stator and rotor, respectively (fig. 3-16). The predominantly used symmetrical stage (figs. 3-15(a) and 3-18) is not the only configuration to be considered, and it is very nearly the least favorable with respect to flow retardation.

The flow coefficient V_m/U of the higher stages must be derived from the flow coefficient of the first (inducer) stage, which is determined by cavitation considerations (fig. 1-18).

(7) The design methods just listed are directly applicable to compressible fluids at flow velocities up to Mach 1, provided the volume flow rate is corrected for changes in the specific volume according to figure 2-7 (which applies to air at moderate temperatures). The subscript o applies to the stagnation conditions, except in V_o and w_o, which are the fictitious velocities achieved by ideal-flow expansion to zero pressure and zero absolute temperature. Figure 3-25 shows cascade design for high subsonic velocities by the mean streamline method for constant width normal to the plane of flow, where the meridional velocity V_m changes proportionally to the specific volume ratio v/v_o. Compressibility leads to a reduced deflection Δw_U or θ (in fig. 3-25) for a given ratio of retardation w_2/w_1, or to a reduced (more severe) ratio of retardation for a given deflection Δw_U or θ. The pressure distribution along the blades can be replaced by the enthalpy distribution.

With supersonic flow at the cascade inlet, the velocity changes abruptly (by normal shock) from supersonic to subsonic according to equation (3-47). Velocity changes in the supersonic flow regime are handled as outlined in section 2.5 in connection with figures 2-36 and 2-37 (see also fig. 3-27). Changes after the normal shock are handled like changes after a subsonic inlet (fig. 3-25), except that retardations after a normal shock must be very conservative.

The retardation by a normal shock must be counted when considering lower limits of the ratio of retardation, but these limits are not known quantitatively for flow with a normal shock.

(8) The deviations of the camber line from the mean streamline are probably lower for high subsonic velocities than for low velocities, where the fluid is practically incompressible, but the amount of this reduction in deviation is not known. The deviations derived from cascade tests at low Mach numbers cannot be expected to apply to supersonic relative flow.

3.3 Three-Dimensional Aspects of Axial-Flow Turbomachinery Design

3.3.1 Geometric and Mechanical Blade Design Aspects of Axial-Flow Pump Rotors

The preceding section 3.2 describes the hydrodynamic or gas-dynamic design of cylindrical flow sections through axial-flow vane systems. These flow sections do not determine the three-dimensional vane or blade shape uniquely. This section describes how the three-dimensional vane or blade shape can be derived from the cylindrical flow sections on the basis of geometric and mechanical design considerations. These considerations are essentially the same for axial-flow turbines as for pumps or compressors, but are discussed in this section primarily with respect to axial-flow pumps.

Figures 3-6 and 3-8 show the tip and root sections of an axial-flow pump system. Two cylindrical sections are generally not sufficient to

describe a system with a hub-tip diameter ratio of 0.5 (see fig. 3-5). A third cylindrical flow section at the radius $r = 0.75\ r_o$ is shown in figure 3-29; this section is developed by the same mean streamline method and for the same flow conditions as the sections in figures 3-6 and 3-8. On the left side in figure 3-29, only the mean streamline and the resulting mean camber line of the blade section are shown. The corresponding blade section is shown on the right side.

The blade or cascade sections shown in figures 3-6, 3-8, and 3-29 are so far completely dimensionless. The dimensions shown in these three figures bear no meaningful relation to each other, nor to any additional physical condition that may apply.

If all cascades shown in figures 3-6, 3-8, and 3-29 belong to the same axial-flow (rotor) system, the first condition to be satisfied is obviously that the circumferential vane spacing t be proportional to the radius r of the cylindrical flow section considered, that is,

$$2\pi r = Nt \qquad (3\text{-}48)$$

where N is the number of vanes and has, therefore, the same integer value for all cylindrical flow sections of one system. Thus equation (3-48) settles the scale of figures 3-6, 3-8, and 3-29 relative to each other, but not in any absolute sense.

The next question to be answered is how should the various cylindrical vane sections be located relative to each other in the circumferential and axial flow directions.

The mechanical answer is the following: if centrifugal forces are not to exert any bending moments on the blades, the centers of gravity of the cylindrical vane sections (including the effect of internal voids) should fall on one line which is radial and normal to the axis of rotation.

The hydrodynamic or aerodynamic answer is the following: if the blade forces are to be purely circumferential and axial so as to have no effect on the meridional flow, the centers of gravity of the hydrodynamic or aerodynamic blade forces of the various cylindrical blade sections should fall on a radial line normal to the axis of rotation.

Figure 3-30 shows the blade sections of figures 3-6, 3-8, and 3-29 brought to a compatible scale according to equation (3-48) and stacked up so that the centers of vane pressure fall approximately along one radial line represented by point O in this figure. The hydrodynamic condition satisfied here is not in major conflict with the previously stated mechanical requirement. The blade sections shown as dashed lines are discussed later.

The foregoing considerations and equation (3-48) can be satisfied by any whole number of blades N as long as this number is the same for all coaxial, cylindrical blade sections. The dimensions of the cylindrical blade sections in relation to the radial dimensions of the rotor must be determined by the allowable blade bending stress in relation to the hydrodynamic or aerodynamic blade load. The proper starting point for this consideration is the stress specific speed presented in sections 1.2.3 and 1.3.3.2, particularly in the form of equations (1-64) and (1-66). These equations relate the stress specific speed

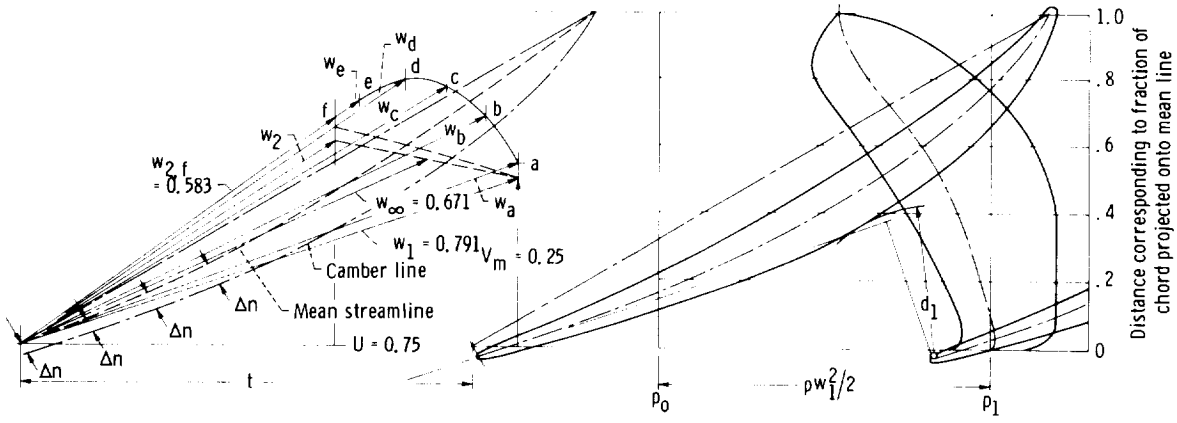

Figure 3-29. – Design of cylindrical midsection r/0.75 r_o. $C_{L,\infty} = 0.56$; $t/l = 0.68$. (See also figs. 3-6 and 3-8.)

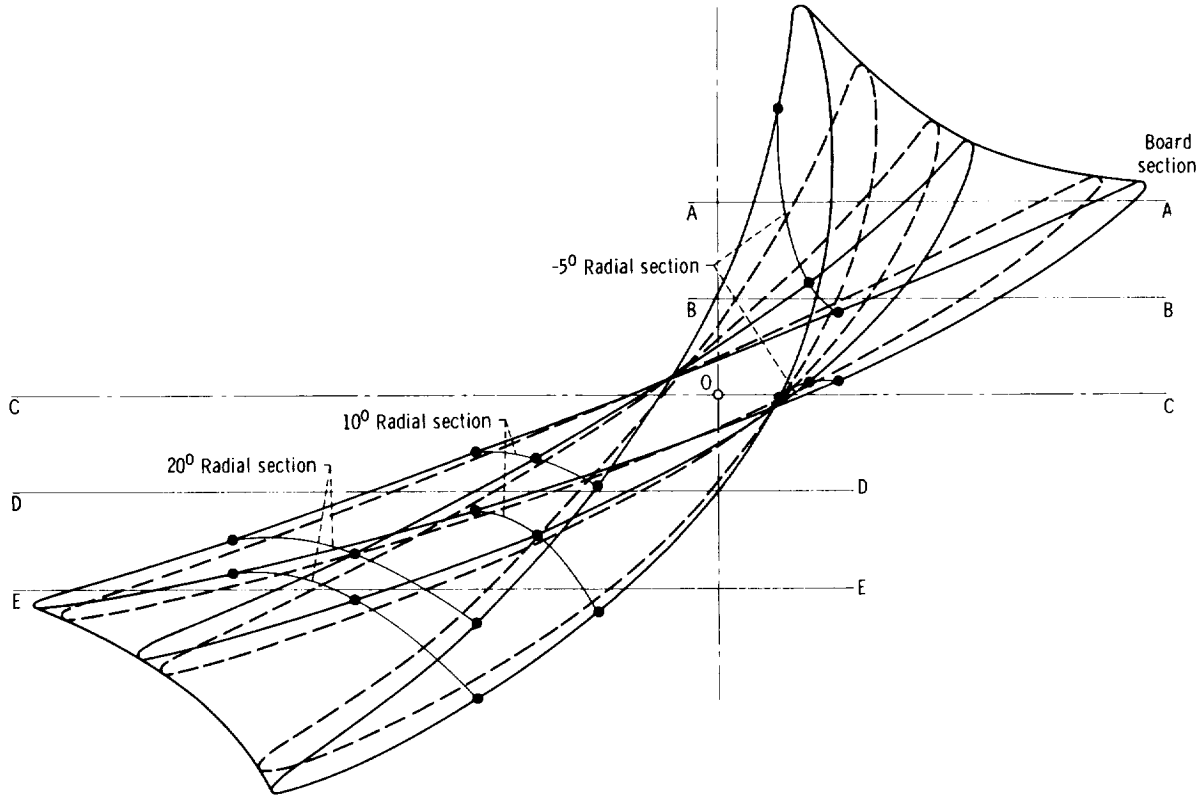

Figure 3-30.—Stacked view of cylindrical blade sections from figures 3-6, 3-8, and 3-29. Dashed lines indicate approximate sections, 0.1 r removed from r_o, 3/4 r_o, and 1/2 r_o sections (solid lines), derived by inlet and discharge flow angles only.

$$n_\sigma = \frac{nQ^{1/2}}{(\sigma_f/\rho_f)^{3/4}} \tag{1-66}$$

to the stress parameters

$$\frac{\rho_f w^2}{2\sigma_f} = \frac{q}{C_L}\frac{m_s}{b^2 l} \tag{1-113}$$

and

$$\frac{\rho_f U_o^2}{2\sigma_f} = q\frac{U_o^2}{C_L w^2}\frac{m_s}{b^2 l} \tag{1-114}$$

where the subscript f denotes fluid, w is the fluid velocity relative to the blade, related to the blade force by the lift coefficient C_L (i.e., w_1 is used with $C_{L,1}$, and w_∞ with $C_{L,\infty}$), m_s is the section modulus of the blade root section, referred to an axis normal to the resultant blade force, b is the blade span (the radial blade length), and l is the chord length. The constant q is 2 for blades cantilevered from the root section, such as those usually used for axial-flow rotors.

The blade section at half the outside radius, shown in figure 3-8, is considered here to be the root section in the mechanical sense. The scheme for determining the section moment of inertia and thereby the section modulus m_s, shown in figure 3-31, is to use a bending axis parallel to the baseline (or chord) of the section. The moment of inertia so determined is probably close to the minimum moment of inertia of this section.

The exact determination of the bending moment acting on this section is somewhat complicated because of the twisted shape of the blade and the nonuniformity of the load distribution. However, an exact determination would not be justified because of the uncertainty of the allowable steady bending stress, which is known to be only part of the total bending stress.

The following simple determination of the number of vanes is based on equation (1-113), which is derived in section 1.3.3.2; it avoids most of the aforementioned complications by using for the

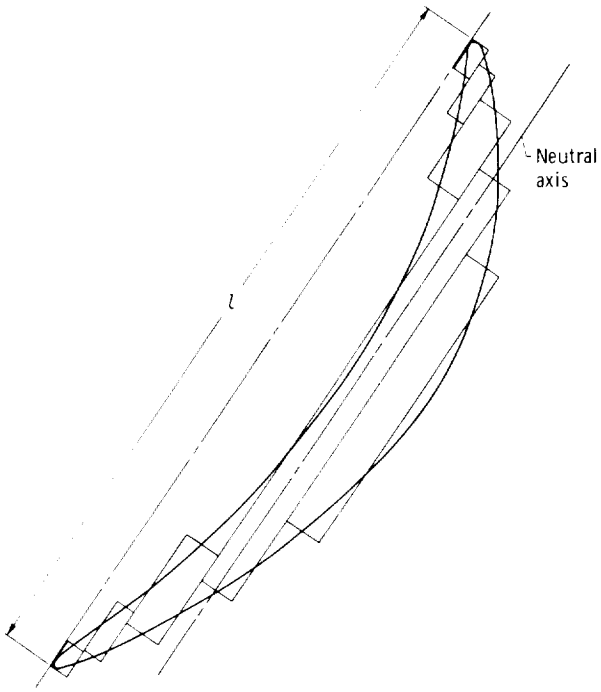

Figure 3-31.—Determination of moment of inertia of blade root section.

relative velocity w and the lift coefficient C_L some reasonable average values of these variables for the entire blade. Furthermore, one may use for the chord length l the chord length of the root section rather than some average value of the entire blade since the length does not vary dramatically with the radial extent of the blade. The use of the root chord length leads to a very desirable simplification.

Calculation of the root section modulus, by using the approximation illustrated in figure 3-31, leads to the following dimensionless expression:

$$\frac{m_s}{l^3} = \frac{1.3}{1000} \tag{3-49}$$

Equation (1-113) can, of course, be converted (with $q=2$) into the form

$$\frac{\rho_f w^2}{2\sigma_f} = \frac{2}{C_L}\frac{m_s}{l^3}\frac{l^2}{b^2} \tag{3-50}$$

For the vane system considered here, one can use the lift coefficient $C_{L,\infty}=0.56$ (see fig. 3-29) of the midsection $r=0.75\ r_o$, which must be associated with the mean relative velocity $w=w_\infty$ of that section. Thus equation (3-50) can be written

$$\frac{\rho_f w_\infty^2}{2\sigma_f} = \frac{2}{0.56}\frac{1.3}{10^3}\frac{l^2}{b^2}$$

For liquids having approximately the density of water, one can use for the fluid density

$$\rho_f = 2\left(\frac{\text{lb}}{\text{ft}^3}\right)\left(\frac{\text{sec}^2}{\text{ft}}\right)$$

The allowable stress of the blade material should be estimated conservatively, since the most destructive vibratory stresses are not included. It is assumed that

$$\sigma_f = 8000\frac{\text{lb}}{\text{in.}^2} = 1.152\times10^6\frac{\text{lb}}{\text{ft}^2} \tag{3-51}$$

Finally, it is assumed that the representative mean relative velocity $w_{\infty,av}$ is 100 feet per second, somewhat higher than the mean relative velocity of the $r=0.75\ r_o$ section in order to carry out the load averaging process in the most probable manner. (This writer would estimate that $w_{\infty,av}$ should be assumed to be between 1.1 and 1.2 times the vectorial mean w_∞ of the $r=0.75\ r_o$ section.) With the foregoing assumptions, one finds

$$\frac{\rho_f w_\infty^2}{2\sigma_f} = \frac{2\times10^4}{2\times1.152\times10^6} = \frac{1}{115.2} \tag{3-52}$$

and, according to equation (3-50),

$$\frac{l^2}{b^2} = \frac{10^3}{115.2}\frac{0.56}{2.6} = 1.86$$

or

$$\frac{l}{b} = 1.37 \tag{3-53}$$

At the root section (fig. 3-8), $l/t=2.155$. Furthermore, according to figure 3-5,

$$b = r_o - r_{root} = r_o - 0.5r_o = 0.5r_o \tag{3-54}$$

and $t=(2\pi r_o)(0.5)/N$, where N is the number of vanes, so that

$$l = 2.155t = 2.155\frac{\pi r_o}{N} \tag{3-55}$$

Substituting equations (3-54) and (3-55) into equation (3-53) yields

$$1.37 = \frac{2.155\,\pi}{0.5\,N}$$

or

$$N = \frac{2.155\,\pi}{1.37 \times 0.5} \approx 10 \qquad (3\text{-}56)$$

Equation (3-56) indicates that 10 vanes satisfy the foregoing assumption about the steady bending stress in the root section of the blade. It must be remembered that, according to the suggestion made in reference 55, an equal vibratory stress should be assumed, which should be combined (at right angles) with the steady-state stress in a modified Goodman diagram (fig. 31 of ref. 55).

In the rocket pump field, much higher fluid velocities than $w_{\infty,av} = 100$ feet per second may be employed. The stresses increase with the square of the velocities, just like the head or pressure differences in the machine.

According to equation (3-50), the fluid-induced bending stress σ_f increases proportionally to the square of the aspect (span-chord) ratio b/l of the blades under otherwise similar conditions, that is, increases proportionally to the square of the number of blades for similar cascade configurations, specifically those with the same solidity of the system and similar blade shapes in cylindrical sections.

The three cylindrical blade sections at r_o, 0.75 r_o, and 0.5 r_o shown as solid lines in figure 3-30, in the relative locations given in that figure, determine the vane surfaces by three points along other sections through the vanes and smooth curves drawn through these points, as further explained later in this section. The sections A-A, B-B, C-C, D-D, and E-E normal to the axis of rotation (so-called board sections) and four radial and axial sections at 20°, 10°, 0°, and -5° from the chosen radial axis (O) of the vane were selected for this purpose. The resulting radial and board sections are shown in figure 3-32.

Three points can always be satisfied by a smooth curve with a single curvature. However, the blade surface so determined may not be the hydrodynamically correct vane shape, since certain hydrodynamic conditions have to be satisfied at cylindrical sections between those at r_o, 0.75 r_o, and 0.5 r_o. The most straightforward way to satisfy these conditions is, of course, to develop hydrodynamically additional cylindrical vane sections between the three sections chosen here. Aside from the additional work involved, this method requires a very consistent choice of design parameters (particularly the solidity l/t and the

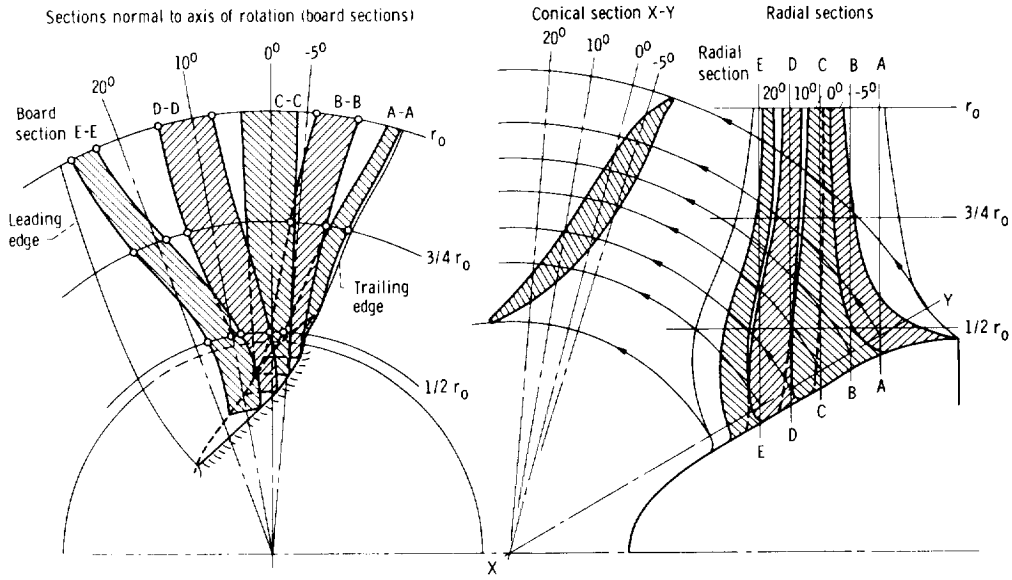

Figure 3-32. – Three-dimensional layout of axial-flow pump rotor.

vane thickness) for the intermediate sections in order to achieve reasonably smooth, three-dimensional vane surfaces. Because this method is difficult and time consuming, an alternative method of vane surface determination is employed here.

From the existing three cylindrical vane sections, three additional vane sections 0.10 r away from these sections are developed by swinging the leading part of the vane about point O (in fig. 3-30) according to the change in the inlet flow angle and the trailing part of the vane about point O according to the change in the discharge flow angle. In other words, the differences between the inlet and discharge flow angles and the vane surface angles along the respective parts of the cylindrical vane sections are kept constant. The inlet and discharge vane edges are assumed to lie on smooth curves drawn through the same vane edges of the existing three vane sections, and the resulting vane sections are corrected to have continuous, smooth contours.

The sections so developed (dashed lines in fig. 3-30) are not treated as equivalent to the three primary vane sections (solid lines), but are used only to obtain an approximation for the tangents to the radial sections and the board sections at the points determined by the three primary cylindrical sections. This approach is particularly helpful for the inward extrapolation of the radial and the board sections from the $r=0.5\ r_o$ section toward the conical hub. However, the continuity and smoothness of the derived radial and board section lines (fig. 3-32) take precedence over the direction of these curves as determined by the auxiliary section shown by dashed lines in figure 3-30.

The extrapolation of the radial sections and board sections toward the hub permits the construction of a conical section X-Y (fig. 3-32), approximately parallel to the hub, placed outside the fillet between the vane and the hub. This section is also a flow section of the vane and must, therefore, have a hydrodynamically acceptable, smooth contour. The direction of its inlet portion is determined by the inlet velocity diagram which can be constructed for the leading edge of this section. The same is true to a somewhat lesser degree for the trailing edge. Attention must be paid to the obvious requirement that all sections through the vane surface must be geometrically compatible with each other.

The contours of the board sections and radial sections in figure 3-32 are called fairing lines, and the geometric process of obtaining smooth vane surfaces by means of these lines is known as fairing. The board sections owe this name to the fact that these sections determine the contours of the boards normal to the axis of rotation from which a wooden rotor of this form, or a pattern (core box) for its production as a casting, can be made.

Since centrifugal forces are radial, such forces generate bending stresses in vane sections in planes normal to the axis of rotation that are not straight and radial, whereas with radial and straight vane sections in such planes, a centrifugal force field generates practically pure tension in the rotor vanes. For this reason, the vane sections A-A, B-B, D-D, and E-E in figure 3-32 are not particularly favorable with respect to centrifugal forces. This is not serious for the liquid-handling rotors considered here because the bending stresses generated by circumferential hydrodynamic forces usually dominate over the centrifugal stresses (see ch.1, sec. 1.3.3.2). For gas-handling rotors, the circumferential and axial extent of the blades is greatly reduced because of the relatively smaller bending loads; this reduction permits much greater aspect ratios b/l, that is, the use of a larger number of radially more slender blades. This change greatly reduces the curvature of blade sections in planes normal to the axis of rotation. This design problem is serious in connection with liquid hydrogen, where bending and centrifugal forces may be of equal importance. This problem is discussed further in section 3.4.

The circumferential overlapping of blades is shown most clearly in the cylindrical sections at r_o (fig. 3-6), 0.75 r_o (fig. 3-29), and 0.5 r_o (fig. 3-8).

3.3.2 Hydrodynamic Effects of Inclination of Vanes Against Radial Direction

The vane or blade layout described in section 3.3.1 is based on the assumption that the stacking axis O of the vane, shown in figure 3-30, is straight, radial, and normal to the axial direction. Since this axis is chosen to coincide with the centers of vane loading, this geometric restriction causes the vane forces to have approximately the circumferential and axial directions, that is, the vane forces have no significant radial component. Thus the vanes have at most only minor effects on the meridional velocity distribution as far as irrotational flow is concerned.

This section discusses effects of departures from this geometric restriction, that is, the effects of an inclination of the vane against the radial direction.

The geometric effect of this inclination of the blade axis O is relatively easy to describe. If this axis is inclined and conceivably deformed to become a simple curve, all cylindrical vane sections are displaced in the circumferential and axial directions as long as point O, where this axis pierces each cylindrical section, retains its position relative to the vane section, and the vane section does not change its orientation relative to the axial and circumferential directions. The board sections and radial sections, of course, change according to the shifting of the cylindrical sections.

However, the inclination of the axis through the centers of pressure of the various cylindrical vane sections affects the flow, as indicated in section 2.7.6, because this axis of the vane action is a bound vortex line (explained in sec. 2.7.6). In the present case, the entire vane action is represented by one vortex line, the axis of the vane, whereas, in section 2.7.6, the vane action is represented by a number of bound vortex lines to obtain a more general representation of the true physical conditions.

Figure 3-33 is an attempt to represent the action of an inclined vane in an axial-flow system by such a single vortex line. The same scheme could also represent part of the vane action, as described in section 2.7.6, but this refinement is not considered here.

Somewhat arbitrarily the inclination of the vane is here assumed to fall approximately within the plane of the vane, although it is recognized fully that a turbomachinery vane is not a plane but more nearly a helical surface. Inclination in the direction described may properly be called sweep, an analogy to the sweep of airplane wings. An inclination normal to the plane of the vane is called tilt. Its hydrodynamic effects are also covered by the considerations in the paragraphs that follow, and its mechanical significance is discussed at the end of this section.

Figure 3-33 shows that, instead of being radial and normal to the axis of rotation, as is line AB, the centerline XY of the vane is inclined against the line AB by an angle of skew λ, as seen in a plane normal to the axis of rotation (sketch at left in fig. 3-33), and by an angle of rake φ, as seen in an axial and radial plane (sketch at lower right in fig. 3-33). As a consequence, the bound vane vorticity which is parallel to the inclined centerline of the vane has three components: the radial component ζ_r, representing the usual vane vorticity, that is, the vane turning action seen in coaxial, cylindrical surfaces such as section N-M with radius r (sketch at upper right in fig. 3-33), the axial component ζ_z, representing the vane vorticity seen in planes normal to the axis of rotation (sketch at left in fig.

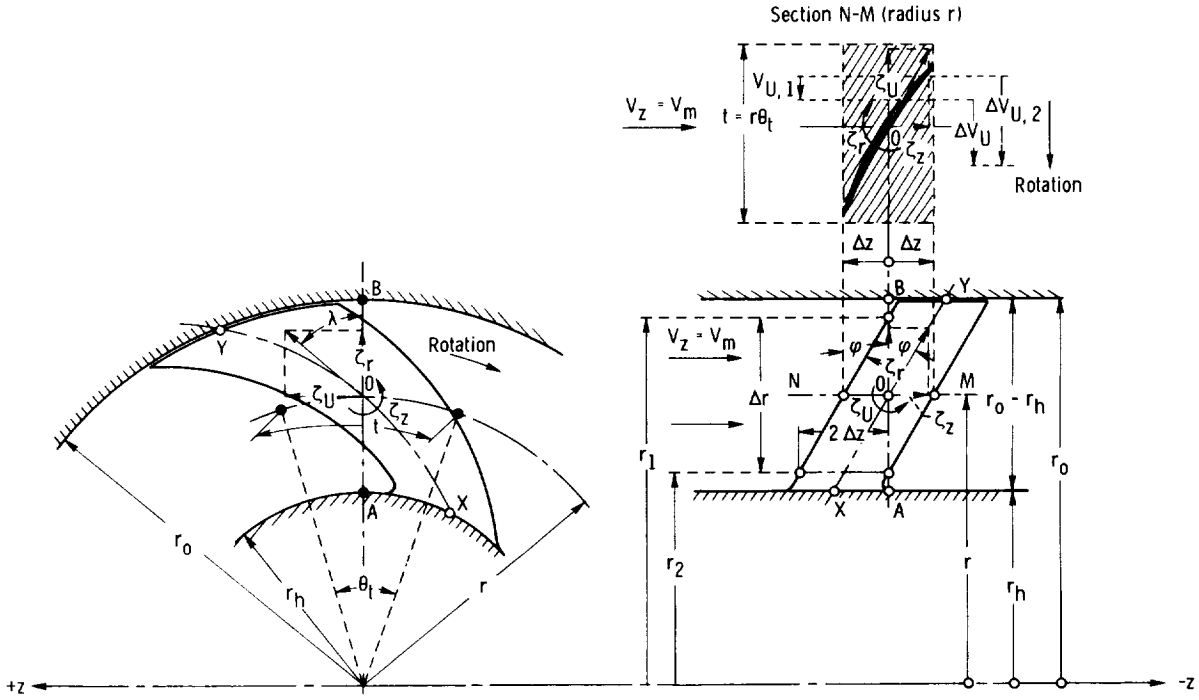

Figure 3-33. – Pump rotor vane with backward skew λ and rake φ.

3-33), and the circumferential component ζ_U, representing the vane vorticity seen in an axial and radial plane (sketch at lower right in fig. 3-33).

The radial component ζ_r is the vane vorticity that one is accustomed to dealing with in any axial-flow vane system, including the case of zero skew and rake. It is related to the change in angular momentum across the vane system seen in the cylindrical section with radius r according to equations (2-A-31) of appendix 2-A:

$$\zeta_r = \frac{\partial V_U}{\partial z} - \frac{\partial V_z}{r\,\partial\theta}$$

where the x-direction of equations (2-A-31) is here assumed to be circumferential, so that $dx = r\,d\theta$, and the y-direction of equations (2-A-31) is now the radial direction. For reasons of axial symmetry, $\partial V_z / r\,d\theta = 0$, so that

$$\zeta_r = \frac{\partial V_U}{\partial z} \tag{3-57}$$

An average value of ζ_r is by definition constant over any axial distance $2\Delta z$ over which the vane action is assumed to take place (say the axial extent of the vane system). Hence

$$\zeta_r\, 2\Delta z = \Delta V_U = V_{U,2} - V_{U,1} \tag{3-58}$$

or for axial flow with $r = \text{constant}$,

$$\zeta_r\, 2\Delta z\, r = r\,\Delta V_U = r(V_{U,2} - V_{U,1}) \tag{3-59}$$

which is the familiar change in angular momentum appearing in Euler's turbomachinery momentum equation (see sec. 2.3).

The axial vorticity component ζ_z has an almost trivially simple significance, which becomes immediately clear by traversing the inclined vane system radially from B to A. At B, that is, in front of the vane system, the angular momentum is $V_{U,1,o}\, r_o$, and at A, behind the vane system, it is $V_{U,2,h}\, r_h$. According to equation (2-A-29) of appendix 2-A,

$$\zeta_z = \frac{1}{r}\,\frac{\partial(rV_U)}{\partial r}$$

and, if ζ_z is assumed to be a constant, average vorticity over the radial extent of the vane system Δr along the plane AB,

$$\zeta_z r_{av}\,\Delta r = \Delta(rV_U) = r_2 V_{U,2} - r_1 V_{U,1} \tag{3-60}$$

In order to have the bound vane vorticity with the components ζ_r, ζ_z, and ζ_U be the only vorticity considered, one must assume the flow in front of as well as behind the vane system to be irrotational, that is,

$$\left.\begin{aligned} r_1 V_{U,1} &= \text{constant} = rV_{U,1} \\ r_2 V_{U,2} &= \text{constant} = rV_{U,2} \end{aligned}\right\} \tag{3-61}$$

Furthermore it is reasonable to assume $r_{av} = r$, that is, r as shown in figure 3-33 is an average of r_1 and r_2. With the last conclusion and equations (3-61), equation (3-60) can be written in the form

$$\zeta_z \Delta r = V_{U,2} - V_{U,1} \tag{3-62}$$

Dividing equations (3-58) and (3-62) and considering that, according to figure 3-33, $\zeta_z/\zeta_r = \tan\varphi = 2\Delta z/\Delta r$ (approximately), one sees that equations (3-58) and (3-62) are completely equivalent, so that the introduction of the axial vorticity component does not express any new facts beyond those expressed by the usual turbomachinery equations when applied to a vane system inclined against a plane AB normal to the axis of rotation by the rake angle φ.

The situation is different with respect to the circumferential inclination of the vanes, called skew. With skew, the circumferential vorticity component ζ_U is normal to the radial and axial plane and thus introduces vorticity, that is, departures from the potential flow pattern, into the meridional flow. For example, the meridional velocity distribution between a cylindrical hub and a coaxial, cylindrical outer shell is not uniform under the influence of skewed (i.e., circumferentially inclined) vanes.

It is evident from figure 3-33 that the skew-induced vorticity of the meridional flow is ζ_U

$= \zeta_r \tan \lambda$. This vorticity extends over the circumferential projection of the vanes, as shown in the sketch at the right in figure 3-33. For the axial symmetry assumed here, every vortex line of this flow field is a circle about the axis of rotation of the vane system. The flow generated by this system of ring vortices constitutes the skew-induced departure of the meridional flow from a straight and uniform axial flow between two coaxial cylinders with the radii r_o and r_h. An exact determination of this departure from the potential meridional flow would be too complex for practical procedures of preliminary design, not only because there are difficulties in solving a flow problem with vorticity prescribed over a part of the flow field, but also because the flow field to be determined is not plane but symmetrically distributed about an axis of revolution with coaxial, cylindrical flow boundaries.

One simplification is suggested immediately from the previously introduced model describing the vane action by a single bound vortex located at the axis of the vane. When combining this model with the assumption of axial symmetry, one arrives at the assumption that the vane action is concentrated at a conical vortex sheet XY in figure 3-33 (sketch at lower right).

Even this model still poses a formidable flow problem, namely, that of the flow induced by a conical, or perhaps flat, vortex sheet normal to the axis of rotation, in which the vortex lines are concentric circles about the axis of rotation and the flow field is bounded by two coaxial cylinders. No general solution of this problem is known to this writer. Even if such a solution were available, its increased number of independent variables (rake angle φ and radius ratio of r_o/r_h) would make its application unduly complicated.

In view of this situation, the design engineer has no other choice but to construct his own model to obtain an approximation which is sufficiently simple for design purposes.

The first simplification to be introduced is the elimination of rake, that is, the elimination of the axial inclination of the vanes shown by the angle φ in the sketch at the lower right in figure 3-33. By this simplification, the vortex sheet formed by the circumferential blade vorticity component ζ_U becomes a plane normal to the axis of rotation. This change may not be too serious because the effect of rake can probably be approximated by subjecting the flow field obtained with the plane vortex sheet to an axial shear deformation equal to the rake of the actual blade. The blade configuration without rake is shown in figure 3-34.

A more severe simplification is obtained by converting the actual, axisymmetric arrangement to a plane arrangement, in which the concentric, circular vortex lines of ζ_U are replaced by parallel, straight vortex lines normal to the plane of the meridional flow. Thereby the effect of ζ_U on the flow along the inner boundary with radius r_h becomes oppositely equal to its effect on the flow along the outer boundary with radius r_o. According to figure 3-33, this situation does not conform to the actual one. However, the simplification achieved by this approximation is sufficient to justify its use for the solution of the design problems. An approximation of the effect of the actual, axially symmetric arrangement is described later in this section.

The scheme for the solution of the flow problem so reduced is shown diagrammatically in figure 3-35. The vortex sheet of ζ_U appears as the vertical line AB, and the radial distance $r_o - r_h$ between the

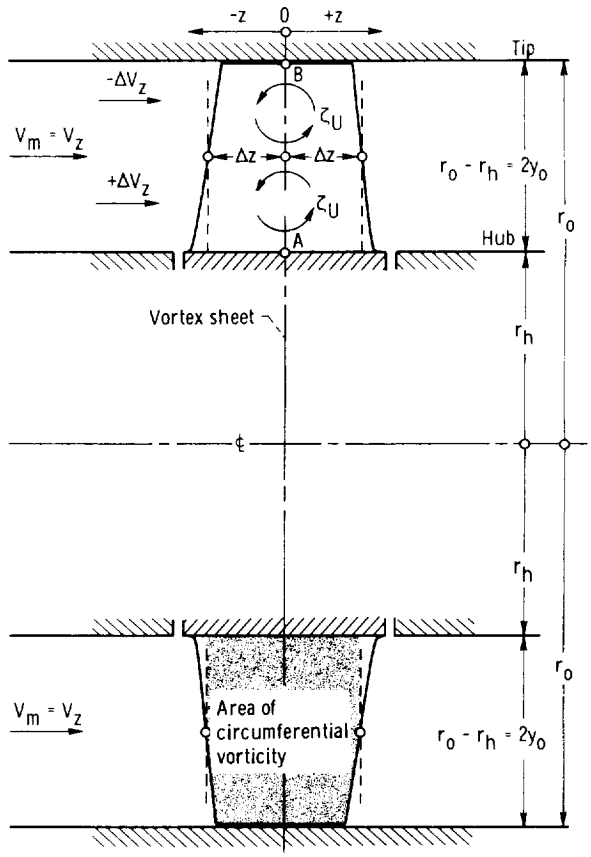

Figure 3-34. – Circumferential vorticity in vane system with skew but without rake.

flow boundaries is designated $2y_o$. The centerline of this flow space is the zero axis of the coordinate y normal to the vortex sheet. This axis is parallel to the assumed flow boundaries.

Two cross-stream coordinates x and y, normal to the axial coordinate z, are used. The coordinate x describes the location of the vortices distributed along the central plane $z=0$, which generate the flow field considered here. The coordinate y describes the (radial) locations at which the axial velocities V_z, generated by the vortex sheet at $z=0$, are determined and plotted.

The lines $x=y=+y_o=$constant and $x=y=-y_o=$constant can be made flow boundaries by reflecting the vorticity along the line AB in these boundaries. This means that the vortices along the line AB must be reflected by oppositely equal vortices along the continuations of the line AB from $x=+y_o$ to $x=+3y_o$ and from $x=-y_o$ to $x=-3y_o$. This reflection is repeated at $x=\pm 3y_o$, $x=\pm 5y_o$, $x=\pm 7y_o$, and so on.

At every point x along the line AB and its continuations, there exists an elementary vortex with the circulation

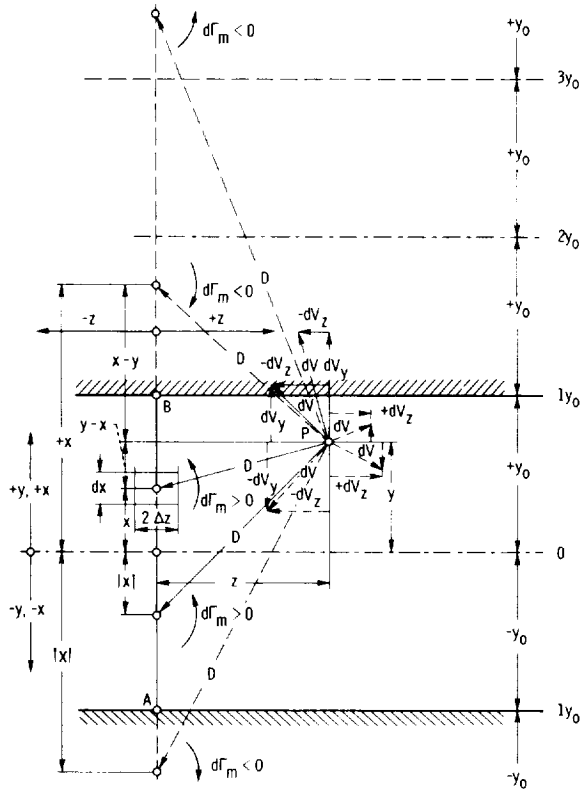

Figure 3-35. – Scheme for deriving changes in meridional velocities from vorticity of meridional flow.

$$d\Gamma_m = \pm\zeta_U\, 2\Delta z\, dx \tag{3-63}$$

where alternating directions of rotation are those indicated in figure 3-36. The circulations between A and B are assumed to be positive. The axial extent $2\Delta z$ of the region having the vorticity ζ_U is here assumed to be negligibly small; this assumption has only a secondary effect on the results obtained outside of the vorticity region with the small extent $2\Delta z$, because Δz cancels out of the final relations.

According to the sketch at the upper right in figure 3-33, it is clear that the circulation of one vane corresponding to the radial vorticity component ζ_r is

$$\Gamma_U = (V_{U,2} - V_{U,1})t = \Delta V_U\, r\theta_t \tag{3-64}$$

and its relation to the radial vorticity component obeys the law that the circulation is equal to the vorticity times the area inside the contour of circulation (see appendix 2-A):

$$\Gamma_U = \zeta_r\, 2\Delta z\, r\theta_t \tag{3-65}$$

As already proved from figure 3-33,

$$\zeta_U = \zeta_r \tan\lambda \tag{3-66}$$

Combining equations (3-64) to (3-66) with equation (3-63) leads to

$$d\Gamma_m = \pm\zeta_r \tan\lambda\, 2\Delta z\, dx$$

and

$$d\Gamma_m = \pm\Delta V_U \tan\lambda\, dx \tag{3-67}$$

where the plus or minus sign is determined by the alternating direction of the elementary circulation, which is assumed to be positive between A and B, that is, for $|x|<|y_o|$.

The determination of the velocity vector induced by the vortex sheet AB (and its reflections) at any arbitrary point P between $y=+y_o$ and $y=-y_o$ is illustrated in figure 3-35. Point P has the coordinates y and z from the centerline $y=0$ and the vortex sheet AB.

The elementary velocity vector dV induced at point P by an elementary vortex with the circulation $d\Gamma_m$ is obviously

$$dV = \frac{d\Gamma_m}{2\pi D} \tag{3-68}$$

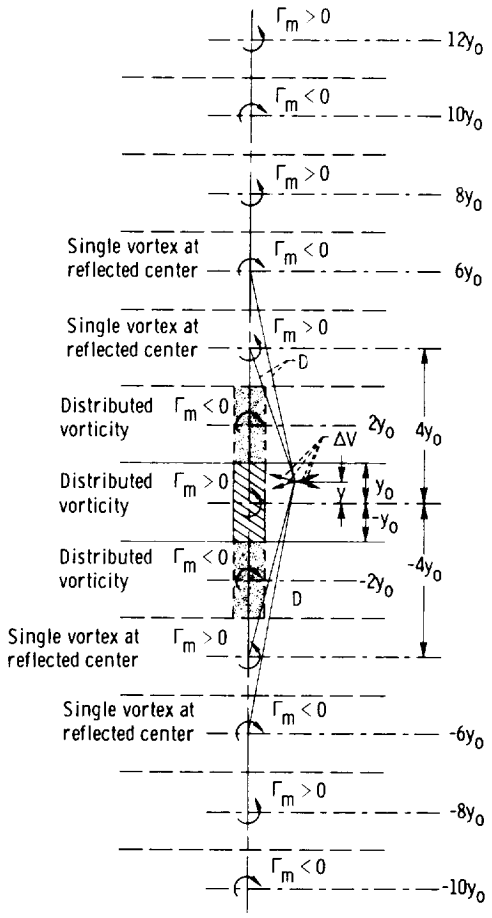

Figure 3-36. – Simplified solution for determination of vorticity-induced meridional velocities.

where D is the distance of point P from the elementary vortex, located along the vortex sheet AB or its reflections. The vector dV is normal to D and has the direction of the circulation $d\Gamma_m$ (counterclockwise if positive).

From figure 3-35, the axial component of dV is

$$dV_z = dV\,\frac{x-y}{D} \tag{3-69}$$

and the y-component is

$$dV_y = dV\,\frac{z}{D} \tag{3-70}$$

which cancels (by virtue of the reflections) at the boundaries $y = \pm y_o$, as required. Only the axial velocity component V_z is considered in the following, because it is of primary importance for the effect of vane skew on the meridional flow.

Combining equations (3-68) and (3-69) leads to

$$dV_z = \frac{d\Gamma_m(x-y)}{2\pi D^2}$$

Evidently

$$D^2 = (x-y)^2 + z^2$$

Therefore using equation (3-67) also gives

$$dV_z = \pm\,\frac{\Delta V_U \tan\lambda}{2\pi}\,\frac{(x-y)\,dx}{(x-y)^2+z^2} \tag{3-71}$$

The integration is carried out separately for the steps from $x=-y_o$ to $x=+y_o$, from $x=+y_o$ to $x=+3y_o$, from $x=-3y_o$ to $x=-y_o$, and so on, because of the alternating signs (direction of circulation) in these various sections. Therefore the total effect of the vortex sheet (and reflections) on the meridional velocity V_z (see fig. 3-36) is

$$\Delta V_z = \frac{\Delta V_U \tan\lambda}{2\pi}\left[\int_{-y_o}^{y_o}\frac{(x-y)dx}{(x-y)^2+z^2} - \int_{y_o}^{3y_o}\frac{(x-y)dx}{(x-y)^2+z^2} + \int_{3y_o}^{5y_o}\frac{(x-y)dx}{(x-y)^2+z^2} - \int_{-3y_o}^{-y_o}\frac{(x-y)dx}{(x-y)^2+z^2} + \int_{-5y_o}^{-3y_o}\frac{(x-y)dx}{(x-y)^2+z^2}\cdots\right] \tag{3-72}$$

This equation can be written in the form

$$\Delta V_z = \lim_{p\to\infty}\frac{\Delta V_U \tan\lambda}{2\pi} \times \sum_{-p}^{p}(-1)^{|r|}\int_{(2r-1)y_o}^{(2r+1)y_o}\frac{(x-y)dx}{(x-y)^2+z^2} \tag{3-72a}$$

where p and r are integers, such that

$$-p \le r \le p$$

and $2ry_o$ is the distance of the center of the vortex sheet AB and of its reflections from the origin $z=y=0$; p marks the extent of the approximation used.

Fortunately the integral of $(x-y)dx/[(x-y)^2+z^2]$ can be found in standard tables of integrals. In section 2 (Mathematics) of Mark's Standard Handbook for Mechanical Engineers (ref. 58), this integral appears in the form

$$\int \frac{(m+nx)dx}{a+2bx+cx^2} = \frac{n}{2c}\ln(a+2bx+cx^2) + \frac{mc-nb}{c}\int \frac{dx}{a+2bx+cx^2}$$

The comparison with the previously mentioned integrand shows that, in the present case, $m=-y$, $n=1$, $a=y^2+z^2$, $b=-y$, and $c=1$, so that $n/2c = 1/2$ and $mc-nb=-y+y=0$. Thus the present integration is simplified to

$$\int \frac{(x-y)dx}{(x-y)^2+z^2} = \frac{1}{2}\ln\left[(x-y)^2+z^2\right] \tag{3-73}$$

where the limits of integration are those given in equation (3-72), and the simplification $y_o=1$ is used.

In carrying out this integration, one finds that, for $|x|>|3y_o|$, the solution for distributed vorticity can hardly be distinguished from that for a single vortex in the center of every interval with the width $2y_o$ above the previously mentioned limits of $|x|$. The validity of this approximation is assured by using the solution expressed by equation (3-73) in most cases up to $|x|=|5y_o|$, except for $z=0$, where it is carried out to $|x|=|7y_o|$.

The circulation of the single vortex located at the center of every step of the length $\Delta x=2y_o$ is, according to equation (2-A-27) of appendix 2-A,

$$\Gamma_1 = \zeta_U\, 2\Delta z\, 2y_o \tag{3-74}$$

where $\zeta_U=\zeta_r \tan\lambda$, as given in figure 3-33.

The circulation per blade is, according to the circumferential section N-M of figure 3-33,

$$\Gamma_U=\zeta_r\, 2\Delta z\, t=\Delta V_U\, t$$

so that $\zeta_r=\Delta V_U/2\Delta z$. Therefore, according to figure 3-33,

$$\zeta_U=\frac{\Delta V_U}{2\Delta z}\tan\lambda$$

With the previously used simplification $y_o=1$, the circulation of every discrete vortex at the centers of the steps $2y_o$ is, in accordance with equation (3-74),

$$|\Gamma_1| = 2\Delta V_U \tan\lambda \tag{3-75}$$

The z-component of the velocity induced at y and z by every one of these vortices can be derived from figure 3-37:

$$\Delta V_z = \frac{\Gamma_1}{2\pi D}\frac{x-y}{D} = \frac{\Gamma_1}{2\pi}\frac{x-y}{(x-y)^2+z^2} \tag{3-76}$$

where the alternating directions of Γ_1 must be taken into account. Using equation (3-75) also, one obtains for the z-components of the velocities induced by all discrete vortices along the axis $z=0$

$$\frac{\pi\Delta V_z}{\Delta V_U\tan\lambda} = \frac{-y}{y^2+z^2} - \frac{2y_o-y}{(2y_o-y)^2+z^2} - \frac{-2y_o-y}{(-2y_o-y)^2+z^2} + \frac{4y_o-y}{(4y_o-y)^2+z^2} + \frac{-4y_o-y}{(-4y_o-y)^2+z^2}\ldots \tag{3-77}$$

This equation can be written in the form

$$\frac{\pi\Delta V_z}{\Delta V_U\tan\lambda} = \lim_{p\to\infty}\sum_{-p}^{p}(-1)^{|k|}\times\frac{2ky_o-y}{(2ky_o-y)^2+z^2} \tag{3-77a}$$

where p and k are integers, such that

$$-p\le k\le p$$

and $2ky_o$ is the distance of each vortex (approximating a vortex sheet of length $2y_o$) from the origin $z=y=0$. As previously, p marks the extent of the approximation used, and where the summation is to be carried out for the vortices located at $x=(0)$, $(\pm 2y_o)$, $(\pm 4y_o)$, $\pm 6y_o$, $\pm 8y_o,\ldots\pm 2ky_o$, $\ldots\pm 2py_o$. The parentheses indicate that in these steps the discrete vortex solution is usually not used to replace the solution with distributed vorticity. The direction of vorticity

is assumed to be positive between A and B in figures 3-35 and 3-37 and to alternate after every step $\Delta x = \pm 2y_o$.

The complete solution described here obviously has the form

$$\frac{2\pi \Delta V_z}{\Delta V_U \tan \lambda} = \sum_{-p}^{p} (-1)^{|r|} \int_{(2r-1)y_o}^{(2r+1)y_o} \frac{(x-y)dx}{(x-y)^2 + z^2}$$

$$+2 \sum_{k} (-1)^{|k|} \frac{2ky_o - y}{(2ky_o - y)^2 + z^2} \qquad (3\text{-}78)$$

where r, k, and p are integers with the same meanings as given after equation (3-72a) and (3-77a). The y values of interest here are those of the physical flow field between $y = -y_o$ and $y = +y_o$, and z continues to be the axial distance from the vortex sheet. The fact that z appears only at its second power conforms to the physically obvious fact that the axial flow field generated by the vortex sheet is the same on both sides of the vortex sheet.

The nature of the numerical solution obtained from equation (3-78) is best described by numerical example. Using $z = 0.5$ and $y = +y_o = 1$ for this purpose, one obtains the following solutions of equation (3-78) as a function of the number of terms used in the second summation: For $x = -5$ to $+5$ (i.e., $-2 \leq p \leq 2$), the first term gives -1.8932. The following table gives the values the parameter $2\pi \Delta V_z / \Delta V_U \tan \lambda$ attains when the second term of equation (3-78) is terminated with the listed values:

$x = +6\, y_o$	-2.290
$x = -6\, y_o$	$\underline{-2.004}$
$x = +8\, y_o$	-1.721
$x = -8\, y_o$	$\underline{-1.942}$
$x = +10\, y_o$	-2.164
$x = -10\, y_o$	$\underline{-1.982}$
$x = +12\, y_o$	-1.801
$x = -12\, y_o$	$\underline{-1.954}$

The results oscillate up and down in steps of two successive summations. This characteristic exists

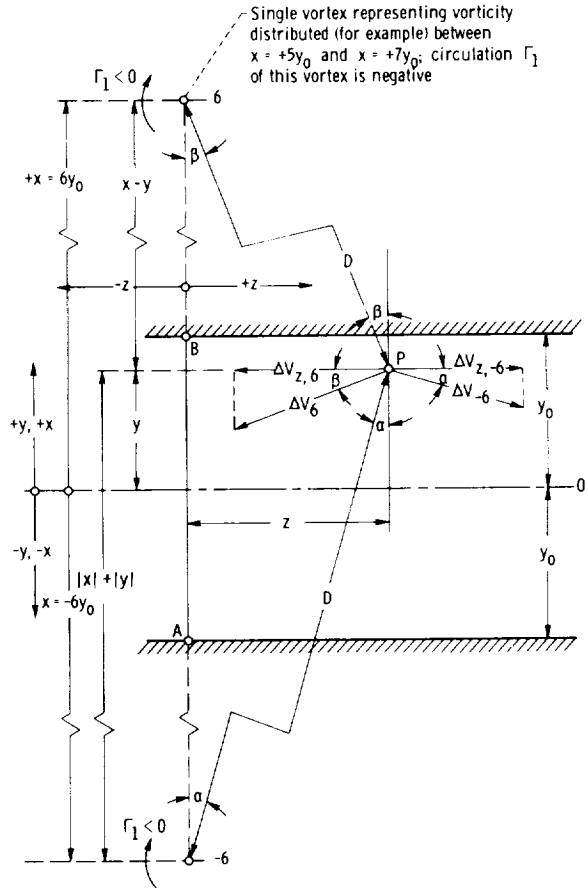

Figure 3-37. – Scheme for deriving changes in meridional velocity from single vortices at centers of reflected flow fields. Shown as an example are velocity changes induced by vortices located at $x = +6y_o$ and $x = -6y_o$, which have negative circulations.

with all y and z values investigated. While this characteristic casts some doubt on the convergence of the second summation in equation (3-78), it is reasonable to assume on physical grounds that there is a solution. The first value after a reversal in the up and down trend of the successive summations (underlined) approaches an optimum approximation of the correct solution. In all cases, the value obtained after adding (algebraically) the effect of the vortex at $x = -12\, y_o$ is used as the solution of equation (3-78).

The solutions so obtained are plotted in figure 3-38 as functions of the position y across the flow field for various values of the distance z from the vortex sheet.

The same solutions are represented by the solid curves in figure 3-39 as functions of the distance z from the vortex sheet for $y = y_o$ and $y = y_o/2$. Figure 3-39 also shows as long- and short-dash

curves the solutions obtained in the same manner by using a single vortex in the center of the physical flow field between $-y_o$ and $+y_o$ and at the centers of all reflections of the flow field in its straight boundaries. This is obviously the flow field of an infinite, straight row of equally spaced vortices with alternating directions of circulation. This flow field is well known, but figure 3-39 shows that it does not constitute an adequate approximation of the flow field generated by a continuous, straight vortex sheet between and normal to two straight and parallel boundaries, which is described by the solid curves.

The last major step in this section is that from an approximation of a plane, two-dimensional vortex flow field to an approximation of the real, three-dimensional, axisymmetric flow field generated by the trailing vortex sheet shed from a vane system with skew (shown in fig. 3-33). As previously, the effect of rake (angle φ in fig. 3-33) is disregarded, so that the axial flow between two coaxial, cylindrical stream surfaces (flow boundaries) is now under the influence of a plane vortex sheet normal to the axis of rotation, with circular vortex lines coaxial with the cylindrical flow boundaries.

As already stated, this flow problem is too complex for the simple design considerations used in this compendium. Instead the plane-flow solution established in the first part of this section is corrected by means of the condition of continuity of the axial flow V_z between two coaxial surfaces, as shown diagrammatically in figure 3-40. The hub surface has the radius r_h, and the blade tip surface the radius r_o. In the notation of the previous plane-flow considerations, figure 3-40 shows that $r_o - r_h = 2\,y_o$.

The condition of continuity of the axial flow in the space of revolution between radius r_h and radius r_o is satisfied by the physical condition that the vorticity along the vortex sheet normal to the axis of revolution cannot generate any net axial flow, that is,

$$\int_{r_h}^{r_o} r\,dr\,\Delta V_z(r) = 0 \tag{3-79}$$

or the rate of flow from left to right in figure 3-40 is oppositely equal to the rate of flow from right to left. This condition can be satisfied approximately by the equation

$$2\pi r_{c,o} \int_C^A \Delta V_z\,dr = -2\pi r_{c,h} \int_B^C \Delta V_z\,dr \tag{3-80}$$

where an axial line $r_{c,o}$ = constant divides the flow diagram DAC into two equal areas, and an axial line $r_{c,h}$ = constant divides the flow diagram EBC into two equal areas. This approximation is considered sufficient, because in order to use the previously derived, plane-flow velocity distribution across the stream, one must assume that the velocity distribution curve DCE in figure 3-40 has the same form as shown in figure 3-38 for the same axial distance z/y_o from the vortex sheet. This assumption is, of course, not exactly true in the same axisymmetric case.

The condition of continuity for the vorticity-induced flow in the space of revolution can be satisfied by varying $r_{o,o}$, the location of the point C, where $V_z = 0$, until equation (3-80) is fulfilled. This process of trial and error can be simplified by using the approximation

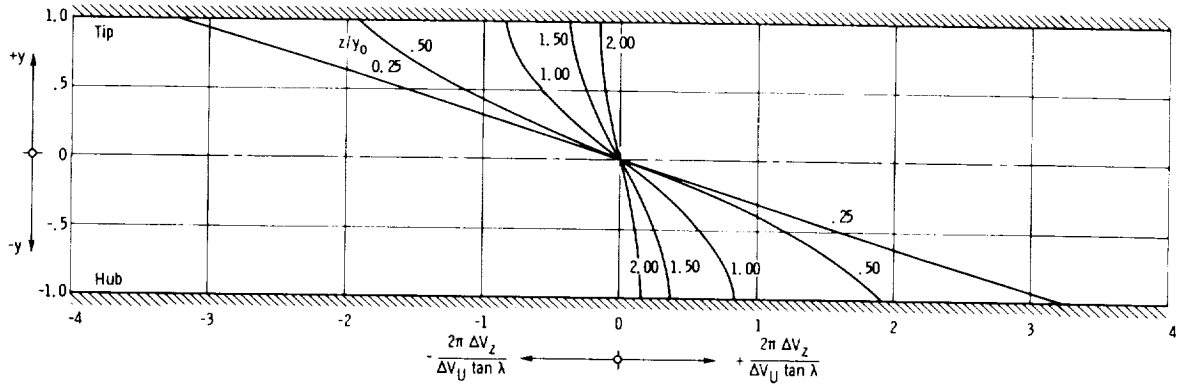

Figure 3-38. – Velocities normal to straight vortex sheet between two straight and parallel flow boundaries at $+y_o$ and $-y_o$. Vortex sheet is normal to boundaries, vorticity is counterclockwise, and z is distance from vortex sheet.

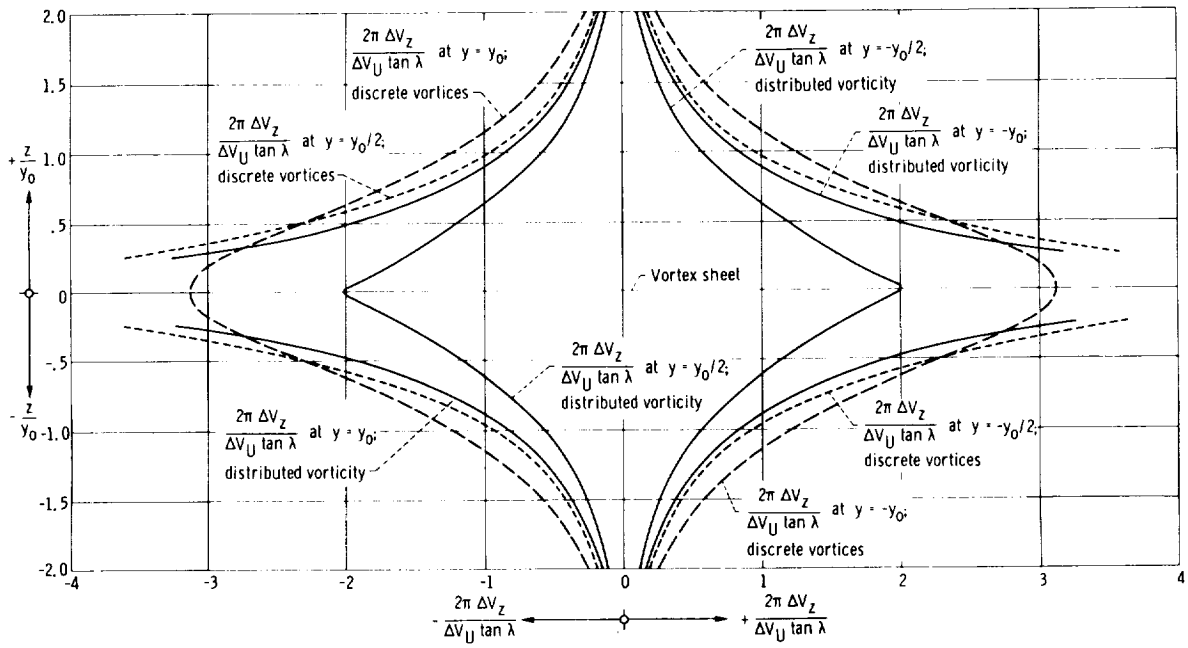

Figure 3-39. – Velocities normal to straight vortex sheet between two straight and parallel boundaries normal to vortex sheet.

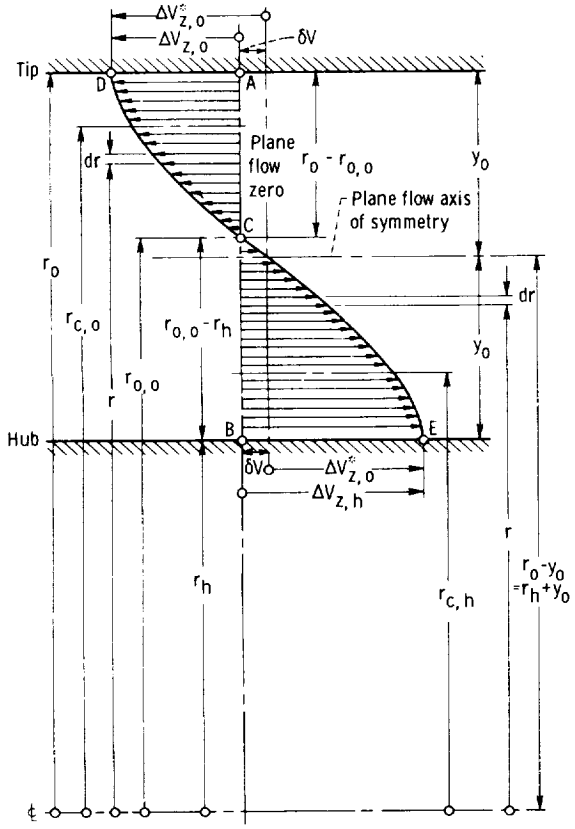

Figure 3-40. – Approximate transformation from plane to axisymmetric flow induced by vortex sheet.

$$\frac{\int_C^A \Delta V_z\, dr}{\int_B^C \Delta V_z\, dr} = \frac{\overline{AD}\times\overline{AC}}{\overline{BE}\times\overline{BC}}$$

$$= \frac{\Delta V_{z,o}(r_o - r_{o,o})}{\Delta V_{z,h}(r_{o,o} - r_h)} = \frac{r_{c,h}}{r_{c,o}} \qquad (3\text{-}81)$$

which assumes (inaccurately) that the curve CD is (relative to AC) geometrically similar to the curve CE (relative to CB). Closer approximations can be found, but are hardly justified in view of other approximations used in this derivation.

It should be evident that the difference between the axisymmetric solution and the plane-flow solution previously derived lies mainly in the fact that, in the axisymmetric solution, the point C, where $\Delta V_z = 0$, does not lie halfway between the inner and the outer flow boundaries, as it does in the plane-flow solution. For the axisymmetric solution,

$$r_o - r_{o,o} < r_{o,o} - r_h \qquad (3\text{-}82)$$

Under the assumptions made here, it follows that

$$\left.\begin{aligned}\Delta V_{z,o} &= (\Delta V^*_{z,o} - \delta V) < \Delta V^*_{z,o} \\ \Delta V_{z,h} &= (\Delta V^*_{z,o} + \delta V) > \Delta V^*_{z,o}\end{aligned}\right\} \qquad (3\text{-}83)$$

where $\Delta V^*_{z,o}$ is the vorticity-induced axial velocity at both flow boundaries obtained by the plane-flow solution.

The inequalities (3-82) and (3-83) express the results of the present, simple approximation of the difference between the (obviously inadequate) plane-flow solution and the present axisymmetric approximation. Inequality (3-82) is probably correct and can be used with confidence. Inequalities (3-83) and equations (3-80) and (3-81) are more questionable, but are the best that can be derived by the simple approximations used in this section. While not accurate, they probably meet the requirements of preliminary design, because they present the most essential characteristics of the axisymmetric flow induced by the trailing vorticity of vanes with backward skew (fig. 3-33). An example of the solutions obtained by this approximation is shown in figures 3-41 and 3-42 for $r_o = 2r_h$. The simplicity of this solution, described previously in connection with figure 3-40, permits the reader to extend this solution to other values of the ratio r_h/r_o. Furthermore this solution approaches the plane-flow solution shown in figures 3-38 and 3-39 as r_h/r_o approaches unity, that is, for very large hub-tip diameter ratios.

Besides the numerical and graphical approximations regarding the effects of either skew or sweep on the meridional flow through turbomachines, one can draw some general conclusions from the foregoing considerations.

For a pump rotor with backward skew, one can conclude from figure 3-33 that the change ΔV_z of the meridional velocity is negative at the outer flow boundary r_o and positive at the inner flow boundary r_h. This situation is favorable for resistance to cavitation, since the blade tips have the highest relative velocity, and it is reduced by a reduction in the meridional velocity. However, the meridional velocity reduction alone also has a major effect on cavitation performance, as expressed by equation (1-42). This is an important reason for using backward skew in pump rotors. For fan or compressor rotors, skew reduces the Mach number of the relative flow normal to the inlet edge (the same effect as with swept airplane wings), but skewing is usually precluded by centrifugal force considerations.

For a hydraulic turbine rotor with the same overall configuration as shown in figure 3-33

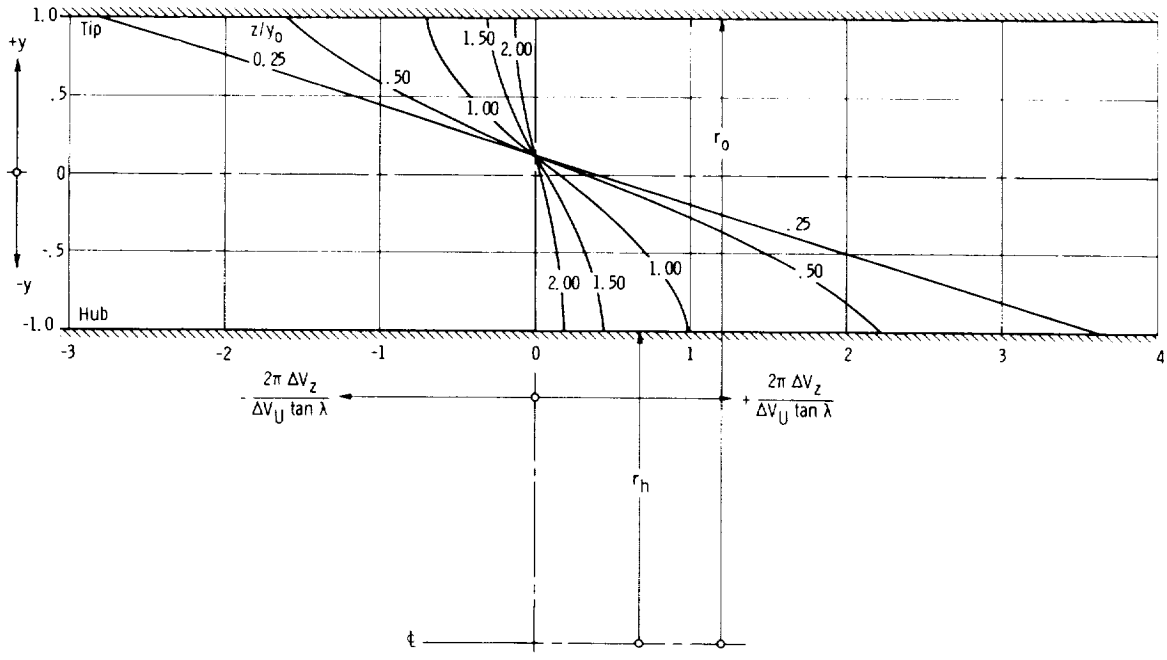

Figure 3-4l. – Approximation of axial velocities in cylindrical space of revolution induced by vortex sheet normal to axis of revolution. Approximately circular vortex lines are coaxial to space of revolution.

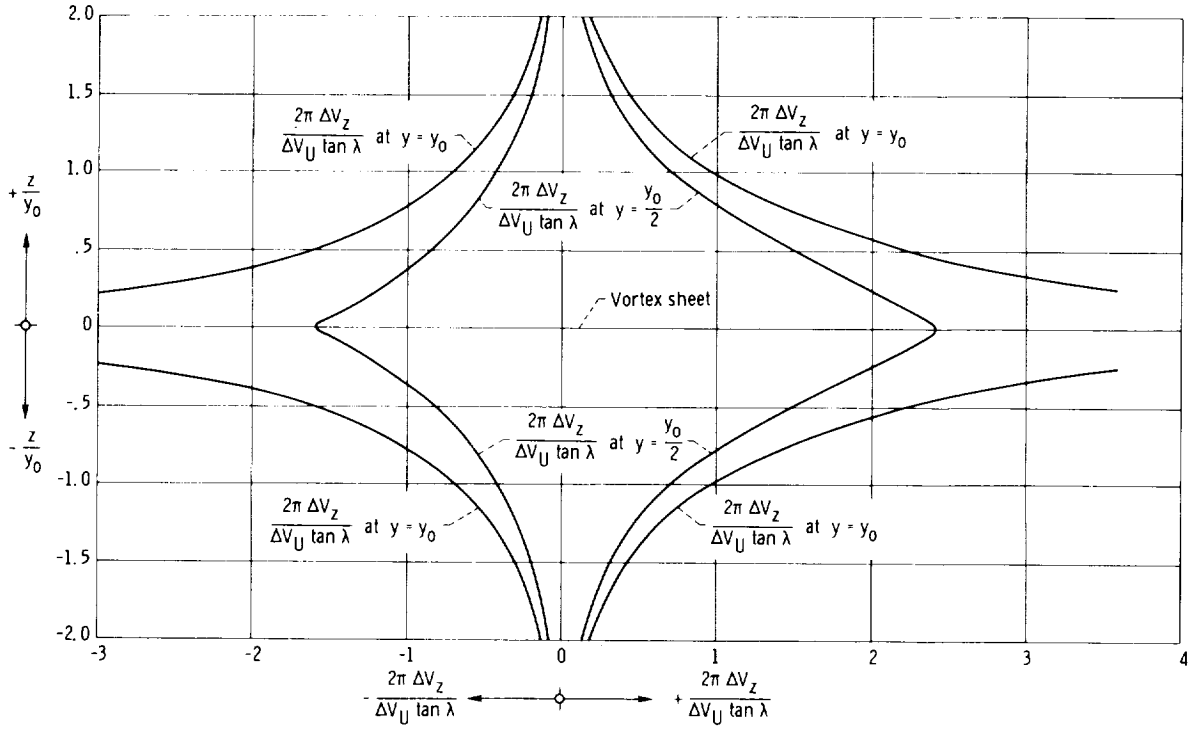

Figure 3-42. – Approximation of vorticity-induced axial velocities in space of revolution shown in figure 3-41 plotted against axial distance z from vortex sheet.

(except for the blade camber) and with the same direction of the meridional flow, the direction of the blade vorticity ζ_r is reversed, since $V_{U,1} > V_{U,2}$. This reverses the direction of the vorticity ζ_U of the meridional flow and thus increases the meridional velocity at the outer flow boundary. The higher meridional velocity is unfavorable for resistance to cavitation. A favorable effect on cavitation resistance can be obtained by designing a turbine rotor with forward skew, that is, in the direction of rotation.

As mentioned previously, figure 3-33 shows a combination of axial and circumferential inclination (rake and skew) such that the resulting inclination (sweep) of the vane falls approximately in the general plane of the vane. One should expect this arrangement to be mechanically favorable with respect to the strength of the vane to resist centrifugal forces. However, the foregoing considerations are definitely not limited to this particular configuration. In fact, in order to simplify the analysis of the effect of circumferential inclination (skew), we have eliminated the geometric consideration of axial inclination (rake). Therefore the vane shown in figure 3-34 must be understood to have only circumferential inclination (skew) as shown in the sketch at the left side in figure 3-33. This gives the skewed vane an inclination normal to its general plane, which is called tilt.

Under the influence of centrifugal forces, tilt introduces a blade bending moment about an axis approximately parallel to that of the minimum section moment of inertia of sections near the blade root. With backward skew, this centrifugal bending moment opposes the hydrodynamic bending moment of a pump blade and may, therefore, have a favorable effect. For a turbine rotor, the hydrodynamic forces have (for the same direction of through flow and of rotation) the opposite direction to that in a pump rotor and, therefore, add to the centrifugal bending stresses. For a turbine rotor, one should, therefore, use either forward skew with little or no rake or backward skew with a rake angle φ larger than that leading to approximately zero tilt, as indicated in figure 3-33.

It should be recognized that with skew (or sweep) the blade is also subjected to a torsional moment whenever the hydrodynamic and the centrifugal bending moments do not cancel each other. This

cancellation of blade bending moments is, therefore, of particular importance for blades with skew.

3.3.3 Design for Small Departures From Strictly Axial Flow in Turbomachines

Moderate departures from a strictly axial direction of the meridional flow exist in many practical cases of axial-flow turbomachinery design, for example, in the case treated in section 3.3.1 (figs. 3-5 and 3-32). There the conical stream surfaces are simply replaced by cylindrical stream surfaces in order to retain the great theoretical and empirical advantages available in the axial-flow field. One can interpret this simplification as a division of the meridional flow into an axial and a radial component, with the hydrodynamic (or gas dynamic) effects of the radial component neglected. If this simplification can be justified, the theory and experience of axial-flow rotors can become available in the mixed-flow machinery field for small departures φ from strictly axial flow (figs. 3-43 and 2-41).

The suggested approximation does not mean that one neglects the changes in distance from the axis of rotation as the flow proceeds along a conical stream surface such as M – N in figure 3-43. At M the vane is properly designed for flow along a cylindrical surface with radius r_M, at N it is designed for flow along a cylindrical surface with radius r_N, and at any intermediate station it is designed for flow along the appropriate cylindrical surface *ZZZ* with radius r_Z. The question is merely whether locally the vane shape can be approximated according to the cylindrical flow at that radius while the meridional flow along the conical stream surface has a radial component

$$V_r = V_m \sin \varphi = V_a \tan \varphi \tag{3-84}$$

and the relative flow has a vorticity (according to eq. (2-103))

$$\zeta_{rel} = -2\omega \sin \varphi \tag{3-85}$$

where ω is the angular velocity of the rotor.

Under the assumption that the radial velocity component V_r is small, it seems reasonable to approximate its direction in planes normal to the axis of rotation in the simplest way possible, which is the one-dimensional assumption that the flow is parallel to the vanes. In other words, the radial flow is assumed to be parallel to vane sections normal to the axis of rotation, such as section A-A in figures 3-43 and 3-44 (a board section). If the vane is a straight, helical surface, such sections are straight and radial, and the radial flow does not have a peripheral velocity component. However, board sections generally are not radial. For example, section A-A of the rotor shown in figures 3-43 and 3-44 is inclined backward by an angle λ, as shown by the sketch at the right in figure 3-43. (The

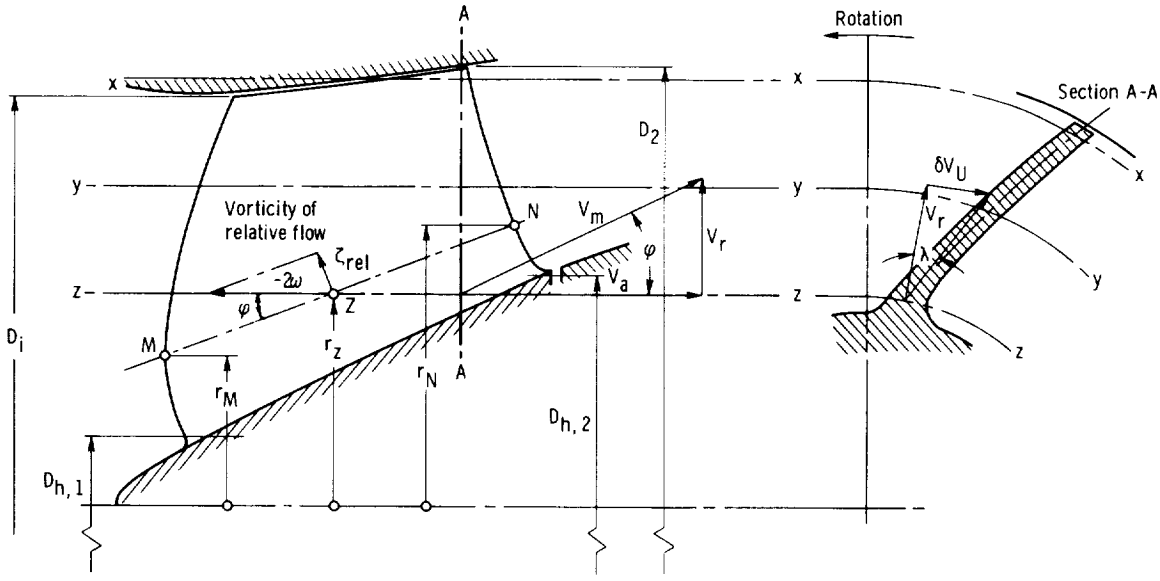

Figure 3-43. – Mixed-flow rotor.

general orientation of board sections is shown by the sketch at the left in fig. 3-32).

The general velocity configuration at any point in a slightly mixed-flow rotor is shown in figure 3-45. Without any radial flow component, the flow in a cylindrical flow section has an absolute velocity vector V_o ending at point A_o and a relative velocity vector w_o ending at B_o. The peripheral components are $V_{U,o}$, ending at D_o and $w_{U,o}$, ending at C_o.

With radial flow but no inclination of vane sections normal to the axis of rotation (straight, radial board sections), the absolute velocity vector (not shown) ends at A′, and the relative velocity vector at B′. The peripheral velocity components remain unchanged.

With the board section inclined by the angle λ against the radial direction, as shown in figure 3-43, the absolute velocity vector V ends at point A, and the relative velocity vector w ends at B. With backward inclination of the board section, the peripheral component V_U of the absolute velocity is reduced by

$$V_{U,o} - V_U = \delta V_U = V_r \tan \lambda \qquad (3\text{-}86)$$

(see fig. 3-43), and the peripheral component w_U of the relative velocity is correspondingly increased.

The foregoing deliberations solve in a straightforward fashion the so-called direct problem, that is, the problem of determining the flow for a slightly mixed-flow rotor (or stator) with a given vane shape. The flow in a cylindrical section, V_o and w_o, is determined according to section 2.5.

The indirect problem, that is, the design problem, is solved by the following process of iteration: One first estimates the inclination λ of board sections near the discharge vane edges and determines (by the condition of continuity) V_m and $V_r = V_m \sin \varphi$

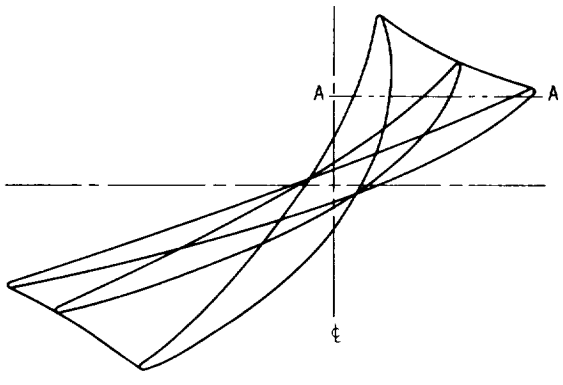

Figure 3-44. – Stacked blade sections.

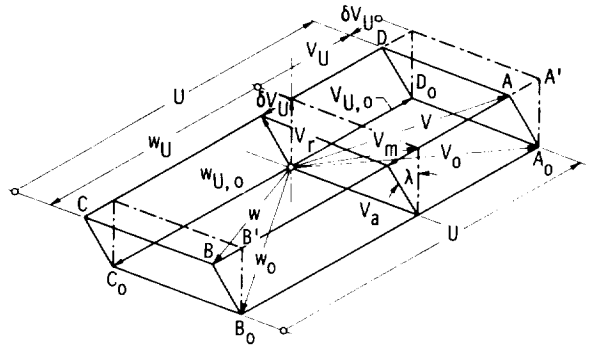

Figure 3-45. – Velocity vector diagram.

from an assumed profile of the rotor like that shown in figure 3-43. For pumps, D_i is known from cavitation considerations (secs. 1.2.2 and 1.3.2), and $D_{h,2}$ is given by the head coefficient $\psi_{h,2} = 2g_o H / U_{h,2}^2$ (secs. 1.2.1 and 1.3.2). The desired peripheral velocity $V_{U,2}$ at the discharge is determined by Euler's turbomachinery equation and the peripheral velocity $V_{U,1}$ of the incoming flow.

From the estimated vane inclination λ at the discharge edges, one determines the change $\delta V_{U,2}$ of the discharge peripheral velocity $V_{U,2}$ (caused by the radial velocity V_r) according to equation (3-86) and from it the discharge peripheral velocities $V_{U,2,o}$ for which the cylindrical vane sections are to be designed. The cylindrical vane sections are determined according to section 3.2 by using particularly the first approximation (sec. 3.2.2). Next one establishes the overall vane shape according to section 3.3.1; this procedure gives a better approximation for the inclination λ of the board sections of the entire vane. Then the foregoing process is repeated except for using a better than first approximation for the design of the cylindrical vane sections, because this iteration is likely to be the last one justified by the approximate character of the entire design process. A similar process applies to the inlet portion of the vane if the meridional flow is not axial.

Still to be answered is the question of what happens in this process to the vorticity of the relative flow ζ_{rel}. This question can be answered by stating that the vorticity -2ω of the radial flow V_r should be taken into account. This problem is considered in section 2.6, and its most practical answer is expressed for the end of radial-flow vane

systems in the form of the Stodola correction (see sec. 2.6.3.5). One should consider whether to apply, at the discharge end of a mixed-flow vane system, an additional negative correction of $V_{U,2}$ of the type expressed by equation (2-142) and figure 2-48, except that the angular velocity ω in equation (2-142) would have to be the angular velocity of the system within the plane development of the conical flow surface M – N in figure 3-43. This angular velocity would obviously be

$$\omega_\varphi = \omega \sin \varphi$$

where ω is the angular velocity of the actual mixed-flow vane system. One would subtract from the peripheral fluid velocity at the discharge, in addition to the previously introduced correction δV_U (which depends on the inclination λ of the board sections), a Stodola correction

$$w_{SA} = \omega_\varphi \frac{d_2}{2} = \omega \frac{d_2}{2} \sin \varphi \qquad (3\text{-}87)$$

where d_2 is the normal distance between two successive vanes at the discharge of the vane system, measured in the development of the conical surface M – N. Consequently one would have to design the cylindrical vane sections for a peripheral discharge velocity $V_{U,2,o}$, which is larger than the actually required velocity $V_{U,2}$ by the sum of the two corrections mentioned, that is,

$$V_{U,2,o} - V_{U,2} = \delta V_U + w_{SA} \qquad (3\text{-}88)$$

where δV_U is given by equation (3-86), and w_{SA} by equation (3-87). This correction is entirely reasonable, but there are no experimental results known to this writer that confirm (or contradict) it.

It is important to observe that, for the discharge conditions, both corrections δV_U and w_{SA} should be evaluated for the mixed-flow angle φ in the discharge region of the vane system. Both corrections are zero for strictly axial meridional flow at the discharge. Furthermore it is of interest that both corrections reverse sign, that is, become additions to $V_{U,2,o}$ when φ is negative (for radially inward mixed-flow rotors).

The Stodola correction applies only to the discharge portion of the vane system, whereas the geometric correction δV_U applies throughout the vane system.

Of course, the Stodola correction is zero for stationary vane systems, whereas δV_U applies to stationary as well as rotating vane systems.

It is reasonable to assume that the considerations of this section should not be applied to meridional flow departing from the axial direction locally by more than about 30°. For larger departures from the axial direction, the vane system should be designed by means of the actual conical stream surfaces, and radial-flow considerations should be applied to the plane developments of these surfaces (see sec. 2.6 and ch. 4).

3.3.4 Design of Axial-Flow Vane Systems With Vorticity in Main Stream

3.3.4.1 *Introduction.*—Vorticity in the main stream results in departures from the familiar potential velocity distributions, that is, from uniform axial velocities in the space between two coaxial cylindrical flow boundaries, and in departures from the law of constant angular momentum $rV_U = \text{constant}$ in the peripheral flow V_U in this space of revolution. The laws of such fluid motions are outlined in section 2.7.

The specific design problems discussed in the present section are

(1) Improvement of the suction specific speed of pump rotors by positive prerotation with radially increasing angular momentum of the flow entering the rotor; laws of this type of fluid motion are described in section 2.7.2 in connection with figures 2-60, 2-61, 2-63, and 2-64

(2) Design of stationary inlet vane systems generating rotation of the flow with radially increasing angular momentum

(3) Design of an axial flow rotor receiving the flow from such a vane system

3.3.4.2 *Improvement of suction specific speed by means of positive, solid-body prerotation at inlet to a pump rotor.*—Positive prerotation,that is, rotation of the incoming fluid in the direction of the rotor motion, is here considered to be generated by a stationary axial-flow vane system.

The peripheral velocity V_U induced by the system is regarded as increasing proportionally to the distance r from the axis of rotation, the familiar solid-body rotation used in the example worked out in figure 2-64 in section 2.7.2. This velocity distribution is chosen because it permits, besides the

graphical solution given in section 2.7.2, also a simple analytical solution on the basis of Bernoulli's equation which lends itself to the intended application to the cavitation performance of axial-flow rotors.

For solid-body rotation (eq. 2-161), the radial distribution of static pressure behind the vane system is particularly simple to calculate by means of the equation of simple radial equilibrium

$$\frac{\partial p}{\partial r} = \frac{\rho V_U^2}{r} \tag{2-162}$$

which is introduced in section 2.7.2. By substituting

$$V_U = V_{U,o}\frac{r}{r_o} \tag{2-161}$$

into equation (2-162) and considering r as the only independent variable, one obtains the following expressions:

$$p_o - p = \int_p^{p_o} dp = \rho \frac{V_{U,o}^2}{r_o^2}\int_r^{r_o} r\,dr$$

$$= \frac{\rho V_{U,o}^2}{2}\left(1 - \frac{r^2}{r_o^2}\right)$$

$$p_o - p = \frac{\rho}{2}\left(V_{U,o}^2 - V_U^2\right) \tag{3-89}$$

where p_o and $V_{U,o}$ are the pressure and the peripheral fluid velocity at the outer radius r_o, and p and V_U are the same variables at any smaller radius r. Since this derivation is intended to be applied to a cavitation problem, the density ρ can be considered constant.

Bernoulli's equation applies to the resultant velocities $V = \sqrt{V_U^2 + V_m^2}$ and $V_o = \sqrt{V_{U,o}^2 + V_{m,o}^2}$, so that

$$p_o - p = \frac{\rho}{2}\left(V_U^2 + V_m^2\right) - \frac{\rho}{2}\left(V_{U,o}^2 + V_{m,o}^2\right) \tag{3-90}$$

Substitution of equation (3-89) into equation (3-90) leads to

$$V_{U,o}^2 - V_U^2 = V_U^2 + V_m^2 - V_{U,o}^2 - V_{m,o}^2$$

Hence

$$V_m^2 - V_{m,o}^2 = 2\left(V_{U,o}^2 - V_U^2\right) \tag{3-91}$$

or

$$\frac{V_m^2 - V_{m,o}^2}{V_{U,o}^2} = 2\left(1 - \frac{V_U^2}{V_{U,o}^2}\right)$$

Substituting equation (2-161) for solid-body rotation gives

$$\frac{V_m^2}{V_{U,o}^2} = 2\left(1 - \frac{r^2}{r_o^2}\right) + \frac{V_{m,o}^2}{V_{U,o}^2} \tag{3-92}$$

which determines V_m as a function of r.

One may, of course, refer everything to some other (intermediate) radius r_A, in which case equation (3-92) would appear in the form

$$\frac{V_m^2}{V_{U,A}^2} = 2\left(1 - \frac{r^2}{r_A^2}\right) + \frac{V_{m,A}^2}{V_{U,A}^2} \tag{3-93}$$

Results of the last equation are compared with those obtained graphically and represented in figure 2-64. The comparison is shown in figure 3-46, which seems quite satisfactory for design purposes.

To evaluate the foregoing results with respect to the cavitation performance of a pump, that is, with respect to its suction specific speed, one must determine the volume flow rate Q connected with the meridional velocity distribution just derived. Obviously

$$Q = 2\pi\int_{r_o}^{r_h} V_m r\,dr \tag{3-94}$$

By substitution from equation (3-92),

$$Q = 2\pi\, V_{U,o} \times \int_{r_o}^{r_h} \sqrt{2\left(1 - \frac{r^2}{r_o^2}\right) + \frac{V_{m,o}^2}{V_{U,o}^2}}\; r\,dr$$

$$Q = 2\pi\, r_o^2\, V_{U,o} \times \int_{r_o}^{r_h} \sqrt{\frac{V_{m,o}^2}{V_{U,o}^2} + 2 - \frac{2r^2}{r_o^2}}\; \frac{r}{r_o}\frac{dr}{r_o} \tag{3-95}$$

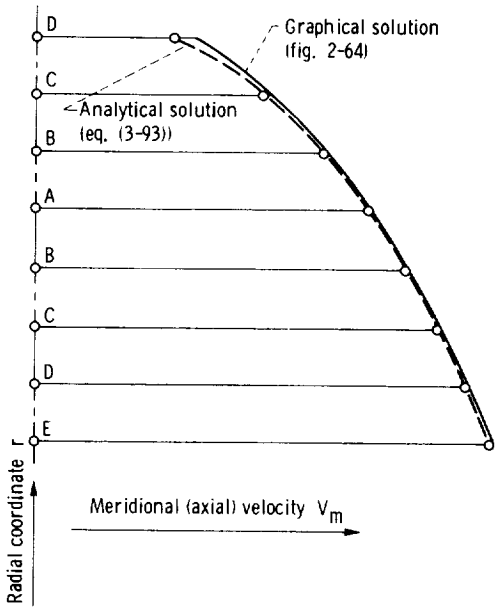

Figure 3-46. – Comparison between graphical and analytical solution for axial flow with vorticity according to solid-body rotation of peripheral flow.

Of course, equation (3-94) can be written directly in the dimensionless form

$$\frac{Q}{2\pi r_o^2 V_{U,o}} = \int_{r_o}^{r_h} \frac{V_m}{V_{U,o}} \frac{r}{r_o} \frac{dr}{r_o} \tag{3-96}$$

which can be evaluated by means of equation (3-92) to obtain equation (3-95) divided by $2\pi r_o^2 V_{U,o}$.

The total inlet head above the vapor pressure required by a pump rotor behind the stationary vane system can be calculated from equation (1-42) in section 1.2.2 in the form

$$H_{sv} = C_1 \frac{V^2}{2g_o} + \sigma_p \frac{w^2}{2g_o} \tag{3-97}$$

where $V^2 = V_U^2 + V_m^2$ and $w^2 = (U - V_U)^2 + V_m^2 = U^2 - 2UV_U + V_U^2 + V_m^2$, so that

$$2g_o H_{sv} = (C_1 + \sigma_p)(V_U^2 + V_m^2) + \sigma_p U^2 \left(1 - \frac{2V_U}{U}\right) \tag{3-98}$$

The law of solid-body rotation, which is assumed to apply, is

$$\frac{V_U}{V_{U,o}} = \frac{r}{r_o} \tag{3-99}$$

Obviously the same law applies to the circumferential velocity U of the rotor, that is,

$$\frac{U}{U_o} = \frac{r}{r_o} \tag{3-100}$$

so that

$$\frac{V_U}{V_{U,o}} = \frac{U}{U_o}$$

or

$$\frac{V_U}{U} = \frac{V_{U,o}}{U_o} = \text{constant} = A \tag{3-101}$$

which is, of course, the ratio of solid-body prerotation. By substitution of these relations into equation (3-98), one obtains

$$2g_o H_{sv} = (C_1 + \sigma_p) V_{U,o}^2 \times \left(\frac{V_U^2}{V_{U,o}^2} + \frac{V_m^2}{V_{U,o}^2}\right) + \sigma_p U_o^2 \frac{U^2}{U_o^2}\left(1 - 2\frac{V_U}{U}\right)$$

$$\frac{2g_o H_{sv}}{U_o^2} = (C_1 + \sigma_p) A^2 \times \left(\frac{r^2}{r_o^2} + \frac{V_m^2}{V_{U,o}^2}\right) + \sigma_p \frac{r^2}{r_o^2}\left(1 - 2\frac{V_{U,o}}{U_o}\right) \tag{3-102}$$

and, by substitution for $V_m^2/V_{U,o}^2$ from equation (3-92),

$$\frac{2g_o H_{sv}}{U_o^2} = (C_1 + \sigma_p) A^2 \times \left(2 - \frac{r^2}{r_o^2} + \frac{V_{m,o}^2}{V_{U,o}^2}\right) + \sigma_p \frac{r^2}{r_o^2}(1 - 2A) \tag{3-103}$$

where one may use the expression

$$\frac{V_{m,o}}{V_{U,o}} = \frac{V_{m,o}}{U_o} \frac{U_o}{V_{U,o}} = \frac{V_{m,o}}{U_o} \frac{1}{A}$$

so that

$$\frac{2g_oH_{sv}}{U_o^2} = (C_1+\sigma_p)\left(2A^2 + \frac{V_{m,o}^2}{U_o^2}\right) - \left[(C_1+\sigma_p)A^2 - \sigma_p(1-2A)\right]\frac{r^2}{r_o^2} \quad (3\text{-}104)$$

It is of interest to evaluate the last equation for zero prerotation, that is, for $A=0$:

$$\frac{2g_oH_{sv}}{U_o^2} = (C_1+\sigma_p)\frac{V_{m,o}^2}{U_o^2} + \sigma_p\frac{r^2}{r_o^2} \quad (3\text{-}105)$$

When $r=r_o$, $V=V_{m,o}$, and $w^2 = U_o^2 + V_{m,o}^2$, equation (3-105) is equivalent to equation (3-97).

If equations (3-96) and (3-104) are to be used for the calculation of the suction specific speed under the influence of solid-body prerotation, the suction specific speed must be transformed as follows:

The number of revolutions per second n is related to the peripheral velocity U_o of the rotor at radius r_o by $n = U_o/2\pi r_o$. With this substitution, the suction specific speed can be written in the form

$$S = \frac{n\sqrt{Q}}{(g_oH_{sv})^{3/4}} = \frac{U_o}{2\pi r_o}\,\frac{\sqrt{Q}\sqrt{\pi}r_o\sqrt{V_{U,o}}U_o^{3/2}}{\sqrt{\pi}r_o\sqrt{V_{U,o}}(g_oH_{sv})^{3/4}U_o^{3/2}}$$

which is readily converted to the terms used in equations (3-96) and (3-104):

$$S = \frac{2^{1/4}}{\pi^{1/2}}\sqrt{\frac{Q}{2\pi r_o^2 V_{U,o}}}\left(\frac{U_o^2}{2g_oH_{sv}}\right)^{3/4}\sqrt{\frac{V_{U,o}}{U_o}} \quad (3\text{-}106)$$

The evaluation of the inlet head coefficient $2g_oH_{sv}/U_o^2$ according to equation (3-104) is shown in figure 3-47 for $C_1 = 1.1$, the same value as used in figure 1-18, and $\sigma_p = 0.2$, the lowest value for which approximately cavitation-free operation can be expected with well-designed vanes. For $(C_1+\sigma_p)A^2 > \sigma_p(1-2A)$, the inlet head coefficient $2g_oH_{sv}/U_o^2$ required to prevent cavitation increases with decreasing r/r_o, because the minimum pressure on the rotor vanes does not occur at the tip section as usual, but at the minimum radius $r=r_h$. With $(C_1+\sigma_p)A^2 < \sigma_p(1-2A)$, the coefficient of r^2/r_o^2 in equation (3-104) is negative, so that the term containing r^2/r_o^2 is added to the first term, that is, $2g_oH_{sv}/U_o^2$ increases with increasing r/r_o and reaches its maximum value at the tip radius $r=r_o$ (as usual). For $(C_1+\sigma_p)A^2 = \sigma_p(1-2A)$, the head coefficient is independent of r/r_o, as shown by line X in figure 3-47. The corresponding value of the prerotation ratio $A = V_{U,o}/U_o$ is 0.2673.

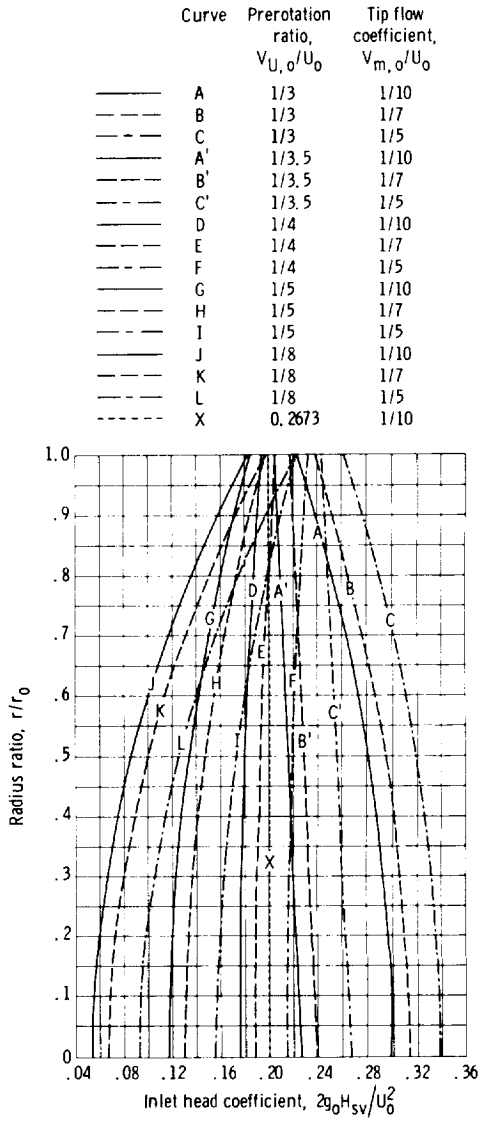

Figure 3-47. – Radial distribution of required H_{sv} for inflow with solid body rotation.

The $2g_oH_{sv}/U_o^2$ values at the tip radius r_o are shown in figure 3-48 as a function of the prerotation ratio $A = V_{U,o}/U_o$ with the tip flow

coefficient $V_{m,o}/U_o$ as a parameter. The values chosen for this investigation were $V_{m,o}/U_o = 1/10$, 1/7, and 1/5. At prerotation values $V_{U,o}/U_o > 0.2673$, the suction head coefficient at the center of rotation ($r_h = 0$) is larger than at the tip and is shown by the nearly straight upper branches of the curves.

The dimensionless volume flow rate $Q/2\pi r_o^2 V_{U,o}$ is determined from equation (3-96) by numerical and graphical procedures, since the designer may not find an analytical solution of equation (3-95). The integrands of equation (3-96) are shown in figure 3-49. Equation (3-95) shows that equation (3-96) depends on only one parameter:

$$\frac{V_{m,o}}{V_{U,o}} = \frac{V_{m,o}}{U_o} \frac{U_o}{V_{U,o}} \tag{3-107}$$

The results of the integration from r_o to $r_h = 0.2\ r_o$ are given in table 3-II together with the head coefficients given in figure 3-48 and the S values calculated according to equation (3-106). The ratio of prerotation $V_{U,o}/U_o$ and the tip flow coefficient $V_{m,o}/U_o$ are also listed.

Figure 3-50 presents graphically the suction specific speeds calculated according to equations (3-96), (3-104), and (3-106) that are listed in table 3-II. The number of points available for this plot from table 3-II is really not sufficient to establish these curves completely, but is sufficient to show the general trend of this relation in a dependable fashion.

The small difference between the curves obtained for the two tip flow coefficients $V_{m,o}/U_o = 0.1$ and 0.2 is remarkable. It is also of practical significance that the maxima of both curves fall between $V_{U,o}/U_o = 0.2$ and 0.267 (short-dash vertical line), the latter being the prerotation ratio at which the minimum pressure shifts from the tip section to the minimum radius ratio r_h/r_o. It is quite possible that the curves have a break at this prerotation ratio, but this investigation is not sufficiently detailed to establish this fact. However, it is of practical importance that one should not select a prerotation ratio in excess of the critical ratio 0.267, partly because the head coefficient $2g_o H_{sv}/U_o^2$ rises (see fig. 3-48) and partly because the most demanding cavitation conditions should not be used at the lower radius ratios, where the flow has to be deflected more strongly than at the tip section.

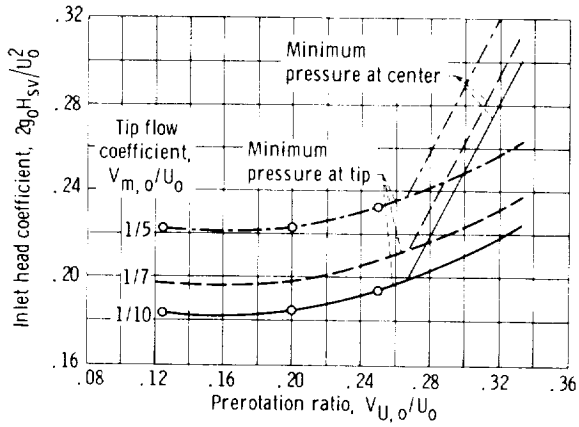

Figure 3-48. – Required inlet head at outer inlet radius r_o as function of solid-body prerotation.

It is of interest that the increase in suction specific speed gained by solid-body prerotation is greater, and reaches over a wider range, than the advantage gained by considering positive prerotation at the tip section without any effect of this prerotation on the meridional velocity distribution (see shaded band in fig. 3-50). The anticipation of this advantage gave rise to the foregoing investigation.

3.3.4.3 *Design elements of axial-flow pump with positive, solid-body prerotation at rotor inlet.*—To illustrate the application of the foregoing results, one must establish the design elements of an axial-flow pump with positive, solid-body prerotation to the extent necessary to demonstrate whether such a design is feasible.

From figure 3-50, it is reasonable to select a prerotation ratio $V_{U,o}/U_o = 0.25$ and a tip flow coefficient $V_{m,o}/U_o = 0.20$. With these values and the previously assumed blade cavitation coefficient $\sigma_p = 0.20$, it should be possible to achieve a suction specific speed of 0.77 (13 200) with only limited cavitation.

Figure 3-51 represents a design engineer's work sheet for the problem presented. The velocity triangles OAB, OCD, and OEF represent the inlet conditions to the pump rotor, which satisfy the previously stated assumptions regarding $V_{U,o}/U_o = 0.25$ and $V_{m,o}/U_o = 0.2$. These triangles also satisfy the condition of solid-body rotation, since the circumferential velocity components $V_{U,1}$ drawn to points A, C, and E are proportional to the radii r_o, 0.8 r_o, and 0.5 r_o.

The axial or meridional velocity distribution corresponding to the solid-body rotation is given by equation (3-92) and represented by the curve GHIJ

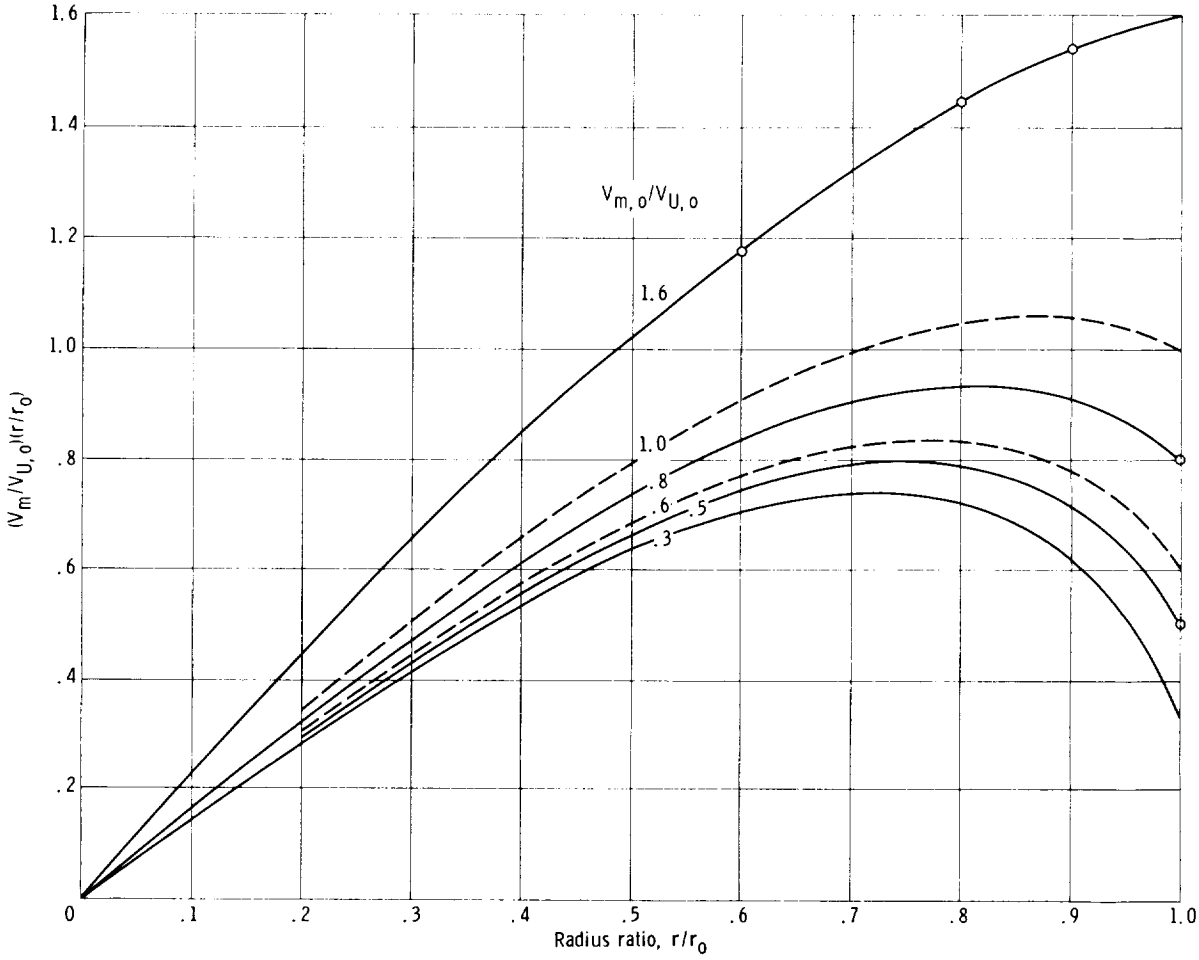

Figure 3-49. – Integrands of equation (3-96).

TABLE 3-II. - CALCULATION OF PREROTATION EFFECT ON SUCTION SPECIFIC SPEED

Ratio of flow to rotational velocity, $V_{m,o}/V_{U,o}$	Prerotation ratio, $V_{U,o}/U_o$	Tip flow coefficient, $V_{m,o}/U_o$	Inlet head coefficient, $2g_oH_{sv}/U_o^2$	Rate of flow coefficient, $\frac{Q}{2\pi r_o^2 V_{U,o}^2}$	Suction specific speed, S
0.3	1/3	0.1	0.298	0.4729	0.66 (11 350)
.5	1/5	.1	.1845	.5126	.76 (13 060)
.6	1/3	.2	.338	.5389	.641 (11 020)
.8	1/4	.2	.2325	.5997	.774 (13 315)
.8	1/8	.1	.1833	.5997	.6604 (11 360)
1.0	1/5	.2	.2225	.6647	.7535 (12 950)
1.6	1/8	.2	.222	.9060	.6956 (11 960)

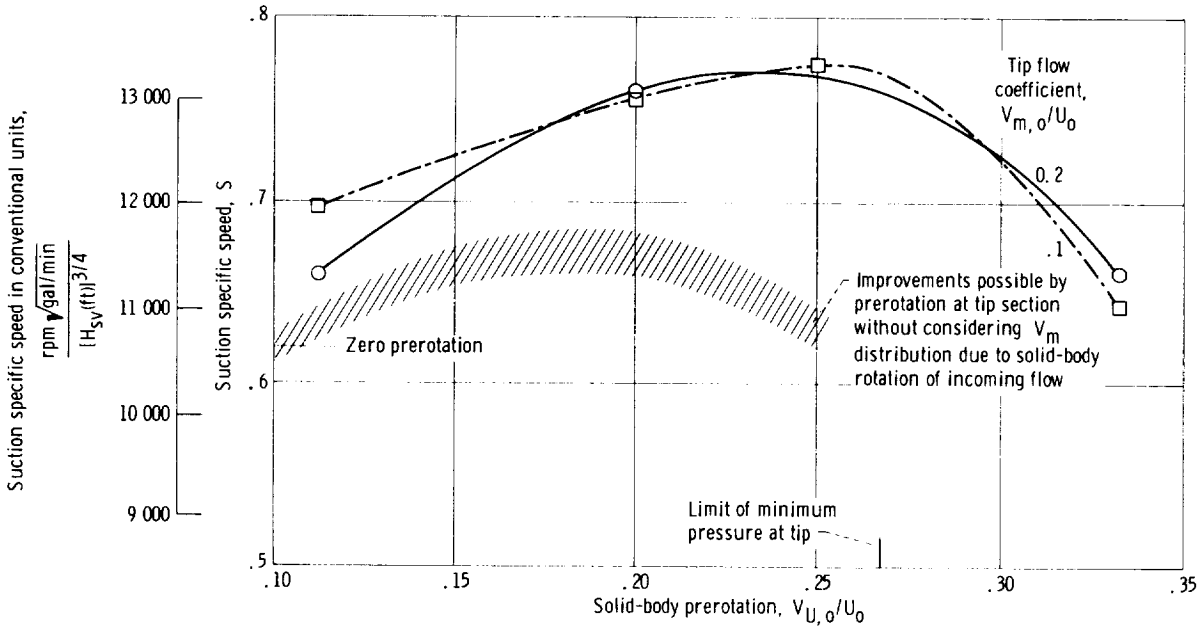

Figure 3-50. – Suction specific speed as function of solid-body prerotation. Hub-tip radius ratio r_h/r_o, 0.2; $C_l = 1.1$; $\sigma_p = 0.2$ in equation (3-97).

plotted against the horizontal r/r_o scale to the right of the origin O; this curve determines the vertical positions of the points A,B,C,D,E, and F above the horizontal coordinate axis through O. The assumed inlet hub radius is $r/r_o = 0.2$, the assumed discharge hub radius is $r/r_o = 0.45$, and the minimum radius of completely developed, cylindrical flow sections is $r/r_o = 0.5$.

To determine the flow at the discharge of the pump rotor, one must, of course, make an assumption about the dimensionless head expected (Euler's turbomachinery equation). It is assumed that, at the minimum flow section ($r/r_o = 0.5$), the relative velocity is turned just slightly beyond the axial direction to point U. A larger or smaller change in the peripheral velocity components w_U and V_U can be assumed; it is essential that this change be substantial, but not unreasonable. In a practical case, this change is prescribed by the head, more specifically, by the head coefficient required by the specific speed. This change in the peripheral velocity component determines the change at all other discharge radii under the assumption of a radially constant head, that is, under the assumption that $\Delta V_U r = \text{constant}$ (radially). This constant (in dimensionless form) is assumed to be

$$\frac{\Delta V_U}{V_{U,o}} \frac{r}{r_o} = 0.8$$

Since one is now concerned with the change ΔV_U of V_U through the rotor, one must remember that $V_{U,o}$ is the peripheral fluid velocity at the inlet to the rotor tip.

The rotor discharge velocities are derived in two steps: First, a new axial inlet velocity distribution is derived from equation (3-92) by applying this equation to a fictitious rotor with a cylindrical hub having everywhere the radius $r_h = 0.45\ r_o$. For this case, equation (3-92) is evaluated with two or three increased values of $V_{m,o}/V_{U,o}$ by estimating these values by the fact that the meridional velocities are inversely proportional to the meridional flow area, which is reduced by the change from $r_h/r_o = 0.2$ to $r_h/r_o = 0.45$. The flow rate for $r_h/r_o = 0.45$ is of course, the same as that for $r_h/r_o = 0.2$. The final curve ZH'I'J' (fig. 3-51) is obtained by interpolation or extrapolation from the curves derived from equation (3-92) by means of various estimated values of $V_{m,o}/V_{U,o}$, as described previously.

Second, a new meridional discharge velocity distribution is derived in the manner to be outlined here for the fictitious rotor with a cylindrical hub ($r_h/r_o = 0.45$) and for a radially constant head or constant change in dimensionless angular momentum $(\Delta V_U/V_{U,o})\ (r/r_o) = 0.8$, which for $r/r_o = 0.5$ gives $\Delta V_U/V_{U,o} = 1.6$, as shown in figure 3-51. This value turns the relative velocity

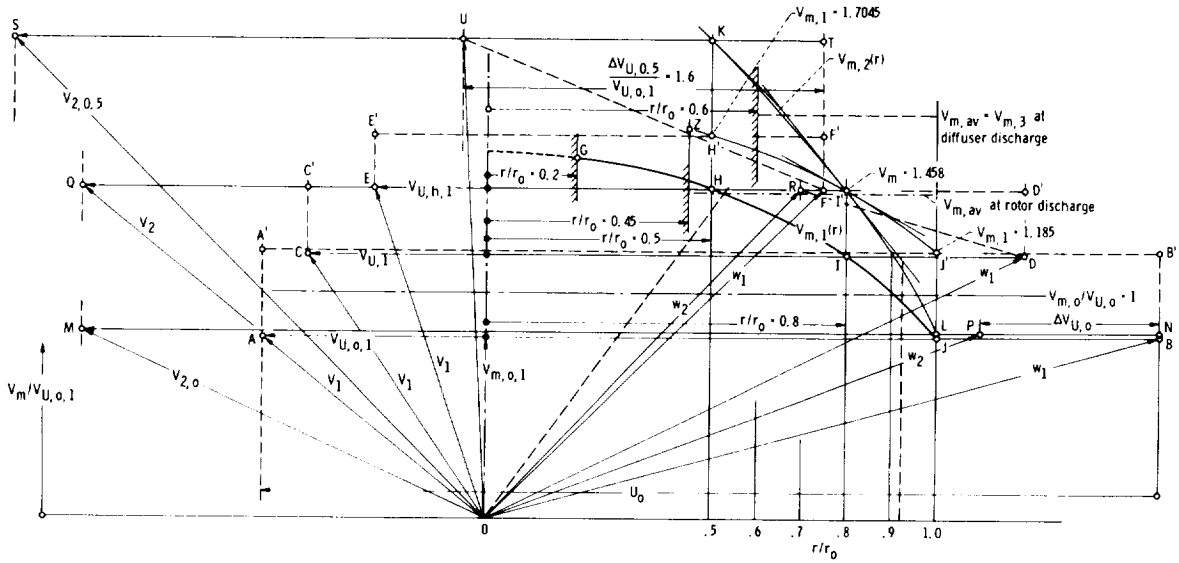

Figure 3-51. – Velocity diagrams and V_m distributions for axial-flow impeller with solid-body prerotation and H_r = constant.

vector in the $r/r_o = 0.5$ section just slightly beyond the axial direction, which constitutes the choice in rotor head previously mentioned. (This particular choice leads to very instructive results, as becomes evident later.)

The physically simplest and, therefore, most reliable way of determining the rotor discharge velocity distribution is based on Helmholtz' law that vorticity remains connected with an inviscid fluid. The vorticity entering the rotor is a trailing vorticity and, therefore, parallel to the flow. Hence

$$\frac{\zeta_{U,1}}{\zeta_{m,1}} = \frac{V_{U,1}}{V_{m,1}} \tag{3-108}$$

For radially constant change in angular momentum ($\Delta V_U r$ = constant), the rotor does not add (or subtract) vorticity to (or from) the flow, so that this vorticity continues to be parallel to the absolute flow. Hence, at the discharge,

$$\frac{\zeta_{U,2}}{\zeta_{m,2}} = \frac{V_{U,2}}{V_{m,2}} \tag{3-109}$$

The radially constant change in angular momentum implies that ζ_m (which controls the circumferential flow) does not change through the rotor, that is, $\zeta_{m,2} = \zeta_{m,1} = \zeta_m$. Hence, by dividing equation (3-109)by equation (3-108), one finds

$$\frac{\zeta_{U,2}}{\zeta_{m,2}} \frac{\zeta_{m,1}}{\zeta_{U,1}} = \frac{\zeta_{U,2}}{\zeta_{U,1}} = \frac{V_{U,2}}{V_{U,1}} \frac{V_{m,1}}{V_{m,2}} \tag{3-110}$$

In all equations of this section, the subscript 1 applies to the flow conditions in front of the fictitious rotor system with a cylindrical hub, and the subscript 2 to the flow conditions behind it.

The incoming vorticity $\zeta_{m,1}$ is connected with solid-body rotation of the flow. Hence, with $\partial V_U/\partial r = V_U/r = V_{U,o}/r_o$,

$$\zeta_{m,1} = \frac{\partial V_U}{\partial r} + \frac{V_U}{r} = 2\frac{V_{U,o}}{r_o} = 2 \tag{3-111}$$

since, for all present considerations, it is most simple to set $V_{U,o} = 1$ and $r_o = 1$, so that all velocities and radii are regarded as divided by $V_{U,o}$ and r_o and are thereby made dimensionless without change in notation. Then equation (3-92) assumes the form

$$V_{m,1}^2 = 2(1 - r^2) + V_{m,o}^2 \tag{3-112}$$

and, for purely axial, meridional flow, that is, for $V_r = 0$,

$$\zeta_{U,1} = \frac{dV_{m,1}}{dr}$$

$$= \frac{-4r}{2\sqrt{2(1-r^2) + V_{m,o}^2}} = -\frac{2r}{V_{m,1}} \tag{3-113}$$

This equation permits the construction of the $V_{m,1}$, r curve from its tangents, provided one starts from a point where $V_{m,1}$ is known. Furthermore

equation (3-113) indicates that the slope of the $V_{m,1}$ curve approaches infinity as $V_{m,1}$ approaches zero. The same construction can be used for the $V_{m,2}$, r curve on the basis of $\zeta_{U,2}$ determined by equation (3-110), provided one starts from a point where $V_{U,2}/V_{U,1}$ and $V_{m,2}/V_{m,1}$ are known.

It is assumed that $V_{m,2} = V_{m,1}$ at $r = r/r_o = 0.8$. At this point, I′ in figure 3-51, the dimensionless velocities are according to previous assumptions $V_{m,2} = V_{m,1} = 1.458$, $V_{U,1} = 0.8$, $\Delta V_U = 1.0$, $V_{U,2} = V_{U,1} + \Delta V_U = 1.8$, and, therefore, $V_{U,2}/V_{U,1} = 2.25$. Furthermore, according to equation (3-113),

$$\zeta_{U,1} = -2 \times \frac{0.8}{1.458} = -1.097$$

Hence, at point I′,

$$\zeta_{U,2} = \frac{dV_{m,2}}{dr} = \zeta_{U,1} \frac{V_{U,2}}{V_{U,1}} = -2.47$$

The tangent so determined permits an estimate of values of $V_{m,2}$ at other radius ratios, and the tangent slopes derived from them by equations (3-110) and (3-113) and $\zeta_{U,2} = dV_{m,2}/dr$ permit the improvement of these estimates by letting the successive tangents intersect each other about halfway between the radii to which they apply. The curve KI′L in figure 3-51 is derived in this manner. It is obvious how the rotor discharge velocity diagrams OMP, OQR, and OSU in figure 3-51 can be constructed from this information. These diagrams, together with the inlet diagrams OAB, OCD, and OEF and with some data on cavitation (or Mach number) characteristics required, permit the design of the cylindrical rotor vane sections at $r = r_o$, 0.8 r_o, and 0.5 r_o according to section 3.2. The diagrams for any other cylindrical sections can be readily derived from the information presented.

Obviously the $V_{m,2}$ curve KI′L has to be checked for compliance with the condition of continuity according to equation (3-96). The curve is found to conform to this condition within approximately 1 percent, which is within the general accuracy of these calculations. Discrepancies up to about 5 percent can be corrected with sufficient accuracy by a parallel, vertical shift of the $V_{m,2}$ curve.

The absolute rotor discharge velocity diagrams present the familar problem of the feasibility of the discharge diffuser vane system.

At first glance one might think that the tip section presents the greatest problem, because of the assumption that the absolute discharge velocity $V_{2,o}$ has to be retarded to $V_{m,o,1}$. However, since the rotor has radially constant vane circulation, it adds a radially uniform energy (head) to the flow. For axial discharge, then, the velocity $V_{m,3}$ of the flow leaving the diffuser must be radially uniform. For the same hub diameter as the discharge of the rotor ($r_h/r_o = 0.45$), this velocity is obviously the average meridional velocity at the rotor discharge (see fig. 3-51). This design involves excessive retardation only at the $r/r_o = 0.5$ section. If a constant tip radius through the diffuser is assumed, an increase in the axial discharge velocity from the diffuser can be accomplished by a continuation of the increase in hub radius through the diffuser. The minimum discharge velocity is assumed to be 0.60 of the maximum diffuser inlet velocity. When the retardation of the flow along the cylindrical surface $r/r_o = 0.45$ is disregarded (because the flow along the hub surface is retarded very little), this velocity is 0.6 $V_{2,0.5}$, which is $V_{m,3} = 1.78\ V_{U,o,1}$ for the velocities shown in figure 3-51. The corresponding hub radius at the diffuser discharge is $r_{h,3}/r_o = 0.60$. The resulting overall design is examined after the vane layout of the inlet guide-vane system is determined.

The inlet vane sections at $r = r_o$ and $r = 0.5\ r_o$ are shown in figure 3-52. For these vane layouts, the first approximation described in section 3.2.2 is used, except that the flow is reversed in comparison with that shown in figure 3-1, and the vane distance d applies to the discharge rather than to the inlet of the system. The inlet velocities shown in figure 3-52 are, of course, those in the actual rotor inlet with $r_h/r_o = 0.2$.

Since the flow is strongly accelerated in the tip section, the lift coefficient C_L is chosen to be 1.6, which is conservative according to figures 2-26 and 3-17. For the $r = 0.5\ r_o$ section, an even more conservative value of $C_L = 1.0$ is selected because the actual circumferential vane spacing $t_{0.5}$ is only half that at the tip section. The vane layouts in figure 3-52 are, of course, dimensionless, and their scales must be adjusted to satisfy the relation

$$\frac{t_o}{t_{0.5}} = \frac{r_o}{r_{0.5}} = \frac{r_o}{0.5\, r_o} = 2 \qquad (3\text{-}114)$$

In addition, the number of vanes must be an integer.

Figure 3-53 shows the profile of the inlet, rotor, and diffuser vane systems discussed. The inlet vane system profile is determined for 10 vanes, whereas the rotor and diffuser system profiles are mere estimates and satisfy only the inlet and discharge hub diameters assumed or determined in the foregoing calculations.

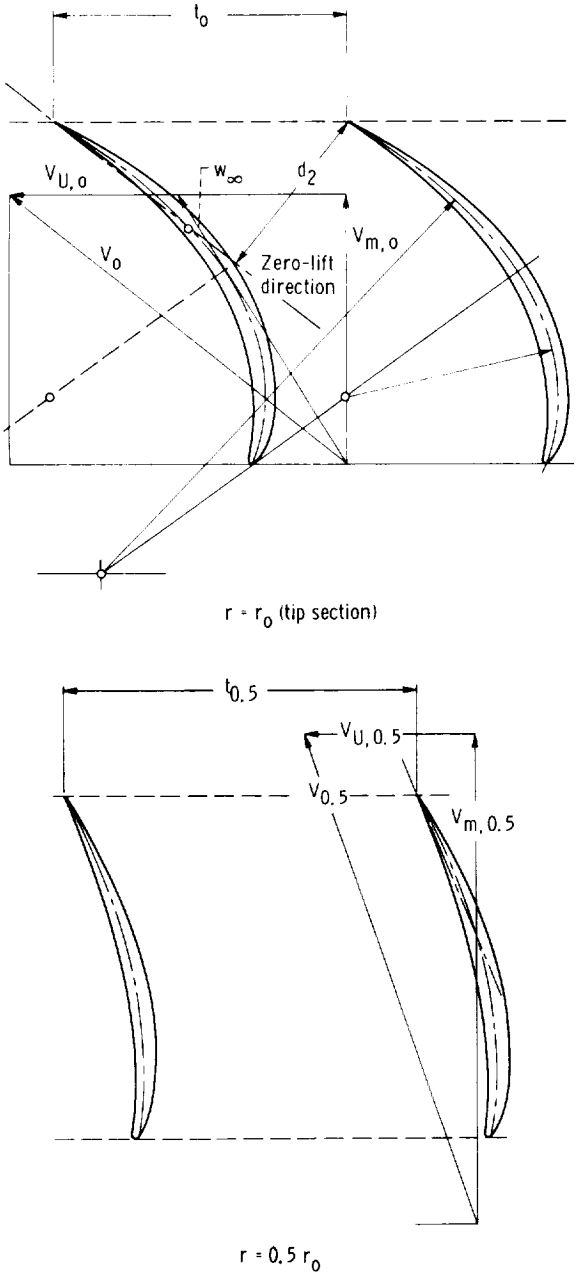

Figure 3-52. – Dimensionless layouts of inlet guide vanes.

The foregoing solution of the problem considered is not the only solution possible. In particular, a radially uniform rotor head may be desirable only for single-stage machines, whereas, in multistage machines, the higher stages can be used to eliminate progressively any radial nonuniformities in total head at the discharge from the first stage (see ref. 33). Thus a radially nonuniform rotor head might be employed to reduce the nonuniformity in the meridional velocity leaving a rotor with radially nonuniform angular momentum (circulation) at its inlet, as described previously.

A second work sheet, figure 3-54, shows the same velocities as figure 3-51 with corresponding points and curves marked by the same symbols, except that the r/r_o scale is vertical, and $V_{U,1}$ and $V_{U,2}$ are plotted in the horizontal direction as a function of r/r_o. For radially constant rotor head (no addition of vorticity by the rotor), the $V_{U,2}$, r/r_o curve MQS can be plotted from the data previously presented, specifically from figure 3-51, where the end points of the V_2 vectors are M, Q, and S. The tangents to this curve (at the same points) are easily derived from the $V_{U,1}, r/r_o$ line A'C'E'O. For the tip conditions, this derivation is represented by the points A' and M and, for $r = 0.5\, r_o$, by the points E' and S, with H_r = constant so that $\zeta_{m,1} = \partial V_U/\partial r + V_U/r = \zeta_{m,2}$. The lines A'A'' and MM'' have the directions of the irrotational $V_U, r/r_o$ curves, where $\partial V_U/\partial r = -V_U/r$. The departures from these directions $\zeta_{m,1}\Delta r$ (where Δr is an arbitrary length) are the same for $V_{U,2}$ as for $V_{U,1}$ as long as the rotor does not add vorticity to the flow, as stated previously for curve MQS.

As mentioned previously, the addition of vorticity by the rotor has the purpose of changing the meridional rotor discharge velocity distribution KI'L to a more uniform shape. The following considerations are simplified by assuming that the desired meridional velocity distribution $V_{m,2}(r)$ is the same at the rotor discharge as at its inlet (curve H'I'J'). The previously used fiction of a cylindrical hub ($r_h = 0.45\, r_o$ = constant) is maintained.

There are (at least) two methods of determining the circumferential rotor discharge velocities $V_{U,2}$ which satisfy the meridional flow condition $V_{m,2} = V_{m,1}$ everywhere. One is that described in section 2.7.2 in connection with figure 2-63, except that, in the present case, this operation has to be carried out for the relative flow leaving the rotor,

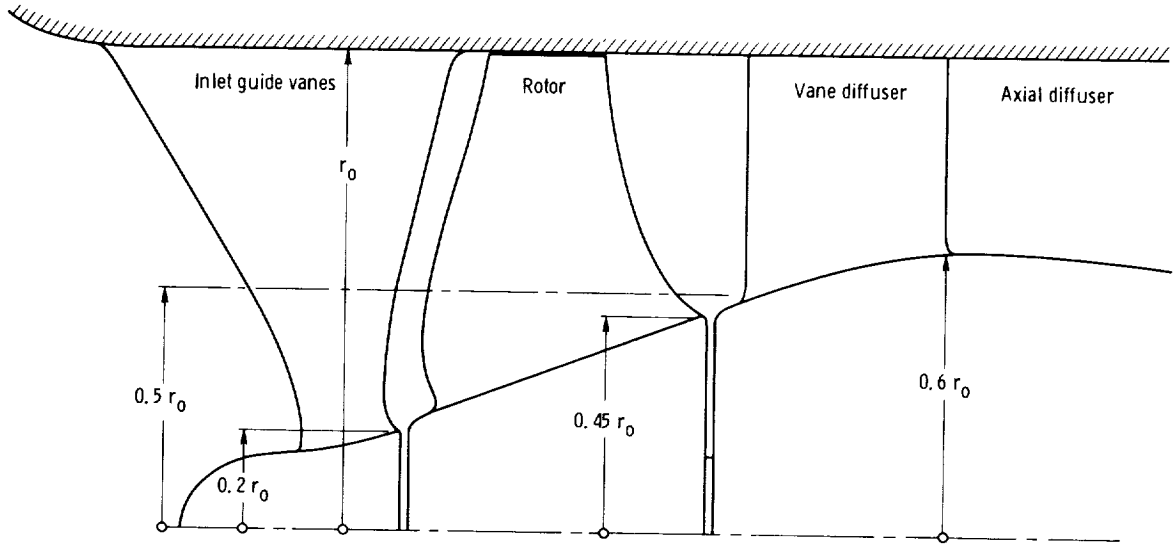

Figure 3-53. – Profile of axial-flow pump with prerotation having radially increasing angular momemtum.

because the vorticity added by the rotor is trailing in figure 3-55 for two steps from $r=0.8\ r_o$: one step to $r=0.9\ r_o$ and the other step to $r=0.7\ r_o$. At $r=0.8\ r_o$, it is assumed that $V_{m,2} = V_{m,1}$. At $r=0.9\ r_o$ and $0.7\ r_o$, the desired meridional velocity $V_{m,2} = V_{m,1}$ differs from that obtained with zero rotor vorticity (curve KI'L) by $\delta V_{m,0.9}$ and $\delta V_{m,0.7}$, respectively, which are the local distances between the curves KI'L and H'I'J' at $r=0.9\ r_o$ and $0.7\ r_o$. The corresponding changes in the peripheral velocity components are derived from the rotor velocity diagrams (fig. 3-55) by swinging the relative velocity vector $w_{2,0.9}$ (at $r=0.9\ r_o$) from its end point U (corresponding to the irrotational rotor flow, curve LI'K, fig. 3-54) to the new end point V determined by the difference in meridional velocity $\delta V_{m,0.9}$. At $r=0.7\ r_o$, the relative velocity vector $w_{2,0.7}$ is swung from its end point X to a new end point Y determined by $\delta V_{m,0.7}$. The end points of the corresponding absolute velocity vectors V_2 are U*, V*, X*, and Y* (at the left side in fig. 3-55).

The process just described can be continued by drawing through the points V' and Y' (fig. 3-54),

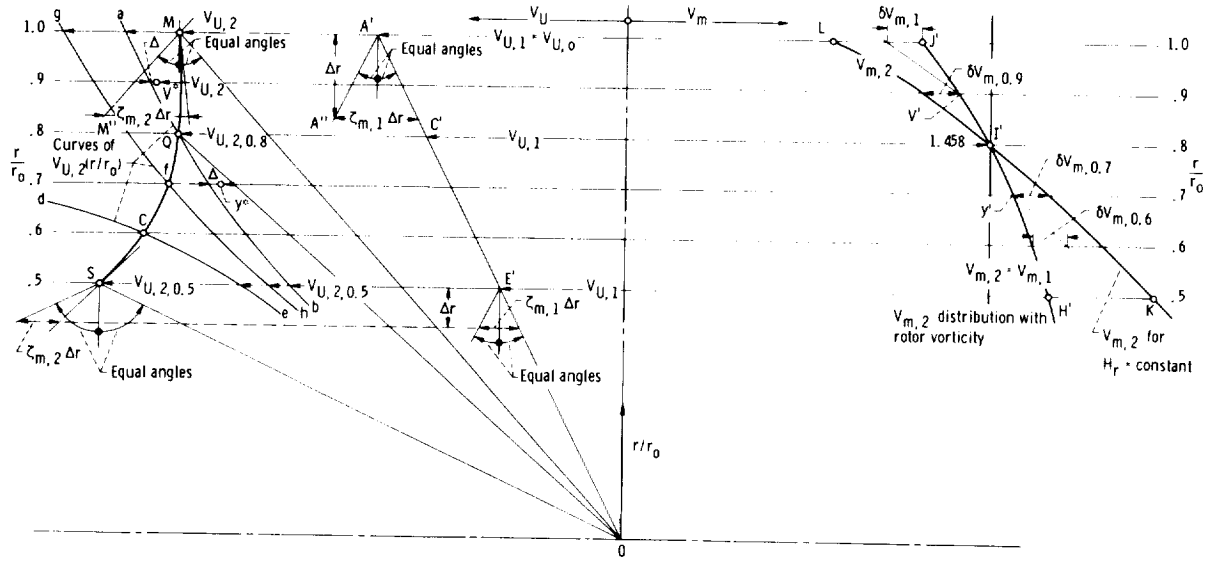

Figure 3-54. – Extension of velocity layout in figure 3-51 to include radially nonuniform rotor head H_r.

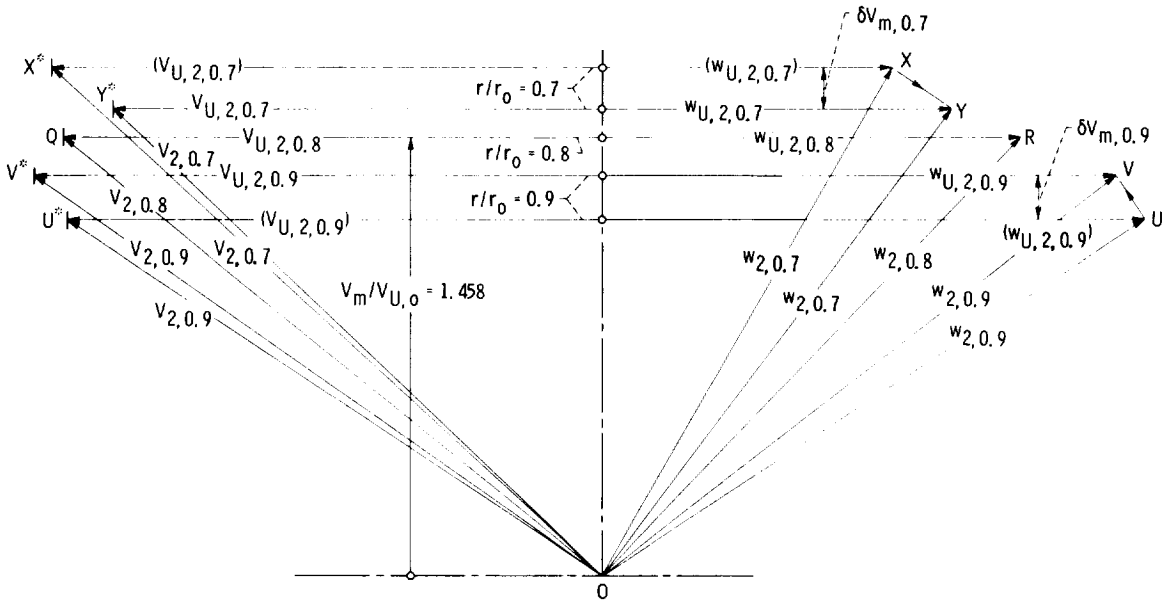

Figure 3-55. – Rotor discharge velocity diagrams with correction for trailing rotor vorticity. Velocity symbols in parentheses refer to rotor discharge with radially constant rotor head.

just reached on the $V_{m,2} = V_{m,1}$ curve H'I'J' at $r = 0.9\ r_o$ and $0.7\ r_o$, short segments of the $V_{m,2}$ curves for zero rotor vorticity. These curves are approximated by their tangents whose inclinations are given by equation (3-110), which, with $V_{m,2} = V_{m,1}$, assumes the form

$$\zeta_{U,2} = \frac{dV_{m,2}}{dr} = \zeta_{U,1} \frac{V_{U,2}}{V_{U,1}} \tag{3-115}$$

where $\zeta_{U,1}$ is given by equation (3-113), and $V_{U,2}$ is the new value arrived at by the preceding steps (points V* and Y*, fig. 3-55). Since the V_m, r curves are not strongly curved, the tangents to these curves can be used to the next stations $r = r_o$ and $0.6\ r_o$ to determine new values of δV_m, after which the preceding process is to be repeated (although not shown in figs. 3-54 and 3-55).

A second method of solving the present problem is based directly on equations (2-172) and (2-175) of section 2.7.3. While physically not as illustrative as the first method, it is under the existing circumstances more practical for obtaining a reasonably complete solution of the problem on hand.

For maintaining the meridional velocity distribution before and after the rotor, it is apparent that

$$\left.\begin{aligned} V_{m,2} &= V_{m,1} \\ \zeta_{U,1} &= \zeta_{U,2} \end{aligned}\right\} \tag{3-116}$$

With this provision and $r_2 = r_1$, as well as $\rho_2 = \rho_1$ (as previously), equation (2-172) reduces to the simple statement

$$\zeta_{m,1} w_{U,1} = \zeta_{m,2} w_{U,2} \tag{3-117}$$

where

$$\zeta_m = \frac{\partial V_U}{\partial r} + \frac{V_U}{r} \tag{3-118}$$

According to equation (3-111), $\zeta_{m,1} = 2V_{U,o}/r_o = 2$ (with $V_{U,o} = 1$ and $r_o = 1$). Hence equation (3-117) is further reduced to

$$\zeta_{m,2} = 2 \frac{w_{U,1}}{w_{U,2}} \tag{3-119}$$

which is easily evaluated by using $w_{U,1} = V_{U,1} - U$ and $w_{U,2} = V_{U,2} - U$. The inlet velocity $V_{U,1}$ is, of course, known, since, for solid-body rotation, $V_{U,1}/V_{U,o,1} = r/r_o$. The calculation is started at a point where the discharge velocity is assumed to be known for the rotor with vorticity, for example, by prescribing the point where the new curve intersects

the old curve MQS (in fig. 3-54) derived for zero rotor vorticity.

Evidently, from equation (3-118),

$$\zeta_{m,2} = \frac{\partial V_{U,2}}{\partial r} + \frac{V_{U,2}}{r}$$

For the determination of $V_{U,2}$ as a function of r only, by means of equation (3-119), the working equation for the numerical evaluation becomes

$$\frac{dV_{U,2}}{dr} = 2\frac{w_{U,1}}{w_{U,2}} - \frac{V_{U,2}}{r} \qquad (3\text{-}120)$$

Selecting point Q at $r=0.8$ as the starting point, where $V_{U,2}=1.8$, $w_{U,2}=V_{U,2}-U=1.8-3.2=-1.4$, and $w_{U,1}=0.8-3.2=-2.4$, one finds

$$\frac{dV_{U,2}}{dr} = 1.18$$

A tangent drawn with this slope through point Q can be extended to $r=0.7$ and $r=0.9$ to permit an estimate of $V_{U,2}$ and calculation of $dV_{U,2}/dr$ for these two radii. The estimate of $V_{U,2}$ can be improved by letting the new tangents at $r=0.7$ and $r=0.9$ intersect the tangent Q about halfway between $r=0.8$ and $r=0.7$ on one side and halfway between $r=0.8$ and $r=0.9$ on the other; thus $V_{U,2}$ and $dV_{U,2}/dr$ are redetermined until satisfactory consistency between $V_{U,2}$ and its derivative is obtained. Convergence is quite good unless $dV_{U,2}/dr$ is much larger than in the present case, as found later. When the described process is repeated, a new $V_{U,2},r$ curve aQb is determined by its tangents.

The values of $V_{U,2}$ reached at $r/r_o=0.9$ and $r/r_o=0.7$ are compared with the values obtained by the first method, shown as points V* and Y* in figure 3-54. The difference Δ between these two sets of results is as small as expected in view of the approximations used with both methods compared.

Other $V_{U,2},r$ curves can, of course, be constructed by beginning at other points along the old curve MQS for zero rotor vorticity. Evidently one cannot start at point S at $r=0.5$, because $w_{U,2}$ goes through zero in the vicinity of this radius and, therefore, according to equation (3-120), the slope of the $V_{U,2}$, r curve increases without bounds. Even an attempt to construct a new $V_{U,2}$, r curve through point c at $r=0.6$ leads to an infinite slope when approaching $r=0.7$. The construction by tangents converges at $r=0.5$, but the resulting curve dce obviously has no practical value.

A new curve constructed through point f at $r=0.7$ converges quite well and has useful, practical significance. It might be of theoretical interest, but hardly of practical interest, to explore where the $V_{U,2},r$ curves cease to stay within finite bounds, since, well before this limit is reached, the solution cannot be used because of excessive variations of the rotor head over the radial extent of the rotor vanes. Already, with the apparently well-behaved curve aQb, the ratio of the rotor head between $r=r_o$ (tip section) and $r=0.5\ r_o$ is about 2.4. For the next higher curve gfh, this ratio is about 2.7 and must reach very high ratios between curves gfh and dce. As already mentioned, head variations encountered with $V_{U,2}$ curves such as aQb and gfh are practically acceptable only in multistage machines, where the higher stages can be used to reduce these nonuniformities in rotor head. The only exception to this statement exists in the field of propulsion pumps and other cases where most of the pump head is converted into kinetic energy, so that radial nonuniformities in head merely result in corresponding nonuniformities in the velocities of the discharging jet.

The foregoing deliberations can only be examples for the application of the laws of vortex flow in turbomachinery to some practical design problems. The laws outlined in section 2.7.3 permit the solution of a large variety of practical design problems. Problems of numerical solutions are today effectively met by means of computers. Essential, in all cases, is close attention to the physical aspects of the overall problem in order to recognize early some mistakes that can always occur in the operations involved, which, although by themselves minor, if undetected, might vitiate the purpose of the work before us.

3.4 Design of Axial-Flow Inducers

3.4.1 Requirements Regarding Suction Specific Speed and Discharge Head of Inducers for Liquid Rocket Pumps and Other Applications

The need for pumps operating at higher suction specific speeds than achievable with little or no cavitation is fairly old. The first extensive need for such pumps arose in steam powerplants, where the condensate pumps receive their flow from the hot well of the condenser. The water in the hot well is

boiling or very close to its boiling point. Therefore the total inlet head H_{sv} of the condensate pump is approximately the difference in elevation between the free water in the hot well and the pump inlet. Since the hot well is usually located close to the lowest floor in the powerplant, this inlet head is often restricted to a few feet.

Such condensate pumps usually operate with very low fluid velocities, so that cavitation damage to impellers of good materials is not serious. In fact, the flow rate is often controlled automatically by varying cavitation as a function of the changing water level in the hot well.

A much more serious demand for pumps of high suction specific speeds has arisen in the field of oxidizer and liquid fuel pumps for rocket engines. Here the weight of the entire pumping unit is of critical importance. The weight of rotating machinery is, for the same head and volume flow rate, about inversely proportional to the speed of rotation. Furthermore there arise major advantages of increased speed if the pump is directly coupled with the driving gas turbine. These advantages include not only lower weight, but also, and at least equally important, simplicity of arrangement, higher reliability, and lower cost.

The inducer was developed to satisfy these conditions. It is an axial-flow rotor with long, helical vanes of low advance ratio or flow coefficient.

Figure 1-18 (ch. 1) reveals at a glance that increased suction specific speeds demand reduced flow coefficients, because curves of constant cavitation parameters σ_p show a maximum in suction specific speed approximately at constant values of $2g_o H_{sv}/V_{m,i}^2$ between 3.0 and 4.0. While at conventional suction specific speeds between 0.5 and 0.6 (8500 to 10 000) the optimum suction specific speed (at zero inlet hub diameter) is reached with $V_{m,i}/U_i$ between 0.25 and 0.35 (see curves for $\sigma_p = \text{constant}$), the corresponding optima at suction specific speeds between 1.5 and 2 fall in the vicinity of $V_{m,i}/U_i = 0.1$. Such suction specific speeds have been reached by conventional, radial-flow condensate pumps with cast impellers.

In the rocket pumps, suction specific speeds between 2 and 3 have been achieved, not, however, with cast impellers but with axial-flow rotors machined with straight, helical blades (at least initially). Machining makes it possible to obtain very thin blades with very sharp leading edges, which are essential for achieving suction specific speeds in excess of 1 (17 200), although such operation is connected with substantial cavitation. Figure 1-18 shows that, at suction specific speeds in excess of 2 (34 400), the flow coefficient $V_{m,i}/U_i$ must be less than 0.1, perhaps as low as 0.05. Obviously the very flat vanes required for such low flow coefficients must be very thin to avoid unreasonably large blockage effects by the vanes, and experience has shown that the high suction specific speeds associated with such low flow coefficients (according to fig. 1-18) can be realized only by using very sharp leading edges of the vanes. The necessity of using machined vanes for such rotors is, therefore, understandable, although today rotors of this type can also be produced by precision casting.

Very thin blades operating in a fairly dense, liquid medium at reasonably high fluid and peripheral blade velocities must have a low aspect ratio, that is, large ratio of the circumferential extent of the blade to its radial extent. Thus there develops the picture of an axial-flow rotor with thin, helical blades and low aspect ratio. Nothing has been derived as yet regarding the solidity (ratio of overlapping) of the vane system of such a rotor. Two considerations give at least qualitative solutions to this problem:

First, figure 1-18 shows that in the range for suction specific speed considered here, 2 to 3 or more (30 000 to 50 000 or more), the blade cavitation parameter $\sigma_p = (p_1 - p_v)/(\rho w_1^2/2)$ must be between 0.05 and 0.01. Such low values preclude the possibility of cavitation-free operation; in fact, cavitiation on the blade surfaces must be expected to be quite extensive. There are two ways of meeting this situation:

(1) One could try to operate an inducer with fully developed cavitation, often called super cavitation. In this case, the cavitation void extends over the entire low-pressure sides of the blades, as described briefly in section 2.5.4.1 and figures 2-21 and 2-22. There is no static-pressure rise through the rotating vane system, and the following vane system receives a rotating system of regions alternately filled with liquid and gas or vapor. Perhaps these regions can be converted into two circumferentially continuous, rotating liquid and gas or vapor masses, as shown in figure 2-22, with the liquid mass entering a radial-flow system. The hydrodynamic properties of such an arrangement have not yet been explored.

(2) The usual solution is to allow the cavitation void to end (collapse) within the first half of the rotating vane channel. After this collapse, the relative flow may be retarded gradually. This retardation is quite limited, because there exists a separated turbulent wake, or at least a very thick boundary layer, behind the cavitation void. (The situation is comparable to that in supersonic flow of a gas with a normal shock in the vane channel, described in sec. 3.2.7 and by fig. 3-27.) This solution clearly requires a solidity of the vane system well in excess of unity, but the actual value of the solidity must be determined by additional considerations of the pressure distribution, possibly by the previously described mean streamline method.

Second, in addition to being required to operate at high suction specific speed, inducers must generate sufficient head H to permit operation of the following pump stage without extensive cavitation. This head requirement is given as one of the design criteria for inducers in reference 59.

Operation without extensive cavitation has been achieved reliably with suction specific speeds up to 0.5 and 0.6 (8500 and 10 000), whereas completely cavitation-free operation requires still lower suction specific speeds. These figures apply only to impellers with hub diameter at the impeller inlet not more than 40 percent ($D_{h,2}/D_{i,2} \leqq 0.4$), like those shown in figures 3-56 and 3-57. Larger hub diameter ratios, such as used in multistage, axial-flow pumps beginning with the second stage (see fig. 1-39), call for correspondingly lower suction specific speeds of the stage following the inducer.

Evidently the total inlet head (above vapor pressure) of the stage following the inducer is

$$H_{sv,2} = H_{sv,1} + \mathrm{H}_1 \tag{3-121}$$

where the subscript 1 applies to the inducer, that is, the first stage, and the subscript 2 to the second stage. Continuing with this definition of subscripts, one finds (for constant n and Q)

$$\frac{S_1}{S_2} = \frac{H_{sv,2}^{3/4}}{H_{sv,1}^{3/4}} = \frac{(H_{sv,1} + H_1)^{3/4}}{H_{sv,1}^{3/4}} \tag{3-122}$$

and, therefore,

$$\frac{S_1^{4/3}}{S_2^{4/3}} = 1 + \frac{H_1}{H_{sv,1}}$$

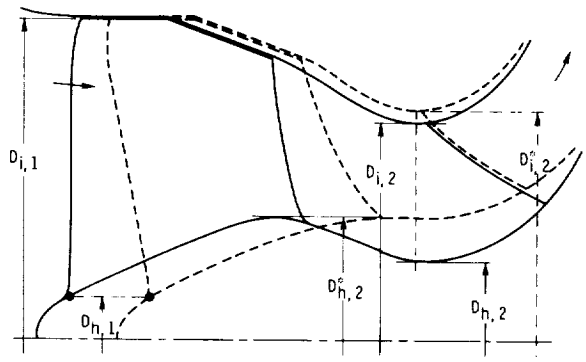

Figure 3-56. – Two low-head inducers in combination with radial-flow impeller inlet.

or

$$\sigma_{H,1} = \frac{H_{sv,1}}{H_1} = \frac{1}{S_1^{4/3}/S_2^{4/3} - 1} \tag{3-123}$$

which permits the determination of the basic specific speed of the inducer stage:

$$n_{S,1} = S_1 \sigma_{H,1}^{3/4} \tag{3-124}$$

From the specific speed, one can calculate a number of design parameters according to equations (1-24) to (1-26). In order to appreciate the practical significance of these and the foregoing relations, one should evaluate an example numerically.

Assume that the suction specific speed of the inducer is $S_1 = 2.4$ (41 250) and the suction specific speed of the following radial-flow or mixed-flow pump is $S_2 = 0.5$ (8600), values which should be achievable with an inlet hub diameter ratio not over $D_{h,2}/D_{i,2} = 0.4$ (see fig. 3-56).

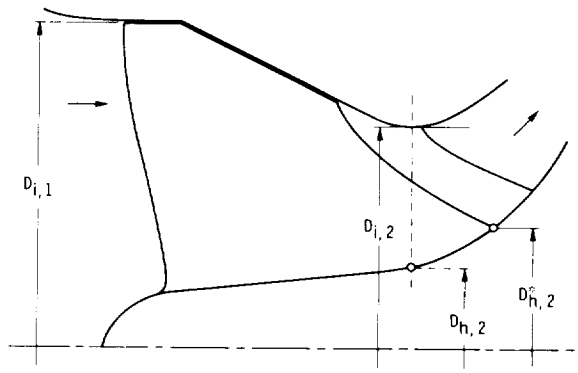

Figure 3-57. – Close coupling of inducer and radial-flow impeller. (Rapid contraction from $D_{i,1}$ to $D_{i,2}$ is problematic.)

From equation (3-123), one obtains

$$\sigma_{H,1} = \frac{1}{4.8^{4/3} - 1} = \frac{1}{7.1} \tag{3-125}$$

and, from equation (3-124),

$$n_{S,1} = \frac{2.4}{7.1^{3/4}} = \frac{2.4}{4.34} = 0.553\ (9500) \tag{3-126}$$

which is a reasonable value for an axial-flow pump (see figs. 1-8 and 1-9). In order to verify this contention, one can determine the discharge hub diameter ratio $D_{h,2}/D_{i,1}$ of the inducer from equation (1-26), because at $D_{h,2}$ the head coefficient $\psi_{h,2} = 2g_o H/U_{h,2}^2$ can be estimated, and the flow coefficient $V_{m,i}/U_i$ is approximately given by the suction specific speed by using figure 1-18.

As in previous cases, the head coefficient at the discharge hub diameter $\psi_{h,2}$ can be assumed to be unity. Reading the flow coefficient $V_{m,i}/U_i = 0.08$ (corresponding to $S_1 = 2.4$ and $2g_o H_{sv}/V_{m,i}^2 = 3.3$) from figure 1-18, one obtains from equation (1-26) with $D_{h,1}/D_{i,1} = 0.2$ the result $D_{h,2}/D_{i,1} = 0.385$. Fortunately this ratio is slightly less than the maximum hub ratio of the impeller following the inducer, for which the suction specific speed of 0.5 can be assumed to be achievable if the inlet diameter $D_{i,2}$ of the radial-flow or mixed-flow impeller following the inducer is equal to the inlet diameter $D_{i,1}$ of the inducer. This assumption may not be correct, however, because the impeller inlet diameter $D_{i,2}$ must approximately satisfy the flow coefficient $V_{m,i,2}/U_{i,2}$, which is appropriate for the impeller suction specific speed $S_2 = 0.5$. Figure 1-18 shows that, for this S_2, the optimum flow coefficient is approximately $V_{m,i,2}/U_{i,2} = 0.3$.

When the notation associated with the solid contours in figure 3-56 is used, the condition of continuity for axial flow leads to the relation

$$V_{m,i,1} D_{i,1}^2 \left(1 - \frac{D_{h,1}^2}{D_{i,1}^2}\right) = V_{m,i,2} D_{i,2}^2 \left(1 - \frac{D_{h,2}^2}{D_{i,2}^2}\right) \tag{3-127}$$

which can readily be rewritten in the form

$$\frac{V_{m,i,1}}{U_{i,1}} \frac{U_{i,2}}{V_{m,i,2}} \frac{1 - D_{h,1}^2/D_{i,1}^2}{1 - D_{h,2}^2/D_{i,2}^2} = \frac{D_{i,2}^3}{D_{i,1}^3} \tag{3-128}$$

With $D_{h,1}/D_{i,1} = 0.2$ and $D_{h,2}/D_{i,2} = 0.4$, as assumed previously,

$$\frac{0.08}{0.3} \times \frac{0.96}{0.84} = 0.3048 = \frac{D_{i,2}^3}{D_{i,1}^3}$$

Hence $D_{i,2}/D_{i,1} = 0.673$, and

$$\frac{D_{h,2}}{D_{i,1}} = \frac{D_{h,2}}{D_{i,2}} \frac{D_{i,2}}{D_{i,1}} = 0.4 \times 0.673 = 0.2693$$

which is substantially less than the inducer discharge hub diameter ratio of 0.385 calculated previously on the basis of the inducer head coefficient $2g_o H/U_{h,2}^2 = 1$ assumed for this diameter.

Figure 3-56 illustrates in solid lines the inducer and impeller inlet profile (plane radial section containing the axis of revolution) which satisfies the diameters established by the foregoing calculations. This profile shows

(1) A rather abrupt necking of the hub diameter after the inducer discharge in order to connect the inducer discharge hub diameter with a smaller impeller inlet hub diameter ($0.4\ D_{i,2}$).

(2) An even more rapid reduction in outside diameter from the inducer inlet to the following impeller inlet. The design criteria in reference 59 suggest that this reduction in outside diameter does not begin (axially) before the flow enters the completely enclosed inducer vane passage. Nevertheless a reduction in outside diameter, shown by solid lines in figure 3-56, may lead to hydrodynamic stability problems, because the radially converging part of the inducer passage constitutes in its outer portion a radially inward-flow impeller with its as yet unsolved problems.

There is a critical speed problem connected with these variations in hub diameter, since the nearest bearing is probably located behind the radial- or mixed-flow impeller, that is, to its right in figure 3-56. This problem can probably be reduced by the closely coupled arrangement shown in figure 3-57, in which the inducer discharge hub diameter is moved under the impeller inlet and into the back shroud of the (radial- or mixed-flow) impeller. The reduction in axial length (overhang) achievable in this manner is limited, because the axial extent of the inducer is largely determined by the steepness of the inward slope at its outer contour. The slope shown in figure 3-57 is the steepest this writer would attempt to use. Furthermore radial sections through the inducer vanes shown in figure 3-57 are, no doubt, inclined toward the inlet side, and this inclination emphasizes the problem of mechanical strength in the design of this inducer.

The necking of the hub between the inducer discharge and the impeller inlet, shown in figure 3-56, can also be avoided by giving the impeller inlet an increased hub diameter ratio. This ratio can be increased by rewriting equation (3-128) in the form

$$\frac{V_{m,i,1}}{U_{i,1}}\,\frac{U_{i,2}}{V_{m,i,2}}\left(1-\frac{D_{h,1}^2}{D_{i,1}^2}\right)=\frac{D_{i,2}^{*3}}{D_{i,1}^3}\times\left(1-\frac{D_{h,2}^{*2}}{D_{i,1}^2}\,\frac{D_{i,1}^2}{D_{i,2}^{*2}}\right) \qquad (3\text{-}129)$$

where $D_{h,2}^*/D_{i,1}$ is the given discharge hub diameter ratio of the inducer (0.385 in this case). The numerical evaluation of equation (3-129) now assumes the form

$$\frac{0.08}{0.3}\times 0.96=0.256=\frac{D_{i,2}^{*3}}{D_{i,1}^3}-0.1483\frac{D_{i,2}^*}{D_{i,1}}$$

which has the solution $D_{i,2}^*/D_{i,1}=0.7125$.

The inducer and impeller profile resulting from the last figure and from the assumption that the impeller inlet hub diameter is equal to the inducer discharge hub diameter (determined by the inducer head) is shown in figure 3-56 in dashed lines. Intuitively one favors this form of the profile for mechanical reasons. This choice is probably correct when comparing the profile with others having the conventional inducer and impeller arrangements shown in figures 1(a) to (d) of reference 59. On the other hand, this change in hydrodynamic design increases the impeller inlet head $H_{sv,2}$ required for reasonably cavitation-free operation of the impeller.

The fact that the increase in $D_{i,2}$ increases the relative velocity at the periphery of the impeller inlet must be taken into account in the impeller design with respect to the retardation of the relative flow.

The present considerations on inducers with discharge hub diameter ratios of less than (say) 0.5 would be incomplete without a brief discussion of the question of whether a radially nonuniform inducer head might be advantageous for the combination of the inducer and a radial- or mixed-flow impeller. This question is suggested by the fact that the inlet head required to avoid or limit cavitation in an impeller with an axial inlet is usually greater at the outer portions of the impeller inlet than at its inner portions. At first glance, it seems to be easy to generate more head at the outer periphery of the inducer discharge than at its hub. While this is true in principle, the degree to which the inducer head can be varied from the hub to the outside of its discharge deserves further investigation.

A design for radially nonuniform inducer head is easily derived for an inducer with a radially uniform total head at its inlet. Departures from the flow associated with uniform inducer head appear in the form of vorticity trailing from the inducer blades, so that the velocity components representing this departure from irrotational flow are normal to the relative flow leaving the inducer. The principles of this characteristic of vortex flow in turbomachines are outlined in section 2.7.2 with reference to figure 2-63, except that, in the present case, the relative velocity leaving the inducer takes the place of the absolute velocity shown in figure 2-63.

A simple approximation of this process is shown in figure 3-58, which applies to inducers of the general form shown in figure 3-56 in dashed lines. Velocities carrying the subscript i apply to the outermost stream surface, while velocities without this subscript apply to a stream surface having a diameter about half that of the outermost stream surface, that is, a diameter a little greater than the hub discharge diameter. The velocity vectors representing the potential velocity distribution leading to a radially constant inducer head are shown by solid lines, while those representing the discharge flow with vorticity leading to a radially nonuniform inducer head are shown in dashed lines, and the velocity symbols of this vortex flow are distinguished by primes.

For a reduction in meridional velocity (at a diameter $D_2=D_{i,1}/2$) to about one-half ($V'_{m,2}=V_{m,2}/2$), the head at that stream surface is reduced from its potential value by approximately 14 percent ($V'_{U,2}/V_{U,2}=0.86$). The head at the outermost stream surface is increased by approximately 18 percent ($V'_{U,i,2}/V_{U,i,2}=1.18$), if, at this stream surface, an increase in meridional velocity of $V'_{m,i,2}/V_{m,2}=1.83$ is assumed. This assumption is yet to be checked by the condition of continuity.

The variations in meridional velocity assumed here are as large as possible, since, for a discharge hub diameter slightly smaller than $D_{i,1}/2$, the meridional velocity there may drop to zero. This

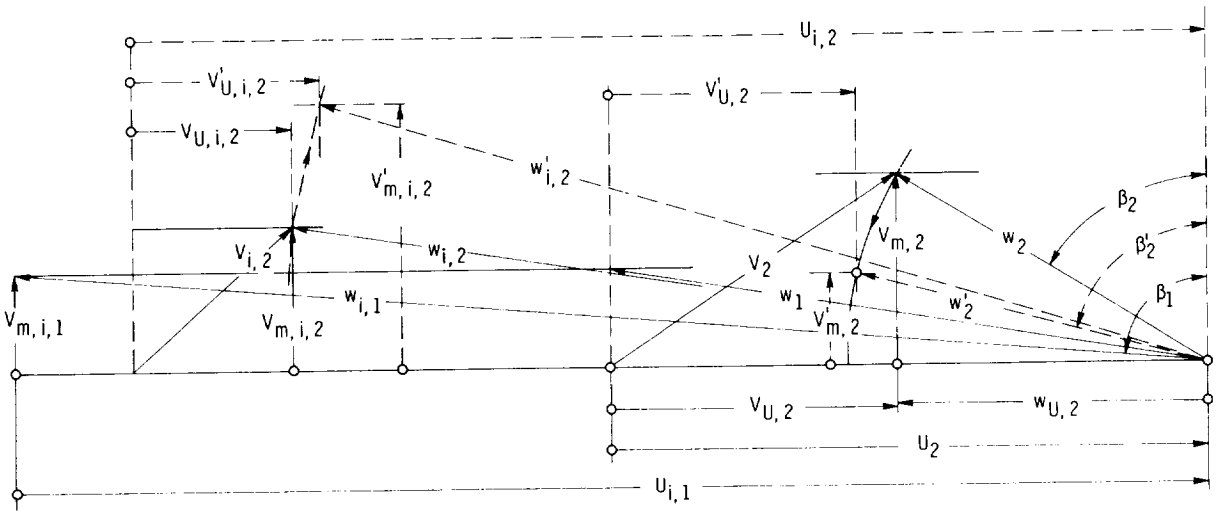

Figure 3-58. – Inducer velocity diagrams with nonuniform inducer head.

example, therefore, gives an indication of the maximum radial variations in inducer head (+18 percent and −14 percent) that one can hope to achieve in this manner. It is doubtful whether these variations are sufficient to justify departures from the constant-head design. On the other hand, the change in relative flow angle, from β_2 to β'_2, associated with a reduction in head and meridional velocity near the hub may be quite significant and desirable, because the flow angle achieved by this departure from the constant-head design brings the resulting inducer vane shape much closer to a helical surface than the flow angle β_2 associated with the constant-head design.

The foregoing considerations regarding the inducer head required to prevent major cavitation in the second-stage inlet have been applied primarily to the so-called low head inducers, that is, to inducers with a hub diameter ratio of less than 0.5 at their discharge, like those in figures 3-56 and 3-57 as well as figures 1(a) to (d) of reference 59. The same considerations apply with (at least) one modification also to the so-called high-head inducers shown in figures 1-39 and 3-59, as well as figures 1(e) and (f) of reference 59. The conventional designations (low-head and high-head) are, of course, related to the difference in discharge hub diameters of these two types of inducers, since the inducer head is more or less dictated by the discharge hub diameter ratio through the condition (assumed here) that the head coefficient referred to this diameter $\psi_{h,2} = 2g_o H/U^2_{h,2}$ is approximately constant.

The most significant difference between high-head and low-head inducers lies in the fact that in the latter the hub-tip diameter ratio of the inlet to the second-stage impeller is not a variable of major significance, since this ratio is fairly low, say not greater than 0.4 or 0.5, as assumed. In this case, the effect of this ratio on the suction specific speed is less than 14 percent and can be considered a minor correction of the S values appearing, for example, in figure 1-18. In this respect, the analysis of high-head inducers must be altered from the foregoing procedure.

The physical relation to be observed is, still, that the inlet head to the inducer $H_{sv,1}$ plus the head generated by the inducer H_1 must be equal to or larger than the inlet head above vapor pressure $H_{sv,2}$ required to operate the second stage without major cavitation. The second relation that can be considered in a simple manner is the condition of continuity of the meridional flow.

The head generated by the inducer is, by definition of the head coefficient ψ,

$$H_1 = \frac{\psi U^2}{2g_o} \tag{3-130}$$

Thus ψ is determined by the peripheral blade velocity U. As stated previously, the maximum value of ψ at the minimum discharge diameter (i.e., the discharge hub diameter of the inducer) is the only one that can be generally predicted. As in other cases, it is assumed that $\psi_{h,2} = 1$ at the discharge hub diameter of the inducer, that is, that

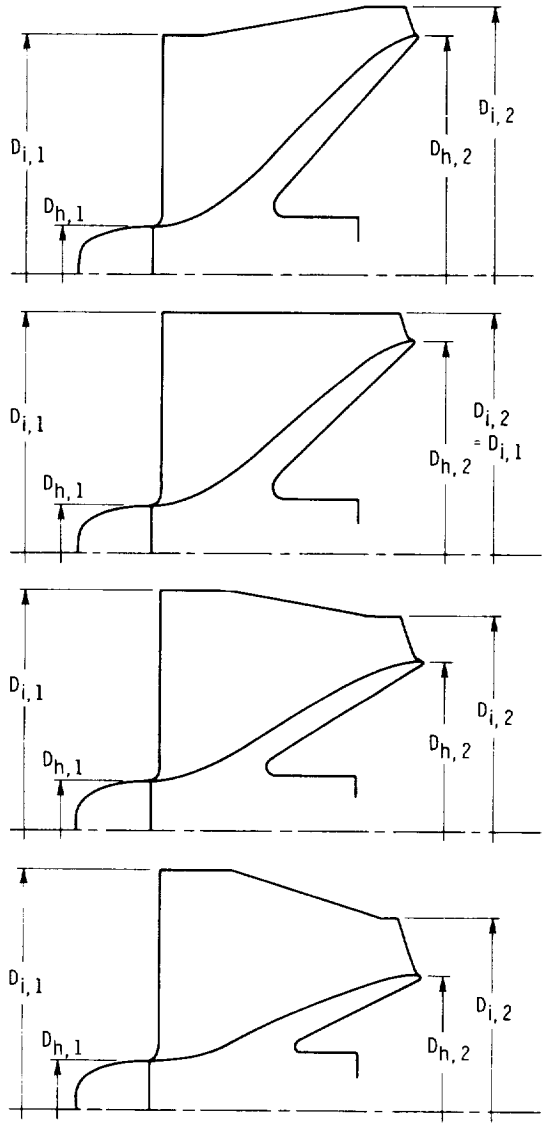

Figure 3-59. – High-head inducer profiles for $K_2 = 1.5$.

$$H_1 = \frac{U_{h,2}^2}{2g_o} \tag{3-131}$$

When the outlet diameter (D_i according to fig. 1-20) is used, this can be written in the form

$$H_1 = \frac{U_{i,1}^2}{2g_o} \frac{D_{h,2}^2}{D_{i,1}^2} \tag{3-132}$$

that is, the inducer head changes for constant speed of rotation according to the square of the discharge hub diameter ratio $D_{h,2}/D_i$.

Obviously the second-stage inlet head $H_{sv,2}$ is given, as previously, by the relation

$$\frac{H_{sv,2}}{H_{sv,1}} = \frac{H_{sv,1} + H_1}{H_{sv,1}} = 1 + \frac{H_1}{H_{sv,1}} \tag{3-133}$$

where the last term is the reciprocal of the Thoma parameter σ_H of the inducer.

The inlet head above vapor pressure required by the second stage for reasonably cavitation-free operation is expressed best by the cavitation parameter $2g_o H_{sv,2}/V_{m,i,2}^2$, which varies relatively little for optimum conditions (see fig. 1-18). At the fairly low suction specific speed required for operation without major cavitation in the second stage, this parameter has a value of about 4 (see fig. 1-18), so that

$$H_{sv,2} = \frac{4V_{m,i,2}^2}{2g_o} \tag{3-134}$$

A corresponding relation can be written for the required inlet head $H_{sv,1}$ of the inducer. In this high range of suction specific speed, the optimum value of the cavitation parameter is read from figure 1-18 to be $2g_o H_{sv,1}/V_{m,i,1}^2 = 3.3$, so that

$$H_{sv,1} = 3.3 \frac{V_{m,i,1}^2}{2g_o} \tag{3-135}$$

The relation between the inducer head H_1 and the second-stage inlet head $H_{sv,2}$, expressed previously by equation (3-133), may now be written in the form

$$\frac{H_{sv,2}}{H_{sv,1}} = 1 + \frac{H_1}{H_{sv,1}} = K_2 \frac{4}{3.3} \frac{V_{m,i,2}^2}{V_{m,i,1}^2} \tag{3-136}$$

where the minimum value of K_2 is 1, which gives the second stage just the inlet head required; larger values ($K_2 > 1$) indicate that the inducer generates more head than required to keep cavitation in the second stage below specified limits.

From the condition of continuity, it is evident that

$$V_{m,i,1}\left(D_{i,1}^2 - D_{h,1}^2\right) = V_{m,i,2}\left(D_{i,2}^2 - D_{h,2}^2\right)$$

so that

$$\frac{V_{m,i,2}}{V_{m,i,1}} = \frac{D_{i,1}^2}{D_{i,2}^2} \frac{1 - D_{h,1}^2/D_{i,1}^2}{1 - D_{h,2}^2/D_{i,2}^2} \tag{3-137}$$

Combining equations (3-132) to (3-137), one obtains the following expression:

$$1+\frac{U_{i,1}^2}{3.3V_{m,i,1}^2}\frac{D_{h,2}^2}{D_{i,1}^2}=K_2\frac{4}{3.3}\frac{D_{i,1}^4}{D_{i,2}^4}\frac{\left(1-D_{h,1}^2/D_{i,1}^2\right)^2}{\left(1-D_{h,2}^2/D_{i,2}^2\right)^2} \qquad (3\text{-}138)$$

Again using $V_{m,i,1}/U_{i,1}=0.08$, so that $U_{i,1}^2/3.3V_{m,i,1}^2=47.3$, and $4/3.3=1.212$, one finds

$$K_2=\frac{\left(1+47.3D_{h,2}^2/D_{i,1}^2\right)\left(1-D_{h,2}^2/D_{i,2}^2\right)^2}{1.212\left(D_{i,1}^4/D_{i,2}^4\right)\left(1-D_{h,1}^2/D_{i,1}^2\right)^2} \qquad (3\text{-}139)$$

which, for ease of calculation, can be converted into the form

$$K_2=\frac{\left[1+47.3\left(D_{h,2}^2/D_{i,2}^2\right)\left(D_{i,2}^2/D_{i,1}^2\right)\right]\left(1-D_{h,2}^2/D_{i,2}^2\right)^2}{1.212\left(1-D_{h,1}^2/D_{i,1}^2\right)^2}\times\frac{D_{i,2}^4}{D_{i,1}^4} \qquad (3\text{-}140)$$

The numerical evaluation of this equation for $D_{h,1}/D_{i,1}=0.2$ is given in figure 3-60. Below $K_2=1$, the curves do not have any direct design significance and are, therefore, presented as dashed lines.

Figure 3-59 illustrates the physical meanings of equation (3-140) and figure 3-60 by showing the inducer profiles resulting from this equation and figure for $K_2=1.5$, that is, the inducer profiles resulting under the plausible assumption that the first (inducer) stage supplies to the second stage 1.5 times the inlet head $H_{sv,2}$ required for reasonably low cavitation in the second stage. Only the values of $D_{h,2}/D_{i,2}$ larger than those corresponding to the maximum values of K_2 in figure 3-60 are considered in figure 3-59, since only these values apply to high-head inducers.

Figure 3-60 indicates that lower discharge hub diameter ratios $D_{h,2}/D_{i,2}$ than shown in figure 3-59 are readily usable in the range where the K_2 curve lies above the assumed K_2 value (1.5), which means that the ratio of available to required second-stage inlet head K_2 is larger than that assumed in figure 3-59. In other words, the $D_{h,2}/D_{i,2}$ values shown in figure 3-59 are maximum values for $K_2=1.5$, so that the head developed by the inducer is the highest possible under the assumed conditions.

It should be observed that $D_{i,2}$ is the outer inlet diameter of the second stage, and for this reason, the subscripts i and 2 are used.

The foregoing considerations and their results, illustrated by figures 3-56 to 3-60, present the diameters required for high-head inducers under given assumptions. The following sections give the design requirements for blade flow sections (cylindrical sections) resulting from the cavitation conditions under which inducer blades must operate.

3.4.2 Vane Inlet Design of Axial-Flow Inducers

As noted previously, according to figure 1-18 and the underlying equations (1-42) to (1-49) as well as equation (1-50c), a substantial increase in suction specific speed is necessarily connected with a reduction in the flow coefficient $V_{m,i}/U_i$ and particularly with a reduction in the vane cavitation number $\sigma_p=(p_1-p_v)/(\rho w_i^2/2)$ to values which are much lower than those achievable with cavitation-free operation. Some conclusions regarding the vane shape are drawn in the preceding section 3.4.1. In the present section, more specific conclusions are derived regarding the vane shape required to permit very low σ_p values with the accompanying cavitation.

Obviously, to account for the cavitation void expected on the suction side of the vanes, one must delete the equality sign in equation (3-1), to state

$$d_1>t\cos\beta_1 \qquad (3\text{-}141)$$

which means that the normal inlet distance d_1 between successive vanes must be substantially, say 10 percent, larger than the distance required to admit the relative flow approaching the vane system without any increase in relative velocity. This is so

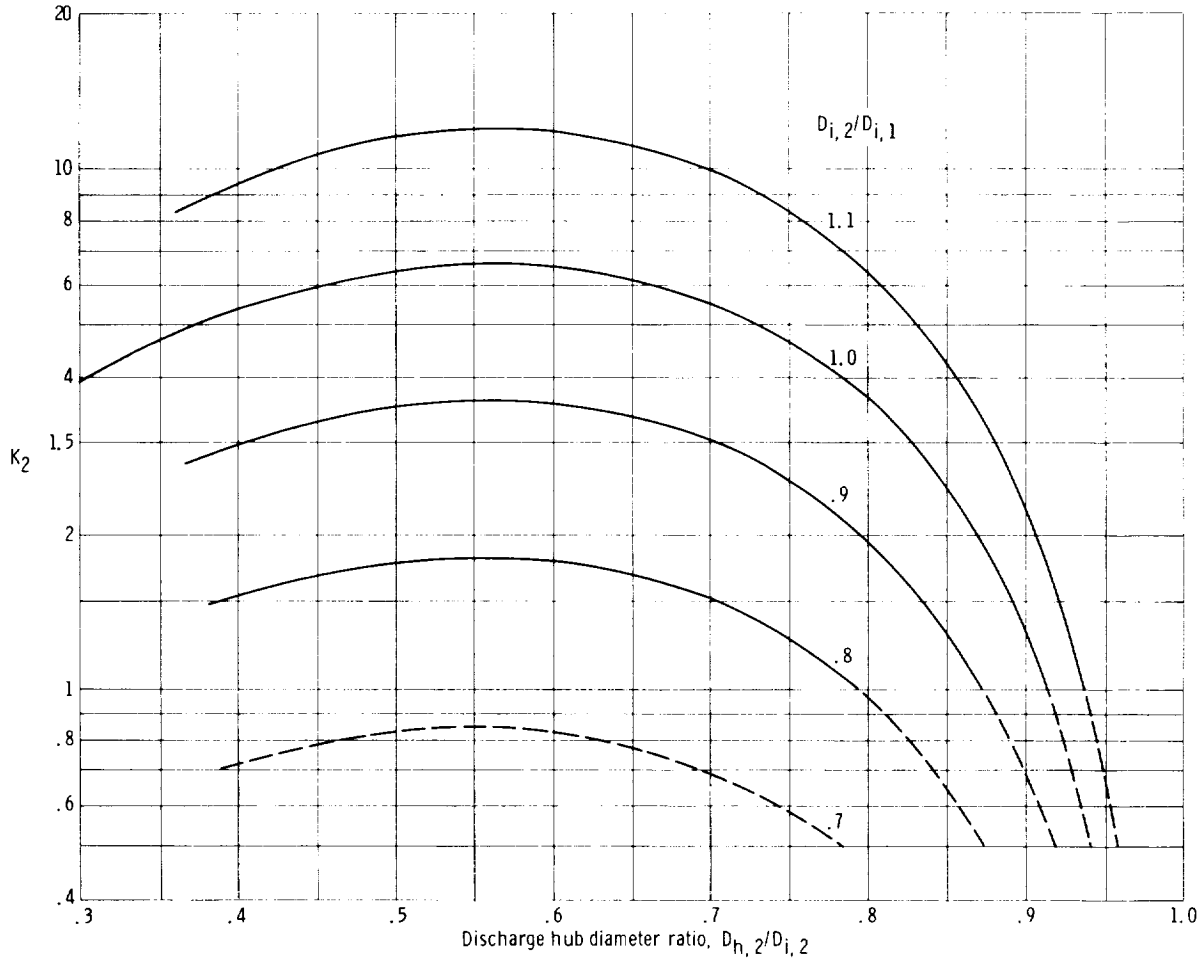

Figure 3-60. – Ratio K_2 of inlet head supplied by inducer to second stage divided by inlet head required by second stage. Inlet hub diameter ratio $D_{h,1}/D_{i,1}$, 0.2.

because, adjacent to a cavitation void, this velocity has already attained its maximum value.

As mentioned in section 3.4.1, the existence of very low blade cavitation numbers can be met either by a cavitation void covering the entire low-pressure side of the blade or by a cavitation void ending within the vane channel of the inducer. In this section, only the second of these two forms of cavitation is considered; it is the form used almost exclusively in practical inducer design and operation.

Reference 59 makes the plausible suggestion that the low-pressure side of the vane should stay everywhere within the bounds of the cavitation void shed from a sharp leading edge, so that the cavitation void does not have to be larger than it would be under the ideal conditions prescribed by the given, low value of the cavitation number σ_p. The simplest approximation for this boundary of the cavitation void (also suggested in ref. 59) is a straight line through a sharp leading edge in the direction β_1 of the oncoming, relative flow with the velocity w_1 (see fig. 3-61). If the wedge angle α_w of the leading vane end is to be finite and practical, the leading side of the vane must be substantially steeper than the trailing (low-pressure) side, that is, the leading side vane angle β_v (measured against the axial direction) must be smaller than the trailing side vane angle. Hence, with reference to figure 3-61,

$$\beta_v + \alpha_w \leqq \beta_1 \tag{3-142}$$

Furthermore it is suggested in reference 59 that the low-pressure side of the vane should stay within the cavitation void up to a rate of flow 10 percent larger

than the design capacity. By this rule and with reference to figure 3-62,

$$\cot(\beta_v + \alpha_w) = 1.10 \cot\beta_1 = 1.10 \frac{V_{m,1}}{w_{U,1}} \qquad (3\text{-}143)$$

so that the equality sign in equation (3-142) is to be deleted.

Finally, reference 59 suggests that the direction β_v of the leading side of the vane is determined by making the angle of attack α between the leading side and the inlet relative velocity w_1 a value between 0.35 and 0.5 of $\pi/2 - \beta_v$, the larger values applying to relatively thicker blades. The preferred value is the mean between these limits

$$\alpha = 0.425\left(\frac{\pi}{2} - \beta_v\right) \qquad (3\text{-}144)$$

which is used in figure 3-61 on the basis of the following derivation. According to figures 3-61 and 3-63,

$$\frac{\pi}{2} - \beta_v = \frac{\pi}{2} - \beta_1 + \alpha$$

or

$$\beta_v = \beta_1 - \alpha$$

Substituting into equation (3-144) gives

$$\alpha = 0.425\left(\frac{\pi}{2} - \beta_1 + \alpha\right)$$

or

$$\alpha - 0.425\,\alpha = 0.575\,\alpha = 0.425\left(\frac{\pi}{2} - \beta_1\right)$$

Hence

$$\alpha = 0.739\left(\frac{\pi}{2} - \beta_1\right) \qquad (3\text{-}145)$$

This equation can obviously be used to derive a relation between β_1 and β_v in the form

$$\beta_v = \beta_1 - 0.739\left(\frac{\pi}{2} - \beta_1\right)$$

$$\frac{\pi}{2} - \beta_v = \frac{\pi}{2} - \beta_1 + 0.739\left(\frac{\pi}{2} - \beta_1\right)$$

$$\frac{\pi}{2} - \beta_v = 1.739\left(\frac{\pi}{2} - \beta_1\right) \qquad (3\text{-}146)$$

where the factor 1.739 corresponds to 0.425 in equation (3-144). If this factor in equation (3-144) were 0.5, one would find

$$\frac{\pi}{2} - \beta_v = 2\left(\frac{\pi}{2} - \beta_1\right)$$

and, if the same factor had its minimum value of 0.35, the result would be

$$\frac{\pi}{2} - \beta_v = 1.54\left(\frac{\pi}{2} - \beta_1\right)$$

One can, therefore, conclude that

$$\frac{\pi}{2} - \beta_v = (1.54 \text{ to } 2)\left(\frac{\pi}{2} - \beta_1\right) \qquad (3\text{-}147)$$

The foregoing considerations and rules establish the leading-edge design of inducer vanes empirically. It is desirable to relate these rules to the actual flow pattern to be expected. In addition to an illustration of the previously mentioned approx-

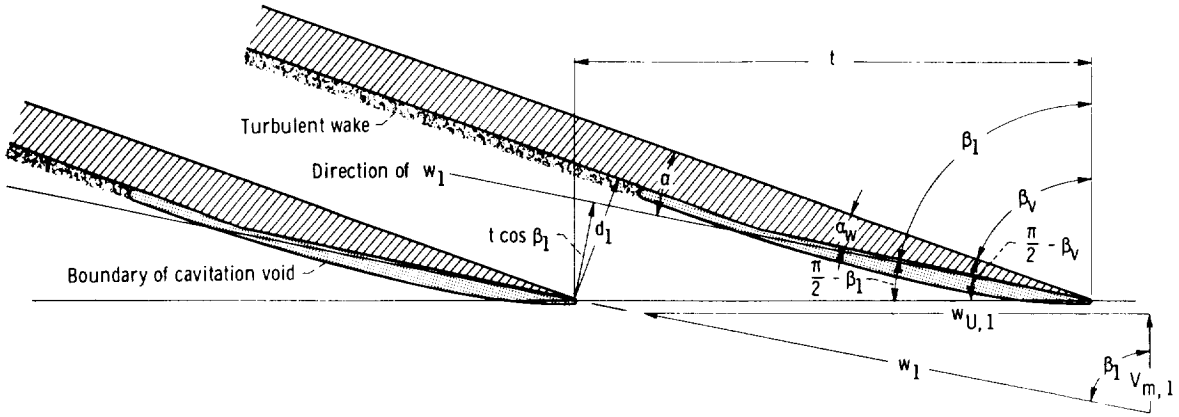

Figure 3-61. – Inducer vane inlet configuration.

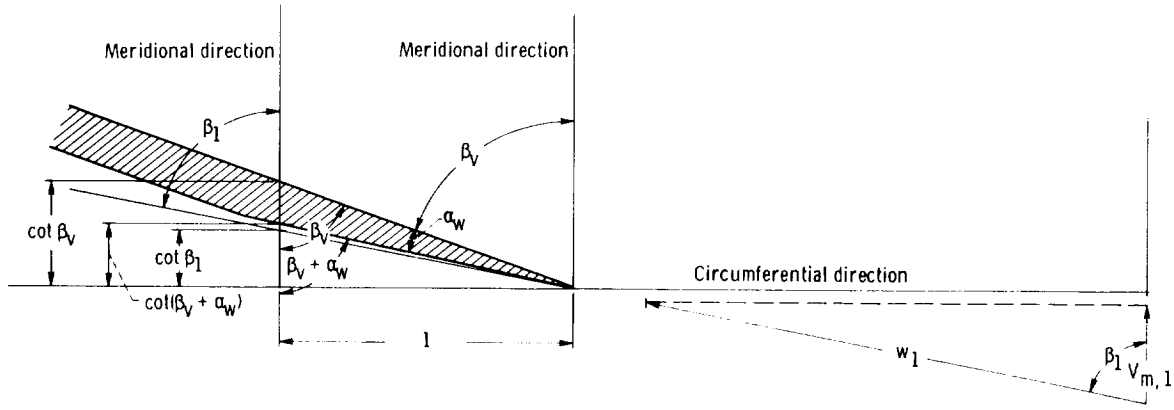

Figure 3-62. – Inlet vane and flow angles.

imation of the cavity boundary (by a straight line through the sharp leading edge in the direction of the incoming relative velocity w_1), figure 3-61 includes an estimate of the actual boundary of the cavitation void with the void itself represented as a dotted region. The origin of the cavitation void at the sharp leading edge is shown enlarged in figure 3-64. Both figures indicate that the vane thickness at the leading edge could be increased over the sharp-edged wedge contour without increasing the size of the cavitation void. Reference 59 suggests a maximum leading-edge radius r_1 of not more than 0.01 t, that is, of not more than 1 percent of the circumferential vane spacing, or a total leading-edge thickness not greater than 0.02 t.

No doubt the form of the leading edge is important in this connection. This geometry is shown in figure 3-63 for a flow coefficient $V_{m,1}/w_{U,1} = 0.1$. Beveling the leading edge in the circumferential direction (as shown by the line ab) is, of course, mechanically quite simple. Under the assumption of a zero leading-edge thickness after beveling, the circumferential width of the leading-edge cut shown in figure 3-63 is approximately

$$\tau_1 = 0.15\, t = 15\, r_1 \qquad (3\text{-}148)$$

The sharp edge between the leading side of the vane and the circumferential cut would, of course, have to be blunted by polishing, as indicated in figure 3-63 by $\tau_{n,o} = r_1$, so that the rounded leading edge would be slightly behind the theoretical leading edge generated by the circumferential cut.

The foregoing equations (3-141) to (3-148) and figures 3-61 to 3-64 describe the design of the inlet portion of inducer vanes on empirical grounds. On the other hand, the actual contour of the cavitation void shown in figures 3-61 and 3-64 can be determined theoretically on the basis that pressure and velocity along the boundary of a cavitation void are constant. Perhaps the oldest solution of this problem for a straight system of parallel, straight vanes is given in reference 9, where the problem is solved for $\sigma_p = 0$. This publication is valuable insofar as it includes an introduction to the hodograph method for solving this type of problem. More recent publications are references 60 and 61, which apply directly to inducers of turbopumps.

From reference 59, one receives the impression that the previously mentioned theoretical solutions

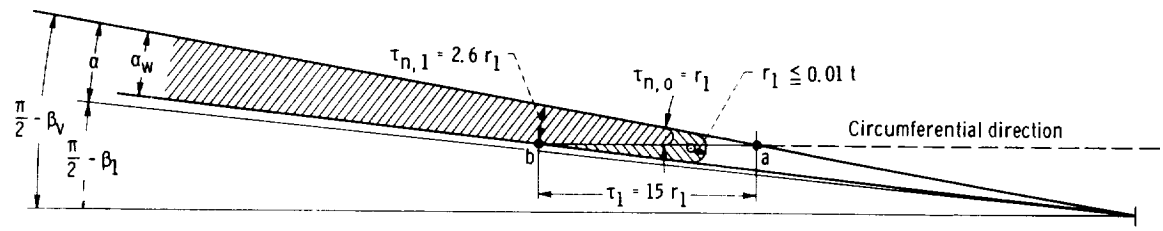

Figure 3-63. – Leading-edge geometries for $V_{m,1}/U = 0.10$.

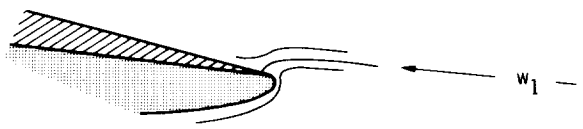

Figure 3-64. – Leading-edge flow configuration.

are fairly successful. Yet the empirical approach outlined in this section is the only solution described in reference 59. This writer considers the empirical solution the most dependable one, partly because the cavitation voids in inducers often differ in appearance markedly from the theoretical model and partly because measurements by Ruggeri et al. (refs. 42 and 43) indicate that the pressure in a cavitation void is not uniform (see fig. 2-79, sec. 2.8.4), whereas its uniformity is the basis of the theoretical approach. The empirical approach outlined previously, therefore, seems to be the only dependable rule available for the design of the inlet portion of inducer vanes.

3.4.3 Design of Entire Vane Section of Axial-Flow Inducers

With the exception of the inlet portion of the vane, the design of cylindrical sections through axial-flow inducers can follow the same principles as described in sections 3.2.2 and 3.2.4 for axial-flow vane sections in general. However, there is at least one important difference to be observed with respect to inducer vane sections, the fact that the leading edge of the vane is designed with a positive angle of attack. This angle, together with the existence of a cavitation void on the low-pressure side, determines the pressure distribution over the leading portion of the vane. Thus there is a design condition different from the prescribed minimum pressure condition usually observed when designing a vane system for zero or limited cavitation. This difference between the vane design for inducers and that for other axial-flow vane systems is the principal subject of this section.

While the pressure distribution in a vane system operating with extensive cavitation can be determined by theoretical means (see refs. 9, 60, and 61), a much simpler, quasi-one-dimensional approach is employed here, partly because the doubtful assumption of uniform cavity pressure seems to have only a minor effect on the results obtained with this approach and partly because simplicity of reasoning is important for design work.

Figure 3-65(a) illustrates the intended procedure, considering the flow areas of the system in relation to the flow conditions in a section a-a inside the system. This section has an, as yet unknown, axial distance y_a from a line connecting the leading edges of the vanes.

The relative velocity through this section varies from $w_{a,min}$ along the high-pressure side of the vane to $w_{a,max}$ along the cavitation void on the low-pressure side. Evidently, if constant cavity pressure p_v is assumed,

$$\frac{\rho w_{a,max}^2}{2} + p_v = \frac{\rho w_1^2}{2} + p_1$$

Hence

$$\frac{w_{a,max}^2}{w_1^2} = 1 + \frac{p_1 - p_v}{\rho w_1^2/2} = 1 + \sigma_p \qquad (3\text{-}149)$$

For example, with a cavitation number $\sigma_p = 0.02$, which is quite common with cavitating inducers, $w_{a,max}/w_1 = 1.01$, that is, $w_{a,max}$ is only 1 percent larger than w_1. If cavity pressure is not exactly constant, $w_{a,max}$ may be closer to w_1 than indicated by the foregoing approximation.

Furthermore, considering that the flow within section a-a can be assumed to have uniform energy,

$$p_{a,max} + \frac{\rho w_{a,min}^2}{2} = p_v + \frac{\rho w_{a,max}^2}{2}$$

$$p_{a,max} - p_v = \Delta p_a = \frac{\rho}{2}\left(w_{a,max}^2 - w_{a,min}^2\right)$$

$$\Delta p_a = \rho \frac{w_{a,max} + w_{a,min}}{2}(w_{a,max} - w_{a,min})$$

and, with $(w_{a,max} + w_{a,min})/2 = \overline{w}_a$, which is a mean relative velocity in section a-a, one finds

$$\Delta p_a = \rho \overline{w}_a (w_{a,max} - w_{a,min})$$

Since (by definition of $\overline{w}_a$) $w_{a,max} - w_{a,min} = 2(w_{a,max} - \overline{w}_a)$,

$$\Delta p_a = 2\rho \overline{w}_a (w_{a,max} - \overline{w}_a) \qquad (3\text{-}150)$$

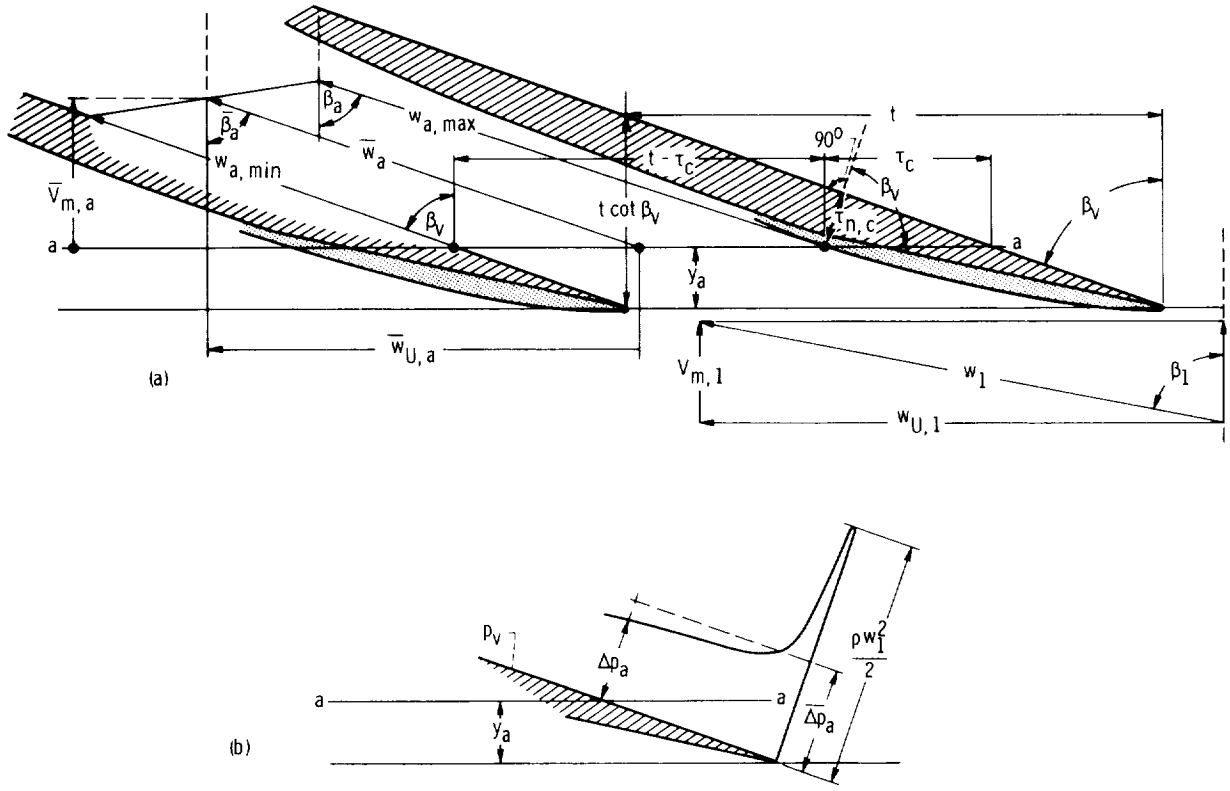

(a) Inducer vane system inlet.
(b) Vane pressure distribution near leading edge.
Figure 3-65. – Approximation of flow in inducer vane system.

The condition of continuity obviously demands that

$$tV_{m,1} = (t-\tau_c)\bar{V}_{m,a} \tag{3-151}$$

where τ_c is the circumferential vane thickness plus the circumferential thickness of the cavitation void (see fig. 3-65(a)). Furthermore

$$\bar{w}_a = \frac{\bar{V}_{m,a}}{\cos\bar{\beta}_a} \tag{3-152}$$

where the mean flow angle $\bar{\beta}_a$ in section a-a can be only slightly larger than β_v (see fig. 3-65(a)).

From equations (3-151) and (3-152), one finds

$$\bar{w}_a = \frac{V_{m,1}}{\cos\bar{\beta}_a}\frac{t}{t-\tau_c} = \frac{V_{m,1}}{w_1} \times \frac{w_1}{\cos\bar{\beta}_a}\frac{t}{t-\tau_c} = \frac{\cos\beta_1}{\cos\bar{\beta}_a} w_1 \frac{1}{1-(\tau_c/t)}$$

or

$$\bar{w}_a = A w_1$$

where

$$A \equiv \frac{\cos\beta_1}{\cos\bar{\beta}_a}\frac{1}{1-(\tau_c/t)} \tag{3-153}$$

so that, according to equation (3-150) and with the small difference between $w_{a,max}$ and w_1 neglected,

$$\Delta p_a = 2\rho w_1^2 A(1-A)$$

or

$$\frac{\Delta p_a}{\rho w_1^2/2} = 4A(1-A) \tag{3-154}$$

The ratio $\cos\beta_1/\cos\bar{\beta}_a$ varies only from 0.72 for $\cot\beta_1 = 0.05$ to 0.62 for $\cot\beta_1 = 0.15$ when the

rules outlined in section 3.4.2 are used for β_v and it is assumed that $\bar{\beta}_a$ is 1° larger than β_v, as shown in figure 3-65(a). Therefore A and thereby the vane face pressure coefficient $\Delta p_a/(\rho w_1^2/2) = 4A\ (1-A)$ vary primarily with blockage ratio τ_c/t.

The relation between the vane face pressure coefficient and the blockage ratio (including the cavitation void) calculated from equations (3-154) and (3-153) is shown in solid lines in figure 3-66. The points where these curves drop to $\Delta p_a/(\rho w_1^2/2) = 0$ obviously mark the condition which can only be described as cavitation choking, since the rate of flow is here restricted by cavitation and the condition of continuity. This condition cannot be approached closely because of the uncertainties involved in the calculations leading to these curves and because of irregularities in the flow. The dashed line AB connects the points at which τ_c/t is 80 percent of its value at the choking condition $\Delta p_a = 0$. This ratio is somewhat arbitrarily assumed to be the highest blockage ratio which can be used in design to be reasonably sure of avoiding cavitation choking. According to figure 3-66, then, the pressure coefficient $\Delta p_a/(\rho w_1^2/2)$ cannot be lower than its values at the points where the dashed line AB intersects the curves describing the relation between this pressure coefficient and the blockage ratio.

Higher pressure coefficients obviously involve lower blockage ratios than indicated by the points at which the line AB intersects the respective pressure coefficient curves. The upper limits of this pressure coefficient are, therefore, given by the lowest values of the blockage ratio τ_c/t which are mechanically feasible. Such lower limits are not directly evident, because τ_c is not measured normal to the vane. The corresponding thickness measured normal to the vane is evidently, according to figure 3-65(a),

$$\tau_{n,c} = \tau_c \cos \beta_v \tag{3-155}$$

This relation is represented graphically in figure 3-67, where $\tau_{n,c}$ is made dimensionless in the same manner as previously by division by the circumferential vane spacing t. The flow coefficient $V_{m,1}/w_{U,1}$ is obviously cot β_1 (see fig. 3-61), and β_1 is related to β_v by equation (3-146). It should be clear that $\tau_{n,c}$ includes an assumed thickness of the cavitation void as does τ_c.

The lower practical limit of the thickness ratio $\tau_{n,c}/t$ is assumed to be 0.025. Thus, for example, a

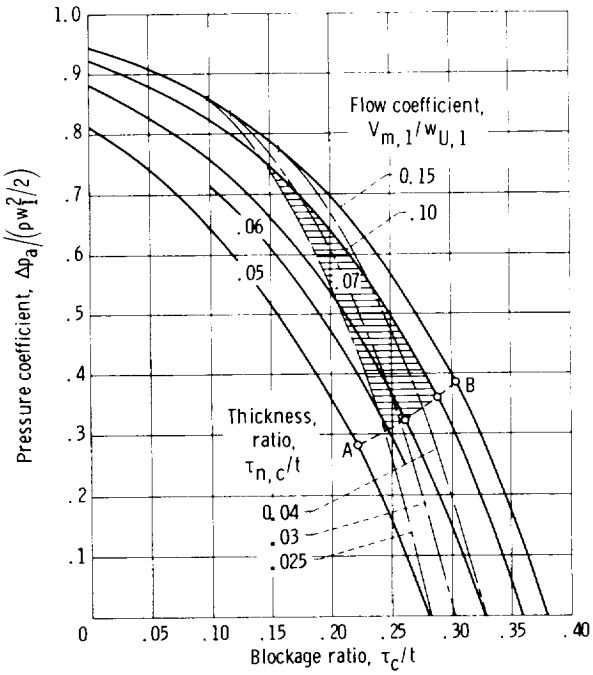

Figure 3-66. – Pressure coefficient at pressure side of vane near inlet as a function of blockage ratio.

three-vane inducer 10 inches in diameter, with $t = 10\pi/3 = 10.47$ inches, has $\tau_{n,c} = 0.025 \times 10.47 = 0.26$ inch; this value is here considered a minimum for an inducer 10 inches in diameter, because the actual vane thickness must be less, certainly not more than 0.20 inch, since $\tau_{n,c}$ includes the thickness of the cavitation void.

The horizontal line $\tau_{n,c}/t = 0.025$ in figure 3-67 is transferred to figure 3-66 and appears there as a dash-dot curve marked with the same thickness ratio. The corresponding curves are drawn for $\tau_{n,c}/t = 0.03$ and 0.04.

The solid curve for $V_{m,1}/w_{U,1} = 0.05$ lies entirely to the left of the dash-dot curve for $\tau_{n,c}/t = 0.025$, so that this flow coefficient cannot be reached with the assumed minimum vane plus the cavity thickness ratio $\tau_{n,c}/t = 0.025$. The minimum flow coefficient that can be reached with the stated minimum thickness ratio is established approximately by adding part of the curve for a flow coefficient of 0.06 to this diagram. This curve intersects curve AB just slightly to the right of the curve $\tau_{n,c}/t = 0.025$, so that $V_{m,1}/w_{U,1} = 0.06$ is just slightly above the minimum flow coefficient that can be reached with this thickness ratio. The minimum pressure coefficient $\Delta p_a/(\rho w_1^2/2)$ usable under the rules adopted here is approximately 0.3,

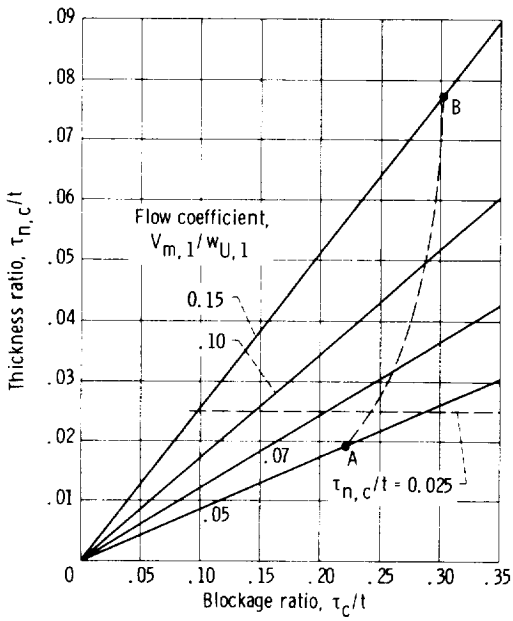

Figure 3-67. – Blockage analysis of inducer vane system.

and its maximum value for $V_{m,1}/w_{U,1} = 0.06$ is only slightly higher (0.34).

Furthermore, when it is assumed that flow coefficients higher than 0.1 are of only limited practical value in the rocket pump field (see fig. 1-18), the foregoing restrictions lead to the conclusion that the shaded area in figure 3-66 is the only usable area in the field of application discussed here.

When these results are used, it must be remembered that the various assumptions made to arrive at the diagram in figure 3-66 and its underlying equations are quite hypothetical, considering the complexity of the actual flow, which is discussed further in section 3.4.5. Figure 3-66 can, therefore, serve only as a means of general orientation. For example, it indicates that the inducer flow coefficient probably has a lower practical limit, here estimated to be 0.06. From figure 1-18, one must conclude that this leads to an upper limit of the suction specific speed obtainable under the assumptions made here, without thermal effects on cavitation.

As yet there is no indication of the location along the vane at which the face presssure coefficient, just established to be between 0.35 and 0.7, is to be expected. This location can be approximated as follows: If $\overline{\Delta p}_a$ is the average vane pressure difference from the leading edge to section a-a along the pressure surface (see fig. 3-65(b)) and y_a is the axial distance of section a-a from the leading edge, the change in circumferential momentum is related to the circumferential blade force by

$$\overline{\Delta p}_a y_a = A^*\left(w_{U,1} - \overline{w}_{U,a}\right)\rho(t - \tau_c)\overline{V}_{m,a} \qquad (3\text{-}156)$$

where $(t-\tau_c)\overline{V}_{m,a} = tV_{m,1}$ is the volume flow rate per vane and per unit height normal to the plane of the flow. The coefficient $A^* < 1$ expresses the fact that in a nonuniformly distributed flow like that shown in figure 3-65(b) the regions with the greatest momentum change have the least flow per unit area, and vice versa. However, this effect can hardly be major.

Combining equations (3-150) and (3-156), one obtains the relation

$$2\overline{w}_a(w_{a,max} - \overline{w}_a)\frac{\overline{\Delta p}_a}{\Delta p_a} y_a = A^*(w_{U,1} - \overline{w}_{U,a}) \times (t-\tau_c)\overline{V}_{m,a} \qquad (3\text{-}157)$$

From figure 3-65(b), it is evident that, under the assumption of a pressure distribution expressed by this figure, $\overline{\Delta p}_a/\Delta p_a > 1$. As explained previously, with $A^* < 1$,

$$\frac{\overline{\Delta p}_a}{\Delta p_a}\frac{1}{A^*} \equiv B > 1 \qquad (3\text{-}158)$$

but may not be very much larger than 1, since the departures of $\overline{\Delta p}/\Delta p_a$ and A^* from unity are not expected to be very large. With the notation introduced by equation (3-158), equation (3-157) can be written in the form

$$2\frac{w_{a,max} - \overline{w}_a}{w_{U,1} - \overline{w}_{U,a}} B = \frac{t-\tau_c}{y_a}\frac{\overline{V}_{m,a}}{\overline{w}_a} = \frac{t-\tau_c}{y_a}\cos\bar{\beta}_a \qquad (3\text{-}159)$$

since $\overline{V}_{m,a}/\overline{w}_a = \cos\bar{\beta}_a$ is evident from figure 3-65(a). From the same figure, it is reasonable to make y_a dimensionless by dividing by $t\cot\beta_v$, that is, by the rise (or advance) of the pressure face of

one vane over the leading edge of the following vane. This introduces the ratio

$$Y = \frac{y_a}{t \cot \beta_v} = \frac{y_a}{t} \frac{\sin \beta_v}{\cos \beta_v} \tag{3-160}$$

With this notation, equation (3-159) can be written in the form

$$2 \frac{w_{a,max} - \overline{w}_a}{w_{U,1} - \overline{w}_{U,a}} BY = \left(1 - \frac{\tau_c}{t}\right) \sin \beta_v \frac{\cos \overline{\beta}_a}{\cos \beta_v} \tag{3-161}$$

Figure 3-68 shows that, for a typical velocity diagram drawn with $V_{m,1}/U = 0.1$, the ratio $(w_{a,max} - \overline{w}_a)/(w_{U,1} - \overline{w}_{U,a})$ is within drafting accuracy equal to $1/\sin \overline{\beta}_a = 1.017$, that is, the ratio is practically unity. When $\overline{\beta}_a - \beta_v = 1°$ is assumed, the ratio $\cos \overline{\beta}_a / \cos \beta_v$ is -0.914 and $\sin \beta_v$ is approximately 0.98, so that $\sin \beta_v \cos \overline{\beta}_a / \cos \beta_v = 0.896$. Hence equation (3-161) reduces to the form

$$2BY = \left(1 - \frac{\tau_c}{t}\right) \frac{0.896}{1.017} = \left(1 - \frac{\tau_c}{t}\right) 0.881$$

From figure 3-66, one may conclude that an average, useful value of τ_c/t is approximately 0.24. With this value, one finds $BY = 0.335$. Since B is slightly, say about 10 percent, larger than unity, it is reasonable to conclude that

$$Y \approx 0.3 \tag{3-162}$$

as shown in figure 3-65(a). Thus the vane face pressure coefficient shown in figure 3-66 applies for a solidity of 1 to a point less than one-third of the vane length removed from the leading edge. Since inducer vane systems usually have solidities much greater than 1, the point to which the $\Delta p_a/(\rho w_1^2/2)$ values in figure 3-66 apply lies very close to the leading edge, for example, at a distance slightly less than one-sixth of the vane length for a system with a solidity of 2.

The foregoing results require some additional analysis before they are ready to be used in the design of inducer vane sections. Particularly there should be an estimate of how the momentum or head rise from the inlet to section a-a (fig. 3-65) compares with the total momentum or head rise accomplished in the entire cylindrical section considered. Such an estimate permits the establishment of an approximate relation between Δp_a (as given by eq. (3-154) and fig. 3-66) and the vane pressure difference over the remainder of the blade after section a-a.

The rise in angular momentum from the inlet to section a-a is expressed by equation (3-156), which obviously contains the mean vane pressure difference from the leading edge to section a-a. On

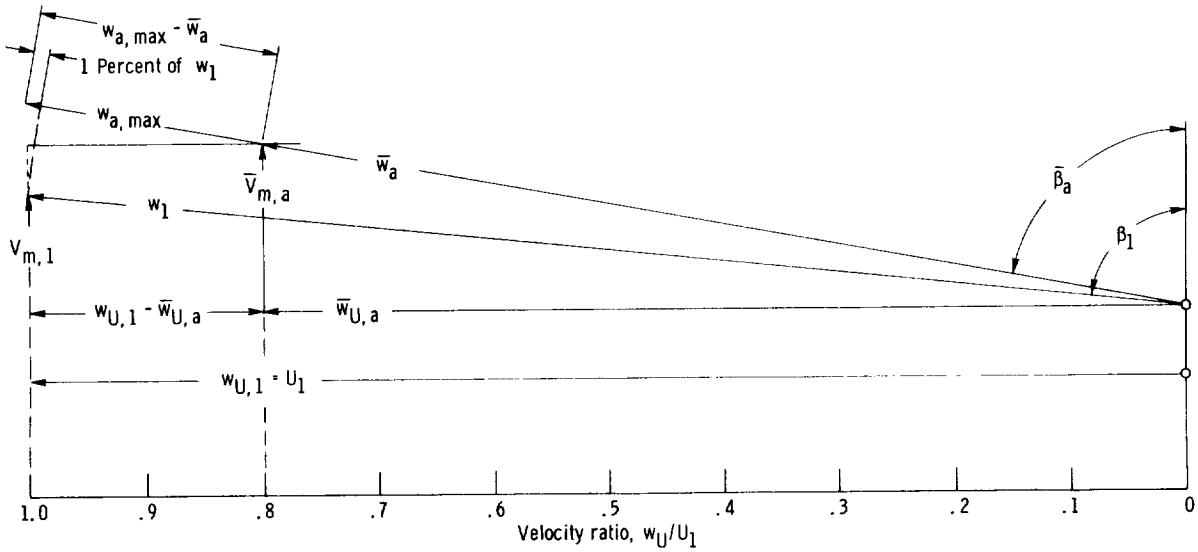

Figure 3-68. – Velocity diagrams for $V_{m,1}/U = 0.1 = \cot \beta_1$ at axial distance $y_a = 0.3\ t \cot \beta_v$ from leading edge. For reasons of clarity, $w_{U,1} - w_{U,a}$ and $w_{a,max} - w_a$ are shown at twice their correct size.

the other hand, equation (3-154) and figure 3-66 describe the local vane pressure difference Δp_a at section a-a. These two relations can be combined in the form

$$\overline{\Delta p}_a = \Delta p_a \frac{\overline{\Delta p}_a}{\Delta p_a} = A^* \Delta V_{U,a} \rho \frac{t}{y_a} V_{m,1} \qquad (3\text{-}163)$$

where $\Delta V_{U,a} = w_{U,1} - \overline{w}_{U,a}$ and $tV_{m,1} = (t - \tau_c) V_{m,a}$.

The desired result is here derived for $\Delta p_a / (\rho w_1^2/2) = 0.4$ and for a flow coefficient $V_{m,1}/w_{U,1} = \cos \beta_1 = 0.07$, which in figure 3-66 is associated with $\tau_c/t = 0.24$ and has an acceptable location within the shaded area of practically useful and possible design conditions.

With $\Delta p_a = 0.4 \ \rho w_1^2/2$, and when equation (3-160) is used, equation (3-163) can be written in the form

$$\frac{\Delta V_{U,a}}{U} = 0.2 \frac{\overline{\Delta p}_a}{\Delta p_a} \frac{1}{A^*} \frac{w_1}{U} Y \frac{\cos \beta_v}{\sin \beta_v} \frac{w_1}{V_{m,1}}$$

With the notation introduced by equation (3-158), as well as the trigonometric relations between the velocity ratios and the inflow angle β_1 (see fig. 3-61), one finds

$$\frac{\Delta V_{U,a}}{U} = 0.2 B \frac{1}{\sin \beta_1} Y \frac{\cos \beta_v}{\sin \beta_v} \frac{1}{\cos \beta_1} \qquad (3\text{-}164)$$

With the flow coefficient $\cot \beta_1 = 0.07$, one obtains $\beta_1 = 86°$ and according to equation (3-146), $\beta_v = 83.04°$. Using the previously derived value $Y = 0.3$ and for B the estimated value of 1.1, one obtains

$$\frac{\Delta V_{U,a}}{U} = 0.22 \times \frac{1}{0.9976} \times 0.3 \times \frac{0.1212}{0.9926} \times \frac{1}{0.06983} = 0.1157$$

This velocity ratio can readily be converted into the head coefficient applying to section a-a:

$$\psi_a = \frac{2 g_o H_a}{U^2} = 2 \eta_h \frac{\Delta V_{U,a}}{U} = 1.7 \times 0.1157 = 0.1967$$

where the so-called hydraulic efficiency η_h is assumed to be 0.85.

The foregoing evaluations of equation (3-163) apply primarily to the tip section of an inducer, because of the assumed flow coefficient $\cot \beta_1 = 0.07$. Figure 3-66 shows that substantially larger diameters are not possible, because 0.07 is close to the minimum flow coefficient feasible under the assumptions used here. The maximum total head coefficient of the tip section with diameter $D_{i,2}$ can be estimated from the head coefficient $\psi_{h,2} = 2 g_o H / U_{h,2}^2$ by the relation

$$\psi_i = \psi_{h,2} \frac{D_{h,2}^2}{D_{i,2}^2} \qquad (3\text{-}165)$$

For the frequently assumed value $\psi_{h,2} = 1$, this equation is obviously reduced to the simple form

$$\psi_i = \frac{D_{h,2}^2}{D_{i,2}^2} \qquad (3\text{-}166)$$

Consider, for example, a so-called high-head inducer having a discharge diameter ratio $D_{h,2}/D_{i,2} = 0.8$ (see fig. 3-59, particularly the second drawing from the top). With $\psi_{h,a} = 1$, it is seen from equation (3-166) that $\psi_i = 0.64$. If $\psi_a = 0.2$, it follows that $\psi_i/\psi_a = 3.2$ and, therefore, that the total momentum and head rise in the tip section is 3.2 times this rise up to section a-a. However, as previously shown on the basis of the approximate relation (3-162), the vane length from the inlet to section a-a is only about one-sixth of the entire vane length. The mean vane pressure difference over the rest of the vane after section a-a must, therefore, be only about one-half of the mean vane pressure difference $\overline{\Delta p}_a$ from the leading edge to section a-a. Consequently this vane is necessarily leading-edge loaded.

This situation is even more pronounced with the so called low-head inducers. Consider a typical case with $D_{h,2}/D_{i,2} = 0.4$. According to equation (3-166), this value leads to $\psi_i = 0.16$. With radially increasing inducer head, as described in connection with figure 3-58, ψ_i could be increased to about 0.2, but not much more. Thus, for low-head inducers, the momentum and head rise reached at section a-a is at least as great or greater than the entire momentum and head rise required at the tip section.

This conclusion does not mean that the tip section of the vane could end at section a-a. One reason why it could not is that it would operate with the cavitation void passing through the system to its discharge side, which would change the action of the system, as explained briefly in section 2.5.4 by means of figure 2-21. A second, related reason is that the earlier assumption that the mean flow angle

β_a in section a-a would be only slightly larger than β_v would be invalid. A (straight) extension of the vanes beyond section a-a would be necessary to permit closing of the cavitation void within the system and to even out the flow before it leaves the system, since in section a-a the change in angular momentum is essentially zero for the streamline along the cavitation void and is twice its mean value for the streamline along the pressure face of the vane. Nevertheless the extension of the vane (in the tip section) beyond section a-a has only indirect reasons, as indicated, if the required change in angular momentum is already accomplished in section a-a. In addition to the closing of the cavitation void and the equalization of the active flow, this extension of the vanes must also permit the gradual dissipation of the turbulent wake behind the cavitation void shown in figure 3-61. Generally the minimum solidity of inducer vane systems must be somewhat larger than unity, as becomes more evident in section 3.4.5

For vane sections where the increase in angular momentum $\Delta V_U/U$ is distinctly larger than 0.12, the mean streamline method may be employed to obtain a reasonable vane pressure distribution. One might be tempted to assume a rather abrupt increase in static pressure after the point of closure of the cavitation void. This is not likely to be a valid assumption because of the existence of a turbulent wake in this region (see fig. 3-61). One should assume instead a gradual pressure rise after the closure of the cavitation void. Even ahead of an assumed point of closure (estimated from the wall pressure and the mean flow pressure), the cavity pressure can be expected to rise in the direction of the flow, because of dispersed liquid in the cavity. This assumption is in accordance with the work by Ruggeri, et al. (refs. 42 and 43) represented in section 2.8.4 by figure 2-79. It is important to maintain a very conservative pressure gradient behind the cavitation void, since the turbulent wake following the termination of this void (see fig. 3-61) is very prone to separation in an adverse pressure gradient.

3.4.4 Summary of Procedure for Design of Inducer Vane Systems Based on Frictionless Flow Through Axial-Flow Inducers

This section summarizes the results of the foregoing sections 3.4.2 and 3.4.3 and of reference 59 on the basis of the idealized flow considerations employed in these sections. These considerations exclude (except for overall efficiency) the effects of fluid friction (viscous or turbulent) and of the secondary fluid motions induced thereby. (Only in one instance were local fluid friction effects considered, when recognizing the existence of a turbulent wake behind a closing cavitation void.)

The method of designing cylindrical vane sections of inducers emerging from these considerations is the following:

(1) The design is based on the direction of the relative velocity w_1 of the flow before entering the vane system. This direction is expressed by the angle β_1 measured from the axial (or meridional) direction.

(2) The low-pressure side of the vane should not touch the boundary of the cavitation void, which is approximated by a straight line through the leading edge of the vane having the direction β_1 of the oncoming relative flow w_1. This rule should be satisfied up to a flow 10 percent in excess of the design flow. With the notations given in figures 3-61 and 3-62, this rule assumes the form

$$\cot(\beta_v + \alpha_w) = 1.10 \cot \beta_1 = 1.10 \frac{V_{m,1}}{w_{U,1}} \qquad (3\text{-}143)$$

where β_1 and $V_{m,1}$ express the design flow rate.

(3) The leading portion of the vane is wedge-shaped, as shown in figure 3-61. The pressure face near the leading edge is straight and has the direction β_v determined by the empirical relation

$$\frac{\pi}{2} - \beta_v = (1.54 \text{ to } 2)\left(\frac{\pi}{2} - \beta_1\right) \qquad (3\text{-}147)$$

which is intended to assure an adequate wedge angle α_w. A factor of 1.739 corresponds to 0.425 in equation (3-144), according to equation (3-146).

(4) The low-pressure side of the vane, as described by item (2), should turn in the direction β_v of the leading side of the vane in a region from $0.5\,t$ to $0.8\,t$ removed from the leading edge (see fig. 3-61). The desired vane thickness is important in this choice.

(5) The leading edge may be shaped approximately according to figure 3-63.

(6) In section a-a (fig. 3-65(a)), at an axial distance from the leading edges of approximately $y_a = 0.3\,t \cot \beta_v$, the leading face pressure above the

vapor pressure is approximately given by equations (3-154) and (3-153) and by figure 3-66. These equations and this figure are derived by a quasi-one-dimensional consideration under the assumption that the cavitation void extends through section a-a.

(7) On the basis of the results quoted under item (6), one can estimate the momentum and head rise up to section a-a (fig. 3-65(a)) from equation (3-164). For a flow coefficient $V_{m,1}/w_{U,1} = 0.07$, with $U = w_{U,1}$, the momentum rise up to section a-a is $\Delta V_{U,a} \approx 0.12\ U$, which is for high-head inducers a substantial part, say one-third, of the total momentum rise of the tip section. For low-head inducers, it is about equal to the total momentum rise of the tip section.

(8) If the total circumferential deflection expected from the cylindrical vane section considered is not substantially larger than $\Delta V_U = 0.12\ w_{U,1}$, the pressure face of the vane can continue approximately under the angle β_v to the trailing edge, and the suction face curves can continue gradually to meet the trailing edge at a small, final vane thickness. The vane must extend considerably beyond section a-a to permit cavity closure and equalization of the flow. The solidity required to accomplish this is empirically found to be never less than unity. The pressure on the suction side of the vane starts with the vapor pressure p_v and begins to rise gradually somewhat before the (estimated) end of the cavitation void (beyond section a-a). The pressure on the high-pressure side of the vane starts with Δp_a at section a-a (given in figs. 3-66 and 3-65(b)) and smoothly approaches the discharge pressure of the system, which is $p_2 = p_1 + \rho(w_1^2 - w_2^2)/2$. In estimating the discharge relative velocity w_2, one should take the boundary layers into account. A vane system designed as outlined here is expected to generate somewhat more head than indicated by the mean change in angular momentum predicted for section a-a.

(9) If the total circumferential deflection required from the cylindrical vane section considered is substantially larger than $\Delta V_U = 0.12\ w_{U,1}$, the mean streamline method permits the design of the vane section with a smooth transition from the inlet portion designed according to the preceding consideration. Up to section a-a (axial distance y_a), the vane pressure distribution is given by p_v on the suction side and Δp_a (from fig. 3-66) on the high-pressure side. Near the leading edge, the stagnation pressure is reached, as indicated in figure 3-65(b), but this pressure distribution should be plotted against the axial coordinate y as previously described for the mean streamline method of design. The pressure along the suction side of the vane begins to rise slightly above the vapor pressure somewhat before the (estimated) end of the cavitation void. The subsequent pressure rise toward the discharge static pressure of the mean flow must be very gradual to avoid separation under the influence of the turbulent wake behind the cavitation void. Separation is avoided by selecting a low lift coefficient, certainly lower than the pressure difference $\Delta p_a/(\rho w_1^2/2)$ near the leading end of the vane; that is, the lift coefficient $C_{L,1}$ should be lower than 0.4. For inducer vanes, this value leads to leading-edge-loaded profiles in contrast to vane systems designed for little or no cavitation, where uniform loading or trailing-edge loading should be preferred.

(10) The three-dimensional layout of the entire inducer vane can follow the same principles as described and used in section 3.3.1. The geometric and mechanical problem is often more difficult with inducers than with more-standard, axial-flow pump rotors because of the large circumferential (angular) extent of the inducer vanes. No general solution of this problem is known to this writer. However, in the rocket pump field, the problem is met by using far-reaching compromises in favor of mechanical design and ease of manufacture.

3.4.5 Effects of Fluid Friction on Flow in Axial-Flow Inducers

Inducers for suction specific speeds in the range between 2 and 3 (35 000 and 50 000) must, according to figure 1-18, have flow coefficients between 0.10 and 0.06. Furthermore the solidity of the vane system is usually in the vicinity of 2 in the tip section and considerably larger near the hub. These values imply a very large ratio of blade chord to the average normal distance between the blades, so that the effects of fluid friction must be expected to be quite large. For example, with a solidity of 2 and a flow coefficient of 0.08, this ratio can be estimated to be about 12, so that the vane boundary layer cannot be expected to remain small compared with the normal distance between the vanes.

In addition, bending stress considerations outlined in section 1.3.3.2 indicate that, for inducers with relatively small hub diameters, the number of blades must be fairly small, say 3 or 4, so that a vane system with a solidity of 2 covers a

substantial angular extent, often more than π. In such inducers, the radii of curvature of the relative flow along the blades, which are nearly equal to the distances of the streamlines from the axis of rotation, are of the same order of magnitude as the radial extent of the blades and of the flow field next to the blades. This fact and the large angular extent of the vanes lead to a very significant effect of centrifugal forces on the flow in the vane boundary layers, as described in section 2.5.7 and figure 2-38. Specifically the radial motion in the boundary layers must be strong, and the resulting secondary flow is of more than just local importance, considering the previously mentioned thickness of the vane boundary layers. The secondary flow, usually confined to the relatively thin boundary layers, must be expected to occupy in inducers major portions, or the entire cross section, of the flow channel between the vanes near the discharge end of the rotor vane system. Figure 3-69 shows a cross section of the expected vane channel flow which has been confirmed by experimental observations, particularly those by Lakshminarayana reported in reference 62. The entire outer half of the vane channel is, as expected, occupied by boundary-layer fluid at the inducer discharge. Only in the region within the inner half of the vane channel is the flow not strongly influenced by the boundary layers. Under these circumstances, inducers of the type described here would be expected to have hydrodynamic characteristics substantially different from those predicted on the usual basis of a frictionless fluid corrected merely for the real efficiency. The previously mentioned investigations by Lakshminarayana had the purpose of clarifying this matter, and the following presentation is essentially an excerpt from reference 63, focusing attention on only those results that may be of major interest for the design engineer.

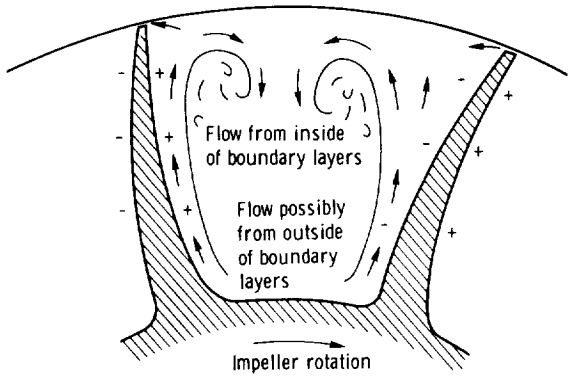

Figure 3-69.—Cross section through vane channel flow near inducer discharge. (This drawing applies qualitatively to any radial section between normal to vanes and parallel to axis of rotation.)

Lakshminarayana's investigations were carried out by means of a large-scale (3-ft-diam) model of an axial-flow inducer designed for a suction specific speed of 2.9 (50 000). The model is operated in air, since only fluid friction effects, not the cavitation characteristics, are under investigation. Important data on the model are given in table 3-III. The test inducer was originally designed (by the mean streamline method) for radially uniform head at radially uniform through flow velocity. A modification was necessary to permit reasonable fairing of the various sections, leading to a slightly higher theoretical (i.e., ideal-flow) head in the midsection ($r/r_o = 0.75$) than at the root and tip sections of the vanes.

The hub and tip sections of the inducer are shown in figure 3-70, and the axial end view of the vane as well as the circumferential projection of radial sections through this vane are shown in figure 3-71. In spite of the previously mentioned minor compromises in favor of fairing, the radial sections are far from straight, but are still mechanically acceptable.

The most important departures from the velocity and momentum distributions derived by frictionless flow considerations are obtained by velocity measurements behind the test inducer. Figure 3-72 shows the locations of the stations at which such measurements were made. These are the stations referred to in figures 3-73 to 3-76, which give test results from reference 63.

Figure 3-73 shows the measured variation of the absolute, circumferential velocities at various distances behind the test inducer. The dramatic departure from the design velocity distribution is immediately evident; the measured velocities increase with increasing distance from the axis of rotation rather than decreasing as assumed for the design. The increase can only be explained by the flow distribution at the discharge of the vane channel, shown diagrammatically in figure 3-69. The flow in the outer regions is under the influence of boundary friction and, because of the high stagger angles of the vanes (angles against the axial direction, table 3-III and fig. 3-70), acquires greater absolute angular momentum than it would

TABLE 3-III. - INDUCER CHARACTERISTICS

[Subscript t denotes vane tip; radius ratio $R = r/r_o$.]

Tip diameter, in.	36.5
Hub-tip ratio at outlet	0.5
Hub-tip ratio at inlet	0.25
Radial clearance, in.	0.0625
Design suction specific speed, S	50 000
Flow coefficient, $\varphi = V_z/U_t$	0.065
Blade chord, in.	
Tip (R = 1.0)	82.96
Midspan (R = 0.75)	63.18
Hub (R = 0.5)	49.94
Solidity	
Tip	2.86
Midspan	2.91
Hub	3.50
Number of vanes	4
Average angular wrap, deg	290
Lift coefficient of blade based on mean velocity	
Tip	0.0966
Midspan	0.163
Hub	0.307
Reynolds number based on tip radius	6.60×10^5
Reynolds number based on relative velocity and chord at midradius	1.75×10^6
Maximum deviation of camber line from mean streamline, $(\Delta n/L)_{max}$	
Hub	0.02
Midspan	0.01075
Tip	0.00637
Blade angle at inlet	
Hub	75°30'
Midspan	83° 30'
Tip	86°15'

without friction. The effectiveness of this increase in angular momentum is discussed later.

Somewhat startling is the apparent decrease in angular momentum with increasing distance from the rotor in a vaneless space of revolution. This apparent contradiction is explained, at least partly, by the axial velocity distribution shown in figure 3-74, since only the local mass flow ($\rho V_z \times$ area) times the circumferential velocity component ($V_\theta = V_U$) represents the transport in angular momentum. It should also be considered that the axial velocity component V_z is generally a small component of the total absolute velocity, so that its measurement is necessarily less accurate than that of the absolute velocity and its peripheral component.

Figure 3-74 indicates that the axial velocity component decreases near the hub with increasing distance from the rotor, and this effect suggests back flow and separation of the axial flow component after station 5 in figure 3-72. In reference 63, this separation is explained as being caused by the radial flow inside the blade boundary layers and in the blade wakes. References 62 and 64 report observations and flow measurements of this separation which indicate that it is the same for a stationary and a rotating hub surface behind the inducer. (This result is surprising, because the

C-4

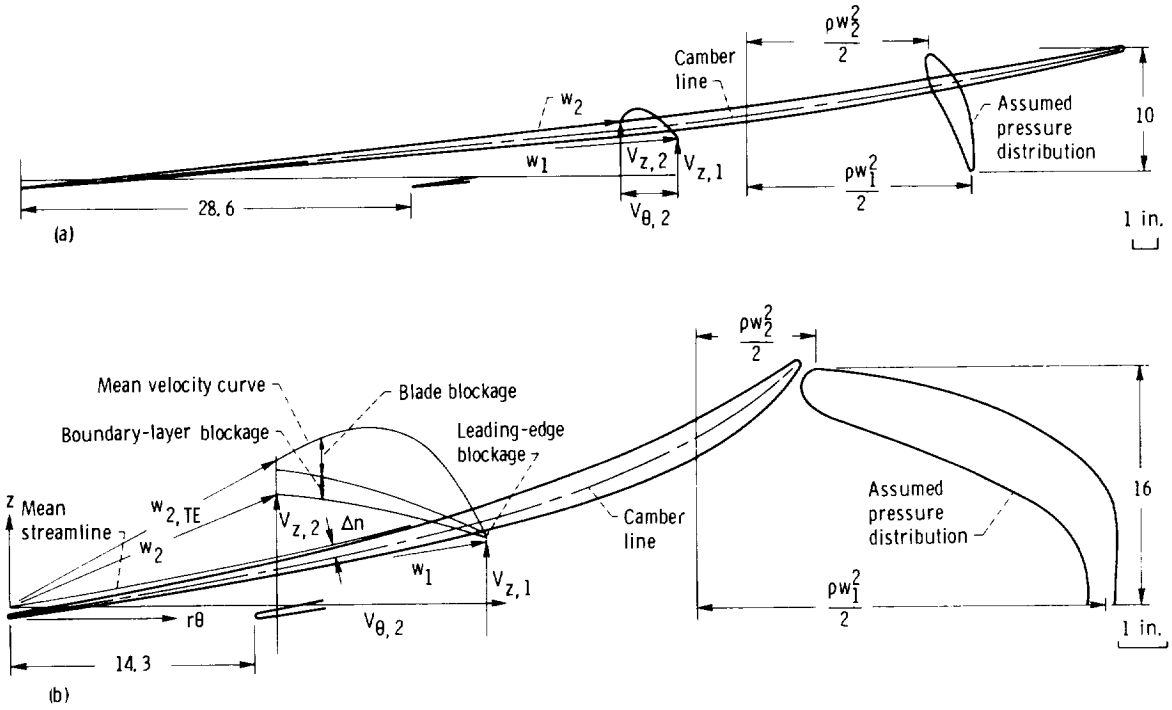

(a) Development of cylindrical tip section ($r/r_t = 1.0$).
(b) Development of cylindrical root section ($r/r_t = 0.5$).
Figure 3-70. – Design of blade profiles. (Dimensions in inches.)

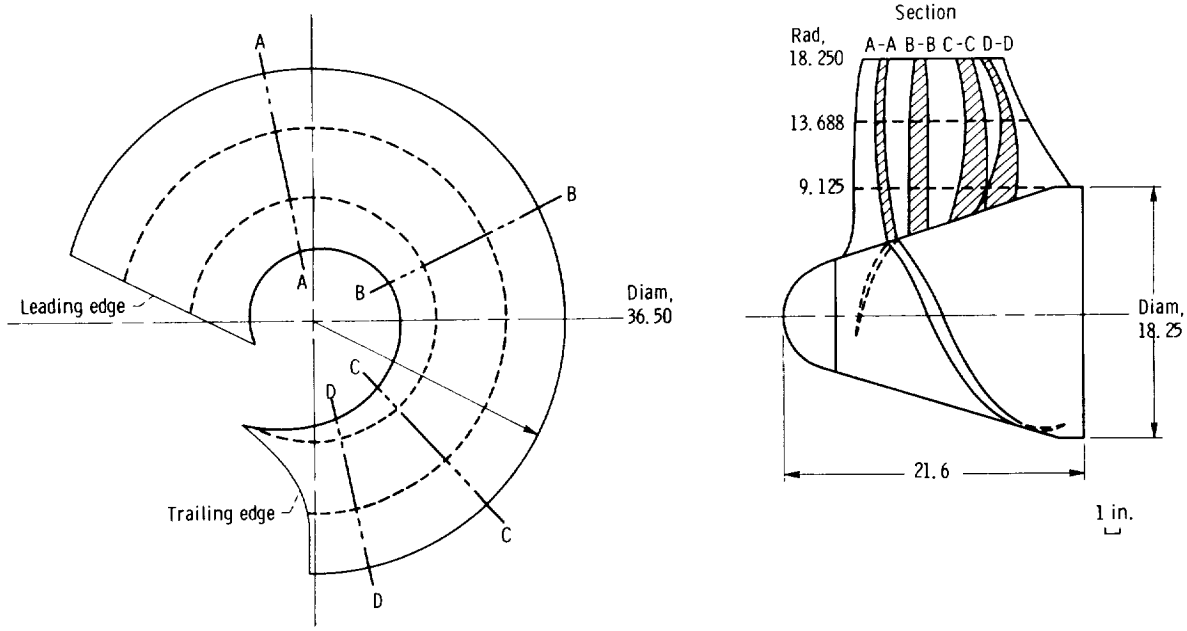

Figure 3-71. – Axial view and circular projection of inducer blade. (Dimensions in inches.)

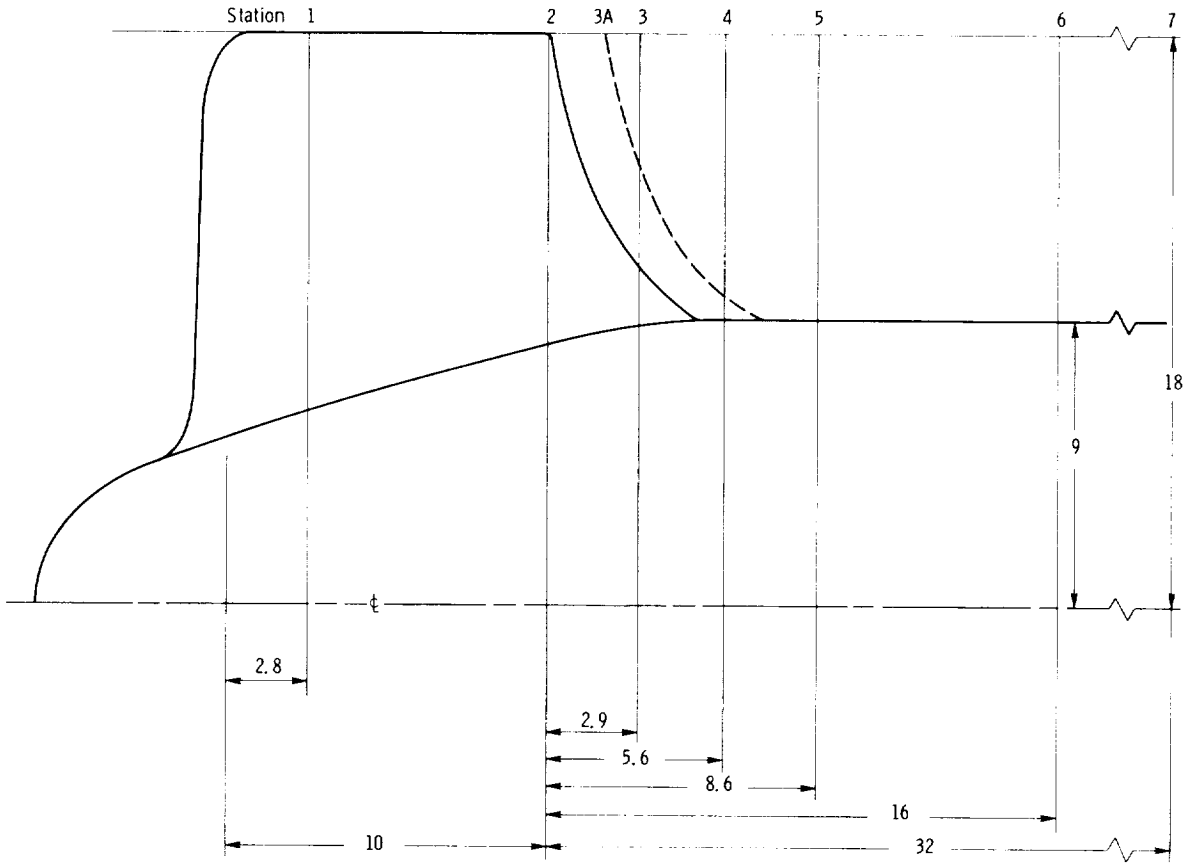

Figure 3-72. – Locations of flow measuring stations. (Dimensions in inches.)

motion of the boundary should have a significant influence on the boundary-layer flow.) An alternative (or additional) explanation for the separation of the axial flow from the hub is the static-pressure rise along the hub (see fig. 3-76). This pressure rise is mainly dictated by the circumferential flow, which has, in general, much higher velocities than the axial flow. Although this pressure rise appears to be small according to figure 3-76, it can be estimated to be about $5V_z^2/2g_o$, which is ample to explain the separation of the axial flow V_z.

Figure 3-75 shows the total head rise, measured behind the impeller, as a function of the radius ratio and of the distance behind the impeller. When these curves are compared with those in figure 3-73, it should be considered that in the controlling relation

$$\psi_T = \frac{2g_o H}{U_t^2} = 2\eta_h \frac{V_\theta U(r)}{U_t^2} = 2\eta_h \frac{V_\theta}{U_t} \frac{r}{r_t} \qquad (3\text{-}167)$$

the local hydraulic efficiency η_h varies very strongly as a function of the radius ratio as well as of the distance from the impeller. This efficiency falls off very rapidly with increasing r/r_t in the outer regions of the flow. The local hydraulic efficiency increases with increasing distance from the impeller; this effect certainly deserves further scrutiny. It is significant that the radial increase in the circumferential velocity shown in figure 3-73 is confirmed by a similar radial increase in the measured total head (fig. 3-75). This result should be fairly dependable in spite of the highly disturbed (unsteady) flow conditions under which all measurements of this investigation had to be taken.

Another dependable measurement is the previously mentioned static pressure at the outer and inner cylindrical walls of the flow field considered. It is also useful to interpolate between the outer and inner wall pressures at the same station (3,4,5, etc.), because the tangents to the $p(r)$ curves at each end are easily calculated from the circumferential velocity near each wall (outside a thin boundary layer). The results of such wall

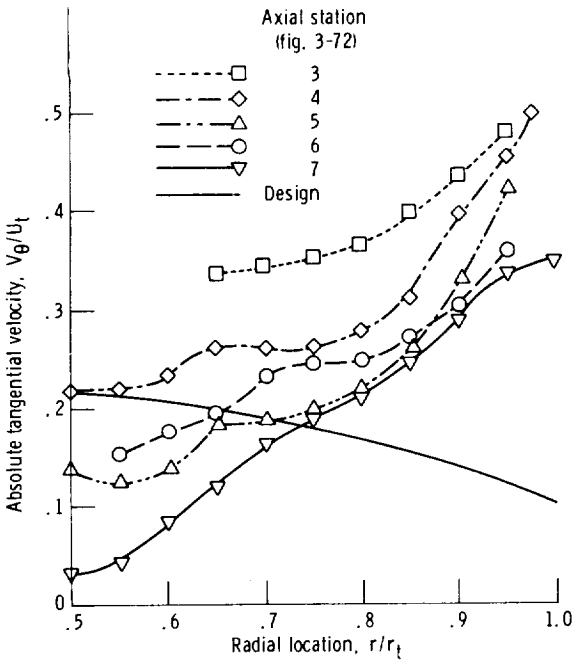

Figure 3-73. – Radial variation of absolute tangential velocity at various axial locations. Subscript a denotes circumferential component; subscript t denotes tip of vanes. (From ref. 63.)

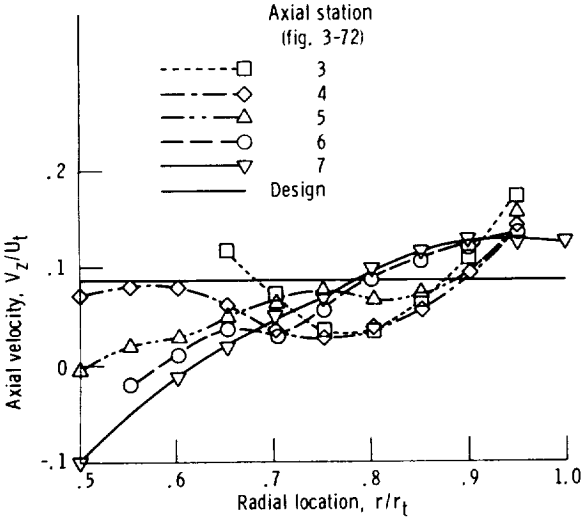

Figure 3-74. – Radial variation of axial velocity at various axial locations. Subscript z denotes axial or meridional component; subscript t denotes tip of vanes. (From ref. 63.)

pressure measurements are presented in figure 3-76 in terms of a static head coefficient:

$$\psi_S = \frac{2g_o h}{U_t^2} \tag{3-168}$$

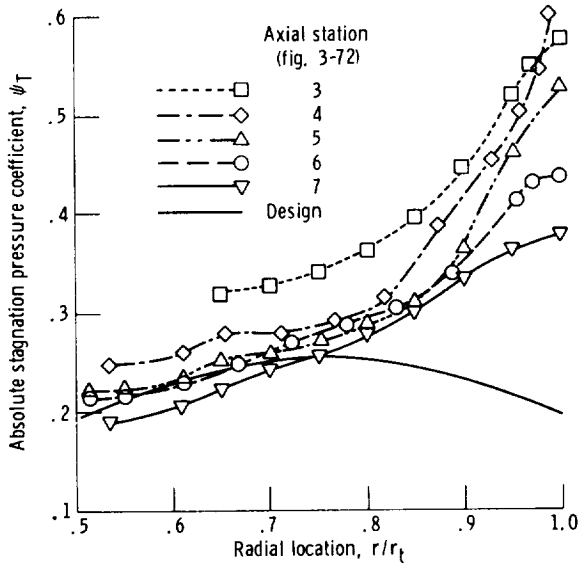

Figure 3-75. – Radial variation of absolute stagnation pressure coefficient at various axial locations. Subscript T refers to total head H in $\psi_T = 2g_o H/U_t^2$; subscript t denotes tip of vanes. (From ref. 63.)

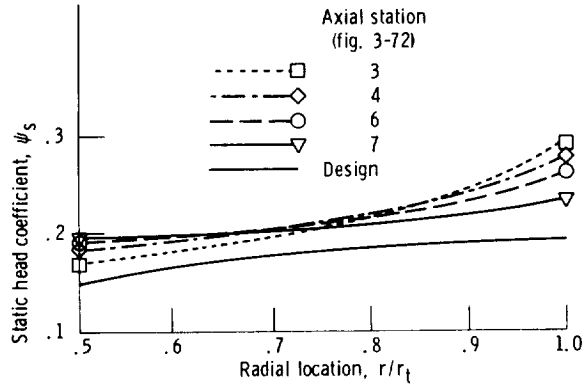

Figure 3-76. – Radial variation of static head coefficient at various axial locations. Subscript s refers to static head h in $\psi_s = 2g_o h/U_t^2$; subscript t denotes tip of vanes. (From ref. 63.)

where h is the static head.

It is of considerable interest that even the static head coefficient is somewhat higher than its design value, but the difference between the measured and the design value is far less than for the total head coefficient (fig. 3-75). Since it is not known how much of the kinetic energy in the highly disturbed flow represented by figure 3-75 can be recovered, it seems reasonable to consider that the measured static-pressure distribution (fig. 3-76) is a safe indication of the minimum head that can be expected from the inducer described by table 3-III

and figures 3-70 and 3-71. By comparing the test curves in figure 3-76 with the design curve in figure 3-75, one can conclude that the useful static head developed by an inducer with extensive fluid friction effects may not differ a great deal from that calculated by the usual design methods. Of course, the required torque is much higher than the design torque and may be more appropriately represented by measured values of ψ_T and V_θ/U_t (figs. 3-73 and 3-75), if these values are properly weighted for mass flow distribution. This distribution can be obtained by replotting the V_z/U_t curves in figure 3-74 against r^2/r_t^2, so that they represent the annulus area.

The aforementioned estimate of the useful inducer head is too conservative if the inducer is used, without a diffuser, in connection with an impeller, as shown in figures 3-56 and 3-57, because this impeller receives the total angular momentum leaving the inducer. It is particularly important to estimate the true angular momentum in the outer regions of the flow annulus between the inducer and the impeller in order to design the inlet to the impeller vane system properly to receive this flow. Only a fairly crude approximation is possible in this respect, since the actual flow leaving the inducer is generally not known. The excess angular momentum (over its design value) in the outer regions of the inducer discharge may well be less than indicated by figures 3-73 and 3-75, but some excess angular momentum in the outer regions must be assumed to exist. In view of the magnitude of possible departures from the design flow (by factors between 2 and 3), some flow measurements between the inducer and the impeller are a necessity for good impeller design.

The four-blade test inducer for which test results are presented in figures 3-73 to 3-76 is shown in table 3-III and figures 3-70 and 3-71 to have an extremely high solidity (2.86 at the tip). This solidity was chosen for the early tests in order to emphasize fluid friction effects. However, for practical application the solidity of the four-blade inducer tested is probably excessive and is likely to lead to low efficiency. For this reason, the test inducer was also investigated with three and with two vanes of the same shape.

All inducer models were tested at the same flow coefficient, Reynolds number, and blade angles (see table 3-III). The test results obtained with three and two blades are not presented here in detail, because they do not indicate behavior or flow pattern fundamentally different from those observed with the four-blade test inducer. However, the most essential effects of reducing the solidity of the test inducer from reference 64 are given here:

(1) The performance of the inducer improves continuously with decreasing solidity, the two-blade inducer showing substantial improvement over the four- and three-blade inducers. This change is to be expected, because inducers are designed for acceptable performance with cavitation, and this type of design results in solidities that are much higher than would be optimum with respect to fluid friction.

(2) The static-pressure (or head) rise increases continuously with decreasing solidity at all radii. The average static head coefficient for the four-blade inducer was 0.21 (see fig. 3-76); for the three- and two-blade inducers, the average head coefficients were 0.31 and 0.375, respectively.

(3) The stagnation pressure (or head) rise coefficient also increases continuously with decrease in blade number at all radii. The mass-averaged values are 0.4, 0.476, and 0.584, respectively, for the four-, three-, and two-blade inducers. The radial gradient of head rise coefficient $\partial\psi_T/\partial r$ is almost constant from hub to tip for the two-blade inducer, unlike that at other solidities, where a steep rise is observed near the tip.

(4) The axial velocity profile is qualitatively similar downstream of all the inducers tested. The steep rise in axial velocity toward the tip observed in three- and four-blade inducers is absent in the two-blade configuration, but the extent of the separated zone (or back-flow region) near the hub increases continuously with decrease in solidity. Very near the trailing edge (at station 3 in fig. 3-72), the axial velocity is radially uniform for the two-blade inducer, unlike that for the three- and four-blade inducers, where the minimum velocity occurs at midradius. This difference indicates the dominant influence of blade blockage, which is large for the four-blade inducer.

(5) The tangential velocity V_θ distribution shows a trend similar to the ψ_T distribution. But the large values of dV_θ/dr observed in the four- and three-blade inducers are reduced substantially in the two-blade configuration.

(6) The hydraulic efficiency (local as well as overall) increases continuously with decrease in solidity.

The results of the investigation of fluid friction effects in inducers are summarized at the end of reference 63. Reference 64 constitutes a summary of the entire project. No summary of these findings is given here. There are only a few comments on the practical application of the results quoted in this section:

(1) There is as yet no convincing reason why one should depart significantly from the design procedures outlined in sections 3.4.1 to 3.4.4, although it is known that fluid friction influences the flow in inducers significantly. In particular, the consideration of fluid friction does not justify a return to the (mechanically convenient) so-called flat-plate inducer design (actually having helical blades of constant pitch). Even with ideal, or nonviscous, flow conditions, the flat-plate inducer leads to radially increasing meridional velocity and pump head, that is, it departs from the desired uniform flow and head distribution in the same direction as a well-designed inducer under the influence of fluid friction. In other words, under any assumption, the flat-plate inducer must be expected to depart from the desired (uniform) flow distribution farther than an inducer designed by the usual methods for radially constant head (the so-called vortex design).

(2) The actual flow leaving the inducer must be recognized as one of radially increasing angular momentum. The degree of this departure from radially constant angular momentum is generally not predictable. Before a vane system following an inducer of the type described here is designed, it is highly desirable to measure the velocity distribution of the flow leaving the inducer. The departures from radially uniform angular momentum may be appreciable, the angular momentum always increasing with radius.

(3) In view of the fluid friction effects outlined in this section, one should be tempted to reduce the solidity of the outer portions of inducer vane systems as far as possible. Hence one should know the minimum solidity required to insure (a) closure of the cavitation void, (b) dissipation of the wake behind the cavitation void, and (c) a reasonable degree of equalization of the uneven velocity distribution in the presence of a cavitation void. (Items (b) and (c) are, of course, closely related.) References 60 and 61 offer some answers to these questions, but further experimental work would seem necessary before the answers are dependable under the complex, actual flow conditions in an inducer.

A progressively increasing reduction in solidity (vane chord) with increasing radius necessarily leads to a substantial departure of the leading and trailing vane edges from the radial direction. For the leading edge, there is a combination of backward skew and rake, called sweep, as shown in figure 3-33 and discussed in section 3.3.2. Fortunately backward sweep is advantageous for the performance of inducers and, if coupled with a reduction in vane chord (or solidity) in the outer portions of the vane, has obvious advantages regarding the mechanical strength of the vanes (see ref. 59). For substantial sweep (as shown, e.g., in fig. 3-33), one should estimate its effect on the oncoming velocity distribution as outlined in section 3.3.2. To do so, one must make an assumption regarding the part of the total vane vorticity that is generated by the swept portion of the vane, since the entire blade usually has little or no sweep. For the leading-edge loading used in inducers, the swept part of the vane vorticity may be in excess of one-half at the tip and between one-quarter and one-third at the root.

(4) With proper design considerations and experimentation, it should be possible to reduce the large-scale secondary fluid motions in inducers by more or less known means such as fences, appropriately designed slots in the outer portion of the vane (constituting high-lift devices), and perhaps an approximately cylindrical shroud between the hub and tip diameters. Other methods have been suggested.

Such methods of inducer improvement should be explored if the opportunity to do so presents itself. However, aside from mechanical complication and manufacturing difficulties, most methods of this type introduce additional skin friction. It is not certain that a reduction in large-scale secondary motions brings significant advancements if obtained by the addition of skin friction.

(5) High-head inducers with large discharge hub diameters, such as shown in figure 3-59, are not subjected to major effects of fluid friction and can be designed for fairly high increases in head along conventional lines, for instance, by the mean streamline method. The inlet portion of the vanes must be designed according to section 3.4.2 wherever the vane cavitation coefficient is sufficiently low that extensive cavitation is expected.

The success frequently achieved with high-head inducers raises the question of whether inducers used in combination with standard centrifugal pump impellers should not be redesigned to form a hydrodynamic unit with the centrifugal impeller.

Chapter 4

Hydrodynamic and Gas-Dynamic Design of Radial- and Mixed-Flow Turbomachinery

4.1 Introduction

The theoretical principles of radial- and mixed-flow turbomachinery are outlined in section 2.6 as far as they are directly applicable to the design of this type of machinery as treated in this compendium. It is pointed out there that the design principles of radial- and mixed-flow turbomachines are to a large extent the same if the flow of the latter can be approximated as proceeding along straight, conical stream surfaces which can be developed into planes (see fig. 2-41). Within these surfaces and planes, the flow can be treated as proceeding along radial planes normal to the axis of rotation.

In the design process, one must consider the fact that in truly radial-flow systems the flow and the vane shape can be assumed to be identical in parallel, plane stream surfaces normal to the axis of rotation (see fig. 2-40). In mixed-flow or conical-flow systems (fig. 2-41), however, the streamlines and the vane shapes in different conical stream surfaces generally cannot be identical. The flow in truly radial-flow systems may be treated as two-dimensional, whereas flow in an entire conical-flow system must be treated as three-dimensional, because corresponding points in various conical stream surfaces are at different distances from the axis of rotation. Nevertheless the flow in each conical stream surface can be treated as two-dimensional, particularly if the various conical stream surfaces are parallel to each other.

Furthermore, as pointed out in section 2.6, the relative flow in a radial-flow rotor is fundamentally different from the flow through the same vane system at rest, because the relative flow through the rotating system has a uniformly distributed vorticity

$$\zeta_{rel} = -2\omega \tag{4-1}$$

where ω is the absolute angular velocity of the truly radial-flow system. The design of radial-flow stator systems is, therefore, fundamentally different from that of rotating, radial-flow systems. Recall that such a difference does not exist for the individual cylindrical flow sections of axial-flow vane systems, although the entire axial-flow vane system is different for stator and rotor.

In addition to the previously mentioned characteristics of radial- and mixed-flow systems in contrast with axial-flow systems, mixed-flow systems present an inherently three-dimensional design problem as soon as the meridional stream surfaces cannot be approximated by straight, conical surfaces, that is, as soon as the meridional flow changes within the vane system from approximately axial to approximately radial, or vice versa, as shown, for example, in figures 1-7 and 1-25. In this case, the meridional stream surfaces have double curvature and cannot be developed into a plane, so obviously there is a special problem regarding the description of the flow and vane shape within these surfaces. Rotors with doubly curved meridional stream surfaces are called Francis rotors, but vane

systems of this type are used also as passages between successive stages of radial- or mixed-flow pumps and compressors (see fig. 1-28, example C). It is obvious that rotor and stator vane systems of this type must occupy an important place in the design of radial- and mixed-flow turbomachinery.

The general philosophy of treatment continues to be the same as indicated in the Introduction of chapter 3. Primary attention is given to preliminary design in the sense of establishing the general design form of a machine, rotor, or stator. In this formative stage, the design of radial- and mixed-flow machines is dominated by graphical procedures still more than the design of axial-flow machines. Even similarity considerations, beyond the calculation of a few specific speeds, depend on the existence of a general design form before the specific speeds can be translated into ratios of dimensions, and the general design forms of radial- and mixed-flow machines vary over a much wider range than those of axial-flow machines.

Furthermore most radial- and mixed-flow vane systems have a higher solidity and lower aspect ratio (vane span/vane length) than usually used in the axial-flow field (except in inducers), characteristics which increase the importance of real-flow effects. Unfortunately, the empirical background of experimental cascade data, so important for axial-flow machines, is not available in the field of radial- and mixed-flow machines. This entire situation makes radial- and mixed-flow machinery design still more dependent on geometric procedures, simple (though rational) approximations, and empirical data than is the design of axial-flow turbomachinery. The practical orientation of design procedure, already used in chapter 3, is, therefore, even more justified in this chapter.

The effects of compressibility can be taken into account by the same principles as outlined and used in chapters 2 and 3, specifically sections 2.4 and 3.2.7. These principles can be applied effectively only to the inlet and discharge conditions of any one vane system. The detailed investigations outlined in section 3.2.7 can apply only to stationary vane systems, specifically to the diffusers of compressors with sonic or supersonic rotor discharge velocities. This chapter shows that an essentially one-dimensional application of the laws of compressible fluid flow is relatively simple and straightforward.

Since the principles of compressible fluid flow differ from those of incompressible fluids, mainly by changes in the volume flow rate, the fluid mechanics used in this chapter are called hydrodynamic.

4.2 Geometry of Radial-Flow Vane Systems

The geometry of axial-flow vane systems as seen in the development of coaxial, cylindrical sections through the system is essentially Cartesian, with the axial and circumferential coordinates being (in the development) straight and normal to each other. In contrast, the most natural coordinate system of radial-flow systems as seen in flow surfaces normal to the axis of rotation, or in the development of conical flow surfaces, is a polar coordinate system. As a consequence, the geometries in these two types of systems are substantially different; in particular, the concept of what is simple in these two systems is quite different. In the Cartesian system, the simplest geometric construction is obviously a straight line. In the polar system, this is true only for radial lines. Generally a line with a constant inclination (angle) against the coordinate directions (radial and circumferential) must be considered the simplest line, and it is a logarithmic spiral. As shown in section 2.6.2, the same curve is also the streamline of an absolute, axisymmetric ideal flow between two planes normal to the axis of rotation, because the radial as well as the circumferential components of this flow change in inverse proportion to the radius, so that their ratio remains constant. The equation of the logarithmic spiral is

$$\varphi - \varphi_1 = \tan \beta_r \ln \frac{r}{r_1} \tag{4-2}$$

where φ is the angular coordinate, φ_1 is the initial value of φ, β_r is the angle between the curve and the radial direction (β_r = constant), r is the radial coordinate, and r_1 is the initial value of r. Figure 4-1 shows an approximate, graphical construction of a logarithmic spiral out of circular arcs, derived in chapter 22 of reference 14. In figure 4-1, $\beta_\varphi = \pi/2 - \beta_r$ is the inclination of the spiral against the circumferential direction, which is used because of its obvious geometric relation to the radial direction of the system shown in figure 4-2.

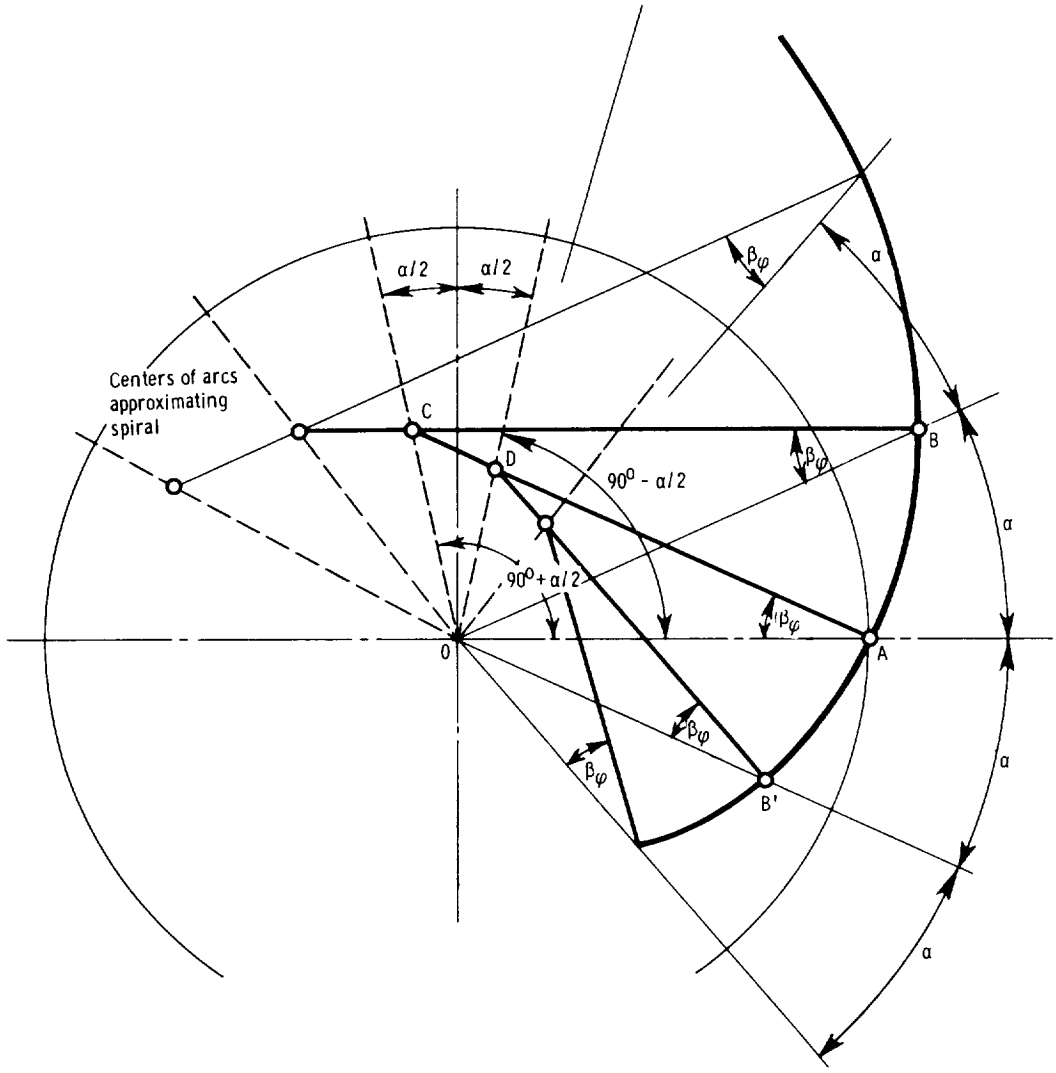

Figure 4-1. – Construction of logarithmic spiral out of circular arcs.

For finite angular steps, α, the angle of the curve derived according to figure 4-1, is, of course, not strictly constant. From figure 233 of reference 14, one can derive the following relation between the construction angle β_φ used in figure 4-1 and the average angle of inclination $\beta_{\varphi,av}$ of the resulting approximation of a logarithmic spiral:

$$\frac{\beta_\varphi}{\beta_{\varphi,av}} = \frac{1}{1+(1/4)(\alpha/2)^2(\sin\beta_\varphi\cos\beta_\varphi)/\beta_\varphi} \qquad (4\text{-}3)$$

where all the angles β_φ, $\beta_{\varphi,av}$, and α, must be measured in radians. (Note that eq. (4-3) is different from the equation derived in ref. 14 because a mistake made in that reference has been corrected.)

The results obtained from equation (4-3) are shown in figure 4-3. There is no significant difference between β_φ and $\beta_{\varphi,av}$ for angular steps α below 20°.

Because of the accumulation of errors, the construction shown in figure 4-1 should not be used for a large number of steps . For long spirals, equation (4-2) gives more accurate coordinates. It is convenient to use the equation in the form in which, if any two points of a logarithmic spiral are given, a third one can be found. From figure 4-4 and equation (4-2), it can be seen that, for $\Delta\varphi_1 = \Delta\varphi_2$,

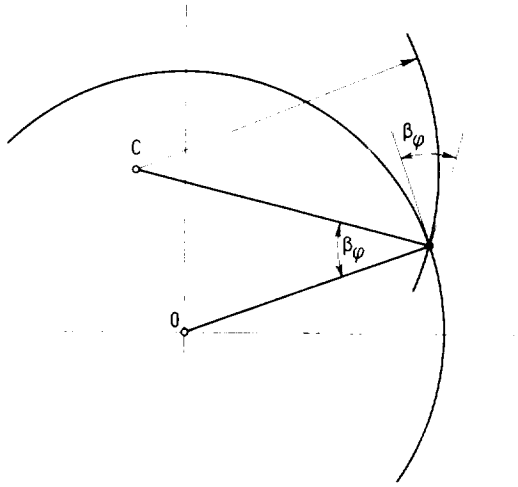

Figure 4-2. — Inclination of circular arc against peripheral direction in polar system in relation to directon of its radius against radial direction of system.

$r_A/r_B = r_B/r_C$, considering that $\Delta\varphi$ can be equated to $\varphi - \varphi_1$ in equation (4-1). Even the operation $r_A/r_B = r_B/r_C$ can be carried out graphically, as shown in figure 4-5, since the triangles AOB and BOC in that figure are similar.

It should be evident that, by repeating the process described, one can derive from two points of a logarithmic spiral any number of additional points of the same spiral.

Compared with other methods, the stepwise construction of a logarithmic spiral (fig. 4-1) has the advantage of permitting generalization to the construction of spirals with moderate variation of the spiral angle β_φ (and β_r). This construction may, therefore, be used to draw a smooth, spiral connection between two radii where the desired curve has prescribed angles $\beta_{\varphi,1}$ and $\beta_{\varphi,2}$. The limit of this

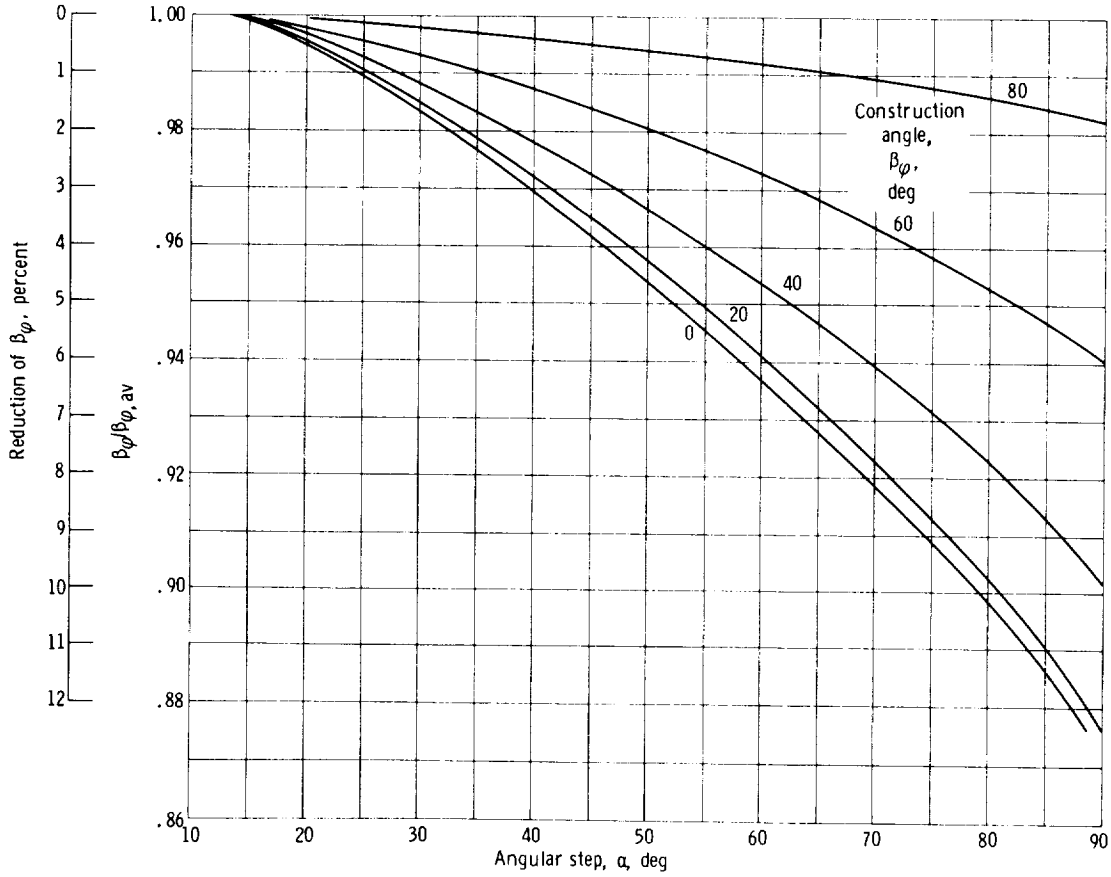

Figure 4-3. — Construction angle β_φ in figure 4-1 in relation to average angle $\beta_{\varphi,av}$ of resulting logarithmic spiral.

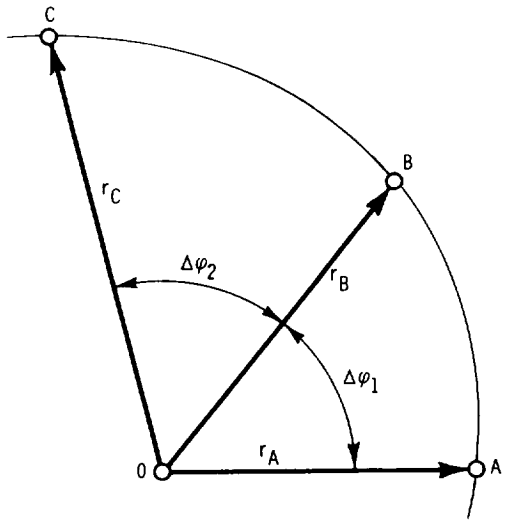

Figure 4-4. – Radial coordinates of logarithmic spiral.

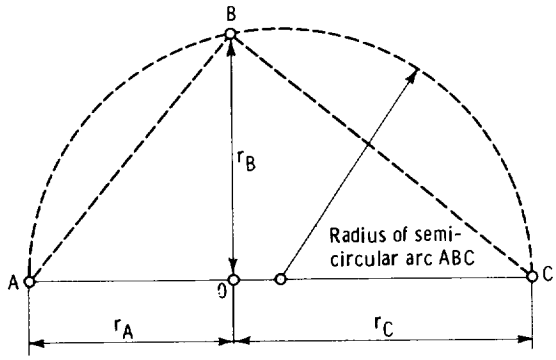

Figure 4-5. – Graphical solution of relation $r_A/r_B = r_B/r_C$.

construction by means of circular arcs is obviously reached when successive normal lines such as ADC and BC in figure 4-1 are parallel, so that the circular arc degenerates into a straight line. The curvature of the line may well change from one direction to the other, the change suggesting that the construction by means of circular arcs may no longer be the most practical.

A construction merely by the tangents to the desired curve is more general for large variations in the angle β_φ or β_r and is illustrated in figure 4-6 for a linear change in β_r (designated in fig. 4-6 merely as β) as a function of the radial coordinate r of the system.

The changes in r for this step-by-step construction are more or less arbitrary, conveniently chosen from the graphical solution. Important is the fact that a flow line (perhaps a vane centerline) with

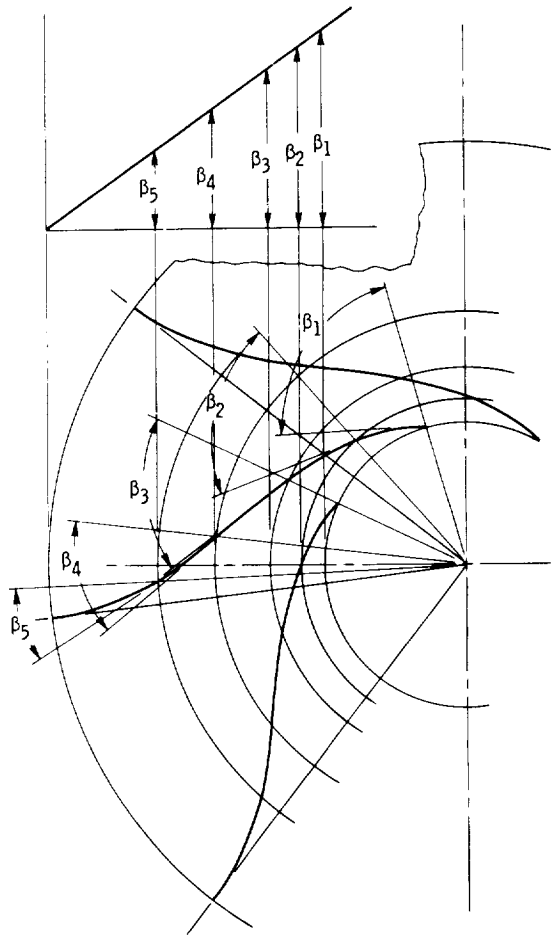

Figure 4-6. – Curve with linearly varying inclination.

strongly varying curvature results from a very simple variation of the flow angle β, a fact which illustrates the concept of so-called simple curves in a radial-flow (polar) system. It is of interest that vane shapes of the type shown in figure 4-6 have been used successfully in the field of radial-flow hydraulic turbines of fairly low specific speeds.

4.3 Hydrodynamic Design of Radial-Flow, Rotating Vane Systems

It should be evident from the preceding section that the description of curves in radial-flow systems by means of circular arcs has distinct practical advantages. This method is, therefore, used in the present section for the description of vanes in radial-flow rotors, primarily those of centrifugal pumps. The design forms discussed here apply also to radial-flow compressors and turbines with vanes

curved in only one direction over the entire vane length (see, e.g., figs. 2-40 and 2-41), whereas vanes with changing direction of curvature require, for at least part of their extent, design methods similar to that illustrated by figure 4-6.

The methods described here apply to strictly radial-flow rotors as well as to the development of straight, conical stream surfaces in mixed-flow rotors.

In the simplest case, to be discussed in this section, the rotor vanes are to be designed entirely from the inlet and discharge velocity diagrams of the rotor, which can determine only the inlet and discharge portions of the vane systems. The design process, therefore, consists in designing these two portions of the vane system independently of each other and in finding a suitable, smooth connection between these two portions.

Figure 4-7 shows the inlet portion of a radially outward-flow pump or compressor rotor, or the discharge portion of a radially inward-flow turbine rotor. The subscript used in figure 4-7 appies to the former and should be changed to 2 if applied to a turbine. In the following, only the inlet to a pump or compressor rotor is considered.

The vane shape shown in figure 4-7 is essentially determined by the vane angles $\beta_{\varphi,o}$ and $\beta_{\varphi,i}$ at the end points A and B and by the vane distance d_1 measured from point A. The angles $\beta_{\varphi,o}$ and $\beta_{\varphi,i}$ are very nearly equal to the flow angle $\beta_{\varphi,1}$, defined by $\sin \beta_{\varphi,1} = V_{m,1}/w_1$. However, the vane distance d_1 is not necessarily determined in the same manner as for axial-flow vane systems (fig. 3-1 and eq. (3-1)), because the relative velocity $w_{1,1}$ in section AD (having the width d_1) is not necessarily the same as w_1 before entering the vane system. (The equality sign in eq. (3-1) is obviously based on the assumption $w_{1,1} = w_1$.)

If the flow between the inlet and section AD is not influenced by the vanes, $w_{1,1}$ is larger than w_1 in front of the system. If it is assumed there is no rotation of the absolute flow before it enters the system,

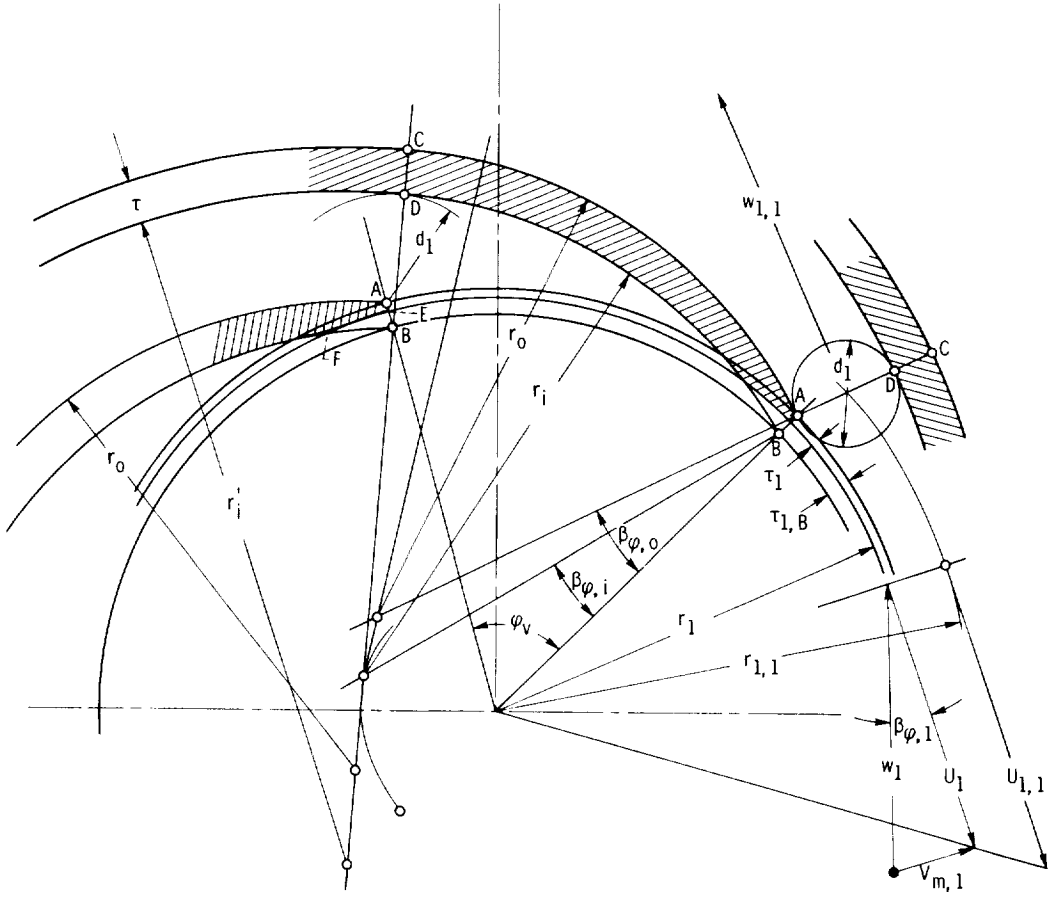

Figure 4-7. – Inlet to radially outward-flow pump rotor (or discharge from radially inward-flow turbine rotor).

$w_{1,1}$ can be approximated by the relation

$$\frac{w_{1,1}}{w_1} = \frac{r_{1,1}}{r_1} \tag{4-4}$$

where the relative velocity is assumed to vary in proportion to its peripheral component, which, under the foregoing assumption of no influence of the rotor system on the flow, is oppositely equal to the peripheral velocities of the rotor. Under this assumption, the inlet vane distance d_1 is smaller than that expressed by equation (3-1) for axial-flow systems and may be approximated by the relation

$$d_1 \geqq \frac{r_1}{r_{1,1}} t_1 \sin \beta_{\varphi,1} \tag{4-5}$$

where $t_1 = r_1 \varphi_v$ is the circumferential vane spacing at the radius r_1.

If, on the other hand, the rotor system imparts a significant positive rotation to the absolute flow between the inlet edges and section AD, the equality sign in equation (4-5) has to be deleted. In this case, it is fairly customary to ignore the ratio $r_1/r_{1,1}$, that is, to return to equation (3-1) in the form

$$d_1 \gtrless t_1 \sin \beta_{\varphi,1} \tag{4-6}$$

where the larger than and smaller than signs are usually ignored.

The foregoing considerations determine the pump inlet vane shape from the inlet vane angles $\beta_{\varphi,o}$ and $\beta_{\varphi,i}$ and from the normal vane distance d_1. These parameters are not quite sufficient for the design of the vanes. In particular, the vane thickness τ must be selected, usually on the basis of strength and manufacturing considerations. As a rule, the vane thickness is kept as small as possible within safety limits. However, with the vane distance d_1 properly determined, there is no reason (except weight) why the vane thickness should truly be as small as possible. The vane thickness at the vane ends $\tau_{1,B} = AB$ is usually less than the average vane thickness τ. Even then, this end thickness of cast vanes is usually greater than desirable at the inlet if cavitation or compressibility considerations apply. A circumferential cut EF in figure 4-7 (radius r_1), is desirable to reduce the thickness τ_1 of the leading edge as far as desired.

From the critical section AD toward the outside of the rotor, the normal vane distance d (or the cross section between the vanes) must usually be increased for hydrodynamic reasons. This can be easily accomplished by increasing the radius of curvature of the vanes, as, for example, from radius r_i to radius r_i' in figure 4-7. In this figure, the opposite vane surfaces are almost parallel at section AD, but a moderate divergence of the vane channel at its minimum section AD would be equally acceptable. This divergence is easily produced by a slight increase in the radii r_i and r_o, which leads to slight reduction in the angles $\beta_{\varphi,1}$ and $\beta_{\varphi,i}$ at the leading edge (A and B) and a slight increase in the corresponding vane angles at D and C. The circular-arc construction is very convenient for executing minor changes of the vane shape in an orderly fashion.

Figure 4-8 shows the discharge vane ends of a standard centrifugal pump or compressor rotor with backward-bent vanes. The layout is based on the discharge velocity diagram shown in figure 2-45 and derived according to Euler's turbomachinery equation (sec. 2.3), the condition of continuity, and various other considerations given in sections 2.6.3.4 to 2.6.3.6.

The fictitious velocity w_2^* in figure 2-45 is related by the condition of continuity to the cross section of the vane channel connected with the discharge vane distance d_2. (This writer's attention was called to this use of the vane channel cross section by O. Dorer, of the Worthington Pump and Machinery Corp., in 1935.) The discharge vane angle $\beta_{\varphi,2}$ (in this case referred to the low-pressure side of the vane) has no direct relation to the discharge velocity diagram, since the direction of the vane in figure 2-45 must be some average direction of the discharge portion of the vanes. This condition has a definite meaning only if this portion of the vane has a constant vane angle and is infinitely thin, as assumed in section 2.6.3.4 (i.e., for thin vanes curved according to a logarithmic spiral). Generally, in pumps, the vane angle β_φ (measured against the peripheral direction) decreases from E (opposite to B) to A in figure 4-8.

The vane distance d_2 at the vane channel discharge (point B) is shown in figure 4-8 to be divergent by the angles δ_1 and δ_2 at the two sides of the vane channel. For constant width normal to the layout in figure 4-8, this divergence (which could be a convergence) applies to the cross section between the vanes and may, therefore, have hydrodynamic significance regarding separation in the rotor passages. This writer has had good results with designing the low-pressure side of the vanes so that the angles of divergence δ_1 and δ_2 are zero. The

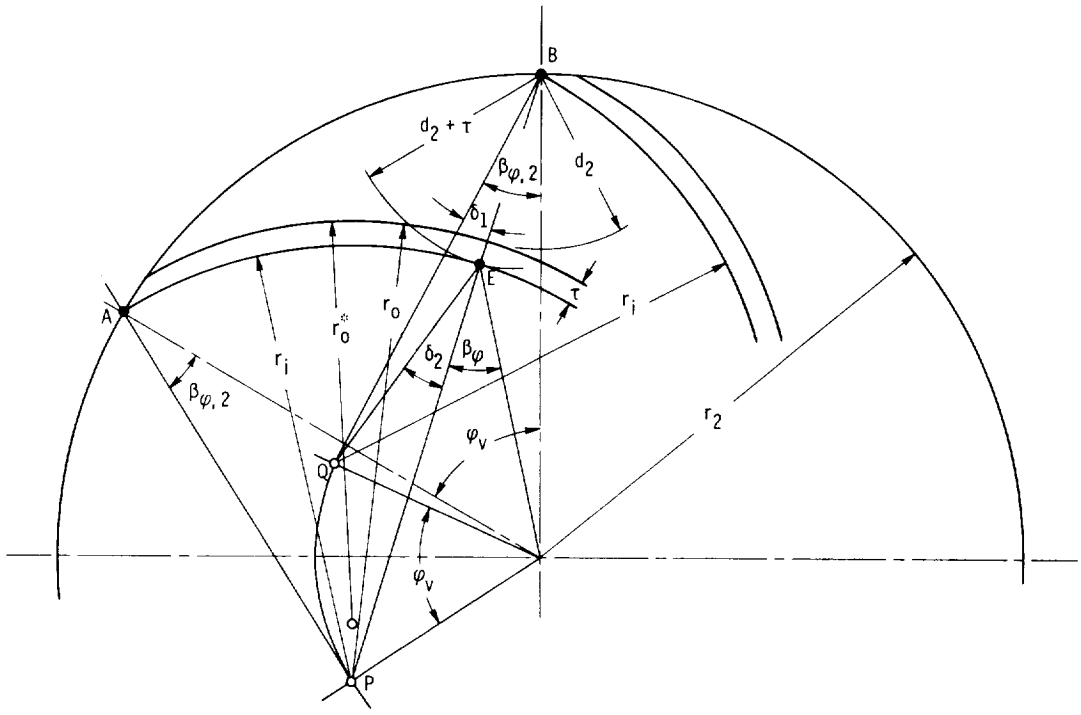

Figure 4-8. – Discharge vane ends of radially outward-flow pump or compressor rotor.

geometric construction which accomplishes this is shown in figure 4-9 and should be self-explanatory if it is understood that the triangles BCD and QOP are geometrically equal to each other (except for direction). It can readily be seen that the vane angle β_φ at E (measured against the peripheral direction) is in this case significantly larger than the corresponding vane angle $\beta_{\varphi,2}$ at the discharge end of the vanes.

The design for parallel vanes at the discharge cross section, shown in figure 4-9 for infinitely thin vanes, applies to vanes of finite thickness if the vane thickness is constant at point E. Such a construction is shown in figure 4-10. This figure also shows that the vane thickness may still be reduced from τ to τ_2 if the radius of the leading side of the vanes is reduced from r_o to r_o^* at some distance a from the trailing edge, as long as this distance is less than the distance AE in figure 4-9.

With the vane ends designed according to figures 4-7 to 4-10, yet to be determined is a method for connecting these vane ends with each other in a hydrodynamically and geometrically satisfactory fashion. A hydrodynamic solution of this problem is described in the next section and is, therefore, not considered here in detail. However, in many practical cases, a simple geometric solution is acceptable, provided this solution considers some elementary hydrodynamic requirements. The most important, and often sufficient, requirement of this type is that the cross section between the vanes should change in a simple, approximately monotone manner from the last definitely determined cross section of the inlet portion (usually AD in fig. 4-7 with vane distance d_1) to the first well-determined cross section of the discharge portion (usually the cross section measured from the vane end B having the normal vane distance d_2). Such a monotone change in cross section is approximately satisfied by a second requirement, namely, that the vane angle change in a simple, reasonable monotone manner from the last (outermost) determined vane angle of the inlet portion to the first (innermost) determined vane angle of the discharge portion.

The foregoing condition of the vane angles can be satisfied approximately by a single circular arc as illustrated in the two diagrams shown in figure 4-11. In either case, point A is the starting point of the

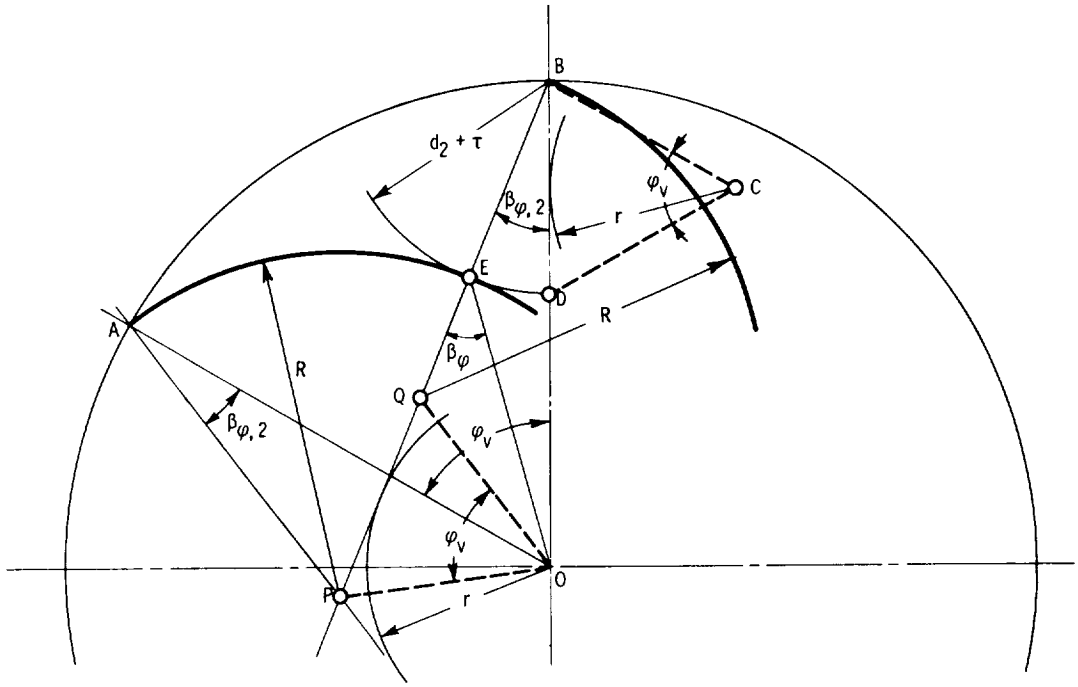

Figure 4-9. – Circular arc construction of vane ends of radial-flow pump rotor to be parallel at their outer ends and at opposite part of vane.

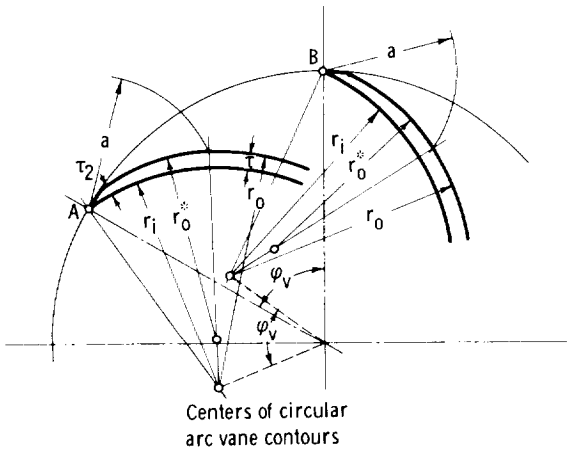

Figure 4-10. – Circular arc construction of suitable thickness distribution over outer ends of vanes of centrifugal pump or compressor rotors.

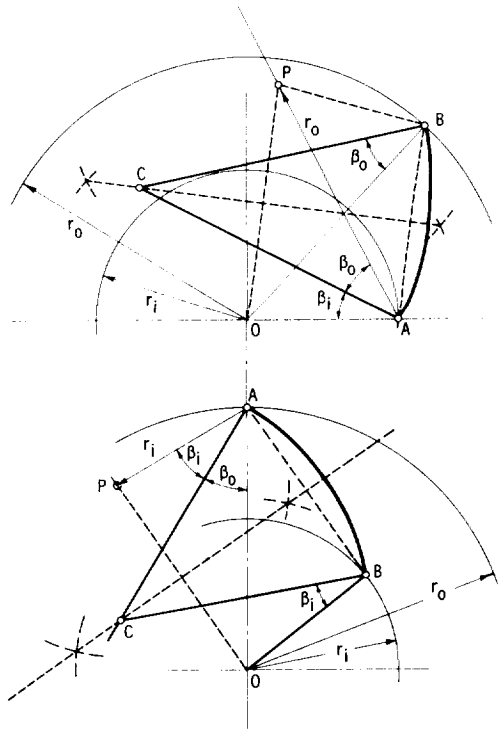

Figure 4-11. – Circular arc construction of curve with prescribed angles at two given radii r_i and r_o in polar coordinate system.

construction. The radii r_i and r_o as well as the vane angles β_i and β_o at these radii (measured from the peripheral direction) are given. The construction is based on the symmetry of the figures OABPC (upper diagram) and OBAPC (lower diagram) with respect to the broken line through C which is normal to OP. The first point to be located from point A is point P by means of β_i, β_o, r_o, or r_i as in-

dicated. The normal line OP and the line through A under the angle β_i or β_o determine the center C of the arc AB.

Before this elementary consideration of radial- and conical-flow rotors is closed, it is proper to call attention to the background of the design of such rotors previously outlined in chapter 2, particularly section 2.6. Specifically the selection of the number of vanes (not mentioned so far in the present section), or the equivalent selection of the vane spacing φ_v in figures 4-7 to 4-10, is described in section 2.6.3.3 as given by the lift coefficient (eq.(2-130)), and the latter is limited by the retardation of the relative flow w_2/w_1. For radial-flow rotors, there is no better information available than that developed for axial-flow vane systems represented by figure 2-26 and the approximation in figure 3-17. As in many cases, an answer regarding the number of vanes or the angular vane spacing φ_v can be obtained only by successive approximations. The lift coefficient $C_{L,\infty}$ is related to the vane spacing ($t_2 = \varphi_v r_2$) and the vane length, while the vane shape (which determines the vane length) is given by the inlet and discharge portions (figs. 4.7 and 4.8) with φ_v as an essential variable. Generally one estimates the vane length from the inlet and discharge flow angles and the inlet and discharge radii r_1 and r_2. With an estimated lift coefficient and vane length and the given inlet and discharge velocity diagrams, one can calculate the vane spacing $t_2 = r_2\varphi_v$ and select a number of vanes. From it, one can design the inlet and discharge portions of the vanes, and from them the whole vane. If the resulting vane length is sufficiently different from the estimated vane length to require a change in the number of vanes, the design process has to be repeated. As a rule, the second approximation of the vane shape is adequate.

Finally it is necessary to review critically the initial three-dimensional assumptions underlying the foregoing design considerations. Radial flow is assumed to proceed along surfaces normal to the axis of rotation, and mixed flow along conical surfaces coaxial with the axis of rotation.

Figures 2-40 and 2-41, which are typical for these two forms of flow, indicate that the meridional flow is likely to depart somewhat from the assumed plane or conical flow at the inlet where the flow direction changes from axial to radial or conical and thus involves a velocity component normal to the assumed plane or conical stream surface. This departure from the assumed flow can be kept quite small if the passage width normal to the assumed meridional stream surface is small compared with the distance r_1 of the leading vane edges from the axis of rotation (see fig. 4-12). For radial-flow pump or compressor rotors of low specific speed such as shown in figure 4-12, the vane distance r_1 should be made substantially larger than half of the axial inlet diameter D_i. If this sizing is not possible (for reasons of cavitation or compressibility considerations), the inlet vane edges extend into the region of the inlet flow curvature, as shown in figure 4-13 (typical for a rotor of higher specific speed). For such a rotor, the axial inlet velocity component $V_{a,1}$ must be taken into account as illustrated in figure 4-14. Figure 4-14(a) shows the three-dimensional inlet velocity diagram under the simplifying assumption of zero prerotation. Figure 4-14(b) presents the relation among the radial, axial, and meridional velocity components in the meridional flow configuration. Specifically it shows by the similarity of the triangles ABC and ADB that

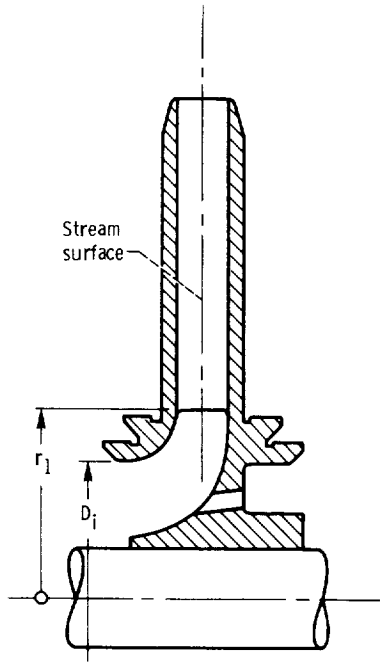

Figure 4-12. – Radial-flow pump rotor with inlet meridional flow close to radial direction.

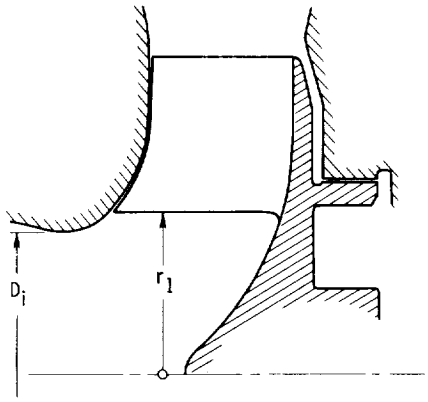

Figure 4-13. – Radial-flow pump rotor with inlet meridional flow departing from radial direction.

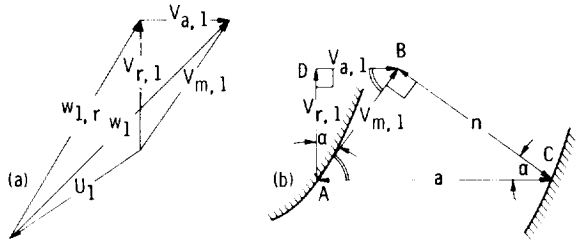

(*a*) *Inlet velocity diagram. Zero prerotation.*

(*b*) *Velocity components in meridional flow.*

Figure 4-14. – Treatment of axial velocity component at inlet to radial-flow vane system

$$\frac{n}{a} = \cos\alpha = \frac{V_{r,1}}{V_{m,1}} \tag{4-7}$$

and

$$aV_{r,1} = nV_{m,1} \tag{4-8}$$

that is, that the condition of continuity is satisfied if the product of the radial velocity component and the axial width is multiplied by the local circumference of the meridional flow passage. Thus, the inlet portion of the vanes (fig. 4-7) can be designed by using the radial instead of the meridional velocity component according to equation (4-8), provided the vanes are cylindrical and parallel to the axis of rotation so as to satisfy the axial component $V_{a,1}$ (fig. 4-14(a)). (Obviously such cylindrical vanes are the simplest to manufacture.)

The two shaded curves in figure 4-14(b) are not necessarily the solid flow boundaries of the meridional flow passage, but may be considered as successive meridional streamlines. This interpretation renders equation (4-8) more accurate than it is when applied to the entire passage width. Furthermore this refinement permits consideration of nonuniformities of $V_{m,1}$ and $V_{r,1}$ across the meridional flow passage, derived from the curvature of the meridional streamlines according to section 2.2, particularly figure 2-3. However, this consideration would lead to some departures from the cylindrical vane shape previously mentioned and thereby to complications regarding the axial velocity component. This type of problem is discussed in section 4.4.

While rotors of low specific speeds such as shown in figure 4-12 rarely involve significant flow components normal to the plane meridional flow surface, as discussed previously, such narrow rotors must be expected to be subject to major effects of fluid friction, which may modify certain conclusions regarding separation or stall in radial-flow rotors. As previously, in the absence of good information on real-flow effects in radial-flow rotors, one has no choice but to use the information on such effects developed for axial flow vane systems. In particular, one is forced to use axial flow data on stall limits described by the lift coefficient as a function of the ratio of retardation of the relative flow (see figs. 2-26 and 3-17), perhaps with more conservative values for radial- than for axial-flow machines in view of the results by Johnston quoted in section 2.6.3.7. On the other hand, lower (i.e., more aggressive) ratios of retardation have been used with reasonable success for radial-flow compressors.

In radial-flow rotors like that shown in figure 4-12, one must expect that shroud effects on the flow between the vanes and shrouds (described in sec. 2.6.3.8, particularly fig. 2-57) may assume a dominating influence. There is probably no part of the relative flow which is not strongly influenced by fluid friction, whereas, in good axial-flow machines (except inducers), fluid friction effects are strong only within boundary layers of limited thickness along the vanes, casing wall, and hub. Conclusions derived under these flow conditions cannot be expected to apply to rotors (or stators) in which fluid friction influences the entire flow. In addition, it must be considered that the flow along rotating shrouds moves under the influence of friction from the high-pressure toward the low-pressure side of

the vane channel and presumably generates on the low-pressure side a very thick boundary layer which has an increased pump head in rotors with backward-bent vanes.

In view of this situation, the writer feels that the previously mentioned limits on lift coefficient and ratio of relative flow retardation do not apply to radial-flow rotors of low specific speeds (less than 0.06, or 1000) and that ratios of retardation lower than $w_2/w_1 = 0.6$ may well be acceptable in this low-specific-speed range. Furthermore, for the same reason, one must be very careful in applying in this range either empirically or theoretically justified rules about the head coefficient $C_H = V_{U,2}/V^*_{U,2}$ (see fig. 2-45 and secs. 2.6.3.3 to 2.6.3.8). This situation is similar to that described in section 3.4.5 with respect to axial-flow inducers, except that no detailed experimental investigations, such as described there, have been carried out on radial-flow pumps or compressors of low specific speeds. Since the extensive experimental investigations on axial-flow inducers have not yet led to definite design rules considering fluid friction, one must be somewhat pessimistic regarding the prediction of the performance of radial-flow pumps and compressors of low specific speeds (per stage). At present, this type of pump or compressor is designed on the basis of test results obtained with comparable machines of this type.

4.4 Hydrodynamic Design of Rotating Vane Systems With Transitions Between Axial and Radial Flow

4.4.1 Design by Inlet and Discharge of Vane System

This section describes the design of rotating vane systems which extend well into the regions of axial and radial flow, so that there is a strong change of the direction of the meridional flow within the vane system. In this case, the meridional stream surfaces have strong double curvature and cannot be developed into planes. Furthermore the method of dealing only with the radial component of the meridional flow, described in section 4.3 in connection with figures 4-13 and 4-14, is no longer applicable, partly because the radial flow component may approach zero and partly because cylindrical vanes meet the outer shroud under a very unfavorable (small) angle α, as shown in figure 4-15.

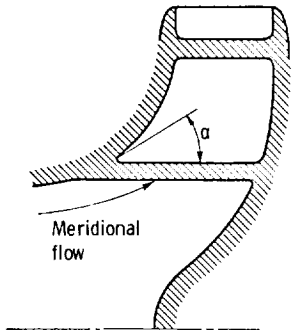

Figure 4-15. – Cylindrical vane for axial and radial flow.

The same figure also shows the unfavorable relation between the direction of the meridional flow and the direction of a cylindrical vane.

Both disadvantages of the cylindrical vane can be avoided (or minimized) by twisting the inner vane end in relation to the outer end as shown in figure 4-16. Since this twisting constitutes a major complication of the vane shape and the manufacturing methods required, one usually goes one step farther

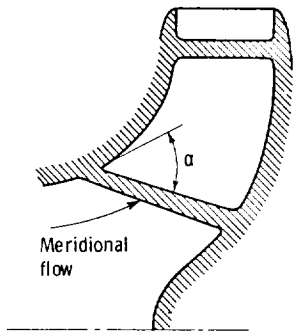

Figure 4-16. – Conical and twisted vane for axial and radial flow.

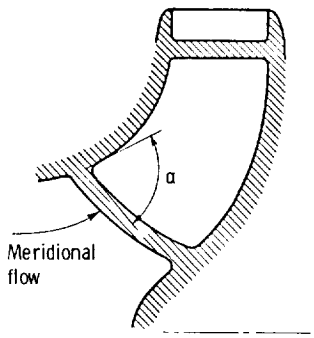

Figure 4-17. – Double-curved and twisted Francis vane for axial and radial flow.

and gives the radial vane sections a curvature (fig. 4-17), which further improves the relation between the vane and the meridional flow as well as the outer shroud. This type of pump or turbine rotor is usually referred to as a Francis rotor.

Figure 4-18 illustrates the design of a Francis pump rotor with axial inlet and approximately radial discharge, using primarily the inlet and discharge portions of the vanes.

The discharge portion, shown at the left in figure 4-18, is represented by a plane section normal to the axis of rotation, designed as described in section 4.3 in connection with figures 4-8 to 4-10. The inlet portion is designed by means of a number of straight, conical sections approximating the inlet portions of the meridional stream surfaces. Two of these surfaces, AAA and BBB, are shown developed into planes. The vane sections in these developments are designed as described in section 4.3 in connection with figure 4-7. Strange as it seems, very favorable results have been obtained by assuming a uniform meridional velocity along the inlet edges of the vanes; this method is discussed further in sections 4.4.2 and 4.4.3.

By approximating the inlet portions of a number of stream surfaces, I, II, III, IV, and V, by conical sections, one can determine successive radial sections 1, 2, 3, and 4 through the inlet portion of the vanes. Of course, a process of trial and error is required before the conical sections (such as AAA and BBB) as well as the radial sections 1, 2, 3, and 4 form smooth and simple curves.

The connection between the outer and the inner vane portions so determined has to be established geometrically by the continuity of the vane slope from the inlet to the discharge portions of the vanes. This process is illustrated in figure 4-18 only with respect to the back-shroud contour V. The meridional distance δ between successive radial vane sections 1, 2, 3, 4, etc. is plotted in this case against the distance from the axis of rotation. This distance δ between the radial sections should form smooth curves along all meridional stream surfaces I to V. Note, however, that the radial sections through the outer and inner vane portions may have to be rotated circumferentially relative to each other by a finite angle; that is, beginning with the inlet sections 1, 2, 3, and 4, the outer portion may finally

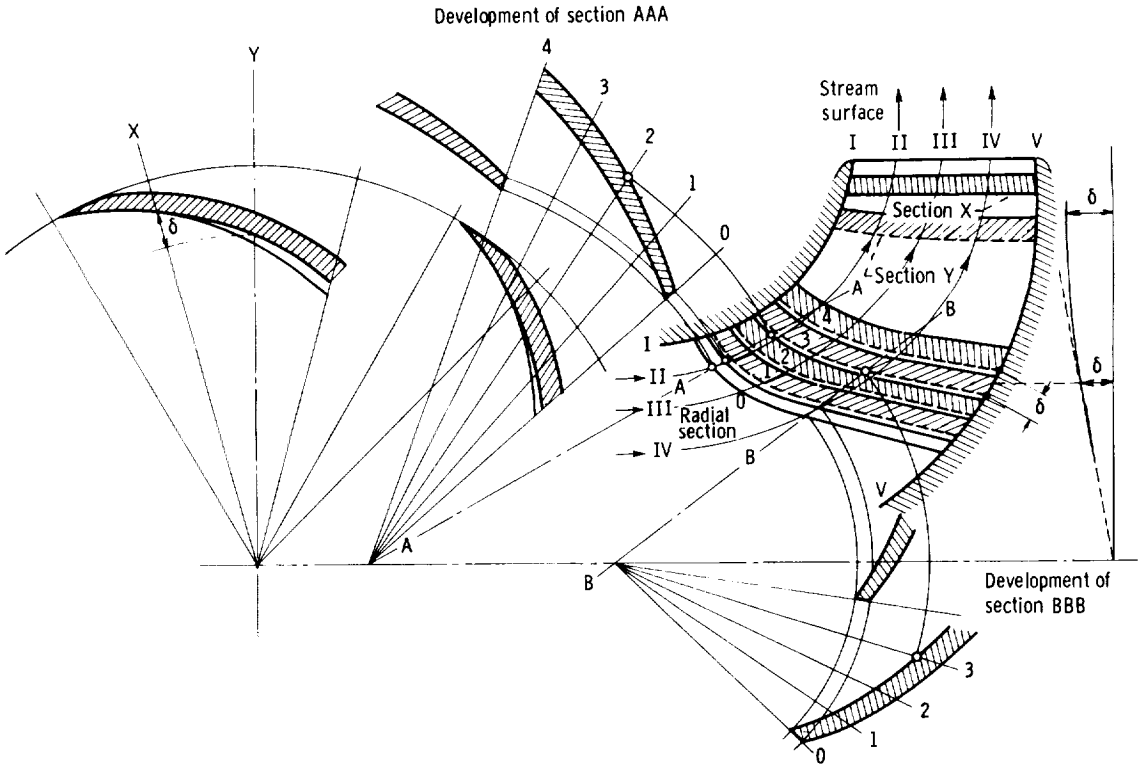

Figure 4-18. – Views of Francis pump rotor showing inlet and discharge portions of vanes.

not be described by the sections X and Y but by sections at intermediate angles and displaced circumferentially from sections X and Y.

Furthermore all radial sections containing the axis of rotation must form smooth curves, by changing gradually and progressively from sections 1, 2, 3, and 4 to the radial sections through the outer portion of the vane. It should be evident that this design process is one of trial and error and may involve some minor changes in the radial sections 3 and 4 as well as in the radial sections through the outer portion of the vane.

Evidently the angular spacing between vanes must be the same for the inner and outer portions. It must be selected by means of an estimated vane length, the inlet and discharge velocity diagrams, and an estimated lift coefficient based on the maximum retardation of the relative flow, which in pumps nearly always occurs along the outer shroud.

It is clear that this vane design process is not very definite. A more systematic process for the same type of Francis rotor is described in section 4.4.2.

A somewhat different design problem exists with radial-flow rotors having very high peripheral velocities, more precisely, very low centrifugal stress coefficients $\sigma_c/\rho_S U^2$, or centrifugal stress specific speeds in excess of 0.1 or 0.2 (see secs. 1.3.3.1 and 1.3.3.2 and fig. 1-46). In such cases, the form of sections normal to the axis of rotation is determined almost entirely by mechanical considerations and must, therefore, be considered as prescribed independently of the flow in the rotor. This design problem is discussed in connection with a fairly typical case, where the stress coefficient is sufficiently low to demand approximately straight radial vane sections in planes normal to the axis of rotation (see, e.g., the lower part of fig. 1-46). This requirement applies to radial-flow compressors with pressure ratios per stage of 4 or higher and to rocket pumps raising the pressure of liquid hydrogen by more than 1000 pounds per square inch per stage. In such cases, the inlet and discharge portions of the rotor vane system have to be designed more or less independently of each other, and the connection between these two portions is dictated geometrically by the mechanically prescribed vane shape.

The following example is worked out under the assumption that the retardation of the relative flow in the rotor should stay within limits which can be estimated to be acceptable with respect to separation or stall. Specifically the ratio of the relative discharge velocity w_2 to the maximum inlet relative velocity $w_{1,o}$ should not be lower than 0.6.

This writer is well aware of the fact that this empirical rule is usually not observed for radial-flow pump or compressor rotors with radial vanes, which are often designed under the assumption of separated flow in the rotor passages. This practice may be an important reason why this type of radial-flow machine has not as yet achieved the efficiencies (around 90 percent) that were reached by centrifugal pumps with backward-bent vanes more than 40 years ago. It is, therefore, desirable to make a serious attempt to keep a radial-flow, radial-vane rotor within limits of unstalled operation, although these limits are not really known in the radial-flow field, the previously mentioned limit of $w_2/w_{1,o} > 0.6$ having been reasonably confirmed only for axial-flow machines.

To stay within this limit, the fluid must be admitted to the rotor with considerable rotation in the direction of the rotor motion and thus reduce the inlet relative velocity. For the reason given at the beginning of section 2.7.2, this rotation is so-called solid-body rotation, that is,

$$\frac{V_U}{V_{U,o}} = \frac{r}{r_o} \tag{4-9}$$

as shown on the left side in figure 4-19. The velocities shown in this figure apply to the rotor shown in figure 4-20.

The maximum peripheral fluid velocity $V_{U,o}$ at the rotor inlet diameter (cylindrical section O) is determined by a series of successive approximations from the relative discharge velocity w_2 (fig. 4-19) so that $w_2/w_{1,o} > 0.6$. The final value of this ratio is 0.62, because of previously neglecting the effect of vane thickness, which tends to increase this ratio.

The inlet and discharge cross sections $(D_i^2 - D_h^2)\pi/4$ and $D_2 \pi b_2$ are made equal so that for a practically incompressible fluid the mean, meridional inlet and discharge velocities are equal. (To maintain the last relation for a compressible fluid, one would have to reduce b_2 proportionally to the reduction in specific volume, as described later.)

The meridional inlet velocity distribution in section A-A is determined according to the laws of

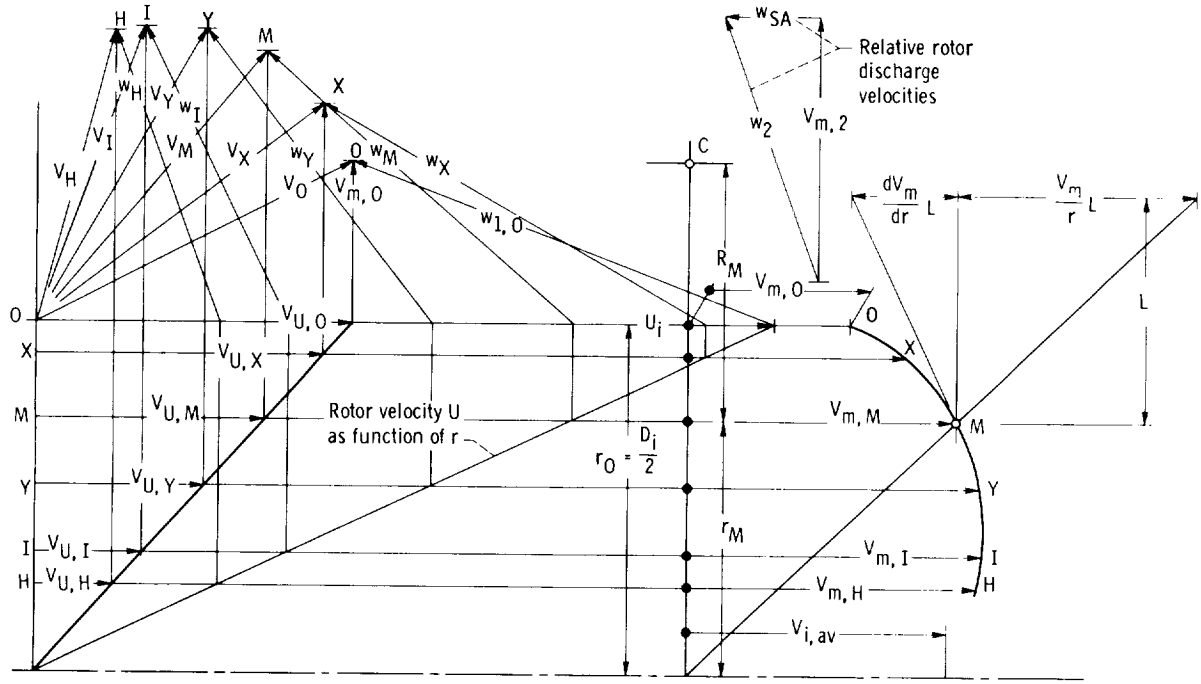

Figure 4-19. – Velocities approaching radial-flow pump rotor with radial vanes.

flow with vorticity presented in sections 2.7.2 and 2.7.3. An attempt to do so by the graphical method described in section 2.7.2 (figs. 2-63 and 2-64) was not successful, because the radial steps required to obtain acceptable accuracy were impractically small. On the other hand, the analytical solution given in section 2.7.3 turned out to be quite simple.

If an irrotational inlet velocity distribution of the stationary inlet guide-vane system is assumed, the left side of equation (2-173) is zero when applied to this system. Thus the right side of the same equation, describing the velocity distribution in section A-A (fig.4-20), reduces (with the angle $\varphi = 0$ and the subscript 2 dropped) to the form

$$V_U\left(\frac{dV_U}{dr} + \frac{V_U}{r}\right) + V_m\left(\frac{dV_m}{dr} - \frac{V_m}{R}\right) = 0 \qquad (4\text{-}10)$$

Since the coordinate n in equation (2-173) is equivalent to r in section A-A, r is the only independent variable in equation (4-10), and it justifies the total derivatives in this equation. In this equation, r is the distance from the axis of rotation, and R is the local radius of curvature of the meridional streamlines. It so happens that over a large portion of section A-A these streamlines are, in a radial section, concentric to one center C, and this approximation is used in the solution of equation (4-10).

For solid-body rotation, obviously $dV_U/dr = V_U/r$, so that equation (4-10) assumes the form

$$2\frac{V_U^2}{r} = -V_m\left(\frac{dV_m}{dr} - \frac{V_m}{R}\right) \qquad (4\text{-}11)$$

or

$$2\frac{V_U^2}{V_m^2} = -\frac{dV_m}{dr}\frac{r}{V_m} + \frac{r}{R}$$

$$\frac{dV_m}{dr}\frac{r}{V_m} = -2\frac{V_U^2}{V_m^2} + \frac{r}{R}$$

$$\frac{dV_m}{dr} = \frac{V_m}{r}\left(-2\frac{V_U^2}{V_m^2} + \frac{r}{R}\right) \qquad (4\text{-}12)$$

The last expression is evaluated in figure 4-19 by a horizontal line at an arbitrary distance L above r. Obviously

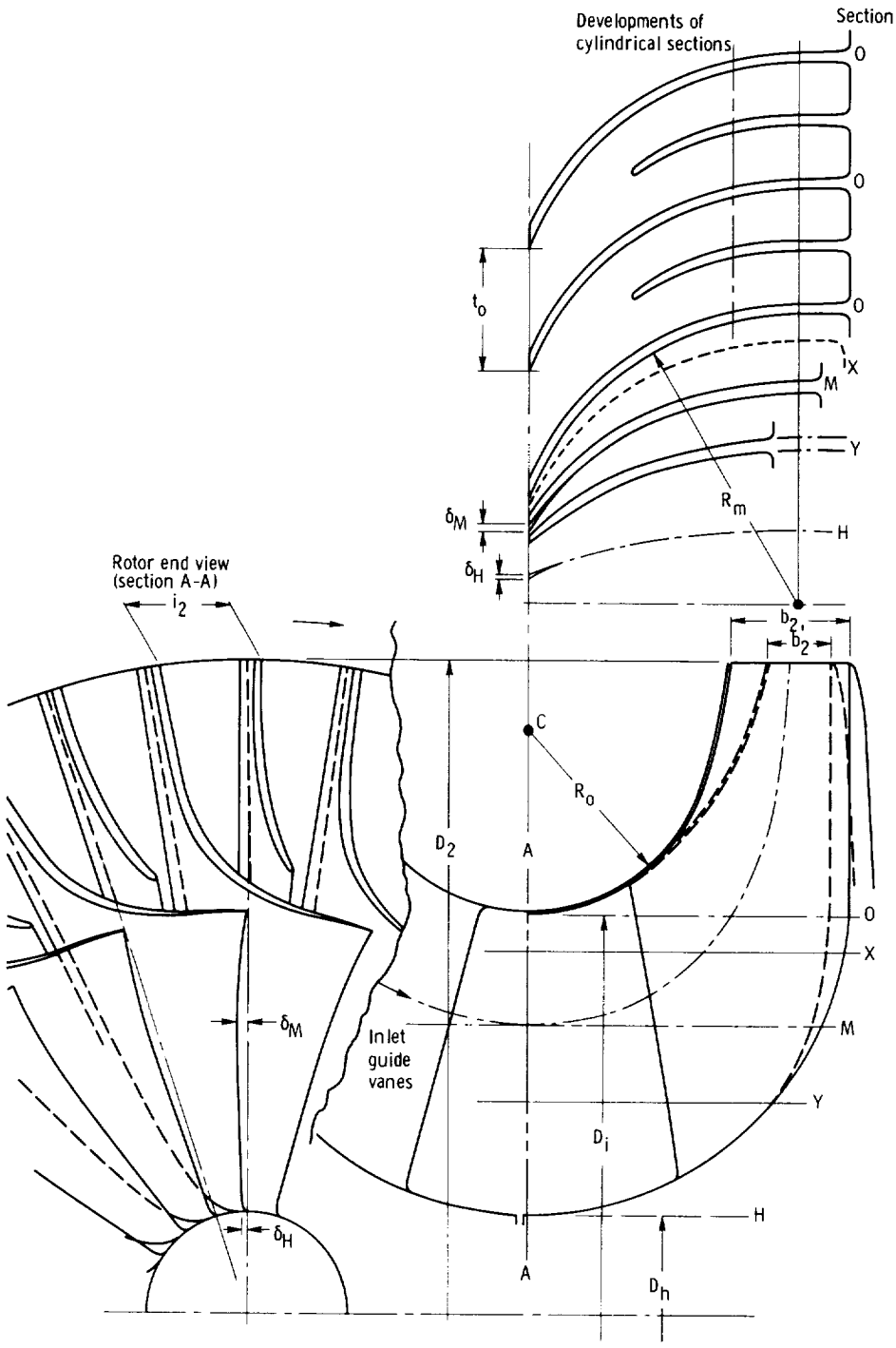

Figure 4-20. – Radial-flow pump rotor with radial vanes.

$$\frac{dV_m/dr}{V_m/r} = -2\frac{V_U^2}{V_m^2} + \frac{r}{R} \qquad (4\text{-}13)$$

Starting, as usual, at an estimated point where $V_m = V_{i,av}$ is determined by the one-dimensional condition of continuity, one can construct a V_m, r curve from its tangents as indicated in figure 4-19. Successive tangents should intersect about halfway between the r values to which they apply.

The V_m,r curve is constructed beginning at the midradius r_m, which divides the area of the meridional flow section A-A into two equal parts. The value of V_m at that radius is estimated, after some trial and error, to be about 3 percent higher than the average meridional velocity $V_{i,av}$ in section A-A (as well as at the discharge of the rotor).

The inlet velocity vector diagrams corresponding to the V_m values so determined as well as to the V_U values of the assumed solid-body prerotation are also shown in figure 4-19. In the upper part of figure 4-20 are shown a number of cylindrical vane sections of which the high-pressure sides at the leading vane edge are tangential to the relative velocity vectors shown in figure 4-19. The vane sections at various radii are related to each other by being located and deformed circumferentially, so that vane sections normal to the axis of rotation are radial. To satisfy the vane directions prescribed by the inlet velocity diagrams, the leading edges of the vane depart from this law of a helical surface by δ_M at the midsection M and by δ_H at the hub section H. These departures from the helical vane shape (defined by radial sections normal to the axis of rotation) are very small and can hardly be expected to jeopardize the mechanical quality of the vanes with respect to centrifugal forces. The vane thickness increases from the vane tips toward the center of rotation approximately according to figure 1-32 and suggests a centrifugal stress coefficient of about $\rho_S U^2/2\sigma_c = 2$.

The number of vanes is determined from the vane lift coefficient:

$$C_{L,\infty} = 2\frac{V_{U,2}}{w_\infty}\frac{t_2}{l}\left(1 - \frac{V_{U,1}\, r_1}{V_{U,2}\, r_2}\right) \tag{2-130}$$

which, if one chooses the ratio of retardation to be $w_2/w_{1,o} = 0.62$, should be about unity when axial-flow data are used as previously. From the velocity diagram in figure 4-21 and from the ratio of discharge to inlet diameter of 1.625, one can scale $V_{U,2}/w_\infty = 3.34$, $V_{U,1}/V_{U,2} = 0.284$, and $r_1/r_2 = 0.615$ along the outer shroud. With $C_{L,\infty} = 1$, one finds

$$\frac{l}{t_2} = 2 \times 3.34 \times 0.825 = 5.51$$

which leads to between 42 and 43 vanes when the full vane length along the outer shroud is used. Actually a 40-vane rotor is shown in figure 4-20.

Such numbers would result in an extremely close vane spacing at the rotor inlet unless one reduces the length of every second vane as shown in figure 4-20. The average vane length-spacing ratio is thereby reduced to $l/t_2 = 3.9$. On the other hand, the mean relative velocity w_∞ is larger than assumed from the effect of the finite vane thickness and leads to $V_{U,2}/w_\infty = 3.087$, so that

$$C_{L,\infty} = 2 \times 3.087 \times \frac{0.825}{3.9} = 1.306$$

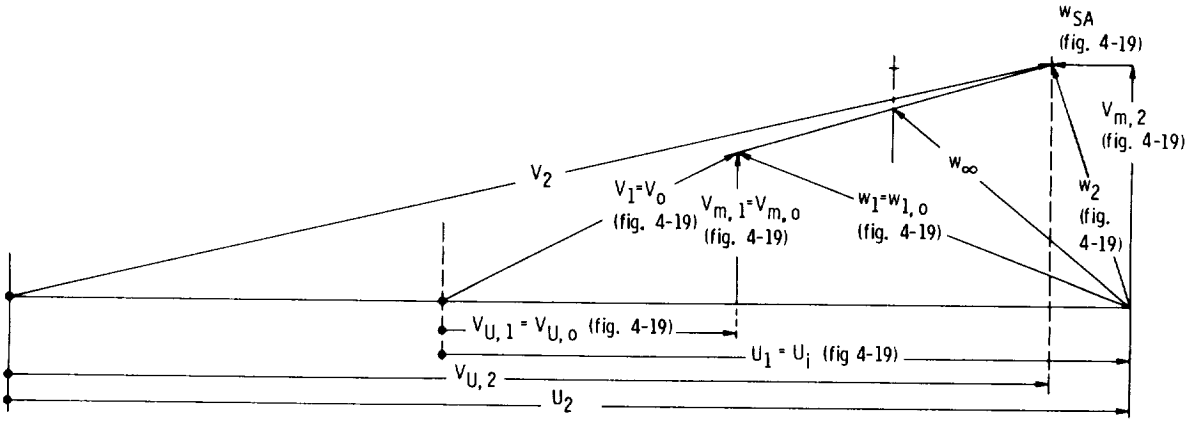

Figure 4-21. – Discharge and inlet velocity diagrams at outer shroud of radial-flow rotor shown in figure 4-20.

which can still be considered acceptable until experimental results for rotors of this type give a better foundation for their design.

Beyond the previously stated consideration, the vane shape of the rotor having radial blade elements is determined by any one cylindrical section through the vane system. One usually uses for this purpose the section having the inlet diameter D_i (section O in fig. 4-20) because the relative inlet velocity is a maximum in this section, and it is, thus, dynamically or hydrodynamically the most critical section. The design principles at the inlet to this section are approximately those of axial-flow pumps and compressors. For example, the initial radius of curvature of the vanes can be chosen in relation to the vane spacing t_o by some approximate consideration of a local (inlet) lift coefficient in relation to a local retardation of the relative flow. In section O of figure 4-20, this radius of vane curvature is chosen to be constant from the inlet to the point where the vane reaches the axial direction, since there is no reason for departing from this simple shape. In other cylindrical sections (X, M, Y, and H), the vane shape becomes elliptic by the law of a helical surface, except very near the leading edge, where the pressure side is made parallel to the relative velocity as described previously. Thus, for one cylindrical section, such as O, the law of a helical surface (radial sections normal to the axis of rotation), the direction of the vane near its leading edge, and the vane thickness distribution determined by the stress coefficient $\rho_S U^2/2\sigma_c$, together with the minimum thickness at the vane tip, determine the entire vane shape between the bounding surfaces of revolution. Under these conditions, no independent design consideration can be given to the flow in the rotor passages between the inlet and the discharge, although the frictionless flow in these passages can be determined as outlined in section 2.7.6.

It should be mentioned that a strictly radial vane shape in sections normal to the axis of rotation is not the mechanically most desirable vane shape if the density of the fluid is sufficient to generate significant bending stresses in the vanes, as would be true with liquid hydrogen. In this case, one can advantageously incline the vanes backward against the radial direction, so that the resulting centrifugal bending forces cancel the hydrodynamic bending forces to some extent.

The rotor form shown in figure 4-20 was first used for centrifugal compressors. Although more recently this rotor received serious consideration in connection with pumps for liquid hydrogen, it is, nevertheless, appropriate to describe briefly how the effects of compressibility of the fluid can be taken into account in a simple manner. These considerations are here limited to gases which can be treated by the laws applicable to air, as outlined in section 2.4.

Since the flow in the passages between the inlet and the discharge of the rotor is not considered in detail for the design of this rotor, it is sufficient for the consideration of compressibility effects to determine the change in specific volume and volume flow from the rotor inlet to the rotor discharge only and to take care of the transition between these two stations geometrically, that is, by gradual changes in the lateral flow boundaries of the rotor.

The velocities are the same as previously assumed for an incompressible fluid and shown in figure 4-19, except that for compressible flow the velocities must be given as thermodynamically dimensionless, definite values (Mach numbers or ratios to V_o as defined by eq. (2-21)).

Since the meridional streamline picture is not required for the design process considered here, it is sufficient to carry out the intended compressibility considerations on a one-dimensional basis, that is, to use only average values of the meridional velocity in any one cross section, provided this velocity does not come close to the local acoustic velocity, which is to be avoided in any event because of the danger of choking. (On the other hand, it is of interest to note that the inlet vane design shown in figure 4-20 has been used successfully up to a Mach number of 1 of the relative inlet velocity $w_{1,o}$, when the leading vane edges have been thin and sharp.)

The determination of the inlet cross section $(D_i^2 - D_H^2)\pi/4$ for a given average meridional inlet velocity $V_{i,av}/V_o$ (notation of sec. 2.4) and a given mass or weight flow is straightforward, since the specific volume can be read from figure 2-7, where V_o is derived from the given inlet stagnation enthalpy of the absolute flow. If the inlet cross section is prescribed, the inlet velocity $V_{i,av}$ is obtained by successive approximations as described in section 2.4.

As assumed previously, the meridional discharge velocity $V_{m,2}$ is assumed to be equal to the average inlet velocity $V_{i,av}$. The discharge stagnation enthalpy of the absolute discharge flow is

$$h_{o,2} = h_{o,i} + H_r \tag{4-14}$$

where $h_{o,i}$ is the stagnation enthalpy of the absolute flow entering the rotor, and H_r is the rotor head determined by Euler's turbomachinery equation (2-18).

By the definitions for the enthalpy introduced in section 2.4, one can use for the absolute inlet stagnation conditions the simple (although fictitious) relation

$$h_{o,i} = C_p T_{o,i} \tag{4-15}$$

where the specific heat at constant pressure C_p is assumed to be constant at all temperatures up to $T_{o,i}$. (This assumption is valid for air up to $T_{o,i} = 600°$ R and is approximately correct up to about $T_{o,i} = 800°$ R.) By the same definitions, for the discharge stagnation conditions (of the absolute flow),

$$T_{o,2} = \frac{h_{o,2}}{C_p} \tag{4-16}$$

where $T_{o,2}$ is subject to the same limitations as previously stated for $T_{o,i}$. A useful approximation of C_p for $T_{o,2}$ slightly larger than 800° R is described later.

The compression in the rotor is, of course, polytropic, so that the isentropic equations (2-28) to (2-30) must be replaced by the corresponding polytropic relations. In particular, the specific volume at the discharge stagnation conditions $v_{o,2}$ is related to the specific volume at the inlet stagnation conditions $v_{o,i}$ by the polytropic equation

$$\frac{v_{o,2}}{v_{o,i}} = \frac{T_{o,i}^{1/(n-1)}}{T_{o,2}^{1/(n-1)}} \tag{4-17}$$

The polytropic exponent in the equation

$$pv^n = \text{constant} \tag{4-18}$$

is related to the polytropic efficiency, which for compression assumes the form

$$\eta_r = \frac{1-1/\gamma}{1-1/n} \tag{4-19}$$

This relation can readily be converted into

$$n = \frac{1}{1-(1/\eta_r)(1-1/\gamma)} \tag{4-20}$$

where η_r is the polytropic efficiency of the rotor alone. Thus equation (4-17) can be solved to obtain the ratio of the stagnation specific volumes from the inlet to the discharge of the compressor rotor. However, for the rotor design, one needs the actual specific volumes v_i and v_2, not their stagnation values. The relation between the actual specific volume and the stagnation volume is given (for air at temperatures below 800° R) by figure 2-7 and can be expressed as

$$\left.\begin{aligned} \frac{v_i}{v_{o,i}} &= f\left(\frac{V_{i,av}}{V_{o,i}}\right) \\ \frac{v_2}{v_{o,2}} &= f\left(\frac{V_2}{V_{o,2}}\right) \end{aligned}\right\} \tag{4-21}$$

Values of these quantities can be read from figure 2-7 as soon as $V_{i,av}/V_{o,i}$ and $V_2/V_{o,2}$ are known. The value of $V_{i,av}/V_{o,i}$ is either assumed or derived as mentioned previously from the inlet cross section $(D_i^2 - D_H^2)\pi/4$, the inlet gas condition (since $V_{o,i} = \sqrt{2g_o h_{o,i}}$), and the mass or weight flow rate.

The absolute discharge velocity V_2 can be scaled from the rotor discharge velocity diagram (fig. 4-21), where the quantities U_2, $V_{m,2}$, and w_{SA} are calculated from

$$\frac{U_2}{U_i} = \frac{D_2}{D_i}$$

$$V_{m,2} = V_{i,av}$$

$$w_{SA} = U_2 \frac{t_2}{D_2} = U_2 \frac{\pi}{N}$$

in which N is the number of vanes. Finally $V_{o,2} = \sqrt{2g_o h_{o,2}}$, where $h_{o,2}$ is given by equation (4-14).

From the foregoing information, one can evaluate equations (4-21) by means of figure 2-7. What is ultimately needed is the ratio of the

discharge to inlet volume flow rate Q_2'/Q_1, which is proportional to the corresponding ratio of specific volumes:

$$\frac{Q_2'}{Q_1} = \frac{v_2}{v_i} = \left(\frac{v_2 v_{o,i}}{v_{o,2} v_i}\right) \frac{v_{o,2}}{v_{o,i}} \tag{4-22}$$

where the prime designates the compressible flow rate and the term in parentheses is determined from equations (4-21) and the last multiplier by equation (4-17).

Since the discharge width b_2 (fig. 4-20) was determined by $Q_2 = Q_1$, the new width b_2' for compressible flow is given by

$$b_2' = b_2 \frac{Q_2'}{Q_1} \tag{4-23}$$

because it is still assumed that $V_{m,2} = V_{i,av}$, as for incompressible flow.

To illustrate the foregoing considerations, we assume that the rotor shown in figure 4-20 handles air at an inlet stagnation temperature $T_{o,i}$ of 80° F (539.7° R). The rotor peripheral velocities are $U_2 = 1700$ feet per second and $U_i = 1046$ feet per second. The specific heat of air at the assumed temperature is $C_p = 186.8$ foot-pounds per °R, so that $h_{o,i} = 186.8 \times 539.7 = 100\ 816$ foot-pounds per pound.

The discharge velocity diagram in figure 4-21 is assumed to apply to the mean, meridional stream surface. The rotor head is

$$H_r = \frac{U_2 V_{U,2} - U_1 V_{U,M}}{g_o} \tag{4-24}$$

Scaling from the velocity diagrams in figures 4-19 and 4-21, one finds

$$H_r = \frac{(1700 \times 1568) - (762 \times 326)}{32.2} = 75\ 069 \text{ ft-lb/lb}$$

It might be mentioned in passing that the maximum relative inlet velocity (scaling from fig. 4-19) is $w_{1,o} = 640$ feet per second, which corresponds to a Mach number of about 0.57, and the absolute rotor discharge velocity (scaling from fig. 4-21) is $V_2 = 1612$ feet per second, which corresponds to a Mach number of about 1.17.

According to equation (4-14), $h_{o,2} = 100\ 816 + 75\ 069 = 175\ 885$ foot-pounds per pound, and the corresponding discharge stagnation temperature is $T_{o,2} = 175\ 885/188 = 936°$ R, where C_p is approximated by an average value between 0° R (fictitious) and 1000° R.

From equation (4-17), one obtains the stagnation specific volume ratio

$$\frac{v_{o,2}}{v_{o,i}} = \left(\frac{539.7}{936}\right)^{1/(n-1)} = 0.5766^{1/(n-1)}$$

Assuming a polytropic rotor efficiency of 93 percent (as doubtlessly more than half of the total losses occur in the diffuser after the rotor), one obtains from equation (4-20)

$$n = \frac{1}{1-(1/0.93)(1-1/1.39)} = \frac{1}{1-0.302} = 1.433$$

$$\frac{1}{n-1} = \frac{1}{0.433} = 2.3095$$

and, according to equation (4-17),

$$\frac{v_{o,2}}{v_{o,i}} = 0.5766^{2.3095} = 0.2804$$

Furthermore, with scaling from the velocity diagrams,

$V_{i,av} = 369$ ft/sec

$V_2 = 1612$ ft/sec

$V_{o,i} = \sqrt{2 g_o 100\ 816} = 2548$ ft/sec

$V_{o,2} = \sqrt{2 g_o 175\ 885} = 3365.6$ ft/sec

Hence

$$\frac{V_{i,av}}{V_{o,i}} = \frac{369}{2548} = 0.1448$$

and, from figure 2-7,

$$\frac{v_i}{v_{o,i}} = 1.05$$

$$\frac{V_2}{V_{o,2}} = \frac{1612}{3365.6} = 0.479$$

$$\frac{v_2}{v_{o,2}} = 1.920$$

Therefore, according to equation (4-22),

$$\frac{Q_2'}{Q_1} = \frac{v_2}{v_i} = \frac{1.92}{1.05} \times 0.2804 = 0.5127$$

that is, in this example, the volume flow rate is reduced from the inlet to the discharge of the rotor to slightly more than one-half. The same velocities as in the preceding case of an incompressible fluid can be maintained by reducing the discharge width of the rotor from b_2 to b_2', where $b_2' = 0.505\ b_2$. Figure 4-20 shows, in dashed lines, this change in rotor width and the required gradual transition from the rotor discharge to its inlet, where there is no change in volume.

It is interesting to observe that in the rotor for an incompressible fluid the axial width changes in the radial part of the rotor in inverse proportion to the distance from the axis of rotation in order to maintain a constant average meridional velocity as far as possible on the simple basis of this design. Accomplishing the same thing for a compressible fluid would require increasing the width of the rotor from the discharge diameter toward the inlet very much faster than in inverse proportion to the distance from the axis of rotation.

It should be observed that the specific speed of the rotor shown in figure 4-20 is the same whether the rotor is handling an incompressible or a compressible fluid if the specific speed is calculated for the inlet rate of volume flow. On the other hand, when calculated for the discharge volume flow of the rotor, the specific speed of the rotor for a compressible fluid is (for the particular conditions considered here) lower by a factor of $\sqrt{0.5127} = 0.716$ than the specific speed of the corresponding rotor for an incompressible fluid. The specific speed for a compressible fluid is still lower when referred to the discharge volume of the entire compressor stage, since the volume flow is further reduced by the compression in the stationary diffuser passages of the stage (or single-stage machine).

It is also of interest to determine the stagnation pressure ratio of the entire stage $p_{o,3}/p_{o,i}$, where the subscript 3 denotes the final discharge condition of that stage. This ratio is found as follows:

$$H_r = h_{o,2} - h_{o,i} = h_{o,i}\left(\frac{h_{o,2}}{h_{o,i}} - 1\right) = h_{o,i}\left(\frac{T_{o,2}}{T_{o,i}} - 1\right)$$

where $h_{o,2} = h_{o,3}$ and $T_{o,2} = T_{o,3}$.

For isentropic changes, the relation between the stagnation temperature ratio and the stagnation pressure ratio is given by equation (2-30). The corresponding relation for polytropic changes is obviously

$$\left(\frac{T_{o,3}}{T_{o,i}}\right)^{n/(n-1)} = \frac{p_{o,3}}{p_{o,i}}$$

or

$$\frac{T_{o,3}}{T_{o,i}} = \left(\frac{p_{o,3}}{p_{o,i}}\right)^{(1-1/n)} \tag{4-25}$$

Hence

$$H_r = h_{o,i}\left[\left(\frac{p_{o,3}}{p_{o,i}}\right)^{(1-1/n)} - 1\right]$$

$$\frac{H_r}{h_{o,i}} + 1 = \left(\frac{p_{o,3}}{p_{o,i}}\right)^{(1-1/n)}$$

$$\frac{p_{o,3}}{p_{o,i}} = \left(\frac{H_r}{h_{o,i}} + 1\right)^{1/(1-1/n)}$$

If one is interested in the pressure ratio of the entire stage or single-stage machine, one must determine n from the estimated polytropic efficiency of the entire stage. Assuming this efficiency to be 83 percent, one finds from equation (4-20) with $\eta = 0.83$ in place of η_r

$$n = \frac{1}{1-(1/0.83)(1-1/1.39)} = 1.51067$$

so that $1/(1-1/n) = 2.9582$ and

$$\frac{p_{o,3}}{p_{o,i}} = \left(\frac{75\ 069}{100\ 816} + 1\right)^{2.9582} = 5.188 \tag{4-26}$$

The corresponding overall volume ratio is, according to equation (4-18),

$$\frac{v_{o,3}}{v_{o,i}} = \left(\frac{p_{o,i}}{p_{o,3}}\right)^{1/n} = 0.1928^{0.662} = 0.3363 \qquad (4\text{-}27)$$

which can be compared with the previously determined volume ratio of the rotor alone, $v_{o,2}/v_{o,i} = 0.2804$.

The foregoing calculations of volume and pressure changes in the machine can be greatly simplified by the use of a suitable diagram showing the relation among the principal variables: temperature, specific volume, and pressure. This writer found that the logarithmic temperature-volume diagram described in chapter 18 (sec. 89) of reference 14 is particularly useful, because thermal changes appear in this diagram as practically straight lines with slopes proportional to $\gamma - 1$ for isentropic changes and $n - 1$ for polytropic changes. Lines of constant pressure are also straight, and the enthalpy can be read from a scale almost proportional to T, instead of requiring the determination of an area. However, the presentation of this method of calculation does not fall within the intended scope of this compendium.

4.4.2 Design of Francis Rotor Vane Systems by Conformal Mapping

In order to consider the entire vane surface in the design of Francis rotor vane systems (figs. 4-17 and 4-18), one must represent the intersection of the vanes with the meridional stream surfaces in a manner permitting the design of the vane sections from the prescribed or desired directions of flow. To do so by means of three-dimensional models of the stream surfaces would be quite complicated and costly. It is, therefore, necessary to represent the intersections of the vane with the meridional stream surfaces in a plane.

The meridional stream surface between an axial inflow and an approximately radial discharge forms a doubly curved surface which cannot be developed into a plane without significant changes in its local linear dimensions. The most widely known transformation of a doubly curved surface into a plane is the Mercator projection of the Earth's surface. It is conformal insofar as small areas are represented in a geometrically similar manner to the actual geometry on the globe. On the other hand, there are major changes in the scale of projection, so that Greenland appears on the Mercator map disproportionately large compared wth equatorial regions, and the polar regions appear, indeed, infinitely large.

The same principle of conformal mapping was first applied to Francis type turbomachinery by Prasil (refs. 65 and 66). The basic principle used in this application is purely geometric and may be described as follows:

First, the surface of revolution to be represented conformally on a plane is intersected by radial planes containing the axis of revolution and having a constant angular distance $\Delta\varphi$ from each other (see fig. 4-22). In the turbomachinery field, $\Delta\varphi$ is preferably a simple fraction (1/2, 1/3, 1/4, 1/5, etc.) of the angular distance between succcessive vanes, that is,

$$\Delta\varphi = \frac{2\pi}{AN} \qquad (4\text{-}28)$$

where A is preferably an integer, and N must be an integer, since it is the number of vanes.

The circumferential distance between successive radial planes along the surface of revolution is

$$b(r) = r\,\Delta\varphi \qquad (4\text{-}29)$$

where r is the mean local distance from the axis of revolution. The intersections of the radial planes with a surface of revolution mark meridional lines on that surface.

Second, one can draw on the surface of revolution coaxial circles spaced by the variable distances $b(r)$ along that surface, this distance $b(r)$ between the coaxial circles being equal to the circumferential distances $b(r)$ between the radial planes at the same distance r from the axis of rotation, given by equation (4-29). The distance r from the axis is measured from the middle of every step $b(r)$ as shown in figure 4-22. The graphical determination of the points 1, 2, 3, 4, 5, and 6, establishing the circles of the same numbers on the surface of revolution, involves a brief process of trial and error, or a graphical procedure described later.

The circles so determined and the meridional lines of intersection between the surface of revolution and the radial planes establish on the surface of revolution a network of orthogonal lines with equal, mean distances $b(r)$ in both orthogonal directions. This network approaches a network of squares as $\Delta\varphi$ approaches zero.

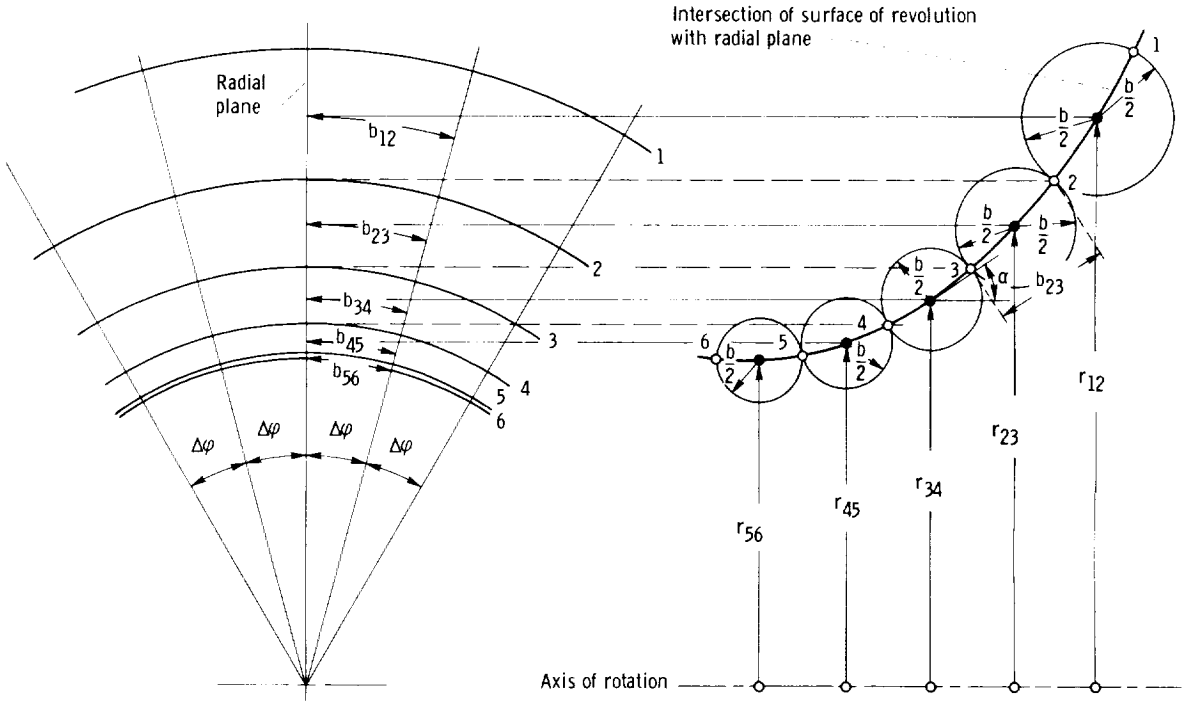

Figure 4-22. – Coordinate lines on surface of revolution for conformal mapping.

The network of lines so established may be correlated with a network of orthogonal lines on a plane surface called the plane of representation. This plane could be, for example, a network of concentric circles and radial lines with the radial spacing between the circles and the circumferential spacing between the radial lines being locally equal to each other (see, e.g., the lower part of fig. 2-42). However, it is simpler to choose in the plane of representation a chessboardlike system of straight, orthogonal, parallel lines with a constant spacing a. Such a system is used in the following considerations.

Since the line spacing $b(r)$ on the surface of revolution varies proportionally to r, it should be possible to find or select a particular distance r_1 from the axis of rotation where $b(r) = a$, so that

$$\left.\begin{aligned} \frac{b(r)}{r} &= \frac{a}{r_1} \\ \text{or} \\ \frac{b(r)}{a} &= \frac{r}{r_1} \end{aligned}\right\} \qquad (4\text{-}30)$$

The second expression is obviously the local scale ratio of the surface of revolution to the plane of representation and applies also to any pair of correlated parts Δb and Δa of the line spacings $b(r)$ and a, so that

$$\frac{\Delta b}{\Delta a} = \frac{r}{r_1} \qquad (4\text{-}31)$$

By means of this relation, one can transform any figure drawn in the plane of representation into a corresponding figure on the surface of revolution, and vice versa, since Δb and Δa may be distances of any point in the figure from a nearby coordinate line. The distance r from the axis of rotation is, of course, measured from the center of Δb as illustrated in figure 4-22 with respect to the line spacing $b(r)$.

It is easy to show that corresponding figures on the surface of revolution and in the plane of representation are conformal to each other, that is, that they have the same angles, by proving that angles against one of the coordinate directions are the same for corresponding figures.

Designate the meridional coordinate on the surface of revolution by m and the corresponding coordinate in the plane of representation by y. Designate the circumferential coordinate on the surface of revolution by $r\varphi$ (with r = constant so that $d(r\varphi) = rd\varphi$) and the corresponding coordinate in

the plane of representation by x. Designate the angle of any line against the circumferential direction by β_φ and against the x-direction by β_x. Evidently

$$\left.\begin{aligned}\tan\beta_\varphi &= \frac{dm}{r\,d\varphi}\\ \tan\beta_x &= \frac{dy}{dx}\end{aligned}\right\} \tag{4-32}$$

Furthermore, at any one point on the surface of revoluton, $r=$ constant, so that, according to equation (4-31),

$$\frac{dm}{dy} = \frac{r}{r_1} = \frac{r\,d\varphi}{dx} \tag{4-33}$$

Hence

$$\frac{dm}{r\,d\varphi} = \frac{dy}{dx} \tag{4-34}$$

and, therefore, according to equation (4-32),

$$\beta_\varphi = \beta_x \tag{4-35}$$

which proves that angles at corresponding points are the same on the surface of revolution and in the plane of representation, that is, that corresponding figures in these two surfaces are conformal.

If the foregoing conformal transformation is applied to Francis rotors, it has purely geometric, not hydrodynamic, significance, that is, it does not apply to relative flow pictures in the two surfaces considered, since even a frictionless relative flow of an incompressible fluid is neither irrotational nor two-dimensional. The laws of fluid motion must, therefore, be satisfied in the actual flow field along the surface of revolution. The conformal representation of the vane sections in a plane can be used hydrodynamically only for one-dimensional considerations, and then only with reservations.

The foregoing design principles are applied in the following example to the design of a Francis pump rotor having characteristics of practical significance and a basic specific speed with which in the past overall efficienices of about 90 percent have been obtained. While to some extent typical, the design presented here does not correspond to any existing pump rotor, and its actual performance is, therefore, not known. The design merely represents the best design methods available to this writer, and more than half of the pump rotors designed by this method have been successful.

It is assumed that the basic specific speed of the single-suction pump to be designed is $n_S=0.12$ (2064, with Q in gal/min) and its suction specific speed is $S=0.58$ (9976). The suction specific speed corrected for $D_h/D_i=0.35$ is $S_o=0.61916$ (10 649). From figure 1-18, we select $V_{m,i}/U_i=0.35$ with $2g_oH_{sv}/V_{m,i}^2=2.85$. Choosing tentatively $\psi=2g_oH/U_2^2=1.0$, one derives from equation (1-24) the outside to inlet diameter ratio:

$$\left(\frac{D_2}{D_i}\right)^{3/2} = \frac{1}{n_S\times 2.1078}\left(\frac{U_2^2}{2g_oH}\right)^{3/4}\left(\frac{V_{m,i}}{U_i}\right)^{1/2}\left(1-\frac{D_h^2}{D_i^2}\right)^{1/2} \tag{4-36}$$

$$= 3.9536\times 1\times 0.59161\times 0.93675 = 2.19105$$

$$\frac{D_2}{D_i} = 2.19105^{2/3} = 1.68695$$

which establishes the major diameters of the rotor, D_i, D_2, and D_h as ratios. It should be recognized that $\psi=2g_oH/U_2^2=1$ is an arbitrary (empirical) choice, so that the ratio D_2/D_i may yet have to be altered in order to have an acceptable ratio of retardation w_2/w_i along the outer shroud.

Still to be determined is the change in the average meridional velocity from the inlet to the discharge of the rotor. For an incompressible fluid, a constant meridional velocity (as assumed in sec. 4.4.1) would lead to the relation

$$\pi D_2 b_2 = (D_i^2 - D_h^2)\frac{\pi}{4}$$

where the vane thickness blockage is ignored. This relation leads to

$$\frac{b_2}{D_2} = \frac{D_i^2}{D_2^2}\frac{1-D_h^2/D_i^2}{4}$$

$$\frac{b_2}{D_2} = 0.3514 \times \frac{0.8775}{4} = 0.07709 \tag{4-37}$$

However, there is no reason for keeping the meridional velocity constant, since only the retardation (if any) of the relative flow between the vanes has a recognized significance regarding the real-flow effects in the vane passages.

A low meridional velocity at the impeller (rotor) discharge may have advantages regarding the volute or diffuser passages following the rotor (see sec. 4.5). Assuming arbitrarily that the meridional velocity is reduced from rotor inlet to discharge to one-half ($V_{m,2}/V_{m,i} = 1/2$) results in

$$\frac{b_2}{D_2} = 0.1542 \tag{4-38}$$

Empirically it can be assumed that the impeller width or retardation of the meridional flow lies between the values given by equations (4-37) and (4-38). A somewhat arbitrary choice is required. Assume

$$\frac{b_2}{D_2} = 0.13$$

so that

$$\frac{V_{m,2}}{V_{m,i}} = \frac{0.0771}{0.13} = 0.593$$

or

$$\frac{V_{m,2}}{V_{m,i}} = 0.6$$

which leads to

$$\frac{b_2}{D_2} = \frac{0.0771}{0.6} = 0.1285$$

In view of the approximate character of the foregoing considerations,

$$\left.\begin{aligned} &\frac{b_2}{D_2} = 0.13 \\ &\text{and} \\ &\frac{V_{m,2}}{V_{m,i}} = 0.6 \end{aligned}\right\} \tag{4-39}$$

are selected for the following considerations.

Equations (4-39), the result of equation (4-36), and the foregoing assumption $D_h/D_i = 0.35$ determine the profile of the rotor as far as possible on the basis of the simple considerations used here (see fig. 4-23).

It is assumed that the fluid enters the rotor without rotation about the axis, so that $V_{U,i} = 0$. As a consequence,

$$\psi = \frac{2g_o H}{U_2^2} = 2\eta_h \frac{V_{U,2}}{U_2} \tag{4-40}$$

The so-called hydraulic efficiency η_h covers only losses which reduce the pump head, not losses which merely increase the required torque, and is, therefore, higher than the overall efficiency. The hydraulic efficiency is conservatively assumed to be $\eta_h = 0.90$. Using, furthermore, the earlier assumption that $2g_o H/U_2^2 = 1$, one finds, from equation (4-40),

$$\frac{V_{U,2}}{U_2} = \frac{1}{2\eta_h} = 0.5556$$

Scaling from the velocity vector diagrams in figure 4-24, one finds the retardation ratio of the relative flow along the outer shroud is $w_2/w_i = 0.736$, which is acceptable if the lift coefficient is selected accordingly to be fairly low. A conservative value $C_{L,\infty} = 1.0$ is selected tentatively in order to determine the number of vanes.

The profile of the rotor shown in figure 4-23 is developed to a large extent empirically. Its axial length is made as small as possible in order to ease the mechanical problems connected with the application of this rotor. On the other hand, the radius of curvature R_i of the outer shroud at the rotor inlet should be as large as possible in order to minimize the inlet cavitation problem. (An attempt to make R_i not much smaller than the radial width $(D_i - D_h)/2$ of the passage at the inlet resulted in $R_i = 0.923\ (D_i - D_h)/2$.) The axial extent of the rotor is minimized by reducing the radius of the shroud curvature below R_i between the inlet and the radial portion. This change should be acceptable since the relative flow in the rotor passages has a strong circumferential component and is, therefore, subjected to far less curvature than visible in the rotor profile.

The circumferential cross section $2\pi rb$ measured normal to the two boundaries of the axially symmetric flow passage is previously described to be in-

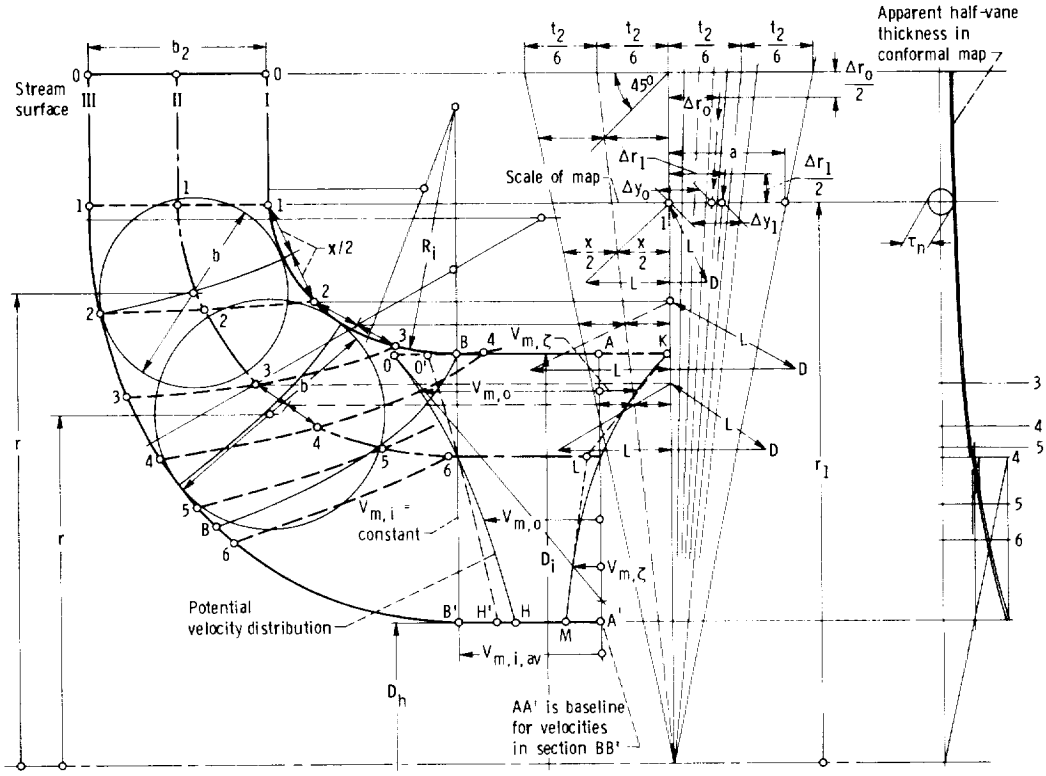

Figure 4-23. – Profile of Francis rotor locating circles for conformal mapping of three meridional stream surfaces of revolution.

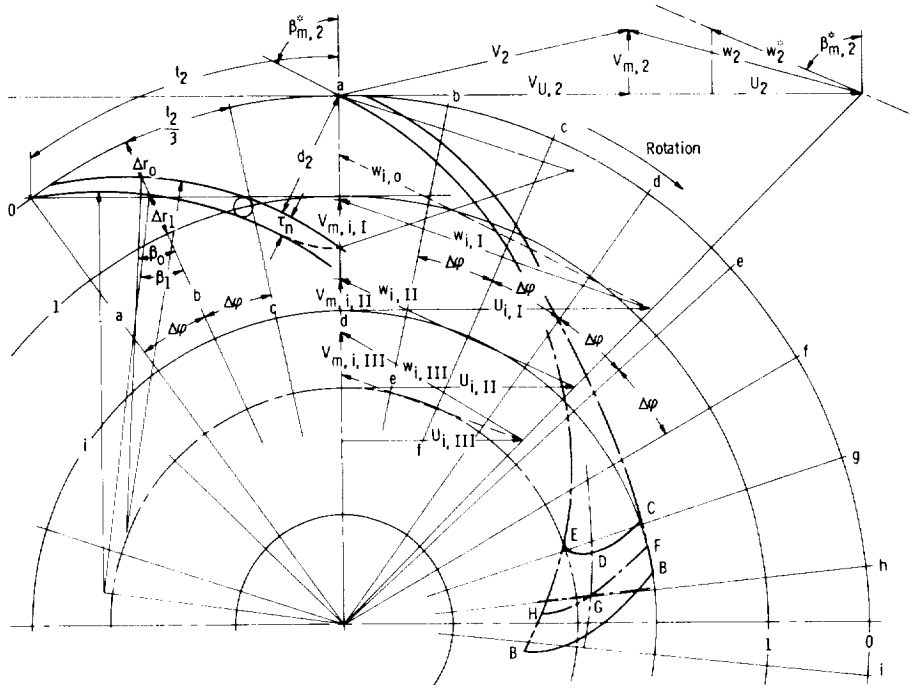

Figure 4-24. – End view of outer vane end and of constant-head lines at inner vane end and basic velocity diagrams of Francis pump rotor.

creasing toward the discharge of the rotor. All that is required is that it increase along a smooth curve as shown in figure 4-25. This curve is derived by trial and error in connection with the inner contour of the back shroud of the rotor.

To determine the number of vanes from the lift coefficient, one must estimate the length of the vane. For the estimate along the outer shroud, it is necessary to obtain an average vane angle along that contour. The inlet vane angle is given by the inlet velocity diagram. The discharge vane angle is estimated from the discharge velocity diagram as indicated in sections 2.6.3.4 to 2.6.3.6 and figure 2-45 and as shown in figure 4-24. The discharge flow angle measured against the meridional direction is $\beta^*_{m,2} = 66°$. The mean vane angle must be smaller to account for the vane blockage, which increases the meridional velocity.

Let s_m be the meridional vane length measured along a meridional flow line in the section shown in figure 4-23. Evidently the vane length is approximately

$$l = \frac{s_m}{\cos \beta_{m,av}} \tag{4-41}$$

Scaling s_m from figure 4-23, one finds $s_m/D_2 = 0.286$ measured along the outer shroud from the maximum to the minimum diameter. Furthermore one can estimate from existing rotor designs that

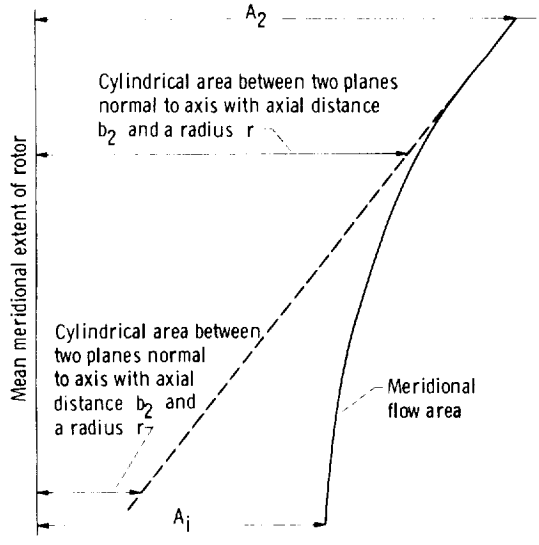

Figure 4-25. – Meridional flow area distribution.

$\beta_{m,av} = 63°$. Hence equation (4-41) gives the following result:

$$\frac{l}{D_2} = \frac{0.286}{0.4540} = 0.63$$

Estimating w_∞ to be $(w_i + w_2)/2 = 0.547\ U_2$ and using the previously determined ratio $V_{U,2}/U_2 = 0.5556$, one calculates from equation (2-130), with $C_{L,\infty} = 1.0$ and $V_{U,1} = 0$,

$$\frac{l}{t_2} = 2\frac{V_{U,2}}{w_\infty} = 2\frac{0.5556}{0.547} = 2.0314$$

and, with $l/D_2 = 0.63$,

$$\frac{D_2}{l}\frac{l}{t_2} = \frac{D_2}{t_2} = \frac{2.0314}{0.63} = 3.2245$$

so that the number of vanes is

$$N = \pi \times 3.2245 = 10.13$$

Using $N = 10$, one obtains $C_{L,\infty} = 1.013$, which is acceptable but not final, since the actual vane length is likely to be different from that given by equation (4-41) with an estimated value of $\beta_{m,av}$.

Before the vane is laid out by conformal mapping, it is desirable to design the discharge end of the vane in a preliminary fashion described in section 4.3 in connection with figures 4-8 to 4-10, because the simple design method given there is applicable to the discharge portion of the presently considered impeller and, therefore, offers a good check of the part of the design developed by conformal mappling.

The discharge vane distance d_2 is determined by the condition of continuity, with a uniform, fictitious velocity assumed in this cross section (see figs. 2-45 and 4-24). This distance is easily determined by comparison with the inlet cross section

$$Q = V_{m,i}\frac{D_i^2\pi}{4}\left(1-\frac{D_h^2}{D_i^2}\right) = w_2^* b_2 d_2 N$$

so that

$$\frac{d_2}{D_i} = \frac{V_{m,i}}{w_2^*}\frac{D_i\pi(1-D_h^2/D_i^2)}{4b_2 N} \qquad (4\text{-}42)$$

Using the diameter ratios from figure 4-23 and the velocity ratios from the diagrams in figure 4-24, one finds

$$\frac{d_2}{D_i} = 0.6692 \times 4.572 \times \frac{\pi}{4} \times \frac{0.8875}{10} = 0.211$$

The outer vane end is designed according to figures 4-9 and 4-10 and is shown in figure 4-24. The vane thickness τ_n is chosen to be 2 percent of the outside rotor diameter, with a slight reduction toward the discharge vane end.

For the vane layout by means of conformal mapping, it is necessary to determine the stream surfaces of the meridional flow. The objective is to establish the intersections between the vanes and these surfaces, since these intersections can be assumed to determine the vane action on the flow.

For this impeller layout, three meridional stream surfaces, I, II, and III, are considered (fig. 4-23), I and III coinciding with the inner surfaces of the outer and inner shrouds and II located halfway between surfaces I and III according to the local circumferential cross sections of the meridional flow. The central stream surface II is, therefore, established under the assumption that the meridional velocity V_m is constant over any one cross section of this flow. This assumption is sufficiently close for the establishment of flow surface II and is discussed further later.

The dimensionless scale of the orthogonal network of meridional lines and coaxial circles on the meridional stream surfaces of revolution is established by the angular spacing $\Delta\varphi$ between the radial and axial planes. This scale was chosen to be one-third of the vane spacing, that is, 12° for 10 vanes. Successive radial sections are marked a, b, c, d, etc. for each vane, the sequence beginning at the discharge edge and proceeding in the direction of rotation (against the relative flow). Since figure 4-24 shows two vanes, it must show two scales a, b, c, d, etc.

The next step is to establish on surfaces I, II, and III coaxial circles 0, 1, 2, 3, etc. spaced at intervals meridionally equal to the circumferential spacing between the radial planes a, b, c, etc. at the mean radius (distance from the axis of rotation) of each meridional step. The principle involved is outlined previously and illustrated in figure 4-22. It is rather simple to satisfy this principle graphically by the operation suggested by Victor Potondy (formerly of Goulds Pumps Inc., Seneca Falls, N.Y.) and illustrated in figure 4-23 for the step from 0 (outside periphery) to 1. In a diagram such as figure 4-23 showing the spacing between the circles as a function of the distance r from the axis of rotation (shown to the right of the impeller profile), one draws a line under 45° (as shown). The intersection of this line with the dashed line showing one-half of the spacing as a function of r gives the radial position of the center of the first step from 0 to 1. This solution is, of course, valid only if the surface of revolution is a plane normal to the axis, as it is between stations 0 and 1 in figure 4-23. An extension of the method to a general surface of revolution such as shown in figure 4-22 and figure 4-23 below station 1 is shown in figure 4-26.

The meridional spacing between successive circles on the surface of revolution is $x(r) = r\,\Delta\varphi$, where r is the distance of the center of $x(r)$ from the axis of rotation. The diagram $x(r) = r\,\Delta\varphi$ is shown in figure 4-23 to the right of the rotor profile and at the left side in figure 4-26 at an enlarged scale. The meridional spacing between circles 1 and 2 is designated x_{12}, and the spacing is assumed to be sufficiently small to neglect the difference between the chord length 12 and the length measured along the curved surface of revolution in the meridional direction.

In the $x(r)$ diagram (at the right in fig. 4-23 and at the left in fig. 4-26), one draws through point A (corresponding to point 1) a line parallel to the estimated direction of the chord 12 on the surface of revolution. Along this line, one marks from point A an arbitrary length L ending at D. (The length is preferably somewhat larger than the expected one-half chord length, in order to obtain good accuracy.) Along a line through D paralled to the axis of rotation, one plots the same length L, from E to B. A straight line from A to B intersects

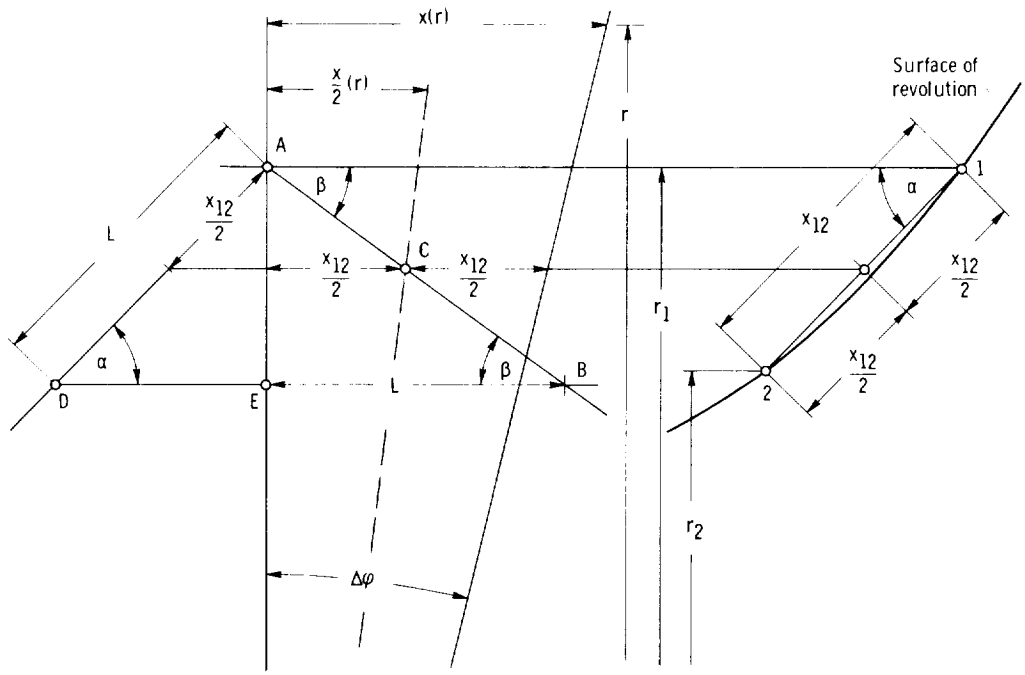

Figure 4-26. – Construction of spacing between coaxial circles on surface of revolution for conformal mapping; sin α = tan β.

the broken $x(r)/2$ line at C, which marks the chord center of the desired chord x_{12} and thereby determines the magnitude of $x_{12}/2$ from the $x(r)$ diagram, as shown in figure 4-26.

If the initial estimate of the direction of the chord 12 and thereby of the line AD is significantly wrong, one can reiterate, but, with a little experience in estimating the step x_{12}, this reiteration is rarely required.

The same construction is shown in figure 4-23, only for three steps, one from 1 to 2 and one from 2 to 3 along stream surface I and another from 3 to 4 along stream surface II. The same method is used for all steps to which it applies. (It does not apply to nearly cylindrical parts of the stream surface.)

With the network of orthogonal lines so established on all stream surfaces I, II, and III (circles 1, 2, 3, etc. and meridional lines along the radial planes a, b, c, etc. in figs. 4-24 and 4-27), one is ready for the design process by conformal mapping.

To begin, one selects more or less arbitrarily a radius r, at which the scales of the impeller drawing and of the plane of conformal representation are the same. The radius of the three points marked 1 in figure 4-23 is selected to be r_1, which gives a convenient size for the conformal representations of the intersections of the vanes with the three surfaces I, II, and III. The constant spacing a of the straight, orthogonal lines in the plane of representation (fig. 4-27) is, therefore,

$$a = \frac{2\pi r_1}{AN} = \frac{2\pi r_1}{30} \tag{4-43}$$

according to equation (4-28) and the choice of $N = 10$ and $A = 3$.

The design method consists in designing the vane sections I, II, and III in the plane of representation. Since this representation is conformal, the direction of the vane section is known from the inlet and discharge velocity diagrams, by using at the discharge the direction of the fictitious relative velocity vector w_2^* (see figs. 2-45 and 4-24) determined according to sections 2.6.3.4 to 2.6.3.6. The inlet vane angle is very nearly equal to the angle of the inlet relative velocity (see figs. 3-1 and 4-7). The real problem in this case is the determination of the meridional velocity component at the inlet. The peripheral component of the absolute inlet flow is here assumed to be zero to avoid unnecessary complication of the overall problem.

It would be natural to assume at the inlet a potential meridional velocity distribution determined

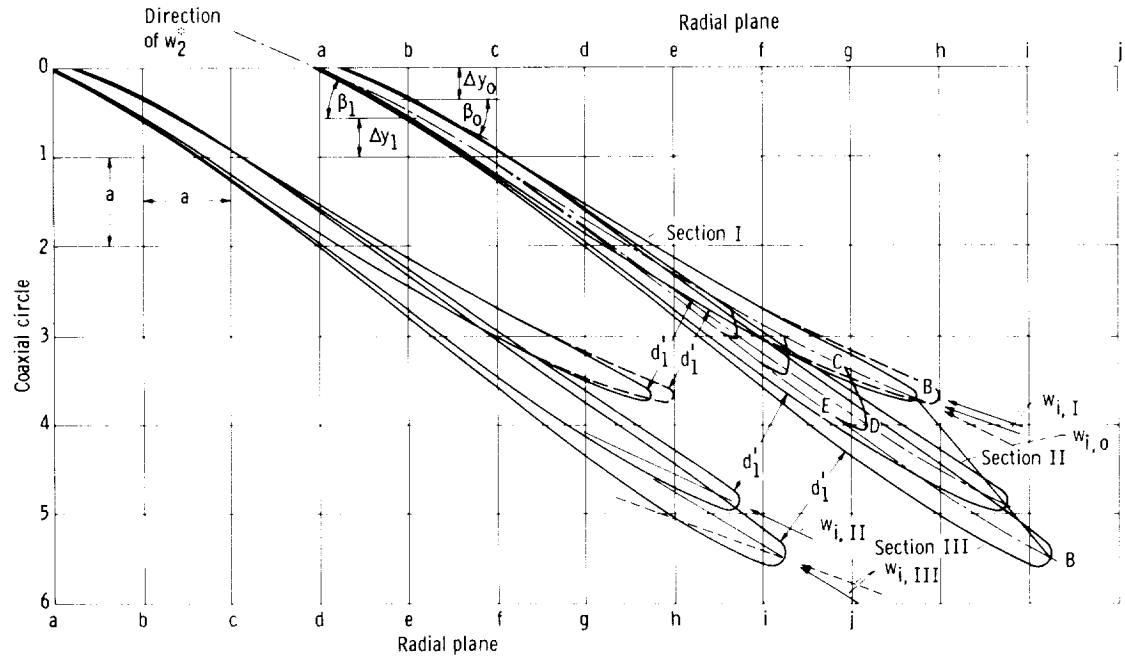

Figure 4-27. – Conformal representation of Francis pump rotor vanes.

from the radii of curvature at the inner and outer flow boundaries as outlined in section 2.2. This approximation of the potential inlet velocity distribution is shown in figure 4-23 as curve OH, plotted from the baseline AA′ to the right of the impeller inlet. This meridional velocity distribution could also be assumed to exist along the inlet edges BB of the vanes. Strange as it seems, vanes designed according to this assumption have usually shown poorer results than vanes designed according to the more elementary (one-dimensional) assumption of a uniform meridional velocity distribution along the inlet edges of the vanes. In the next section, an attempt is made to explain this result by theoretical approximations. At present, the empirical rule $V_{m,i} = \text{constant}$ is used as the primary design criterion, however, with some attention to the potential velocity distribution of the meridional inflow. The meridional flow area distribution shown in figure 4-25 indicates that it is justified to assume the mean meridional velocity distribution to be the same at the vane inlet edge BB as in the so-called eye cross section with an outside diameter D_i and an inside diameter D_h.

With the inlet and discharge vane angles so determined, it must still be considered that these directions of flow (particularly at the inlet) do not consider the blockage effect of the finite vane thickness, which increases the meridional velocity component in the central portions of the vanes more than at the vane ends. In other words, in their central portions, the vanes must be steeper than at their ends.

In the conformal map, centerlines of the vanes are drawn parallel to w_i at the inlet, parallel to w_2^* at the discharge, and somewhat steeper than either end in the central portions of the vane to account for blockage. It should be recognized that the difference between w_2^* and the true relative velocity w_2 takes the vorticity of the relative flow into account. The vertical location of the vane inlet edges is determined by the empirically assumed vane inlet edge as shown in figure 4-23 (subject to revision, if necessary), so that only the horizontal extent of each vane section in the conformal map (i.e., the circumferential extent of the actual vane section) needs to be determined by the smooth connection between the inlet and discharge portions and the previously mentioned requirement that the vane must be somewhat steeper in its central portion than at the vane ends.

In the present case, the process outlined previously is greatly facilitated by the existence of a preliminary layout of the outer vane portion according to the geometric principles described in connection with figures 4-9 and 4-10. The result of

such a layout is shown in figure 4-24. The transfer of this layout into the conformal map (fig. 4-27) is illustrated for two points in the radial and axial section b removed from the discharge edge by $\Delta\varphi = 2\pi/30$. The transformation of the radial distances Δr_o and Δr_1 from the nearest coordinate circles 0 and 1 into the corresponding distances Δy_o and Δy_1 in the conformal map is shown in the $x(r), r$ diagram in figure 4-23 and should be self-explanatory. Furthermore the conformal nature of this transformation permits the transfer of all vane angles from the physical layout (fig. 4-24) to corresponding points on the conformal map. This transfer is facilitated by the fact that the physical layout of the outer vane end was constructed out of circular arcs, so that the vane angle against the peripheral direction is directly given by the angle between radial lines, as shown in figures 4-2 and 4-24. The conformal representation of the outer vane end is, therefore, given by points along the curve and its tangents. This method is a very reliable determination of a curve.

It should be noted that the outer vane end so designed agrees in direction very satisfactorily with the fictitious velocity w_2^* shown in figure 4-24 and transferred to figure 4-27.

The outer vane end so determined establishes the vane centerline (dash-dot line) in that region (fig. 4-27), which can then be continued smoothly toward the leading edge, where its direction is given by the relative velocity of the oncoming flow. The construction of the outer vane end according to figure 4-9 automatically leads to the steepening of the vanes in the central portions of the vane, which is previously described as dictated by the blockage effect of vanes with finite thickness.

The complete vane section shape is determined by placing the half-vane thickness symmetrically around the vane centerline. A constant vane thickness in the physical system obviously leads to an increase in the apparent vane thickness toward the leading end of the conformal vane layout (fig. 4-27). This apparent thickness is inversely proportional to the local distance r from the axis of rotation. Its construction is shown at the right in figure 4-23, and it can be used directly in the conformal map. The actual vane thickness remains, of course, not constant to the vane ends. The reduction in thickness toward the discharge end is included in the geometric construction used (see fig. 4-10), and toward the leading edge the change in thickness is best accomplished graphically in the conformal map.

The vane section I (outer shroud, fig. 4-23) shows in its conformal representation (fig. 4-27) two leading-edge shapes. The shape developed first entirely on the basis of the relative velocity associated with a uniform meridional approach velocity $V_{m,i}$ = constant is shown in dashed lines, and the relative velocity is represented by solid velocity vectors $w_{i,I}$. Figure 4-23 also shows a potential meridional velocity $V_{m,o}$ whose radial distribution is represented by the solid curve HO. Experience has shown that this departure from the uniform meridional velocity distribution is too large and that a meridional velocity distribution halfway between the uniform $V_{m,i}$ and the potential $V_{m,o}$ distribution in figure 4-23 gives better results, particularly with respect to cavitation. This intermediate meridional velocity distribution is shown in figure 4-23 by the dashed line H′O′. Its upper end O′ is used in the conformal map (fig. 4-27) for the construction of a revised vane section I, shown in solid lines, which is used in this design example. The normal inlet vane distance d_1' increases approximately in proportion to the intermediate meridional velocity (with end point O′) along flow section I. While this criterion, derived from equation (3-1) and figure 3-1 (of ch. 3), does not apply exactly to the conformal map (fig. 4-27), it does constitute a reasonable approximation and thus confirms the vane section I shown in solid lines in figure 4-27. In the next section 4.4.3, an attempt is made to improve the halfway approximation used here for the meridional inlet velocity along flow section I.

The difference between the uniform meridional inflow velocity and the potential meridional velocity distribution $V_{m,o}$ is shown in figure 4-23 to be practically zero at the central flow surface II, so that no halfway velocity approximation is required. However, along the inner stream surface III, a design compromise similar to that along the outer surface I is required, with point H′ (fig. 4-23) used as the end point for the local meridional velocity. The difference between this compromise velocity and the uniform velocity $V_{m,i}$, of course, runs along stream surface III in the opposite direction from that along stream surface I, so that the dashed, potential velocity vector $V_{m,i}$ along surface III (in figs. 4-23 and 4-27) is flatter than the solid velocity vector corresponding to $V_{m,i}$ = constant. Figure 4-27 shows only one vane section for stream surface III, designed for inflow about halfway between the solid and the dashed velocity vectors $w_{i,III}$.

The three vane sections I, II, and III shown in the conformal map (fig. 4-27) establish the vane shape along the three surfaces of revolution I, II, and III shown in figure 4-23. It remains to transform the information contained in the conformal map back into the physical layout of the rotor vanes and to fill in the three-dimensional vane shape between the stream surfaces I, II, and III. Both objectives can be accomplished by constructing out of the conformal representations a sufficient number of plane, radial and axial sections through the vanes to define their shape.

Radial and axial sections are represented in the plane of conformal representation (fig. 4-27) by the vertical lines a, b, c, etc. The points of intersection between these lines and the conformal vane contours, when transferred into the rotor profile in figure 4-23, determine three points of a radial (and axial) section through each side (or surface) of the vane. By judiciously drawing smooth fairing curves through every set of three points, one fills in the vane surface between the three stream surfaces I, II, and III. The fairing curves can be drawn in such a manner as to achieve a favorable angle between the blade and shroud surfaces, which is an important objective when designing Francis vanes for turbomachinery rotors (see figs. 4-15 to 4-17).

Figure 4-28 shows the radial fairing sections through the vane so derived from figure 4-27. Also shown are the curves of meridional distances between successive radial sections previously introduced in connection with figure 4-18. Plotted along the projections of the centers of each meridional vane surface step are solid curves which represent the meridional distances between the upper or leading vane surfaces and dotted curves which represent those between the lower vane surfaces. Only along the outer shroud section I has a minor adjustment been made, primarily in section d. The change is so small that it could have been ignored for practical purposes. This accuracy indicates that the process of conformal mapping, if carried out carefully, is a practically useful method of Francis vane design.

The radial sections shown in figure 4-28 may be used directly for the manufacturing of rotor blades. However, other sections may be more appropriate for specific manufacturing methods. Sections 1, 2, 3, etc., normal to the axis of rotation, are required for production of a so-called core box in wood and are, therefore, termed "board sections" (see figs. 4-28 and 4-29). The pressure or leading side of the

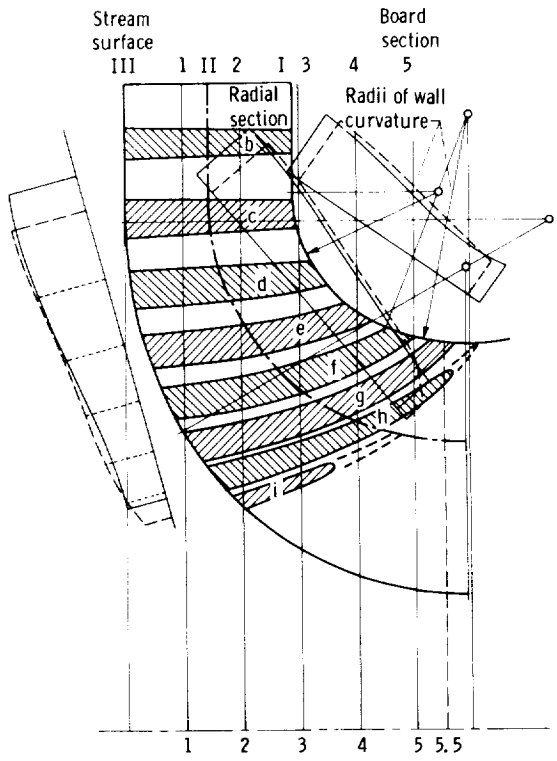

Figure 4-28. – Radial sections through Francis rotor.

vanes is shown by dashed lines in figure 4-29. The identification of the board sections by numbers 1, 2, 3, etc. should not be confused with the same numbering of the coaxial circles on the stream surfaces of revolution used in figures 4-23 and 4-27. For reasons of clarity, a fairly small number of board sections is used in this presentation. A somewhat larger number of board sections is usually required.

The design method described in this section has been used successfully since the second half of the 1930's. Figures 4-30 to 4-32 show one of the best impellers developed toward the end of that period. In connection with a twin-volute casing of the type shown in figure 4-54 (section 4.5.2), this impeller led to overall pump efficiencies between 90 and 92 percent (depending on the quality of the surface finish) with an impeller diameter of about 12.5 inches. Also the cavitation performance was highly satisfactory. However, other considerations such as those presented in section 4.4.4 are necessary to give this method of design the required level of dependability.

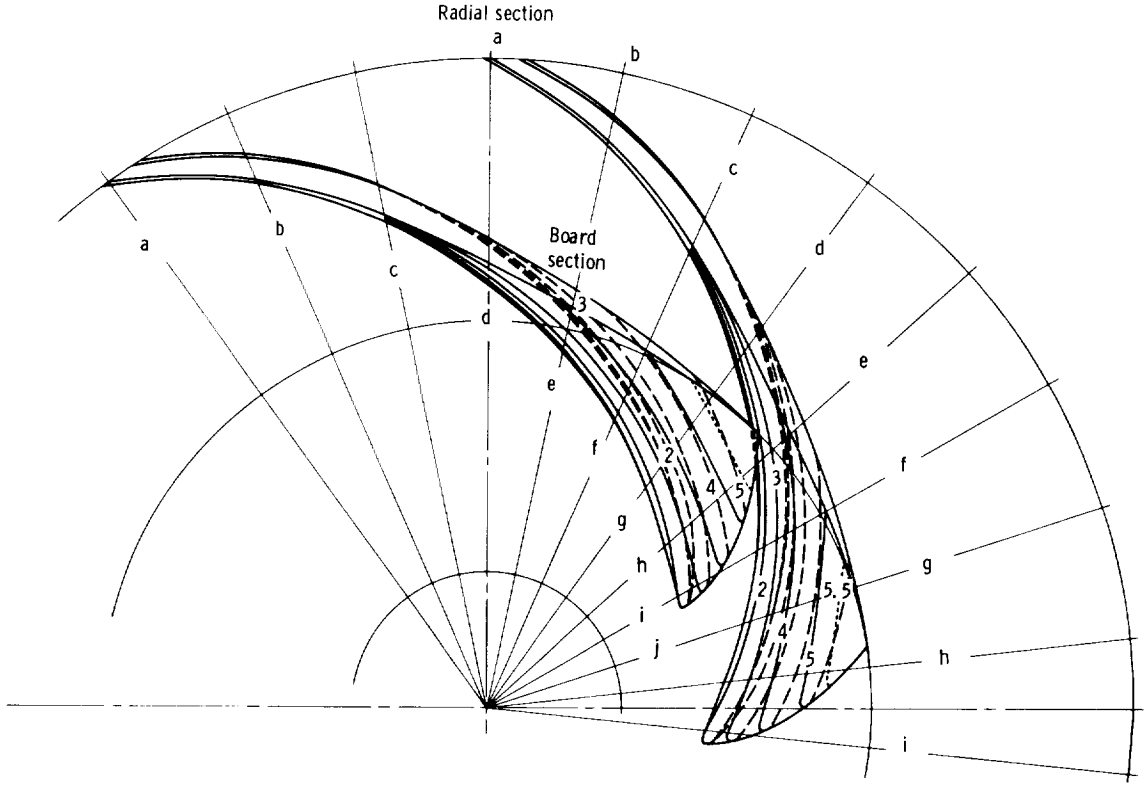

Figure 4-29. – Vane layout with board sections of Francis pump rotor.

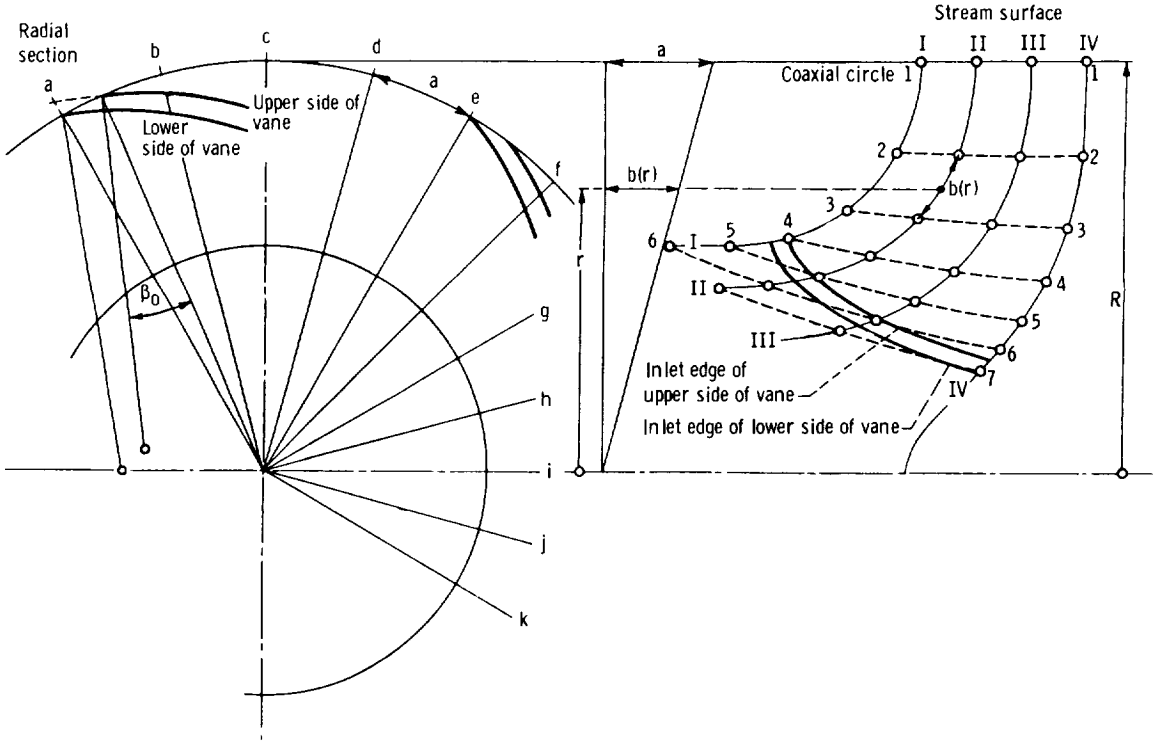

Figure 4-30. – Views of Francis impeller designed and tested in late thirties showing coaxial circles and radial sections for conformal mapping.

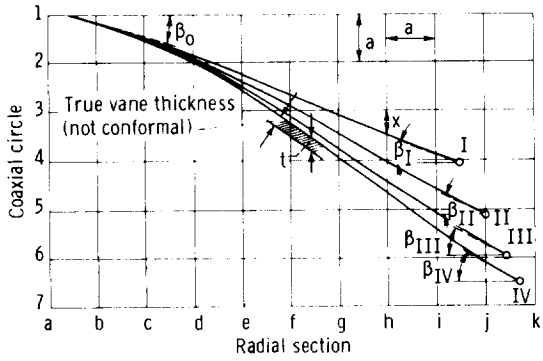

Figure 4-31. – Conformal vane layout of Francis impeller designed and tested in late thirties.

4.4.3 Approximation of Effect of Vane Vorticity on Meridional Flow

The principles of the effect of bound vane vorticity on the meridional flow are outlined in section 2.7.6. In the example treated there, this effect of vane vorticity is unfavorable insofar as the meridional velocity distribution across the flow space of revolution is, under the influence of vane vorticity, less uniform than its distribution for irrotational meridional flow. However, it is pointed out at the end of section 2.7.6 that, for vanes whose shape is not dictated by centrifugal stress considerations, it may well be possible to achieve a favorable effect of the vanes on the meridional velocity distribution. Specifically one can shape the vanes in such a manner that they aid in deflecting the meridional flow from the axial toward the radially outward direction. This is accomplished by taking radial sections through the vane shapes as shown in figure 4-28, with the upper (outer) sides of the vane sections b to h considered to be the leading and, therefore, the high-pressure sides of backward-bent vanes such as shown in figure 4-29. It is evident that, without vane action and without rotation of the fluid about the axis of symmetry, the outer boundary I of the meridional flow passage shown in figures 4-23 and 4-28 would be the low-pressure, high-velocity side of the meridional flow. With the high-pressure sides of the vanes facing this low-pressure side of the meridional flow passage (fig. 4-28), the vane action tends to reduce the pressure and velocity differences across the meridional stream. These differences are ordinarily associated with the deflection of a flow,

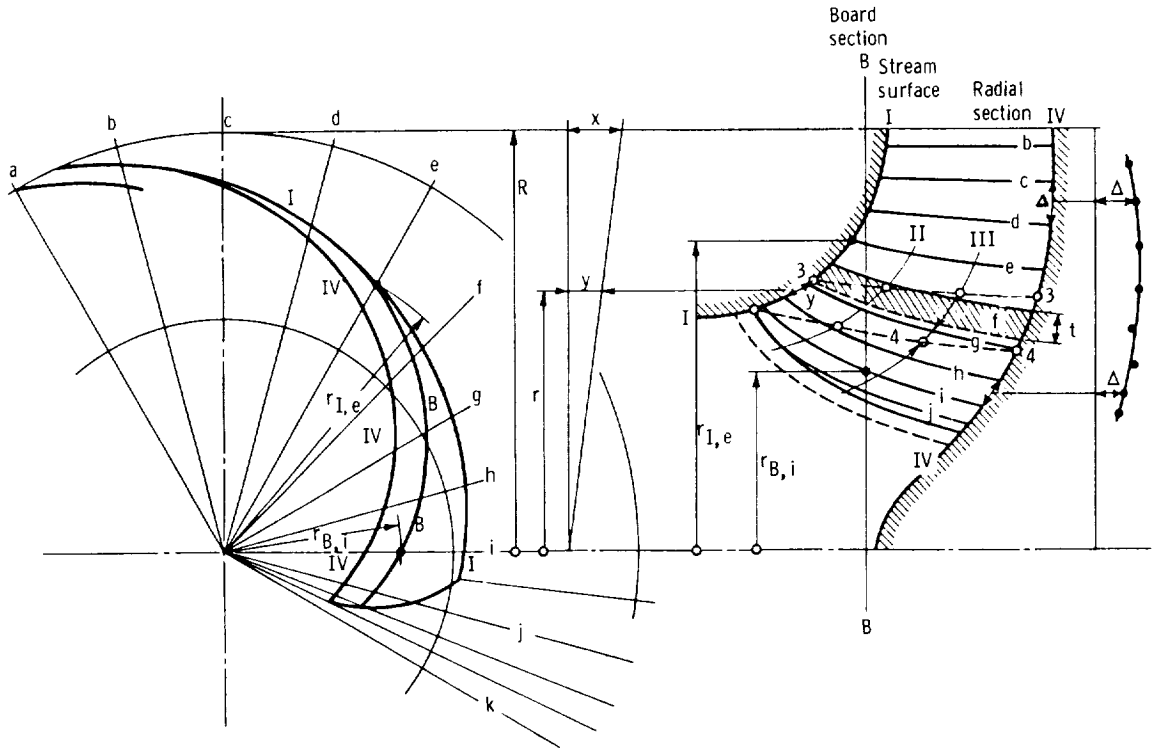

Figure 4-32. – Layout of Francis impeller designed and tested in late thirties showing contour and one board section (left) and radial sections (right).

in this case the deflection from the axial to the radial direction. A reduction in these cross-stream pressure and velocity differences is an advantage in accomplishing a certain deflection of the flow, which is, therefore, aided by action of vanes of this shape (fig. 4-28). This aid by the vanes does not exist with vanes having radial blade elements, such as shown in figure 4-20, where radial sections through the vanes are straight and normal to the axis of rotation and, therefore, have no force action toward the outer boundary of the meridional flow passage.

The empirical assumption of a uniform meridional velocity across the meridional flow, used in section 4.4.2, indeed implies that the vanes are assumed to have such a favorable effect. To derive the vane action on the meridional flow in detail would be quite complicated and would exceed the general scope of the present treatment. However, it is in order to seek a general indication of whether the vane shape derived under the assumption of uniform meridional flow tends to justify this assumption. An attempt to find such an indication is now made by analyzing the bound vane vortex lines used in section 2.7.6.

As in section 2.7.6, the vane vortex lines are determined by the lines or surfaces of constant rotor head. These lines or surfaces are determined under the one-dimensional assumption that the relative flow in the rotor passages is parallel to the centerlines of the vanes.

Figure 4-33 shows the relative velocity diagrams derived under this assumption for the stations (coaxial circles) 1, 2, 3, etc. along the stream surfaces I, II, and III. The meridional velocities V_m are derived by the one-dimensional condition of continuity from the cross section $2\pi rb$ of the space of revolution (figs. 4-23 and 4-25) and from the vane blockage (fig. 4-27) and are plotted in figure 4-34. Drawing the one-dimensional relative velocity vectors w^* parallel to the vane centerline at the stations (1, 2, 3, etc.) concerned, one obtains the local absolute velocity component V_U^*. Its product with the local peripheral velocity V_U^*U is proportional to the local head increase over the inlet head, with the approximation that the head coefficient $V_U/V_U^* = C_H$ is constant over a local region of the meridional flow. The product V_U^*U is plotted in figure 4-34 against the meridional extent of the flow, stations 1, 2, 3, etc. Horizontal lines through this plot locate points of constant head $V_U^*U = g_o H_r^*$ as a function of the meridional extent 1, 2, 3, etc. of the flow along each of the meridional stream surfaces.

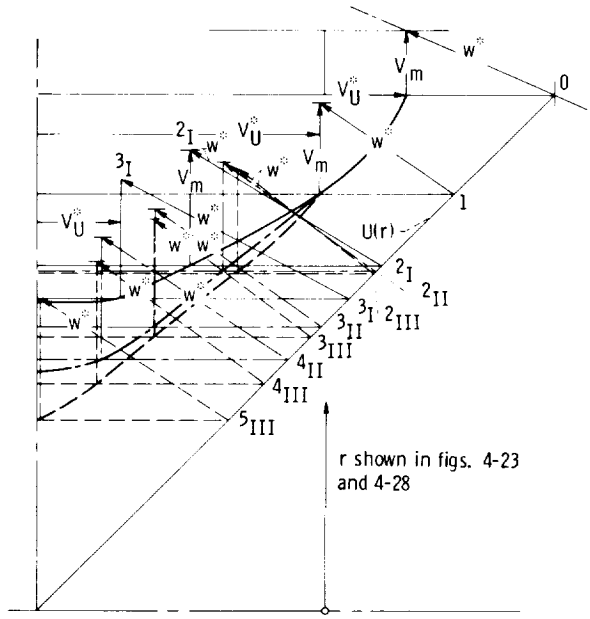

Figure 4-33. – One-dimensional relative velocity diagrams in Francis pump rotor.

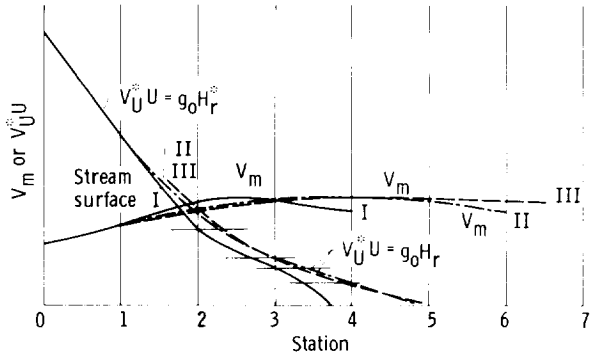

Figure 4-34. – Meridional velocity and one-dimensional rotor-head distribution in Francis pump rotor.

The corresponding lines of constant head are plotted first in the conformal map, figure 4-27. The line closest to the leading edge BB is marked CDE and is transferred to figures 4-24 and 4-35. In both figures, a dash-dot line FGH is drawn halfway between the leading edge and the first constant-head line (CDE). The line FGH may be considered the first bound vortex line of the vane, and its inclination against the radial direction λ may be considered to determine the circumferential vorticity component ζ_U, that is, the vorticity of the meridional flow. (See the development of the conical section IGF in fig. 4-35. This section agrees with the

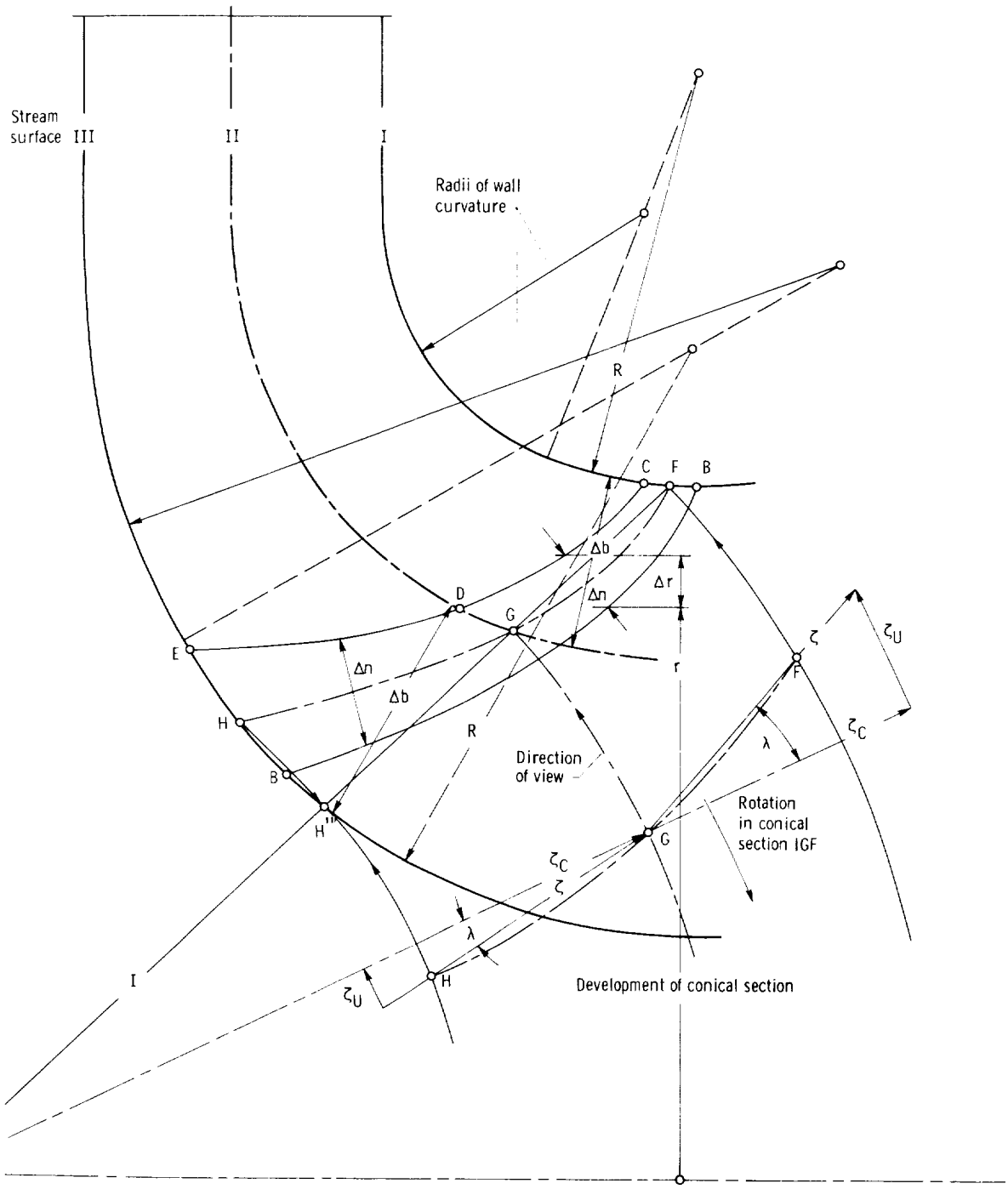

Figure 4-35. – Bound vortex line near leading edge.

vortex line mainly in its outer part FG, because this part is of greatest importance.)

Here it is necessary to identify the direction of the meridional velocity $V_{m,\zeta}$ induced by the vorticity ζ of the bound vane vortex line HGF.

The impeller end view shown in figure 4-24 indicates that the direction of the angular momentum generated is clockwise; that is, in figures 4-23 and 4-35, the peripheral fluid velocity V_U as well as its increase ΔV_U from the leading edge toward line

CDE point away from the observer. This orientation determines the direction of the vorticity vectors ζ_C, ζ, and ζ_U shown in figure 4-35 by the rule used herein that the vorticity direction is counterclockwise when looking in the direction of the vorticity vector. Specifically the direction of ζ_U can be derived directly from the geometric fact that the outer end F of the bound vortex line HGF trails circumferentially behind its inner end H, as shown at the lower right in figure 4-24.

Since the development of the conical section IGF is viewed in figure 4-35 from the suction side, or inside, it follows that the vorticity vector ζ_U of the meridional flow points in the radial (and axial) sections through the impeller shown in figures 4-23 and 4-35 toward the observer; that is, the vorticity of the meridional flow (expressed by ζ_U) is in the clockwise direction. This means that the velocity $V_{m,\zeta}$ induced by ζ_U at the outer shroud (diameter D_i in fig. 4-23) is directed counter to the incoming flow with the velocity $V_{m,i,o}$ and at the hub (diameter D_h) in the direction of the incoming flow.

As outlined in chapter 11 of reference 14, it is desirable to divide the meridional flow into two parts: an irrotational part $V_{m,o}$ and another part having the vorticity ζ_U. Evidently

$$\zeta_U = \zeta_c \tan \lambda \tag{4-44}$$

where ζ_c is the vane vorticity component in a meridional plane (see figs. 2-70 and 4-35). Designating the velocity representing the vorticity ζ_U by $V_{m,\zeta}$ obviously satisfies the equation

$$\frac{V_{m,\zeta}}{R} + \frac{\partial V_{m,\zeta}}{\partial b} = \zeta_U \tag{4-45}$$

where R is the radius of curvature of the meridional streamlines, and b is the coordinate across and normal to the meridional flow as used in section 2.2.

According to equation (2-181), the vane vorticity component ζ_c is

$$\zeta_c = \frac{1}{r}\frac{\Delta(rV_U)}{\Delta n} = \frac{V_U}{r}\frac{\Delta r}{\Delta n} + \frac{\Delta V_U}{\Delta n} \tag{4-46}$$

where Δn is the normal distance between two vane vortex lines representing a difference in angular momentum $\Delta(rV_U)$ such as seen in a radial and axial plane (see fig. 4-35).

Using finite differences in equation (4-45) also and combining equations (4-44) to (4-46) lead to

$$\frac{V_{m,\zeta}}{R} + \frac{\Delta V_{m,\zeta}}{\Delta b} = \left(\frac{V_U}{\Delta n}\frac{\Delta r}{r} + \frac{\Delta V_U}{\Delta n}\right)\tan \lambda \tag{4-47}$$

The velocity distribution $V_{m,\zeta}$ must not have a finite flow rate over the cross section considered, since the condition of continuity should be satisfied by the irrotational velocity distribution $V_{m,o}$ and in addition must obey the equation

$$\frac{V_{m,o}}{R} + \frac{dV_{m,o}}{db} = 0 \tag{4-48}$$

The following considerations apply primarily to the $V_{m,\zeta}$ distribution between G and F in figure 4-35, as an attempt is made to approximate the $V_{m,\zeta}$ value at F ($V_{m,\zeta,F}$), although the same reasoning can also be used for the part HG of the same curve. For a simple (approximately linear) $V_{m,\zeta}$ distribution between G and F and with $\int_H^F V_{m,\zeta} r\, db = 0$, it can be assumed that $V_{m,\zeta}$ at $G(V_{m,\zeta,G})$ is quite small. Hence $|V_{m,\zeta,F} - V_{m,\zeta,G}| = |\Delta V_{m,\zeta}| > |V_{m,\zeta}|$ between G and F. Furthermore it can be seen from figures 4-23 and 4-35 that $R > \Delta b$. Hence, to obtain a first approximation, one is justified in neglecting in equation (4-47) $V_{m,\zeta}/R$ in comparison with $\Delta V_{m,\zeta}/\Delta b$.

Furthermore, for a linear increase in V_U from the leading edge BB to the constant-head line CDE, it is easy to see that on the average between the leading edge and the line CDE

$$\frac{\overline{V_U}}{\Delta n} = \frac{1}{2}\frac{\Delta V_U}{\Delta n}$$

In addition, it can be seen from figure 4-35 that $\Delta r/r$ is quite small, since $\Delta r \leqq \Delta n$. One is, therefore, justified in neglecting in equation (4-47) for the first approximation $(V_U/\Delta n)(\Delta r/r)$ in comparison with $\Delta V_U/\Delta n$. Equation (4-47) may, therefore, be reduced (by the first approximation) to

$$\frac{\Delta V_{m,\zeta}}{\Delta b} = \frac{\Delta V_U}{\Delta n}\tan \lambda$$

or

$$\Delta V_{m,\zeta} = \Delta V_U \frac{\Delta b}{\Delta n}\tan \lambda \tag{4-49}$$

In this equation $\Delta b/\Delta n$ as well as tan λ can be scaled from figure 4-35, and ΔV_U is obtained by interpolation between the values given in figure 4-33. The resulting $\Delta V_{m,\zeta}$ is plotted in figure 4-23 from the baseline A-A′, by using point L as the zero point and obtaining two straight lines SL and LM approximating the curve for the outer and inner portions separately. The smooth, solid curve KM shown tends to average these two straight lines, which are not tangents to this curve. The curve is an estimate of $V_{m,\zeta}$ as a function of the coordinate across the section B-B′.

At the upper point B, the normal section B-B′ meets the leading edges of the vanes along the outer shroud. At this point, it is justified to assume that the velocity departure from the irrotational velocity distribution ($V_{m,o}$ described by line OH in fig. 4-23) is $\Delta V_{m,\zeta}/2$, since the vane vorticity covers only half of the flow field adjacent to this point B. The same assumption is applied to other points of this velocity distribution, since all meridional velocities of section B-B′ are to be applied to the leading edges of the vanes (BB in figs. 4-23 and 4-35), for which this reasoning is correct. The resulting meridional velocity distribution in section B-B′ and approximately along the leading edge BB is shown as the dashed curve O′H′ in figure 4-23.

The new velocity distribution curve O′H′ is appreciably closer to the previously assumed uniform velocity distribution $V_{m,i}$ = constant than the potential velocity distribution OH. At the same time, it is clear from the sketch of the vane inlet region shown in figure 4-24 that the inclination of the bound vortex line HGF is largely due to the inclination of the leading edge BB against a meridional plane. Thus a favorable effect of the vanes on the meridional inlet velocity distribution depends primarily on the inclination of the leading vane edge, as shown in figures 4-24 and 4-29, with the vane edge at the inner shroud leading circumferentially relative to the vane edge at the outer shroud.

One can draw the conclusion that the meridional velocity at the inlet to a Francis rotor vane system can be made almost uniform by an inclination of the leading vane edge. This conclusion supports the previously mentioned empirical justification for using a uniform meridional velocity distribution in the design of this type of rotor. Nevertheless some recognition of departures from the uniform velocity distribution is desirable.

4.4.4 Design of Radial-Flow, Rotating Vane Systems by Mean Streamline Method

As pointed out in chapter 27 of reference 14, the mean streamline method is in principle also applicable to radial-flow vane systems. However, the problems associated with this application are not described in that reference.

It is stated in reference 14 that the equilibrium between the circumferential momentum change and the vane force, previously described in section 2.5.5 (eqs. (2-77) and (2-78)), assumes in radial-flow systems the form of the equilibrium between the moment of the vane force and the change in the moment of momentum (angular momentum) of the flow. For radial-flow vane systems, it is advantageous to express this relation in terms of the absolute rather than the relative flow. By analogy to equations (2-77) and (2-78), this reasoning leads to the expression

$$\frac{\rho\,\Delta Q}{N}\,\frac{\partial(rV_U)}{\partial r}\,dr = \Delta b_x \Delta p_x r\,dy \tag{4-50}$$

where the axial coordinate y in equations (2-77) and (2-78) has been replaced by the meridional distances, also designated by y. As previously, ΔQ is the volume flow rate between two adjacent meridional stream surfaces with the normal distance Δb_x. The subscript x is an index, designating any station 8, 7, 6, etc. along the meridional flow, as shown in figure 4-36; N is the number of vanes; and Δp is the vane pressure difference.

Since, by the condition of continuity, $\rho\,\Delta Q/N$ = constant, one may write equation (4-50) in the form

$$V_U dr + r\,dV_U = \text{constant}\ \Delta b_x \Delta p_x r\,dy \tag{4-51}$$

considering that the radius r is in this investigation the only independent variable.

As in the case of axial-flow vane systems, the integration of equation (4-51) is carried out in a limited number of finite steps, and equation (4-51) may, therefore, be written in the form

$$V_{U,x}\frac{\Delta r_x}{r_x} + \Delta V_{U,x} = \text{constant}\ \Delta b_x \Delta p_x \Delta y_x \tag{4-52}$$

where x varies through the finite steps 8 to 7 to 6 etc. to 0.

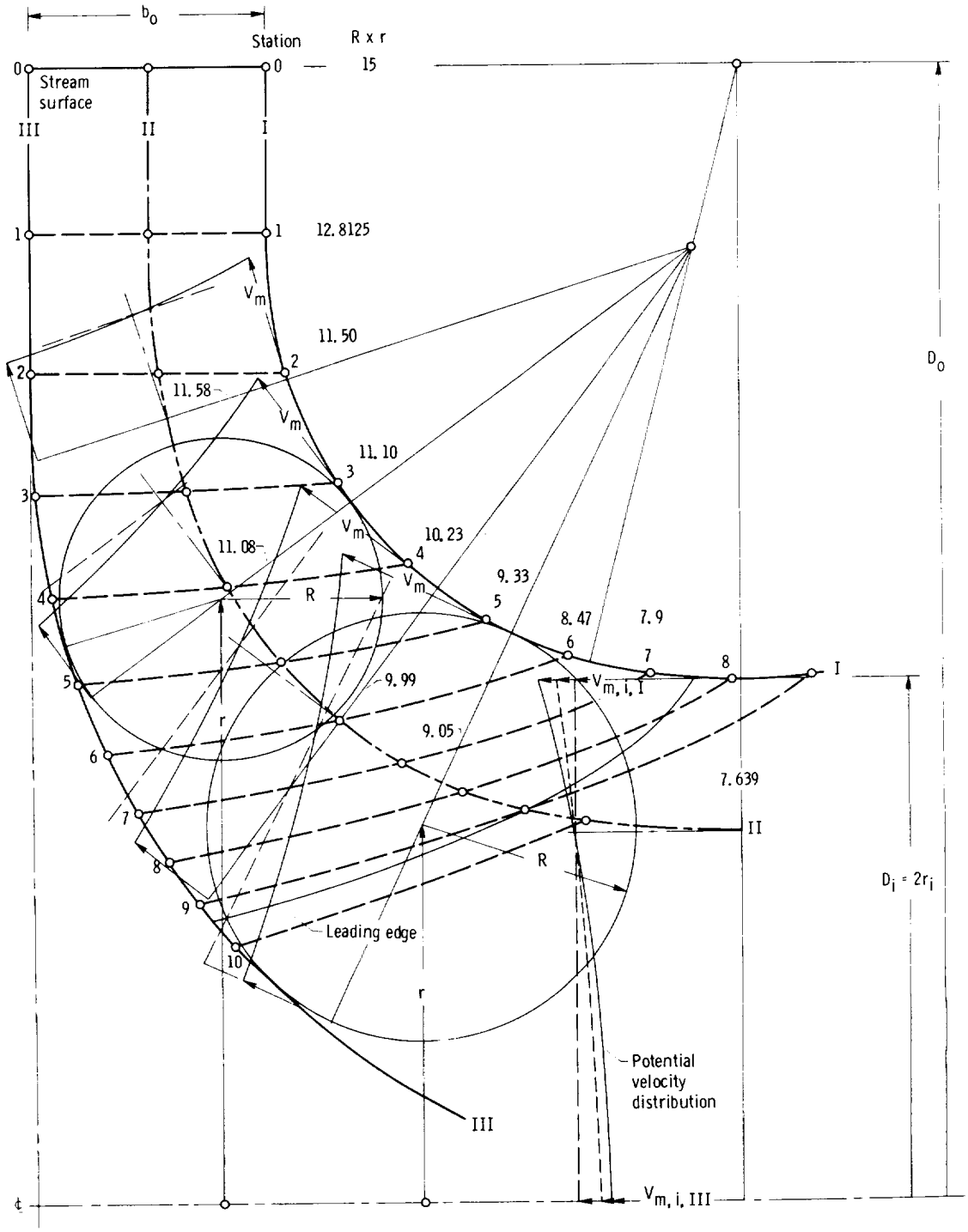

Figure 4-36. – Radial section through impeller with intersections 1, 2, 3, etc. by coaxial circles used for conformal mapping of vanes.

The solution of equation (4-52) is described in connection with a definite design example. The example chosen is a single suction pump with a basic specific speed of 0.086 (1480). The impeller is overhung, so that the shaft or hub diameter D_h at the impeller inlet is zero. The flow is assumed to enter the impeller without angular momentum. On this basis, the suction specific speed is assumed to be 0.52 (8940), which leads to a Thoma head ratio $\sigma_H = H_{sv}/H$ of slightly less than 1/10, so that this example is a convenient reference case. By extremely careful design and experimental development, such a pump can be made very nearly free from cavitation. This writer is acquainted with the design characteristics of one such pump which has 90 percent efficiency when used with a single-volute casing. This value is close to the maximum achievable efficiency of centrifugal pumps (see also fig. 1-12 of ch. 1). Some empirically confirmed design characteristics are available for this example.

The aforementioned estimate of the suction specific speed is, according to figure 1-18 and the corresponding equations, associated with a flow coefficient $V_{m,i}/U_i = 0.38$ and a blade cavitation number $\sigma_p = 0.26$ which is probably the lowest with which cavitation-free operation is achievable. The flow coefficient $V_{m,i}/U_i$ is chosen to be slightly higher than its optimum value with respect to the suction specific speed S and σ_p in order to minimize the inlet relative velocity as far as possible without reducing S substantially.

The most familiar relation between the basic specific speed and the design characteristics of the impeller is

$$n_s = \frac{nQ^{1/2}}{(gH)^{3/4}} = \frac{1}{2^{1/4}\pi^{1/2}} \left(\frac{U_o^2}{2gH}\right)^{3/4} \times \left(\frac{V_{m,i}}{U_i}\right)^{1/2} \left(\frac{D_i}{D_o}\right)^{3/2} \qquad (4\text{-}53)$$

where the subscript o refers to the outlet diameter, and the subscript i refers to the inlet diameter of the impeller (see ch. 1, sec. 1.2.1). With $n_s = 0.086$ and $V_{m,i}/U_i = 0.38$, one finds

$$\left(\frac{U_o^2}{2gH}\right)^{3/4} \left(\frac{D_i}{D_o}\right)^{3/2} = \frac{0.086 \times 2^{1/4} \times \pi^{1/2}}{0.38^{1/2}} = 0.29406 \qquad (4\text{-}54)$$

The aforementioned existing pump of the same basic specific speed with an efficiency of 90 percent has a head coefficient $2gH/U_o^2$ of approximately 1.085 with satisfactory, stable operation. This value of the head coefficient is, therefore, chosen for the pump to be designed here and, according to equation (4-54), leads to

$$\frac{D_i}{D_o} = (0.29406 \times 1.085^{3/4})^{2/3} = 0.46063$$

Furthermore the impeller discharge width b_o is empirically chosen to be slightly over one-tenth of the outlet diameter D_o (actually $b_o = 0.104\ D_o$).

The inside contours of the outer shroud and of the inner or back shroud of the impeller, resulting from the previously mentioned dimensions, are shown in figure 4-36. The numbered points marked on the shroud contours I and III, and on the central stream surface II, have the same significance with respect to the conformal representation of these surfaces as in figures 4-22 and 4-23 (explained in sec. 4.4.2). Furthermore figures 4-36 and 4-37 show without a definite scale the changes in the meridional flow cross sections between the shroud contours I and III, given by the products Rr of the circles inscribed between the shroud contours. Only two of these circles are shown.

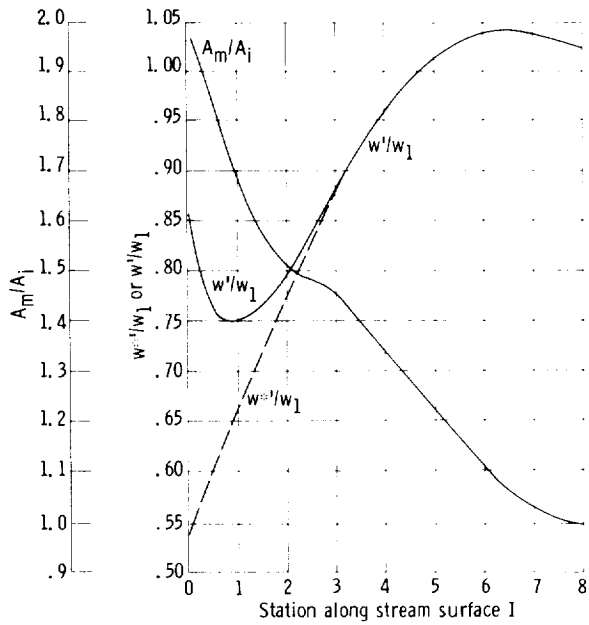

Figure 4-37. – Meridional area A_m and relative rotor fluid velocity w' with blockage correction as functions of meridional flow station along outer shroud contour I.

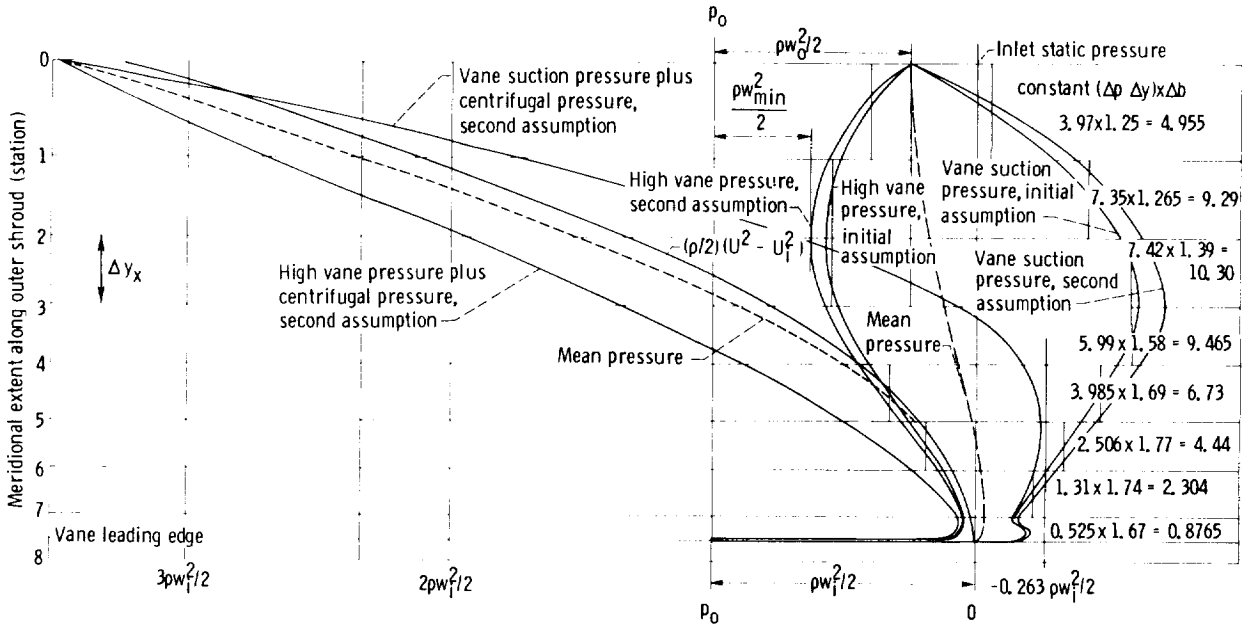

Figure 4-38. – Pump vane pressure distribution designed to meet pressure coefficient $\sigma_p = 0.263$.

The velocity distributions in the cross sections of the meridional flow are approximated according to equation (2-6) with the assumption of irrotational meridional flow ($\zeta_m = 0$). An exception is made at the inlet cross section (fig. 4-36), where the actual meridional velocity distribution (dashed line) is assumed to be about halfway between the irrotational velocity distribution and a uniform velocity distribution. This assumption is intended to approximate the influence of the swept vane inlet on the meridional velocity distribution (see sec. 4.4.3). It also considers the transition from a straight inlet duct to the curved impeller passage.

The next step constitutes the only element by which the design method outlined in this section differs fundamentally from the methods used previously. As indicated previously, this step aims to design the impeller vanes so that a prescribed or assumed pressure distribution is generated along the vanes. This pressure distribution must satisfy the requirements established by the cavitation conditions under which the pump is expected to operate. Specifically the absolute pressure drop at the vane inlet must not be greater than $\sigma_p \rho w_1^2/2$, where the cavitation parameter σ_p should in this example not be higher than 0.26, the value previously derived from the suction specific speed by means of the diagram in figure 1-18. An attempt to satisfy this requirement is shown in figure 4-38. The present considerations are restricted to the flow along the outermost shroud contour I (fig. 4-36), because the pressure reduction leading to cavitation is likely to be most severe at this stream surface, where the inlet relative velocity is the highest.

The ordinate in figure 4-38 is the meridional length or distance y along the stream surface I, and the stations from 8 to 0 are the same as those marked in figure 4-36 along this stream surface. In figure 4-38, pressures are plotted in the horizontal direction, and the line 0-0 signifies the static pressure at the leading edge of the vane. It can be seen in figure 4-36 that the leading-edge line meets the stream surface I between stations 7 and 8, and the pressure curves in figure 4-38 start at a point between the same stations.

The pressure-velocity relation which governs the pressure curves in figure 4-38 is equation (2-108) in section 2.6. The subscript 1 in that equation refers here to the station at the leading edge of the vane and can, therefore, be replaced by i. The subscript 2 refers here to any station along the flow through the vane system of the rotor and may, therefore, be omitted. With this understanding, and since we are considering here static pressures rather than head values, equation (2-108) should be written in the form

$$p_{st}-p_{st,i}=\frac{\rho}{2}(U^2-U_i^2)+\frac{\rho}{2}(w_i^2-w^2) \qquad (4\text{-}55)$$

Two pressure diagrams are shown in figure 4-38: one representing only the second part of the right side of equation 4-55 (i.e., $(\rho/2)(w_i^2-w^2)$), which gives the vane pressures without the pressure rise due to the centrifugal force field, and one representing the entire equation (4-55). The difference between these two diagrams is obviously $(\rho/2)(U^2-U_i^2)$, represented by a curve so marked.

The vane pressures representing only $\rho(w_i^2-w^2)/2$ are marked "High vane pressure" and "Vane suction pressure." According to equation 4-52, the partial vane force is approximated by the mean vane pressure difference Δp_x acting over a certain part of the vane length Δy_x, in this presentation the distance between successive stations (8 to 0) along the stream surface I, and over a certain width Δb_x normal to the stream surface. In this case, Δb_x is assumed to be proportional to the normal distance between the stream surfaces I and II.

A preliminary check of the general shape of the pressure distribution assumed shows that it does, with some margin, satisfy the cavitation requirement $\sigma_p=0.26$ after $\rho(U^2-U_i^2)/2$ is added. It also has to be established whether this pressure distribution would generate a vane lift coefficient compatible with reasonable requirements for the overall design of the impeller.

In the arbitrary scale used in the original impeller layout and in the pressure diagram in figure 4-38,

$$\Sigma_{LE}^{o}\Delta p\ \Delta y\ \Delta b=48.361$$

and the lift coefficient referred to the inlet relative velocity w_i is

$$C_{L,i}=\frac{\Sigma_{LE}^{o}\Delta p\ \Delta y\ \Delta b}{(\rho w_i^2/2)\Sigma_{LE}^{o}\Delta y\ \Delta b}=\frac{48.361}{69.4}=0.698 \qquad (4\text{-}56)$$

where the subscript LE denotes the leading edge.

The average relative velocity is $w_\infty/U_o=(w_i+w_o)/2U_o=0.46$, whereas the inlet relative velocity on the same dimensionless basis is 0.493, where w_i and w_o are taken from the velocity diagrams in figure 4-39, derived from the assumed head coefficient 1.085 and from the previously assumed dimensionless impeller dimensions. Therefore the lift coefficient referred to w_∞ is

$$C_{L,\infty}=\frac{w_i^2}{w_\infty^2}C_{L,i}=\frac{0.493^2}{0.46^2}0.698=0.80 \qquad (4\text{-}57)$$

From the inlet and discharge velocity vector diagrams at the meridional stream surface I and the length of this meridional streamline as scaled from figure 4-36, one can estimate the vane length l to be $0.89\ D_o$. From this estimate and equation (2-116) with $V_{U,1}=0$, it is easy to obtain an approximation for the number of vanes, which is between 11 and 12. This number is higher than suggested on empirical grounds and raises the question of whether the vanes could not be somewhat more highly loaded than indicated by the curve marked "Initial assumption" shown in figure 4-38.

The vane pressure distribution marked "Second assumption" (fig. 4-38) represents a nearly proportional increase of the pressure differences generated by the vanes. By this increase in vane loading, the number of vanes can be reduced to 10. Adding to the second assumption of the vane pressures the centrifugal pressure $\rho(U-U_i^2)/2$ indicates that the resulting pressure distribution including the centrifugal pressure has a minimum still slightly above the critical pressure ($0.26\ \rho w_i^2/2$), and thus the cavitation requirements are met, although perhaps with not quite the margin of safety that might be desired to compensate for the inaccuracies necessarily associated with the approximate design process presented here.

With the second assumption of the vane pressure distribution accepted, it remains to show the effect of this pressure distribution on the change in angular momentum generated by the vanes.

Since the flow is assumed to enter the impeller without any angular momentum, Euler's turbomachinery equation appears here in the form

$$\frac{\rho\ \Delta Q}{N}rV_U=\Sigma_{r,i}^{r}(\Delta p\ \Delta y\ \Delta b\ r) \qquad (4\text{-}58)$$

In comparison with the discharge moment of momentum previously derived from the assumed rotor head coefficient $\psi_r=2gH_r/U_o^2=1.085/\eta_h$, equation (4-58), which applies to any distance r from the axis of rotation, can be made dimensionless as follows:

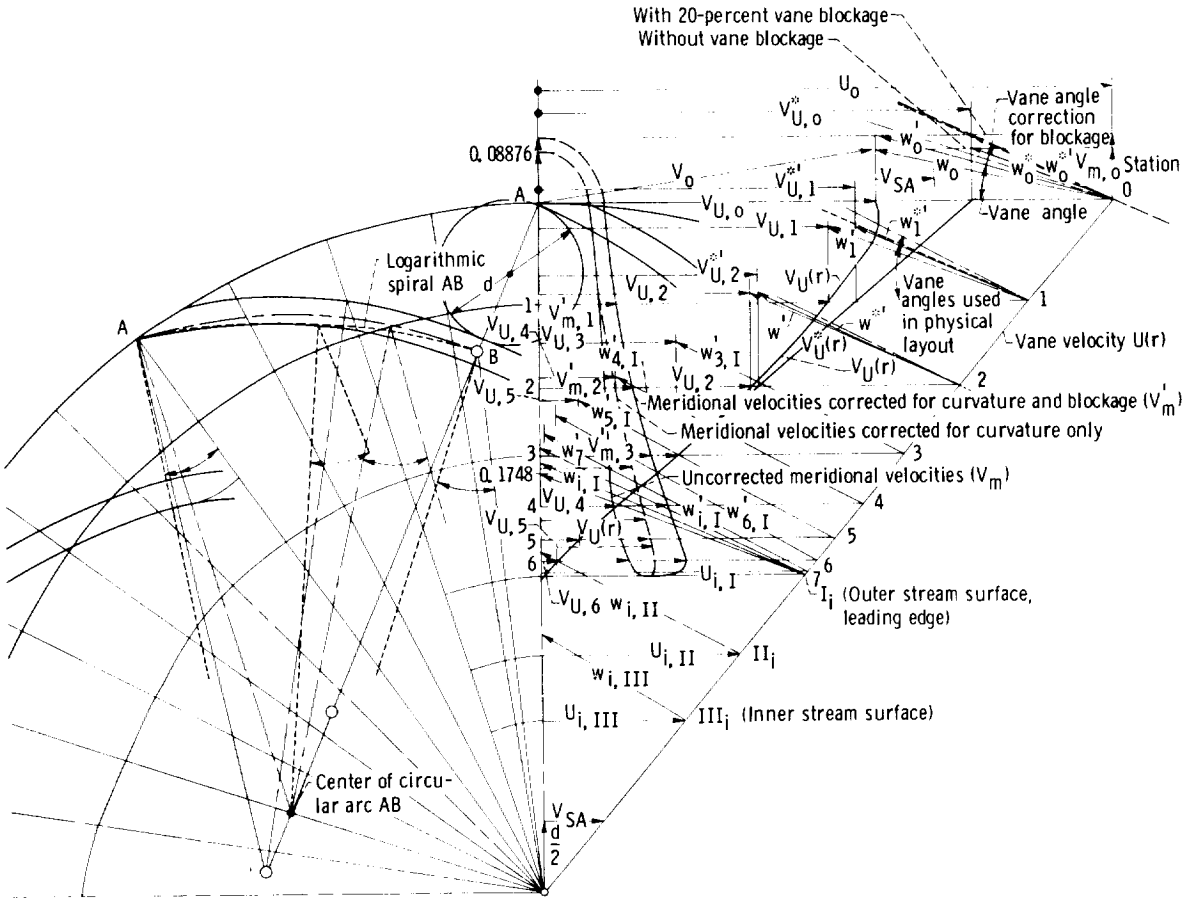

Figure 4-39. – Vane end layout and velocity distribution through impeller.

$$\frac{rV_U}{r_o V_{U,o}} = \frac{\Sigma_{r_i}^{r}(\Delta p\ \Delta y\ \Delta b\ r)}{\Sigma_{r_i}^{r_o}(\Delta p\ \Delta y\ \Delta b\ r)} \qquad (4\text{-}59)$$

From equation (4-59), it is easy to plot V_U as a function of the distance r from the axis of rotation. This has been done in figure 4-39, by using $V_{U,o} = 0.59\ U_o$, from $\psi_r = 1.085/\eta_h$, and $\eta_h = 0.92$.

In the same figure is shown the meridional velocity V_m, first, as derived by the condition of continuity from the meridional cross sections in the form Rr in figure 4-36, second, as corrected for the curvature of the meridional flow on the basis of equation (2-6) (irrotational flow ($\zeta_m = 0$) except for the inlet section), and, third, as corrected for curvature and also for blockage by the vanes and the boundary layers. This method of presentation permits plotting the velocity vector diagrams along stream surface I as a function of the distance r from the axis of rotation, as done in figure 4-33. In other words, the angles of the relative velocities in the impeller are now known as a function of the distance from the axis of rotation and, thereby, as a function of the stations (LE to 0) along the meridional stream surface I.

The angles of the relative flow, corrected for curvature and blockage, are assumed to be essentially the same as the vane angles from the impeller inlet to station 3. From there on, the fictitious peripheral velocity component V_U^*, which determines the (equally fictitious) relative velocity w^* defined to be parallel to the vanes, departs from the actual V_U values along an approximately straight line as a function of r, as shown in figure 4-39. This straight line is drawn so as to end at the outer periphery of the impeller at $V_{U,o}^*$, derived from the desired $V_{U,o}$ value by the theoretical and empirical relations given in sections 2.6.3.4 to 2.6.3.6. This process establishes the vane shape as a function of the pressure distribution along the vane for stream surface I.

The same process could be carried out for stream surfaces II and III. However, since the pressure distribution along these stream surfaces is with respect to cavitation not as important as for stream surface I, this writer feels that the vane angles along the additional stream surfaces II and III should rather be determined by geometric considerations, as outlined in the following part of this section.

At the left side in figure 4-39 is shown a design of the discharge ends of the vanes which was used successfully by this writer during the lively development period in the thirties. The principal idea of this design is to end the rotor vane passage at the discharge without divergence. The geometric method of accomplishing this objective is shown diagrammatically in figure 4-9, which applies primarily to the low-pressure side of the vane. The comparison between this vane shape and that derived from the vane pressure distribution is discussed briefly at the end of this section.

By the nature of conformal mapping, it is evident that the vane angles given in figure 4-39 determine directly the shape of the vane centerline along section I in the conformal representation shown in figure 4-40. The vane angle (measured from the circumferential direction) increases near the inlet to compensate for the vane blockage and then decreases very slowly. It does not show strongly the previously mentioned characteristic of being a maximum along the central portion of the vane and diminishing toward both vane ends (for comparison see fig. 4-27).

If the physical vane thickness were approximately constant along the vane (except at the vane ends) the thickness appearing in the conformal map would increase toward the inlet in inverse proportion to the distance from the centerline of the impeller. This is true for impellers with small or moderate dimensions, where the physical vane thickness is determined by foundry considerations and is essentially constant. In the case of a rather large impeller or advanced manufacturing techniques, the physical vane thickness can be permitted to decrease toward the inlet, so that the thicknesses appearing in the conformal map increase only slightly toward the inlet and decrease only very near the leading edge.

As mentioned previously, this writer suggests selecting the vane shapes along stream surfaces II and III from geometric considerations rather than according to a prescribed pressure distribution. The

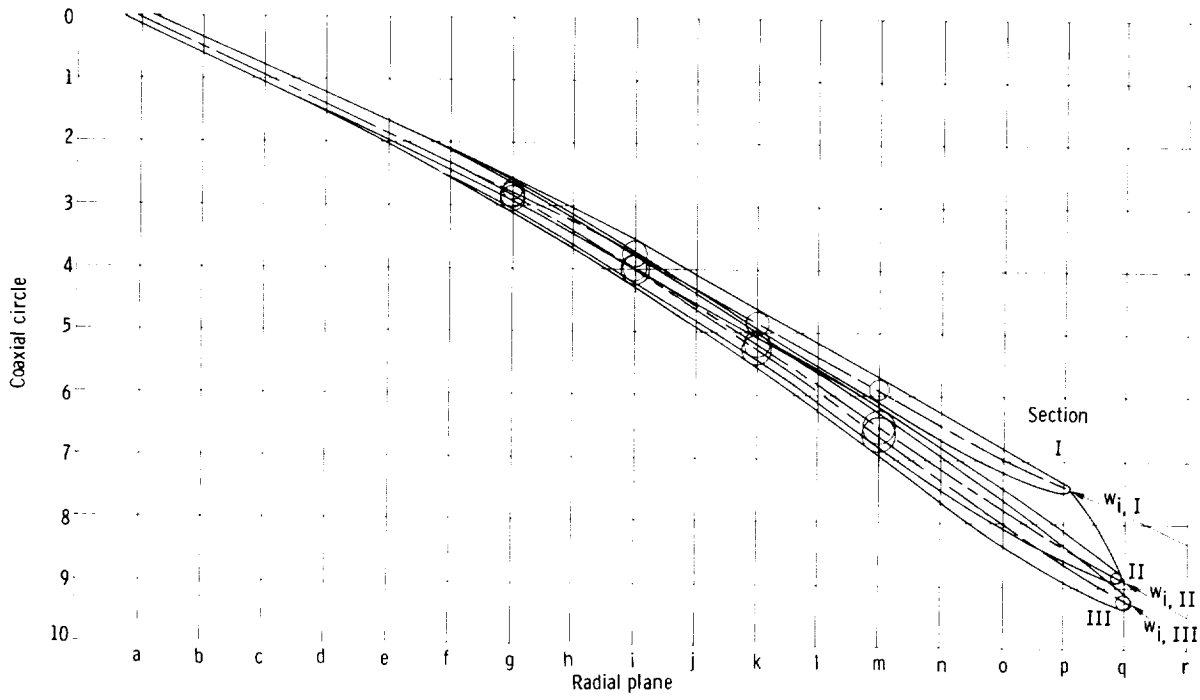

Figure 4-40. – Conformal map.

principal geometric consideration is the shape of the radial vane sections (see figs. 4-18 and 4-28), determined by the requirement that the vanes must meet the side shroud under a reasonable angle. The locations of the leading edges of the vanes in the conformal map are given by the place where the leading edge meets the meridional stream surfaces II and III (fig. 4-36), and the direction of the vane at this point is determined in the conformal map by the direction of the relative velocities at the inlet (w_i in fig. 4-39). The discharge end of the vane has in the present case the same shape in all three stream surfaces, because near the discharge the vane has an axially cylindrical shape. In order to obtain satisfactory shapes for the radial vane sections, one must draw the conformal representations of vane sections II and III closer to each other than those of sections I and II. With these restrictions in mind, it is not too difficult to draw the conformal representations of vane sections II and III as shown in figure 4-40. The vane thickness appearing in the conformal map can be derived from those of section I by the law of conformal mapping (eqs. (4-30) and (4-31)), so that the physical thickness is approximatey constant along each radial section. Thus the vane blockage along stream surfaces II and III is larger than along stream surface I, a difference which should not be too serious since the inner parts of the vane passages, where this increased blockage exists, have basically lower relative velocities than prevailing along stream surface I.

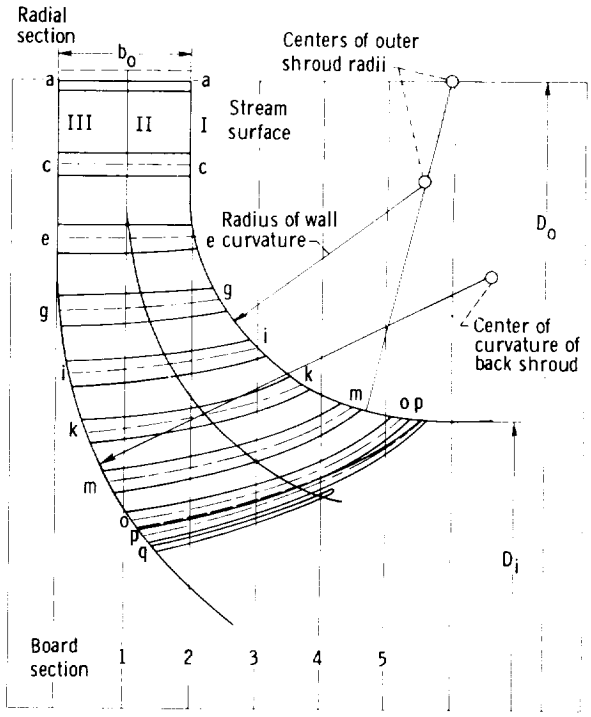

Figure 4-41. – Radial vane sections.

From this stage of design on, the design process is essentially the same as described in section 4.4.2. The resulting radial vane sections are shown in figure 4-41. For clarity, in this illustration only every second radial section, a, c, e, etc., is shown except in the immediate vicinity of the leading edge, where all radial sections, o, p, and q, are shown in order to define this vane end adequately.

For most manufacturing processes, it is necessary to develop also an end view of the vane, such as shown in figure 4-42. Here again the number of board sections, 1, 2, 3, 4, and 5, is not sufficient, but at the scale of this drawing it is impossible to show a practically adequate number of board sections without making the figure unreadable. It should be mentioned that deriving the curved lines in figure 4-42 accurately from the radial sections in figure 4-41 would require a larger number of radial sections than shown in figure 4-41.

The end view (fig. 4-42) permits making a comparison between the vane shape derived from the assumed vane pressure distribution (fig. 4-38) and an older design for the discharge end of the vane shown in figures 4-39 and 4-9. For this purpose, the logarithmic spiral, curve AB, shown as a dotted curve in figure 4-39, is also drawn in figure 4-42, where it is very close to the centerline of the vane derived from the pressure distribution. Yet the actual vane shape shown in figure 4-39 differs significantly from that indicated by the dotted logarithmic spiral. No conclusion can as yet be drawn from this comparison.

Some attention must be paid to the maximum vane pressure near station 2 in figure 4-38, appearing in the diagram to the right of the stagnation pressure p_0, which does not show the pressure rise due to the centrifugal force field. If this maximum vane pressure were to approach the inlet stagnation pressure p_0, the corresponding relative velocity w_{min} would approach zero at that part of the high-pressure side of the vanes. This situation could hardly be acceptable in view of the condition of continuity of the relative flow, which is tacitly assumed to be satisfied in the mean streamline method.

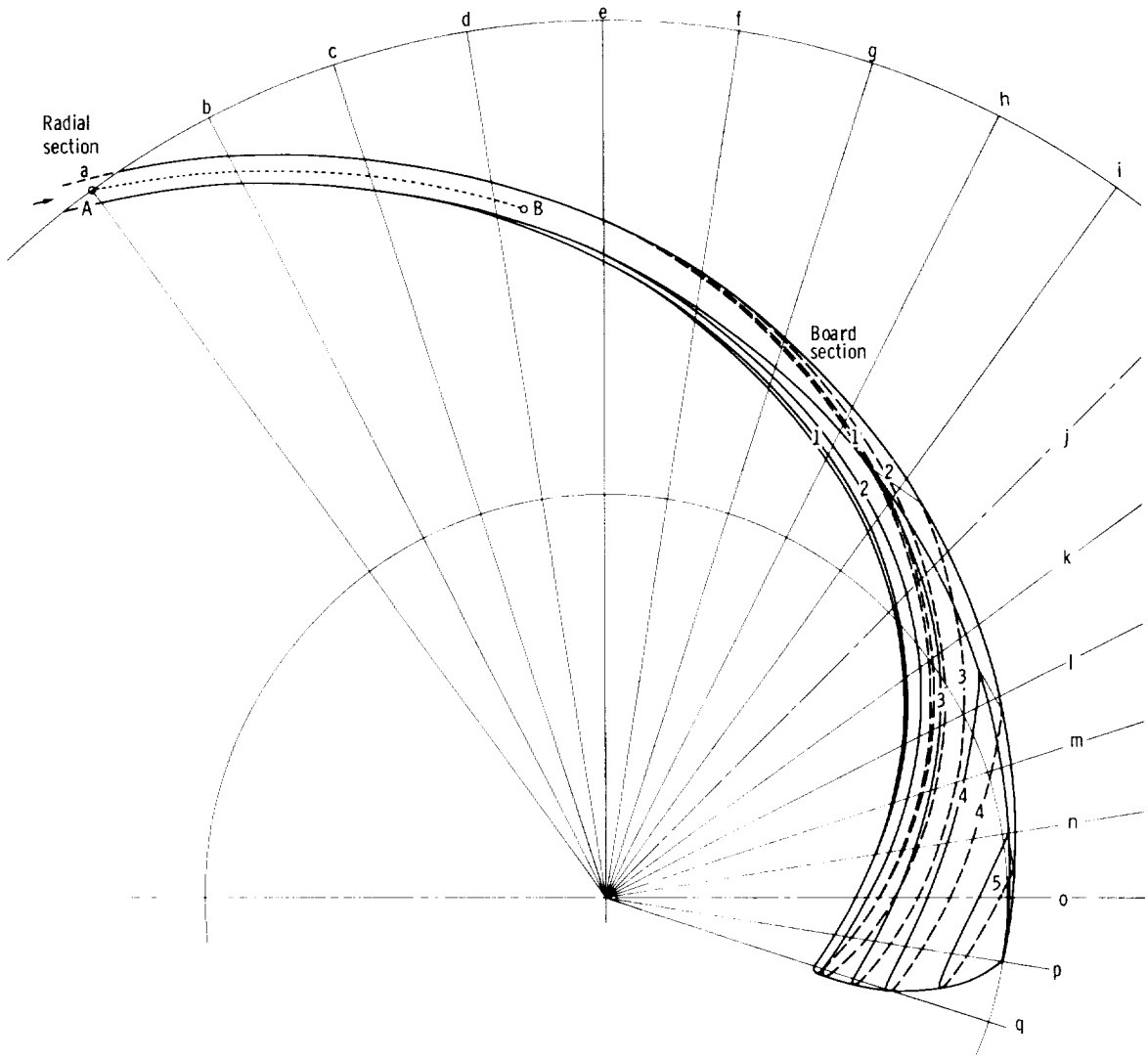

Figure 4-42. – Axial view of vane with board sections.

4.4.5 Manufacturing Considerations of Three-Dimensional Vane Design

The design forms described in the preceding section are fairly complicated, since they have been developed on the basis of hydrodynamic principles with only little or no attention to geometric or mechanical considerations. An exception is the design shown in figure 4-20, a vane shape determined by the centrifugal forces.

As soon as manufacturing principles enter into the design problem, it is desirable to consider the vane shape not only by its intersection with the meridional stream surfaces of revolution, but also by its overall geometric characteristics in space. The most obvious, and perhaps the simplest, example of such a surface in space is a straight, helical surface, shown diagrammatically in figure 4-43. It represents correctly the vane surface of an axial-flow rotor near its inlet from a body of fluid with uniform axial velocity and zero absolute rotation, so that its circumferential velocity relative to a rotating vane system is proportional to the distance from the axis of rotation (see fig. 4-44). In the moment the absolute flow acquires significant angular momentum, the flow follows the pattern depicted in figure 4-45, which involves a significant departure from that for a straight helical surface of constant pitch (angle β in fig. 4-43). The realities of turbomachinery flow, therefore, involve variations in the pitch angle which are not governed by the law of a helical curve of constant inclination against the

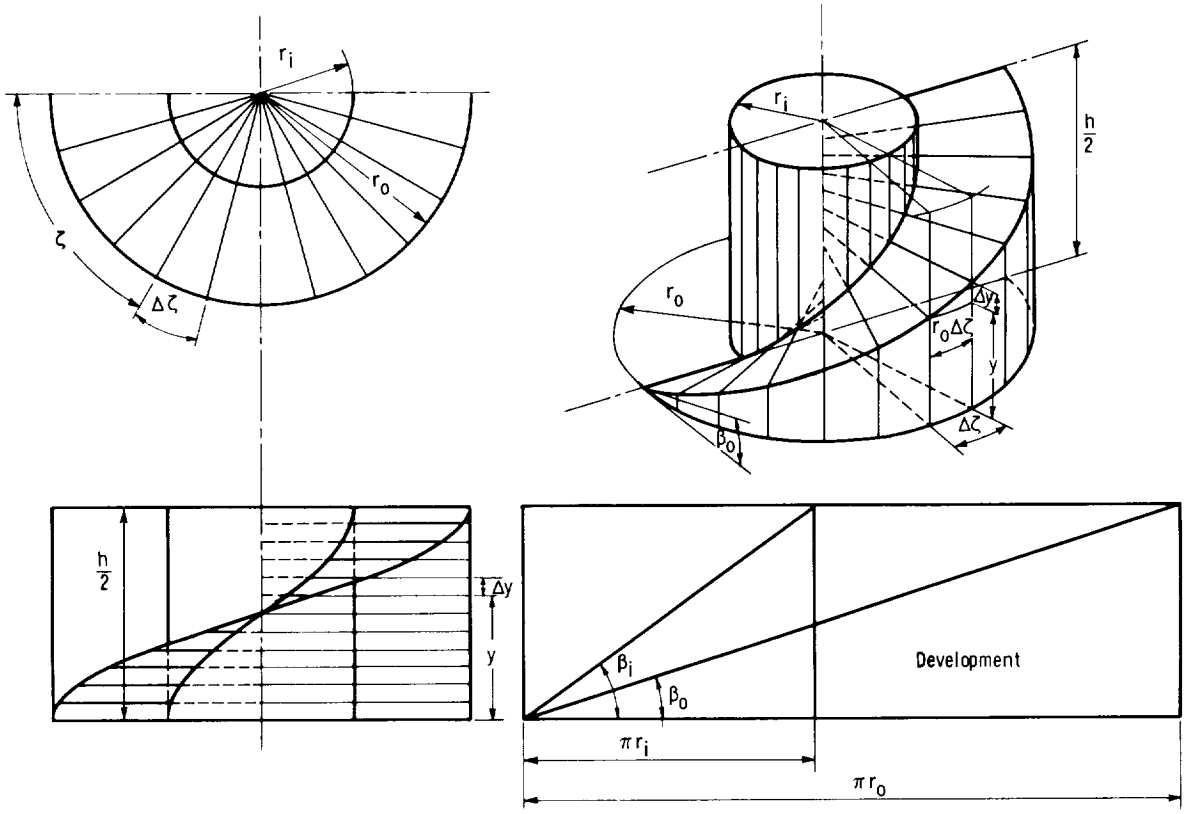

Figure 4-43. – Straight helical surface.

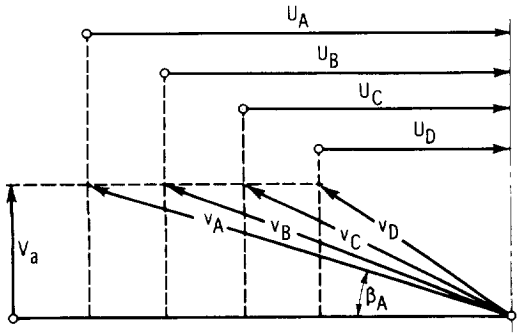

Figure 4-44. – Inlet vector velocity diagram as related to straight helical surface.

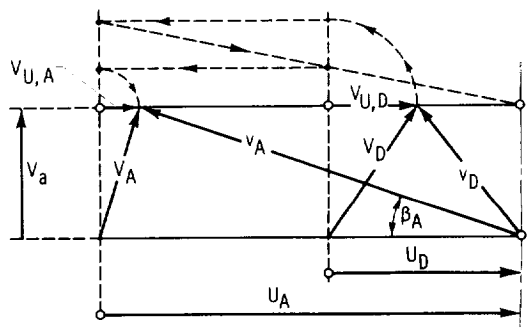

Figure 4-45. – General vector velocity diagram departing from straight helical surface.

axial direction. Actual hydrodynamic rotors demand not only variations of the pitch angle β at the same radius, but also variations of the angle γ, the inclination of the generating line against the axial direction (see fig. 4-46).

Under these conditions, it is well to consider the somewhat extreme case depicted in figure 4-47. Here the Francis rotor vane design derived in section 4.4.2 is converted to straight fairing sections, intersecting with the meridional stream surfaces I and II at the same points (or diameters) as in the previously developed radial section shown in figure 4-28. Thus the flow sections along the meriodional stream surfaces I and II are the same as assumed previously, whereas the intersection with stream surface III is different. It can be shown that this deviation is not of major hydrodynamic significance, whereas the intersection of the radial

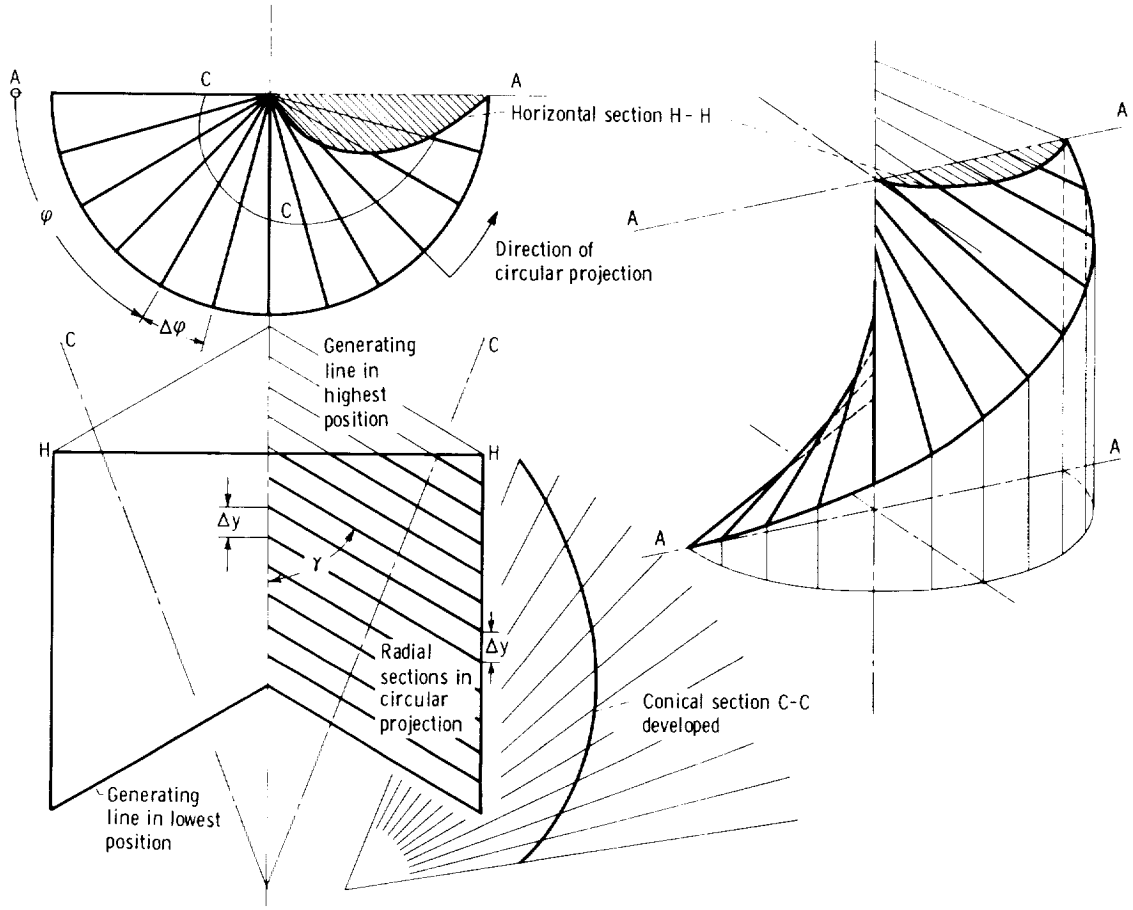

Figure 4-46. – Conical helical surface.

sections b, c, d, etc. with the outer shroud is less favorable than that in figure 4-28. The intersection of the radial sections b, c, d, etc. with the back shroud turns out to be somewhat more favorable than that in figure 4-28, but the flow conditions near the outer shroud, surface I, are less favorable and probably of greater significance because of the higher relative velocities involved there.

The vane layout shown in figure 4-47 can be interpreted as a greatly generalized helical surface, with varying pitch angle β as well as inclination γ of the generating lines against the axial direction. The resulting departures from a conical, helical surface in figure 4-46 have a somewhat complicated relation to the path of the tool needed to generate this surface (here assumed to be a slightly conical end mill). The tool diameter d_t must be sufficiently small to accommodate the minimum vane distance at the inlet of a pump rotor, and the path of the tool is related to the desired vane surface as shown in figure 4-47 (approximate development of conical section A-O). Thus the tool-path design is by no means simple, but is reasonably well defined. (The radial sections shown in fig. 4-47 are not exactly straight for a conical milling cutter with straight sides.)

Even the straight helical vane surface (i.e., a surface with a right angle between the generating line and the axis of rotation) (fig. 4-43) has important practical applications if the pitch angle β alone is varied as shown in figure 4-20. The relation between the (essentially radial) position of the tool and the vane surface is determined by considerations similar to those illustrated in figure 4-47, by section A-O. It may be of interest to mention that the generation of a vane surface such as shown in figure 4-20 has been used successfully, including the generation of the vanes of reduced length shown in that illustration.

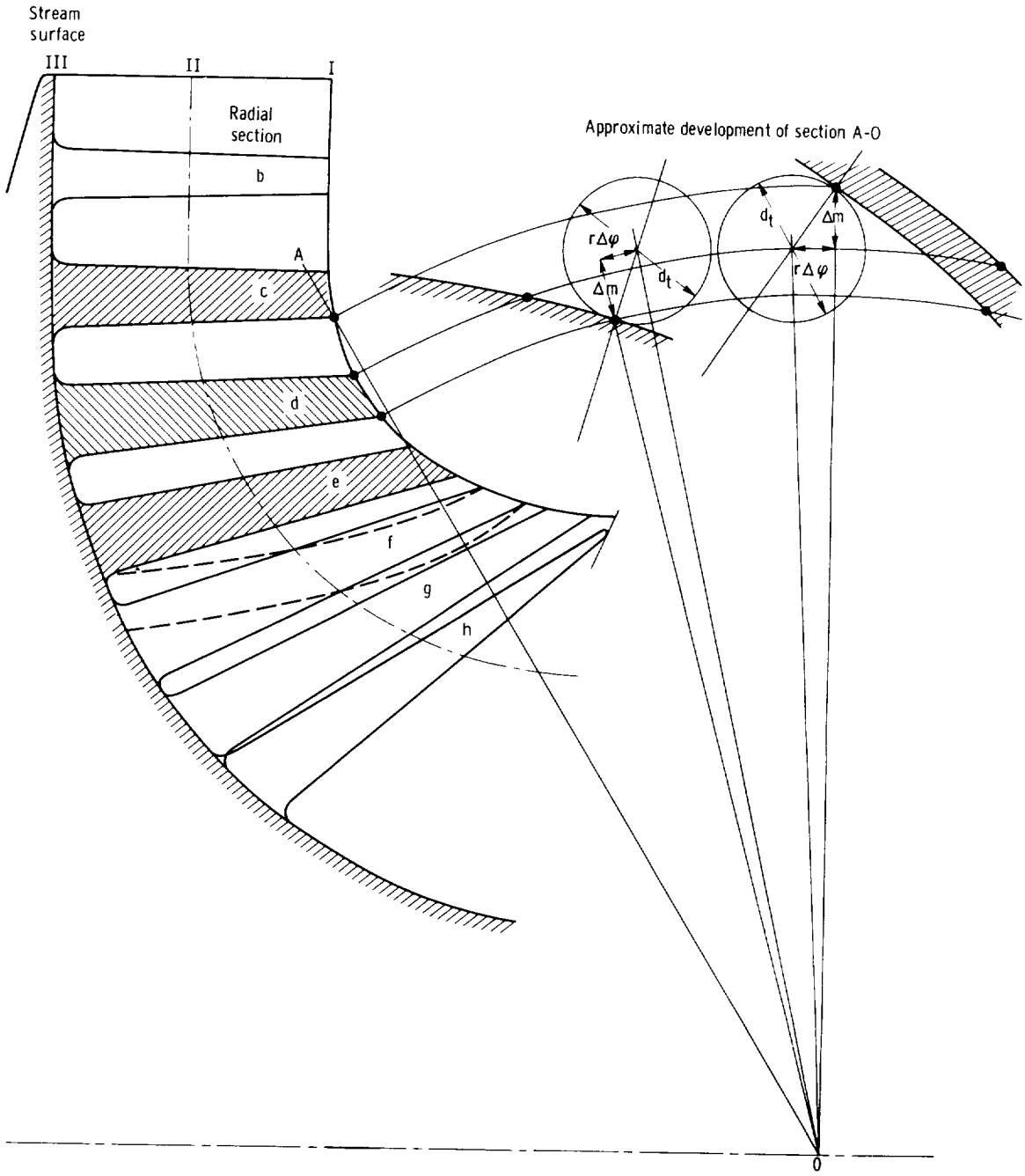

Figure 4-47. – Mechanical simplification of Francis rotor.

There is an additional modification of Francis pump impeller vanes that deserves to be mentioned, although it does not seem to have general, geometric interpretation.

During the past 10 or 20 years, it has been found in the commercial pump industry that Francis pump vanes can be withdrawn from a foundry core by a turning or rolling motion, as shown diagrammatically in figure 4-48. This withdrawal is possible if a set of parallel sections through the vane form approximately concentric circles about a common axis. Minor deviations from this law are required to provide the vane with a certain draft in the direction of rotating withdrawal from the core.

Figure 4-48 illustrates this process. One begins by selecting a direction of the parallel, equally spaced

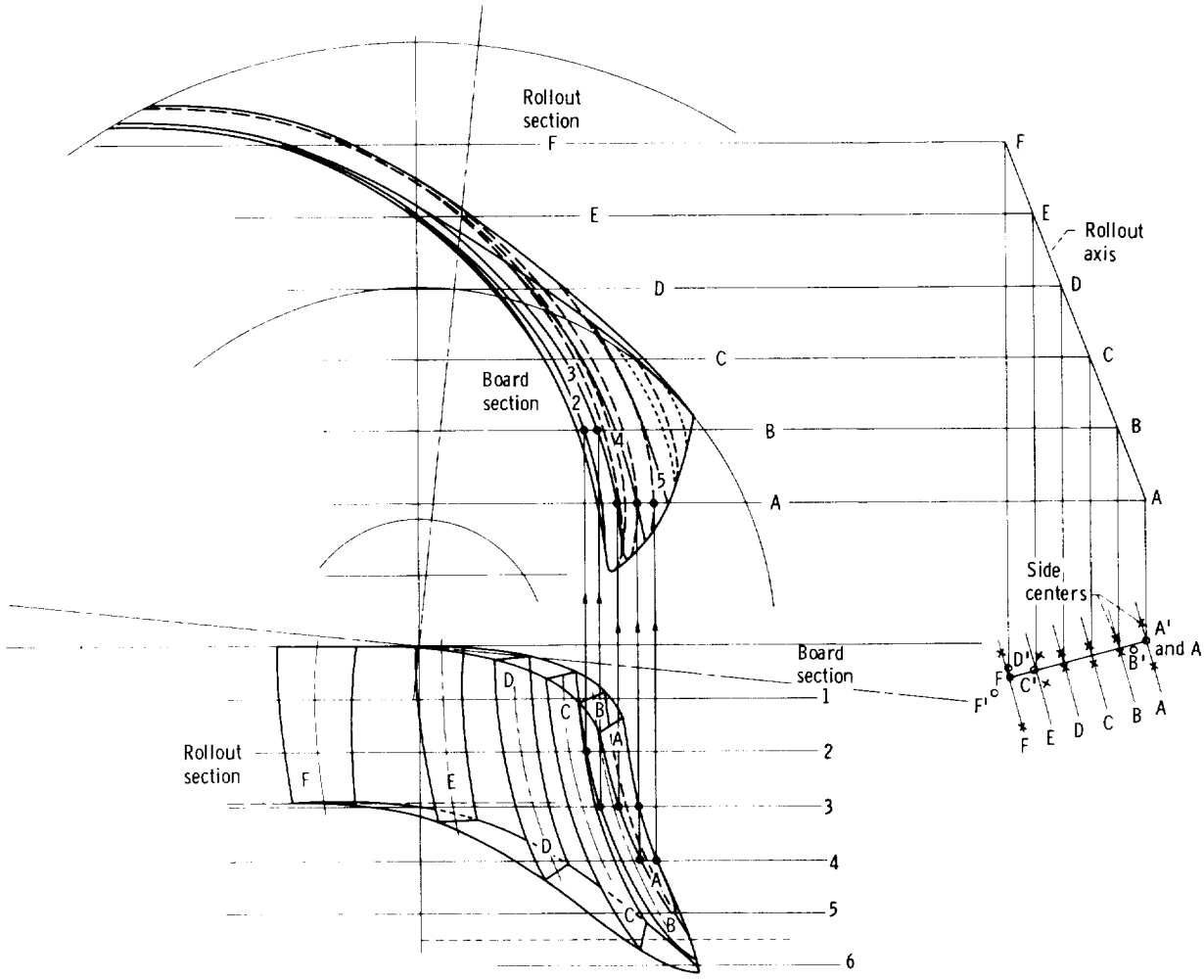

Figure 4-48. – Modification of Francis rotor vane for rollout. (Center E′ falls beyond limits of this figure.)

sections A, B, C, etc. along which the circular withdrawal lines are to be established. These sections should be approximately parallel to the cylindrical discharge vane end, to avoid major changes in that part of the vane. Then the parallel sections A, B, C, etc. are derived from an existing Francis vane layout such as that shown in figure 4-29. All points so obtained for the sections are for each section approximated by circular arcs about one center A′, B′, C′, etc., as shown in figure 4-48. (The center E′ actually falls somewhat beyond the limits of this figure.)

To permit rollout, all these points should really coincide and form an axis normal to the planes of the sections A, B, C, etc. It was in this form that the method was first introduced to this writer through Victor Potondy. This strict requirment is quite restrictive and demands considerable departure of the final vane shape from that originally derived (fig. 4-29). This writer suggests relaxing this requirement by permitting the axis of rollout to be not exactly normal to the planes of the rollout sections A, B, C, etc. With this relaxation, the rollout centers do not need to coincide exactly in the planes of sections A, B, C, etc., but must be equally spaced along a straight line so as to fall along a straight axis in space. This shift of the original centers A′, B′, C′, etc. is shown in figure 4-48, with the new centers being equally spaced along the line AF. (The new center A is assumed to coincide with the original center A′.)

With the assumed inclination of the rollout axis against the direction normal to the sections A, B, C, etc., the rollout sections are not strictly circular but

elliptic. For only slight inclinations of this axis, the departure from the circular arc rollout sections can be neglected.

The new rollout centers, equally spaced along the line A(A′)F, apply primarily to the centerlines of the rollout sections. When the sides of these sections are also approximated by circular arcs, the centers of one side must all fall on one side of the line AF, and the centers of the other side on the opposite side of the line AF (see fig. 4-48). The slightly irregular spacing of these side centers permits an improved approximation of the vane sides originally derived from figure 4-29, without violating the rules of rollout.

The rollout sections so established determine a vane shape slightly different from that originally derived, such as presented in figure 4-29. However, the agreement between figures 4-29 and 4-48 is nearly within manufacturing accuracy of sand castings.

The rollout sections may now be reconverted into a new set of board sections, also shown in figure 4-48. However, the rollout sections themselves can be used for manufacturing purposes or as templates for the vane surface formed by the newly determined board sections.

Evidently the procedure just described can be greatly improved and facilitated by modern computer techniques (called lofting). However, for completely new developments, it is advisable first to use graphical methods (such as described) in order to obtain a test impeller by which rollout and hydrodynamic characteristics can be determined experimentally before programming for automatic computation.

4.5 Hydrodynamic Design of Stationary Radial- and Mixed-Flow Vane and Duct Systems

4.5.1 Hydrodynamic Design of Stationary Radial-Flow Vane Systems

Stationary radial-flow vane systems are found either as radially inward-flow nozzle systems of hydraulic turbines, or radial-flow gas turbines, or as diffusers following radially outward-flow pump or compressor rotors. The inward-flow vane systems of turbines are usually fairly easy to design on a one-dimensional basis, partly because of the accelerated flow in such systems and partly because such systems have in most practical cases a rather high solidity. For these reasons, this section deals primarily with radially outward-flow vane diffusers as used on the outside of radial-flow pump or compressor rotors. However, the principles described apply also to other stationary radial-flow vane systems.

The effect of compressibility of the fluid can be taken into account for such systems in a one-dimensional manner as outlined in section 2.4. All design considerations described in the following apply also to compressible fluids provided one makes the required corrections for changes in the volume flow rate given in section 2.4. Therefore no further attention is given here to the case of compressible fluids.

For incompressible, frictionless fluids, radial-flow vane systems between parallel walls (normal to the axis of rotation) can be derived from straight systems of parallel vanes (secs. 2.5 and 3.2) by the process of conformal mapping, described for this case in section 2.6.2. By this method, the ideal flow characteristics of stationary radial-flow vane systems are given by those of straight systems of parallel vanes which have been extensively investigated by theoretical as well as experimental methods.

As pointed out in section 2.6.2, this theoretical background of stationary radial-flow vane systems does not apply to the real flow characteristics of such systems. In particular, the retardation of the flow, which is decisive for the separation or stall of the flow, is not the same in a radial-flow system and in its conformal representation by a straight system of parallel vanes. The separation or stall characteristics must, therefore, be explored in the actual radial-flow system, and the resulting flow limitations must be transformed into the straight system by the laws of conformal mapping (sec. 2.6.2). In other words, the experimentally determined real-flow characteristics of straight systems of parallel vanes (separation or stall) do not apply to a conformal radial-flow system. Obviously this fact reduces the practical value of the conformal relation between radial and straight parallel systems considerably.

In view of the foregoing considerations, the design of radial-flow vane systems is here pursued directly, by using the mean streamline method described in sections 2.5.5 and 3.2.4. Figures 4-49 and 4-50 show this design process for two cases which differ from each other primarily by the angle

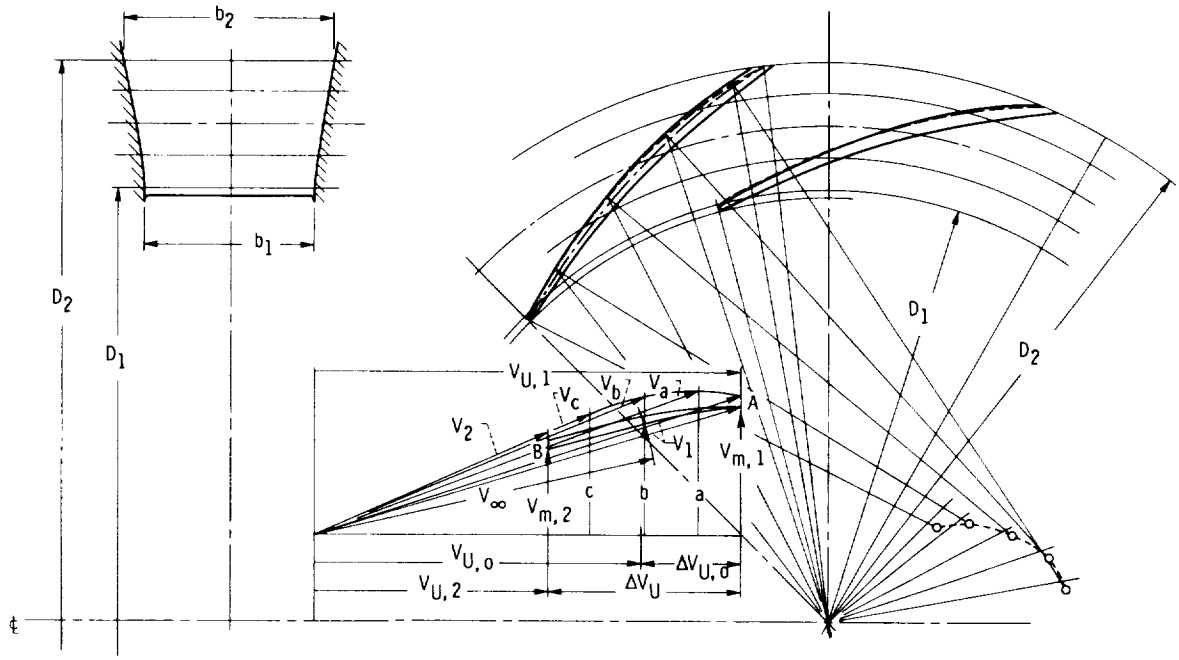

Figure 4-49. – Radial-flow vane diffuser with moderate wall divergence; 12 vanes.

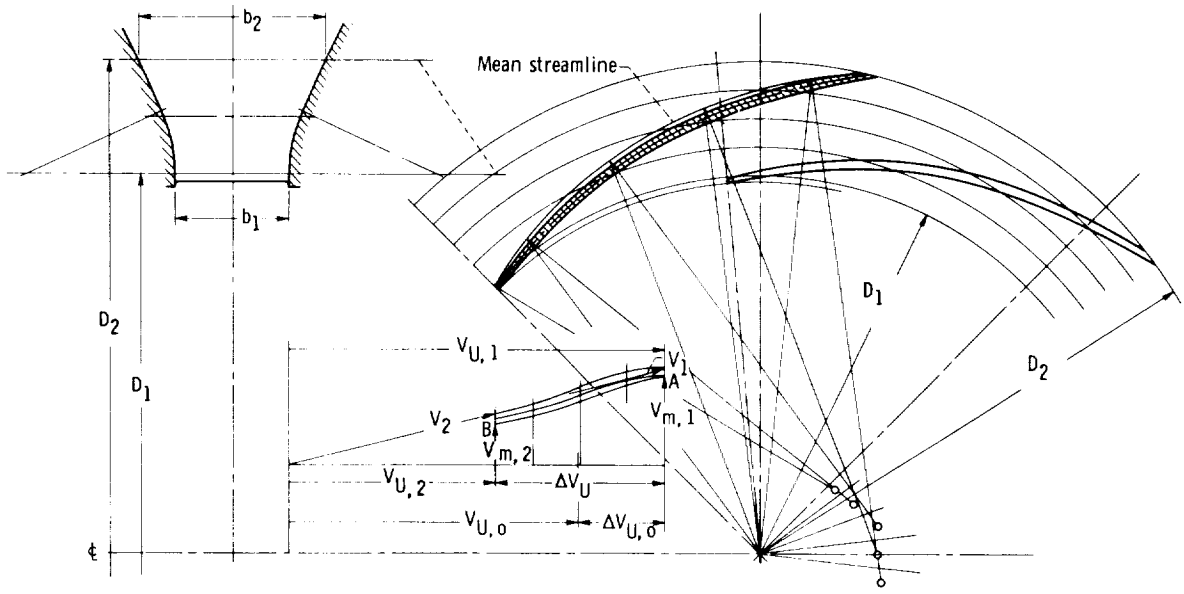

Figure 4-50. – Radial-flow vane diffuser with high wall divergence; nine vanes.

of the incoming flow against the circumferential or radial direction and by the divergence of the lateral walls expressed by the ratio b_2/b_1. The change in the circumferential velocity component is the same in both cases, with $V_{U,2}/V_{U,1}=0.55$, this change being divided into four steps, 22, 28, 28, and 22 percent. The reason for the low ratio of retardation is explained later.

With the aforementioned changes in the peripheral velocity component, the prescribed changes in the channel width b give the variation in the meridional velocity and in the absolute velocity

from the inlet to the discharge without considering vane and boundary-layer blockage. This variation is shown in figures 4-49 and 4-50 by the curve AB. In figure 4-49, above this curve is shown a second curve representing an estimated effect of the boundary layers on the meridional (radial) velocity, and above the second curve a third curve representing an estimated effect of the finite vane thickness. The resulting mean velocity vectors are drawn to the successive stations on the third curve. This entire process is the same as that described in section 2.5.5 and by figure 2-31 with respect to straight systems of parallel vanes.

The velocity vectors so derived give the direction of the mean flow at the successive flow stations through the system. From it, one can construct the mean streamline in the same manner as described in section 4.2 in connection with figure 4-1, except that the angle β_φ is in the present case not constant, since it varies with the direction of the mean flow velocity vectors. In figure 4-49, the mean streamline so derived is shown by a dashed line coinciding partly with the pressure surface of the vane, whereas, in figure 4-50, the mean streamline is well separated from the vane and can, therefore, be marked clearly.

The deviation of the mean camber line of the vane from the mean streamline is determined by the lift coefficient

$$C_{L,\infty} = 2\frac{V_{U,2}}{V_\infty}\frac{t_2}{l}\left(1 - \frac{V_{U,1}}{V_{U,2}}\frac{r_1}{r_2}\right) \tag{4-60}$$

which is derived from the equations (2-127) and (2-128) in the same manner as equation (2-130) in section 2.6.3.3 except for replacing w_∞ by V_∞. Since the vane systems considered here reduce the angular momentum, so that $V_{U,1}r_1 > V_{U,2}r_2$, the lift coefficient turns out to be negative. From figure 4-49, one finds

$$\left.\begin{aligned} C_{L,\infty}\frac{l}{t_2} &= -0.540 \\ C_{L,\infty} &= -0.446 \end{aligned}\right\} \tag{4-61}$$

and, from figure 4-50,

$$\left.\begin{aligned} C_{L,\infty}\frac{l}{t_2} &= -0.555 \\ C_{L,\infty} &= -0.4205 \end{aligned}\right\} \tag{4-62}$$

For the relation between the maximum normal deviation of the camber line from the mean streamline and the vane chord angle, one has no information other than that given in figure 2-33 for straight systems of parallel vanes. For β_v larger than 60° (measured from the radial direction), one finds for figure 4-49

$$\left(\frac{\Delta n}{l}\right)_{\max} = -0.05 \times 0.446 = 0.0223 \tag{4-63}$$

and for figure 4-50

$$\left(\frac{\Delta n}{l}\right)_{\max} = 0.05 \times 0.4205 = 0.021 \tag{4-64}$$

These values are used in figures 4-49 and 4-50. The distribution of the normal deviation Δn along the vane has to be estimated and should be qualitatively similar to that given by figure 2-34. The thickness distribution is derived from the previously assumed vane blockage as indicated in sections 2.5.5 and 3.2.4.

It remains to discuss the choice of an abnormally low ratio of retardation, $V_{U,2}/V_{U,1} = 0.55$, and the corresponding choice of the lift coefficient or of the solidity l/t_2 according to equations (4-61) and (4-62).

The low ratio of retardation can be justified qualitatively by the fact that in a radial-flow vane diffuser the low-pressure side of the vane, which is usually expected to be subject to separation (stall), is in most cases the concave side of the vane, in contrast to conditions in straight systems of parallel vanes. It is shown in section 3.2.3 that the flow along a concave wall is unstable (i.e., it tends toward increased turbulence) and is, therefore, more resistant to separation than the flow along a convex wall. Thus a radial diffuser should be more resistant to separation than an axial-flow diffuser, and a diffuser such as shown in figure 4-50 more so than the diffuser shown in figure 4-49. However, no quantitative prediction can as yet be made regarding this difference between radial and axial dif-

fusers, so that the choice of $V_{U,2}/V_{U,1}=0.55$ is at present hypothetical only.

The design of radial-flow vane diffusers, as described previously in connection with the mean streamline method, has not yet been verified experimentally. The only accurate record of dependable tests of radial-flow vane diffusers available to this writer dates back to the late thirties, when models of large twin-volute and diffuser pumps were tested at the California Institute of Technology. Figure 4-51 shows a diffuser design of the Worthington Pump and Machinery Corporation which produced overall pump efficiencies of 89.8 and 89.9 percent at 8 and 7 cubic feet per second, respectively, both at the same speed of rotation and, of course, at favorable basic specific speeds (0.12 and 0.11, respectively; see fig. 1-12).

Figure 4-52 shows the mean velocities in this old diffuser at the two rates of flow just given, in the same form as used in figures 4-49 and 4-50. This form is similar to the velocity diagrams developed in sections 2.5.5 and 3.2.4 in connection with the mean streamline method, except that in figure 4-52 the displacement thickness of the boundary layers was not taken into account. The ratios of retardation in the old, but successful, diffuser were as low as or lower than those assumed and discussed in the previous design examples (figs. 4-49 and 4-50).

Furthermore the mean ratio of the radial velocity component to the mean peripheral velocity was about 0.2 in the old diffuser (fig. 4-52), whereas in figure 4-49 it is about 0.36 and in figure 4-50 about 0.24.

The vane lift coefficients of the old diffuser were 0.29 and 0.49 at 8 and 7 cubic feet per second, respectively, that is, in the same range as those derived from figures 4-49 and 4-50 (see eqs. (4-61) and (4-62)).

The solidity of the diffuser with 11 vanes was $l/t_2=1.576$. It is very informative that the old dif-

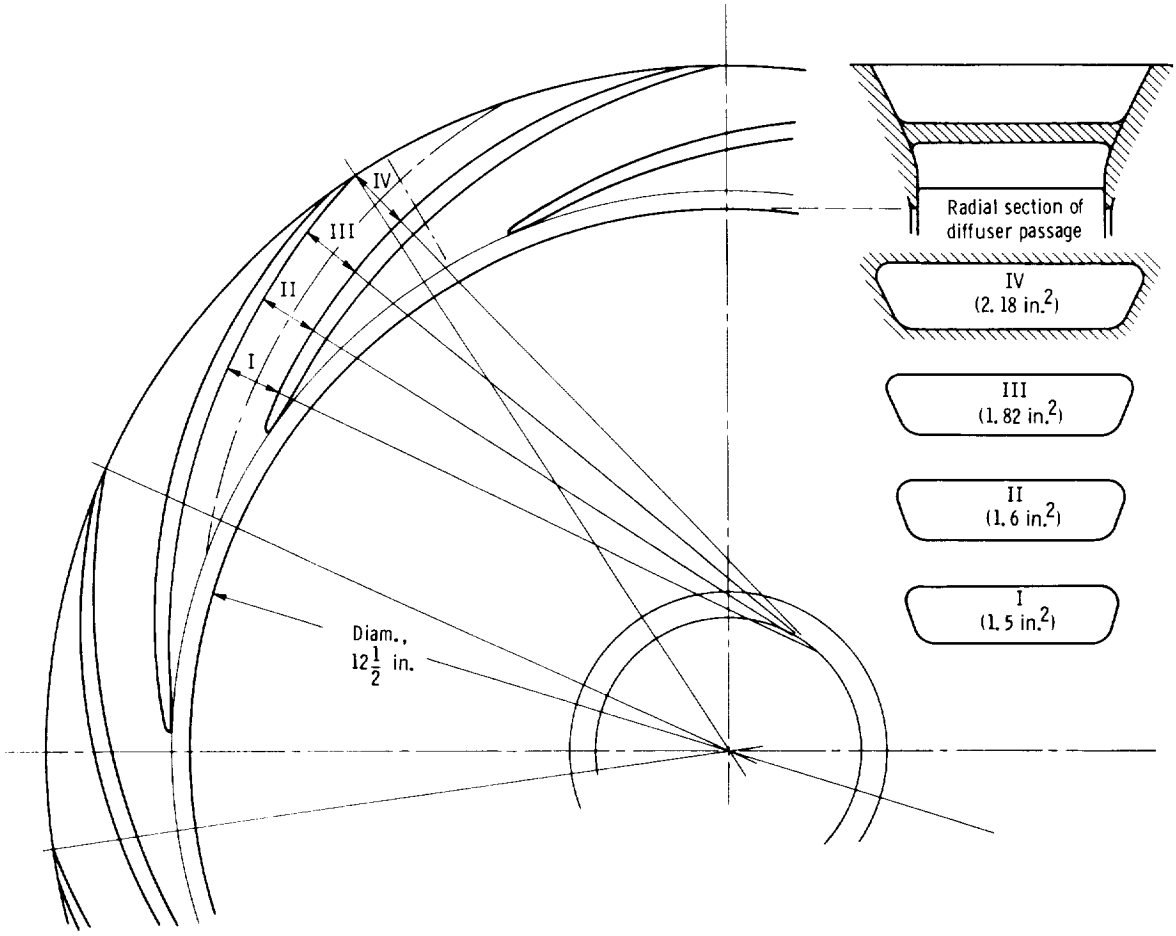

Figure 4-51.—Centrifugal pump vane diffuser designed and tested in late thirties; 11 vanes.

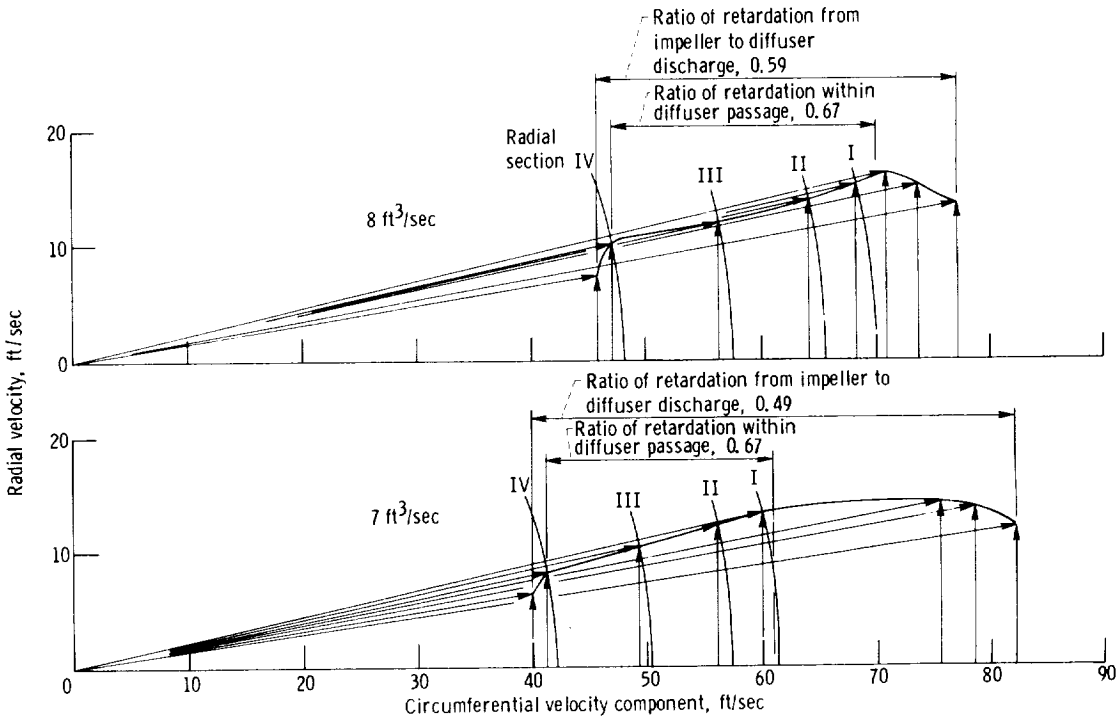

Figure 4-52. – Velocities in radial-flow pump diffuser shown in figure 4-51.

fuser form shown in figure 4-51 was also tested with 9 instead of 11 vanes, with the same impeller and no change in the diffuser vane shape. At 8 cubic feet per second (and the same speed of rotation), the performance was essentially unchanged, while the lift coefficient was, of course, increased from 0.29 to $0.29 \times 11/9 = 0.355$. However, in the vicinity of 7 cubic feet per second and a lift coefficient of $0.49 \times 11/9 = 0.60$, there were unmistakable signs of separation or stall by a strong, downward departure of the head and efficiency curves from those obtained with 11 diffuser vanes. This means that at a total ratio of retardation from the impeller to the diffuser discharge of 0.49 (see fig. 4-52) a vane lift coefficient of 0.60 is sufficient to cause stall, whereas test results obtained with straight cascades of parallel vanes (fig. 2-26) indicate that the same or somewhat higher lift coefficients are generally safe with respect to stall provided the ratio of mean flow retardation is above 0.6. The generally assumed dependence of the maximum allowable lift coefficient on the mean flow retardation is, therefore, confirmed by this old observation with a well designed radial-flow vane diffuser.

It is evident that systematic experimentation with radial-flow diffusers is necessary before such diffusers can be designed with confidence. Until then, fairly low lift coefficients and solidities well in excess of unity seem to be indicated. While it is possible that the solidity of $l/t_2 = 1.32$ shown in figure 4-50 is adequate at the lift coefficient given in equation (4-62), the solidity of 1.21 shown in figure 4-49 may well be too low for the suggested lift coefficient. It is comforting to know that the 11-vane diffuser shown in figure 4-51 was satisfactory under the flow conditions shown in figure 4-52, so that this design can be used as a proven design example.

4.5.2 Hydrodynamic Design of Volute Casings

The volute or spiral casing is the most efficient form of collector of the flow leaving a radial or mixed-flow pump or compressor rotor, or a radial-flow vane diffuser, provided the circumferential velocity component of the flow is substantially larger than the radial or meridional velocity component. In turbines, the volute or spiral casing leads the flow to the radially inward-flow nozzle ring or vane system, in order to supply this nozzle or vane system with a circumferentially uniform flow at its inlet.

Figure 1-28 shows as example A a volute casing surrounding a radial-flow rotor directly, while example B shows the same type of casing around a radial-flow diffuser or nozzle vane system surrounding the rotor. The tangential nozzle leading the fluid to or from the volute is included in the following description of volute casing design.

A so-called single volute such as shown in figure 4-53 extends over 360° as a single passage, surrounding the rotor and stationary vane system (if used) completely, and has only one passage leading to or from it to a single, usually straight, discharge or supply duct.

The so-called double volute or twin volute comprises two passages, each extending over 180° around the rotor or stationary vane system (if used), and has two tangential passages, circumferentially 180° apart, leading to or from it to the discharge or supply duct(s). If the ducts are to be joined, one is usually placed around one of the two volute passages as shown in figure 4-54, whereas, if they are to be separated, they are arranged as shown in figure 4-55.

When the twin-volute design shown in figure 4-54 is used for a pump (or compressor), almost the entire retardation of the flow from the rotor discharge to the discharge from the casing takes place within one of the discharge passages between A and E. This nearly straight-line retardation is discussed later. The flow from the other volute is retarded from section A'B' to section CD, with little or no retardation from section CD to the discharge section FG. This writer had good results with somewhat faster retardation in the beginning of the loop from A'B' to CD than in its later portion. The radial dimension of this loop remains almost constant, so that the axial width of this passage is increased very gradually. This design tends to minimize the radial dimension of this passage and should be favorable for this curved flow (see its section CD in fig. 4-54). The cross section from CD to

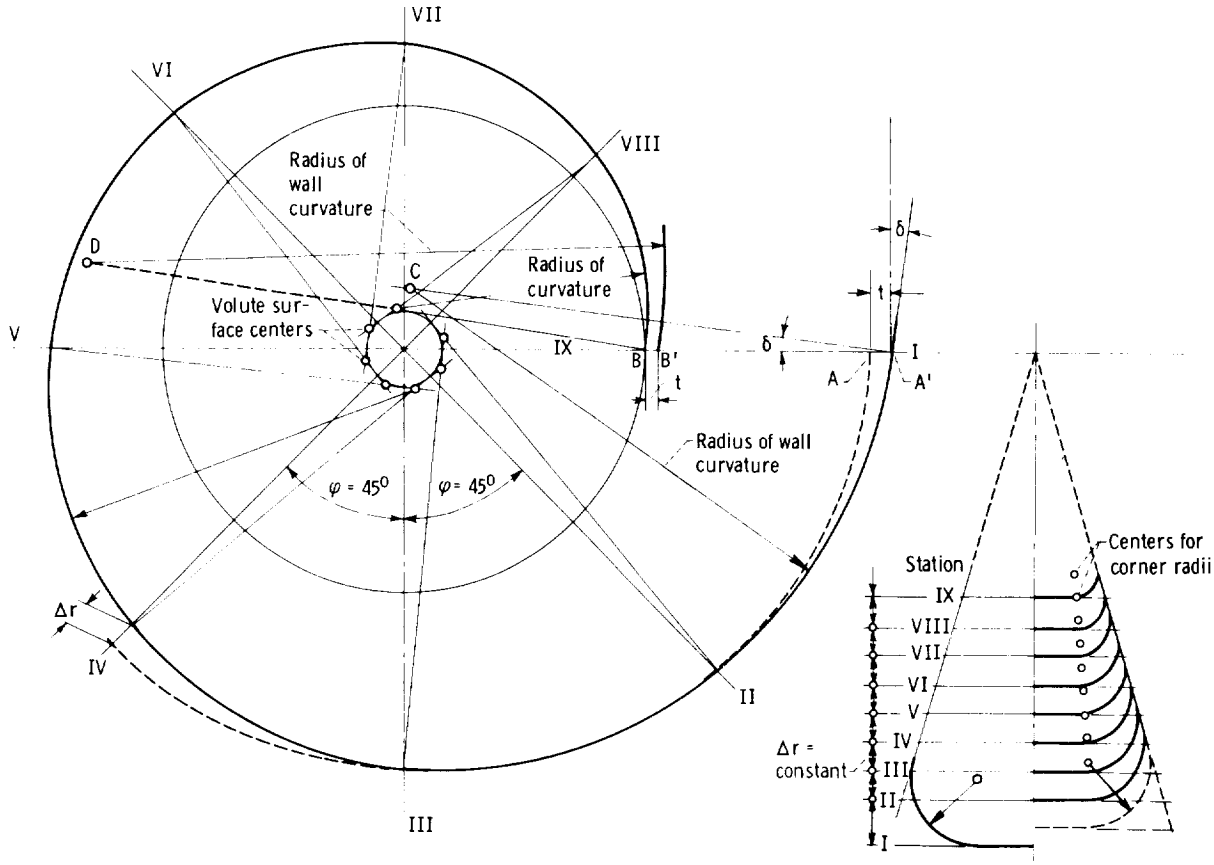

Figure 4-53. – Single-volute layout.

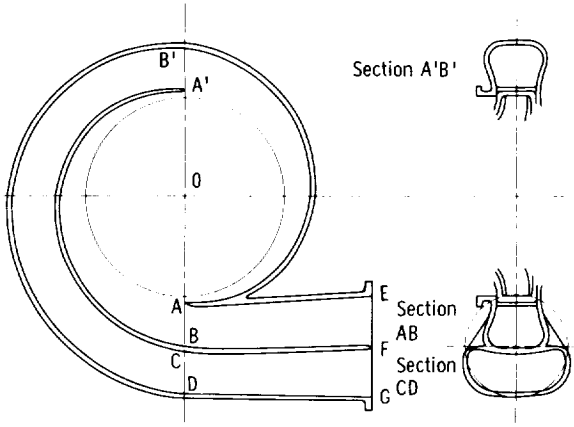

Figure 4-54. – Double or twin volute with joining discharge (or supply) ducts.

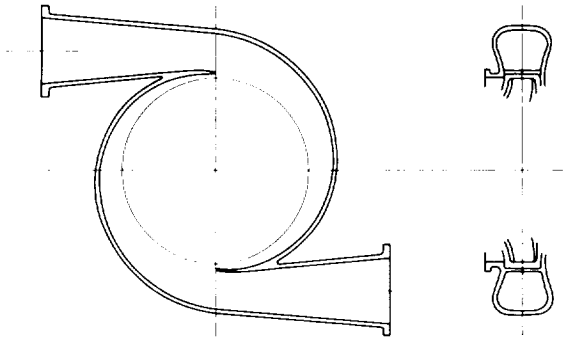

Figure 4-55. – Double or twin volute with separated discharge (or supply) ducts.

FG in figure 4-54 remains almost constant. While the extension of the central splitter from B and C to F involves some foundry difficulties, this extension seems, nevertheless, necessary for good performance.

Triple volutes, quadruple volutes, etc. comprise three, four, or more passages, each extending over 120°, 90°, or smaller fractions of 360° around the rotor and stationary vane system (if used). Such multiple volutes have of course three, four, or more tangential passages 120°, 90°, or smaller fractions of 360° displaced from each other (see fig. 4-56). These passages are but rarely joined into a single discharge or supply duct except quite far away from the machine. Evidently multiple volutes can be regarded as vane (or duct) diffusers with the number of volutes being the number of vanes in the diffuser.

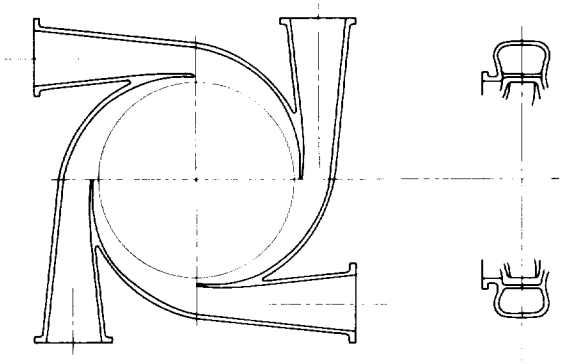

Figure 4-56. – Quadruple volute (or four-vane diffuser) with separate discharges.

The hydrodynamically simplest form of a volute is one between two parallel walls normal to the axis of rotation. The frictionless and incompressible flow between these walls is a vortex source or vortex sink, with its streamlines forming logarithmic spirals as described in section 2.6.2. The outer wall of this type of a volute casing should, therefore, have the form of a logarithmic spiral with the same angle against the peripheral or radial directions as the flow at the inner circular section of the volute, that is, at the outer periphery of the rotor or stationary vane system surrounded by the volute. The peripheral component of the flow in the volute obviously follows the law of constant angular momentum, and the radial component satisfies the condition of continuity for radial flow between parallel walls, that is, both components are inversely proportional to the distance from the axis of rotation. The ideal flow in the volute is, therefore, the same as that in a vaneless space of revolution. A more rapid change in the flow velocity (diffusion in the case of a pump or compressor) can take place only after the flow has left (or before it enters) the volute proper, that is, in the passage leading tangentially away from or toward the volute.

The foregoing characteristics of volute flow can be taken as valid also if the volute is not designed as confined axially by parallel end walls. A form of volute design frequently used or approximated is that shown in figure 4-53. Here the axial end walls are coaxial, conical surfaces with the apexes meeting along the axis of rotation. In this case, the increase in the area of radial sections through the volute is proportional to the distance from the axis of rotation provided this distance increases by constant steps Δr. Applying this relation along any

stream surface in the volute, but in particular along the outer contour of the volute, one finds that a constant value of increase in radius Δr = constant is associated by the condition of continuity with a constant change in the angular coordinate φ. Proportionality between the angular coordinate φ and the radial coordinate r leads to an Archimedian spiral; its graphical construction is depicted in figure 4-57. The application of this construction is shown in figure 4-53. Also included is a departure from this construction to be used when approaching the discharge (or inlet) cross section AB of the volute casing. (The continuation of the Archimedian spiral leads to point A, whereas the volute contour must run through point A′ to account for the finite thickness t of the tongue or splitter.)

Since the most important portion of the diffusion in volute pumps or compressors without vane diffusers occurs in the tangential discharge nozzle (or nozzles) of the casing, the design of this part of a volute casing deserves particular attention.

For centrifugal pumps, the highest efficiencies have been achieved with volute casings surrounding the rotor without a stationary guide vane system (see fig. 1-28, example A). The rotor discharge width is usually made substantially smaller than the axial width of the casing without detrimental effects on efficiency (the rotor width usually being between 65 and 85 percent of the casing width, this ratio increasing with the basic specific speed). In this case, radial sections through the volute are usually not circular. Rather these sections have a shape such as shown in figure 1-28, example A, and in figure 4-53. For the discharge nozzle of the volute, this shape requires a transition from a noncircular section to a (usually) circular section of the final discharge duct, as shown in figure 4-58. A favorable transition is designed by means of a number of sections A, B, C, etc. radial and parallel to the duct and by a number of cross sections 0, 1, 2, 3, etc. normal to the centerline of the duct. The longitudinal sections A, B, C, etc. must, of course, be free of unnecessary changes in direction. The angle between these sections and the centerline of the duct usually varies between 3° and 8°; that is, its average value is somewhat larger than the customary 3½° for straight ducts with circular cross section, particularly if the duct following the diffusing nozzle is straight for a considerable length. (Such angles of divergence can be justified by a high degree of large-scale turbulence in the volute.)

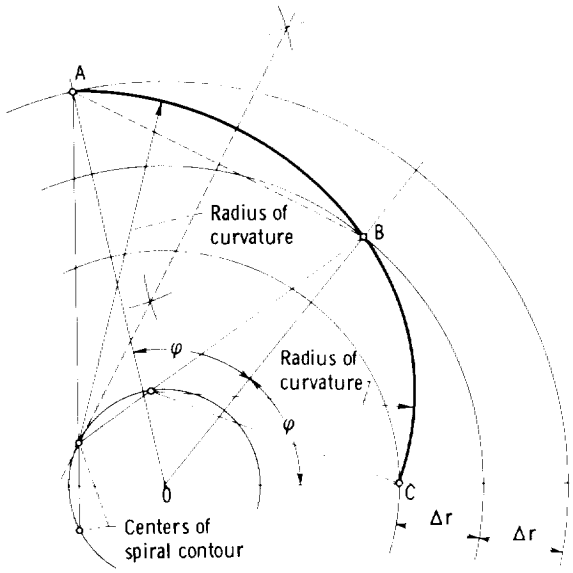

Figure 4-57. – Archimedian spiral approximated by circular arcs.

Volute casings located radially outside of vane diffusers of pumps or of nozzle rings of turbines usually have approximately circular radial sections with the exception of the inner portion where the volute joins the stationary vane system (see fig. 1-28, example B). In this case, the transition to a duct with circular cross section constitutes no significant design problem. For pumps or compressors, this transition is a straight, conical duct with an enclosed angle of divergence usually equal to, or slightly smaller than, 7°. For turbines, one usually makes the maximum cross section of the volute about equal to that of the approaching duct in order to minimize skin-friction losses in the volute. The greatest part of the acceleration toward the rotor takes place in the stationary guide vane system inside the volute.

The flow rate through a volute casing is determined by the so-called throat area A′B′ in figure 4-53. For an open volute of a centrifugal pump, that is, a volute without a stationary vane system, the relation between the throat area A_{th} = A′B′ and the volume flow rate Q is

$$Q = \alpha N A_{th} V_{th} \tag{4-65}$$

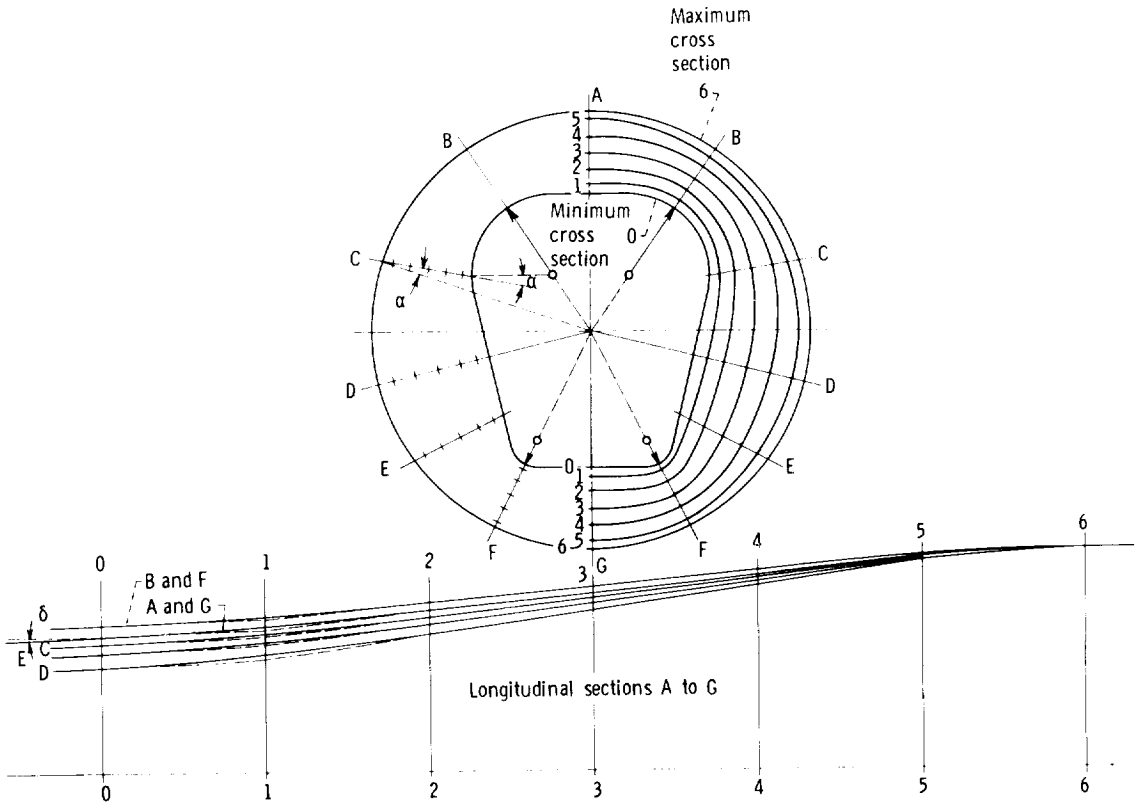

Figure 4-58. – Layout of discharge from pump volute casing.

where α is a correction factor for the boundary-layer displacement area in the throat, which may be estimated to be in the vicinity of 0.9; N is the number of volutes ($N=1$ for a single volute, $N=2$ for a double volute, etc.); and V_{th} is the mean velocity in the throat.

The throat velocity V_{th} is related to other velocities in the system by the law of constant angular momentum, for example, to the peripheral component $V_{U,o}$ of the absolute velocity at the outer periphery of the rotor by the relation

$$V_{th}r_{th} = V_{U,o}r_o \tag{4-66}$$

where r_{th} is the distance of the center of gravity of the throat section from the axis of rotation, and r_o is the radius of the rotor where $V_{U,o}$ is assumed to exist. The relations (4-65) and (4-66) are very generally valid not only for volute casings, but also for vane diffusers, where A_{th} and r_{th} can be defined analogously to their definitions with respect to a volute by the inlet area, adjacent to the inlet vane edge of a radially outward-flow vane diffuser. In the application to diffusers, the correction factor α may well be somewhere between 0.9 and unity and should increase generally with the number of volute passages.

For volutes with stationary vane systems, the radius r_o and the circumferential velocity $V_{U,o}$ in equations (4-65) and (4-66) apply, of course, to the outside diameter of the stationary vane system.

The actual radial velocity distribution in volute casings does not conform uniformly to the law of constant angular momentum, probably because of secondary motions, which must be expected to be radially outward in the center and radially inward near the side walls of the volute. Nevertheless the law of constant angular momentum holds closely for the mean velocity in any complete radial section through the volute. This relation is expressed by equation (4-66); it is compatible with equation (4-65) only under the design flow conditions with some allowance α for the effects of skin friction.

For volute pumps without stationary vane systems, the flow rate determined by equations (4-65) and (4-66) is usually that of maximum efficiency, particularly if the average velocity in the throat section of the volute is the highest mean

velocity in confined cross sections of the machine. This is generally true for single-suction pumps with specific speeds of 0.10 or less (and for double-suction pumps with specific speeds of 0.14 or less). For substantially higher specific speeds, the maximum mean velocities usually occur at the rotor inlet, so that this part of the pump determines the flow rate of best efficiency. For specific speeds between 0.10 and 0.18 for single-suction pumps, both the casing throat and the rotor inlet passage must be expected to influence the point of best efficiency. Theoretically, of course, there is an influence for a much wider range of specific speeds.

If the flow departs significantly from the condition expressed by equations (4-65) and (4-66), the flow conditions along the open part of the volute casing (the part directly exposed to the rotor) cannot be uniform in the circumferential direction since they involve variations in momentum and pressure. With a single volute, this nonuniformity leads to a significant unbalanced radial force acting on the rotor, whereas, for multiple volutes, these forces should be balanced as long as the flow conditions in every volute are equal to those in all other volutes of the same system. Thus the ducting connected with all volutes of one machine, as well as their discharge pressures, must be exactly the same. While this condition is apparently not completely satisfied in practice (see, e.g., fig. 4-54), it is, nevertheless, true that twin and other multiple volute casings (as well as vane diffusers) lead to substantially lower force actions on the rotor than a single-volute casing at substantially off-design conditions.

The unbalanced forces acting on the impeller of a volute pump have been expressed by a simple similarity consideration. It is assumed that the unbalanced force per unit area is proportional to the pump head H times the fluid weight per unit volume and that this unbalanced pressure acts on an area equal to the discharge diameter D_o times the discharge width b_o of the impeller. The resulting relation is obviously

$$F = k_F g_o \rho H D_o b_o \tag{4-67}$$

where k_F is a coefficient of proportionality to be determined theoretically or by test. So far, only its experimental determination has led to practically useful results.

For single-volute pumps, the highest values of k_F occur near the zero-flow (shutoff) conditions and cover the range $0.3 \leq k_F \leq 0.65$. The unbalanced force does not go to zero at the design operating conditions, where k_F is about 0.1, but may be somewhat higher. Double- and multiple-volute pumps have a more nearly constant value of k_F over the entire operating range of positive flow rates and positive rotation, this value being in the same range as that of single-volute pumps at design conditions. This characteristic is an important reason for using double and multiple volutes or vane diffusers.

The foregoing values of k_F apply only to time-averaged values of the unbalanced radial forces acting on the impeller of centrifugal pumps. All turbomachinery rotors are also subjected to unsteady forces which are considerable and sometimes destructive if the machine is operated beyond its stall point (for pumps and compressors, at reduced flow rates) or with high degrees of cavitation.

As mentioned previously, the highest efficiencies of centrifugal pumps have been achieved with single- and double-volute casings without a stationary vane system (values between 90 and 92 percent under very exacting laboratory conditions). Investigations of the discharge velocity distribution of efficient centrifugal pump impellers indicate that the volute casing with greater width than the impeller discharge is not very sensitive to the actual velocity distribution at the impeller discharge, a fact which may be one of the reasons for the high efficiencies obtained. This empirical fact may be considered to be in conflict with the equally empirical observation that vaneless diffusers (vaneless, radially extending spaces of revolution with more or less parallel side walls) have so far never led to exceptionally high efficiencies.

There are several reasons for the difficulties encountered with vaneless diffusers:

(1) The side-wall boundary layer of the circumferential flow cannot be expected to sustain the higher radial pressure gradient of the flow with higher circumferential velocity in the axially central parts of the diffuser. One may, therefore, expect radial backflow near the side walls, that is, major axial nonuniformities of the radial velocity component. One accidental observation seems to suggest that the flow at the side walls is exactly circumferential, but this observation was made with a slightly conical (mixed-flow) vaneless diffuser (about 15° or 20° from the radial direction) and may, therefore, not generally be valid.

(2) An experiment with a radially deep vaneless diffuser (D_2/D_1 between 1.5 and 2) revealed with a good impeller with radial vanes (see fig. 4-20) the existence of major circumferential irregularities of the flow at the outer discharge of the diffuser (there were regions of zero discharge). These irregularities disappeared when a screen was wrapped around the periphery of the impeller (rotating with the impeller); evidently a vaneless diffuser greatly increases nonuniformities of the flow leaving the impeller. With the screen, the flow irregularities at the impeller discharge (diffuser inlet) were apparently sufficiently reduced to prevent their amplification in the vaneless diffuser. In this respect, the vaneless diffuser has the opposite characteristic to that of the volute (without stationary vanes), which is rather insensitive to flow irregularities at the impeller discharge.

(3) The flow in a vaneless diffuser is probably unstable, because skin friction on the side walls causes the flow to have radially decreasing angular momentum (Prandtl's stability criterion, see also sec. 3.2.3). This instability agrees with the observations under item (2) and makes the vaneless diffuser particularly sensitive to flow reductions below the design conditions. Under such reduced flow, any vane system (or volute) at the outer periphery of the vaneless diffuser must act as a brake on the circumferential flow component and thus further reduces the angular momentum in the outer portion of the diffuser; this reduction increases the aforementioned instability of the diffuser flow.

(4) The observations in items (1) to (3) explain why the losses in efficiency connected with vaneless diffusers are hardly measurable in the diffuser itself, but become apparent in the vane or duct system following the diffuser.

The foregoing comments are not intended to discourage further investigations of vaneless diffusers. On the contrary, such investigations are necessary to permit the use of vaneless diffusers in some cases and to improve our understanding of the favorable characteristics of volute casings. The instability of the flow in a vaneless space of revolution may be the reason why optimum efficiencies have been achieved with small radial distances between the impeller discharge and the tongue (or splitter) of a volute or between the impeller and the vanes of a vane diffuser. In this connection, it should be mentioned that volute pumps (without stationary vanes) are advantageously designed with a very small ratio of the radial to the peripheral component of the absolute flow at the impeller discharge. (This relation may be one reason why an axial gap between the impeller and the side walls of a volute casing is not harmful.)

4.5.3 Hydrodynamic Design of Passages Between Successive Stages of Radial-Flow Pumps on the Same Shaft

The design of passages between the successive stages of radial-flow, multistage pumps may well be considered one of the major problems of radial-flow pump design. Usually there exists a considerable reduction in efficiency as soon as radial-flow pumps have to be arranged in several stages on the same shaft. This reduction indicates that the hydrodynamic connection between such stages constitutes, at best, an incompletely solved problem.

The most reliable, and so far the most efficient, solution of this problem consists in carrying the flow outside the casing (by a straight discharge from the volute), curving the flow back toward the centerline of the pump as efficiently as possible, and turning the flow to the axial direction to enter the impeller of the next stage. A design form satisfying these requirements is shown in figure 4-59. The radial dimension of the elbow cross section outside the casing is smaller than the axial dimension, and the cross section of the duct changes subsequently to a smaller axial and a larger circumferential dimension in order to accommodate the turn into the impeller of the next stage; thus the axial distance between successive stages is minimized. The radial return to the next stage is characteristic for entering any axial inlet to a pump by a duct essentially normal to the axis of rotation. The necessarily sharp turn into the axial direction does constitute a significant flow problem, and it is common to many pumps with a side inlet. This problem can be solved by giving the flow a substantial acceleration when it turns from radial to axial at the impeller inlet. Thus, for a return passage such as shown in figure 4-59, the flow must be retarded in this passage to a substantially lower velocity than required at the inlet to the next stage. This requirement is the reason why the fairly great length of the loop shown in figure 4-59 is important for favorable hydrodynamic performance of this design form.

The flow can and should be retarded quite rapidly in the straight, tangential diffuser leaving the volute casing, where the total cone angle of an equivalent diffuser with circular cross section

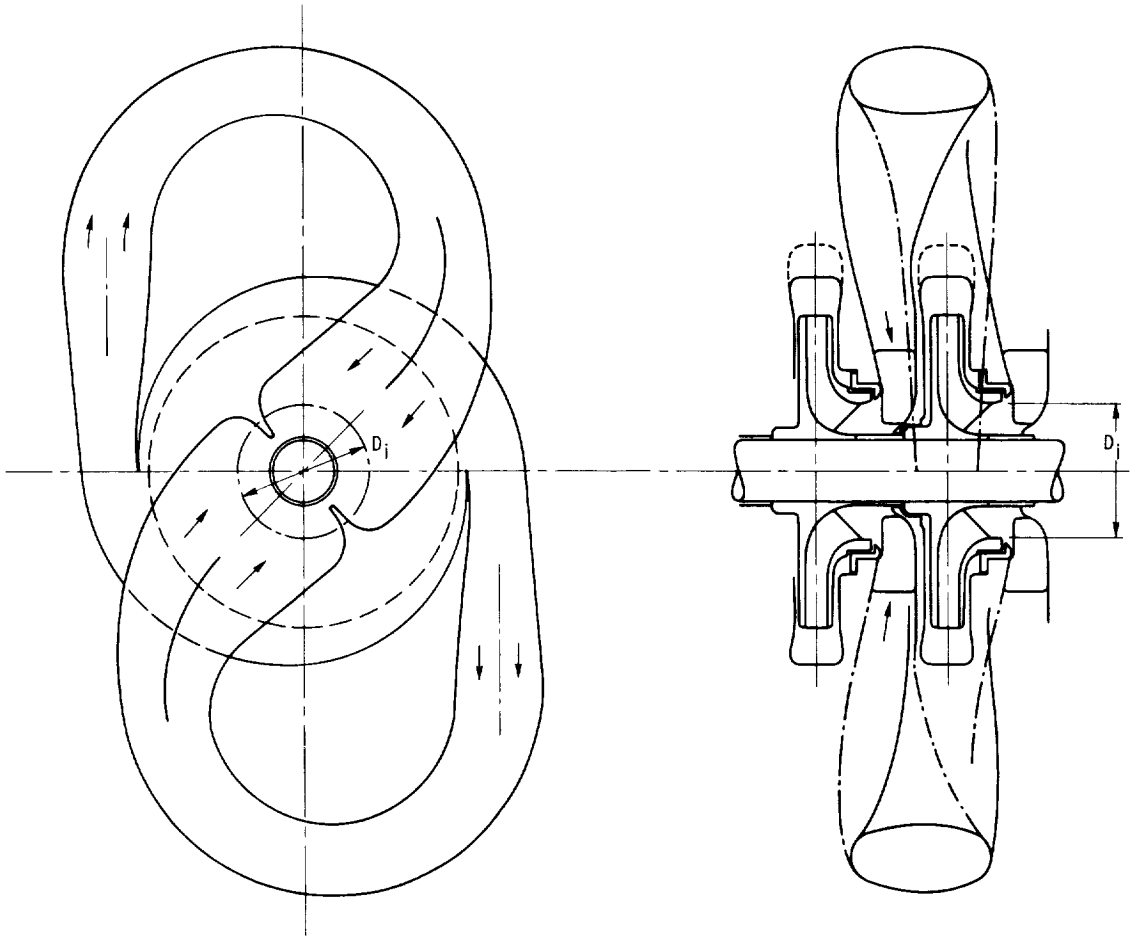

Figure 4-59. – Crossover from twin volute to following stage on same shaft.

should not be less than the familiar 7° and may be as large as 10° because of the high degree of turbulence in this passage. In the following elbow and return passage, the total rate of diffusion must be much less, perhaps equivalent to a cone angle of 2° to 3° for most of this passage. The rate of diffusion should approach zero just before the flow turns to the axial direction, where it must be accelerated. The wall radius of curvature in this last turn is less than normally desired in order to minimize the axial stage distance and thereby the bearing span.

A crossover such as shown in figure 4-59 is particularly advantageous when connecting two successive stages with back-to-back impellers. In this case, the external elbow or loop crosses over the second-stage impeller and casing, yet there is ample circumferential space between the external loops for the discharge passage(s) of the second-stage casing.

The external crossover design shown in figure 4-59 is obviously not usable if the outside dimensions of the pump casing are severely restricted for some practical reason. In that case, the external loop can be placed tightly around the volute casing, as shown in figure 4-60 for a quadruple volute. This drawing indicates only the hydrodynamic design in principle and ignores the mechanical arrangement necessary to solve the assembly problem. This problem has to be solved separately in relation to the chosen casing construction, horizontally or vertically split (fig. 1-40).

For the same impeller size, the crossover passages shown in figure 4-60 are not nearly as long as those of the external loop design shown in figure 4-59. The rate of diffusion is, therefore, limited for the tight crossover design (fig. 4-60), and it dictates higher velocities in the crossover passages (compared with the impeller discharge velocity V_0) than

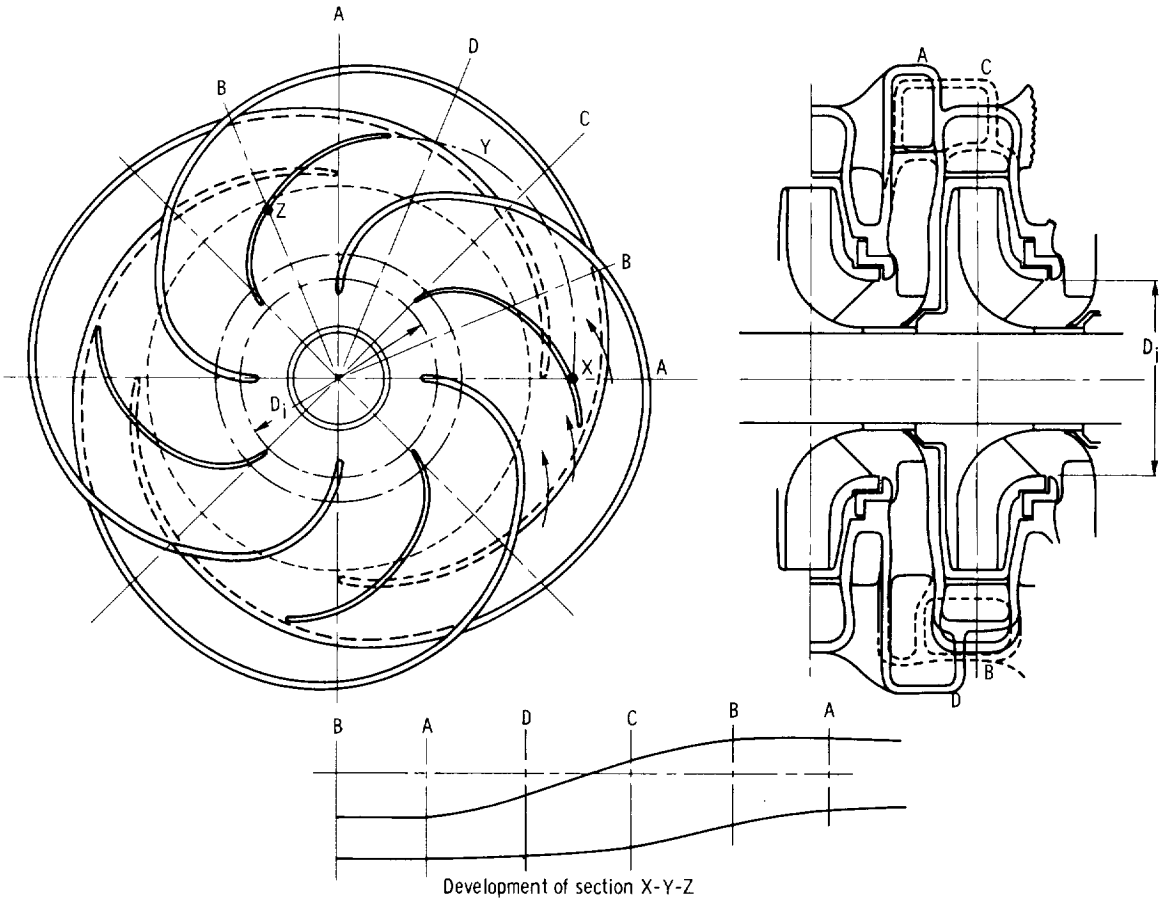

Figure 4-60. – Crossover from quadruple volute.

for the external loop design, particularly as the flow approaches the inlet to the next impeller. These higher velocities are almost certain to lead to increased hydrodynamic losses due to flow distortion at the inlet to the second-stage impeller shown in figure 4-60. A design of this type has been used for many years in connection with twin volutes in the field of high-pressure boiler feed pumps, with only moderate success regarding efficiency. In this case, a quadruple-volute (or four-vane diffuser) design can be expected to be more efficient than a single- or a twin-volute design, because the cross sectional dimensions of the casing passages decrease with increasing number of volutes, so that the ratio of crossover length to the cross-sectional dimension (i.e., a dimensionless length of these passages) increases with increasing number of volutes.

For the design indicated in figure 4-60, the distribution of the rate of diffusion along the crossover passage should follow a law similar to that previously described in connection with the external loop design, that is, the rate of diffusion should be a maximum at the beginning of that passage and a minimum at its end. Whether one can achieve, with the rates of diffusion suggested previously, velocities lower than the mean inlet velocities of the second impeller remains to be determined for individual cases. To improve the likelihood of this achievement, one should select high meridional impeller inlet velocites, that is, high inlet flow coefficients $V_{m,i}/U_i$ for all except the first radial-flow stage. This choice should be possible since all these stages have, as a rule, very low suction specific speeds.

The design process consists here in wrapping the discharge vane system of one stage as tightly as possible around the volute system of the same stage and diverting it around that system so as to enter the impeller of the next stage within a minimum of axial distance between the stages. It is hoped that

figure 4-60 illustrates this geometric design process. From the foregoing remarks, it should be evident that this solution of this design problem is more successful the larger the number of volutes or diffuser vanes. Hence a multivane diffuser leading along a curved passage from one stage to the next (see fig. 1-28, example C) might offer a hydrodynamically and geometrically satisfactory solution.

The connection between successive stages shown diagrammatically in figure 1-28, example C, suggests that a three dimensionally curved vane system may serve this purpose. Figures 4-61 to 4-63 illustrate the design of such a vane system by the method of conformal mapping previously discussed in section 4.4.2 with respect to Francis pump rotors. Details of this method were developed especially for this publication in order to illustrate the application of conformal mapping of the curved stream surfaces to the design of vane systems of this type. There are no test results available on the hydrodynamic qualities of this design form.

First, an impeller profile is assumed which, in an actual case, would be derived from the prescribed

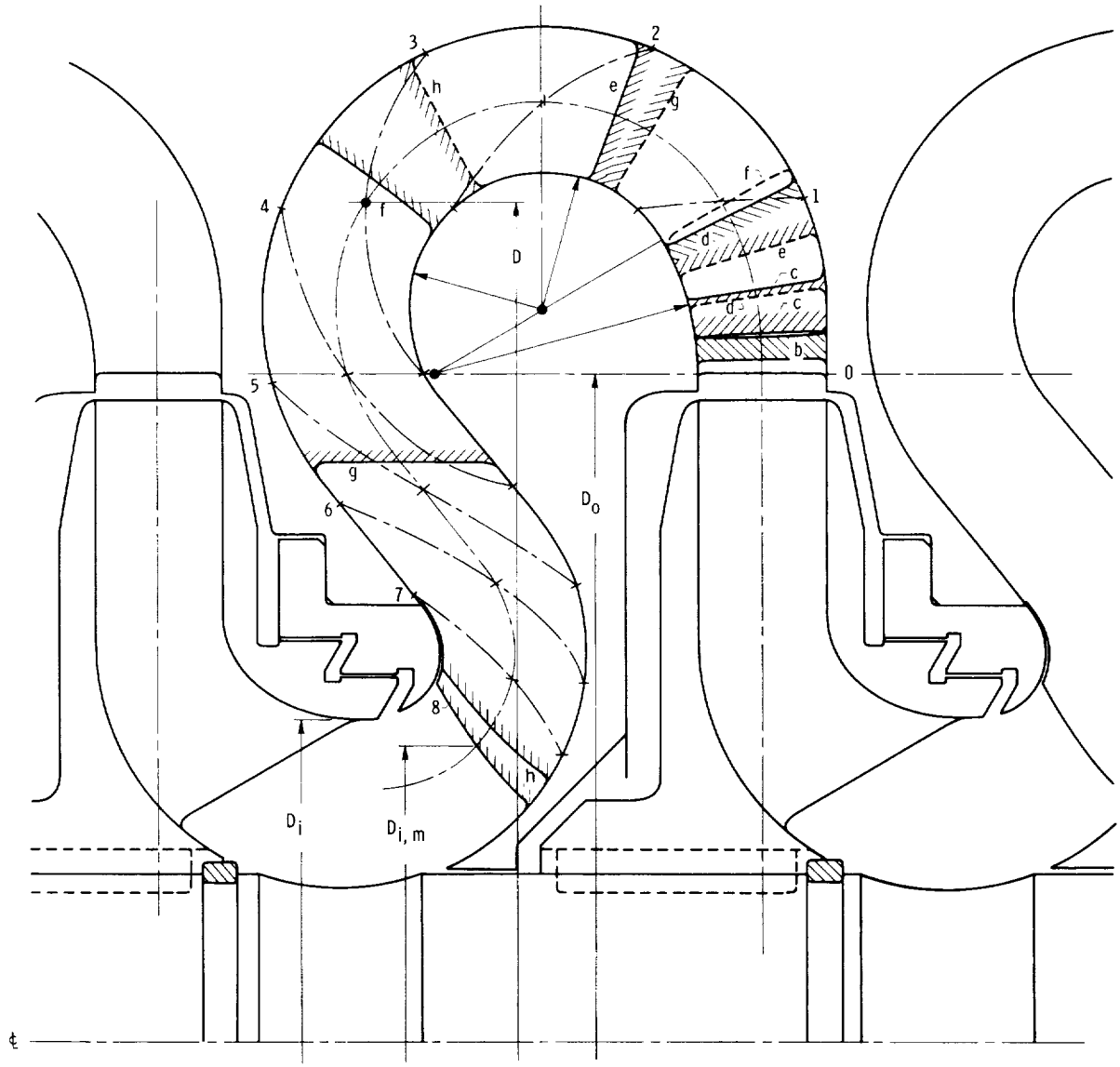

Figure 4-61. – Vane diffuser between successive radial-flow stages. (0 to 8 denote coaxial circles spaced by law of conformal mapping; b to h denote radial sections through vanes obtained by conformal mapping (fig. 4-63).)

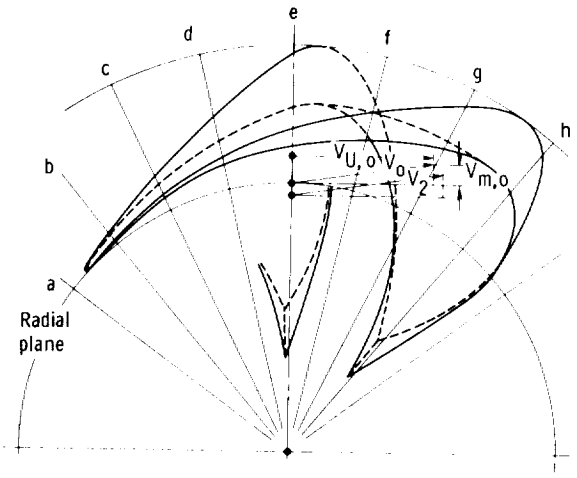

Figure 4-62. – Vane of diffuser between successive radial-flow stages; nine vanes.

operating conditions in the form of the basic specific speed. Second, a curved space of revolution is developed that provides for continous passages from the impeller discharge to the inlet of the next impeller. In the present case, this space is assumed to diverge for a short distance after the impeller discharge and then to continue at constant width (normal to the walls of the space) until shortly ahead of the next impeller inlet.

Next, one establishes a mean meridional stream surface midway between the two shroud surfaces of the space of revolution so established. This mean meridional stream surface is shown by a dash-dot line in figure 4-61.

Along the two shroud surfaces and the mean stream surface, one establishes a network of coaxial circles and meridional lines, 1, 2, 3, etc. in figure 4-61 and a, b, c, etc. in figure 4-62, in exactly the same manner as described in section 4.4.2, by using figures 4-22, 4-23, and 4-26, with the local spacings between successive meridional lines and coaxial circles being equal. Circles of the same number on the shroud and mean surfaces are connected in figure 4-61 by dash-dot lines. A network of straight, equally spaced, orthogonal lines corresponding to the circles and meridional lines on the three curved surfaces of revolution is given in the plane of conformal representation, shown in figure 4-63.

Instead of drawing centerlines of the vane sections in the plane of representation, as described in section 4.4.2, it is in the present case preferable to start the design process in the plane of representa-

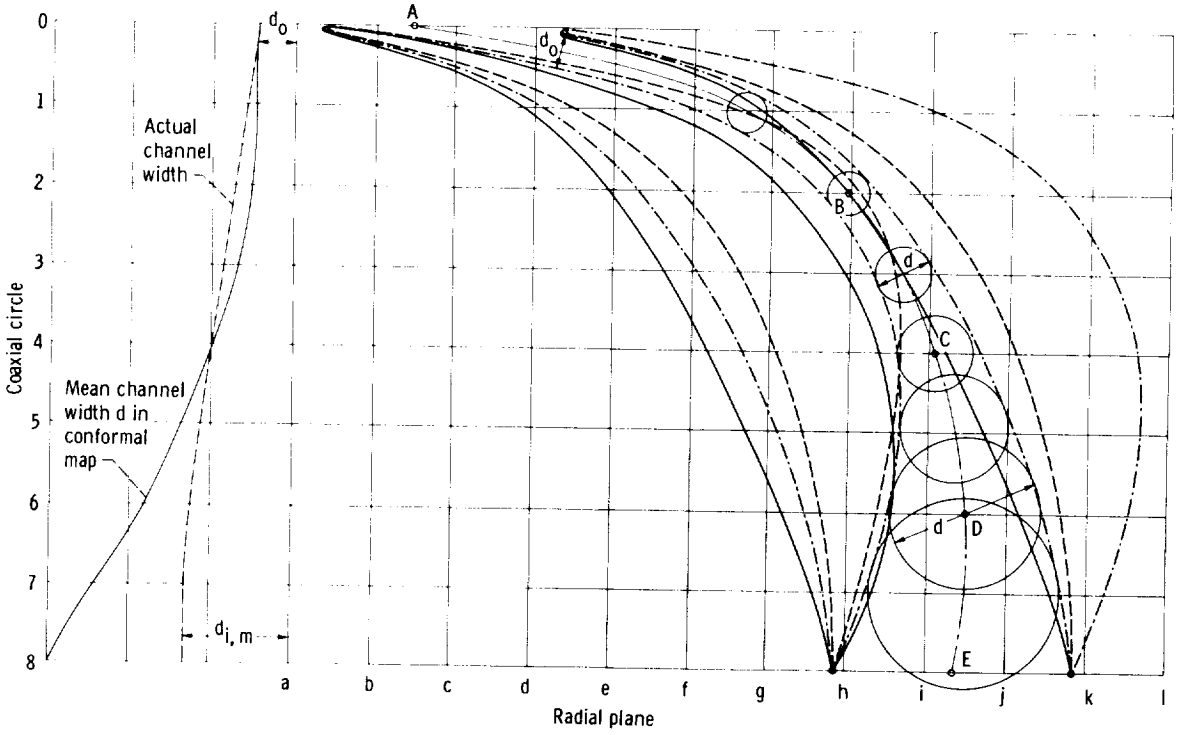

Figure 4-63. – Conformal map of vane between successive radial-flow stages.

tion with a centerline A, B, C, D, E of the space between the vanes, because with the very high solidity of the vane system to be designed here the one-dimensional design process to be used is concerned primarily with the space (channel) between the vanes.

The centerline of the vane channel has at its starting point A the direction of the absolute flow leaving the impeller (see fig. 4-62). If the flow is to leave this vane in the meridional direction, that is, without any circumferential component (as assumed here), the geometric centerline of the vane channel should overturn by an estimated amount, since the flow cannot be expected to follow the geometric centerline of the channel exactly. This overturning is shown between points D and E of the centerline in figure 4-63.

To determine the width of the vane channel d normal to its centerline, one must first determine the number of vanes or vane channels. Considering that the peripheral velocity component at the discharge from this vane system is zero, the lift coefficient of every vane in that system is, according to equation (2-130),

$$C_{L,\infty} = 2 \frac{V_{U,o}}{V_\infty} \frac{t_o}{l} \tag{4-68}$$

where

$$t_o = \frac{D_o \pi}{N} \tag{4-69}$$

in which N is the number of vanes.

From the foregoing equations, and with estimated values of $l/D_o = 1.17$ and $V_{U,o}/V_\infty = 1.56$, one obtains $C_{L,\infty} = 0.93$ with an assumed number of vanes $N = 9$.

The vane distance varies from $d_o = t_o V_{m,o}/V_{U,o}$ to $d_{i,m} = D_{i,m}\pi/N$, and this variation is plotted in dashed lines to the left of the plane of representation (fig. 4-63) as a function of the meridional distance in the conformal representation. This vane distance is assumed to increase first linearly with the meridional distance and then to remain constant for a moderate stretch. This variation in vane distance implies a more rapid increase in vane channel area at the beginning of the passage, where the distance between the shroud walls first increases and then remains constant. This rapid increase in vane channel area agrees with the design philosophy of the previously described examples.

The actual channel width plotted to the left of the conformal map in figure 4-63 can readily be transformed into the normal channel widths appearing in the conformal map by the law of conformal transformation:

$$d = d_o \frac{D}{D_o} \tag{4-70}$$

This process is carried out for the mean stream surface in figure 4-61, and the results are again represented by dash-dot lines in the plane of representation (fig. 4-63) to give the vane contours in the conformal representation along the mean meridional stream surface.

The condition considered controlling for the entire vane and channel surfaces is that the vane and channel walls must meet the outer and inner shroud surfaces approximately at right angles. In the first part of the vane channel, with predominantly circumferential flow, this condition is satisfied if the radial vane and channel wall sections, appearing in figure 4-61, meet the shroud contours at right angles.

The vane contour along the mean stream surface, derived from the channel centerline and the channel width (transformed to the conformal map as described previously), is transferred to the physical mean stream surface appearing in figure 4-61. Through the points so obtained along the dash-dot mean streamline, lines are drawn normal to the outer and inner contours of this flow space to mark points along the shroud surfaces which can be transferred conformally to the plane of representation (fig. 4-63). The outer shroud vane contours are represented there by solid lines, and the inner shroud vane contours by dashed lines.

From the point where the radial vane sections become axial (180° from the inlet section 0 in a radial plane, figure 4-61), the radial section lines remain axial. While this is a more or less arbitrary rule, it leads to a reasonable overall vane and channel shape.

The points transferred by this rule from the mean stream surface to the outer and inner shroud surfaces, when transferred to the conformal map (by the laws outlined in sec. 4.4.2), form on this map reasonable and continuously curving contours and, therefore, are acceptable. The total channel cross sections arrived at in this manner must be checked in some simple manner. In this example, these cross sections are found to be quite reasonable.

The vane contours so obtained along the outer and inner shroud surfaces are transferred to the axial end view shown in figure 4-62. There the vane contours present a geometrically consistent picture. It is, of course, possible to derive from the radial vane sections (fig. 4-61) and from the vane contours in figure 4-62 also board sections, that is, plane sections normal to the axis of rotation, and for that matter any other sections that would be helpful for the manufacturing process.

The actual channel width shown at the left in figure 4-63 is very nearly proportional to the cross-sectional channel area, because the channel width normal to it and shown in figure 4-61 is approximately constant. This relation indicates (by scaling) an increase in channel cross section by a factor of approximately 3, first rapid and later slow, as a zero rate of diffusion is approached. This change in cross section must be considered a hydrodynamically very severe total retardation of the flow. However, this retardation is dictated by the inlet and discharge flow conditions prescribed for this system, that is, the retardation from the absolute velocity leaving the impeller to the absolute velocity entering a similar impeller under similar flow conditions. This retardation is, therefore, the same for any duct system connecting successive stages; specifically it is the same for the three different crossover systems shown in figures 4-59 to 4-63. Which of these arrangements is hydrodynamically most advantageous can at present be answered only by experiment. As mentioned in the beginning of this section, the arrangement shown in figure 4-59 has an efficiency advantage over other arrangements because of the high retardation that is possible in a straight discharge from a volute casing. A multivane diffuser form using straight (tangential) diffuser passages is quite efficient. It is, of course, very similar to a multiple volute, as shown, for example, in figure 4-56.

In closing, we must answer the question of why the velocities entering a discharge or crossover duct system from a radial-flow impeller must be rather high in comparison with the total head of the stage.

It is a well-supported empirical fact that for standard centrifugal pump impellers (having backward-bent vanes and zero rotation of the incoming flow) the head coefficient $\psi = 2g_o H/U_o^2$ should have values near unity in order to achieve acceptable efficiencies. (Actually ψ is a function of the basic specific speed, and $\psi = 1$ applies to specific speeds between 0.1 and 0.12. For lower specific speeds, ψ should be greater than 1, but usually not over 1.1, because with higher ψ values the pump performance may become unstable. For specific speeds higher than 0.12, the head coefficient should be less than unity. For $n_s = 0.2$, the head coefficient is usually about 0.9.)

For $\psi = 1$, the peripheral component of the absolute impeller discharge velocity is $V_{U,o} = \psi U_o/2\eta_h = 0.56\ U_o$ for $\eta_h = 0.9$, and it is correspondingly higher for lower efficiencies. Thus $V_{U,o}^2/2g_o = 0.31\ H$, that is, the kinetic energy at the impeller discharge is about one-third of the net pump head, a proportion which illustrates the importance of the hydrodynamic quality of the stationary vane or duct system following the impeller. The situation is still more severe for pumps or compressors with radial impeller vanes (see fig. 4-20), where $V_{U,o}$ is at least $0.8\ U_o$, so that $V_{U,o}^2/2g_o$ is at least $0.4\ H$.

The empirical fact that for basic specific speeds around 0.1 head coefficients ψ below unity usually lead to poor efficiencies is commonly attributed to disk friction losses on the outside of the impeller shroud(s) and on the stationary shroud whenever an open impeller is used (see fig. 4-20). It is easy to show that the disk friction torque increases for a given angular velocity with the rotor diameter raised to a power of 5 and, therefore, with $\psi^{-5/2}$. Thus a reduction in ψ from unity to 0.9 increases the disk fricton losses by 30 percent. Moreover it is not certain that disk friction is the only reason for the effect of ψ on the efficiency, so that this effect could be greater.

Chapter 5

Some Mechanical Design Considerations of Turbomachinery

5.1 Introduction

Some mechanical design characteristics are discussed in sections 1.2.3 and 1.3.3 of chapter 1 on the basis of simple similarity considerations. None of these considerations are repeated in this chapter, but, in many cases, the results form the basis for this chapter.

The mechanical design of turbomachinery constitutes a very broad subject, particularly if rotor dynamics is considered. This chapter is not intended to cover all of this extensive field, nor to give a detailed stress analysis of stationary and rotating parts of turbomachines.

Instead the considerations of sections 1.2.3 and 1.3.3 are extended as far as possible by considerations of sufficient simplicity to permit their application in the early phases of preliminary design. This approach excludes, for example, the type of stress considerations employed by departments of stress analysis after the design forms of the machine and its parts have been established in a general manner. The only considerations presented are those which are usable for the initial establishment of a stress-determined design form and do not depend on extensive use of computers, because in the formative phase of design, the design engineer must be able to decide quickly which design form has a reasonable chance of meeting the requirements of the prescribed operating conditions. This approach to, and limitation of, the subject is the same as that used in the preceding chapters with respect to hydrodynamic design, although, in many cases, the latter has been carried to greater detail than is done in this chapter with respect to mechanical design problems.

Even with the limitations just mentioned, this chapter cannot make any claim to completeness. It simply covers a limited number of design problems which have come to the attention of this writer. No doubt there are numerous other design problems which should be treated, or at least mentioned, but with which this writer did not have sufficient contact to permit their treatment. The reason for this somewhat unsatisfactory situation is probably that the hydrodynamic (or gas-dynamic) design of turbomachines permits a fairly systematic approach, whereas there is no equivalent system for treatment of the mechanical design of turbomachines. This may partly be due to the fact that the overall design form of turbomachines is mainly determined by hydrodynamic considerations, although not entirely, as demonstrated in section 1.3.5 of chapter 1.

5.2 Stress Design of Rotating Parts

5.2.1 Elastic Stresses in Flat, Rotating Disks

The design of coaxially rotating disks is discussed in section 1.3.3.1, under the assumption of equal and uniformly distributed circumferential and radial stresses. In this case, the thickness distribution is a function of the stress coefficient $\rho_s U_1^2/2\sigma_c$, where the subscript 1 refers to a radius r_1 with a circumferential and radial stress σ_c (see figs. 1-31 and 1-33).

Generally circumferential and radial stresses in rotating disks are neither equal nor uniformly distributed. Equality is, in fact, impossible if the disk has a hole at its center, where the radial stress is either zero or a compressive stress, as in the case of a press or shrink fit on a shaft.

The elastic stress distribution in rotating disks is treated competently in references 2 and 67 and is not treated in detail in this compendium. Only a fundamental differential equation governing the stresses in a rotating disk of uniform temperature is derived, since it is the basis for other work in this field. This derivation is limited to the equilibrium of forces and neglects the compatibility of deformations (see the beginning of Sec. 5, ref. 58).

Figure 5-1 shows two radial sections through an axially symmetric disk, one normal to and one parallel to the axis of rotation. This figure defines the notation used in the equations that follow. It is evident from this figure that

$$\sigma_r br\, d\theta + \sigma_\theta b\, dr\, d\theta = (\sigma_r + d\sigma_r) \times (b+db)(r+dr)d\theta + \rho_s b\, dr\, r\, d\theta\, r\omega^2 \qquad (5\text{-}1)$$

where the left side expresses the radially inward forces acting on the element shown, and the right side the radially outward forces. This equation can be reduced algebraically to the form

$$(\sigma_\theta - \sigma_r)b\, dr - \sigma_r\, db\, r - d\sigma_r\, br = \rho_s b\, dr\, r^2\omega^2$$

and further to

$$b(\sigma_r - \sigma_\theta) + \sigma_r r\frac{db}{dr} + br\frac{d\sigma_r}{dr} + \rho_s br^2\omega^2 = 0 \qquad (5\text{-}2)$$

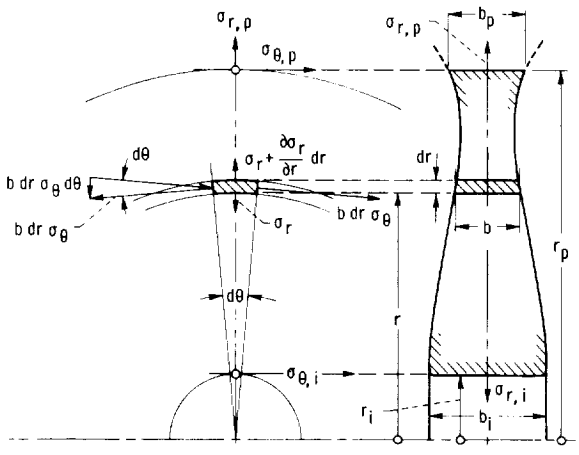

Figure 5-1. – Derivation of elastic stresses in rotating disks.

which is completely equivalent to equation (k) on page 72 of reference 67. From this equation, one can derive by various methods of integration the elastic stress distribution of a rotating disk with given dimensions. In all cases, the stresses are assumed to be uniform in the axial direction (i.e., the thickness-radius ratio is assumed to be reasonably small), and the disk is assumed to be flat (i.e., symmetrical to a plane normal to the axis of rotation, not dished). References 2, 58, and 67 present various methods of integrating equation (5-2). The integration must start with a prescribed radial stress at either the inside or (usually) the outside perimeter of the disk. The circumferential stress at this perimeter is usually not given, but must be assumed, and the assumption must be changed until the given boundary condition at the other perimeter is satisfied.

This process of trial and error can be eliminated by making use of the fact that elastic stress fields can be superimposed on each other. The method of solution is as follows: assume the aforementioned integration is started at the outer (peripheral) boundary with a prescribed radial stress $\sigma_{r,p}$ (e.g., a centrifugal blade pull, averaged over the circumference of the disk) and an assumed circumferential stress $\sigma_{\theta,p}$, which is generally of the same order of magnitude as $\rho_s U_p^2/2$ (in consistent units), where the subscript p refers to the outer (peripheral) boundary of the disk.

Assume furthermore that at the end of the integration there appears at the inside boundary ($r=r_i$) a radial stress $\sigma_{r,i,1}$ which violates the physical boundary condition at r_i since there the radial stress is usually $\sigma_{r,i}=0$ (or a fairly low compressive stress).

Next integrate equation (5-2) for the same disk at rest (i.e., for $\omega=0$) with $\sigma_{r,p}$ assumed to be 0 and $\sigma_{\theta,p}$ assumed to have any convenient value, say 1, 100, or the like. This second integration yields again a certain radial stress $\sigma_{r,i,2}$ at the inner boundary $r=r_i$.

All stresses so obtained for the disk at rest may now be changed by the ratio $\sigma_{r,i,1}/\sigma_{r,i,2}$, so that at $r=r_i$ the radial stress of the disk at rest is now $\sigma_{r,i,1}$. This new stress distribution is subtracted from the stresses obtained by the first integration of equation (5-2) for the rotating disk, and thus the unacceptable radial stress $\sigma_{r,i,1}$ obtained by the first integration is canceled. The stresses obtained by this subtraction, therefore, satisfy the boundary conditions at $r=r_p$ and $r=r_i$, because the stresses calculated for the disk at rest are obtained for zero

radial stress at the outer periphery of the disk, so that the subtraction of these stresses from those obtained by the first integration does not change the prescribed radial stress $\sigma_{r,p}$ at the outer periphery.

The solution of equation (5-2) described previously gives the elastic stress distribution for a rotating disk with a given thickness distribution $b(r)$ and db/dr. Thereby equation (5-2) can be integrated numerically in finite radial steps. Other methods of integration are described in references 2, 58, and 67. All these methods solve the familiar direct problem of finding the stresses in a disk of given shape rotating at a given speed with given inner and outer boundary conditions.

The indirect problem, that is, the design problem of finding the shape (thickness distribution) of that disk for a given stress distribution is solved by the familiar method using a disk of constant stress (see sec. 1.3.3.1), but only for the case of equal and uniformly distributed radial and circumferential stresses. Obviously this solution is particularly simple in this case since the first and third terms in equation (5-2) vanish. However, this solution excludes the possibility of a hole in the center of the disk (or anywhere else) because the stress normal to the periphery of a hole must vanish.

At first glance, equation (5-2) seems solvable (numerically) for the thickness distribution $b(r)$ if one assumes certain stress distributions $\sigma_r(r)$ and $\sigma_\theta(r)$. However, not every stress distribution assumed leads to a usable thickness distribution. As noted previously the most desirable stress distribution, $\sigma_r = \sigma_\theta =$ constant throughout the disk, is incompatible with any hole through the disk.

In order to solve equation (5-2) for the thickness distribution $b(r)$ in the general case of a hole through the center of the disk, one would have to first assume a practically useful thickness distribution $b(r)$, in particular, one that justifies the earlier assumption of a uniform stress distribution in the axial direction (i.e., across the disk) and then solve for the stress distribution as outlined previously. With a hole in the center of the disk, this stress distribution invariably shows a very rapid increase in the circumferential stress toward the inner boundary (i.e., the circumference of the central hole).

If the general stress level is unsatisfactory, say too high, one can try to solve for the thickness distribution with a lower stress distribution, a distribution which retains the same general form, in particular, the rapid rise of the circumferential stress toward the central hole. The assumed stress distribution should be kept somewhat flexible to correct for incompatibilities between the radial and the circumferential stresses during the process of integration. This writer is not aware of any attempts at form design of rotating disks by this method, so that its feasibility is not yet assured; successful use is almost certain to depend heavily on the experience and skill of the engineer carrying out this process. The assumption of a different thickness distribution with a lower thickness ratio b_p/b_i and solution for the stress distribution may be a more practical procedure.

In closing the discussion of elastic stresses in rotating disks, we reduce the governing differential equation (5-2) to dimensionless form and, thus, maintain the general practice of this compendium in this respect.

Dividing equation (5-2) by $\rho_s r_p^2 \omega^2 b_p$ and rearranging leads to the following dimensionless equation:

$$\frac{b}{b_p}\frac{\sigma_r-\sigma_\theta}{\rho_s r_p^2\omega^2} + \frac{\sigma_r}{\rho_s r_p^2\omega^2}\frac{db}{dr}\frac{r_p}{b_p}\frac{r}{r_p} + \frac{b}{b_p}\frac{r}{r_p}\frac{d\sigma_r}{dr}\frac{r_p}{\rho_s r_p^2\omega^2} + \frac{b}{b_p}\frac{r^2}{r_p^2} = 0 \qquad (5\text{-}3)$$

Introducing the dimensionless variables

$$\left.\begin{aligned} \frac{b}{b_p} &= B \\ \frac{r}{r_p} &= R \\ \frac{\sigma_r}{\rho_s r_p^2\omega^2} &= S_r \\ \frac{\sigma_\theta}{\rho_s r_p^2\omega^2} &= S_\theta \end{aligned}\right\} \qquad (5\text{-}4)$$

reduces equation (5-3) to the form

$$B(S_r - S_\theta) + S_r R\frac{dB}{dR} + BR\frac{dS_r}{dR} + BR^2 = 0 \qquad (5\text{-}5)$$

which is the same as equation (5-2) except that it is expressed in dimensionless variables. The variables S_r and S_θ are obviously equivalent to the reciprocals of the stress coefficient used in section 1.3.3.1. The dimensionless disk thickness B shows that all disks of the same thickness distribution referred to the thickness b_p at the outside radius r_p (see fig. 5-1) have the same stress distribution irrespective of the thickness-radius ratio. This result was obtained under the assumption of a uniform stress distribution in the axial direction (across the disk). This assumption limits the validity of the result to low thickness-radius ratios (i.e., to fairly thin disks).

Furthermore, as mentioned previously, the results apply only to disks which are symmetrical with respect to a plane normal to the axis of rotation.

5.2.2 Mean Stress Design of Flat, Rotating Disks

A relatively very simple approximation for the stresses in rotating disks is that based on the assumption of a uniformly distributed circumferential stress, called the mean stress. (The importance of the mean stress in the design of rotating disks was brought to the attention of this writer by Ronald B. Smith.) On the basis of what is said in section 5.2.1, this assumption would seem to be a very poor approximation for disks with a central hole, since the elastic circumferential stress rises rapidly toward the circumference of the central hole. In reality, the mean-stress approximation is not that bad, if the high elastic stress near the hole, or at some other places, exceeds the yield stress of the disk material. With ductile materials, since deformations after the yield stress is passed can be a multiple of the elastic deformations, the yielding portions of the disk do not accept more than the yield stress and pass part of their load on to the surrounding portions of the disk which are still in the elastic state. Thus, while the yielding portions are limited to the constant yield stress, the less stressed elastic portions are more highly stressed than according to the elastic stress analysis, so that the entire stress distribution becomes more uniform. Therefore it approaches that of the mean-stress assumption, which should, in fact, be completely satisfied when the entire disk has reached the yield stress. This hypothesis is reasonably well supported by tests of rotating disks to failure, which takes place at approximately the same mean stress almost independently of the form of the disk, for example, the presence or absence of a central hole (ref. 68).

Furthermore, after limited portions of the disk have yielded, the disk at rest would be expected to be prestressed, with the yielded portions in compression and the remaining portions in tension. If the deformation in yielding does not exceed the maximum elastic deformation of the material, repeated stressing does not necessarily involve major repeated yielding, so that the initial local yielding does not necessarily lead to a significant reliability risk (associated with fatigue failure).

The foregoing reasoning can be only approximately accurate. Nevertheless it seems to have sufficient practical value to warrant developing the mean-stress method in sufficient detail to be used for preliminary design.

In order to develop the mean-stress method, one considers the disk to be divided into two equal parts separated by a plane containing the axis of rotation. The centrifugal forces tend to separate these two parts along this plane, and the separating force F generates in the plane of separation a mean stress $\sigma_{\theta,m}$, so that

$$F = \sigma_{\theta,m} A \tag{5-6}$$

If A is the radial and axial section through the disk shown in figure 5-2, F must be the component of the centrifugal force of the one-quarter of the disk which is normal to the separating radial and axial plane OB in figure 5-2.

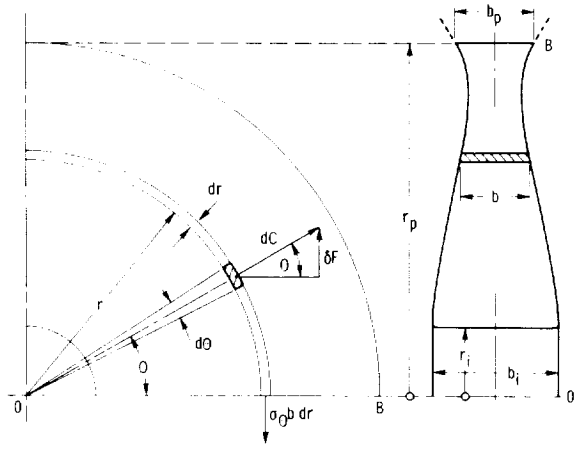

Figure 5-2. – Approximation of circumferential stress in rotating disk as hoop stress.

In order to determine the separating force F, divide the disk into a large number of rings of radius r, axial width b, and radial thickness dr. The centrifugal force acting on an element of this ring is

$$dC=\rho_s r\, d\theta\, b\, dr\, r\omega^2$$

Therefore its component δF normal to the plane of separation OB is

$$\delta F=dC\sin\theta=\rho_s\omega^2 r^2\, dr\, b\sin\theta\, d\theta \tag{5-7}$$

and the force dF acting on section OB is

$$dF=\rho_s\omega^2 r^2\, dr\, b\int_o^{\pi/2}\sin\theta\, d\theta=\rho_s\omega^2 r^2\, dr\, b \tag{5-8}$$

This force is resisted by the hoop stress according to the familiar relation

$$dF=b\, dr\,\sigma_\theta=\rho_s\omega^2 r^2\, dr\, b$$

so that the hoop stress is

$$\sigma_\theta=\rho_s\omega^2 r^2=\rho_s U^2 \tag{5-9}$$

a relation which is presented in subsection 1.3.3.1. This hoop stress is, of course, not constant as a function of the radius. It is related to the mean circumferential stress $\sigma_{\theta,m}$ by the equation

$$\sigma_{\theta,m}A=\int_{r_i}^{r_p}\sigma_\theta b\, dr=\rho_s\omega^2\int_{r_i}^{r_p} br^2\, dr \tag{5-10}$$

where the last integral is obviously the area moment of inertia I of section OB (area A) with respect to the axis of rotation.

From equation (5-10), it follows that

$$\sigma_{\theta,m}=\rho_s\omega^2\frac{\int_{r_i}^{r_p} br^2\, dr}{A}=\rho_s\omega^2\frac{I}{A}=\rho_s\omega^2 r_I^2 \tag{5-11}$$

where r_I is the radius of gyration of section OB (with area A), and, therefore,

$$r_I^2=\frac{I}{A}$$

or

$$r_I=\sqrt{\frac{I}{A}} \tag{5-12}$$

Figure 5-3 shows graphically the determination of I/A by showing the distribution of b at a greatly enlarged scale and by dividing r by r_p. Evidently, from equation (5-11),

$$\frac{r_I^2}{r_p^2}=\frac{\int_{r_i}^{r_p} b(r^2/r_p^2)dr}{A}=\frac{\int_{r_i}^{r_p} b(r^2/r_p^2)dr/r_p}{\int_{r_i}^{r_p} b\, dr/r_p} \tag{5-13}$$

so that the radius of gyration r_I divided by r_p appears as the square root of the ratio of the two areas, marked in figure 5-3 as ABCD and AECD. The br^2/r_p^2 curve AE can be derived from the $b(r)$ curve AB either numerically or graphically by the lines UVWXY and the ratio given by equation (5-13) by planimetric or numerical determination of the areas ABCD and AECD.

For the example shown in figure 5-3, $r_I^2/r_p^2=0.3059$ and $r_I/r_p=0.553$. The stress coefficient $\rho_s U^2/2\sigma$ (introduced in sec. 1.3.3.1) is, according to equation (5-11), $\rho_s U_I^2/2\sigma_{\theta,m}=0.5$, that is, the same as for a freely rotating, thin hoop. The stress coefficient referred to the outside radius r_p is

$$\frac{\rho_s U_p^2}{2\sigma_{\theta,m}}=\frac{\rho_s U_I^2}{2\sigma_{\theta,m}}\frac{r_p^2}{r_I^2}=\frac{0.5}{0.3059}=1.6345 \tag{5-14}$$

which characterizes the stress in the disk as described in sections 1.2.3 and 1.3.3.1 and permits, for example, the determination of the stress specific speed or a comparison with a stress specific speed given by the operating conditions, including the properties ρ_s and $\sigma_{\theta,m}$ of the disk material.

The ratio of the mean stress $\sigma_{\theta,m}$ used here to the yield stress σ_y of the material $\sigma_{\theta,m}/\sigma_y<1$ may well be considered the factor of safety because $\sigma_{\theta,m}=\sigma_y$ leads to unlimited yielding and thereby to failure. Furthermore attention must be paid to the question of whether at the operating temperature the material is still sufficiently ductile to justify the

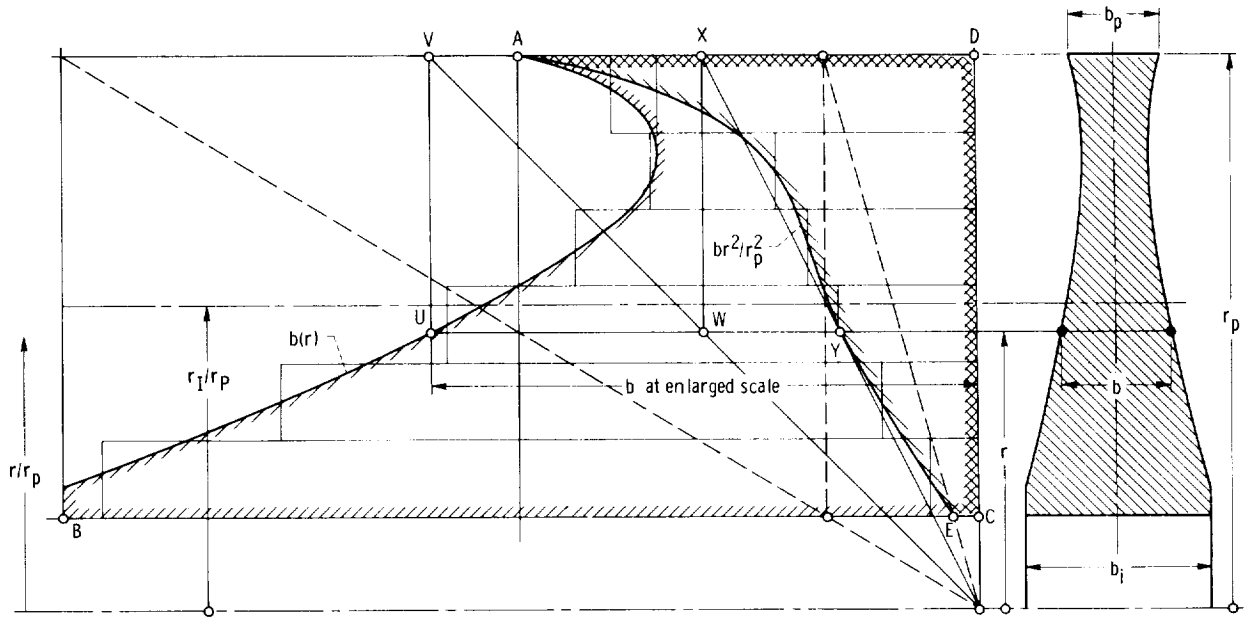

Figure 5-3. – Determination of radius of gyration of radial section through disk.

assumptions connected with the use of the mean stress.

The indirect or design problem of rotating disks calls for the determination of the disk thickness distribution $b(r)$ from a given stress coefficient. For the mean-stress method, equation (5-14) shows that the ratio of the radius of gyration r_I to the outer radius r_p is determined by the stress coefficient $\rho_s U_p^2/2\sigma_{\theta,m}$. Equation (5-13) shows that this ratio of radii determines the ratio of area ABCD to area AECD in figure 5-3. This area ratio does not determine the thickness distribution uniquely, but limits the choice of this distribution considerably for a given outer disk thickness b_p, which is usually prescribed by the vane system, the axial spacing between successive vane systems, and the like. In particular, the ratio b_i/b_p, while not uniquely determined by the stress coefficient and the resulting area ratio in figure 5-3, does increase with the stress coefficient, so that, if one design form fails to satisfy the required stress coefficient $(\rho_s U_p^2/2\sigma_{\theta,m})$, a profile having a higher b_i/b_p is likely to meet the requirements of a higher stress coefficient. However, no simple relation between b_i/b_p and the stress coefficient is as yet available.

Before the discussion on rotating disks is closed, it is necessary to define the r_p of the outer periphery of the disk somewhat more closely than done by the foregoing illustrations. From figure 1-33, it is evident that r_p has a different meaning than either r_1 or r_o used in chapter 1.

The radius r_p and all other variables with the subscript p refer to the maximum diameter of the disk which is capable of sustaining a circumferential tensile stress σ_θ. That this is not necessarily the maximum diameter of the disk is illustrated in figure 5-4, which shows the so-called fir-tree fastening of blades at the periphery of the disk. Obviously no circumferential tensile stress can be carried across the fir trees, so r_p must be the root radius of the fir trees. There are other forms of blade fastening where the determination of r_p is not

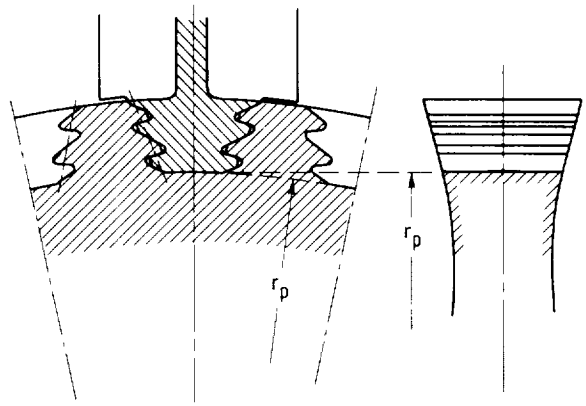

Figure 5-4. – Definition of r_p for rotating disk.

as simple as in figure 5-4, but useful approximations of r_p can always be found on the basis of the foregoing general definition. It should be obvious that parts of the disk extending outside r_p must be included with the blades when calculating the radial stress $\sigma_{r,p}$ at the perimeter with radius r_p.

5.2.3 Remarks on Thin-Walled, Hollow Bodies of Revolution in Bending

Hollow bodies of revolution which are subject to a bending moment are used in turbomachinery design primarily in connection with rotors of relatively large diameter, as shown, for example, in figure 1-39. No particular problem arises if, as shown in that figure, the wall thickness is sufficient to prevent deformation of the cross sections of the body from their original circular shape. In this case, the bending stiffness of the body can be based on the area moment of inertia of its circular, ring-shaped cross sections in the same manner as customary for solid shafts.

However, if the wall thickness of the body is small, the foregoing assumption that its cross sections remain circular when subjected to a bending moment is no longer justified. Rather the body is deformed as shown in figure 5-5 (greatly exaggerated), so that its cross sections do not remain circular, but become egg-shaped. As a consequence, there exists a deformation in bending which would not exist if the cross sections would remain circular and which is much greater than that which would exist without out-of-round deformations.

It would be very difficult, if not impossible, to predict theoretically the bending deformation due to out-of-round deformations. Certainly, this theoretical prediction would be too complicated for preliminary design considerations. Instead it would be more practical to eliminate out-of-round deformations by appropriate design measures. Figure 5-6 shows the most obvious way in which this can be accomplished, that is, by a flat diaphragm normal to the axis of rotation. This diaphragm does not need to be thick to prevent out-of-round deformations, as long as it is prevented from buckling by something like the rim on the inner boundary shown in figure 5-6.

The reinforcement against out-of-round deformation is required only at places where the outer shell changes its direction in relation to the axis of rotation. Cylindrical and straight conical shells do not require such reinforcement.

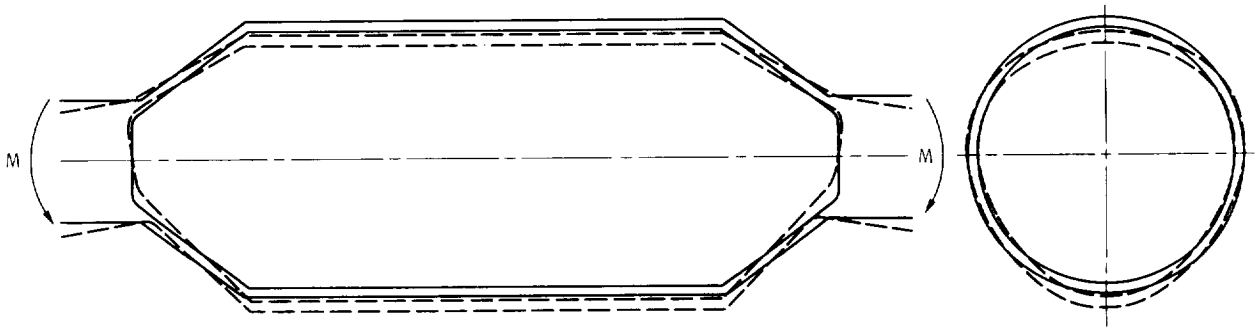

Figure 5-5. – Exaggerated deformation of thin-walled body of revolution under bending moment M.

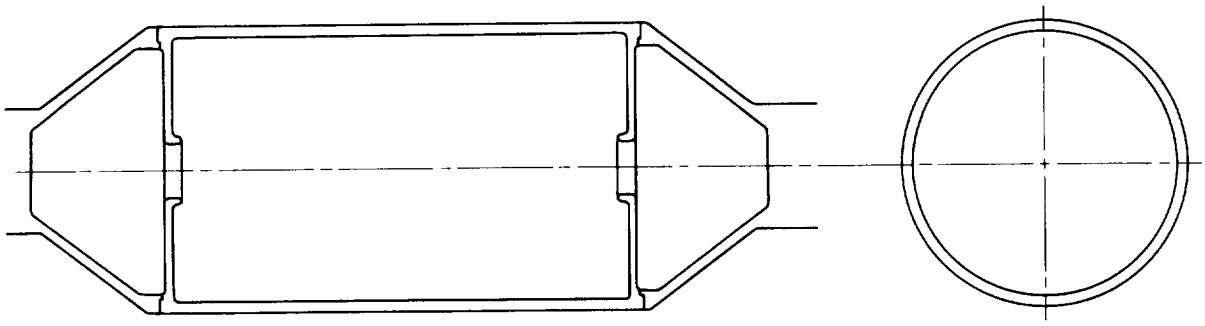

Figure 5-6. – Reinforcement against out-of-round deformations of thin-walled body of revolution under bending moment.

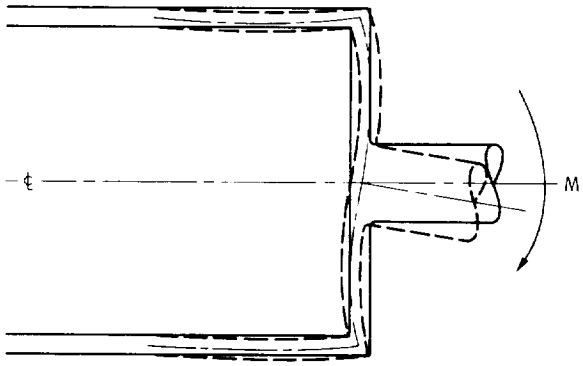

Figure 5-7. – Alternative form of deformation of thin-walled body of revolution under bending moment M.

An alternative form of deformation of a thin-walled body of revolution is shown in figure 5-7. In this case, the unacceptable deformation takes place mainly in a flat, disk-shaped member connecting two parts of the body having substantially different diameters.

Again a theoretical prediction of this form of deformation would be quite complex, certainly too complicated to be carried out in connection with preliminary design. Instead one should introduce some simple form of reinforcement preventing the deformation shown in figure 5-7. One possible form of such reinforcement is shown diagrammatically in figure 5-8. As in the previously described case, this example is intended to call attention to certain forms of deformation which might be overlooked in the process of preliminary design and to the principles of their prevention.

The foregoing considerations are not limited to rotating thin-walled bodies of revolution. They apply to any hollow, fairly thin-walled body of revolution under bending. In the present case, it is left to the intuition of the design engineer to decide when a body should be considered thin-walled in the sense of the foregoing considerations. The examples shown in figures 5-5 and 5-7 certainly require the reinforcements in figures 5-6 and 5-8. The axial-flow pump rotor shown in figure 1-39 may be a borderline case, where a detailed deformation analysis is necessary to decide whether reinforcement against out-of-roundness is required.

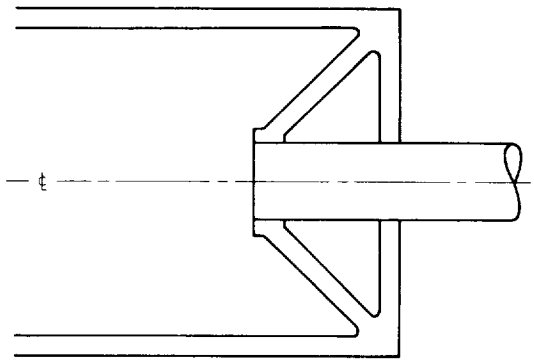

Figure 5-8. – Alternative reinforcement of thin-walled body of revolution against bending moment.

5.3 Stress Design of Turbomachinery Casings

5.3.1 Introduction

The simplest forms of casing design are discussed in section 1.3.3.3. Among them are the cylindrical casing form and the spherical casing form. Figure 1-39 gives examples for both, since the discharge portion of the casing can advantageously be spherical. The simplicity of the casing design is, in fact, one very important advantage of multistage axial-flow pumps for high absolute pressures.

This section deals primarily with the mechanical design problems of volute casings. Volutes constitute a complex and severe design problem whenever used in connection with high absolute casing pressures. They have been used this way for many years in the field of high-head hydraulic turbines, where the strength of the volute casing depends almost entirely on internal vanes called stay vanes. Volute pumps for pressures of the order of 1000 pounds per square inch (or more) have been used in the rocket pump field.

High-pressure volute casings are designed mechanically on the basis of three different reinforcement principles: external radial ribs, axial extensions of the casing with a force-carrying connection with the end covers, and, finally as previously mentioned, internal force-carrying vanes. These three methods of design are described in sections 5.3.2, 5.3.3, and 5.3.4. Section 5.3.5 deals with some design details. In accordance with the general philosophy of this compendium, the stress analysis is restricted to considerations of sufficient simplicity to be applicable to the formative phases of preliminary design.

5.3.2 Volute Casings Reinforced Against Internal Pressure by External Radial Ribs

Pump volute casings without diffuser vanes can and have been made resistant to high internal

pressures by selecting a sufficiently large casing wall thickness. This solution can be used only where basic specific speeds are low, say 0.06 or less; where the absolute dimensions are fairly small, where the wall thickness dictated by foundry considerations is sufficient to resist the internal pressure; where it is unnecessary to minimize the weight of the machine; and where simplicity of form is more important than the cost of the additional material.

In other instances, it is necessary to make a volute casing without diffuser vanes resistant to the internal gage pressure by selecting an external design form which provides the required strength without excessive wall thickness. Figure 5-9 shows a single-volute casing reinforced by external radial ribs. As shown in figures 4-54 to 4-56, the same form of reinforcement is applicable to twin- and multiple-volute casings, which, of course, require radially smaller ribs than a single-volute casing for the same total flow areas.

In figure 5-9, the impeller discharge pressure p in excess of the ambient pressure is assumed to exist internally between the outer contour of the volute passage and wearing rings. The pump inlet pressure inside the wearing rings is assumed to be equal to the external (ambient) pressure and, therefore, has no effect on the casing stresses. Departures from this assumption are easily considered by applying the inlet gage pressure inside the wearing rings.

The radial component of the internal pressure is taken up by approximately circumferential stresses in the volute walls, which are not considered because they are of secondary importance compared with the bending stresses produced by the axial component of the internal pressure; the latter produce a toroidal moment tending to open the horseshoe-shaped radial sections through the volute casing. The axial pressure forces acting on the end covers are transmitted to the volute casing by the net bolt forces A (not including seal pressure). The stresses in the end covers are discussed in section 5.3.3.

There are two mechanical design characteristics of the volute casing shown in figure 5-9 which deserve special consideration:

The first is the tongue, or splitter, of the casing, which, of course, provides a far stiffer connection between the two axial halves of the casing than the external ribs. This stiffness causes a considerable stress concentration at the tongue. This stress concentration can never be completely avoided with this design form, but it can be reduced to a tolerable level by the design detail shown in figure 5-9, that is, the cylindrical, axial extensions on both sides of

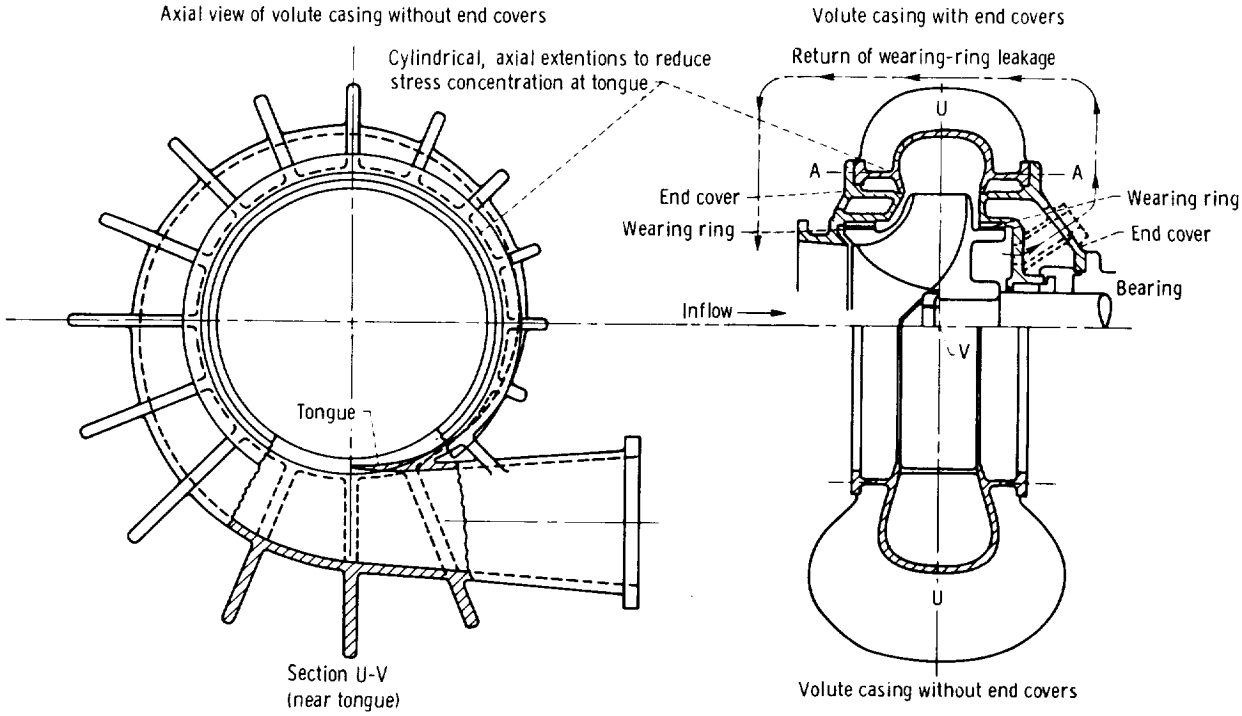

Figure 5-9. – Single-volute casing reinforced against internal pressure by external ribs.

the casing which carry the flanges necessary to attach the end covers of the casing. If these cylindrical extensions have distinctly larger radius than the distance of the end of the tongue from the axis (as shown), the axial force they transmit does not load up the end of the tongue but only the thicker portions a fair distance from its relatively thin end. Any stress concentration at the thin end of the tongue is, thereby, reduced to a significant degree. Without this design feature, the stress concentration at the end of the tongue might well lead to local failure.

The second design characteristic that deserves consideration, even in only preliminary phases of design, is the effect of beam curvature on the stresses in the curved elements consisting of a radial rib and the connected part of the casing wall. At first, it might appear reasonable to neglect the effect of curvature in a preliminary design consideration. However, as shown by the following discussion, the effects of beam curvature are sufficient in this instance to render the results obtained on the basis of a straight beam not only inaccurate but also incorrect in a fundamental fashion. The effects of beam curvature (curvature of the radial ribs and the wall as seen in radial, and axial, sections) must, therefore, be considered even for preliminary calculations.

Stresses in a curved beam can be analyzed in a fairly rigorous fashion on the basis of the general theory of elasticity. This analysis might be quite complex for a beam shaped according to radial sections through the casing shown in figure 5-9. The cross section of this beam covers approximately the spacing from rib to rib and is, therefore, T-shaped, with the casing shell forming the horizontal part of the T and the radial rib forming the vertical part. The following simplified analysis is carried out under the classical assumption that plane sections normal to the curved beam (i.e., radial sections relative to the curved beam) continue to be plane after deformation. This situation is shown in figure 5-10, which represents a section in the plane of the curved beam, that is, in the plane of one of the ribs in figure 5-9.

To be considered is an element between two radial sections AB and DC having a circumferential extent measured by the angle $d\varphi$. Assume section DC remains unchanged under the influence of forces and moments applied to this element; then section AOB is displaced to A'OB' (vastly exaggerated in the figure), that is, AB is rotated about O by the angle $\Delta d\varphi_b$, while, according to the foregoing assumption A'OB' continues to be a straight line. The location of point O, or the magnitude of the radius r_o, is defined as the point and radius of zero stress, wherever this occurs.

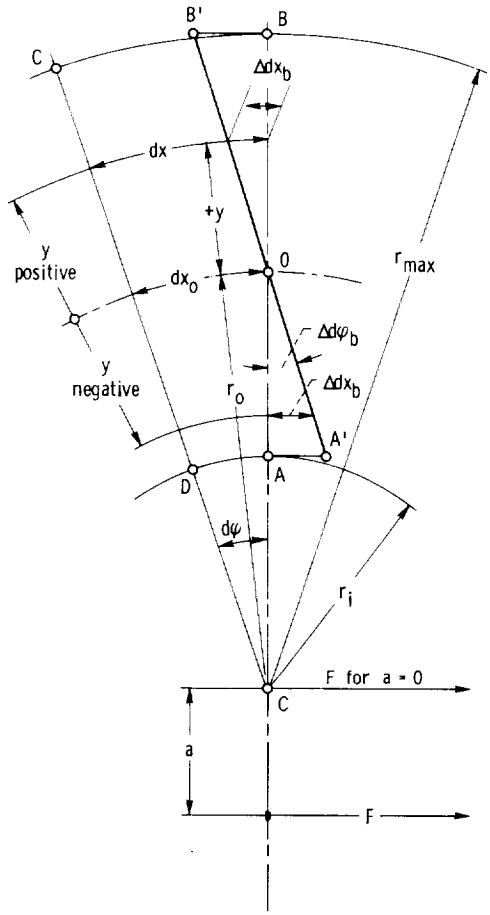

Figure 5-10. – Diagram for deformations in curved beam.

Evidently

$$\left.\begin{aligned} dx &= (r_o + y)d\varphi \\ dx_o &= r_o\, d\varphi \\ \Delta dx_b &= y\, \Delta d\varphi_b \\ \frac{\Delta dx_b}{dx} &= \frac{\sigma_b}{E} \quad \text{at the same } r \end{aligned}\right\} \qquad (5\text{-}15)$$

Hence

$$\frac{\sigma_b}{E} = -\frac{y}{r_o + y}\frac{|\Delta d\varphi_b|}{d\varphi} = -\frac{y/r_o}{1 + y/r_o}\frac{|\Delta d\varphi_b|}{d\varphi} \quad (5\text{-}16)$$

where σ_b is the bending stress only and does not include the uniformly distributed tensile stress σ_o. (Tensile stresses are counted as positive.)

For the total stress $\sigma = \sigma_o + \sigma_b$, equation (5-16) assumes the form

$$\frac{\sigma}{E} = \frac{\Delta dx_o}{r_o\, d\varphi} - \frac{y/r_o}{1 + y/r_o}\frac{|\Delta d\varphi_b|}{d\varphi} \quad (5\text{-}17)$$

where Δdx_o is the uniform deformation caused by σ_o only. If F is the axial force exerted on cross section U-V (see figs. 5-9 and 5-11), this section being normal to the axis of rotation of the machine (right side of fig. 5-9), then

$$F = \sigma_o \int_{r_{min}}^{r_{max}} b\, dy = \sigma_o A \quad (5\text{-}18)$$

where A is the area of a cross section normal to figure 5-10, and b is the width of the same cross section as indicated in the right side of figure 5-11. The moment of this force is

$$F(r_o + a) = -\int_{r_i}^{r_{max}} \sigma_b b y\, dy \quad (5\text{-}19)$$

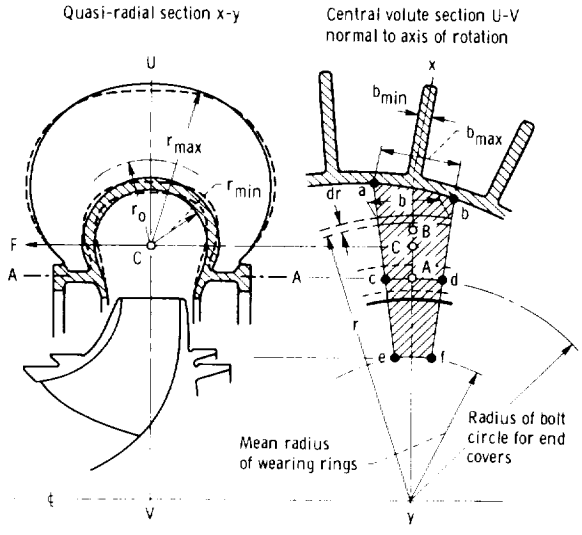

Figure 5-11. – Simplified curved-beam approximation of radial volute section.

where a is the radial distance of the force F from the center of curvature C, shown in figure 5-10, and the negative sign results from the definition of $+y$ given in figure 5-10.

A general solution of equations (5-16) to (5-19) is attempted here by using two simplifying assumptions which were introduced by Föppl in his classical treatment of the curved beam in bending, given in reference 69. It is assumed that the vector of the force F applied to the curved beam passes through the center of curvature of the beam, so that (in eq. (5-19) and fig. 5-10) $a = 0$. Furthermore it is assumed, according to Föppl (ref. 69) that the axis of zero bending stress ($\sigma_b = 0$), designated by O in figure 5-10, coincides with the center of gravity of the cross section considered and that its location is, therefore, known. This assumption cannot be correct, since according to equations (5-16) and (5-17) the stress distribution is not linear as usually assumed for straight beams in bending. This second assumption by Föppl is examined critically later in this section, after some results have been obtained by using the two simplifications just mentioned.

The first assumption ($a = 0$) is shown in figure 5-11 to be a reasonably good approximation if the general form of radial volute sections shown in figure 5-9, and by dashed lines at the left side in figure 5-11, is replaced by a cross section with circular contour, shown by solid lines at the left side in figure 5-11. This approach is quite acceptable. The internal pressure force per rib acts on the center of gravity B of the area acdb, whereas the pressure acting on the casing end covers, area cefd, is transmitted to the volute casing at the point A, representing a bolt force at the end flange of the casing. The center of curvature C of the curved volute cross section has a very reasonable relation to the points A and B (with uniform static pressure assumed), since the distance BC times the area acdb is approximately equal to the distance AC times the area cefd. This approximate equality was found, without being intended, from the assumed layout of the volute casing. Thus, in equation (5-19), the assumption $a = 0$ can be used as a fair approximation.

The fact that the reinforcing ribs are not strictly radial, so that section x-y is not exactly plane, is ignored in the following considerations, because the departure of the direction of the ribs from the radial direction is usually much smaller than shown in figure 5-11.

Since the solution to the uniform tensile stress σ_o is rather trivial on basis of equation (5-18), one is

concerned primarily with the solution of equations (5-16) and (5-19) relative to the bending stress σ_b. This solution is attempted by introducing the following dimensionless variables:

$$\left.\begin{aligned} y' &= \frac{y}{r_o} \\ \text{and, therefore,} \\ dy' &= \frac{dy}{r_o} \\ b' &= \frac{b}{b_{max}} \\ \sigma_b' &= \frac{\sigma_b}{E} = \frac{-y|\Delta d\varphi_b|}{(r_o+y)d\varphi} = \frac{-y'}{1+y'}\,\frac{|\Delta d\varphi_b|}{d\varphi} \end{aligned}\right\} \quad (5\text{-}20)$$

where the notation is derived from figure 5-10.

The negative sign results from the deformation assumed in figure 5-10, which causes tension in the inner fibers and compression in the outer fibers, where a negative deformation is associated with the compression of fibers in the region $y>0$. As usual, tensile stresses are considered positive.

With the variables introduced by equations (5-20) and the assumption $a=0$, equation (5-19) appears in the form

$$F = E\frac{|\Delta d\varphi_b|}{d\varphi} b_{max} r_o \int_{r_{min}}^{r_{max}} b'\,\frac{y'}{1+y'}\,y'\,dy' \quad (5\text{-}21)$$

Evidently, according to figure 5-11 (right side),

$$F = pA_{aefb} \quad (5\text{-}22)$$

where p is the internal static pressure above ambient acting on the area aefb. When the last of the equations (5-20) is used, that is, applied to $y=y_i$ and $r_i=r_{min}$ (see fig. 5-12), where $\sigma_b=\sigma_{b,i}$, equation (5-21) can be written in the form

$$p = -\sigma_{b,i}\frac{b_{max}\,r_o}{A_{aefb}} \int_{r_{min}}^{r_{max}} b'\,\frac{y'/(1+y')}{y_i'/(1+y_i')}\,y'\,dy' \quad (5\text{-}23)$$

The bending stress $\sigma_{b,i}$ at the inner boundary of the beam is expected to be of primary importance since it is to be added to the uniform tensile stress σ_o (eq.

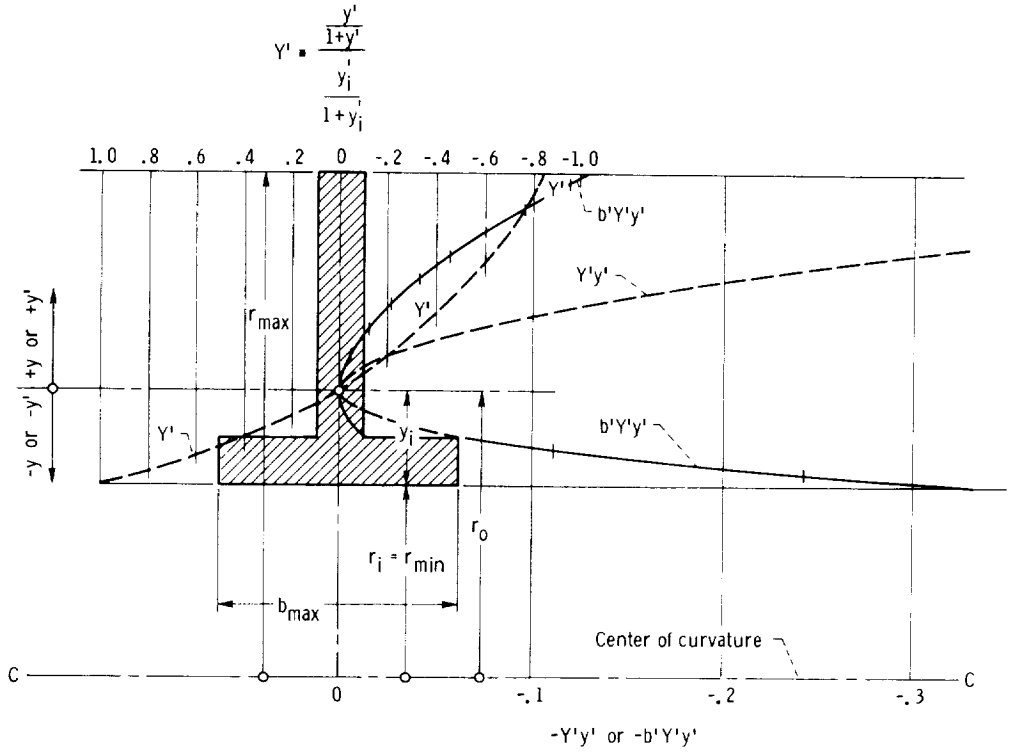

Figure 5-12. – Determination of bending stress in strongly curved beam, for example, in volute casing shown in figure 5-11.

(5-18)) and the combination may well be the maximum total stress.

The numerical solution of equation (5-23) is shown in figure 5-12, where

$$Y' = \frac{y'/(1+y')}{y_i'/(1+y_i')}$$

With the ratios of dimensions scaled from figures 5-11 and 5-12 (the rib and wall thickness from fig. 5-12 only), the following approximate results are obtained:

$$\frac{y_i'}{1+y_i'} = -\frac{1}{2}$$

$$\frac{b_{max}\, r_o}{A_{aefb}} = 0.72$$

$$\int_{r_{min}}^{r_{max}} b'\, Y' y'\, dy' = -0.067$$

the last of which, by equation (5-23), leads to

$$\frac{p}{\sigma_{b,i}} = 0.72 \times 0.067 = 0.048$$

$$\sigma_{b,i} = 20.8\, p$$

To this value of the bending stress, which is a tensile stress, one must add the uniformly distributed tensile stress σ_o, which, according to equations (5-18) and (5-22) is

$$\sigma_o = \frac{F}{A} = \frac{pA_{aefb}}{A}$$

where A is the area of the T-shaped cross section of the volute wall. According to figures 5-11 and 5-12, the area ratio is approximately $A_{aefb}/A = 4$. Hence $\sigma_o = 4\, p$, and the total maximum stress is

$$\sigma_{max} = \sigma_o + \sigma_{b,i} = 4\, p + 20.8\, p = 24.8\, p$$

It should be understood that the definition of the positive and negative sign of the pressure p is opposite to the previously stated definition of the stress σ, where tension is defined as positive, whereas pressure (compression) is defined as positive with respect to p.

The foregoing results were obtained under the previously mentioned assumptions that (1) the resultant force vector F passes through the center of curvature C and (2) the neutral axis ($\sigma_b = 0$) passes through the center of gravity of the T-shaped cross section of the curved beam (as if it were a straight beam). While the first assumption was demonstrated to be reasonable for the configuration shown in figure 5-11, the second assumption is yet to be checked. This consideration is given by Timoshenko in reference 70 in analytical form. In this section, the required demonstration is given graphically.

The condition to be satisfied is that the total force exerted by the bending stresses alone must be zero (see ref. 70), that is,

$$\int_{r_i}^{r_{max}} \sigma_b b\, dy = 0 \qquad (5\text{-}24)$$

With the notation introduced by equations (5-20) and (5-16), equation (5-24) can be written in the form

$$E\frac{|\Delta d\varphi_b|}{d\varphi}\int_{r_i}^{r_{max}} \frac{y/r_o}{1+y/r_o}\, b\, dy$$

$$= E\frac{|\Delta d\varphi_b|}{d\varphi} r_o b_{max}\int_{r_i}^{r_{max}} \frac{y'}{1+y'}\, b'\, dy' = 0 \qquad (5\text{-}25)$$

where with any substantial pressure loading $E|\Delta d\varphi_b|/d\varphi$ is not zero, so that the condition to be satisfied reduces to

$$\int_{r_i}^{r_{max}} \frac{y'}{1+y'}\, b'\, dy' = 0 \qquad (5\text{-}26)$$

This condition is satisfied in figure 5-13 by trial and error. First, the integrand is plotted against y' for the neutral axis (AA) running, according to Föppl's assumption, through the center of gravity of the section, which results in the irregular line A'A'A'A'A'. Numerical integration yields

$$\left|\int_{y=0}^{r_{max}} \frac{y'}{1+y'}\, b'\, dy'\right| \cong 0.75 \left|\int_{y=0}^{r_i'} \frac{y'}{1+y'}\, b'\, dy'\right|$$

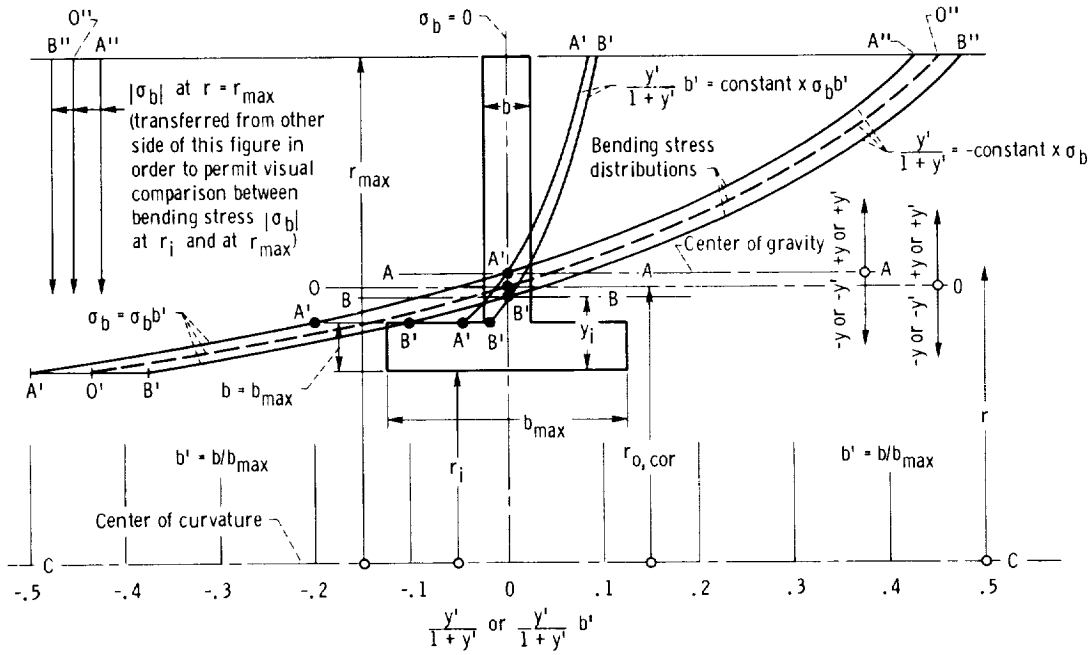

Figure 5-13. – Determination of neutral axis of curved beam.

so that

$$\int_{r_i}^{r_{max}} \frac{y'}{1+y'} b'dy' < 0$$

which does not satisfy equation (5-24). Second, it is assumed (arbitrarily) that the distance y_i of the neutral axis from r_i is three-fourths of this distance y_i previously assumed (fig. 5-12). Under this assumption, one obtains the irregular line B'B'B'B'B', with the neutral axis BB, and the integration yields

$$\left| \int_{y=0}^{r_{max}} \frac{y'}{1+y'} b'dy' \right| \cong 1.2 \left| \int_{y=0}^{r_i} \frac{y'}{1+y'} b'dy' \right|$$

so that

$$\int_{r_i}^{r_{max}} \frac{y'}{1+y'} b'dy' > 0$$

This equation shows that by this assumption one has overshot the goal set by equation (5-24).

According to equations (5-16) and (5-20), the relation between the dimensionless variables used in figure 5-13 and the bending stress σ_b is

$$\frac{y'}{1+y'} b' = -\sigma_b b' \frac{d\varphi}{\Delta d\varphi_b E}$$

or

$$\frac{y'}{1+y'} = -\sigma_b \frac{d\varphi}{\Delta d\varphi_b E}$$

where $d\varphi/\Delta d\varphi_b E$ = constant for any one geometric configuration and pressure loading of the casing.

Evidently the irregular lines A'A'A'A'A' and B'B'B'B'B' in figure 5-13 can be converted by division by b' into smooth $y'/(1+y')$ curves A''A'A'A' and B''B'B'B', which represent the (dimensionless) stress distributions A''A'A'A', according to the earlier assumption that $\sigma_b = 0$ at the center of gravity, and B''B'B'B', for the assumed different location of the neutral axis BB. The preceding evaluation of equation (5-24) indicates that the true stress distribution must lie between the smooth curves A''A'A'A' and B''B'B'B', slightly closer to the B''B'B'B' than to the A''A'A'A' curve. The dashed curve O''O' may, therefore, be accepted as an adequate approximation of the true bending stress distribution, with a third location of the neutral ($\sigma_b = 0$) axis OO.

In order to determine the scale of the new stress curve O''O', one must introduce the corrected value of r_o (locating the new neutral axis) into equation (5-23) and into the y' values used therein; that is, using the corrected r_o value, one repeats the process shown in figure 5-12. This revised

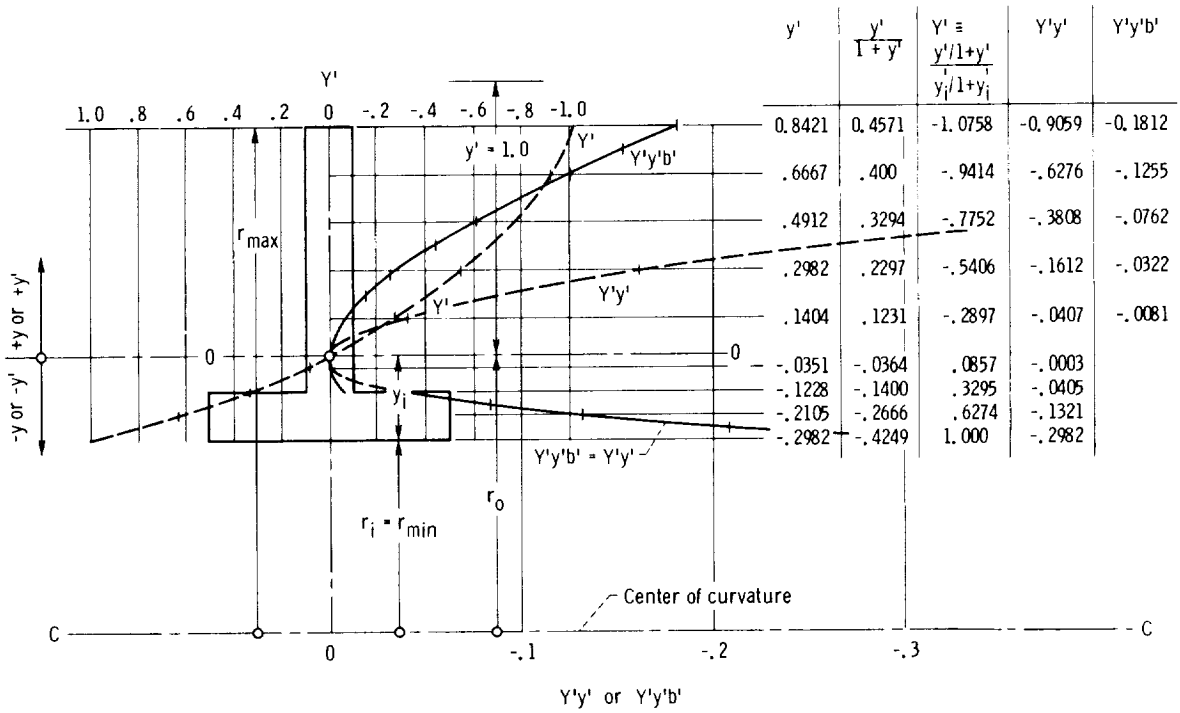

Figure 5-14. – Determination of bending stresses in strongly curved beam (volute casing section) with neutral axis corrected (see fig. 5-13).

determination of the bending stress distribution is shown in fugure 5-14 and, according to equation (5-23), leads to the result $p/\sigma_{b,i} = 0.057$ (i.e., $\sigma_{b,i} = 17.5\ p$). The comparison with the previous result $\sigma_{b,i} = 20.8\ p$ reflects the effect of the shift of the neutral axis derived from equations (5-25) and (5-26).

The addition of the uniform stress σ_o, of course, the same as described previously, leads to a total stress at r_i of $\sigma_{b,i} + \sigma_o = (17.5 + 4)\ p = 21.5\ p$, which is by a factor of $21.5/24.8 = 0.87$ lower than the value obtained when disregarding the shift of the neutral axis from the axis through the center of gravity. With the corrected r_o value, the bending stress σ_b at the inside wall of the beam is about equal to the compressive stress at the maximum distance r_{max} from the center of curvature, and even with the departures from the corrected location (OO) investigated in figure 5-13 (curves A″A′A′ and B″B′B′), the difference in the stress σ_b between the inside r_i and the outside r_{max} of the curved beam does not exceed 25 percent of the mean value of the stresses at r_{max} and r_i. On the other hand, if one had ignored the curvature of the beam completely by assuming a linear stress distribution, the bending stresses would have been proportional to the distance from the center of gravity of the section, that is, 2.25 times greater at the outermost boundary than at the innermost boundary. As mentioned previously, this solution could not be regarded as a useful approximation. The principal effect of curvature of a beam in bending is, therefore, the nonlinearity of the bending-stress distribution rather than the resulting departure of the neutral axis from the center of gravity of the section. The original assumption that the neutral axis passes through the center of gravity of the cross section considered may, therefore, still be accepted as a first approximation, but a better approximation for the location of the neutral axis is fairly easy to obtain, as shown in figure 5-13.

It is evident that the numerical results, while dimensionless, nevertheless represent only an example and will change with departures from the dimensionless geometric configuration shown in figures 5-11 and 5-12. In the more general design process, it may be well to consider two simple design principles:

(1) If the stresses are obtained for an assumed configuration and if the wall and rib thicknesses are not very large compared with other local dimen-

sions of the casing, stresses may be assumed to be inversely proportional to the wall and rib thicknesses. Thus moderate discrepancies in stresses encountered with the first approximation of a design can be corrected approximately by corresponding changes in the wall and rib thicknesses.

(2) As a first approximation, one might be tempted to consider b_{max} as equal to the circumferential distance between successive radial ribs. This assumption would be based on circumferentially uniform bending stresses in the volute casing between successive ribs. Actually these bending stresses must be expected to be a maximum near the juncture between the rib and the casing wall and to diminish with increasing circumferential distance from the rib. Therefore, if the calculated bending stress is to represent the maximum rather than an average bending stress, b_{max}, as used in the foregoing calculations, must be made somewhat smaller than the circumferential distance between successive ribs measured along the wall of the casing.

As already mentioned, in principle, the reinforcement of twin or multiple volutes with separate discharge nozzles can be handled by external ribs just like this type of reinforcement for single-volute casings. However, a twin-volute casing with joining discharge (or inlet) ducts such as shown in figure 4-54 presents a somewhat different problem in the part where the discharge duct of one volute is wrapped tightly around the outside of the inner volute. Figure 5-15 shows the reinforcement of this type of a twin-volute casing by means of external radial ribs.

It is immediately evident that in the twin-duct part of the casing the radial extent of the ribs is dramatically reduced in comparison with that in a single-volute casing having the same total duct area. The radial extent of the ribs at this part of the casing is even less than the height of the ribs reinforcing the single-volute part of the casing, because the outer duct constitutes a very effective reinforcement of the inner volute of the twin-duct part. Thus the twin-volute construction shown in figure 5-15 has not only a hydrodynamic advantage (the balancing of radial hydrodynamic forces), but

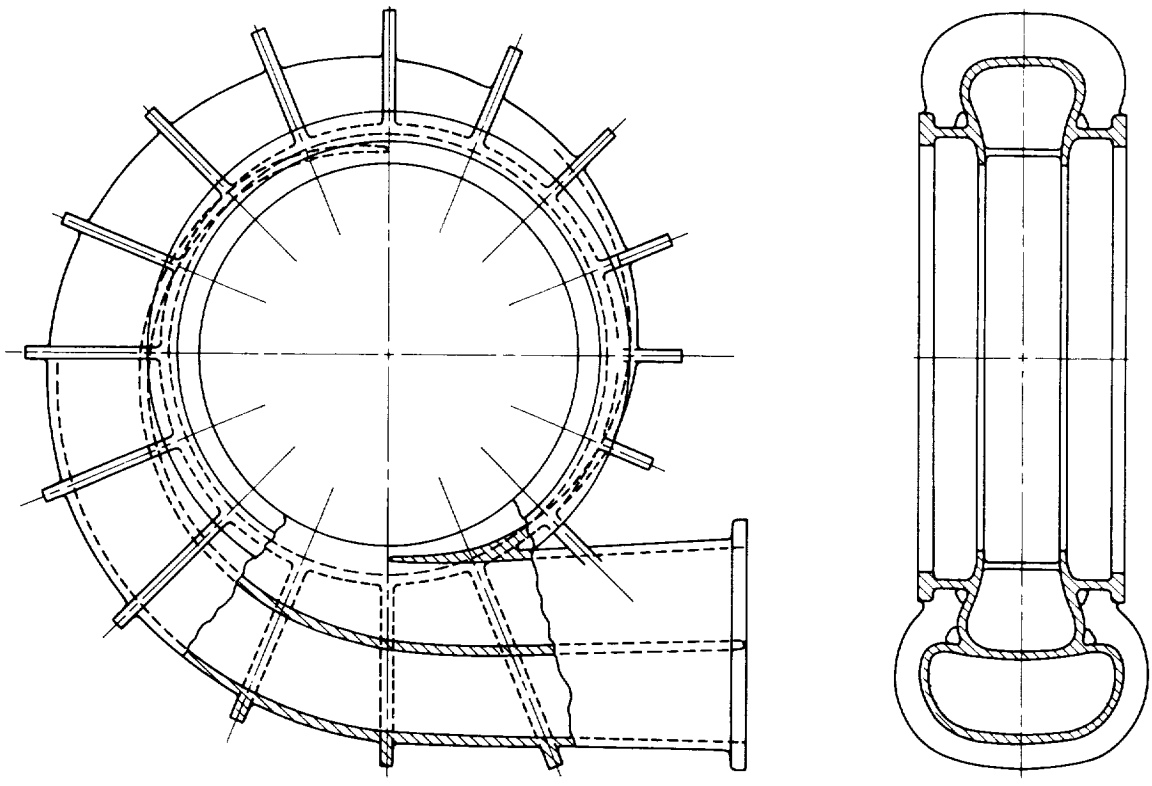

Figure 5-15. – Twin-volute casing reinforced against internal pressure by external ribs.

also a major mechanical advantage regarding the strength of the casing with respect to internal pressures.

The design shown in figure 5-15 minimizes the stress concentration at the two tongues (or splitters) of the casing in the same manner as previously described in connection with figure 5-9.

5.3.3 Volute Casings Reinforced Against Internal Pressure by Form of Pressure-Resisting Parts of Casing

The moments tending to open up a volute casing under internal pressure can be reduced by increasing the diameter of the axial and cylindrical extensions shown in figures 5-9 and 5-15 toward the flanges holding the end covers. In this way, the toroidal bending load on the volute is replaced by the axial load on the end covers, and the somewhat complex stressing of the end covers is increased. The more-or-less flat end covers can resist an axial load only by circumferential stresses in a structure of some axial depth. This is discussed in greater detail later in this section.

The aforementioned reasoning leads to surrounding the volute casing by an essentially cylindrical casing covered on both ends by more-or-less flat covers of sufficient axial depth to resist the internal pressure. However, there must be a more favorable shape than the cylindrical shape to accomplish this purpose. A shape approximating a sphere would be more favorable, partly because the spherical shape is most effective against internal pressure (see sec. 1.3.3.3, eq. (1-121a)) and partly because an approximately spherical shape results in a somewhat smaller flange diameter for the end cover(s). In 1936, this reasoning led to a form of casing design for the high-head pumps of the Colorado River Aqueduct which was similar to that shown in figure 5-16. In this case, the radial rib construction discussed in the previous section would have required rib thicknesses which were not feasible because of foundry considerations. Thus a combination of external radial ribs and the design principle shown in figure 5-16 was used. Later this design principle was used successfully without external ribs. It is evident that this design principle uses circumferential stresses to retain the internal pressure. Figure 5-16 shows the pump with a vertical shaft merely because the first pumps using this design principle had this arrangement. Obviously the direction of the shaft generally has no effect on the design of the pump casing.

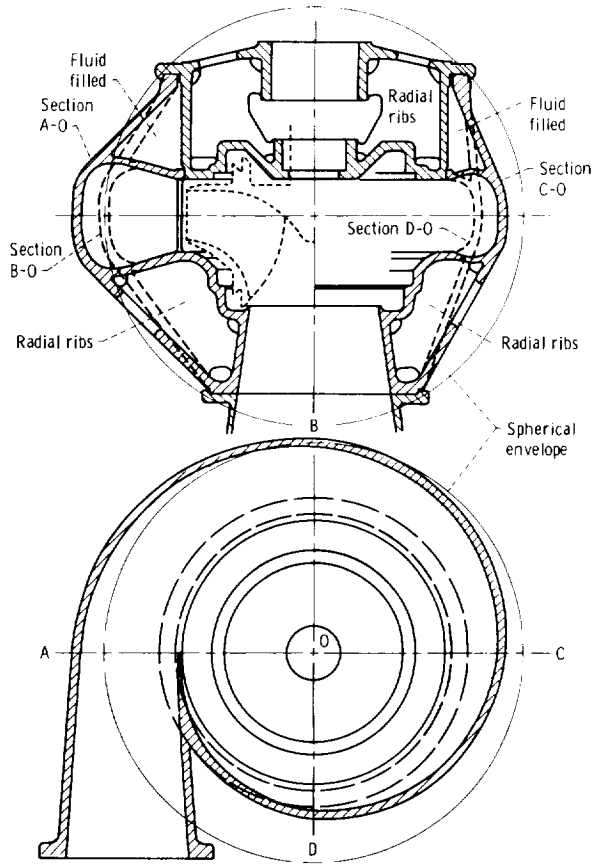

Figure 5-16. – Single-volute casing reinforced against internal pressure by form of casing and cover.

Figure 5-16 shows how this design conforms to, and departs from, a spherical envelope. While the departures are appreciable, the approximation of a spherical shape is unmistakable. Note that the regions outside the active flow passages which are filled with fluid are not expected to transmit shear forces. In contrast, the regions where there are radial ribs do transmit significant shear forces and are connected to the outside pressure. This is further explored later in this section.

Also note that the upper and lower parts of the casing shown in the upper drawing in figure 5-16 represent two somewhat different design principles within the same general design philosophy. It would have been equally possible to use bolted flanges on both sides of the casing; however, one removable cover is sufficient to meet the requirements of assembly.

The design principles illustrated in figures 5-16 and figures 5-17 are, of course, also applicable to twin and multiple volutes, with similar advantages of greater compactness and axial symmetry as for

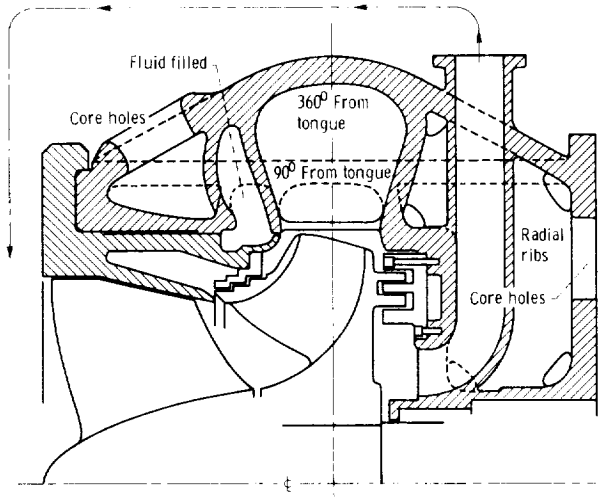

Figure 5-17. – Alternative form of volute casing reinforced against internal pressure by form of casing.

casings reinforced by external ribs (fig. 5-15). With the twin-volute design shown in figure 4-54, the external passage of the twin part of the casing should be placed outside the pressure carrying, quasi-spherical shell; that is, this shell should be the dividing wall between the inner volute and the outer passage and should extend axially (and quasi-spherically) toward the end covers or form part of one of these covers as shown in figure 5-16. Twin- and multiple-volute casings lead to very advantageous design forms in connection with the principle described in this section. The accompanying illustrations show the single-volute casing form merely because it constitutes the most difficult application of the design principles described here.

With some fluids, it is necessary to minimize the fluid volume inside the machine. In particular, stagnant fluid bodies are sometimes not acceptable. The fluid-filled regions outside the active flow passage must in such cases be eliminated or minimized. Figure 5-17 shows a design form applicable under this restriction. The fluid-filled space outside the volute is reduced to the minimum volume required to avoid a stress concentration at the tongue (or splitter) of the casing. The rest of the volume which is filled with fluid in figure 5-16 is occupied in figure 5-17 by a ring structure with varying radial cross sections, its inner volume being connected to the outside of the casing. The core holes in the outer shell must be minimized in circumferential extent and in number, because the outer shell carries the entire axial force resulting from the internal pressure.

The design principles discussed here are applied in the design shown in figure 5-17. It is a radial-flow pump combined with an axial-flow inducer and has a removable end cover on the inlet side of the pump, in contrast to the design shown in figure 5-16. None of these variations should interfere with a clean application of the design principles described.

The foregoing deliberations of this section are largely qualitative in nature. Yet to be added are some simple considerations that can be used to approximate the stresses generated in the force-carrying parts of the casing by a given internal gage pressure. It is even more desirable to obtain information regarding the structural form and wall thicknesses required to withstand the internal pressure.

The design forms described lead to two different kinds of considerations. First, in this approach, the pressure-carrying parts of the casing are shaped in such a manner as to approximate simple forms with known stress-pressure relations. The two forms considered are the circular cylinder and the sphere. For small wall thickness t, the stress-pressure relations are

$$\sigma = p\frac{r}{t} \tag{5-27}$$

for the circular cylinder and

$$\sigma = p\frac{r}{2t} \tag{5-28}$$

for the sphere. Even the thicknesses shown in figure 5-17 are small within the definition of this term as applicable to the approximate calculations used in preliminary design.

Obviously no design can achieve the stress-pressure relation of a thin-walled sphere (eq. (5-28)). Even the relation for circular cylinders (eq. (5-27)) may be too optimistic for casings designed according to the previously described principles. Yet equation (5-27) may offer a usable first approximation, if the radius r is interpreted to apply to the maximum casing radius.

Second, both end covers shown in figure 5-16 and the right end cover in figure 5-17 are essentially flat structures normal to the axis of rotation and extending significantly in the axial as well as the radial direction. This type of structure is called here

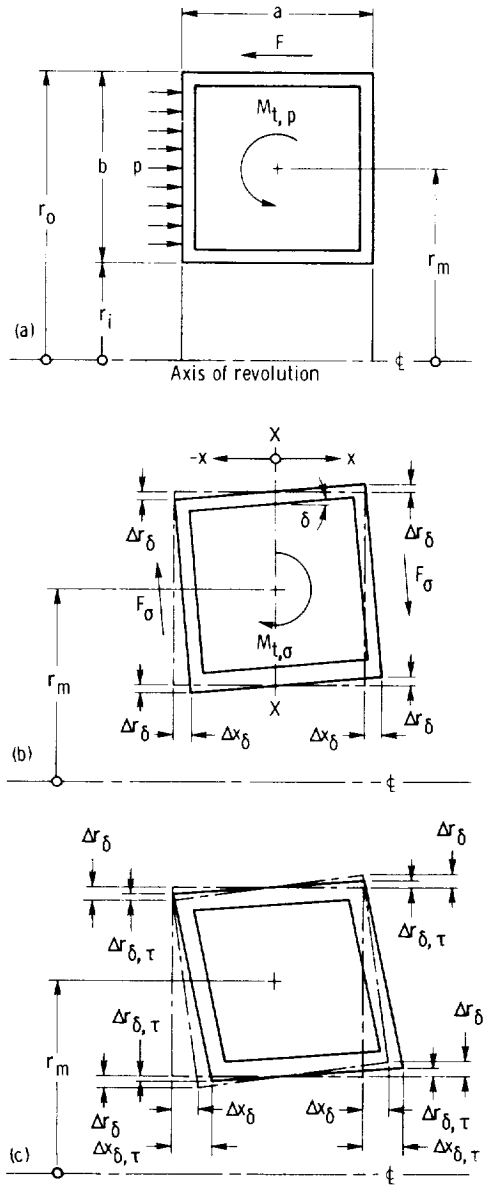

(a) Undeformed girder.
(b) Rotation.
(c) Rotation plus shear.
Figure 5-18.—Deformations of ring girder under axial forces with toroidal moment.

a ring girder (see fig. 5-18). The principal forces acting on this structure in the applications considered here are axial; they are the internal pressure p acting on one face of the ring girder and the opposing holding force F acting along the outer periphery of the ring girder (see fig. 5-18(a)). These forces form a ring-shaped couple, which is called here a toroidal moment $M_{t,p}$ in figure 5-18(a).

The most obvious effect of this toroidal moment is a rotation of all radial sections through the ring girder by an angle δ, as shown in figure 5-18(b). This rotation causes an expansion $\Delta r_\delta = \delta(a/2)$ of one side of the ring girder and a corresponding radial compression on the other side, which generate circumferential tensile and compressive stresses and corresponding radial forces F_σ with a toroidal moment $M_{t,\sigma}$ oppositely equal to the moment $M_{t,p}$ of the external force acting on the ring girder.

In addition to the rotation, the external forces and the circumferential stresses cause a shear deformation of the ring girder, as shown in figure 5-18(c). The shear deformation increases the axial deformation Δx and reduces the radial deformation Δr and thus the toroidal moment opposing the axial forces; that is, the shear deformation reduces considerably the elastic resistance of a ring girder to the axial forces considered here.

Shear deformations of a ring girder can be reduced substantially by radial, plane ribs. Such ribs are shown in figures 5-16 and 5-17 in the regions subject to shear forces and deformations. With such ribs, it is possible for a first approximation to consider shear deformations negligible, that is, to calculate the stresses in a ring girder on the basis of a pure rotation of its radial sections, as shown in figure 5-18(b).

The ring stresses σ generated by the rotation of the radial sections can be approximated by assuming that Δr_δ is a function of x only, not of r:

$$\sigma = E\frac{\Delta r_\delta(x)}{r} = E\frac{x\delta}{r} \tag{5-29}$$

where x is the axial distance from the neutral axis XX, which is a plane normal to the axis of rotation.

The toroidal moment $M_{t,\sigma}$ of the ring stresses is

$$M_{t,\sigma} = \int_A \sigma x\, dA = E\delta\int_A \frac{x^2}{r}\, dA \tag{5-30}$$

where A is the cross-sectional area of the ring girder, and the angle of rotation δ is assumed to be constant. The toroidal moment $M_{t,\sigma}$ is (obviously) oppositely equal to the moment of the applied forces $M_{t,p}$.

The last integral in equation (5-30) is not commonly encountered in strength of materials, but can be evaluated numerically for any cross section of the ring girder if one determines the location of the neutral axis XX by the condition that

$$\int \frac{x^2}{r} dA \tag{5-31}$$

has the same absolute value to the right and to the left of the neutral axis. If one assumes first that the neutral axis runs through the center of gravity of the cross section, one obtains a better approximation of the location of the neutral axis by plotting $(x^2/r)dA$ as a function of x and r and dividing this volume into two equal parts by a plane $x = \text{constant}$.

After the integral (5-31) has been determined in this manner, one can solve equation (5-30) for the (small) angle of rotation δ (in radians), subsequently solve equation (5-29) for the ring stress as a function of x and r, and then obtain the maximum stress by inspection.

As in other instances discussed previously, the foregoing solution is not directly applicable to the solution of the design problem, that is, the determination of the ring cross section (area and form) from the allowable stress and the applied forces. To accomplish this, we introduce a radial mean value of the ring stress

$$\sigma_m = \sigma \frac{r}{r_m} \tag{5-32}$$

where r_m is a mean radius, as shown in figure 5-18. With this mean stress, equation (5-29) can be written in the form

$$\sigma_m = E \frac{\Delta r_\delta(x)}{r_m} = \frac{E}{r_m} x\delta \tag{5-33}$$

and equation (5-30) in the form

$$M_{t,\sigma} = \int_A \sigma_m(x)\, x\, dA = \frac{E\delta}{r_m} \int_A x^2\, dA \tag{5-34}$$

where the last integral is the familiar moment of inertia of the cross-sectional area A with respect to the neutral axis XX, which can now be assumed to run through the center of gravity of the cross section.

An allowable maximum value of mean stress σ_m can be derived by equation (5-32) from the maximum allowable actual stress σ_{max} by the relation

$$\sigma_{m,max} = \sigma_{max} \frac{r_i}{r_m} \tag{5-35}$$

where r_i must be measured near x_{max}.

From equation (5-33), one finds

$$\frac{E\delta}{r_m} = \frac{\sigma_{m,max}}{x_{max}} \tag{5-36}$$

and, by substitution of this value, equation (5-34) can be solved for the required moment of inertia of the cross-sectional area A with respect to the axis XX. As mentioned previously, the toroidal moment $M_{t,\sigma}$ is oppositely equal to the toroidal moment $M_{t,p}$ of the applied forces. The moment of inertia permits the design of the cross-sectional area A under the geometric constraints of this section of the casing, as should be clear from figures 5-16 and 5-17.

The casing extension and cover at the left side in figure 5-17 can in principle be treated in the same manner as described previously. The ring girder at the left side comprises the axial extension of the volute together with the bolted-on insert or end cover. The difference between this ring girder and that shown at the right side is mainly that the latter has a very much smaller, minimum radius r_i and thereby a smaller radius ratio r_i/r_m. Consequently, according to equation (5-35), for the same σ_{max}, one obtains a lower allowable maximum mean stress $\sigma_{m,max}$ for the right side of this structure than for the left.

This reasoning, while correct regarding stresses, is misleading regarding deformations, which, for the same maximum stress, might be greater for the left side than for the right. If this relation is not acceptable, one would select a somewhat lower maximum stress σ_{max} (in eq.(5-35)) for the design of the left side than for the right.

These stress determinations constitute a practical limit of preliminary design considerations. After the establishment of a general design form, a deformation analysis can be carried out, and, if desirable, the design can be corrected mainly by changes in the wall thicknesses rather than by changes in the overall design.

It is evident from figures 5-16 and 5-17 that the radial sections through the ring girders forming the end covers are not uniform in the circumferential direction, particularly where the end cover forms an integral part of the casing (lower part of the casing shown in the upper drawing in fig. 5-16 and right cover in fig. 5-17). In general, one should select the radial section adjacent to the largest volute section for design considerations and possibly use reduced wall thicknesses adjacent to the smaller volute sections. If this is done, the design procedures outlined in this section must be carried out for at least two different radial sections through the casing, for example, the largest and the smallest sections shown in figures 5-16 and 5-17.

5.3.4. Volute Casings Reinforced Against Internal Pressure by Internal Vanes

As mentioned previously, the oldest method of reinforcing volute casings against high internal pressures is probably the use of internal guide vanes of sufficient cross section to carry the axial load imposed by the internal pressures. This method is used almost exclusively in the field of hydraulic turbines.

In pumps, however, contrary to early expectations, volute casings without a multiplicity of internal guide vanes give higher efficiencies and usually a smoother head-capacity curve than volute casings with internal guide vanes. Therefore external reinforcements against the internal pressure have been developed and used in the pump field only. Nevertheless internal guide vanes can be an important means of reinforcing pump volute casings against high internal pressures provided such vane systems are designed hydrodynamically as well as mechanically more effectively than was done in some earlier cases. While the hydrodynamic design of diffuser vane systems is outlined in section 4.5.1, their mechanical design still requires some careful consideration.

As in sections 5.3.2 and 5.3.3, the considerations presented in this section are limited to cases where the meridional flow entering and passing through the vane diffuser into the volute is radial. The diffuser vanes are formed by generalized cylindrical surfaces with their generating lines parallel to the axis of rotation of the machine. Under these conditions and under the assumption that the impeller inlet pressure is approximately the ambient pressure, a section through the diffuser vane system normal to the axis of rotation carries in

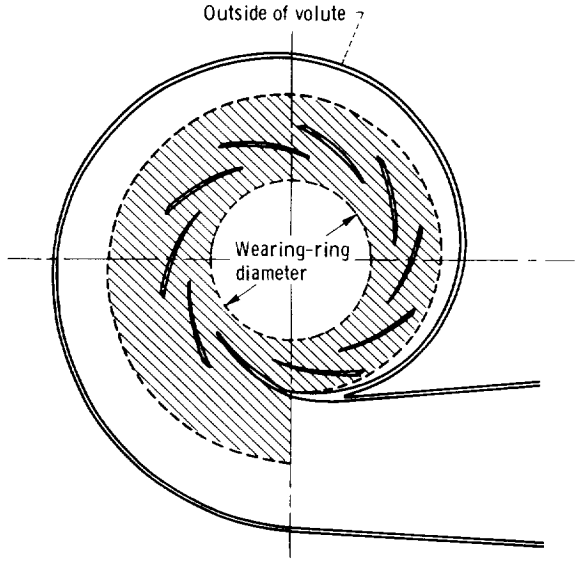

Figure 5-19. – Axial pressure load on vane system inside volute casing.

tension the internal pressure load from a radius halfway between the outside of the volute and the vane system to some minimum radius determined by the pressure-breakdown devices around the impeller. Figure 5-19 shows the pressure area concerned here including, of course, the load on the end covers.

The diffuser vanes carry nearly the entire axial pressure force (unless the casing is reinforced against the internal pressure by some other means). Thus the design of the diffuser vane system is subjected to a mechanical requirement in addition to the hydrodynamic requirements described in chapter 4 (sec. 4.5.1).

Let us assume that the diffuser vane sections derived by hydrodynamic considerations only are not sufficient to carry the axial pressure force. This may well be true for the vane systems shown in figures 4-49 and 4-50. Then the vane design must be changed to increase the vane thickness. The left side of figure 5-20 shows such a modification of the diffuser vane system presented in figure 4-50. An increase in vane thickness increases the blockage and, thereby, the meridional velocity component within the vane system. Therefore the vertical distance between the zero-blockage curve AB and the uppermost curve in the velocity diagram in figure 4-50 must be increased. This increase is shown in figure 5-20; it results in an increased steepness in the midsections of the vanes. For the same ratio of outside to inside radius of the system, vane length is reduced. The same ratio of vane

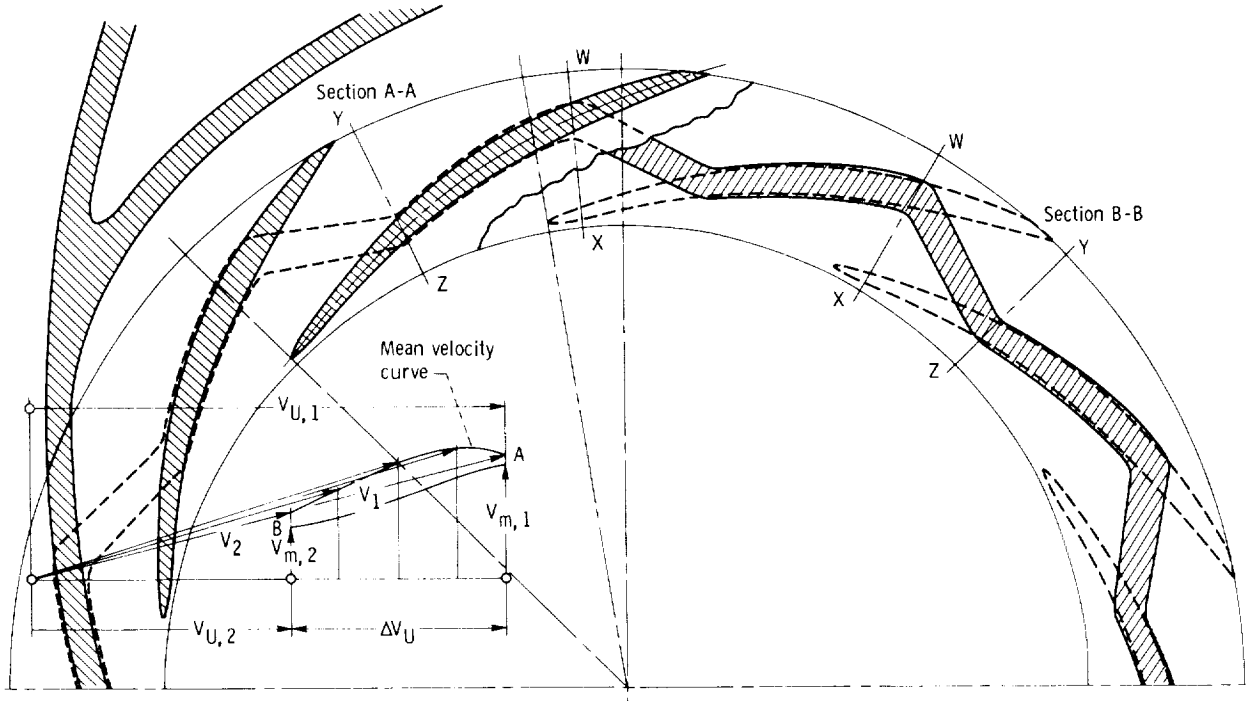

Figure 5-20. – Diffuser vanes and supports to carry internal casing pressure. Number of vanes, 10. (For locations of sections A-A and B-B and for sections W-X and Y-Z, see figs. 5-21 and 5-22.)

length to spacing is maintained by reducing the circumferential vane spacing proportionately and increasing the number of vanes in inverse proportion. In the present case, the number of vanes is increased from 9 in figure 4–50 to 10 in figure 5–20.

It is difficult or impossible to predict the maximum diffuser vane thickness-length ratio that is achievable in the manner just indicated. The thickness-length ratio shown in figure 5–20 is probably not a maximum, but it may not be possible to increase this ratio a great deal further before the efficiency of the pump would suffer significantly. In any event, this writer does not believe that bolts can be passed axially through diffuser vanes at high internal pressures without substantial, and probably intolerable, sacrifices in efficiency. However, just the use of the diffuser vanes as force-transmitting members causes considerable mechanical difficulty, chiefly because of the danger of stress concentrations at the thin vane ends. Figures 5–20 and 5–21 show a solution of this problem which avoids this danger. This solution is based on the principle that if the force-transmitting elements to the right and left of the diffuser passage do not extend to the vane ends, these ends necessarily have a lower stress than the

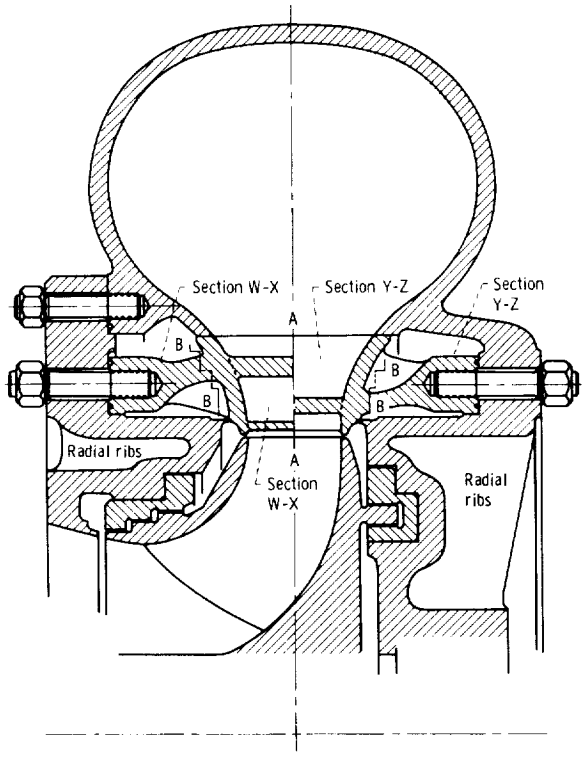

Figure 5-21. – Single-volute casing reinforced against internal pressure by diffuser vanes. (For locations of sections W-X and Y-Z and for sections A-A and B-B, see fig. 5-20.)

central portion of the vane (see sec. B-B at the right in fig. 5-20). Figure 5-21 shows that section B-B is gradually tapered into the circular flanges on both sides of the vane diffuser which transmit the axial vane forces to the casing and the end cover. Figures 5-19 and 5-21 indicate that the axial pressure forces applied radially inside and radially outside these diffuser flanges are approximately equal, so that the toroidal bending moment at the connection between the diffuser structure and the end cover or casing is not excessive and is carried jointly by the connected parts.

The question arises of whether the vane diffuser shown in figures 5-20 and 5-21 could be cast integrally with the volute casing. The answer is affirmative; such a casting is shown in figure 5-22. From the point of view of stress design, the only disadvantage of the integral construction is the fact that only the inner, not the outer, vane ends are stress relieved. It is difficult to say how serious the stress concentration at the outer vane ends would be. This stress concentration could be reduced by small external ribs (shown in fig. 5-22) located near the radial sections W-X, which would transmit the volute force toward the central parts of the diffuser vanes.

From a practical point of view, the separate diffuser shown in figure 5-21 has distinct advantages. It permits the use of different materials for the diffuser and the volute casing and greatly simplifies the foundry and cleaning problems encountered with the integral construction. In fact, modern methods would permit machining the separate diffuser out of a solid ring.

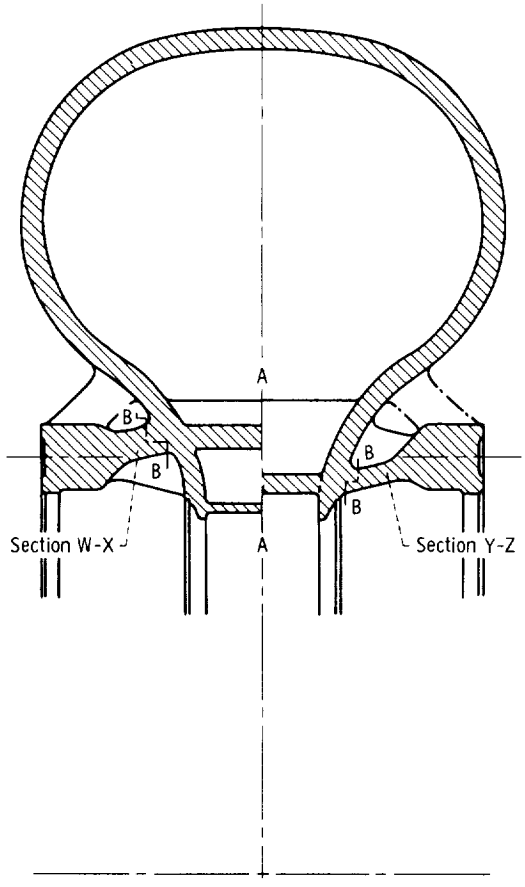

Figure 5-22. – Single-volute casing cast integrally with vane diffuser. (For sections A-A and B-B and for locations of sections W-X and Y-Z, see fig. 5-20.)

It should be recognized that the radial dimensions of a volute casing with a vane diffuser are very much larger than those of a volute casing without a vane diffuser for the same flow rate and head. This is due not only to the geometric effect of the diffuser, which increases the inside diameter of the volute, but also to the fact that the discharge velocity of the vane diffuser is much lower than the discharge velocity of the impeller (for the same head). One can estimate that, for the same capacity, head, and specific speed, the flow sections of a volute with a vane diffuser are about twice as large as those of a volute without a vane diffuser. The latter requires, therefore, as a rule, considerable diffusion after the flow has left the volute.

5.3.5 Concluding Remarks

It is not certain that the following remarks apply exclusively to the casings of turbomachinery. However, reference is made primarily to the preceding sections 5.3.2, 5.3.3, and 5.3.4 on casing design.

Regarding the arrangement of forces, the reinforcement of a volute casing by internal guide vanes is the most direct solution of this problem. Figure 5-19 shows that the diffuser vanes are located in a favorable position within the area whose pressure is being carried by these vanes, so that the vanes are loaded practically in pure tension. All that needs to be done is to transmit this tension to the end covers and the inner parts of the volute in a manner avoiding excessive loading of the relatively thin vane ends. Since the outer wall of the volute is also loaded in practically pure tension, all parts carrying the pressure force can be quite uniformly loaded where these parts pass through the central plane of the casing.

In contrast to this favorable situation, the stress distribution in the central plane of a volute casing reinforced by external radial ribs (fig. 5-9) is quite nonuniform. Since the ribs and the joining parts of the casing are loaded in bending in addition to tension, the outer parts of the ribs are in compression. The inner parts of the ribs and the casing wall must, therefore, carry in tension the pressure load plus the compressive force of the ribs. Hence the total cross-sectional area required to carry this load must be substantially greater than in a casing reinforced by internal vanes, because the distribution of the tensile stresses in a ribbed casing is quite uneven (figs. 5-11 to 5-14). However, this judgment is only relative, since under similar conditions all areas are proportional to one another, and, as stated previously, the areas of a volute with diffuser vanes are much larger than those of a volute without diffuser vanes. Nevertheless the force transmission can be regarded as much more efficient in a casing with internal vanes than in a casing reinforced entirely by external ribs.

Finally, for volute casings reinforced against the internal pressure by the shape of the casing, one has two different situations to consider: The outer shell of the volute casing is obviously in very nearly pure tension, as should be obvious from the central section normal to the axis of rotation, shown in the lower drawing in figure 5-16. With respect to pressure resistance, this situation is analogous to the high efficiency of a spherical casing. On the other hand, the end covers shown in figures 5-16 and 5-17 do not follow the spherical principle, but resist the internal pressure as ring girders. A ring girder resists axial forces by forming a toroidal moment from tensile and compressive ring stresses as described in section 5.3.3. It is somewhat dubious how direct this form of resistance to internal pressures can be considered.

Thus the three forms of casing design considered can be regarded as follows with respect to the directness of the force transmission:

(1) Volute with internal force-carrying guide vanes: very direct, but the casing size and, therefore, the pressure forces are relatively large; indirect in the flat end covers.

(2) Volute reinforced by external radial ribs: roundabout, mainly by bending stresses; indirect in the flat end covers.

(3) Volute reinforced by the form of the casing: very direct in the outer casing shell; indirect in the flat end covers.

It would be advantageous if the three casing design forms could be characterized by a common design principle. Professor Leyer of the Technical University in Stuttgart, Germany, attempted to do something along this line by introducing the concept of force flux into mechanical design. Unfortunately he did not define this potentially valuable concept with a reasonable degree of scientific rigor. As a consequence, the concept was at times strongly attacked by scientifically oriented engineers who justly contended that such a concept must be defined to have any useful meaning.

On the basis of the examples given here, one is tempted to define directness of force flux through a mechanical structure by the relative absence of bending in the structure, or by the uniformity of stress distribution in the force-transmitting members of the structure.

Whenever the cross-sectional dimensions of a structural element are substantial compared with its overall dimensions, experienced design engineers draw lines into the structure to represent something like a flux of forces in the material. Usually such lines resemble streamlines of a potential fluid motion. As such, these flux lines are more closely spaced at the inside than at the outside of a curved structural member. If this is meant to indicate increased local stresses (a stress concentration) near a concave boundary of a structural member, this intuitive representation has a qualitative value for the design engineer and might be associated with the concept of a force flux in the material. Yet this intuitive representation of stresses in a structural member should not be accepted and used without some critical considerations.

The stress distribution in a solid is not a vector field like the flow of a frictionless fluid; it is a tensor field, and, therefore, its representation by force lines is inherently incorrect. However, if the force lines are defined to be parallel to the so-called principal directions which are free from shear stresses then, under plane, two-dimensional stress conditions, an orthogonal system of lines has a definable meaning. If the boundaries of the solid have no shear stresses (as usual), so that the boundary has one of the principal directions, and if the principal stress parallel to the boundary dominates (as usual), the force lines drawn parallel to the boundaries have a useful meaning, at least close to the free boundary. When drawn like streamlines, these lines indicate correctly a local stress increase at a concave boundary, but the magnitude of this stress increase is greater than the

corresponding velocity increase in a potential flow field. For example, the stress at a circular hole in an infinite flat plate in one-dimensional tension is three times the uniform stress at infinity, whereas the corresponding fluid velocity increases only by a factor of 2 (see ref. 71, which is generally very valuable).

An example of stress design in this sense is the axial connection between the diffuser vanes and the force transmitting circular flanges, shown in figures 5-20 to 5-22. The maximum departure from the axial direction is 15° in sections W-X and Y-Z.

Thus it is possible to use the concept of force flux also for local design detail by drawing the force flux lines like streamlines, even though the actual stress increases are greater than indicated by this picture. The previously mentioned criterion of directness of force flux indicated by uniformity of stress distribution and absence of bending moments applies locally as well as to the force-carrying structure as a whole.

While the foregoing considerations are only qualitative, it is hoped that they will aid in establishing design forms that are favorable with respect to stress during the process of preliminary design. It is obvious that the foregoing considerations regarding stress concentrations are useful approximations (for preliminary design) only as long as the stresses are not expected to exceed (substantially) the yield stress of the material.

5.4 Hydrostatic Balancing of Axial Forces Acting on Turbomachinery Rotors

With single-suction hydrodynamic rotors, there is generally an unbalanced axial force because the axial hydrodynamic force acting on the inlet side is lower than that on the corresponding area on the opposite side.

For axial-flow machines, the axial thrust of the rotating vane system is the frontal discharge area times the static discharge pressure of the system, minus the frontal inlet area times the static inlet pressure, plus the difference in axial momentum of the flow leaving and entering the system. To be added is the static pressure difference across the rotor times the hub (and shroud) areas exposed to the inlet and discharge static pressures. For the axial-flow shrouded rotor vane system shown in figure 5-23, this can be expressed as

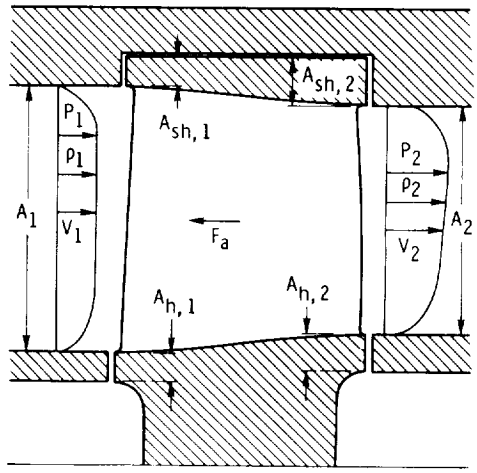

Figure 5-23. – Meridional view of thrust balance on axial-flow rotor vane system.

$$F_a = p_2 A_2 - p_1 A_1 + \rho_2 V_2^2 A_2$$

$$- \rho_1 V_1^2 A_1 + p_2 (A_{h,2} + A_{sh,2}) - p_1 (A_{h,1} + A_{sh,1})$$

where F_a is the resulting thrust, p and V are radially averaged pressure and axial fluid velocity, respectively, A is annular area as defined in figure 5-23, the subscripts 1 and 2 denote the inlet and discharge respectively, of the vane system, and the subscripts h and sh denote hub and shroud, respectively. The foregoing equation obviously does not include the axial forces acting on the rotor inside the hub ring of the vane system.

The right side of figure 1-39 shows the balancing of the thrust of a multistage axial-flow rotor by means of a balance drum at the discharge end of the rotor. The drum diameter is calculated by the equation just given from the static pressure in the space behind (to the right of) the drum. The pressure in this space is slightly higher than the inlet static pressure, because this space is connected to the inlet passage of the pump. In the case shown in figure 1-39, the balance drum has a diameter about halfway between the hub and tip diameters, which reflects the assumption that about one-half of the total pressure rise takes place in the rotor vane system and one-half in the stator vane system (symmetrical stages). This may not always be the case.

Since all static pressures involved are not known exactly, the thrust balance achievable by the foregoing considerations can be only approximate. The unbalanced part of the thrust must be taken up by a thrust bearing.

C-5

The thrust on single-suction, radial-flow rotors is usually balanced by a ring-shaped pressure-breakdown device (wearing ring) on the outside of the back shroud as shown, for example, at the left side in figure 1-39 and in figures 5-17 and 5-21. As a first approximation, one would give the back wearing ring the same diameter as the suction-side wearing ring. As shown empirically, for optimum thrust balance, the back wearing ring should have a slightly larger diameter than the suction side wearing ring, because the average static pressure between the rotating shrouds and the casing covers is slightly lower on the suction side than on the back side. This difference can be attributed to the fact that, on the suction side, the flow in this space probably has a radially (outward) decreasing angular momentum and, thereby, an instability which should increase the disk friction.

The space inside the back wearing ring must, of course, be connected to the suction side of the impeller, either by an external passage (or passages), as shown in figure 5-17, or by axial holes through the hub of the impeller. (See fig. 5-24, where this method of venting is applied to a different form of pressure breakdown, described in the next paragraph.)

Instead of a back wearing ring, one can use radial ribs or vanes on the outside of the back shroud in order to reduce the pressure near the center of the space outside the back shroud. If it is assumed that the fluid in this space rotates like a solid body with the impeller, the radial static head drop from the outside to the inside of such a vane system can be expressed as

$$\Delta h = \frac{U_o^2 - U_i^2}{2g_o} \tag{5-37}$$

where subscript o refers to the outside of the vane system (except in $g_o = 32.2$ ft/sec^2), and the subscript i to the inside. This static head change is actually somewhat less than given by equation 5-37, since the assumption of solid-body rotation is not exactly satisfied. Yet the static head change in this so-called pumpout vane system is approximately equal to that in the impeller, so that this method of balancing the axial thrust of radial-flow impellers is justified, particularly for open impellers, that is, impellers without a shroud on the suction side (see, e.g., fig. 4-20). Nevertheless the method of balancing the axial thrust by means of pumpout vanes is probably less accurate than when using a back wearing ring. Furthermore the pressure behind the back shroud may well depend on the axial clearance between the pumpout vanes and the casing wall, and this relation is mechanically unstable if closing this clearance reduces the pressure behind the shroud (and vice versa). Finally pumpout vanes should probably not be used in connection with diffuser pumps where the diffuser side walls should be lined up with the inside shroud walls of the impeller (see fig. 5-21), so that the pumpout vanes would have to operate in an essentially closed space and would be in danger of overheating.

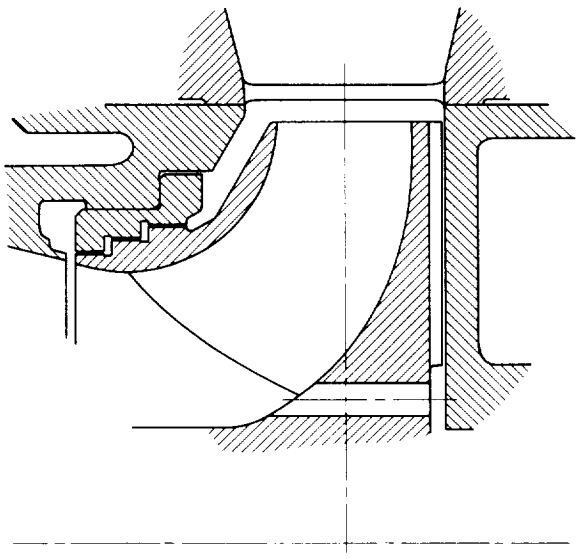

Figure 5-24. – Axial thrust balancing by external vanes on back shroud of impeller.

Throttling devices for pressure breakdown (see figures 1-39 and 5-21) can be made self-balancing if the clearance in at least one of several throttle

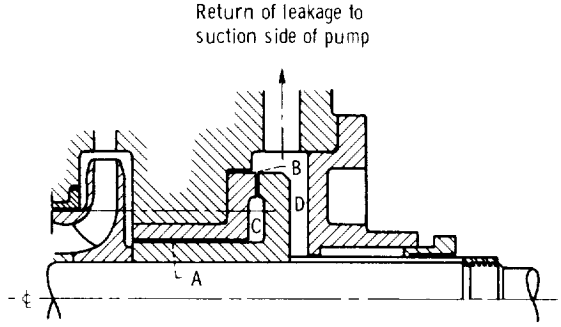

Figure 5-25. – Balance disk and drum.

surfaces changes appropriately as a function of the axial position of the rotor.

Figure 5-25 shows the principal and oldest form of such a self-balancing device, the combination of one throttle surface A having constant clearance with a plane throttle surface B having variable clearance. If the pump rotor moves to the left, the clearance at B is reduced, and the pressure in the space C builds up to a higher value, so that it automatically counteracts the initial movement. The opposite movement produces the same counteracting effect by lowering the pressure in the space C. With this type of a balancing device, the thrust of the impeller(s) is balanced exactly, and a thrust bearing is not required. In the United States, a thrust bearing is usually used with this type of balancing device partly as a safety measure and partly to take care of unsteady operating conditions (e.g., starting conditions, which can be quite complex). Originally no thrust bearings were used in Europe in connection with self-balancing devices.

The particular arrangement shown in figure 5-25 has been used extensively in connection with multistage radial-flow pumps. However, other arrangements are certainly possible, for example, the cylindrical throttle surface after the balance disk or the disk placed between two cylindrical throttle surfaces. The principle of the functioning of this type of balancing device would not be changed by such modifications of arrangement.

There is a more substantial change in arrangement of liquid rocket pumps that has been used successfully since the sixties. It is shown in figure 5-26 in connection with a multistage axial-flow pump such as shown at the right in figure 1-39; it changes the high-pressure end and the thrust balancing device of the axial-flow pump shown in that figure. If there is a small motion to the left (fig. 5-26), the clearance at A decreases while the clearance at B increases; thus there is a decrease in pressure in the space C, and the initial axial movement is counteracted. A motion in the opposite direction causes an increase in pressure in the space C and again the initial motion is counteracted.

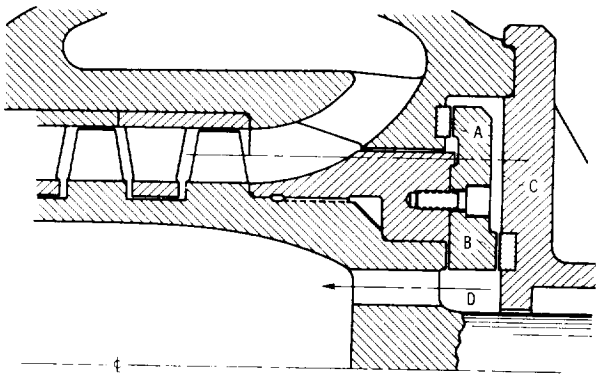

Figure 5-26. – Double-facing balance disk.

The axial force reaction with the arrangement shown in figure 5-26 should be greater than for the arrangement shown in figure 5-25, the upstream motion closing the upstream opening at A also opens the downstream opening at B. This sequence causes a very rapid decrease in pressure in the space C and, thus, strongly counteracts the initial motion.

In figure 5-26, the return of the leakage flow is shown through the inside of the rotor, although this return of the flow could be accomplished by an external passage, as indicated in figure 5-25 (see also fig. 5-17).

Furthermore the connection of the double-faced balance disk shown in figure 5-26 with a multistage axial-flow pump has a purely historic basis, since it represents the first applications of this balancing device in the rocket pump field. There is no reason why the double-faced balance disk could not be applied as well to single-stage or multistage radial-flow pumps. For single-stage radial-flow pumps, the back shroud of the impeller could form a double-faced balance disk extending radially somewhat beyond the outside diameter of the impeller. Of course, this design would involve some increase in disk friction losses.

Generally, at least the outer balance disk face operates with very small axial clearance, because the outside diameter of the disk must be minimized in order to avoid unnecessary disk friction losses. (Note that disk friction torque increases with the fourth power of the disk diameter.) Occasional contact between the stationary and rotating disk faces is, therefore, difficult to avoid. Consequently a great deal of attention must be paid to the selection of the material for the mating disk faces, indicated in figure 5-26 by double crosshatching of the stationary face material. However, any detailed consideration of this problem falls outside the scope of this compendium.

The same problem leads to the modification of the disk shape illustrated in figure 5-27 for the disk arrangement shown in figure 5-25; this modification has been used with gratifying success.

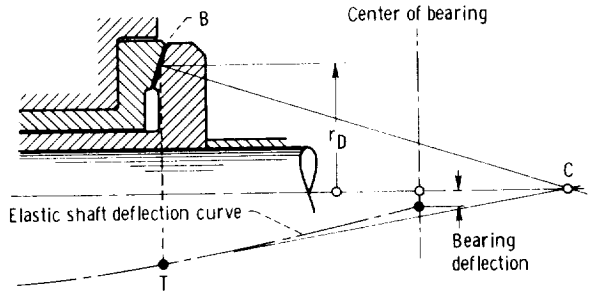

Figure 5-27. – Effect of rotor deflection on balance disk design.

In general, the stationary and rotating disk faces do not remain parallel to each other when the centerline of the rotor is deflected, as shown at an enlarged scale in figure 5-27. Since the deflection may not be constant, the only way to avoid the resulting difference in disk clearance between diametrically opposing sides is to give the disk faces approximately spherical shape, concentric to point C (fig. 5-27), where a tangent to the deflection curve of the rotor intersects the straight axis of rotation. In view of the small amount of actual deflection, the spherical disk surface can be approximated by a straight conical surface in order to simplify the problem of machining. Even if the curve of elastic deflection of the rotor cannot be determined with great accuracy, an approximation of it constitutes a marked improvement over plane disk surfaces normal to the axis of rotation.

While to the best knowledge of this writer the foregoing modification of balance disk design has been used successfully only in connection with the disk-drum combination shown in figure 5-25, there is no reason why this modification cannot be used to good advantage in connection with the double-faced disk design shown in figure 5-26. Of course, the angles of the two conical disk surfaces would not be the same, but they would differ in proportion to the mean radius r_D of each surface (see fig. 5-27).

There is also the possibility of substantially reducing the hydrostatic axial thrust on single-suction rotors by a special arrangement of successive stages of multistage pumps.

For a two-stage pump, the principle of this method of thrust reduction is illustrated in figure 5-28. This so-called back-to-back arrangement reduces the end thrust without any special balancing

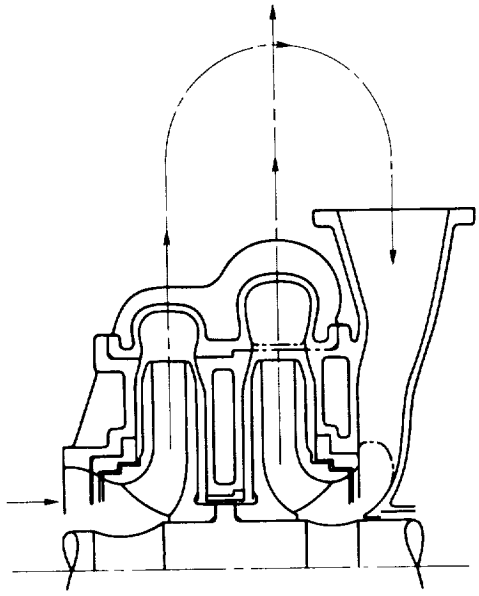

Figure 5-28. – Back-to-back two-stage radial-flow pump.

device to a fraction of the unbalanced thrust of one impeller, depending on the relative diameter of the pressure-breakdown device between the two stages. If this diameter is equal to the wearing ring diameter, the unbalanced thrust is equal to that of one impeller (i.e., one-half of the total thrust), whereas the unbalanced thrust approaches zero as the area inside the pressure-breakdown device becomes negligibly small compared with the area inside the wearing ring surfaces.

The crossover passage between the two stages may be designed similarly to that shown in figure 4-59 and described in connection with that figure.

The same principle of thrust balancing is applicable to multistage pumps, as shown in figure 5-29. In this case, the diameter of the pressure-breakdown device between the two central stages is equal to the wearing ring diameter; this arrangement is mechanically advantageous in order to

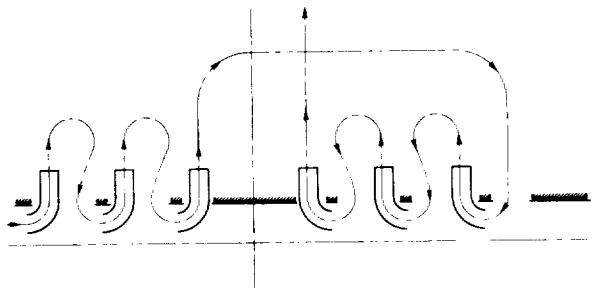

Figure 5-29. – Back-to-back multistage radial-flow pump.

obtain increased shaft stiffness. The unbalanced end thrust of the entire pump is, therefore, equal to the unbalanced thrust of three stages (i.e., to one-half of that of the entire pump), unless one introduces a pressure-breakdown device on the right end of the pump (as shown) with a diameter equal to the wearing ring diameter. This device balances the pump completely within the limited accuracy of cylindrical pressure-breakdown and balancing devices. In any event, it is desirable to have a pressure-breakdown device at that end of the pump, since otherwise the stuffing box or shaft seal would be subjected to one-half of the total pump pressure.

The application of the same balancing principle to multistage axial-flow pumps is illustrated in figure 5-30. In this case, the balancing of the thrust on the relatively large hub (of the higher stages) requires a pressure-breakdown device, as shown at the right end of the pump.

The residual thrusts of the pumps shown in figures 5-28 to 5-30 can, of course, be balanced completely by means of the self-compensating balancing devices shown in figures 5-25 to 5-27, except that, with the back-to-back arrangements discussed here, such devices would operate only under one-half of the total pump pressure, and there would be a corresponding reduction in leakage losses. Whether this advantage is sufficient to justify the complications of the back-to-back arrangement is questionable and must be decided primarily on the basis of reliability considerations. This may be the reason why the arrangement shown in figure 5-30 has, to the knowledge of this writer, not yet been used, whereas the design forms shown in figures 5-28 and 5-29 are frequently employed, particularly in the commercial pump field.

It should be evident that the foregoing discussion of axial forces acting on rotors of turbomachines does not begin to cover all possible configurations of such forces, nor the various design forms which have been used, or should be considered, to minimize or eliminate these forces. At best section 5.4 presents a few solutions in this class of design problems and perhaps can be expected to stimulate further developments in this and related fields.

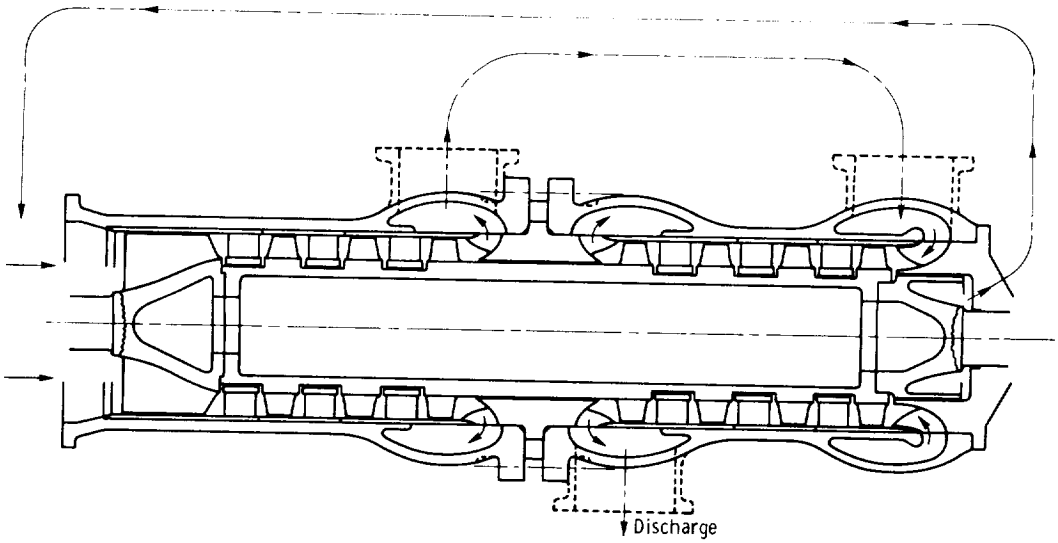

Figure 5-30. – Multistage axial-flow pump with axially opposed rotors.

References

1. Prandtl, Ludwig; and Tietjens, O. G.: Applied Hydro and Aeromechanics. McGraw-Hill Book Co., Inc., 1934.
2. Stodola, Aurel (Dr. Louis C. Lowenstein, transl.): Steam and Gas Turbines, with a Supplement on the Prospects of the Thermal Prime Mover. Vols. I and II. McGraw-Hill Book Co., Inc., 1927. Reprinted by Peter Smith, New York, 1945.
3. Lawaczeck, F.: Turbinen und Pumpen, Theorie und Praxis. Julius Springer, 1932.
4. Busemann, A.: Verdichtungsstösse in ebenen Gasströmungen (Compression Shocks in Two-Dimensional Gas Flows). In Gilles, A.; Hopf, L.; and von Karman, Theodor: Vorträge aus dem Gebiete der Aerodynamik und Verwandter Gebiete (Aachen, 1929), Springer (Berlin), 1930, pp. 162-169.
5. Prandtl, Ludwig; and Busemann, Adolph: Näherungsverfahren zur zeichnerischen Ermittlung von ebenen Strömungen mit Überschallgeschwindigkeit (Approximate Graphical Methods for Determining Two-Dimensional Supersonic Flows). In Stodola, A.: Festschrift, Orell Füssli Verlag (Zürich & Leipzig), 1929, pp. 499-509.
6. Bullock, R. O.; and Johnsen, I. A., eds.: Aerodynamic Design of Axial-Flow Compressors. NASA SP-36, 1965.
7. Thoma, D.: Neuere Anschauungen über Hydrodynamik der Wasserturbinen (New Viewpoints about Hydrodynamics of Water Turbines). In von Karman, T.; and Levi-Civita, T.: Vorträge aus dem Gebiete der Hydro und Aerodynamic, Julius Springer (Berlin), 1924, p. 240.
8. Weinig, Fritz: Die Stroemung um die Schaufeln von Turbomaschinen. Johann Ambrosius Barth (Leipzig), 1935. Also translation by NACA: Flow Past the Blades of Turbomachines, 1944.
9. Betz, A.; and Petersohn, E.: Anwendung der Theorie der freien Strahlen (Application of the Theory of Free Jets). Ing.-Arch., vol. 2, 1931, pp. 190-211.
10. Ackeret, J.: Zum Entwurf dichtstehender Schaufelgitter (On the Layout of Close-Spaced Vane Cascades). Schweiz. Bauz., vol. 120, no. 9, Aug. 29, 1942, pp. 103-108.
11. Savage, Melvyn: Analysis of Aerodynamic Blade-Loading-Limit Parameters for NACA 65-($C_{10}A_{10}$)10 Compressor-Blade Sections at Low Speeds. NACA RM L54L02a, 1955.
12. Lieblein, Seymour; Schwenk, Francis C.; and Broderick, Robert L.: Diffusion Factor for Estimating Losses and Limiting Blade Loadings in Axial-Flow Compressor Blade Elements. NACA RM E53D01, 1953.
13. Lieblein, Seymour; Analysis of Experimental Low-Speed Loss and Stall Characteristics of Two-Dimensional Compressor Blade Cascades. NACA RM E57A28, 1957.
14. Wislicenus, George Friedrich: Fluid Mechanics of Turbomachinery. Second ed. Dover Publications, 1965.
15. Howell, A. R.: Fluid Dynamics of Axial Compressors. Development of British Gas Turbine Jet Units, Inst. Mech. Eng. (London), 1947, pp. 441-452.
16. Emery, J. C.; Herrig, L. J.; Erwin, J. R.; and Felix, A. R.: Systematic Two-Dimensional Cascade Tests of NACA 65-Series Compressor Blades at Low Speeds. NACA Rep. 1368, 1958.
17. Dunavant, James C.: and Erwin, John R.: Investigation of a Related Series of Turbine-Blade Profiles in Cascade. NACA TN 3802, 1956.
18. Erwin, John R.; Savage, Melvyn; and Emery, James C.: Two-Dimensional Low Speed Cascade Investigation of NACA Compressor Blade Sections Having a Systematic Variation in Mean-Line Loading. NACA TN 3817, 1956.
19. Westphal, Willard R.; and Godwin, William R.: Comparison of NACA 65-Series Compressor-Blade Pressure Distributions and Performance in a Rotor and in Cascade. NACA TN 3806, 1957.
20. Schulze, Wallace M.; Erwin, John R.; and Ashby, George C., Jr.: NACA 65-Series Compressor Rotor Performance with Varying Annulus-Area Ratio, Solidity, Blade Angle, and Reynolds Number and Comparison with Cascade Results. NACA TN 4130, 1957.
21. Pfleiderer, C.: Die Kreiselpumpen (Centrifugal Pumps). Julius Springer (Berlin), 1924. (Revised second ed., 1932.)
22. Prandtl, Ludwig: Essentials of Fluid Dynamics. Translation of Führer durch die Stromungslehere. Third ed., Hafner Publishing Co., 1952.
23. Smith, L. H., Jr.: Secondary Flow in Axial-Flow Turbomachinery. Trans. ASME, vol. 77, Oct. 1955, pp. 1065-1076.
24. Weske, J. R.: Investigation of Blade Characteristics. Trans. ASME, vol. 66, no. 5, July 1944, pp. 413-420.
25. Hawthorne, W. R.: Secondary Circulation in Fluid Flow. Proc. of Roy. Soc. (London), Series A, vol. 206, no. 1086, May 7, 1951, pp. 374-387.
26. Kucharski, Walther: Strömungen einer Reibungsfreien Flüssigkeit Bei Rotation Fester Körper: Beiträge zur Turbinentheorie (Flow of a Friction-Free Fluid During Rotation of Solid Bodies: Contributions to Turbine Theory). R. Oldenbourg (München), 1918.
27. Spannhake, W.: Konforme Abbildung (Conformal Mapping). In Hydraulische Probleme (Hydraulic Problems). V.D.I. Verlag (Berlin), 1926.
28. König, E.: Potentialströmung durch Gitter (Potential Flow Through Cascades). Z. Angew. Math. Mech., vol. 2, no. 6, 1922, pp. 422-429.
29. Sörenson, E.: Potentialströmung durch rotierende Kreiselräder (Potential Flow Through Rotating Turbomachines). Z. Angew. Math. Mech., vol. 7, no. 2, Apr. 1927, pp. 89-106.
30. Busemann, A.: Das Förderhöhenverhältnis radialer Kreisel pumpen mit logarithmisch-spiralignen Schaufeln (The Head Ratio of Radial, Centrifugal Pumps with Logarithmic Spiral Vanes). Z. Angew. Math. Mech., vol. 8, no. 5, Oct. 1928, pp. 372-384.
31. Johnston, James P.: The Effects of Rotation on the Boundary Layers in Turbomachine Rotors. Fluid Mechanics, Acoustics, and Design of Turbomachinery, Part 1, NASA SP-304, 1970, pp. 207-242.
32. Smith, Leroy H., Jr.: Three-Dimensional Flow in Axial Flow Turbomachinery. Doctoral Dissertation, Johns Hopkins Univ., 1954.

33. Smith, L. H., Jr.; Traugott, S. C.; and Wislicenus, G. F.: A Practical Solution of a Three-Dimensional Flow Problem of Axial-Flow Turbomachinery. Trans. ASME, vol. 75, July 1953, pp. 789-803.

34. Batchelor, George Keith: An Introduction to Fluid Mechanics. Cambridge Univ. Press (London), 1967, sec. 5.3.

35. Wattendorf, Frank L.: The Ideal Performance of Curved-Lattice Fans. The Von Karman Anniversary Volume, Calif. Inst. Tech., 1941, pp. 285-292.

36. O'Brien, M. P.; and Folsom, R. G.: The Design of Propeller Pumps and Fans. Univ. Calif., Berkeley, Publ. Eng., vol. 4, no. 1, 1939, pp. 1-18.

37. Smith, L. H., Jr.: Secondary Flow in Axial-Flow Turbomachinery. Trans. ASME, vol. 77, Oct. 1955, pp. 1065-1076.

38. Lorenz, H.: Neue Theorie und Berechnung der Kreiselräder (New Theorie and Calculation of Turbomachines). R. Oldenbourg (Munich and Berlin), 1906.

39. Bauersfeld, W.: Die Konstruction der Francis-Schaufeln nach der Lorenzschen Turbinentheorie (The Layout of Francis Vanes According to the Lorenz Turbine Theory). Z. Ver. Deut. Ing., vol. 56, 1912, pp. 2045-2051.

40. Hamrick, Joseph T.; Ginsburg, Ambrose; Osborn, Walter M.: Method of Analysis for Compressible Flow Through Mixed-Flow Centrifugal Impellers of Arbitrary Design. NASA TN 2165, 1950.

41. Holl, J. W.: The Effect of Surface Irregularities on Incipient Cavitation. Ph. D. Thesis, Pennsylvania State Univ., 1958.

42. Gelder, Thomas F.; Ruggeri, Robert S.; and Moore, Royce D.: Cavitation Similarity Considerations Based on Measured Pressure and Temperature Depressions in Cavitated Regions of Freon 114. NASA TN D-3509, 1966.

43. Ruggeri, Robert S.: Experimental Studies on the Thermodynamic Effects of Developed Cavitation. Fluid Mechanics, Acoustics, and Design of Turbomachinery, Part 1, NASA SP-304, 1970, pp. 377-401.

44. Plesset, Milton S.: The Tensile Strength of Liquids. Cavitation State of Knowledge, J. M. Robertson and G. F. Wislicenus, eds., ASME, 1969, pp. 15-25.

45. Plesset, Milton S.: Physical Effects in Cavitating Flows. Fluid Mechanics, Acoustics, and Design of Turbomachinery, Part I, NASA SP-304, 1974, pp. 341-354.

46. Knapp, Robert T.; Daily, James W.; and Hammitt, Frederick G.: Cavitation. McGraw-Hill Book Co., Inc., 1970.

47. Ripken, J. F.; and Killen, J. M.: Gas Bubbles: Their Occurrence, Measurement, and Influence in Cavitation Testing. Cavitation and Hydraulic Machinery, F. Numachi, ed., Inst. High Speed Mechanics (Japan), 1963, pp. 37-54.

48. Gilmore, Forrest R.; and Plesset, Milton S.: Scaling Laws for Incipient Cavitation Noise. Rep. 26-1, Calif. Inst. Tech., 1950.

49. Stahl, H. A.; and Stepanoff, A. J.: Thermodynamic Aspects of Cavitation in Centrifugal Pumps. Trans. ASME, vol. 78, Nov. 1956, pp. 1691-1963.

50. Billet, Michael L: Thermodynamic Effects on Developed Cavitation in Water and Freon 113. M. S. Thesis, Pennsylvania State Univ., 1970.

51. Holl, J. William; and Wislicenus, George F.: Scale Effects on Cavitation. J. Basic Eng., vol. 83, Sept. 1961, pp. 385-400.

52. Hollander, A.: Thermodynamic Aspects of Cavitation in Centrifugal Pumps. J. Am. Roc. Soc., vol. 32, no. 10, Oct. 1962, pp. 1594-1595.

53. Ruggeri, Robert S.; and Moore, Royce D.: Method for Prediction of Pump Cavitation Performance for Various Liquids, Liquid Temperatures, and Rotative Speeds. NASA TN D-5292, 1969.

54. Horlock, J. H.: Axial Flow Compressors; Fluid Mechanics and Thermodynamics. Butterworth (London), 1958.

55. Liquid Rocket Engine Axial-Flow Turbopumps. NASA Space Vehicle Design Criteria. NASA SP-8125, April 1978.

56. Wattendorf, Frank L.: A Study of the Effect of Curvature on Fully Developed Turbulent Flow. Proc. Roy. Soc. (London), Series A, vol. 148, no. 865, Feb. 15, 1935, pp. 565-598.

57. Eskinazi, Salamon; and Yeh, Hsuan: An Investigation on Fully Developed Turbulent Flows in a Curved Channel. J. Aeronaut. Sci., vol. 23, no. 1, Jan. 1956, pp. 23-34.

58. Baumeister, Theodore, ed.: Mark's Standard Handbook for Mechanical Engineers. Seventh ed. McGraw-Hill Book Co., Inc., 1967.

59. Jakobsen, Jakob K.: NASA Space Vehicle Design Criteria for Liquid Rocket Engine Turbopump Inducers. NASA SP-8052, 1971.

60. Stripling, L. B.; and Acosta, A. J.: Cavitation in Turbo Pumps—Part 1. J. Basic Eng., vol. 84, Sep. 1962, pp. 326-338.

61. Stripling L. B.: Cavitation in Turbo Pumps—Part 2. J. Basic Eng., vol. 84, Sep. 1962, pp. 339-350.

62. Lakshminarayana, B.: Visualization Study of Flow in Axial Flow Inducer. J. Basic Eng., vol. 94, Dec. 1972, pp. 777-787.

63. Lakshminarayana, B.: Experimental and Analytical Investigation of Flow Distribution in Rocket Pump Inducers. Fluid Mechanics, Acoustics, and Design of Turbomachinery, Part 2, NASA SP-304, 1970, pp. 689-731.

64. Gorton, C. A.; and Lakshminarayana, B.: Analytical and Experimental Study of Mean Flow and Turbulence Characteristics Inside the Passages of an Axial Flow Inducer. (PSU-AERSP-74-2, Pennsylvania State Univ., NASA Contract NGL-39-009-007.) NASA CR-134682, 1974.

65. Prasil, Franz: Technische Hydrodynamik (Technical Hydromechanics). Second ed., Julius Springer (Berlin), 1926, p. 287.

66. Prasil, Franz: Zur Geometrie der Konformen Abbildungen von Schaufelrissen (On the Geometry of Conformal Mapping of Vane Contours). Schweiz. Bauztg., Bd. 52, Heft 7, Aug. 15, 1908, pp. 85-88; Bd. 52, Heft 8, Aug. 22, 1908, pp. 102-105.

67. Timoshenko, Stephen; and Goodier, J. N.: Theory of Elasticity. Second ed. McGraw-Hill Book Co., Inc., 1951, ch. 3, sec. 30.

68. Robinson, Ernest L.: Bursting Tests on Steam Turbine Disk

Wheels. Trans. ASME, vol. 66, no. 5, July 1944, pp. 373-386.

69. Föppl, August: Vorlesungen über technische Mechanik (Lectures on Technical Mechanics). Vol. III, Festigkeitslehre (Strength of Materials). Tenth ed. Teubner (Leipzig and Berlin), 1927, pp. 240-244.

70. Timoshenko, Stephen: Strength of Materials: Advanced Theory and Problems. Part II. Third ed. Van Nostrand, 1956.

71. Peterson, Rudolph Earl: Stress Concentration Design Factors, Charts and Relations Useful in Making Strength Calculations for Machine Parts and Structural Elements. John Wiley & Sons, Inc., New York, 1974.

1. Report No.	2. Government Accession No.	3. Recipient's Catalog No.
NASA RP-1170		

4. Title and Subtitle	5. Report Date
Preliminary Design of Turbopumps and Related Machinery	October 1986
	6. Performing Organization Code
7. Author(s)	8. Performing Organization Report No.
George F. Wislicenus	E-7389
	10. Work Unit No.
	535-05-01
9. Performing Organization Name and Address	11. Contract or Grant No.
George F. Wislicenus 351 Golf Court (Oakmont) Santa Rosa, California 95405	NAS3-13475
	13. Type of Report and Period Covered
	Reference Publication
12. Sponsoring Agency Name and Address	14. Sponsoring Agency Code
National Aeronautics and Space Administration Lewis Research Center Cleveland, Ohio 44135	

15. Supplementary Notes

16. Abstract

This compendium pertains primarily to the pumps used in large liquid-fuel rocket engines. The term "preliminary design" denotes the initial, creative phases of design, where the general shape and characteristics of the machine are being determined. The compendium is intended to provide the design engineer responsible for these initial phases with a physical understanding and background knowledge of the numerous special fields involved in the design process. Primary attention is directed to the pumping part of the turbopump and hence is concerned with essentially incompressible fluids. However, compressible flow principles are developed. As much as possible, the simplicity and reliability of incompressible flow considerations are retained by treating the mechanics of compressible fluids as a departure from the theory of incompressible fluids. The discussion is presented in five chapters: (1) a survey of the field of turbomachinery in dimensionless form, (2) the theoretical principles of the hydrodynamic design of turbomachinery, (3) the hydrodynamic and gas-dynamic design of axial-flow turbomachinery, (4) the hydrodynamic and gas-dynamic design of radial- and mixed-flow turbomachinery, and (5) some mechanical design considerations of turbomachinery. Theoretical considerations are presented with a relatively elementary mathematical treatment so that the reader is not required to have advanced mathematical methods at his command.

17. Key Words (Suggested by Author(s))	18. Distribution Statement
Design; Turbomachinery; Turbopumps; Axial flow; Radial flow; Incompressible; Compressible	Unclassified – unlimited STAR Category 02

19. Security Classif. (of this report)	20. Security Classif. (of this page)	21. No of pages	22. Price*
Unclassified	Unclassified	395	A17

*For sale by the National Technical Information Service, Springfield, Virginia 22161

NASA-Langley, 1986